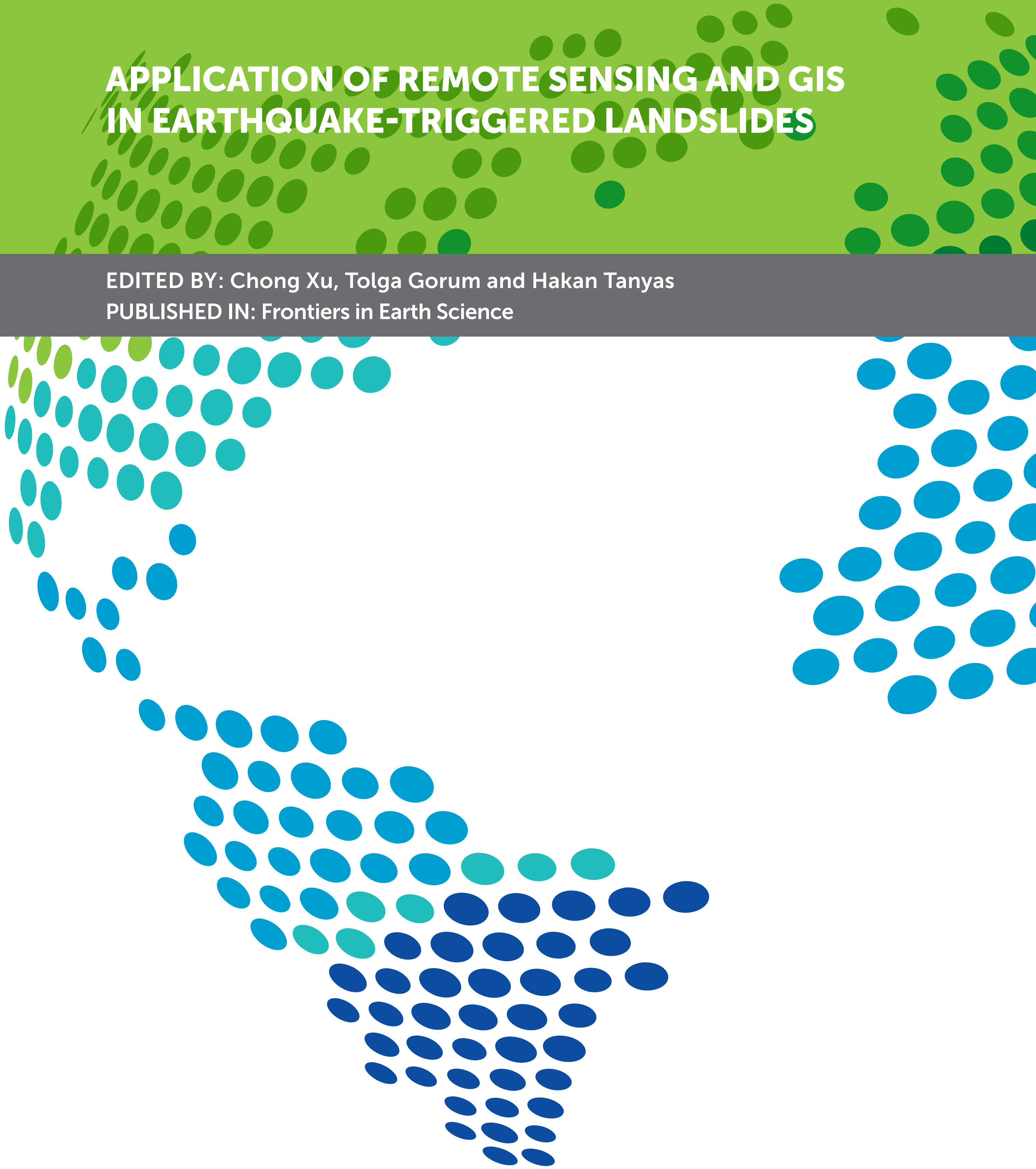

APPLICATION OF REMOTE SENSING AND GIS IN EARTHQUAKE-TRIGGERED LANDSLIDES

EDITED BY: Chong Xu, Tolga Gorum and Hakan Tanyas
PUBLISHED IN: Frontiers in Earth Science

frontiers Research Topics

ISSN 1664-8714
ISBN 978-2-88976-833-2
DOI 10.3389/978-2-88976-833-2

About Frontiers

Frontiers is more than just an open-access publisher of scholarly articles: it is a pioneering approach to the world of academia, radically improving the way scholarly research is managed. The grand vision of Frontiers is a world where all people have an equal opportunity to seek, share and generate knowledge. Frontiers provides immediate and permanent online open access to all its publications, but this alone is not enough to realize our grand goals.

Frontiers Journal Series

The Frontiers Journal Series is a multi-tier and interdisciplinary set of open-access, online journals, promising a paradigm shift from the current review, selection and dissemination processes in academic publishing. All Frontiers journals are driven by researchers for researchers; therefore, they constitute a service to the scholarly community. At the same time, the Frontiers Journal Series operates on a revolutionary invention, the tiered publishing system, initially addressing specific communities of scholars, and gradually climbing up to broader public understanding, thus serving the interests of the lay society, too.

Dedication to Quality

Each Frontiers article is a landmark of the highest quality, thanks to genuinely collaborative interactions between authors and review editors, who include some of the world's best academicians. Research must be certified by peers before entering a stream of knowledge that may eventually reach the public - and shape society; therefore, Frontiers only applies the most rigorous and unbiased reviews.
Frontiers revolutionizes research publishing by freely delivering the most outstanding research, evaluated with no bias from both the academic and social point of view. By applying the most advanced information technologies, Frontiers is catapulting scholarly publishing into a new generation.

What are Frontiers Research Topics?

Frontiers Research Topics are very popular trademarks of the Frontiers Journals Series: they are collections of at least ten articles, all centered on a particular subject. With their unique mix of varied contributions from Original Research to Review Articles, Frontiers Research Topics unify the most influential researchers, the latest key findings and historical advances in a hot research area! Find out more on how to host your own Frontiers Research Topic or contribute to one as an author by contacting the Frontiers Editorial Office: frontiersin.org/about/contact

APPLICATION OF REMOTE SENSING AND GIS IN EARTHQUAKE-TRIGGERED LANDSLIDES

Topic Editors:
Chong Xu, Ministry of Emergency Management (China), China
Tolga Gorum, Istanbul Technical University, Turkey
Hakan Tanyas, International Institute for Geo-Information Science and Earth Observation, Netherlands

Citation: Xu, C., Gorum, T., Tanyas, H., eds. (2022). Application of Remote Sensing and GIS in Earthquake-Triggered Landslides. Lausanne: Frontiers Media SA.
doi: 10.3389/978-2-88976-833-2

Table of Contents

frontiers | Frontiers in Earth Science

TYPE Editorial
PUBLISHED 22 July 2022
DOI 10.3389/feart.2022.964753

EDITED AND REVIEWED BY
Stefano Luigi Gariano,
Institute for Geo-Hydrological
Protection (IRPI), Italy

*CORRESPONDENCE
Chong Xu,
xc11111111@126.com

SPECIALTY SECTION
This article was submitted to
Geohazards and Georisks,
a section of the journal
Frontiers in Earth Science

RECEIVED 09 June 2022
ACCEPTED 30 June 2022
PUBLISHED 22 July 2022

CITATION
Xu C, Gorum T and Tanyas H (2022),
Editorial: Application of remote sensing
and GIS in earthquake-
triggered landslides.
Front. Earth Sci. 10:964753.
doi: 10.3389/feart.2022.964753

Editorial: Application of remote sensing and GIS in earthquake-triggered landslides

Chong Xu[1,2]*, Tolga Gorum[3] and Hakan Tanyas[4]

[1]National Institute of Natural Hazards, Ministry of Emergency Management of China, Beijing, China, [2]Key Laboratory of Compound and Chained Natural Hazards Dynamics, Ministry of Emergency Management, Beijing, China, [3]Eurasia Institute of Earth Sciences, Istanbul Technical University, Istanbul, Turkey, [4]Faculty of Geo-Information Science and Earth Observation (ITC), University of Twente, Enschede, Netherlands

KEYWORDS

remote sensing, GIS, landslide susceptibility, landslide evolution, landslide inventory map, landslide monitoring, landslide mechanism, earthquake-triggered landslides

Editorial on the Research Topic
Application of remote sensing and GIS in earthquake-triggered landslides

Introduction

Earthquakes have long been recognized as one of the main triggers for landslides across the Earth (Keefer 1984; Tian et al., 2022). The earthquakes we experienced in the last few decades (e.g., the 1994 Mw6.7 Northridge, United States, the 2008 Mw7.9 Wenchuan, China, the 2015 Mw7.8 Gorkha, Nepal, and the 2018 Mw6.6 Hokkaido, Japan, earthquakes) showed that moderate and large earthquakes in mountainous terrain, can produce clusters of several hundred to thousands of landslides in a very short period. In turn, the earthquake-triggered landslides threaten our society by their direct and indirect, long-term effects such as damaged infrastructure, increased debris flows and floods associated with landslide dam failures and downstream river aggradations. As a result, the investigations of earthquake-triggered landslides have received much attention in recent years, due to their probable results of the tragic loss of life and economic devastation. With the rapid development of GIS and remote sensing technologies, valuable progress has been made in the earthquake-triggered landslides research field. The ability and efficiency of extracting large-scale and massive earthquake-triggered landslide data have been greatly improved. The number and quality of earthquake-triggered landslide records are increasing. The susceptibility, hazard, and risk assessment models of earthquake-triggered landslides are becoming more advanced and precise, and the ability to process large-scale and high-precision data is more robust. Remote sensing and GIS technologies have greatly improved the ability of information acquisition and big data analysis of earthquake-triggered landslides. Furthermore, remote sensing and GIS technologies have significantly promoted the progress of identification, mapping, monitoring, early warning, and risk evaluation of earthquake-triggered landslides.

To present the latest achievements in this direction, we organized a Research Topic entitled *Application of remote sensing and GIS in earthquake-triggered landslides*. This Research Topic includes 13 papers covering regional earthquake-triggered landslide mapping and spatial distribution analysis, monitoring and analysis of large-scale individual landslides, landslide susceptibility and hazard assessment, landslide evolution, and changes in rainfall thresholds of debris flow in earthquake-affected areas, etc. Remote sensing and GIS technologies have played an important role in these studies.

Landslide inventory map and spatial distribution analysis

Landslide inventory maps are an essential basis for related research and have achieved rapid development in recent years (Harp et al., 2011; Xu 2015), mainly due to the capability to identify landslides based on high-resolution remote sensing images and to manage and analyze massive landslides based on GIS platform. In this Research Topic, there are three papers in this field. Martinez et al. made an inventory map including 43 coseismic classified landslides triggered by the 2018 Anchorage Mw7.1 earthquake in Alaska, United States, based on comprehensive methods such as field investigations, multi-spectral optical satellite images, LiDAR data, and SAR data. They compared the performance of these techniques, and the results show that the comparison of NDVI data derived from optical satellite images pre- and post-quake, and LiDAR data, are more suitable for identifying soil slumps and rapid soil flows. However, those landslides with small surface deformation can only be detected through field investigations. This study provides a reference for the selection of coseismic landslide mapping methods in subarctic and urban areas.

Building an inventory map of ancient landslides and establishing their connection with historical earthquakes are other relevant works. The old landslide distribution database is one of the critical issues. In this Research Topic, Peng et al. identified 6,876 large-scale active and old landslides in the Southwest of Ordos, China, based on the satellite images from the Google Earth platform. They analyzed the spatial distribution characteristics of these landslides and explored their relationship with a historical earthquake, the 780 BC Qishan earthquake. This work provides an interesting case study of the relationship between ancient landslides and historical earthquakes.

Although the remote sensing image-based visual interpretation method is currently the most crucial approach for establishing landslide inventory maps, the automatic extraction technology of landslides based on remote sensing images has also received extensive attention. In this Research Topic, Comert took the Mw6.7 earthquake in Hokkaido, Japan, on 6 September 2018, as an example and used the random forest method to carry out an experimental study on automatic identification of coseismic landslides and studied the influence of five different sizes of training samples on the results of automatic landslide identification. The datasets include pre- and post-quake differential images and only post-quake images. The results show that the latter had better performance, and the increase in the number of training samples will slightly improve the result accuracy. This work provides a reference for the preprocessing of data and the selection of sample size to automatically identify landslides based on remote sensing data.

GIS has dramatically promoted the spatial distribution analysis of massive landslides. Taking the Mw7.8 earthquake landslide in Gorkha, Nepal, 2015, as an example, Tian et al. analyzed the geometric characteristics of 2,059 landslides with an area larger than 10,000 m^2 based on a landslide inventory map obtained from the visual identification of pre- and post-quake optical satellite images (Xu et al., 2018). They separated these landslides into three types according to their geometry, and the relationships between these landslides and environmental factors are analyzed and compared, respectively. The results showed that landslides with different geometric shapes are more likely to occur in different environments, which provides a case study for further understanding the spatial distribution characteristics of earthquake-triggered landslides. Based on the data of nearly 200,000 coseismic landslides triggered by the 2008 Mw 7.9 Wenchuan, China earthquake (Xu et al., 2014), Liu X. et al. selected some typical watersheds and analyzed the area-frequency distribution relationship of coseismic landslides, and the obtained parameters reflect the landslide density and the proportion of large-scale landslides. They also carried out a hot spot analysis of landslides to evaluate the relationship between the obtained parameters and the spatial distribution of the landslide cluster. This work provides a case study to better understand the landslide area-frequency distribution law.

Monitoring and analysis of large-scale individual landslides

Remote sensing and GIS technology play an increasingly important role in large-scale individual landslide research. The occurrence of many large-scale landslides has a process of initial deformation, deformation acceleration, and failure. Remote sensing and GIS technologies are effective methods for detecting slope deformation. For example, the Baige landslide on the Jinsha River in China in 2018 had significant deformations up to tens of meters within a few years before the final sliding

(Cui et al., 2020). To analyze the creep process of the landslide, Guo et al. examined the vegetation changes on the landslide based on multi-temporal SPOT satellite data. The study showed that the landslide has been creeping about 50 m in the past few years, and the vegetation coverage on the back wall and the body of the landslide decreases significantly as it is closer to the final sliding, which revealed a strong correlation between vegetation change rate and landslide creeping. This work provides a case study for analyzing the deformation process of landslides based on multi-temporal optical remote sensing data. Hu et al. investigated the age of the residual deposits probable from a large landslide on the east bank of the Qiaojia reach of the Jinsha River based on UAV mapping technology and dating technology. They considered the landslide event might be related to an earthquake in AD 624, which provides a shred of evidence from the ancient landslide for subsequent seismic hazard analysis in this area. This work provides a case study for analyzing regional seismic hazards based on large individual landslides supported by remote sensing technology.

Monitoring the *in-situ* seismic response of rock slopes using seismological or geophysical methods can be considered an application of generalized remote sensing technology in the field of landslide monitoring. Based on this method, Huang et al. investigated the response of a high bedrock slope in the mountainous area of southwest China related to the 2019 Changning, China Mw5.7 earthquake. They used environmental noise interferometry to monitor the performance of the rocky slope during the earthquake and located a coseismic rock rupture at a depth of 75 m in the slope that recovered after 2 weeks. This work demonstrates the feasibility of using seismological techniques to analyze coseismic deep fissures in bedrock.

Landslide susceptibility and hazard assessments

Remote sensing and GIS technologies are essential for regional earthquake-triggered landslide susceptibility and hazard assessments. Remote sensing is important for preparing completed and detailed landslide inventory maps and producing environmental thematic maps. The combination of GIS and machine learning models is one of the main methods for this aspect. Machine learning methods and Newmark physical model are the two most common methods. In this Research Topic, we solicited one paper for each of these two methods. In machine learning methods, the selection of landslide samples is an important task. Chen et al. applied a one-class classifier method to generate landslide negative sample data, and performed a rapid earthquake-induced landslide susceptibility analysis in an area affected by the 2008 Wenchuan Mw7. 9 earthquake in China. This work provided a method reference for the production of landslide negative samples in landslide susceptibility and hazard assessments. The application of the Newmark model to regional seismic landslide hazard analysis has received much attention in recent decades, in which the thickness of landslide mass is an important, but difficult, to obtain parameter. Maharjan et al. obtained the median landslide thickness based on pre- and post-quake high-resolution DEMs for subsequent landslide hazard assessment. The results have good spatial consistency with the real distribution of coseismic landslides. It shows that it is feasible to obtain the pre- and post-quake DEMs based on remote sensing technology to obtain the thickness of the landslide mass and conduct a more objective and rapid earthquake-triggered landslide susceptibility and hazard mapping.

Landslide evolution

Massive landslides and strength reduction in hillslope materials related to large earthquakes will have serious secondary effects and severe secondary disasters are likely to occur under subsequent strong aftershocks and heavy rainfall (Fan et al., 2019). Therefore, it is of great significance to study the evolution of landslides in affected areas and the changes in landslide susceptibility after earthquakes. Tanyaş et al. prepared a sequence of multi-temporal landslide inventory maps in three tropics areas affected by major earthquakes. Based on the landslide inventory maps, they analyzed the landslide susceptibility levels pre- and post-quake and concluded that landslide susceptibility returned to pre-quake levels in less than a year. Since the study areas are only parts of the total earthquake-affected area, they are cautious that these observations may not represent the entire area affected by these earthquakes but only the phenomena in the study areas. Guo et al. conducted a study on landslide susceptibility changes in the 2017 Ms7.0 Jiuzhaigou, China earthquake based on machine learning, remote sensing, and GIS technologies. They produced a coseismic landslide inventory map and a post-event landslide inventory map 2 years after the earthquake and found that the total landslide area increased by 1.2 km^2. They compared and analyzed the relationship between the two landslide inventory maps and the influencing factors. The results show that the amplitude in susceptibility in high landslide susceptibility areas is smaller than that in low susceptibility areas. This indicates that the landslide susceptibility in the earthquake-affected area is not a constant state, and reminds us to pay attention to the change of the landslide susceptibility in earthquake-affected areas. Earthquakes have also an important impact on rainfall thresholds of debris flows. Liu S. et al. analyzed the changes in the pre- and post-quake rainfall thresholds for debris flows under the influence of different seismic intensities based on the debris flow records in the affected areas of the 2008 Ms8.0 Wenchuan, 2013 Ms7.0 Lushan and 2017 Ms7. 0 Jiuzhaigou earthquakes in China. The study shows that the post-quake rainfall threshold for debris flows is much lower than that of the pre-quake. In addition, they also considered the influence of earthquake magnitude and focal depth on the change of rainfall thresholds. This study provides support for more objective post-quake debris flow early warning.

Conclusions and prospects

In recent years, with the development of remote sensing, GIS, big data, artificial intelligence, and other high-tech, studies on landslides, especially earthquake-triggered landslides, have achieved rapid expansion, and relevant publications show a growing trend year by year (Huang et al., 2022). The 13 papers in this Research Topic involve multiple directions of remote sensing- and GIS-based seismic landslide research, including landslide inventory mapping, automatic extraction, spatial distribution, and evolution analysis, which have accumulated knowledge for the excellent development of this discipline. However, these studies also raised a few new questions for researchers. For example, in the aspect of automatic landslide extraction, although many advanced landslide extraction models based on remote sensing data have emerged in recent years, it is still a noteworthy direction to develop more scientific and reasonable models and further improve the accuracy. As for landslide inventory maps and their spatial distribution analysis, more high-quality earthquake-triggered landslide mapping is needed to reveal the more general temporal and spatial distribution law of earthquake-triggered landslides. The research on the relationship between ancient landslides and historical earthquakes has always been a concern of researchers (Jibson 1996), but most of the existing work is based on individual landslides or local areas. Remote sensing and GIS technology provide sufficient conditions for creating high-quality ancient landslide inventory maps in broad areas, even in the world. Of course, this great work requires the joint efforts of lots of researchers. As most large landslide that can be preserved for hundreds or even thousands of years, it will undoubtedly be a direction worthy of long-term development. Applying generalized remote sensing such as seismological and geophysical methods in large landslides or seismic slope response is a very meaningful attempt, and it is also a subject growth direction worthy of in-depth exploration.

The increased capacity in remote sensing, geographic information technologies, and computational power contribute to a more thorough understanding of geoenvironmental and earth surface processes. Natural disaster prevention, mitigation, and relief are the eternal subjects of human survival and development. We hope that this Research Topic can promote the development of earthquake-triggered landslide research and attract more researchers to pay more attention to the application of high-tech, such as remote sensing and GIS, in the field of earthquake-triggered landslides.

Author contributions

All authors contributed to the critical review of the papers published in this Research Topic. CX has provided an initial draft of this Editorial which was revised and approved by all the authors.

Funding

This study was supported by the National Institute of Natural Hazards, Ministry of Emergency Management of China (ZDJ2021-14).

Acknowledgments

We deeply thank all the authors for their submissions to this Research Topic and all the reviewers for their valuable comments and suggestions, the Frontiers Editorial Office, and especially Josie Langdon and Ursula Rabar, for their strong supports in all phases of the realization of this Research Topic.

Conflict of interest

The authors declare that the research was conducted in the absence of any commercial or financial relationships that could be construed as a potential conflict of interest.

Publisher's note

References

Cui, Y., Bao, P., Xu, C., Fu, G., Jiao, Q., Luo, Y., et al. (2020). A big landslide on the jinsha river, tibet, china: geometric characteristics, causes, and future stability. *Nat. Hazards.* 104 (3), 2051–2070. doi:10.1007/s11069-020-04261-9

Fan, X., Scaringi, G., Korup, O., West, A. J., van Westen, C. J., Tanyas, H., et al. (2019). Earthquake-induced chains of geologic hazards: Patterns, mechanisms and impacts. *Rev. Geophys.* 57 (2), 421–503. doi:10.1029/2018rg000626

Harp, E. L., Keefer, D. K., Sato, H. P., and Yagi, H. (2011). Landslide inventories: the essential part of seismic landslide hazard analyses. *Eng. Geol.* 122 (1-2), 9–21. doi:10.1016/j.enggeo.2010.06.013

Huang, Y., Xu, C., Zhang, X., and Li, L. (2022). Bibliometric analysis of landslide research based on the WOS database. *Nat. Hazards Res.*. doi:10.1016/j.nhres.2022.02.001

Jibson, R. W. (1996). Use of landslides for paleoseismic analysis. *Eng. Geol.* 43 (4), 291–323. doi:10.1016/S0013-7952(96)00039-7

Keefer, D. K. (1984). Landslides caused by earthquakes. *Geol. Soc. Am. Bull.* 95 (4), 406. doi:10.1130/0016-7606(1984)95<406:lcbe>2.0.co;2

Tian, Y., Xu, C., and Yuan, R. (2022). Earthquake-triggered landslides. *Treatise on geomorphology* 2, 583–614. doi:10.1016/B978-0-12-818234-5.00120-6

Xu, C. (2015). Preparation of earthquake-triggered landslide inventory maps using remote sensing and GIS technologies: Principles and case studies. *Geosci. Front.* 6 (6), 825–836. doi:10.1016/j.gsf.2014.03.004

Xu, C., Tian, Y., Shen, L. L., Xu, X., Zhou, B. G., Ma, S., et al. (2018). Database of landslides triggered by 2015 Gorkha (Nepal) Mw7.8 earthquake. *Seismol. Geol.* 40 (5), 1115–1128. doi:10.3969/j.issn.0253-4967.2018.05.011

Xu, C., Xu, X., Yao, X., and Dai, F. (2014). Three (nearly) complete inventories of landslides triggered by the May 12, 2008 Wenchuan Mw 7.9 earthquake of China and their spatial distribution statistical analysis. *Landslides* 11 (3), 441–461. doi:10.1007/s10346-013-0404-6

frontiers
in Earth Science

ORIGINAL RESEARCH
published: 18 September 2020
doi: 10.3389/feart.2020.572449

Geomorphometry and Statistical Analyses of Landslides Triggered by the 2015 M_w 7.8 Gorkha Earthquake and the M_w 7.3 Aftershock, Nepal

Yingying Tian[1], Lewis A. Owen[2], Chong Xu[1,3], Lingling Shen[4], Qing Zhou[1] and Paula Marques Figueiredo[2]*

[1] Key Laboratory of Active Tectonics and Volcano, Institute of Geology, China Earthquake Administration, Beijing, China, [2] Department of Marine, Earth, and Atmospheric Sciences, North Carolina State University, Raleigh, NC, United States, [3] National Institute of Natural Hazards, Ministry of Emergency Management of China, Beijing, China, [4] Beijing Meteorological Information Center, Beijing Meteorological Service, Beijing, China

The 2015 M_w 7.8 Gorkha earthquake in Nepal and the M_w 7.3 aftershock triggered at least 22,914 landslides that each had areas ≥500 m^2 and lengths and widths ≥20 m. Amongst these landslides, 2,059 had areas >10,000 m^2. Analyses of the landslide geometry, using length (L), width (W), height (H, from the crown to toe), reach angle (arctan value of H/L), and aspect ratio (L/W), show that most of the landslides have aspect ratios of 1.6–3.6 and reach angles of 35–45°. The fitting relationship between H and L is H = 0.87L − 11.11. The steep topography is likely the main factor that controls the landslide runout and planar shape. The landslides are divided into 3 geomorphometric categories using the aspect ratio: LS1 (L/W ≤ 2); LS2 (2 < L/W ≤ 4); and LS3 (L/W > 4). Statistical analyses of these categories with the control factors show that the landslide distribution does not relate to the three large-scale geologic faults that traverse the region, roads, accumulative precipitation before the earthquakes, and the small earthquakes that occurred during the 2012–2015 pre-monsoons in the study area. The 3 landslide categories are sensitive to similar conditions related to curvature, slope position, lithology, and peak ground acceleration. In contrast, the effects of elevation, slope angle, slope aspect, and streams on landslide distribution differ. Moreover, massive landslides (with areas >10,000 m^2) are more likely to occur on the steeper hill slopes that in the higher elevation settings, which provide more substantial gravitational potential energy and long-runout space. As landslides with different geomorphometric shapes have various susceptible conditions, examining the landslide distribution based on their geometric characteristics provides a new way to study the landslide extent and mechanism.

Keywords: 2015 Gorkha earthquake, landslides, Himalaya, geometry, planar geomorphometric shapes, spatial distribution

Edited by:
Juergen Pilz,
Alpen-Adria-Universität Klagenfurt,
Austria

Reviewed by:
Jian Chen,
China University of Geosciences,
China
Saumitra Mukherjee,
Jawaharlal Nehru University, India

****Correspondence:***
Chong Xu
xc11111111@126.com

Specialty section:
This article was submitted to Environmental Informatics and Remote Sensing, a section of the journal Frontiers in Earth Science

Received: *14 June 2020*
Accepted: *26 August 2020*
Published: *18 September 2020*

Citation:
Tian Y, Owen LA, Xu C, Shen L, Zhou Q and Figueiredo PM (2020) Geomorphometry and Statistical Analyses of Landslides Triggered by the 2015 M_w 7.8 Gorkha Earthquake and the M_w 7.3 Aftershock, Nepal. Front. Earth Sci. 8:572449. doi: 10.3389/feart.2020.572449

HIGHLIGHTS

(1) Geomorphometric parameters of landslides triggered by the 2015 Gorkha earthquakes are defined;

(2) Spatial distributions of the landslides of different planar shapes show their vulnerable factor conditions;
(3) Landslides with areas >10,000 m^2 are more likely to occur on the steeper hill slopes and in higher elevation settings;
(4) The terrain and streams are the major factors controlling the spatial distributions of landslides with various shapes and sizes.

INTRODUCTION

Geometric characteristics of earthquake-triggered landslides are associated with factors such as geomorphology, bedrock, soil, topography, vegetation, and seismic ground motion (Yang et al., 2006; Tian et al., 2017). Under strong ground shaking during an earthquake, hill slopes with larger slope angles, higher slope positions, and highly fractured rock masses can generate landslides with a more considerable fall height, smaller width, and larger length/travel distances (Nicoletti and Sorriso-Valvo, 1991). Since they run long distances, such landslides always have relatively greater mobility and likely lead to more significant hazards along their paths. Thus, the geomorphometric features of earthquake-triggered landslides have the potential to be used to study landslide mechanisms and hazard assessment (Hsü, 1975; Corominas et al., 2003; Xu et al., 2016a). Height (H), length (L), width (W), reach angle (arctan value of the height-length ratio, arctan [H/L]), and aspect ratio (length-width ratio, L/W) are primary parameters that can characterize the geometry of a landslide. Our method section below provides our full definitions of these descriptors. Among them, the reach angle and aspect ratio represent the relative mobility and 2-D morphology of landslides, respectively (Heim, 1932; Scheidegger, 1973; Corominas 1996; Xu et al., 2014; Xu and Xu, 2014; Tian et al., 2017; Roback et al., 2018; Tsou et al., 2018). As well, the aspect ratio has relationships with the landslide type (Parise and Jibson, 2000).

On April 25, 2015, an M_w 7.8 earthquake (28.230°N, 84.731°E, known as the Gorkha earthquake) with a focal depth of 8.2 km shook central Nepal, followed by an M_w 7.3 aftershock (27.809°N, 86.066°E) on May 12, 2015, that had a focal depth of 15 km. These earthquakes resulted in >8,800 fatalities and about US $7 billion in economic loss. Field surveys and synthetic aperture radar (SAR) analysis suggest that the earthquake-triggered landslides were the leading cause of the casualties, injuries, and financial damages in the affected area (Collins and Jibson, 2015; Moss et al., 2015; Yun et al., 2015). In all, the 2015 Gorkha earthquakes triggered >47,200 landslides (Xu et al., 2018). The Langtang landslide, in the Rasuwa region of Nepal, was the most colossal slope failure that was triggered by the Gorkha earthquake; it swept across the village of Langtang, resulting in >200 deaths (Collins and Jibson, 2015). Studies on these landslides include field investigations, interpretations of imagery, spatial distribution, and susceptibility assessment (Collins and Jibson, 2015; Kargel et al., 2016; Martha et al., 2016; Regmi et al., 2016; Xu et al., 2016b; Xu et al., 2017; Roback et al., 2018; Tsou et al., 2018), but there was little geomorphometry research. Tsou et al. (2018), e.g., presented a preliminary analysis on the planar geometry of the 912 seismic landslides in the Trishuli Valley, central Nepal following the Gorkha earthquake. In the study by Tsou et al. (2018), the landslide lengths range from 7 to 1,145 m, about 60% of which had aspect ratios (L/W) ≥ 5, and 90% ≥ 1.67. Roback et al. (2018) applied the L/H ratio to study the landslide mobility, showing that most of these landslides had L/H values close to 1 (the average L/H is 1.17). They found that the 38 most highly mobile landslides had L/H ratios >2 and runouts >200 m and mostly in an elevation range of 2,500–3,000 m above sea level (asl).

In this paper, we present an extensive study of the landslides to consider further the geomorphometric features of the landslides triggered by the 2015 Gorkha earthquake and to understand better the variety and nature of earthquake-triggered landslides in high mountain regions. Using the >47,200 landslides of Xu et al. (2018), we study landslides with areas >500 m^2 and lengths and widths longer than 20 m (totally 22,914 landslides) to make an exhaustive analysis of their geometry, including the H, L, W, H/L ratio and aspect ratio. According to their aspect ratios, they are classified into three categories to statistically study their spatial distribution patterns with control factors, including terrain, geology, seismicity, streams, roads, and rainfalls. Our analysis helps in understanding the movement mechanisms of seismic landslides with different geomorphometric characteristics and it is essential to assess geologic hazard in the affected area better, and for similar tectonically active mountain regions.

TECTONIC SETTING AND STUDY AREA

Since the collision with Eurasia plate in the Cenozoic, the Indian plate has continuously moved northward, resulting in the 2,500 km-long Himalayan orogen and creating one of the most tectonically active regions on Earth. Many great earthquakes have shaken the region during the last few centuries, including the 1833 M_w ~ 7.6 Kathmandu, 1905 M_w ~ 7.8 Kangra, 1934 M_w ~ 8.2 Nepal-Bihar, 1950 M_w 8.4 Assam-Tibet, and the 2005 M_w 7.6 Kashmir earthquakes (Berthet et al., 2014; Liu et al., 2015; Elliott et al., 2016; Owen 2017). From north to south, the orogen consists of the Tethyan Himalaya, High/Greater Himalaya, Lesser Himalaya, and sub-Himalaya which are bounded by South Tibetan Detachment System (STDS), Main Central Thrust (MCT), Main Boundary Thrust (MBT), and Main Frontal Thrust (MFT), respectively (Yin and Harrison, 2000; Moss et al., 2015). Amongst these continental-scale structures, the MCT, MBT, and Main Frontal Thrust are the three outcropping branch faults of the basal decollement zone, i.e., Main Himalaya Thrust (MHT), between the Indian and Eurasia continental lithospheric plates within the deep crust (Lavé and Avouac, 2000; Wobus et al., 2006; Liu et al., 2015). The April 25, 2015 M_w 7.8 mainshock and the May 12 M_w 7.3 aftershock were focused on the MHT that dips to the north at an angle of ~10° (**Figure 1B**). The mainshock rupture propagated eastwards for ~140 km and did not reach the topographic surface; there were no identified surface ruptures (Avouac et al., 2015; Hayes et al., 2015; Elliott et al., 2016; Gallen et al., 2017).

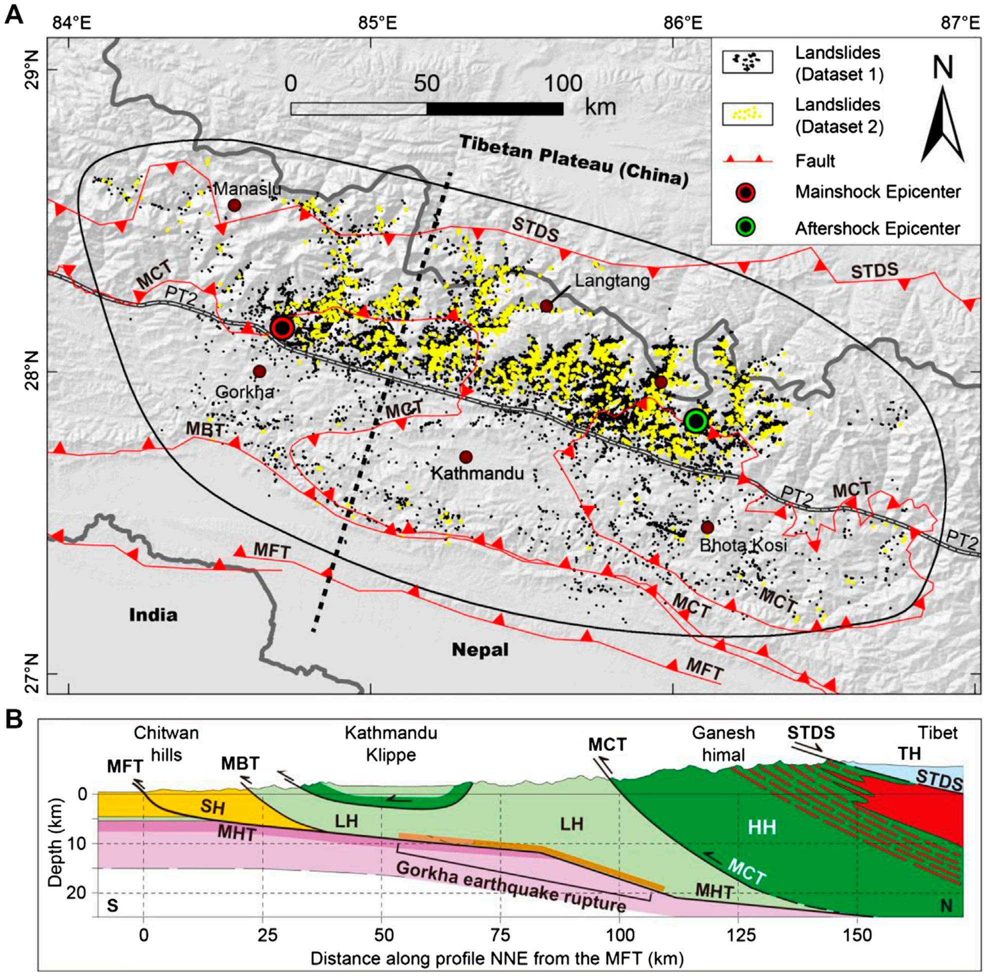

FIGURE 1 | (A) Digital elevation model that highlights the main tectonic structures that traverse the study area (outlined by the quasi-ellipse by the thin black line) and distribution of the 2015 earthquake-triggered landslides and the Gorkha earthquake and its Mw 7.3 aftershock. **(B)** Simplified cross-section across the Ganesh-Langtang Himalaya [from Elliott et al. (2016)], its approximate location is shown as a black dashed line in **(A)**. TH: Tethyan Himalaya, HH: High Himalaya; LH: Lesser Himalaya; SH: sub-Himalaya; STDS: South Tibetan Detachment System; MCT: Main Central Thrust; MBT: Main Boundary Thrust; PT2: Physiographic Transition [digitalized from Whipple et al. (2016)]. Dataset 1 (22,914 landslides that are >500 m^2 and have L and W both >20 m) and Dataset 2 (2,059 landslides, which are >10,000 m^2) are from Xu et al. (2018).

Our study area is a mountainous region with deep gorges in central and eastern Nepal and part of southern Tibet covering ~35,664 km^2 (**Figure 1A**). The transition between Lesser and Higher Himalaya is known as physiographic transition 2 (PT2), and it reflects an abrupt elevation change, which marks the significant northward increase in rock-uplift rate (Hodges et al., 2004; Whipple et al., 2016). The PT2 runs from west to east along an elevation profile of ~2,000 m asl across the study area (**Figure 1A**). The study area rises northwards from ~150 to 8,135 m asl with an average of 2,600 m asl. The areas with elevations exceeding 3,500 m account for 33% of the total study area. Hill slope angles range up to 87° (mainly concentrated in the regions higher than 6,000 m asl) with an average of 27°; 27% of the entire region has hill slopes >35°. The climate is tropical-subtropical monsoonal, with the rainy season from June to September, and the mean annual rainfall varying from 500 to 3,500 mm, and the northern Himalaya is relatively dry (the average rainfall is <1,000 mm; Dahal and Hasegawa, 2008).

DATA AND METHOD

Definition of Landslide Geometry

We define the height (H) of a landslide as the elevation difference between the crown and toe along the movement direction (**Figure 2**). The 10 m-resolution DEM originated from the 30 m-resolution SRTM DEM was applied to estimate the heights for the 22,914 landslides. The length (L) and width (W) of a landslide are the corresponding values of the landslide minimum bounding geometry along the sliding direction (Tian et al., 2017). We separately created the convex hulls (the smallest convex polygon) and the minimum bounding rectangles (we used the rectangle with the smallest width), which enclose each landslide. Then, we calculated and checked the angle between the orientations of the geometries (solid green lines in **Figure 2**) and the line directions linking the highest and lowest points (dash green lines in **Figure 2**) for every landslide. For significant differences, we manually measured (using the measure tool) or

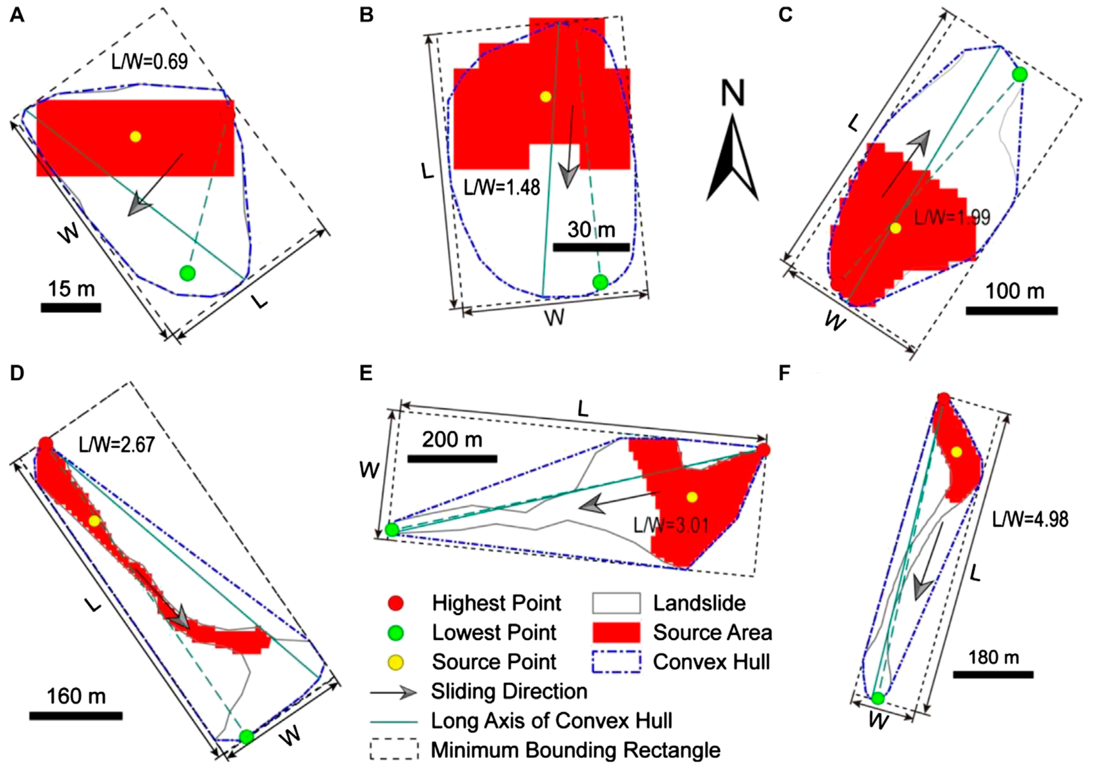

FIGURE 2 | Sketches of landslide length (L) and width (W). Landslide boundaries are real examples selected from the dataset. "L/W" is the aspect ratio/length-width ratio.

chose the most approximate values as landslide L and W (**Figures 2A,D**); and for the smaller differences, we adapted the L and W of the minimum bounding rectangles (**Figures 2B,C** and **2E,F**). All the analysis was conducted using the tools available in ArcGIS 10.5.

Calculating the landslide volume is challenging, and most of the existing methods to calculate the landslide volume use empirical "Area-Volume" relationships (Guzzetti et al., 2009; Larsen et al., 2010; Parker et al., 2011; Xu et al., 2016a). Therefore, in this study, we do not include the landslide volume while talking about landslide geometry.

The reach angle is the arctan value of the height-length ratio (H/L), and the aspect ratio is the length-width ratio (L/W). We use the largest landslide (Langtang landslide) as an example to illustrate the definitions for each geometrical parameter. For the Langtang landslide, its runout is ~3,652 m, and the height is 1,832 m; the H/L ratio, the reach angle, and L/W ratio are ~0.5, 27° and 4.3, respectively (**Figure 3**).

Landslides Triggered by the 2015 Gorkha Earthquake

Combining with field investigations (Tian et al., 2020), Xu et al. (2018) prepared an inventory containing ~47,200 landslides in an area of 35,664 km^2 based on pre- and post-seismic remote sensing images from the Google Earth and the Chinese Gaofen and Ziyuan satellites. The DEM in our research has 10 m-resolution pixels, and aids in identifying 22,914 landslides that are each >500 m^2 in area and have L and W >20 m; each landslide has at least one pixel in its narrowest profile. The Langtang landslide covers an area of ~1,610,957 m^2, while the average landslide area is ~4,435 m^2. Of the >500 m^2 in area landslides, 3,850 landslides (accounting for 16.8% of the total number of landslides) are of 500–1,000 m^2, 10,568 (46.1%) are 1,000–3,000 m^2, 6,437 (28.1%) are 3,000–10,000 m^2, and 2,059 (9%) that are >10,000 m^2 (**Figure 4A**). In the chosen slope failures, 20,238 landslides (accounting for 88.3% of the total) occur on the northern side of the PT2 line (**Figure 1A**) with high altitude and steep terrain.

The maximum slope within each landslide was calculated by obtaining the slope raster derived from the 10 m-resolution DEM to examine the relationships between topography, and landslide size and planar shape. The smallest value of the maximum slopes is ~3°, the steepest slope is ~79°, and the mean value is ~47°. The maximum slopes of ~54% of the chosen landslides concentrate in the range of 45–55° (**Figure 4B**).

The shape of a landslide gives insights into its initial geo-environment and movement process (Niculita, 2016; Taylor et al., 2018). To explore the failure mechanism of landslides in different shapes, other than combined with the landslide 2-D shape, we considered the statistical meaning of each classification by balancing the landslide frequency distribution in each aspect ratio range and classified the landslides into three geomorphometric categories: LS1 (L/W ≤ 2), LS2 (2 < L/W ≤ 4), and LS3 (L/W > 4) (**Figure 6A**). Two datasets that include

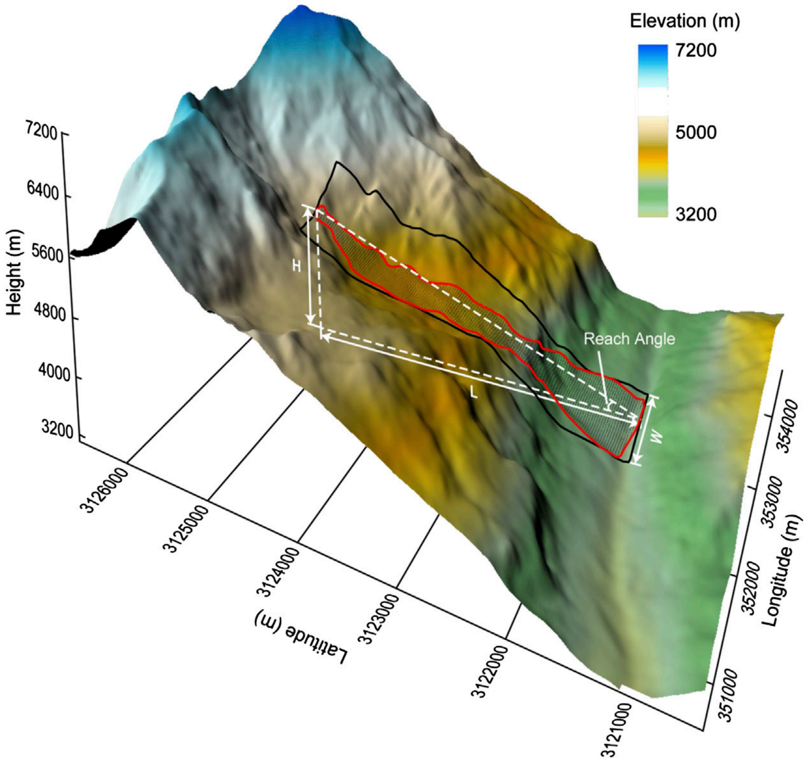

FIGURE 3 | Geometrical parameters illustrated on the Langtang landslide.

22,914 landslides that are >500 m^2 in area with lengths and widths >20 m (named as Dataset 1) and 2,059 large-scale landslides that are >10,000 m^2 from Dataset 1 (named as Dataset 2) (**Figure 1A**) were considered in this study. The landslide source area is where the rupture occurred as well as the majority sliding material from, thus knowing its features is vital for identifying potential landslides and susceptibility mapping (Keefer, 1984; Dai and Lee, 2002; Lee et al., 2008). The source area of a landslide is the grid cells with elevation larger than the median elevation value within each landslide (red areas in **Figure 2**) (Jibson et al., 2000; Wang and Rathje, 2013; Shao et al., 2019). Thus, the source area of each landslide was separated, and its center point (yellow points in **Figure 2**), which links with the control factors. For each geomorphometric type, the number percentage, which equals to the ratio of the landslide numbers in each sub-classification of the setting factors to the total landslide number of this type, is the index being used to explore the distribution characteristics and size effect of landslides with different geomorphometric features.

Control Factors of Landslides

We consider the setting factors, involving terrain (elevation, slope angle, curvature, slope positions, and slope aspect), lithology, streams, roads, and seismology (faults, peak ground acceleration, and small earthquakes before the mainshock) as well as rainfalls in our study. The elevation, slope angle, slope aspect, and curvature derive from the 10 m-resolution DEM mentioned above. The slope position was resampled to 10 m from 90 m-resolution Topographic Position Index (TPI) data downloaded from Geospatial Data Cloud site, Computer Network Information Center, Chinese Academy of Sciences (http://www.gscloud.cn). According to Weiss (2001) and Jenness et al. (2013), hill slope position is divided into six categories based on DEM and slope angles: ridges (TPI > 1 SD), upper slopes (0.5 SD < TPI ≤ 1 SD), middle slopes (−0.5 SD < TPI < 0.5 SD, Slope > 5°), flat slopes (−0.5 SD < TPI < 0.5 SD, Slope ≤ 5°), lower slopes (1 SD < TPI ≤ −0.5 SD) and valleys (TPI < −1.0 SD). TPI refers to the elevation difference between a cell and the average value of its neighborhood around the cell, and the SD is the standard deviation of elevation. The geology bedrock and faults of the region in Nepal were digitalized from geological maps of Yin and Harrison (2000), Dhital (2015), Kargel et al. (2016), and Tiwari et al. (2017), and combined with the digital geology mapping of the rest of the region in China from a geological map on a scale of 1:2,500,000 from the National Geological Data Museum of China (2013). Rock types were classified into 16 categories, as shown in **Figure 5**.

Road data was downloaded from the DIVA-GIS (http://diva-gis.org/download). The river channels were mapped using the 30 m-resolution DEM and hydrology module of the ArcGIS with a grid threshold of flow accumulation >50,000 cells. The 10 m-resolution buffer raster layers were built along the roads and streams in the study area. We built buffers for the streams and roads using the interval of 200 m within the first 1 km-buffer and an interval of 1 km outside to examine the effect of the drainages and roads on different types of landslides.

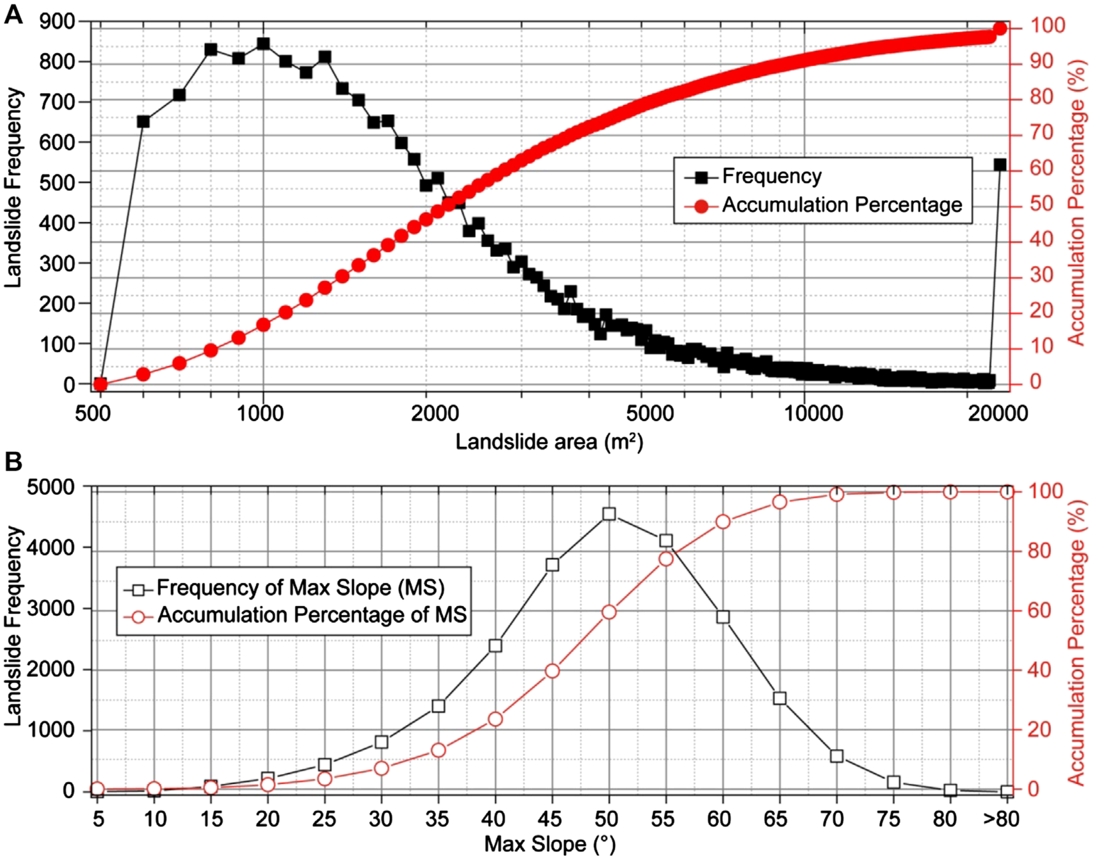

FIGURE 4 | Landslide area **(A)** and maximum slope **(B)** vs. number and accumulation percentage.

Peak ground acceleration (PGA), as a seismic factor, was downloaded from United States Geological Survey (USGS), according to the USGS ShakeMap and local sparse macroseismic reports or measurements ("did you feel it" shake reports) because of few available ground motion stations that were available in Nepal when the earthquake shock the region (USGS, 2015; Kargel et al., 2016).

All the vector layers, including lithology, PGA, and the buffer layers around the faults, roads, and streams, were rasterized into corresponding 10 m-resolution raster layers with reclassified factor information. Then the raster layers were applied to examine the landslide distribution as well as other raster layers of elevation, slope angle, slope aspect, curvature, and slope position.

Rainfall is another triggering factor of landslides. Global Precipitation Measurement data (NASA Earth Observatory, 2019), with a temporal resolution of 1 day and spatial resolution 0.1°, were used to check the relationships among the landslide distribution and antecedent accumulative precipitations (the total rainfalls received before the April 25 Gorkha earthquake at 06:11 UTC and its May 12 aftershock at 07:05 UTC) in varied periods. We considered and mapped the antecedent accumulative precipitations (mm) in the following different periods: for the mainshock, they are 1 day (04/24/2015), 3 days (04/22/2015–04/24/2015), 1 week (04/18/2015–04/24/2015), and 2 weeks (04/11/2015–04/24/2015); for the aftershock, they are 1 day (05/11/2015), 3 days (05/09/2015–05/11/2015), 1 week (05/05/2015–05/11/2015), and 2 weeks (04/28/2015–05/11/2015).

We analyze the effects posed by the regional seismicity before and after the two main 2015 earthquakes from January 2012 through June 2015. The seismicity data for our study area was downloaded from USGS (2019) and was used to explore the potential relationships between the regional seismicity distribution and location of coseismic landslides.

RESULTS AND ANALYSES

Geometrical Parameters

The H, L, and W are 1–1,947 m with an average of 103 m, 20–3,652 m with an average of 132 m and 20–856 m with an average of 43 m, respectively. The aspect ratios range from 0.3 to 15.4, with an average of 3.2, mainly 1.6–3.6 (**Figure 6A**). H/L are 0.03–2.7 with an average of 0.7, and the reach angles range from 2 to 69° with an average of 34° (~55% of the landslides are in the range of 35–45°; **Figure 6B**).

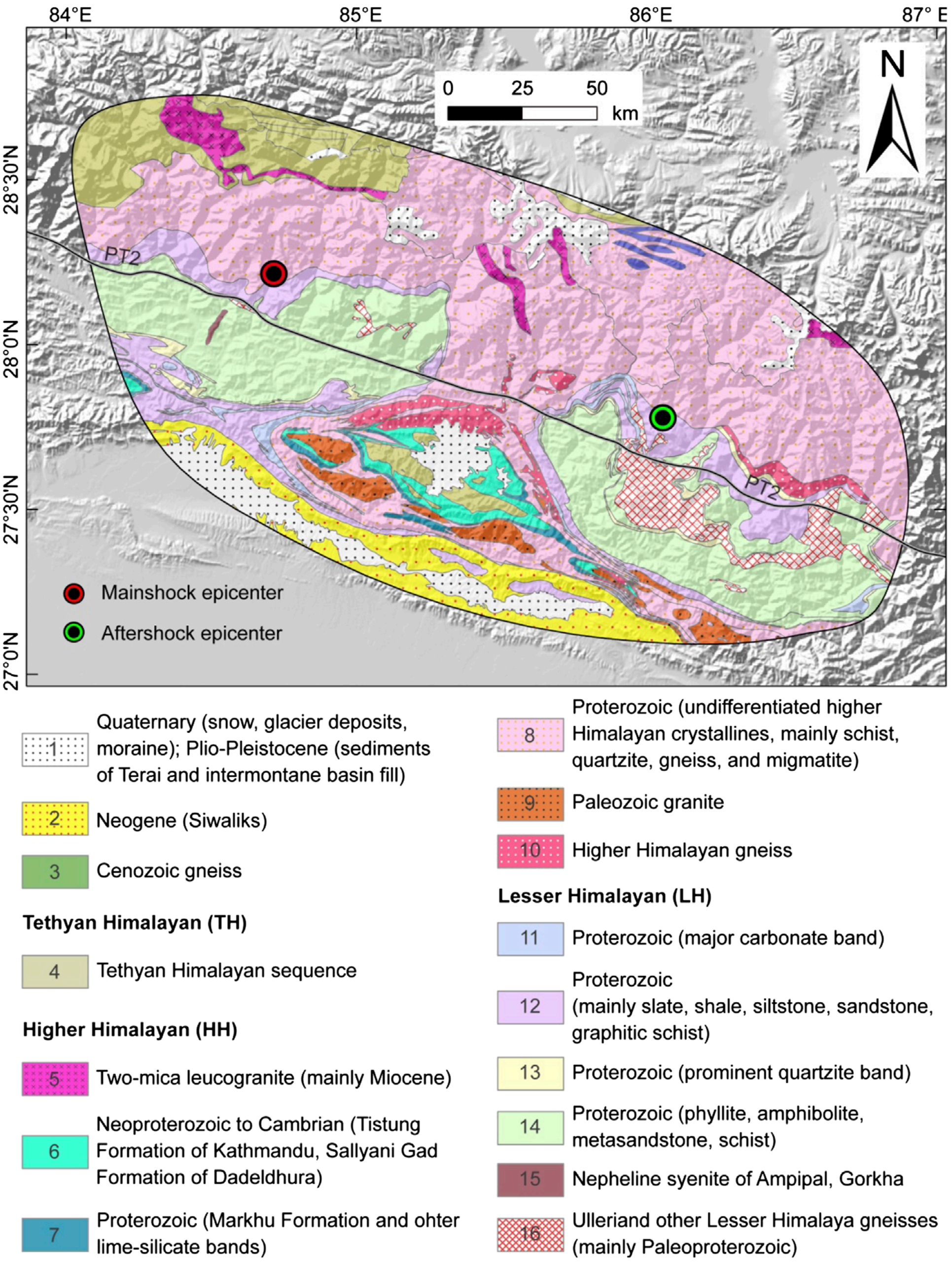

FIGURE 5 | Geology of the study area. The part in Nepal is from Dhital (2015), Kargel et al. (2016), and Tiwari et al. (2017); the area in China is from National Geological Data Museum of China (2013).

A plot using circles of different sizes and colors depicting the landslide size examines the correlations of landslide aspect ratio with terrain (maximum slope) and landslide size (**Figure 6C**). This plot shows that although there is no explicit relationship, most of the landslides are distributed in the enclosed triangle area—above Line 1 ($y = 3.40x + 3.98$), below Line 2 ($y = -1.70x + 80.51$), and on the right side of Line 3 ($x = 0.29$). The smaller landslides have larger ranges for the maximum slope and aspect ratio; however, the larger landslides tend to concentrate in the upper-left corner of the triangle, which means they are likely to develop on the steeper slopes and their main aspect ratios range from 1.0 to 7.0. Specifically, the maximum slopes and aspect ratios for the landslides with an area >8,000 m^2 are generally 40–70° and 1.0–8.5, respectively. The lower limit for the maximum slope range gradually decreases to ~10° for landslides <8,000 m^2. Approximately 700 large landslides have aspect ratios <1.0.

The fitting relationship of H and L for the 22,914 landslides triggered by the 2015 Gorkha earthquake is:

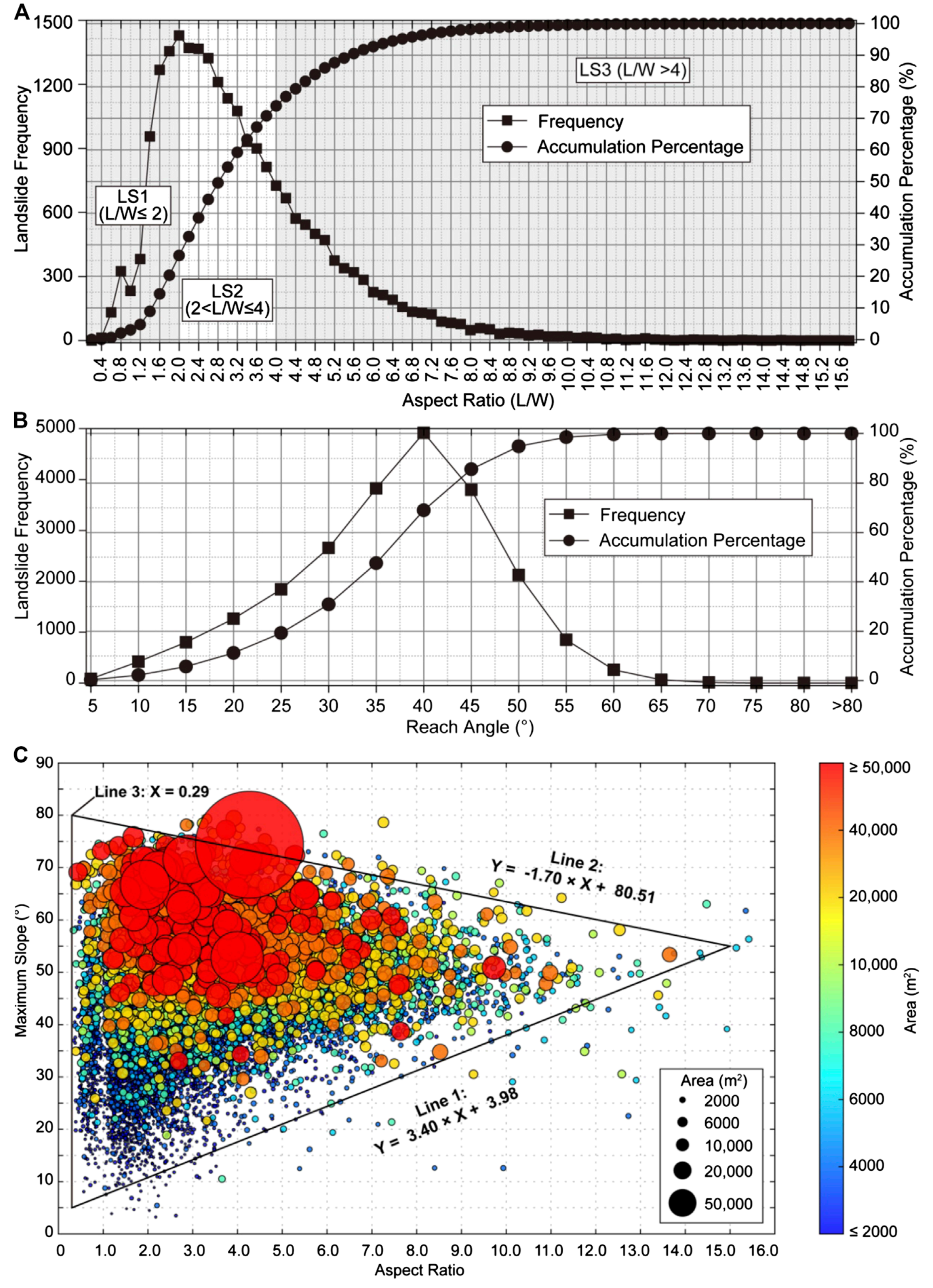

FIGURE 6 | Relationships for aspect ratio **(A)** and reach angle **(B)** vs. landslide number; and **(C)** for the landslide aspect ratio, maximum slope, and area.

TABLE 1 | Classifications of the plane morphology of landslides.

Type	Aspect ratio	Dataset	Number	Percentage (%)
LS1	L/W ≤ 2	Dataset 1 (LS1-1)	6,091	27
		Dataset 2 (LS1-2)	339	16
LS2	2 < L/W ≤ 4	Dataset 1 (LS2-1)	10,851	47
		Dataset 2 (LS2-2)	966	47
LS3	L/W > 4	Dataset 1 (LS3-1)	5,972	26
		Dataset 2 (LS3-2)	754	37

Note: Dataset 1–22,914 landslides that are >500 m² and have L and W both >20 m; Dataset 2–2,059 landslides which are >10,000 m².

$$H = 0.87L - 11.11\left(R^2 = 0.85\right)\left(\textbf{Figure 11}, \text{curve } I'\right) \quad (1)$$

After excluding the largest Langtang landslide, the relationship becomes:

$$H = 0.89L - 13.30\left(R^2 = 0.86\right)\left(\textbf{Figure 11B}, \text{curve } I\right) \quad (2)$$

For the landslides with areas >10,000 m² (excluding the Langtang landslide), the H and L have a relationship of

$$H = 0.76L + 40.77\left(R^2 = 0.69\right)\left(\textbf{Figure 11B}, \text{curve } II\right) \quad (3)$$

The corresponding average values of the reach angles for curve I, I′, and II in **Figure 11** are 41°, 42°, and 37°, respectively.

Planar Geometry

In Dataset 1, 27% are LS1-type, 47% are LS2-type, and 26% are LS3-type landslides (**Table 1**; **Figure 6A**), which we call LS1-1, LS2-1, and LS3-1 (where "-1" denotes Dataset 1) in the following analyses. For landslides >10,000 m² in Dataset 2, these three classes have 16, 47, and 37% for each landslide type. These are called LS1-2, LS2-2, and LS3-2 (where "-2" denotes Dataset 2).

For Dataset 1, ~93% of the LS3-type landslides, 89% of the LS2-type landslides, and 86% of the LS1-type landslides lie in the steep areas north of PT2; for Dataset 2, the percentages of the landslides in the northern part of PT2 are 97, 96, and 97%, respectively. The dominant occurrence of all landslide types distributing in the north of PT2 suggests that the long and large landslides are more prone to developing in the steep higher area.

Spatial Distribution of Landslides and Control Factors

Elevation

The elevation range with the largest area is the 500–1,000 m asl, followed by 1,000–1,500 and 1,500–2,000 m asl (grey columns in **Figure 7A**). The landslide number percentages for all the landslide types are much larger in the elevation ranges of 1,000–3,500 m asl (**Figure 7A**). For the landslides in Dataset 1, LS1-1 and LS2-1 peak in 1,500–2,000 m asl, with percentages ~26 and ~24%, respectively, followed by 1,000–1,500 m asl. Landslides of type LS3-1 mainly concentrate on elevations of 1,500–3,500 m asl. For Dataset 2, the peak percentage (~22%) of LS1-2 is in 1,500–2,500 m asl; for LS2-2 and LS3-2, they (22 and 25%, respectively) are in 2,500–3,000 m asl. Since the percentages on the left-hand side of the peak elevation ranges are much greater than the right-hand side for the LS1-type and LS2-type landslides, we deduced that these 2 kinds of landslides are likely to develop on the lower slopes (such as the free surfaces of the river banks). In comparison, the LS3-type landslides are more common at the higher elevation slopes reflecting by larger percentages on the right-hand side of the peak ranges, and it implies that the narrow landslides tend to form at higher altitudes. Besides, the elevation ranges of the peak percentages for Dataset 2 are much higher than those for Dataset 1. This difference in ranges is possibly because the larger-scale landslides are prone to slopes with much high elevation, which could provide larger gravitational potential energy and long-runout space, as stated by Roback et al. (2018).

Hill Slope Angle

The regions with hill slope angles ranging from 20 to 35° have relatively larger classification areas. The steeper hill slopes are more prone to sliding though their classification areas are relatively small (**Figure 7B**). All of the percentage curves have larger values for slopes of 40–60°. The percentage curve of type LS3-1 firstly increases, then peaks at 40–45° with a percentage of 25% and falls in the slope class of >60°, while the curves for the types LS1-1 and LS2-1 are relatively smoother, especially for the LS1-1, and they both have two peaks in the ranges of 40–45° and 50–60°. The percentage curves of landslides in Dataset 2 have similar trends as those in Dataset 1. However, few landslides in Dataset 2 are present in the area with slope angles <30°. Approximately 30% of the landslides of types LS1-2 and LS2-2 have slope angles of 50–60°, and the maximum percentage for LS3-2 has slope angles of 40–45°. Generally, the slopes with an angle >35° are much more prone to developing longitudinal and elongated landslides, and the large landslides are more common to the steeper slopes than the smaller landslides. This relationship implies that the steep slopes are much easier to slide during shaking, and the stripped debris is more likely to run a long way downward rather than spreading transversely.

Curvature

The curvature range of the study area is −431 to 238. We applied the breakpoints of −4, −0.5, 0.5, and 4 to identify the slope shapes—concave hill slopes (−4 to −0.5), straight hill slopes (−0.5 to 0.5), and convex hill slopes (0.5–4). The regions with curvature ranging from −0.5 to 0.5, hosting the largest classification area are much vulnerable to slide for all the landslide classes, followed by the concave and convex hill slopes (**Figure 7C**). The percentage curve of the LS1-2 type of landslides has similar percentages in the ranges of −4 to −0.5, −0.5 to 0.5, and 0.5–4, which suggests that the possibility for slope failure related to the large-scale landslides with L/W <2 are similar for the straight, concave and convex hill slopes. According to the slope aspect classifications in **Figure 7E**, few areas are horizontal straight and therefore debris does not stay long on inclined straight slopes.

Slope Position

The percentage curves in **Figure 7D** show that the landslides, no matter what planar shape or size, concentrate on the widespread middle slopes. Moreover, in this classification, the percentages of

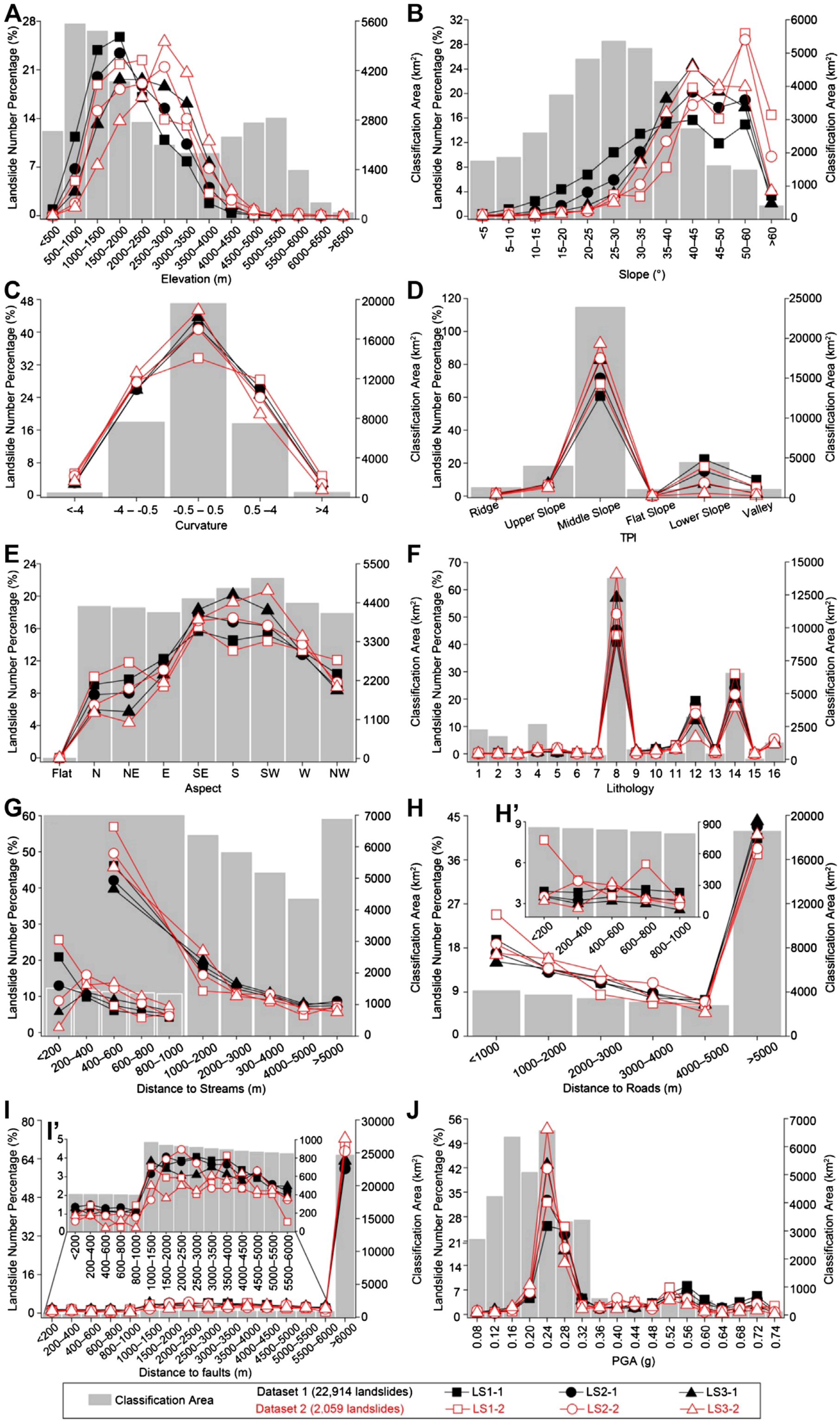

FIGURE 7 | Analyses of the three geomorphometric types of landslides vs. control factors: **(A)** elevation; **(B)** slope; **(C)** curvature; **(D)** slope position/TPI; **(E)** aspect; **(F)** lithology; **(G)** distance from streams; **(H)** distance from roads and **(H')** shows the landslide distribution within 1 km from the roads; **(I)** distance from faults and **(I')** shows the enlarge statistical plot of the distance from faults; and **(J)** PGA. **Figure 5** shows the distribution of bedrock and provides descriptions. LS1-1 (L/W ≤ 2), LS2-1 (2 < L/W ≤ 4), and LS3-1 (L/W > 4) are geometry-based types of landslides for Dataset 1 which includes 22,914 landslides; LS1-2 (L/W ≤ 2), LS2-2 (2 < L/W ≤ 4), and LS3-2 (L/W > 4) are for Dataset 2 which includes 2,059 landslides.

the elongated landslides (LS3), which are ~83% for Dataset 1 and ~93% for Dataset 2, respectively, are particularly larger than the other two types (LS1 and LS2). Besides, few landslides distributed on the flat slopes and the LS1-type landslides are relatively widespread on the lower slopes as well.

Slope Aspect

Figure 7E shows that the SE-, S-, and SW-facing hill slopes are landslide-prone for all types of landslides. The percentages of the LS3-type landslides are notably higher in these aspects, which means that they are much sensitive to the S-facing hill slopes than LS1 and LS2. The southern aspect is consistent with the thrust direction of the hanging wall of MHT, and the rock mass in the thrusting front is relatively fractured. Also, the sunlight and southwest monsoon likely make the south-facing slopes easier to weather.

Lithology

Analysis of landslide number percentages of different geomorphometric types and lithology (**Figure 7F**) shows that the eighth class of the High Himalaya Sequence (Proterozoic: undifferentiated higher Himalayan crystalline rocks, mainly schist, quartzite, gneiss, and migmatite) has the largest classification area and has most of the landslides, followed by the fourteenth (Proterozoic: phyllite, amphibolite, metasandstone, schist) and twelfth (Proterozoic: mainly slate, shale, siltstone, sandstone, graphitic schist) classes of the Lesser Himalaya sequence. In the area covering by the Proterozoic High Himalaya Sequence (class 8), LS3-type landslides are most common, then the LS2-type and the LS1-type landslides, but the trend is opposite in the Less Himalaya sequence area.

Distance From Streams

Of all the landslide types, ≥40% of the landslides are within the 1 km-swath area along the streams (**Figure 7G**). The percentage curves show that the landslide numbers generally decrease with the increasing distance, which indicates that the streams pose much influence on the nearby slopes. However, within the 1 km-swath along the streams, different shapes of landslides show different spatial distribution trends. LS1-type landslides show an evident decrease in numbers as the distance increases from the streams and the percentage curves peak in the area which is <200 m to the streams with the largest percentage of 21% for LS1-1 and 27% for LS1-2; LS3-type landslides are less in the area within 200 m of the streams and more in the 200–400 m-buffer and the peak percentages for LS3-1 and LS3-2 are 11 and 13%, respectively. The curve for LS2-1 decreases directly from 13 to 5%; and LS2-2, it first increases, and peaks with a percentage of 16% then decreases. This pattern suggests that the elongated landslides (LS3) occurred much farther from the stream channels that provide them more space to extend. The oblate or transverse landslides (LS1) are much more susceptible to the influence of the streams, and the locations of the longitudinal landslides (LS2) depends on the landslide size—large landslides are prone to developing farther from the streams while the small ones close to the streams.

Distance from Roads

Other than the largest and farthest class that is >5 km away from the roads, there is a negative relationship between landslide number percentages and the distances from roads, which suggests that the road excavation plays a vital role in triggering landslides (**Figure 7H**). However, the landslide spatial distributions for Dataset 1, within 1 km of the roads, do not correlate with the distances to roads (**Figure 7H'**). For Dataset 2 which contains large landslides, the percentage curves show complex trends—the LS1-2 type of landslides peak in distance ranges of <200 m (number percentage of ~8%) and 600–800 m (number percentage of ~6%) from the roads; LS2-2 and LS3-2 peak in distance ranges of 200–400 and 400–600 m from the roads, respectively. Most roads in the mountainous area are along rivers, and therefore the influence of the streams may mask the effect posed by roads on landsliding.

Distance from Faults

We chose three large-scale exposed faults (STDS, MCT, and MBT), instead of the deep buried MHT, to which these fault root, to study the effect of the faults posed on the spatial distribution of landslides in different shapes. The 200 or 500 m intervals were used to build buffers along these faults. Statistics (**Figure 7I,I'**) show that there is no relationship between landslide distribution and the distance to the STDS, MCT, and MBT.

Peak Ground Acceleration

The PGA values of the study area range from 0.08 to 0.74 g from the Gorkha earthquake. In general, the larger the PGA is, the stronger the ground shaking (assuming other factors such as substrate conditions and topography are the same). However, the landslide distribution does not have a positive relationship with the PGA in the study area. The largest areas of LS1, LS2, and LS3 are all in the class of 0.24 g, followed by the 0.28 g class (**Figure 7J**). The reason may be the uncertainty resulted from the estimation of ground shaking by GMPEs (Ground Motion Prediction Equations), lacking enough real-time measurements of seismic stations (Kargel et al., 2016). On the other hand, this may suggest that the PGA is a triggering factor rather than the predominant factor in controlling the distribution of the earthquake-triggered landslides.

Antecedent Accumulative Rainfalls

Figure 8 shows the contours of the antecedent accumulative precipitations for 1 day, 3 days, 1 week, and 2 weeks before the April 25 Gorkha earthquake and its May 12 aftershock. The landslide density is considerably greater in the northern part of the PT2 line, while the rainfall was less on the north side than the south side. The weather was relatively dry before the mainshock—the 7-day-accumulative precipitation in the area had the densest landslide clusters, was <10 mm, and the 14-day-accumulative rainfall was <40 mm (**Figures 8A–D**). Besides, the rainfall is almost even in the northern part where developed dense landslides. Generally, the distribution of the precipitation before the mainshock does not correlate with the location of the dense landslide clusters. Though the study area received more rainfall during the mainshock and aftershock, and the largest total

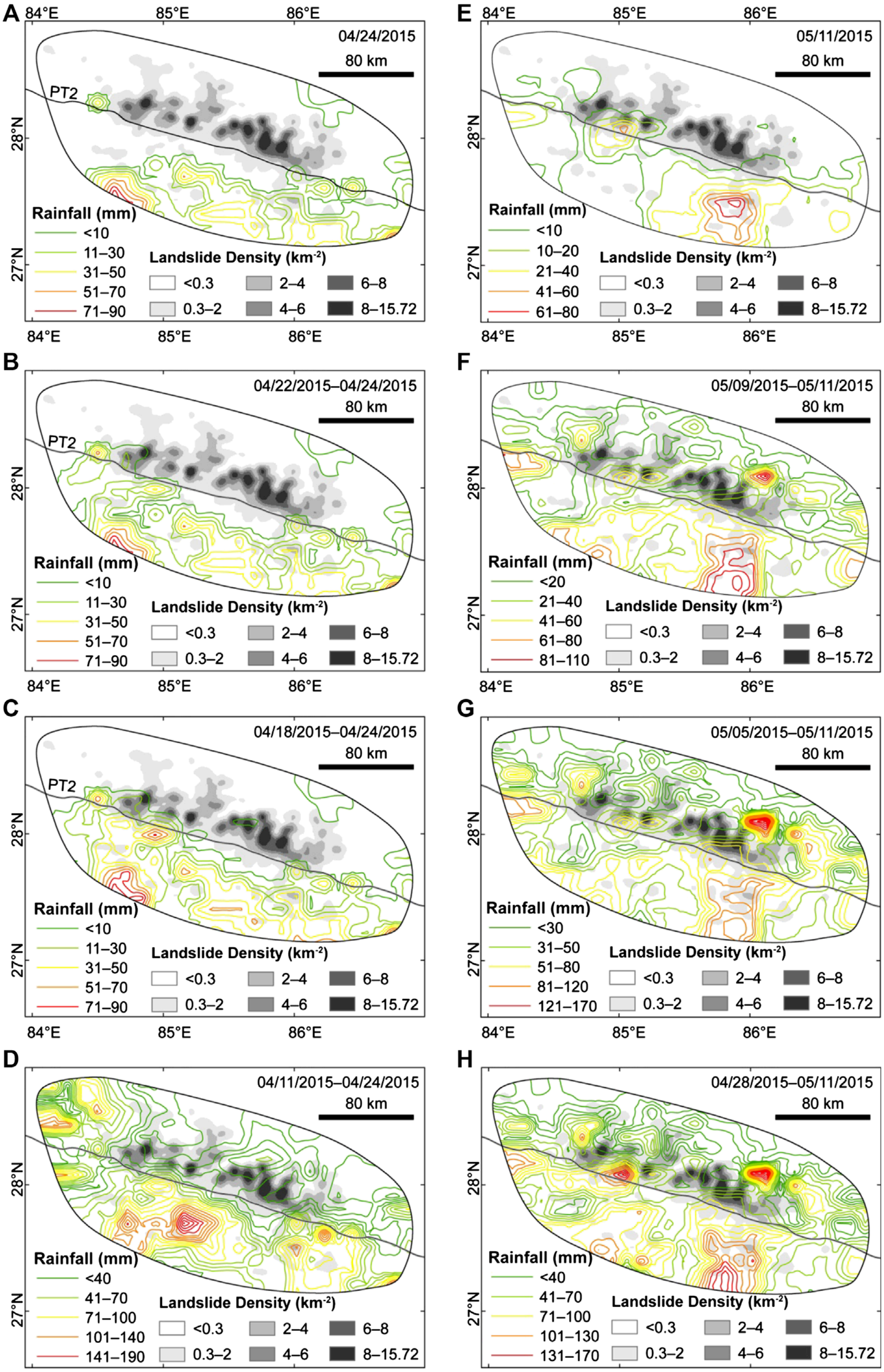

FIGURE 8 | Landslide density vs. antecedent accumulative precipitations (mm) of 1 day, 3 days, 1 week, and 2 weeks before the April 25 mainshock **(A–D)** and 1 day, 3 days, 1 week, and 2 weeks before the May 12 aftershock **(E–H)**. PT2: physiographic transition.

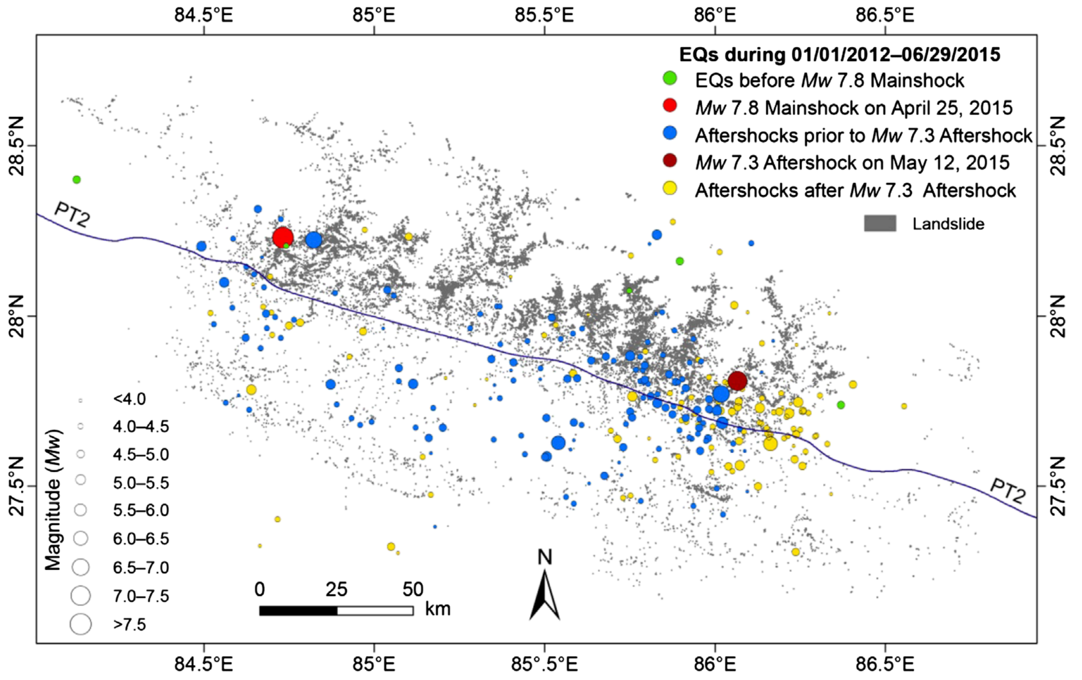

FIGURE 9 | Earthquake-triggered landslides and small magnitude earthquakes that occurred before the April 25 M_w 7.8 mainshock as well as the aftershocks in the seismic area of the 2015 Gorkha earthquakes. EQ is short for earthquakes. Earthquake data are from USGS (2019). Landslide data are from Xu et al. (2018).

rainfall was ~170 mm, the places where most of the dense landslide clusters developed received a total rainfall <70 mm (**Figures 8E–H**). Therefore, the antecedent accumulative precipitation might influence the landslide frequency and location, but it is not the primary control factor for the coseismic landslides related to the 2015 Gorkha earthquakes.

The May 12 aftershock occurred 18 days later than the April 25 mainshock. In comparison with the mainshock, the antecedent accumulative precipitation before the aftershock is greater in different corresponding time spans in the north of PT2 (**Figure 8**). Differentiating the landslides triggered by the mainshock or the aftershock is necessary to examine the influence posed by the rainfalls on landslides triggered by the strong aftershock.

Small Earthquakes Before and After the Mainshock

Totally 267 earthquakes recorded in the area are shown in **Figure 9**. There were 5 of them ($M_w \leq 5.0$) occurred before the main M_w 7.8 event, 80 (including the mainshock) occurred on April 25, and 182 aftershocks occurred after April 25, 2015 Gorkha earthquake, respectively. The majority of the aftershocks were distributed between the locations of the mainshock and the M_w 7.3 strong aftershock, so are the majority of the coseismic landslides. Despite the majority of the aftershocks are located closer to the M_w 7.3 aftershock, they are almost evenly distributed on both sides of the PT2. At the same time, the landslides are mainly located on the northern side of the PT2 and along river channels (**Figure 9**). Even though there is a higher number of coseismic landslides toward the SE, which is coinciding with the location of the aftershocks occurred before the M_w 7.3 strong aftershock, the same is not recognized in the NW, or with the aftershocks after the M_w 7.3. For these reasons, we found no clear correlation between the aftershocks and landslides distributions. Therefore, we deduce that shaking resulted from the earthquakes occurred before the mainshock and the aftershocks have no apparent dominant effects on the distribution of all three geomorphometric types of landslides.

DISCUSSIONS

Landslide Size and the Distribution of Different Shapes of Landslides

The above statistical analyses of landslides with different scales and planar geomorphometric features show that, in general, the large-scale landslides with an area >10,000 m^2 in Dataset 2 have similar failure-prone conditions concerning the predisposing factors with the landslides in Dataset 1. The vulnerable ranges are common in an elevation ranges of 1,000–3,500 m asl, slopes of 40–60°, curvature of −0.5 to 0.5, middle slopes, south-facing slopes, PGA of 0.24 g, and areas covering by the lithology of High Himalaya Sequence and closing to streams and roads (**Figure 7**). Even so, for the landslides with L/W ≤ 2 (LS1 type), the larger-scale landslides have a slightly high elevation (1,500–3,000 m asl, **Figure 7A**) and steeper slope (50–60°, **Figure 7B**) ranges and they are less sensitive to slope curvature (**Figure 7C**). While for LS2 and LS3 types, the large landslides tend to develop in a larger space, so they are more

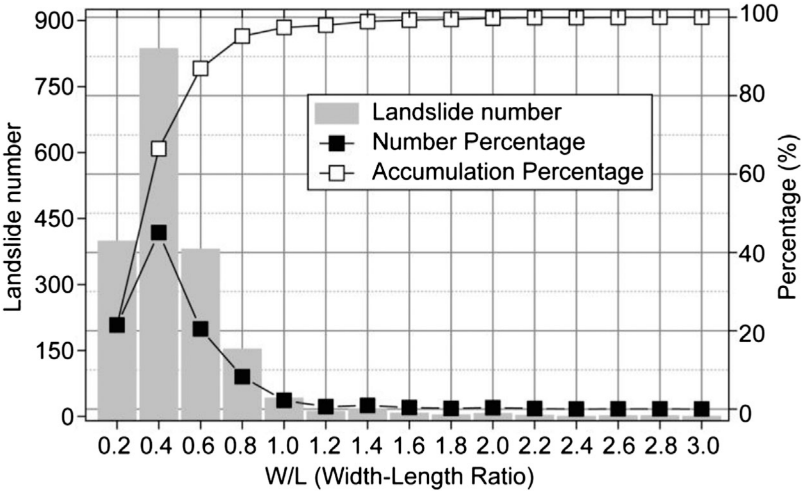

FIGURE 10 | Percentage curves for landslide width-length ratio of this research in the study area of Tsou et al. (2018).

common on the higher elevation (2,500–3,000 m asl, **Figure 7A**) and relatively farther (200–400 m, **Figure 7G**) from the streams.

Comparing With Other Studies

Of the 22,914 landslides, 1,856 landslides were mapped in an area of 465 km^2 in the Trishuli Valley of central Nepal, which is the scope of the study by Tsou et al. (2018). In our study, the L for these landslides range from 20 to 1,119 m with an average L of 165 m, and the W/L values are in 0.07–2.7 (L/W in 0.4–15.4) (**Figure 10**). Despite the similar W/L values, L for the 912 landslides mapped by Tsou et al. (2018) were 7–1,145 m with an average L of 174 m in this region. Also, according to Tsou et al. (2018), landslides with W/L < 0.6 account for 90%, close to 1,614 landslides in our work constituting up 87% of our sample; whereas those of W/L smaller than 0.2 account for 60% of the total according to Tsou et al. (2018), much larger than 398 landslides accounting for 21% of the total as shown by our study. These differences probably result from the landslide sampling rule of our research, i.e., we only considered the landslide with areas >500 m^2 and L and W both >20 m. Another possible reason for the differences is due to the different methods for computing landslide L and W. Tsou et al. (2018) approximated W using the ratio of the landslide area to L. When L is defined, W may be underestimated, resulting in a smaller W/L. While in our method, L and W of the minimum boundary rectangle of the landslide along the slide direction are the effective L and W, which may be closer to real values.

An earthquake of larger magnitude generally produces stronger ground shaking, and the resultant landslides usually have longer runouts and larger aspect ratios (Tian et al., 2017). Thus, the landslides triggered by the 1994 M_w 6.7 Northridge, USA, and the 2013 M_w 5.9 Minxian, China earthquakes, both moderate in magnitude, have relatively smaller average aspect ratios of 2.6 and 2.11, respectively, (**Table 2**). However, the mean aspect ratio (3.2) for the 2015 M_w 7.8 Gorkha earthquake, even the value (3.7) for the landslides >10,000 m^2, is smaller than ratios of the 2010 M_w 7.0 Haiti (3.76) (Xu et al., 2014) and the 2010 M_w 6.9 Yushu (4.15) (Xu and Xu, 2014) earthquakes. Firstly, the larger aspect ratio (L/W) for the Haiti and Yushu cases might as well resulted from underestimating W by defining it as the ratio of landslide area to L (Xu and Xu, 2014; Xu et al., 2014). Also, the topography is a crucial factor in determining the landslide geomorphometry and runout in addition to the triggering factor of the ground shaking. The

TABLE 2 | Landslide's lengths, widths and aspect ratios of five earthquake cases.

Events		Magnitude (M_w)	Landslide number	Length (m)	Mean length (m)	Width (m)	Mean width (m)	Aspect ratio	Mean aspect ratio	References
Minxian[a]		5.9	635	15.3–946.7	60	12.0–284.7	31.6	0.3–8.02	2.11	Tian et al. (2017)
Northridge		6.7	1,052	9–367	69	4–195	26	—	2.6	Parise and Jibson (2000)
Yushu		6.9	2,036	6–415	40	1.7–76.7	10.8	1.5–32.8	4.15	Xu and Xu (2014)
Haiti		7.0	30,828	—	—	—	—	1.37–54.3	3.76	Xu et al. (2014)
Gorkha	Dataset1	7.8	22,914	20–3,652	132	20–856	43	0.3–15.4	3.2	This study
	Dataset2			78–3,652	349	37–856	106	0.23–13.7	3.7	

[a] *1 shows the parameters of the 635 landslides with areas >500 m^2 triggered by the 2013 Minxian, China earthquake.*

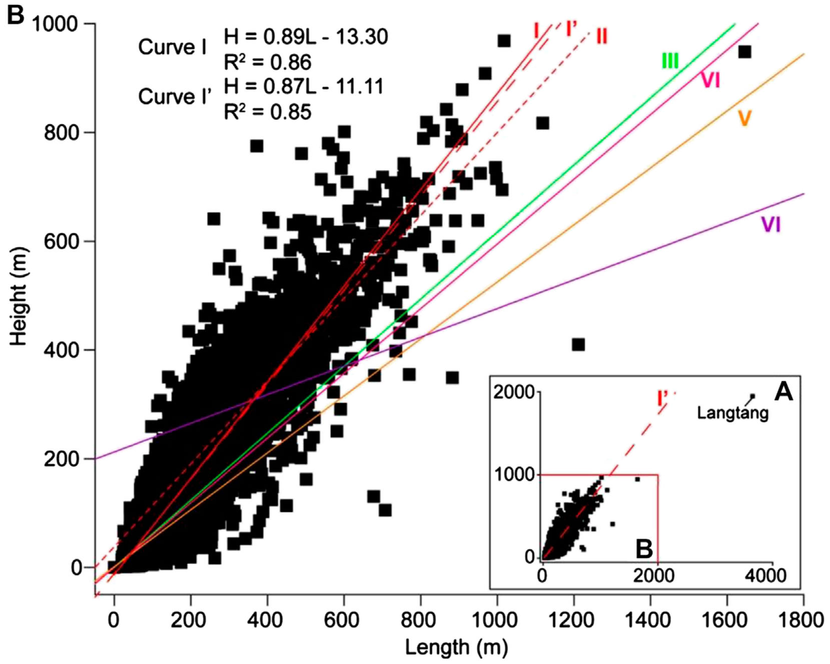

FIGURE 11 | Fitting relationships of landslide length and height. **(A)** Fitting plot with the 22,914 landslides. **(B)** Fitting plots for the 2015 Gorkha earthquake (curve I for landslides (22,913) in Dataset 1 without the Langtang avalanche, curve I' for all landslides (22,914) in Dataset 1 and curve II for landslides (2,059) in Dataset 2) and other existing research (curves III–VI are for landslides in areas related to Minxian, Haiti, Hongkong and Wenchuan cases). **Table 3** provides further details.

V-shape steep topography in Nepal likely blocks landslide masses from running for a long distance, and the sliding debris accumulates in the valley, which would lead to a larger W. Thus, although these landslides have larger lengths, their aspect ratios are relatively small (mainly in 1.6–3.6). However, just as the Yushu earthquake, the earthquake-affected region is an area of gentle slopes (most <30°) on a plateau with sparse vegetation which provides a favorable condition (the longer slope surfaces with few obstacles) for unstable slope masses to run for long distances (Xu et al., 2013). Therefore, although they have a small size, L, and W, the landslides ran a long distance and have large aspect ratios as well as longitudinal shapes (**Table 2**). Another possible reason might be that in our study, the landslide sampling size (account for 49% of the total) is smaller, and we did not examine the landslides with an area of <500 m^2 and L and W > 20 m.

The reach angle of landslides triggered by the 2015 Gorkha earthquake is ~40° (**Figure 11**), which is steeper than those determined from other studies, which include ~32° for the landslides >500 m^2 induced by the 2013 minxian, Gansu, China earthquake (Tian et al., 2017), 31° for landslides triggered by the 2010 Haiti earthquake (Xu et al., 2014), 28° for the rainfall-induced landslides in Lantau Island, Hong Kong (Dai and Lee, 2002), and 15° for the long-runout rock avalanches triggered by the 2008 Wenchuan, Sichuan, China earthquake (Qi et al., 2011) (**Table 3**). The reason for this difference is probably due to the V-shape valleys, high mountains, and gorges in this study area that blocked the landslide masses from advancing long distances.

CONCLUSIONS

We described the geomorphometry of the 22,914 landslides triggered by the 2015 Gorkha earthquake sequence, which have areas ≥500 m^2 and L and W ≥20 m, in an extensive area affected by the earthquakes. Results show that the ranges of L, W, and H are 20–3,652, 20–856, and 1–1,947 m, respectively. The reach angle (arctan H/L) ranges from 2 to 69°, with an average of 34°, and the aspect ratio ranges from 0.3 to 15.4, with an average of 3.2. The height and length have a relationship of $H = 0.87L - 11.11$ ($R^2 = 0.85$), and the fitting average reach angle is ~41°. This average reach angle is much larger than existing studies in other regions. The mean aspect ratio is smaller than those for earthquakes that have smaller magnitude (e.g., Yushu and Haiti earthquakes). One probable reason is that the steep gorges could block the landslide masses from moving long distances, thus resulting in smaller L and larger W as well as a smaller aspect ratio.

The landslides are classified into three geomorphometric types based on their 2-D shape and ratio distributions: LS1 (L/W ≤ 2), LS2 (2 < L/W ≤ 4), and LS3 (L/W > 4). Dataset 1 containing the total 22,914 landslides and Dataset 2 (from Dataset 1 but only includes 2,059 landslides with areas >10,000 m^2) enable the examination of the spatial distributions of the three types of landslides. Results show that, regardless of the size, all the three geomorphometric types of the landslides have similar susceptible ranges including curvature, slope position, lithology, and PGA—they all can occur on straight hill slopes, middle slopes, areas underlain by High Himalayan Proterozoic rocks

TABLE 3 | Fitting relationships of landslide height and length for five study cases.

Event and landslide		Landslide number	Function of height and length	Mean reach angle	References
Landslides triggered by the 2015 Gorkha earthquake	Area ≥500 m^2, length ≥20 m, and width ≥20 m	22,914	Curve I' (**Figure 11**): $H = 0.87L - 11.11$ ($R^2 = 0.85$)	41°	This study
	Area ≥500 m^2, length ≥20 m and width ≥20 m (without langtang landslide)	22,913	Curve I (**Figure 11B**): $H = 0.89L - 13.30$ ($R^2 = 0.86$)	42°	
	Area ≥10,000 m^2 (without langtang landslide)	2,058	Curve II (**Figure 11B**): $H = 0.76L + 40.77$ ($R^2 = 0.69$)	37°	
Landslides triggered by the 2013 Minxian earthquake (area ≥500 m^2)		635	Curve III (**Figure 11B**): $H = 0.6164L + 0.4589$ ($R^2 = 0.7312$)	32°	Tian et al. (2017)
Landslides triggered by the 2010 Haiti earthquake (volume ≥10,000 m^3)		452	Curve IV (**Figure 11B**): $H = 0.595L$ ($R^2 = 0.6972$)	31°	Xu et al. (2014)
Rainfall-induced landslides in Lantau Island, Hong Kong		2,103	Curve V (**Figure 11B**): $H = 0.524L + 1.257$ ($R^2 = 0.87$)	28°	Dai and Lee (2002)
Long runout landslides triggered by the 2008 Wenchuan earthquake		66	Curve VI (**Figure 11B**): $H = 0.2638L + 212.4$ ($R^2 = 0.6716$)	15°	Qi et al. (2011)

(undifferentiated higher Himalayan crystalline rocks, mainly schist, quartzite, gneiss, and migmatite), and PGA of 0.24 g. However, the effects posed by elevation, hill slope angle, slope aspect, and streams are different. The LS3-type landslides are more abundant in areas that are more prone to failure and can provide ample space to extend, which include those with a higher elevation of 1,500–3,000 m asl, hill slopes of 40–45°, and the areas within 200–400 m from the streams. While areas with the highest concentration of LS1-type and LS2-type landslides are at elevations of 1,000–2,000 m asl, slopes of 40–45° and 50–60°, southeast-facing slopes, and within 200 m from the streams. Moreover, the distributions of landslides in Dataset 2 suggest that the large landslides are more likely to occur on much higher and steeper slopes than the small landslides. The roads, three large-scale faults, antecedent precipitations, and the small earthquakes before and after the mainshock do not have dominant impacts on the landslide distribution. In sum, the terrain factors and streams are the major factors controlling the spatial distributions of landslides with various shapes and sizes. Therefore, geometric features of coseismic landslides provide a new view to understand the landslide extent characteristics and mechanism.

One urgent problem is that there is no generally agreed definition for the geomorphometric parameters for earthquake-triggered landslides. Aspect ratios differ because the methods to approximate the L and W for landslides vary. There is a need for a standard method and more case studies to contrast the geomorphometric shapes of earthquake-triggered landslides.

DATA AVAILABILITY STATEMENT

The raw data supporting the conclusions of this article will be made available by the authors, without undue reservation.

AUTHOR CONTRIBUTIONS

CX proposed and participated in designing the study; YT designed the study, analyzed the data and wrote the manuscript; LO participated in designing the study and improved the paper; LS worked on the rainfall data processing; QZ participated in designing the study; PF polished the paper. All authors approved the final version of the manuscript.

FUNDING

This work was supported by the National Natural Science Foundation of China (grant number 41661144037).

REFERENCES

Avouac, J.-P., Meng, L., Wei, S., Wang, T., and Ampuero, J.-P. (2015). Lower edge of locked main Himalayan thrust unzipped by the 2015 Gorkha earthquake. *Nat. Geosci.* 8, 708–711. doi:10.1038/ngeo2518

Berthet, T., Ritz, J.-F., Ferry, M., Pelgay, P., Cattin, R., Drukpa, D., et al. (2014). Active tectonics of the eastern Himalaya: new constraints from the first tectonic geomorphology study in southern Bhutan. *Geology* 42, 427–430. doi:10.1130/G35162.1

Collins, B. D., and Jibson, R. W. (2015). Report No.: 2015-1142. Assessment of existing and potential landslide hazards resulting from the April 25, 2015 Gorkha, Nepal earthquake sequence. Available at: https://www.preventionweb.net/go/47697 (Accessed April 25, 2015)

Corominas, J. (1996). The angle of reach as a mobility index for small and large landslides. *Can. Geotech. J.* 33, 260–271. doi:10.1139/t96-005

Corominas, J., Copons, R., Vilaplana, J. M., Altimir, J., and Amigó, J. (2003). Integrated landslide susceptibility analysis and hazard assessment in the principality of Andorra. *Nat. Hazards* 30, 421–435. doi:10.1023/B:NHAZ.0000007094.74878.d3

Dahal, R. K., and Hasegawa, S. (2008). Representative rainfall thresholds for landslides in the Nepal Himalaya. *Geomorphology* 100, 429–443. doi:10.1016/j.geomorph.2008.01.014

Dai, F. C., and Lee, C. F. (2002). Landslide characteristics and slope instability modeling using GIS, Lantau Island, Hong Kong. *Geomorphology* 42, 213–228. doi:10.1016/S0169-555X(01)00087-3

Dhital, M. R. (2015). *Geology of the Nepal Himalaya–regional perspective of the classic collided Orogen*. Cham, Switzerland: Springer.

Elliott, J. R., Jolivet, R., González, P. J., Avouac, J.-P., Hollingsworth, J., Searle, M. P., et al. (2016). Himalayan megathrust geometry and relation to topography revealed by the Gorkha earthquake. *Nat. Geosci.* 9, 174–180. doi:10.1038/ngeo2623

Gallen, S. F., Clark, M. K., Godt, J. W., Roback, K., and Niemi, N. A. (2017). Application and evaluation of a rapid response earthquake-triggered landslide model to the 25 April 2015 Mw 7.8 Gorkha earthquake, Nepal. *Tectonophysics* 714–715, 173–187. doi:10.1016/j.tecto.2016.10.031

Guzzetti, F., Ardizzone, F., Cardinali, M., Rossi, M., and Valigi, D. (2009). Landslide volumes and landslide mobilization rates in Umbria, central Italy. *Earth Planet Sci. Lett.* 279, 222–229. doi:10.1016/j.epsl.2009.01.005

Hayes, G. P., Briggs, R. W., Barnhart, W. D., Yeck, W. L., McNamara, D. E., Wald, D. J., et al. (2015). Rapid characterization of the 2015Mw 7.8 Gorkha, Nepal, earthquake sequence and its seismotectonic context. *Seismol Res. Lett.* 86, 1557–1567. doi:10.1785/0220150145

Heim, A. (1932). *Bergsturz und Menschenleben (landslides and human lives)*. Vancouver, BC, Canada: BiTech Publishers.

Hodges, K. V., Wobus, C., Ruhl, K., Schildgen, T., and Whipple, K. (2004). Quaternary deformation, river steepening, and heavy precipitation at the front of the higher Himalayan ranges. *Earth Planet Sci. Lett.* 220, 379–389. doi:10.1016/s0012-821x(04)00063-9

Hsü, K. J. (1975). Catastrophic debris streams (sturzstroms) generated by rockfalls. *Geol. Soc. Am. Bull.* 86, 129–140. doi:10.1130/0016-7606(1975)86<129:cdssgb>2.0.co;2

Jenness, J., Brost, B., and Beier, P. (2013). *Land facet corridor designer: extension for ArcGIS*. Available at: http://www.jennessent.com/arcgis/land_facets.htm (Accessed 8 31, 2019).

Jibson, R. W., Harp, E. L., and Michael, J. A. (2000). A method for producing digital probabilistic seismic landslide hazard maps. *Eng. Geol.* 58, 271–289. doi:10.1016/s0013-7952(00)00039-9

Kargel, J. S., Leonard, G. J., Shugar, D. H., Haritashya, U. K., Bevington, A., Fielding, E. J., et al. (2016). Geomorphic and geologic controls of geohazards induced by Nepal's 2015 Gorkha earthquake. *Science* 351, aac8353. doi:10.1126/science.aac8353

Keefer, D. K. (1984). Rock avalanches caused by earthquakes: source characteristics. *Science* 223, 1288–1290. doi:10.1126/science.223.4642.1288

Larsen, I. J., Montgomery, D. R., and Korup, O. (2010). Landslide erosion controlled by hillslope material. *Nat. Geosci.* 3, 247–251. doi:10.1038/ngeo776

Lavé, J., and Avouac, J. P. (2000). Active folding of fluvial terraces across the Siwaliks hills, Himalayas of central Nepal. *J. Geophys. Res. Solid Earth* 105, 5735–5770. doi:10.1029/1999JB900292

Lee, C.-T., Huang, C.-C., Lee, J.-F., Pan, K.-L., Lin, M.-L., and Dong, J.-J. (2008). Statistical approach to earthquake-induced landslide susceptibility. *Eng. Geol.* 100, 43–58. doi:10.1016/j.enggeo.2008.03.004

Li, Z., Liu, J., Wang, W., Ji, C., Zeng, L., Zhang, P., et al. (2015). Tectonic setting and general features of coseismic rupture of the 25 April, 2015M_w 7.8 Gorkha, Nepal earthquake. *Chin. Sci. Bull.* 60, 2640–2655. doi:10.1360/N972015-00559 (in Chinese)

Martha, T. R., Roy, P., Mazumdar, R., Govindharaj, K. B., and Kumar, K. V. (2016). Spatial characteristics of landslides triggered by the 2015 Mw 7.8 (Gorkha) and Mw 7.3 (Dolakha) earthquakes in Nepal. *Landslides* 14, 697–704. doi:10.1007/s10346-016-0763-x

Moss, R. E. S., Thompson, E. M., Scott Kieffer, D., Tiwari, B., Hashash, Y. M. A., Acharya, I., et al. (2015). Geotechnical effects of the 2015 magnitude 7.8 Gorkha, Nepal, earthquake and aftershocks. *Seismol Res. Lett.* 86, 1514–1523. doi:10.1785/0220150158

NASA Earth Observatory (2019). GPM data downloads. Available at: https://pmm.nasa.gov/data-access/downloads/gpm# (Accessed Aug 31, 2019).

National Geological Data Museum of China (2013). Geology map of China with scale of 1:2,500,000. Available at: http://www.ngac.org.cn/Document/Map.aspx?MapId=EC7E1A7A7CF81954E0430100007F182E (Accessed Aug 31, 2019).

Nicoletti, P. G., and Sorriso-Valvo, M. (1991). Geomorphic controls of the shape and mobility of rock avalanches. *Geol. Soc. Am. Bull.* 103, 1365–1373. doi:10.1130/0016-7606(1991)103<1365:gcotsa>2.3.co;2

Niculita, M. (2016). Automatic landslide length and width estimation based on the geometric processing of the bounding box and the geomorphometric analysis of DEMs. *Nat. Hazards Earth Syst. Sci.* 16, 2021–2030. doi:10.5194/nhess-16-2021-2016

Owen, L. A. (2017). Earth surface processes and landscape evolution in the Himalaya: a framework for sustainable development and geohazard mitigation. *Geol. Soc. Spec. Publ.* 462, SP462.9. doi:10.1144/sp462.9

Parise, M., and Jibson, R. W. (2000). A seismic landslide susceptibility rating of geologic units based on analysis of characteristics of landslides triggered by the 17 January, 1994 Northridge, California earthquake. *Eng. Geol.* 58, 251–270. doi:10.1016/S0013-7952(00)00038-7

Parker, R. N., Densmore, A. L., Rosser, N. J., de Michele, M., Li, Y., Huang, R., et al. (2011). Mass wasting triggered by the 2008 Wenchuan earthquake is greater than orogenic growth. *Nat. Geosci.* 4, 449–452. doi:10.1038/ngeo1154

Qi, S., Xu, Q., Zhang, B., Zhou, Y., Lan, H., and Li, L. (2011). Source characteristics of long runout rock avalanches triggered by the 2008 Wenchuan earthquake, China. *J. Asian Earth Sci.* 40, 896–906. doi:10.1016/j.jseaes.2010.05.010

Regmi, A. D., Dhital, M. R., Zhang, J.-q., Su, L.-j., and Chen, X.-q. (2016). Landslide susceptibility assessment of the region affected by the 25 April 2015 Gorkha earthquake of Nepal. *J. Mt. Sci.* 13, 1941–1957. doi:10.1007/s11629-015-3688-2

Roback, K., Clark, M. K., West, A. J., Zekkos, D., Li, G., Gallen, S. F., et al. (2018). The size, distribution, and mobility of landslides caused by the 2015 M_w 7.8 Gorkha earthquake, Nepal. *Geomorphology* 301, 121–138. doi:10.1016/j.geomorph.2017.01.030

Scheidegger, A. E. (1973). On the prediction of the reach and velocity of catastrophic landslides. *Rock Mech.* 5, 231–236. doi:10.1007/BF01301796

Shao, X., Ma, S., Xu, C., Zhang, P., Wen, B., Tian, Y., et al. (2019). Planet image-based inventorying and machine learning-based susceptibility mapping for the landslides triggered by the 2018 Mw6.6 Tomakomai, Japan earthquake. *Remote Sens.* 11, 978, doi:10.3390/rs11080978

Taylor, F. E., Malamud, B. D., Witt, A., and Guzzetti, F. (2018). Landslide shape, ellipticity and length-to-width ratios. *Earth Surf. Process. Landf.* 43, 3164–3189. doi:10.1002/esp.4479

Tian, Y., Owen, L. A., Xu, C., Ma, S., Li, K., Xu, X., et al. (2020). Landslide development within 3 years after the 2015 M_w 7.8 Gorkha earthquake, Nepal. *Landslides* 17, 1251–1267. doi:10.1007/s10346-020-01366-x

Tian, Y., Xu, C., Chen, J., Zhou, Q., and Shen, L. (2017). Geometrical characteristics of earthquake-induced landslides and correlations with control factors: a case study of the 2013 minxian, Gansu, China, M_w 5.9 event. *Landslides* 14, 1915–1927. doi:10.1007/s10346-017-0835-6

Tiwari, B., Ajmera, B., and Dhital, S. (2017). Characteristics of moderate- to large-scale landslides triggered by the M_w 7.8 2015 Gorkha earthquake and its aftershocks. *Landslides* 14, 1297–1318. doi:10.1007/s10346-016-0789-0

Tsou, C.-Y., Chigira, M., Higaki, D., Sato, G., Yagi, H., Sato, H. P., et al. (2018). Topographic and geologic controls on landslides induced by the 2015 Gorkha earthquake and its aftershocks: an example from the Trishuli Valley, central Nepal. *Landslides* 15, 953–965. doi:10.1007/s10346-017-0913-9

USGS (2015). M_w 7.8–36 km E of Khudi, Nepal. Available at: https://earthquake.usgs.gov/earthquakes/eventpage/us20002926/executive#executive (Accessed Aug 21, 2019).

USGS (2019). Search earthquake catalog. Available at: https://earthquake.usgs.gov/earthquakes/search/ (Accessed Oct 10, 2019).

Wang, Y., and Rathje, E. M. (2013). "Regional predictions of earthquake-induced landslides a study of the Niigata-ken Chuestu earthquake." in: 10th international conference on urban earthquake engineering, Tokyo, Japan, March 1–2, 2013.

Weiss, A. (2001). "Topographic position and landforms analysis." in: Poster presentation, ESRI user conference, San Diego, CA, 200, 2001 . Available at: http://www.jennessent.com/downloads/tpi-poster-tnc_18x22.pdf.

Whipple, K. X., Shirzaei, M., Hodges, K. V., and Ramon Arrowsmith, J. (2016). Active shortening within the Himalayan orogenic wedge implied by the 2015 Gorkha earthquake. *Nat. Geosci.* 9, 711–716. doi:10.1038/ngeo2797

Wobus, C. W., Whipple, K. X., and Hodges, K. V. (2006). Neotectonics of the central Nepalese Himalaya: constraints from geomorphology, detrital40Ar/39Ar thermochronology, and thermal modeling. *Tectonics* 25. doi:10.1029/2005TC001935

Xu, C., Tian, Y., Shen, L., Ma, S., Xu, X.-w., Zhou, B., et al. (2018). Database of landslides triggered by 2015 Gorkha (Nepal) M_w 7.8 earthquake. *Seismol. Geol.* 40, 1115–1128. (in Chinese)

Xu, C., Tian, Y., Zhou, B., Ran, H., and Lyu, G. (2017). Landslide damage along Araniko highway and Pasang Lhamu highway and regional assessment of landslide hazard related to the Gorkha, Nepal earthquake of 25 April 2015. *Geoenviron Disasters* 4, 14. doi:10.1186/s40677-017-0078-9

Xu, C., Xu, X., Shen, L., Yao, Q., Tan, X., Kang, W., et al. (2016a). Optimized volume models of earthquake-triggered landslides. *Sci. Rep.* 6, 29797. doi:10.1038/srep29797

Xu, C., and Xu, X. (2014). Statistical analysis of landslides caused by the Mw 6.9 Yushu, China, earthquake of April 14, 2010. *Nat. Hazards* 72, 871–893. doi:10.1007/s11069-014-1038-2

Xu, C., Xu, X., Tian, Y., Shen, L., Yao, Q., Huang, X., et al. (2016b). Two comparable earthquakes produced greatly different coseismic landslides: the 2015 Gorkha, Nepal and 2008 Wenchuan, China events. *J. Earth Sci.* 27, 1008–1015. doi:10.1007/s12583-016-0684-6

Xu, C., Xu, X., and Xu, X. W. (2014). Statistical analysis of landslides caused by the Mw 6.9 Yushu, China, earthquake of April 14, 2010. *Nat. Hazards* 72, 871–1818. doi:10.1007/s11069-014-1038-2

Xu, C., Xu, X., and Yu, G. (2013). Landslides triggered by slipping-fault-generated earthquake on a plateau: an example of the 14 April 2010, Ms 7.1, Yushu, China earthquake. *Landslides* 10, 421–431. doi:10.1007/s10346-012-0340-x

Yin, A., and Harrison, T. M. (2000). Geologic evolution of the Himalayan-Tibetan Orogen. *Annu. Rev. Earth Planet. Sci.* 28, 211–280. doi:10.1146/annurev.earth.28.1.211

Yun, S.-H., Hudnut, K., Owen, S., Webb, F., Simons, M., Sacco, P., et al. (2015). Rapid damage mapping for the 2015Mw 7.8 Gorkha earthquake using synthetic aperture radar data from COSMO-SkyMed and ALOS-2 Satellites. *Seismol Res. Lett.* 86, 1549–1556. doi:10.1785/0220150152

Yang, Z. Y., and Lee, Y. H.(2019). "The fractal characteristics of landslides induced by earthquakes and rainfall in central Taiwan" in Paper presented at the 10th IAEG international congressNottingham, England, 2006.

Conflict of Interest: The authors declare that the research was conducted in the absence of any commercial or financial relationships that could be construed as a potential conflict of interest.

The reviewer (JC) declared a past co-authorship with one of the authors (CX) to the handling editor.

frontiers in Earth Science

ORIGINAL RESEARCH
published: 14 January 2021
doi: 10.3389/feart.2020.610181

Monitoring In-Situ Seismic Response on Rock Slopes Using Ambient Noise Interferometry: Application to the 2019 Changning (Mw 5.7) Earthquake, China

Huibao Huang[1,2], *Shigui Dai*[3] *and Fan Xie*[2]*

[1]Dadu River Hydropower Development Co., Ltd., Chengdu, China, [2]Institute of Geophysics, China Earthquake Administration, Beijing, China, [3]Sichuan Earthquake Administration, Chengdu, China

Study of the mechanical response of rock slopes to moderate earthquakes is important for understanding the local rheology of landslide and earthquake interactions and for mitigating the risks associated with subsurface geological processes in tectonically active mountainous belts. To complement existing point measurements from surface observations (e.g., global positioning system and interferometric synthetic-aperture radar measurements), measuring the ambient noise-based velocity change ($\delta v/v$) allows for remote observations of mechanical state changes of the slope, at depth and continuously in time. We herein investigate the seismic responses of the Pubugou rock slope, a typical steep rock slope in south-west China, to the 2019 Mw 5.7 Changning earthquake. We apply ambient noise interferometry to the slope and measure the coda wave velocity changes at frequencies from 2 to 20 Hz with a 1-h temporal resolution, 2 days before and 14 days after the earthquake. We observe a significant co-seismic wave velocity decrease caused by the Changning earthquake of up to 0.9% followed by a gradual logarithmic recovery process over 2 weeks. The earthquake-induced stress sensitivity of $\delta v/v$ on the slope is estimated as $\sim 3.2 \times 10^{-8}\ \mathrm{Pa}^{-1}$. Through the analysis of the co-seismic and post-seismic $\delta v/v$ with different time lapses of the coda, we characterize the healing process on the slope and also constrain such changes to 75 m in depth. This study highlights the possibility of quantitatively characterizing the slope weakness using moderate earthquakes in mountainous areas in the future.

Keywords: seismic noise, rock slope, seismicity, slow dynamics, velocity change

Edited by:
Chong Xu,
National Institute of Natural Hazards,
China

Reviewed by:
Jia-wen Zhou, Sichuan University,
China
Wentao Yang,
Beijing Forestry University, China

Correspondence:
Fan Xie
xiefan@cea-igp.ac.cn

Specialty section:
This article was submitted to
Geohazards and Georisks,
a section of the journal
Frontiers in Earth Science

Received: *25 September 2020*
Accepted: *12 November 2020*
Published: *14 January 2021*

Citation:
Huang H, Dai S and Xie F (2021)
Monitoring In-Situ Seismic Response
on Rock Slopes Using Ambient Noise
Interferometry: Application to the 2019
Changning (Mw 5.7)
Earthquake, China.
Front. Earth Sci. 8:610181.
doi: 10.3389/feart.2020.610181

INTRODUCTION

Deep-seated rock slopes are widely distributed in the mountainous areas of Sichuan Province, which is one of the most active geohazard regions in China. There are over 300,000 slopes in this area, which are susceptible to a high level of landslide activity (Lin and Wang, 2018). Simultaneously, it is also a seismically active area. Increased seismicity has been recognized in the last decade since the 2008 Wenchuan earthquake (Chigira et al., 2010). According to the earthquake catalogs from Sichuan Earthquake Administration, over 4,000 earthquakes occurred in 2019 with magnitudes ranging from Mw 1 to Mw 5.7.

Mass movement on the damaged rock slopes constitutes a major geological hazard, damaging infrastructure such as dams, roads, railways, and bridges and leading to loss of life. Among a variety of physical parameters (e.g., atmospheric pressure, tide, temperature, and rainfall), seismicity has a strong impact on the damage evolution of the rock slopes as dynamic strain is applied by seismic shaking. Previous studies on seismic hazard assessment on slopes after earthquakes have been based on the statistical analysis of regional inventories of earthquake-triggered landslides (Keefer, 1984; Keefer, 2002). Due to a lack of *in-situ* data and a cost-effective method that is sensitive to the changes of elastic properties, there have been few quantitative studies on earthquake-induced temporal changes on slopes.

Observational evidence (Larose et al., 2015) and theoretical models (Colombero et al., 2017) suggest the earthquake-induced damage is associated with changes in the material's elastic moduli, which lead to failure of the rock slopes. Owing to the heterogeneous elastic nonlinearity, it is hard to quantify such damage on the rock slopes at scales ranging from macroscopic fractures to microscopic contact changes between grains. Nevertheless, it is widely recognized that loss of rigidity is a fundamental signature of the damage development. Therefore, this makes monitoring the changes in elastic wave velocity (Murnaghan, 1951) an ideal method to remotely assess the internal damage development of the rock slopes.

Among the emerging techniques in this field, one promising monitoring approach is ambient seismic noise cross-correlation. This is a passive technique that enables retrieval of impulse responses through cross-correlation of ambient seismic noise recorded at any two sensors. Depending on the multiple scattered coda waves retrieved by the ambient cross-correlation technique (Larose et al., 2006), it is possible to further monitor stress changes of the medium by inferring velocity changes from the phase shift in the coda at different times (Snieder, 2006). This forms the basis of ambient seismic noise interferometry for time-lapse applications. Ambient seismic noise interferometry has been used in geophysics for more than 30 years, e.g., to study the dynamic evolution in faults by monitoring velocity changes caused by nearby earthquakes (Brenguier et al., 2008). This method has been proposed to study the precursor instabilities responsible for landslides. A significant velocity reduction was reported several days before the failure on the Pont Bourquin clay soil of the Swiss Alps (Mainsant et al., 2012). Moreover, the method enhances the knowledge of deformation by environmental variations (e.g., seasonal fluctuations and groundwater infiltration) on slopes with materials composed of clay soil and/or volcanic deposits (Larose et al., 2015).

Monitoring changes of rock slopes during earthquake shaking and the subsequent recovery phase is used to study the dynamic elastic properties of the rock slopes and also to evaluate the damage level. However, to the best of the authors' knowledge, only few observations with limited typology of the slope have successfully tracked co-seismic changes. Even less understood is the healing process due to post-seismic changes when moderate dynamic stress solicitation is applied on rock slopes by a distant earthquake.

This paper focuses on the co-seismic and post-seismic changes on the Pubugou rock slope due to the Changning Mw 5.7 earthquake in 2019. The coda wave velocity changes with a 1-h temporal resolution are measured by applying ambient seismic noise interferometry to continuous recordings on the slope. With these results, some possible explanations and implications of the observations are discussed.

MATERIALS AND METHODS

Study Area

As shown in **Figure 1A**, the Pubugou rock slope is in the middle of the deep-seated bare bedrock alpine valleys of Dadu River between the west margin of Sichuan Basin and the Tibet Plateau. The rock slope is ~800 m from the dam of the Pubugou Hydropower Station (3,600 MW capacity) and is surrounded by active faults characterized by complex Cenozoic structures. There are intense deformations and high levels of seismic activity in this area.

Figure 1B illustrates that the east-facing slope with its height of about 1,180 m above mean sea level (m a.m.s.l.) consists of highly weathered tuffaceous rocks and diabases, in addition to gravels with thin clays on a shallow layer at the upper rear part. The gradient of the slope is approximately 45°. The surface displacement monitoring indicates progressive toppling of the upper part (980–1,180 m a.s.m.l.) at an annual displacement rate of 21 mm/yr. The damaged lower part (< 980 m a.s.m.l.) has been reinforced by removing shallow weathered gravels and rocks and inserting ~100 anti-slide piles with cement grout into drilled holes. Thus, the annual displacement rate in this area is now approximately 3 mm/yr. According to the drilling data provided by a geology study (Yang et al., 2013), intact rocks exist at an average depth of ~70 m. The drilling samples also suggest that the weathering level on the rocky material varies with depth. The strongest weathered material appears at a shallow depth of a few meters.

Data

As illustrated in **Figure 2A**, two observational huts (T01 and T02) were located ~157 m apart on either side of the center part (~990 m a.s.m.l.) of the slope. In such way, a global slope coverage due to limited sensors as well as strong mobile network signal condition was expected. Each hut had a three-component short period seismometer (GL-CS2, GEOLIGHT™) installed, which allowed a relatively flat frequency response from 0.5 to 50 Hz. Each seismometer was digitized by a 24-bit EDAS-24 GN (GEOLIGHT™) at a 100 Hz sampling rate with a system clock error less than 10^{-6} s. The seismic noise data were stored locally in 1-h long records and simultaneously transmitted to the server at Sichuan Earthquake Administration via a mobile network.

A bi-frequency global positioning system (GPS) receptor (GMX902, Leica™) was installed on the roof of each hut, together with a GPS antenna at each hut, to measure the surface deformation along the central part of the slope since April 24, 2019. The hourly global navigation system satellite

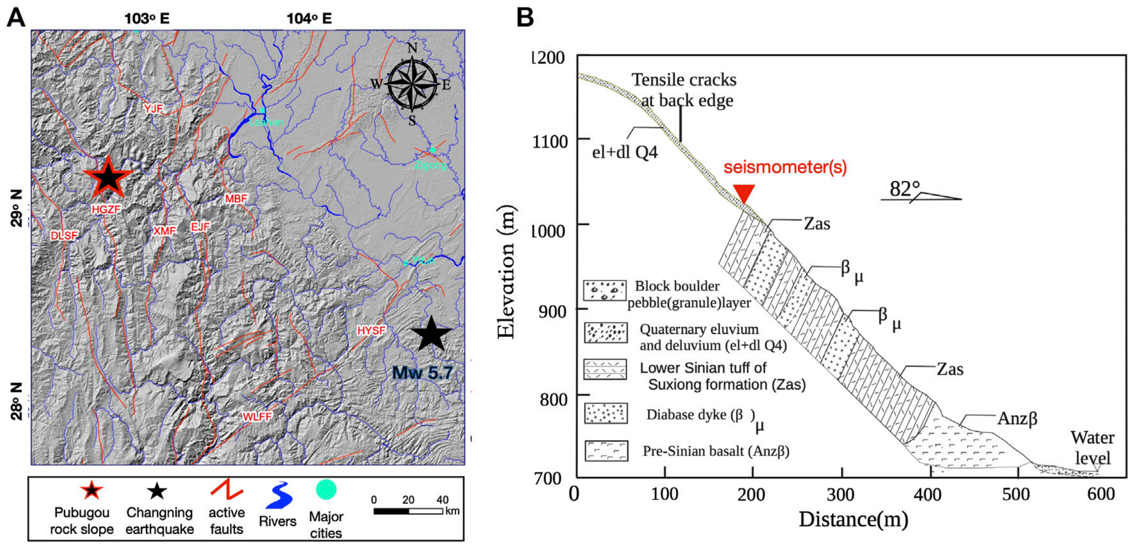

FIGURE 1 | (A) Tectonic settings surrounding the Pubugou slope (the hypocenter of the Changning Mw 5.7 earthquake is indicated by the black star). **(B)** Geological profile of the slope, mainly composed of sedimentary rocks.

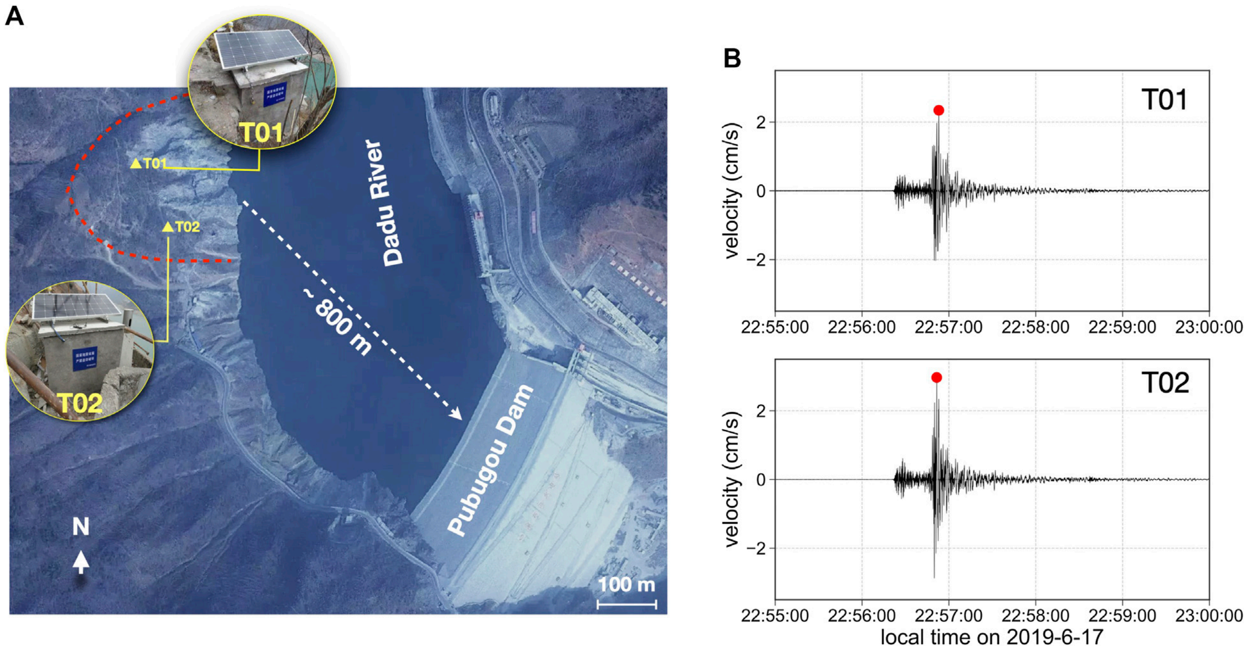

FIGURE 2 | (A) Configuration of two seismic stations (yellow triangles) on the slope (the boundary of the slope is delineated by a red dashed line). **(B)** Peak ground velocity (red circles) due to the Changning Mw 5.7 earthquake recorded for its vertical component by the two stations T01 and T02 on the slope.

(GNSS) measurements were transformed into daily values by averaging over every 24 h. Daily rainfall data were gathered from a weather station on the east bank of the rock slope.

On June 17, 2019, an Mw 5.7 earthquake occurred in Changning county, a region of Sichuan Province in southwest China. Despite the distance between the rock slope and the epicenter of the earthquake being ~221 km, the seismometers on the slope clearly recorded earthquake-induced ground motion. In **Figure 2B**, the seismic shaking intensity is estimated by directly computing the peak ground velocity (PGV) for its vertical component. The measured PGV is 2.34 cm/s for T01 and 2.96 cm/s for T02. Hence, the

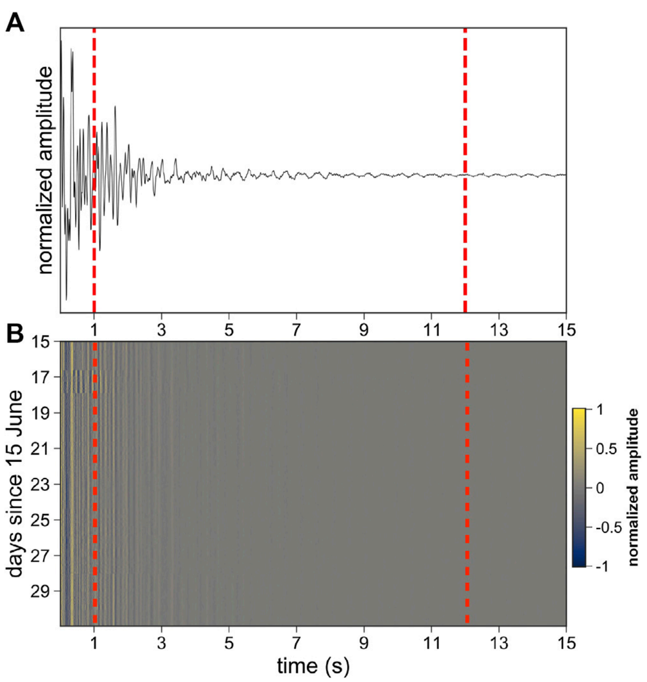

FIGURE 3 | (A) Reference trace averaged over all the correlograms. **(B)** Hourly correlograms from June 15 to June 30, 2019, in the 2–20 Hz frequency range. Vertical red dash lines mark the time window (1–12 s) of the coda used to estimate $\delta v/v$.

approximate PGV is 2.62 cm/s by averaging the PGV value measured at each seismometer.

METHOD

The hourly ambient seismic noise was pre-processed at each seismometer following a standard routine procedure (Larose et al., 2015): the hourly seismic noise was first normalized in the frequency domain between 2 and 20 Hz using the whitening method and then normalized in the time domain using the clipping method with amplitudes exceeding three standard deviations. The purpose of the above steps was to enhance the specific frequency band of the ambient noise and also reduce the impact of spatially isolated noise sources such as earthquakes. Finally, the vertical components of the pre-processed noise values between the seismometers were cross-correlated for each hour with a 15 s time lag. As the cross-correlation functions were asymmetric, due to the anisotropy of the noise propagation direction, the causal and acausal parts of the cross-correlation functions were further averaged.

Figure 3B illustrates the 384 hourly correlograms h_i (i denotes the hour during the period of interest from June 15 to June 30) calculated, along with the reference h_{ref} (**Figure 3A**) that was obtained by averaging all the correlograms.

To understand how changes in seismic velocities can be measured from phase shifts in the correlograms, consider a ray that travels a distance L between two seismometers in time t at velocity v. These quantities are related via

$$L = vt \tag{1}$$

Taking the differential of L,

$$\delta L = t\delta v + v\delta t \tag{2}$$

For a homogeneous velocity change, the ray path does not change ($\delta L = 0$). This yields a relation between the velocity change δv and the change in arrival time δt:

$$\frac{\delta t}{t} = -\frac{\delta v}{v} \tag{3}$$

The change in arrival time scales linearly with lag time, resulting in stretching or compression of the waveform following a decrease or an increase, respectively. Thus, to quantify the temporal changes, the stretching method was applied, which consisted of a grid search testing over a series of candidate velocity changes $\delta v/v_k$ between $h_i(t)$ and the stretched reference signal $h_{\text{ref}}(t(1+\delta v/v_k))$ within a given time window $[t1, t2]$:

$$\text{CC}\left(\frac{\delta v}{v_k}\right) = \frac{\int_{t1}^{t2} h_{\text{ref}}[t(1+\delta v/v_k)]h_i(t)\text{d}t}{\sqrt{\int_{t1}^{t2} h_{\text{ref}}[t(1+\delta v/\text{v}_\text{k})]^2\text{d}t\int_{\text{t1}}^{\text{t2}}\text{h}_\text{i}(\text{t})^2\text{d}t}} \tag{4}$$

The apparent velocity changes $\delta v/v$ can be obtained by maximizing the correlation coefficient $\text{CC}(\delta v/v_k)$. The uncertainty on $\delta v/v$, which is the indicator of the measurement reliability, can be estimated using the theoretical formula proposed by Weaver et al. (2011):

$$\sigma_e = \frac{\sqrt{1-\text{CC}^2}}{2\text{CC}}\sqrt{\frac{6\sqrt{\pi/2}T}{\omega_c^2(t_2^3 - t_1^3)}} \tag{5}$$

where T is the inverse of the frequency bandwidth and ω_c is the central frequency. The lower the uncertainty is, the robuster the measurement is.

RESULTS

Co-Seismic Change

A time window from 1 to 12 s was used (**Figure 3**) to measure the *in-situ* global temporal change using scattered coda waves. **Figure 4A** illustrates the general evolution of the apparent velocity change together with its color-coded uncertainty as a function of time during the period of interest from June 15 to June 30. The uncertainty ($\sim 10^{-5}$) is one or two orders of magnitude smaller than the apparent velocity change ($\sim 10^{-3}$), suggesting that the measurement is consistently good in quality.

We observe a rapid co-seismic velocity drop by ~0.9% on the slope. Simultaneously, the recorded PGV is 2.34 cm/s for T01 and 2.96 cm/s for T02 due to the Changning earthquake. Thanks to the measured PGV, the earthquake-produced dynamics stress on the slope can be estimated using the following equation (Hill et al., 1993):

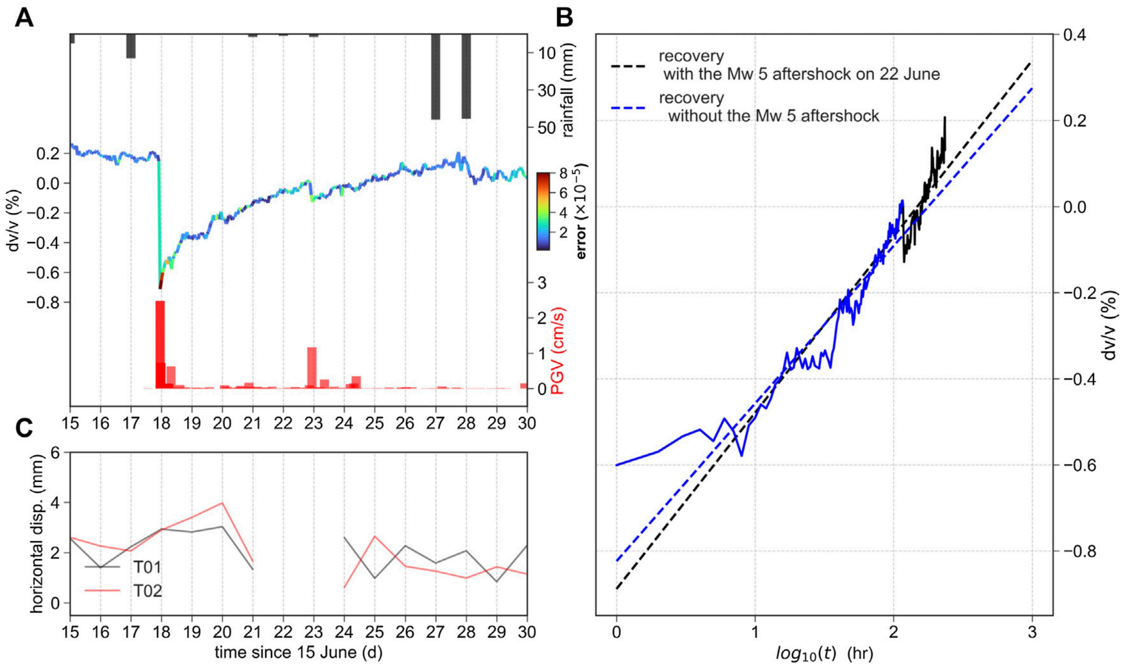

FIGURE 4 | (A) $\delta v/v$ decrease and subsequent recovery due to the Changning Mw 5.7 earthquake. **(B)** $\delta v/v$ as a logarithmic function of recovery time for the earthquake (the black dash line characterizes the recovery time with the Mw 5 aftershock on June 22, and the blue dash line characterizes the recovery time without the Mw 5 aftershock). **(C)** Time series of GNSS horizontal displacements at two stations with a 1-day sampling rate.

$$\Delta\sigma_d = G\frac{PGV}{v_p} \tag{6}$$

where G is the bulk modulus and v_p is the bulk velocity. As with the estimation of physical properties of tuffaceous rocks (Yang et al., 2013), we use $v_p = 1.5$ km/s and $G = 1.6$ GPa. Hence, $\Delta\sigma_d$ is approximately ~280 kPa, and a velocity-stress sensitivity of $\sim 3.2 \times 10^{-8}$ Pa^{-1} can be estimated.

The seismologists (Peng et al., 2010; Gonzalez-Huizar et al., 2012) have reported that even though the earthquake generating PGV remains as low as millimeters per second at a distance of thousand kilometers, the induced stress loading still exists at least 10,000 Pa and has the potential to remotely trigger seismicity. Therefore, such a strong but sudden decease in velocity cannot be influenced by the undrained loading effect due to the groundwater-induced liquefaction of the slope (Lecocq et al., 2017), or by the thermal loading effect due to the air temperate change (Tsai, 2011). The only possible mechanism is attributed to the opening of new or pre-existing cracks/fractures on the slope which decrease the elastic modulus due to the stress loading of earthquake shaking (Bontemps et al., 2020). We interpret that the observed co-seismic velocity drop is caused by the weakness of the slope due to the earthquake-induced dynamic stress transient.

Post-Seismic Change

Almost immediately after the co-seismic velocity drop, a clear logarithmic recovery of the velocity change to the pre-earthquake state is observed over approximately 14 days. Such a healing increase back toward its initial value following a logarithmic evolution after moderate solicitation is referred to as "slow dynamics" (TenCate, 2011).

Slow dynamics is a nonlinear elastic response of the material after imposing a strain of moderate amplitude that does not generate any macroscopic damage and has been found to be universal in granular solids of various compositions ranging from that of the Earth's crust to the inter-grained microscopic cracks of sedimentary rocks or concrete samples of the order of micrometers (TenCate et al., 2000). Hence, we interpret this recovery phase as a nonlinear response to the re-compaction of the opened fractures and micro-cracks due to seismic shaking. Note there was an earthquake sequence that began with an Mw 5.7 earthquake on June 17 and comprised ~600 aftershocks for more than 2 weeks. Within this context, several moderate earthquake-induced ground motion events were recorded on the slope during this period. Among them, there was a 0.1% co-seismic velocity decrease caused by the largest Mw 5 aftershock on June 22 during the healing process, with a PGV value of 1 cm/s on the slope.

In addition, a small velocity fluctuation was observed at the end of the recovery phase. It was noted that such velocity fluctuations occurred after 2 days of precipitations with a total of ~90 mm rainfall. Rather than earthquake shaking (with loading effects that have low PGV values (< 0.1 cm/s)) during these days, the possible main mechanism response for such velocity fluctuations was rigidity decrease due to an augmentation of the water content/pore saturation in the highly weathered granular material of the slope above a certain rainfall threshold (Guzzetti et al., 2008). However, the complex interactions between seismic shaking and rainfall are out of the scope of this work and will be demonstrated in a separate paper.

To quantify the healing process, the logarithmic evolution of $\delta v/v$ can be fitted as follows:

$$\delta v/v = A - m\log_{10}(d) \tag{7}$$

where d is the recovery time in hours, A is the extrapolated $\delta v/v$ after the co-seismic shaking, m is the slope of the logarithmic decay, and $10^{A/m}$ represents the recovery time.

Figure 4B shows the estimation of these parameters with (June 18–27) and without (June 18–22) the Mw 5 aftershock on June 22. The characterized recovery times ($10^{A/m}$) are 146 and 177 h, respectively.

This suggests that the rigidity of the slope experiences a faster recovery process with the effect of additional small seismic event(s). It also implies that even seismic shaking with its PGV value as low as 1 cm/s can accelerate the healing recovery processes by altering the slope's weakness. A possible mechanism for this effect is the re-arranging of existing grains/cracks that favor the closing of opened earthquake-generated micro/macro-fractures (Bontemps et al., 2020).

It is worth noting that compared with ambient noise interferometry, the horizontal displacement (**Figure 4C**) measured at each seismometer site did not show significant co-seismic and post-seismic effects. One reason is that due to low temporal resolution (1 day) of the GNSS measurements, it was hard to track sudden earthquake-induced changes over such a short time. However, such measurements hardly reveal small changes of mechanical properties of the material because they are less sensitive to the state of stress, rigidity, or damage due to their surface measurement configuration.

Different Times in the Coda

The changes are assumed to be in a spatially global homogeneous medium (Snieder, 2006). Thus, velocity change is proportional to a time shift in the later arriving coda waves. However, as a strong heterogeneous material, velocity change in the rock slope is not global, but is influenced by the time in the coda with respect to the sampled domain. Therefore, instead of analyzing a long coda segment as in the previous section, the stretching technique is applied to a series of sliding windows of 3 s in the coda, with the window width corresponding to six periods of applied lowest frequency (2 Hz).

Figure 5 illustrates the velocity changes within seven consecutive shorter time windows centered around t_c = 1.5, 3, 4.5, 6, 7.5, 9, and 10.5 s. The strongest co-seismic velocity reduction and post-seismic recovery process were found at the earliest time of t_c = 1.5 s in the coda. With increasing time, the magnitude of the co-seismic velocity drop decreased from ~0.9% to ~0.1%. Simultaneously, a weaker logarithmic post-seismic recovery process in the later arriving coda was observed. The weakest co-seismic and post-seismic velocity perturbations were observed during the last time window of t_c = 10.5 s in the coda.

As the early coda waves are mostly sensitive to the changes at shallow depths, as well as the weaker bonds between the elements of the weathered tuff rocks, we suggest that earthquake-induced strong ground motion can introduce more opening cracks/fractures, which is the signature of mechanical damage in the form of crack appearance, at a shallow depth of the higher-weathered rock material in the slope.

It is worth noting that the sensitivity to absolute depth requires detailed measurements of the scattering properties of the slope, which are not available for the study area. Nevertheless, the relative depth resolution of coda waves measured at different time lapses of the coda using existing theoretical and numerical testing can be discussed.

DISCUSSION

The *in-situ* apparent velocity evolution on the rock slope due to moderate earthquake shaking raises at least two questions. First, what is the depth sensitivity of the measurements? Second, why is the slow dynamics effect due to earthquake shaking related to the damage features?

To answer the first question, we estimate that the first-order depth resolution for the velocity decrease is due to earthquake. Although the depth sensitivity of coda waves has not yet been fully solved (Obermann and Hillers, 2019), as the study area is neither a layered medium nor a completely solid rock material, we thus evaluate the bulk sensitivity of the scattered coda waves by considering a two-dimensional body wave sensitivity kernel formulation (Obermann and Hillers, 2019):

$$K(s, r, r_0, t) = \frac{1}{p(s, r, t)} \int_0^t p(s, r_0, t') I(r_0, r, t - t') \mathrm{d}t' \tag{8}$$

where s and r are the positions of the stations, r_0 is the local velocity variation, and t is the lapse time. The energy propagator p is calculated by the radiative transfer solution approximation for isotropic scattering of the medium:

$$\begin{aligned} p(s, r, t) = {} & \frac{e^{-ct\ell^{-1}}}{2\pi c\|s - r\|} \delta\left(t - \frac{\|s - r\|}{c}\right) + \frac{e^{\ell^{-1}\left(\sqrt{c^2t^2 - \|s-r\|^2} - ct\right)}}{2\pi\ell\sqrt{c^2t^2 - \|s - r\|^2}} \\ & \times H\left(t - \frac{\|s - r\|}{c}\right) \end{aligned} \tag{9}$$

where $H(x)$ is the Heaviside function and c is the energy velocity.

With an empirical scattering mean free path of ~10 m as well as a bulk energy velocity of ~1,100 m/s, **Figure 6A** gives the theoretical depth sensitivities with respect to the different time lapses (t_c) of the coda, in which sensitivity is normalized by a body wave kernel.

Figure 6B plots the normalized depth sensitivities with values greater than 10% as a function of measured co-seismic velocity reduction at each lapse time. **Figure 6B** shows that the $\delta v/v$ measurement is most sensitive to changes within the top ~100 m, and velocity reduction varies with its depth above ~75 m. This result is in agreement with geological investigation that the intact

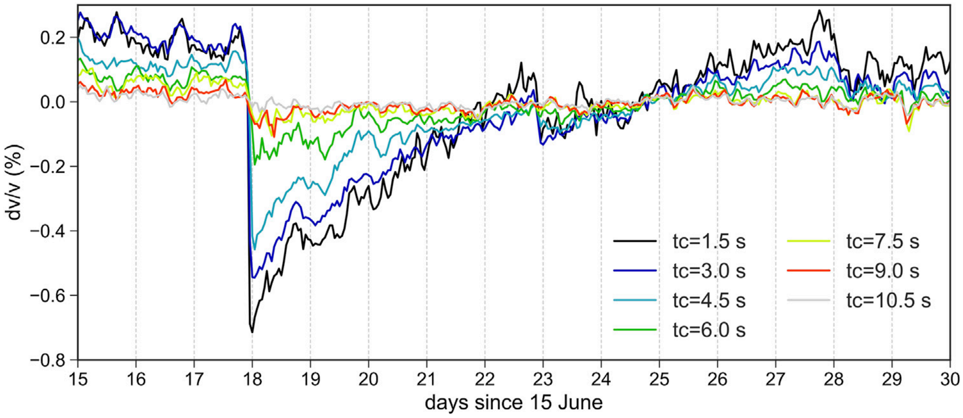

FIGURE 5 | Velocity changes with seven different time lapses of the coda.

rocky material exists to an average depth of ~70 m, where it is less affected by the seismic shaking.

For the second question, due to their direct sensitivity to the higher-order elastic properties of materials, scattered coda waves are more sensitive to the nonlinear elastic response of the material than direct waves (Xie et al., 2018). Compared with nondestructive testing techniques based on common elastic waves, the emerging methods based on coda waves have shown great promise in terms of being more accurate and sensitive in detecting the initiation of damage in various solid materials as early as possible (Xie et al., 2019). As a particularly attractive nonlinear elastic effect, time-logarithmic recovery (slow dynamics) back to the unperturbed elastic modulus following a sharp drop in the elastic modulus (fast dynamics) has been reported in response to moderate mechanical solicitation. Such nonlinear responses were first probed with nonlinear resonant ultrasound spectroscopy and can now be monitored efficiently via velocity changes from coda wave interferometry at various scales (Tremblay et al., 2010).

As far as earthquake-triggered landslides are concerned, some studies have suggested that in contrast to the post-seismic recovery during the dry season, rainfall-produced fluid activities disturbed the post-seismic relaxation process causing a slower recovery time (Bontemps et al., 2020). Laboratory studies have also suggested that the characterized

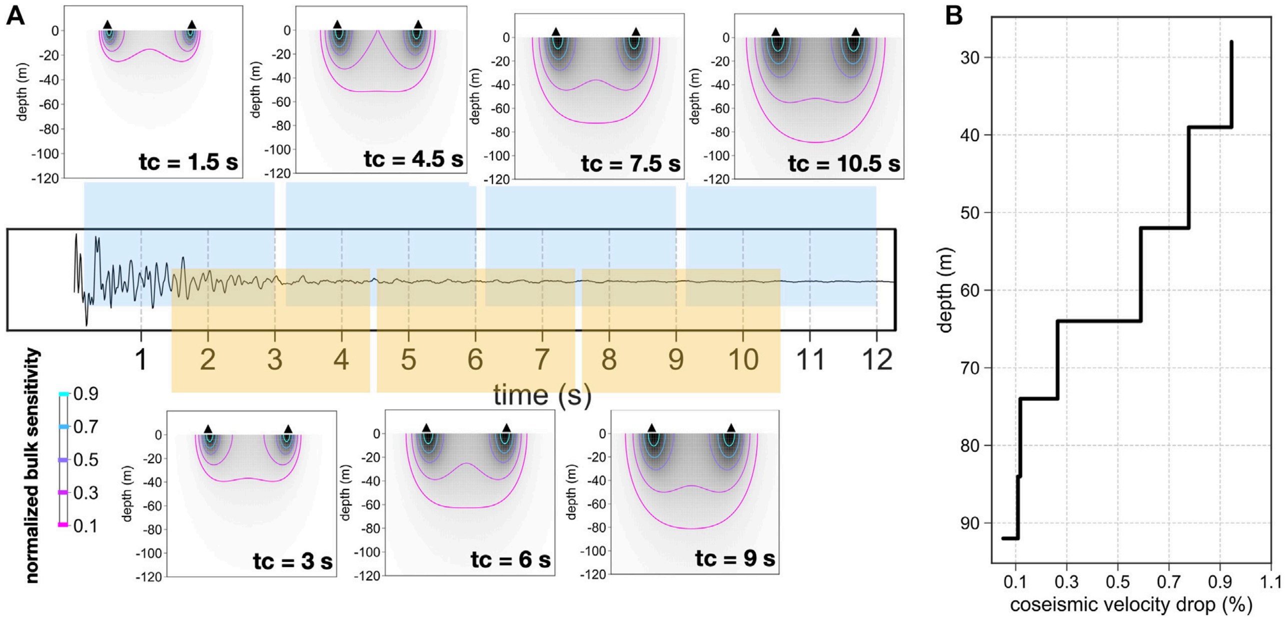

FIGURE 6 | (A) Numerical modeling of the depth resolution of coda waves measured at different time lapses of the coda. **(B)** Kernel depth sensitivity values greater than 10% as a function of measured co-seismic velocity reduction at each lapse time.

recovery times are dependent on the damage of the medium (Tremblay et al., 2010).

In addition, in contrast to seismometer's record, daily GNSS has been applied comprehensively to measure subtle surface mass deformation at a high confidence level of millimeter scale with 24-h static data. It is presumed that the deformation continuously accumulates from months to years, where the GNSS suffices in such high precision level. Nevertheless, there are indeed strong-motion scenarios with rapid deformation (e.g., storm surge loading, pre-eruption volcanic unrest, and earthquakes), which require epoch-wise GPS displacements to capture motions on a wide sub-daily timescale from seconds to hours. However, high-rate GPS solutions to detect sub-daily deformations in a reliable manner are still of great challenges as the magnitudes of such signals are usually close to the lower bound of GNSS carrier-phase measurement precision (Bilich et al. (2008); Geng et al. (2017)). Therefore, so far, it is hard for current GNSS techniques to reveal such small changes of mechanical properties of the rock slope due to their low sensitivity.

To summarize, from scientific point of view, this work quantitatively characterizes the weak but solid dynamic loading effect due to a distant earthquake and subsequent time-dependent recovery process in terms of elastic change using ambient noise interferometry. It is the first time to reveal such physical process inside the rock slope at such highly temporal (1-h) and stress-sensitive ($\sim 3 \times 10^{-8}\ \mathrm{Pa}^{-1}$) ways due to seismic shaking at a distance over 200 km. It facilitates the understanding of on-site damage evolution of the rock slope during the earthquake. From engineering point of view, since seismic shaking is ubiquitous in tectonically active mountainous belts, it has the potential to quantitatively characterize the slope weakness, which is susceptible to nonlinear elastic changes in terms of velocity changes by monitoring the post-seismic relaxation process. It facilitates the *in-situ* seismic hazard assessment of the rock slope during the earthquake which was previously based on the statistical analysis of regional inventories of earthquake-triggered landslides.

CONCLUSIONS

This study has applied *in-situ* ambient noise interferometry to two seismic stations installed on a slope and has measured coda wave velocity changes at frequencies between 2 and 20 Hz with a 1-h temporal resolution, 2 days before and 14 days after an earthquake. The findings are as follows:

(1) Co-seismic wave velocity decreases caused by the Changning earthquake of up to ~0.9% were followed by a gradual logarithmic recovery process over 2 weeks. An earthquake-induced stress sensitivity of $\delta v/v$ on the slope was estimated as $\sim 3.2 \times 10^{-8}\ \mathrm{Pa}^{-1}$.
(2) By analyzing the co-seismic and post-seismic $\delta v/v$ with different coda time lapses, the healing process on the slope was characterized, and such changes were constrained to ~ 75 m in depth.
(3) It may be possible to quantitatively characterize slope weakness using moderate earthquakes in mountainous areas in the future.

DATA AVAILABILITY STATEMENT

The datasets for this study can be obtained from the repository on Figshare: https://figshare.com/articles/dataset/Monitoring_in-situ_seismic_response_on_rock_slope_with_ambient_noise_interferometry_Application_to_the_2019_Changning_Mw_5_7_Earthquake_China/13530911.

AUTHOR CONTRIBUTIONS

HH and FX designed the experiments, analyzed the results, and wrote the paper. SD collected the earthquake catalogue and processed the data acquired. All authors contributed to the manuscript revision.

FUNDING

FX acknowledges funding from the Central Research Institutes of Basic Research and Public Service Special Operations (Grant No. DQJB19B24) and the National Science Foundation of China (Grant No. NSFC41874061).

ACKNOWLEDGMENTS

The authors are grateful to the Editor Chong Xu and three anonymous reviewers for comments and suggestions that significantly improved this manuscript. They also thank the Editor Chong Xu for his efforts on modification of the figures. They thank Sichuan Luopin Science and Technology Company for supporting seismometers, data acquisition system, and maintenance service.

REFERENCES

Bilich, A., Cassidy, J. F., and Larson, K. M. (2008). Gps seismology: application to the 2002 mw 7.9 denali fault earthquake. *Bull. Seismol. Soc. Am.* 98 (2), 593–606. doi:10.1785/0120070096

Bontemps, N., Lacroix, P., Larose, E., Jara, J., and Taipe, E. (2020). Rain and small earthquakes maintain a slow-moving landslide in a persistent critical state. *Nat. Commun.* 11, 1–10. doi:10.1038/s41467-020-14445-3

Brenguier, F., Campillo, M., Hadziioannou, C., Shapiro, N. M., Nadeau, R. M., and Larose, E. (2008). Postseismic relaxation along the san andreas fault at parkfield from continuous seismological observations. *Science* 321, 1478–1481. doi:10.1126/science.1160943

Chigira, M., Wu, X., Inokuchi, T., and Wang, G. (2010). Landslides induced by the 2008 wenchuan earthquake, sichuan, China. *Geomorphology* 118 (3-4), 225–238. doi:10.1016/j.geomorph.2010.01.003

Colombero, C., Baillet, L., Comina, C., Jongmans, D., and Vinciguerra, S. (2017). Characterization of the 3-d fracture setting of an unstable rock mass: from surface and seismic investigations to numerical modeling. *J. Geophys. Res.: Solid Earth* 122 (8), 6346–6366. doi:10.1002/2017jb014111

Geng, J., Jiang, P., and Liu, J. (2017). Integrating gps with glonass for high-rate seismogeodesy. *Geophys. Res. Lett.* 44 (7), 3139–3146. doi:10.1002/2017gl072808

Gonzalez-Huizar, H., Velasco, A. A., Peng, Z., and Castro, R. R. (2012). Remote triggered seismicity caused by the 2011, m9. 0 tohoku-oki, Japan earthquake. *Geophys. Res. Lett.* 39 (10), doi:10.1029/2012gl051015

Guzzetti, F., Peruccacci, S., Rossi, M., and Stark, C. P. (2008). The rainfall intensity–duration control of shallow landslides and debris flows: an update. *Landslides* 5 (1), 3–17. doi:10.1007/s10346-007-0112-1

Hill, D. P., Reasenberg, P. A., Michael, A., Arabaz, W. J., Beroza, G., Brumbaugh, D., et al. (1993). Seismicity remotely triggered by the magnitude 7.3 landers, California, earthquake. *Science* 260, 1617–1623. doi:10.1126/science.260.5114.1617

Keefer, D. K. (1984). Landslides caused by earthquakes. *Geol. Soc. Am. Bull.* 95 (4), 406–421. doi:10.1130/0016-7606(1984)95<406:lcbe>2.0.co;2

Keefer, D. K. (2002). Investigating landslides caused by earthquakes – a historical review. *Surv. Geophys.* 23, 473–510. doi:10.1023/A:1021274710840

Larose, E., Montaldo, G., Derode, A., and Campillo, M. (2006). Passive imaging of localized reflectors and interfaces in open media. *Appl. Phys. Lett.* 88 (10), 104103. doi:10.1063/1.2186112

Larose, E., Carrière, S., Voisin, C., Bottelin, P., Baillet, L., Guéguen, P., et al. (2015). Environmental seismology: what can we learn on earth surface processes with ambient noise?. *J. Appl. Geophys.* 116, 62–74. doi:10.1016/j.jappgeo.2015.02.001

Lecocq, T., Longuevergne, L., Pedersen, H. A., Brenguier, F., and Stammler, K. (2017). Monitoring ground water storage at mesoscale using seismic noise: 30 years of continuous observation and thermo-elastic and hydrological modeling. *Sci. Rep.* 7, 14241–16. doi:10.1038/s41598-017-14468-9

Lin, Q., and Wang, Y. (2018). Spatial and temporal analysis of a fatal landslide inventory in China from 1950 to 2016. *Landslides* 15 (12), 2357–2372. doi:10.1007/s10346-018-1037-6

Mainsant, G., Larose, E., Brönnimann, C., Jongmans, D., Michoud, C., and Jaboyedoff, M. (2012). Ambient seismic noise monitoring of a clay landslide: toward failure prediction. *J. Geophys. Res.: Earth Surface* 117 (F1), doi:10.1029/2011JF002159

Murnaghan, F. D. (1951). *Finite deformation of an elastic solid*. Hoboken, NJ; Wiley

Obermann, A., and Hillers, G. (2019). Seismic time-lapse interferometry across scales, in *Advances in geophysics*, 60. (Amsterdam, Netherlands; Elsevier), 65–143. doi:10.1016/bs.agph.2019.06.001

Peng, Z., Hill, D. P., Shelly, D. R., and Aiken, C. (2010). Remotely triggered microearthquakes and tremor in central California following the 2010 mw 8.8 Chile earthquake. *Geophys. Res. Lett.* 37 (24), doi:10.1029/2010gl045462

Snieder, R. (2006). The theory of coda wave interferometry. *Pure Appl. Geophys.* 163 (2-3), 455–473. doi:10.1007/s00024-005-0026-6

TenCate, J. A., Smith, E., and Guyer, R. A. (2000). Universal slow dynamics in granular solids. *Phys. Rev. Lett.* 85, 1020. doi:10.1103/PhysRevLett.85.1020

TenCate, J. A. (2011). Slow dynamics of earth materials: an experimental overview. *Pure Appl. Geophys.* 168 (12), 2211–2219. doi:10.1007/s00024-011-0268-4

Tremblay, N., Larose, E., and Rossetto, V. (2010). Probing slow dynamics of consolidated granular multicomposite materials by diffuse acoustic wave spectroscopy. *J. Acoust. Soc. Am.* 127, 1239–1243. doi:10.1121/1.3294553

Tsai, V. C. (2011). A model for seasonal changes in gps positions and seismic wave speeds due to thermoelastic and hydrologic variations. *J. Geophys. Res.: Solid Earth* 116 (B4). doi:10.1029/2010jb008156

Weaver, R. L., Hadziioannou, C., Larose, E., and Campillo, M. (2011). On the precision of noise correlation interferometry. *Geophys. J. Int.* 185 (3), 1384–1392. doi:10.1111/j.1365-246x.2011.05015.x

Xie, F., Larose, E., Moreau, L., Zhang, Y., and Planes, T. (2018). Characterizing extended changes in multiple scattering media using coda wave decorrelation: numerical simulations. *Waves Random Complex Media* 28 (1), 1–14. doi:10.1080/17455030.2017.1308042

Xie, F., Li, W., and Zhang, Y. (2019). Monitoring of environmental loading effect on the steel with different plastic deformation by diffuse ultrasound. *Structural Health Monitoring-an International Journal* 18 (2), 602–609. doi:10.1177/1475921718762323

Yang, X., Deng, J., Chen, Q., and Zheng, J. (2013). Characteristics and analysis of deformation of tension-displaced rock mass on right bank at head area of pubugou hydropower station. *Chin. J. Rock Mech. Eng.* 32, 549–552.[in Chinese, with English summary]

Conflict of Interest: Author, HH, is employed by the Dadu River Hydropower Development Co., Ltd. The remaining authors declare that the research was conducted in the absence of any commercial or financial relationships that could be construed as a potential conflict of interest.

frontiers
in Earth Science

ORIGINAL RESEARCH
published: 20 January 2021
doi: 10.3389/feart.2020.633342

Using Google Earth Images to Extract Dense Landslides Induced by Historical Earthquakes at the Southwest of Ordos, China

Du Peng, Xu Yueren, Tian Qinjian and Li Wenqiao*

Key Laboratory of Earthquake Prediction, Institute of Earthquake Forecasting, China Earthquake Administration, Beijing, China

As historical earthquake records are simple, determining the source parameters of historical strong earthquakes over an extended period is difficult. There are numerous uncertainties in the study of historical earthquakes based on limited literature records. Co-seismic landslide interpretation combined with historical documents can yield the possibility of reducing these uncertainties. The dense co-seismic landslides can be preserved for hundreds to thousands of years in Loess Plateau, North China; furthermore, there are notable attribute differences between earthquake landslides and rainfall-triggered landslides. Along the southwestern margin of the Ordos Block, only one severe earthquake has been recorded in the past 3,000 years. The records of "Sanchuan exhaustion and Qishan collapse" provide clues for an investigation of the 780 BC Qishan earthquake. In this study, combined with historical documents, current high-resolution Google Earth images were used to extract historical landslides along the southwestern of the Ordos Block. There were 6,876 landslides with a total area of 643 km^2. The landslide-intensive areas were mainly distributed along the Longxian–Qishan–Mazhao Fault in the loess valley area on the northeastern side of the fault. Loess tableland and river terraces occur on the southwest side of the fault; dense landslides have not been examined due to the topographical conditions in this area. By analyzing the spatial distribution of historical earthquake damage in this region, comparing the characteristics of rainfall-triggered landslides, and combining existing dating results for bedrock collapse and loess landslides, the interpretation of dense historical landslides can be linked to the Qishan Earthquake. The interpretation results are associated with historical records. Analyses of current earthquake cases show that the distribution of dense landslides triggered by strong earthquakes can indicate the episeismic area of an earthquake. In addition, the non-integrated landslide catalog without small- and medium-scale coseismic landslides can be used to effectively determine the source parameters of historical strong earthquakes and perform quantitative evaluations. This study evaluates the focal parameters of the 780 BC Qishan earthquake based on interpretations of the spatial distribution range of historical landslides as representations of the range of the extreme earthquake zone.

Keywords: 780BC Qishan Earthquake, Earthquake-triggered landslides, Loess plateau, Google Earth, seismic parameters

Edited by:
Chong Xu,
National Institute of Natural Hazards,
China

Reviewed by:
Jixiang Xu,
China University of Geosciences,
China
Yulong Cui,
Anhui University of Science and
Technology, China

****Correspondence:***
Xu Yueren
39021865@qq.com

Specialty section:
This article was submitted to
Geohazards and Georisks,
a section of the journal
Frontiers in Earth Science

Received: *25 November 2020*
Accepted: *17 December 2020*
Published: *20 January 2021*

Citation:
Peng D, Yueren X, Qinjian T and Wenqiao L (2021) Using Google Earth Images to Extract Dense Landslides Induced by Historical Earthquakes at the Southwest of Ordos, China.
Front. Earth Sci. 8:633342.
doi: 10.3389/feart.2020.633342

INTRODUCTION

The macro-epicenter, magnitude, range of influence, and rupture scale of historical earthquakes are mostly based on damages recorded in historical documents. However, for earlier historical earthquakes, due to the long history and unknown or missing historical records, determining the relevant seismic parameters is often difficult, or there is significant uncertainty. Previous studies have shown that in addition to fault investigations, the spatial distribution of coseismic landslides can indicate the seismic intensity and rupture zone (Dadson et al., 2004; Meunier et al., 2008; Larsen et al., 2010; Parker et al., 2011; Yuan D et al., 2013). The Wenchuan earthquake produced a 240 km long surface rupture zone. Within the 240 km range, the cumulative number of landslides accounted for 86% of the total landslides triggered by the Wenchuan earthquake, and the cumulative landslide area accounted for 91% of the total landslides triggered by the Wenchuan earthquake. Landslides triggered by the Wenchuan earthquake were mainly distributed in the IX degree area. The landslide area within the IX degree area accounted for 81.1% of the total landslide area while the landslide number accounted for 76.6% of the total landslide number (Du et al., 2020a). The distribution of 5,019 landslides triggered by the Tongwei earthquake in 1718 coincides with X degree isoseismal lines (Xu et al., 2020b). The 7,151 landslides triggered by the Haiyuan M8.5 earthquake in 1920 were distributed within the IX degree area (Xu et al., 2020c). In the Loess Plateau region of China, a large number of valleys, empty areas, and an arid climate have created favorable conditions for the formation and preservation of landslides due to earthquakes. Large-scale dense landslides triggered by historical strong earthquakes can be preserved for decades, hundreds, or even thousands of years. There is a significant difference in the scale between loess landslides due to rainfall and seismic landslides (Xu et al., 2020a). Based on the principle of “connecting the present to the past,” the spatial distribution of preserved large-scale landslides can be used to determine the source parameters of historical strong earthquakes. Similar to analyzing present-day earthquake cases, we can use remote sensing interpretation technologies to perform detailed interpretations and investigations of landslides triggered by historical strong earthquakes, which yield determinations (or modifications) of the magnitude and epicenter parameters of historical earthquakes.

The 780 BC Qishan earthquake, which occurred along the southwestern margin of the Ordos Block in China, was the earliest destructive earthquake recorded in Chinese history. The "Book of Songs" and "Historical Records" clearly record that the earthquake occurred in the second year of King Zhou You. The ground damage included "three rivers exhausted, Qishan collapse, hundred rivers boiled, and hills collapsed". “The high banks turned into valleys,” and “The deep valley became a mausoleum," among other accounts. These records indicate that the earthquake triggered a large number of coseismic landslides. According to these records, this earthquake was a strong event, such that it has attracted the attention of numerous researchers. However, there has been substantial debate over the magnitude of the Qishan earthquake, the macro-epicenter, the range of the extreme earthquake zone, and the seismogenic structure. Various earthquake catalogs have determined the location of the macro-epicenter of this earthquake in Qishan County, Shaanxi Province based on the "Qishan collapse." Scholars suggest that "Sanchuan" in "Sanchuan Exhaust" refers to the present day Jinghe, Weihe, and Luohe rivers. The magnitude is uncertain; various earthquake catalogs generally estimate the magnitude at 6 to ≥ 7. The epicenter intensity is also uncertain; the lack of a consensus yields uncertainty in the assessment of regional seismic activity and seismic risk analysis (Gu, 1983 and **Table 1**).

In addition to studying historical earthquakes on the edge of the Ordos block through limited historical records, a large number of landslides triggered by earthquakes also carry seismic parameter information (e.g., the AD 1303 Hongdong earthquake, AD 1556 Huaxian earthquake, AD 1654 Lixian earthquake, AD 1718 Tongwei Earthquake, and 1920 Haiyuan Earthquake) (Gu, 1983; Department of Earthquake Disaster Prevention, National Seismological Administration, 1995). Except for smaller landslides that have transformed and

TABLE 1 | Records of the 780 BC Qishan earthquake from different documents.

Literature	Estimated epicenter location	Estimated magnitude	Epicenter intensity	Remarks and references
“China Earthquake Catalog” 1960	Guanzhong (epicenter is ominous, likely not far from Qishan)	6–6.75		Sanchuan (Jinghe, Weihe, and Luohe rivers) (Li, 1960)
“China Earthquake Catalog” 1983	Qi’shan (34.5°N, 107.8°E)	6–7		Sanchuan (Jinghe, Weihe, Luohe and rivers). Unknown epicenter (Gu, 1983)
“A brief List of earthquakes in China” 1988	Qi’shan (34.5°N, 107.8°E)	6–7		
Catalog of Strong Earthquakes in Chinese History 1995	Qi’shan (34.5°N, 107.8°E)	≥ 7	≥ IX	Sanchuan (Jinghe, Weihe, and Luohe rivers) (Department of Earthquake Disaster Prevention, National Earthquake Administration, 1995)
“Catalog of Strong Earthquakes in four Provinces (Regions) of Shaanxi, Gansu, Ningxia, and Qinghai”	Qi’shan (34.5°N, 107.8°E)	6–7		Sanchuan (Jinghe river, Weihe river, Luohe river) (Lanzhou Institute of Earthquake Research, State Seismological Administration, 1985)
“Qishan county chronicles”	Qi’shan (34.5°N, 107.8°E)	6–7	VIII	Sanchuan (Jinghe, Weihe, and Luohe rivers)
National Earthquake Science Data Center, China Historical Earthquake Catalog	(34.5°N, 107.8°E)	6.5		

disappeared, larger landslides remain clearly visible on remote sensing images. A large number of dense historical loess landslides are currently preserved along the southwestern margin of the Ordos Block.

This study attempts to implement the interpretation methods detailed in the current strong earthquake landslide survey, combined with a historical literature review and field surveys, and uses current remote sensing images to interpret, in detail, historical landslides along the southwestern margin of the Ordos block. Based on dating results of existing bedrock collapses and loess landslides, historical landslides in the dense area along the southwestern margin of the Ordos block can be linked to the 780 BC Qishan earthquake. In addition, we discuss the possible magnitude, epicenter location, seismogenic structure, and earthquake damage scale associated with the 780 BC Qishan earthquake based on the distribution of landslides.

MATERIALS AND METHODS

Geological Background

The southwestern margin of the Ordos Block has a special structural location, i.e., it is at the forefront of the northeastward expansion of the Tibetan Plateau (**Figure 1**) (Yuan R et al., 2013; Zheng et al., 2013; Zheng et al., 2017; Li, 2018). This area experiences strong tectonic activity and frequent occurrences of both strong historical and current earthquakes. The southwestern margin of the Ordos Block is one of the areas where casualties are extremely tragic (Peng, 1992). The AD1654 Lixian *M*8 earthquake caused 30,000 deaths (Yang et al., 2015). The AD1718 Tongwei M7.5 earthquake caused more than 70,000 deaths, and there is a clear record that a considerable number of deaths are related to the earthquake landslide (Sun et al., 2017). The AD1920 Haiyuan *M*8.5 earthquake caused 270,000 deaths (Cheng et al., 2017), of which more than 100,000 deaths may be directly related to the earthquake landslide (Li et al., 2015). At the same time, this area is a danger zone for strong earthquakes in the future. GPS deformation observation results show that since 1920, the remaining seismic moments on the southwestern margin of the Ordos Block have been accumulating and have been in a state of loss, which has the potential to generate Mw ≥ 7 earthquakes (Li, 2019). The Liupanshan Fault zone and Longxian–Baoji Fault zone are the main fault zones along the southwestern margin of the Ordos Block. Ye et al. (2018) used GPS data inversion to examine the northern section of the Longxian–Baoji Fault zone, finding that this area is in a highly closed state with a greater seismic risk. Previous studies suggest that the middle–south section of the Liupanshan Fault zone and Longxian–Baoji Fault zone are two dangerous areas where strong/major earthquakes may occur in the future. Magnitude estimates of possible earthquakes along the Liupanshan and Longxian–Baoji Fault zones are Mw 7.3 and 7.2, respectively (Du et al., 2018). The Longxian–Qishan–Mazhao Fault is the most active fault in the Longxian–Baoji Fault zone, with a total length of approximately 180 km. This fault is a late Quaternary active fault with an overall NW trend. The fault is mainly left-lateral sliding, accompanied by a certain normal fault (Li, 2018).

Landforms along the southwestern margin of the Ordos Block can be mainly divided into three components: mountains formed by bedrock, the Loess Plateau, and the Weihe Basin. The mountain ranges composed of bedrock include uplift areas, such as Liupan Mountain, Longshan Mountain, Qinling Mountain, Qianyangling Mountain, and Beishan Mountain. They are mainly Precambrian metamorphic basement, granite

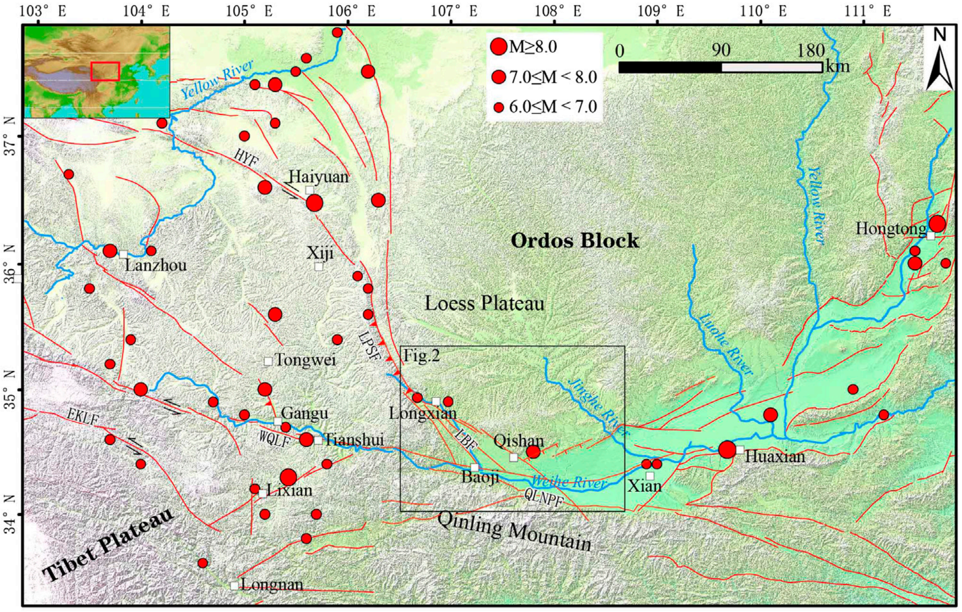

FIGURE 1 | Regional background map. LBF: Longxian Baoji Fault Zone; LPSF: Liupanshan Fault; HYF: Haiyuan Fault; WQLF: West Qinling Fault; EKLF: East Kunlun Fault; QLNPF: West Qinling North Margin Fault; The black box represents the range of **Figure 2**.

bodies, Paleozoic strata, and some Mesozoic strata. The Loess Plateau is covered by Quaternary aeolian loess-paleosol, with thicknesses reaching from 120 to approximately 180 m. The main components of loess are silt or clay, characterized by loose, easily erodible soil. The Loess Plateau is one of the regions with the most serious soil erosion in the world (Li et al., 2019). The eroded landform types include plateaus, beams, and ridges. The terrain is undulating, ravines are vertical and horizontal, and mountains are high and steep. These characteristics create excellent terrain conditions for the occurrence of landslides. The Weihe River Basin includes various levels of loess tableland and Weihe river terraces. The loess plateaus are flat and do not have topographical conditions appropriate for dense landslides.

From the late Holocene to the present, the Baoji area on the southwestern margin of Ordos has been affected by global climate change, the climate has become colder, the intensity of the summer monsoon has weakened, and the winter monsoon has increased. The climate has entered a phase of relatively cold, arid, and scarce precipitation (Deng, 2011). The dry climate along the southwestern margin of the Ordos Block is conducive to the preservation of loess landslides.

Interpretation Method

Satellite images taken before and after earthquakes can be used for detailed interpretation of landslides after modern major earthquakes. The image data used to interpret historical earthquake landslides must conform to the two following requirements: 1) the resolution of the image should be sufficiently high to facilitate the identification of the range of each part of the landslide body through user experience and 2) the area should be covered by the maximum number of temporal images to facilitate comparative interpretations. The interpretation of historical landslides is based on the following. 1) Current earthquake case studies show that only large earthquakes can trigger dense landslides; larger landslides can be preserved for extended periods (Xu et al., 2020a). The scale of landslides caused by moderate earthquakes is limited which has a negligible impact on the interpretation of landslides caused by large earthquakes (Du et al., 2020a). 2) Seismic landslides and rainfall-triggered landslides have distinct characteristics with respect to their duration, area scale, and distribution (Xu et al., 2020a). 3) Large-scale artificially-induced landslides appear as single points or distributed across residential areas; these are also significantly different from dense large-scale landslides. 4) We cannot overlook that earthquake landslides occurred before rainfall or human activity-induced landslides; however, the overall shapes between these landslide types remain clearly distinguishable. We used high-resolution satellite images from Google Earth to systematically interpret historical landslides in the study area and surroundings. Google Earth can provide multi-temporal images with different resolutions of up to 0.15 m. We used Google Earth images of the study area collected from 2005 to 2018, with resolutions of 1–5 m; most areas had an image coverage of more than three times. Google Earth supports a 3-D display at any angle, such that the shape and outline of the landslide can be clearly distinguished. To understand the completeness of the translation, we interpreted it on a river-by-basin basis. In addition, domestic high-resolution satellite images collected by the GF-1, GF-2, and American Keyhole satellites from the 1960s to the 1970s were used as supplementary data sources. If some parts of Google Image are covered by clouds, etc., we used domestic high-resolution satellite image as supplementary data. The Keyhole historical satellite images as a supplementary data source can eliminate the impact of landslides caused by human activity in recent decades. Later field excursions were also used to verify the accuracy of the interpretations. Using Google Earth images, we manually extracted and saved the boundaries of the target landslides as vector files in a kml format. Attribute information for the landslide body was assigned using ArcGIS software. The attribute information included the length and width of the landslide, the elevation of the scarp top and foot edge, and the top and bottom elevations of each located slope.

RESULTS

Interpretation Results

The landslides in the study area had the following image characteristics. 1) There are abnormal arc shapes developed on the rear margin of the landslide body, including "round chair-shaped" and "dustpan-shaped" landslide back wall steep ridges, curved terrain variation lines, and abnormal color lines, among other feature. 2) Landslides protruding toward the bottom of the valley often have slight topography. Landslides often form dammed lakes in the valleys, which occasionally discharge water. The original "V"-shaped loess valley bottom becomes flat terrain, which has been mostly transformed into cultivated land. 3) Most landslides are distributed in the partial deficit areas of steep slopes, such as valleys and rivers. Landslides cause river water to shift to the side of the river where the landslide has not occurred. 4) The valley slopes on both sides of the steep loess valley have abnormally flat cultivated land.

In this study, the historical landslides in the 28,000 km^2 area of the southwestern edge of Ordos was interpreted in detail. **Figure 2** shows the spatial distribution of the interpreted historical landslides. The landslides are mainly distributed along faults to the north of the Longxian–Qishan–Mazhao Fault, east of Longxian, south of Lingtai, and the uplift area of the fault block south of Qianyang. There are 6,876 landslides in this dense area, with a total area of 643 km^2. There are relatively few dense landslides on the Loess Plateau, Weihe river terraces, and floodplains on the southwest side of the Longxian–Qishan–Mazhao Fault due to topographical conditions. At the same time, dense landslides were not interpreted in the bedrock area of the Qishan mountains and north of Fengxiang.

The area density analysis of the interpreted landslides in the study area (**Figure 3**) shows that, although there are landslides in the study area, the high-density areas occur on the northeastern side of the Longxian–Qishan–Mazhao Fault. The area density can reach as high as 28–35% while the area density value at the center of the high-density area is 4- to 5-fold greater than the background density of the Loess Plateau, highlighting this as an abnormal area.

The 6,876 landslides in the dense area were projected onto the projection line along the horizontal and vertical strike of the

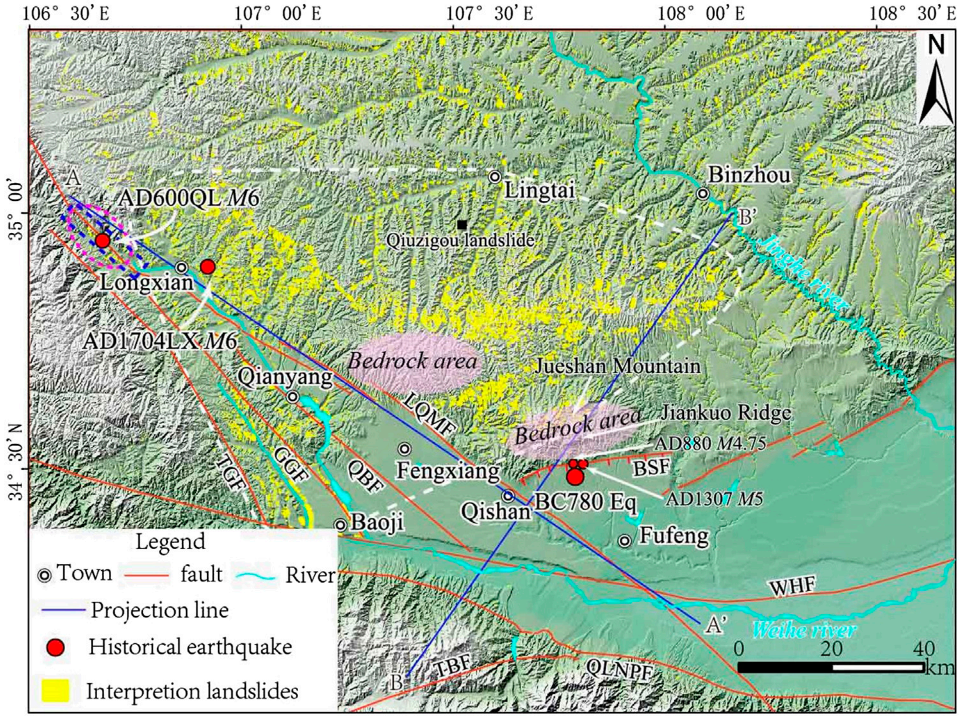

FIGURE 2 | Interpreted historical landslide distribution map at the Southwest of Ordos. LQMF: Longxian–Qishan–Mazhao Fault; QBF: Qianyang–Biaojiao Fault; GGF: Guguan–Guozhen Fault; TGF: Taoyuan-Guichuansi Fault; QLNPF: Qinling North Margin Fault; TBF: Taibai Mountain Fault; WHF: Weihe Fault; and BSF: Beishan Piedmont Fault. The purple dashed oval area is the extreme earthquake zone of the AD 600 Qinlong earthquake (Wang, 2018); the blue dashed rectangle represents the surface rupture of the AD 600 Qinlong earthquake along the Longxian–Qishan–Mazhao fault of the Dazhuangke–Dengjiacao section (Li et al., 2019); the area denoted by the white dotted line is the dense landslide area; and projection lines A–A′ and B–B′ correspond to **Figure 4**.

Longxian–Qishan–Mazhao Fault; we then counted the frequency and cumulative area of the landslides (at 10 km intervals) (**Figure 4**).

Along the strike of the Longxian–Qishan–Mazhao Fault, landslides are mainly concentrated within a range of 90 km between Longxian and Qishan (reaching 6,003 events, accounting for 87.3% of the total number of landslides). The cumulative landslide area is 557.4 km^2, accounting for 86.7% of the total landslide area. The peak appears at approximately 10 km northwest of Qishan County. By projecting the landslide body onto the projection line perpendicular to the strike of the Longxian–Qishan–Mazhao Fault, we observe that the main body of the landslide is distributed on the northeast side of the Longxian–Qishan–Mazhao Fault, where there is a sharp reduction in the number and area of landslides southwest of the fault. This is because the southwest side of the fault is the loess tableland and Weihe River terraces and floodplains, which do not have topographical conditions suitable for large-scale landslides. The landslide-intensive area is distributed unilaterally along the Longxian–Qishan–Mazhao Fault.

Landslide Database and Parameter Statistics

Based on our interpretations, parameter assignments were made for the landslides in dense areas on a case by case basis to establish a coseismic landslide database. The manually assigned attributes of the landslide database included the length, width, elevation of the scarp top and foot edge, and the top and bottom elevations of each located slope. Accorded to these assigned attributes, we calculated several landslide attributes, including the landslide height, H (elevation of the scarp top-elevation of the foot edge), slope difference (the top and bottom elevation difference of each located slope), aspect ratio, and landslide height/slope difference ratio, i.e., H/(R − V).

A statistical analysis of the landslide parameters was conducted based on the coseismic landslide database. The length advantage interval of the historical landslides in the dense area along the southwestern margin of the Ordos Block is 100–500 m; this interval accounts for 82% of the total number of landslides. The width advantage interval is 100–400 m; this interval accounts for 72.6% of the total number of landslides (**Figures 5A,B**). The aspect ratio of the landslide represents the plane spread of the landslide, which ranged from 0.1 to 5.6 for the historical landslides in the dense areas, mainly concentrated between 0.5 and 2.5. This interval accounts for 91% of the total landslides. An aspect ratio of ≤ 0.5 accounted for 5.6% of the total landslides while an aspect ratio of >2.5 accounted for 3.4% of the total landslides, with an average of 1.25 (**Figure 5C**).

The term H/(R − V) refers to the ratio of the height, H, of a landslide to the slope difference (R–V: Ridge–Valley), which represents the ratio of the longitudinal length of the landslide to the slope length where the landslide is located, ranging from 0 to 1. The greater the value of H/(R − V), the greater the proportion of

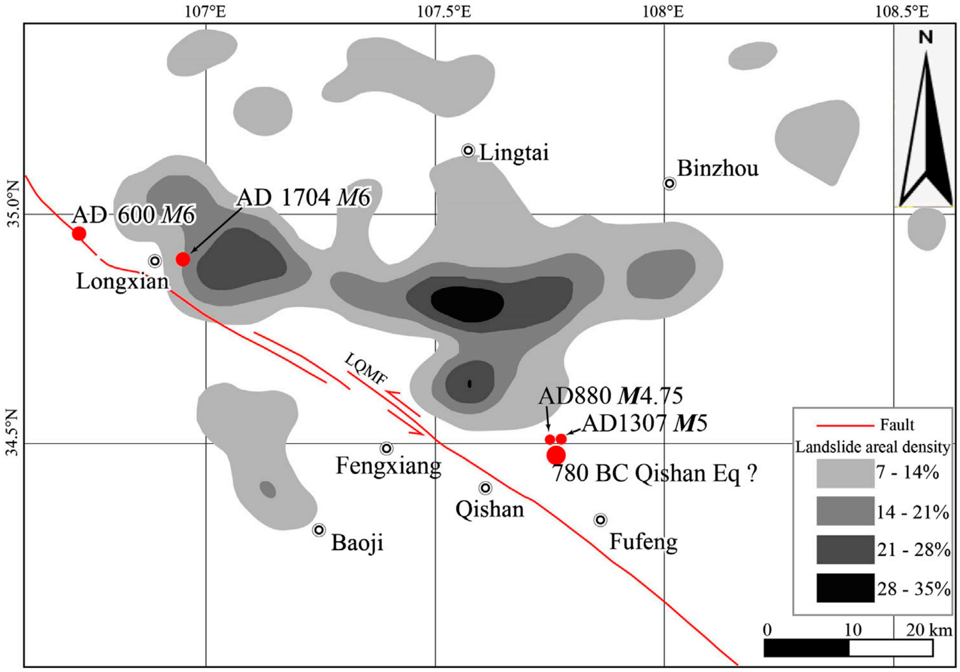

FIGURE 3 | Interpreted historical landslide areal density map. LQMF:Longxian–Qishan–Mazhao Fault; AD 600 M6:AD 600 Qinlong M6 earthquake; AD 1704 M6: AD 1704 Longxian M6 earthquake;

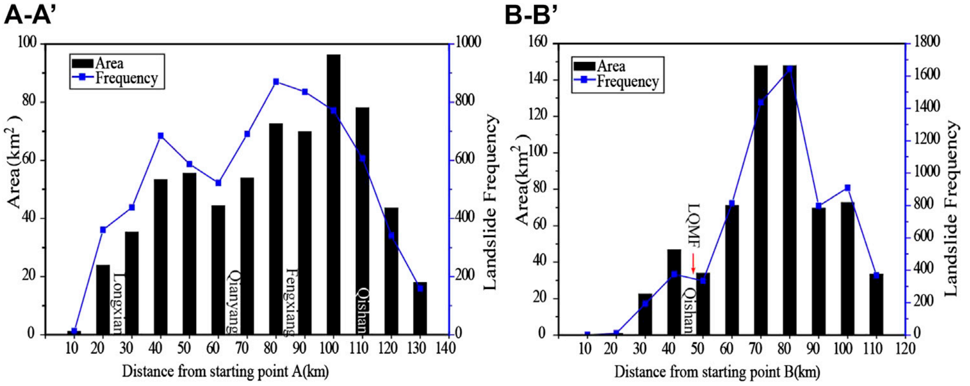

FIGURE 4 | Frequency and cumulative area along strike and vertical strike of the Long xian–Qishan–Mazhao Fault (10 km) (Projection lines A–A′ and B–B′ are shown in **Figure 2**).

landslides in the slope in the longitudinal direction. Among the landslides in the dense areas, 85.4% of landslides have H/(R − V) ratios >0.6 while 57.7% are greater than 0.8 (**Figure 5E**). This shows that the scarp tops of these landslides basically reach the Loess Plateau, with notable landform deficits While the foot edge accumulation basically reaches the bottom of the valley, which can lead to the damming of loess valleys at different scales, forming abrupt landform sedimentary features; these features are consistent with the observation results collected during the field survey (**Figures 6A–D–D**).

In terms of the area, the number of small-area landslides is relatively small; landslides with an area greater than 10,000 m^2 account for 93.2% of the total number of landslides. The area advantage of historical landslides interpreted in the study area is 10,000–200,000 m^2; the number of landslides in this section accounts for 82.3% of the total number of landslides in the dense area of this study (**Figure 5D**).

DISCUSSION

Dense Historical Landslides and the 780 BC Earthquake

In addition to the 780 BC Qishan earthquake, the AD 1704 Longxian earthquake and AD 600 Qinlong earthquake occurred in the study area (**Figure 2**).

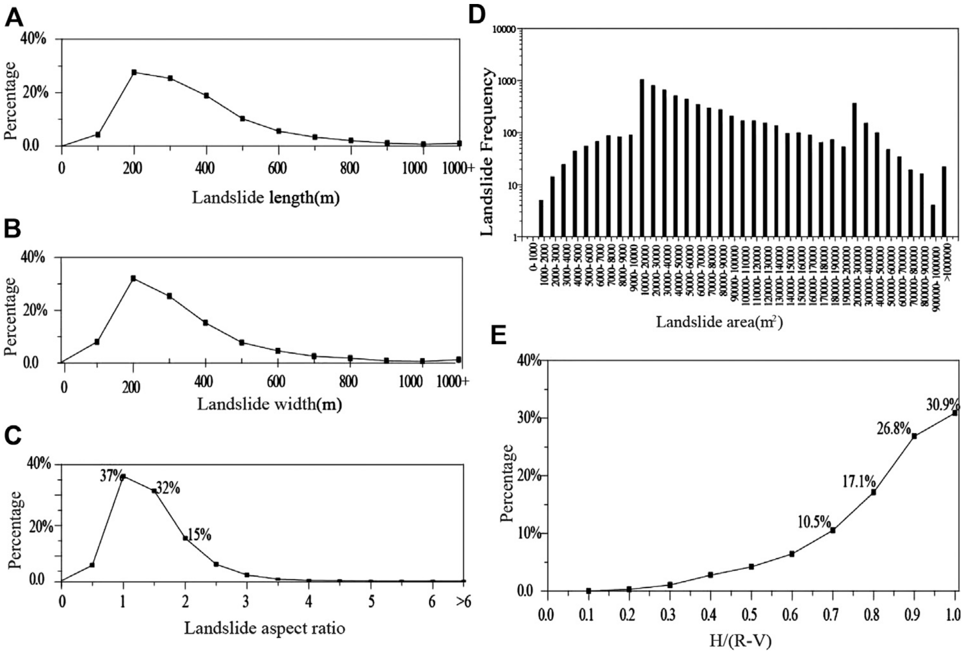

FIGURE 5 | Landslide parameter statistics. **(A)**, statistics on the relationship between landslide length and frequency; **(B)**, statistics on the relationship between landslide width and frequency; **(C)**, statistics on the relationship between landslide aspect ratio and frequency; **(D)**, statistics on the relationship between landslide area and Frequency; **(E)**, statistics on the relationship between landslide H/(R − V) and frequency.

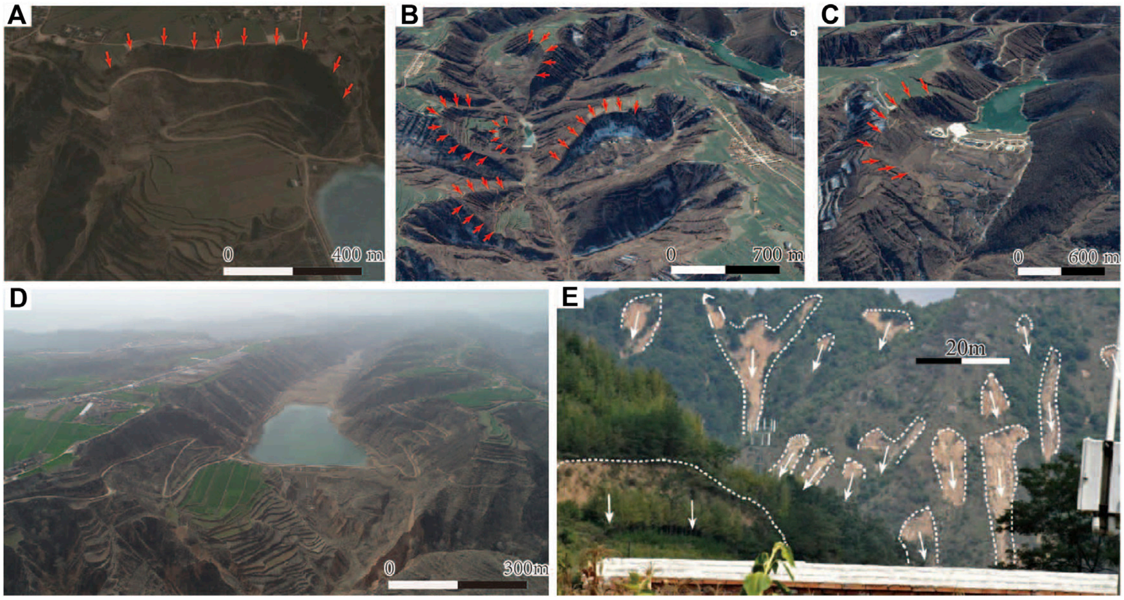

FIGURE 6 | Google images of typical historical landslides and barrier lakes **(A–C)**, UAV. photos of historical landslides(d), and photos of rainfall landslides **(E)**.

Wang (2018) suggested that the seismogenic structure of the AD 600 Qinlong earthquake was due to the Guguan-Caojiawan section of the Liupan Mountain East foot Fault based on an ancient seismic exploration trough, collapsed body, and formation time. Li et al. (2019) proposed that the epicenter of the AD 600 Qinlong earthquake was located 15 km (34.9°N, 106.7°E) northwest of Long County. The epicenters (highly seismic regions) reported in the above two most recent studies are close, providing sufficient evidence. Therefore, we consider that the epicenter of the AD 600 Qinlong M6 earthquake was

15 km northwest of Longxian County (**Figure 2**). For the AD 1704 Longxian earthquake, The "China Earthquake Catalog" (Gu, 1983), published in 1983, set the earthquake at a magnitude of 6, with an epicenter intensity of VII–VIII. As there are relatively few research results on this earthquake, we consider that the epicenter of the AD 1704 Longxian M6 earthquake was in the vicinity of Longxian based on the historical earthquake catalog (Gu, 1983).

In addition to the 780 BC earthquake, there were two earthquakes at a magnitude of approximately 5 that occurred in AD 880 and AD 1037 along the southwestern margin of the Ordos Block. According to the historical descriptions of "Three rivers exhausted, Qi mountain collapse," "Hundred rivers boiled, mountain mounds collapsed. High banks turned into valleys, and deep valleys turned into tombs" recorded in "Book of Songs" and "Historical Records", the damage intensity and scope of the "780 BC Qishan Earthquake" were greater than those of the other two earthquakes. The relevant historical earthquake catalog also sets the magnitudes of these two historical earthquakes in AD 880 and AD 1037 as 4.75 and 5, respectively. Therefore, considering the limited energy of moderate and strong earthquakes, we suggest that the two most recent historical earthquakes, i.e., the "Qishan collapse" and "Qishan collapse again," were only records of earthquake occurrences, not triggers of a large number of landslides. Moreover, the most recent historical earthquakes were more than 1,500 years after the 780 BC earthquake. If the earthquake that triggered the “Qishan collapse” really occurred, records of earthquake damage should theoretically be more abundant than those for the Qishan earthquake in 780 BC; however, there are no other relevant records on these two earthquakes.

According to the interpretation and cataloging results of landslides triggered by earthquakes at a magnitude of approximately 6 (**Table 2**), the scale of landslides triggered by these earthquakes is limited and the range of dense landslides is small. Therefore, although a small part of the landslides at the northwest end of the landslide distribution range in the study area may have been triggered by the AD 600 Qinlong and AD 1704 Longxian earthquakes, the proportion is small and the impact range is limited. The main landslides in the dense area cannot have been triggered by these two earthquakes.

Analyses of the landslides triggered by the Wenchuan earthquake indicate that the far-field effect of strong earthquakes will not trigger large dense landslides outside the extreme earthquake zone (Xu et al., 2014; Du et al. 2020a). Several large earthquakes outside the landslide distribution range are far from the landslide dense area (**Table 3**), such that the possibility of large dense landslides triggered by strong earthquakes outside the range is negligible.

The age of a single landslide is the most powerful evidence to establish a connection between landslides and historical earthquake. Zhou et al. (unpublished, 1993) used lichen geochronology technologies to date 382 bedrock collapses in the Jiankou ridge and Jueshan Mountain region (**Figure 2**). The results showed that the huge collapses in this region were caused by the 780 BC Qishan earthquake. The age of the sediment at the bottom of the landslide dammed lake can represent the age of the landslide. Du et al. (2020b) selected a typical Qiuzigou landslide dam (**Figure 2**) in the study area and obtained ^{14}C dating samples in the bottom sediment of the dammed lake through drilling. These samples are measured by American Beta Laboratories using an accelerator mass spectrometer. The dating results are close to the Qishan earthquake time. Combined with the above age results and comprehensive analysis, we believe that the main body of the dense landslides was most likely caused by the 780 BC Qishan earthquake.

"Incomplete" Historical Landslide Database

Comparing the area–frequency relationship between historical landslides in the dense area (inside the white dotted line in **Figure 3**) along the southwestern margin of the Ordos Block and the Wenchuan earthquake landslide (Du et al., 2020a) (**Figure 7**), there are large differences in the number of landslides in different area intervals. The number of historical landslides in the dense area along the southwestern margin of the Ordos Block is small, ranging from 1 to 10,000 m^2 with only 469 landslides (approximately 6.8% of the total), while the number of landslides due to the Wenchuan earthquake is 32,007, accounting for 61% of the total. This significant difference in the proportion of landslides of <104 m^2 reflects that with the passage of time, small-to-medium-scale historical landslides have basically "disappeared" due to surface processes and man-made transformations, such that they can no longer be identified on current remote sensing images. In particular, the smaller landslides are increasingly rare.

In the 2008 Wenchuan earthquake, small landslides, which accounted for a large proportion of the total, contributed little to the total area of landslides induced by the earthquake (**Figure 8**) (Du et al. 2020a). Large-scale landslides that can be identified today may represent the main body of a historical earthquake landslide; they can also reflect the overall scale of a historical earthquake landslide. Therefore, we discuss medium- and large-scale historical landslides in the dense area along the southwestern margin of the Ordos Block.

In August 2010, partial heavy rain in southeastern Tianshui that triggered a large rainfall landslide. These landslides are generally small in scale, mostly slippery on their slopes, and have a short duration. Rainfall landslides that occurred in 2010 could not be identified in remote sensing images taken after 2016. Some rainfall landslides develop on the back or sidewalls of large earthquake landslides, or on the ridges of loess terraces that have been transformed by humans (Xu et al., 2020a). Xu et al. (2020b) used historical document analysis, remote sensing interpretation, field verification, and other methods to interpret 5,019 landslides triggered by the AD 1718 Tongwei earthquake on both sides of the Tongwei Fault, with a total area of 635 km^2. As this earthquake landslide has clear historical records, it can be used as a typical example of a loess earthquake landslide.

Comparing the area–quantity relationship between historical landslides in dense areas (inside the white dotted line in **Figure 3**), the 2010 Tianshui rainfall landslides, and the AD 1718 Tongwei earthquake landslide (**Figure 9**), rainfall landslides mainly have areas of <10,000 m^2, accounting for 99% of the total landslides. However, there are few small-area landslides in the

TABLE 2 | Interpretation and cataloging results of landslides triggered by earthquakes of approximately M6.

Earthquake cases	Intensity at macro-epicenter	Distribution scale (km)	Size of landslides	References
2013 Minxian M6.6	VIII	Narrow belt, < 15	Small (total area of 1.71 km^2)	Xu et al. (2013)
1970 Xiji M5.5	VII–VIII	4–5	Small	Wang (2003)
1936 Kangle M6 ¾	VIII	8	Rock falls	Zhang et al. (2015)
1936 tianshui town M6.0	VIII	–	Not clear record	Wang et al. (2018)
1837 Minxian M6.0	VIII	–	Not clear record	Zheng et al. (2007)
AD 1125 Lanzhou M7.0	IX	~7	Landslides along the fault	Song et al. (2007)

TABLE 3 | Basic parameters of three historical strong earthquakes around Qishan Longxian and the impact of the earthquake on Qishan Longxian.

Historical earthquake	Distance to landslide dense area (km)	Triggered landslides	Impact of the earthquake on Qishan Longxian	References
1,556 Huaxian *M*8.0	200	The east and west ends of the Huashan Piedmont fault zone	(Qishan) The city, government offices, temples, and houses were destroyed, and the people were crushed to death; (Fengxiang) many people and animals were crushed to death; (Linyou) Destruction of confucian temple	Xu et al. (2018)
1,654 Lixian *M*8.0	190	Between Tianshui Town and Li County	(Baoji) "House destruction, crushing people"; (Fufeng) "Gyeongbok Palace, Yuanyu collapsed, crushing people and animals." (Lin You) "Kilins collapsed, crushing people and animals."; (Qishan, Feng Xiang) "The walls and houses burst up, people and animals can't stand in shock"	Yuan et al. (2017)
1920 Haiyuan *M*8.5	250	Xiji, Haiyuan, Longde area	The Qishan wall collapsed, the ground was cracked and deep gully, people were killed and injured everywhere	Li et al. (2015)

dense areas and within the landslides triggered by the AD 1718 Tongwei earthquake. Landslides with areas >10,000 m^2 accounted for 93.2% and 88.7% of the total in the dense areas and due to AD 1718 Tongwei earthquake, respectively. Therefore, the remaining historical landslides in this study and rainfall landslides can be distinguished by size.

Comparing the length, width, and aspect ratio of historical landslides in the dense area (within the white dotted line in **Figure 3**) with the 2010 Tianshui rainfall landslide and the AD 1718 Tongwei earthquake landslide (**Figure 10**), we observe that 88.4 and 98.9% of the rainfall landslides have a length of ≤100 m and a width of ≤100 m, respectively. The lengths and widths of the historical landslides in dense areas are similar to those of the AD 1718 Tongwei earthquake. Landslides with a length ≤100 m accounted for only approximately 4.2 and 7.2% of the total while landslides with a width ≤100 m accounted for only approximately 7.9 and 14.4% of the total, respectively.

The aspect ratio of historical landslides in dense areas is similar to that of the AD 1718 Tongwei earthquake landslides, mainly between 0.5 and 2.5; landslides in this interval accounts for 89.1% of the total landslides. There is a significant difference between the 2010 Tianshui rainfall landslide and the two earthquakes mentioned above. The landslide aspect ratio for the 2010 Tianshui rainfall landslide ranged from 0.03 to 57.18, with an average value of 3.06. The aspect ratios of rainfall landslides mainly range from 0.5 to 4. The landslides in this interval account for 71% of the total; aspect ratios ≤0.5 account for 5.5% of the total while aspect ratios >4 account for 23.5% of the total, indicating that most rainfall landslides are long and narrow (**Figure 10C**).

Compared with rainfall landslides, there are notable differences with historical landslides in dense areas in terms of their areas, lengths, and widths. The dense historical landslide is highly similar to the AD 1718 Tongwei earthquake landslide in terms of their areas, lengths, and widths. Therefore, there is a clear macroscopic difference between historical earthquake landslides and rainfall landslides. The main part of the landslides in the dense areas was not likely triggered by rainfall events but was more likely triggered by earthquake events. Strong earthquakes can cause such a large-scale landslide. Several earthquakes of magnitudes ≤5 have occurred in the landslide-intensive area and did not trigger large-scale landslides.

Rainfall landslides that occur on the Loess Plateau are generally small in scale and short-lived. Usually, the landslide will be transformed with the restoration of surface vegetation and human activities a few years after its occurrence, such that they can no longer be identified in high-resolution satellite images. Medium- and large-scale landslides triggered by earthquakes will cause significant changes in local landforms, which generally endure for an extended period. Although various natural and man-made modifications may have contributed to these landslides, their basic shapes can still be identified (Xu et al., 2020b).

We note that the previous discussion only points out the differences between historical earthquake landslides and rainfall landslides from a macro perspective. Individual large-scale rainfall landslides may be characterized by continuous activity;

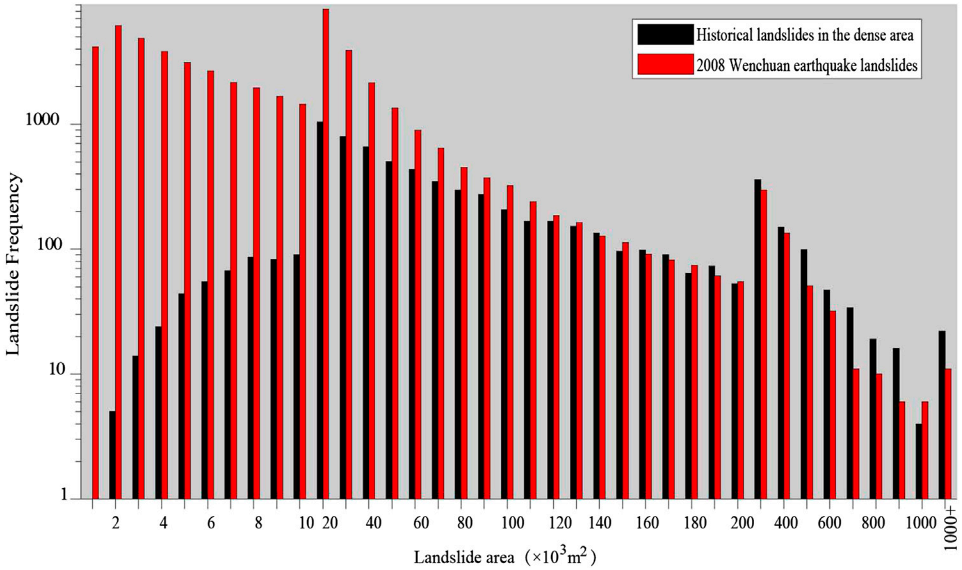

FIGURE 7 | Comparison of the area-frequency relationship between the Qishan earthquake landslide and Wenchuan earthquake landslide.

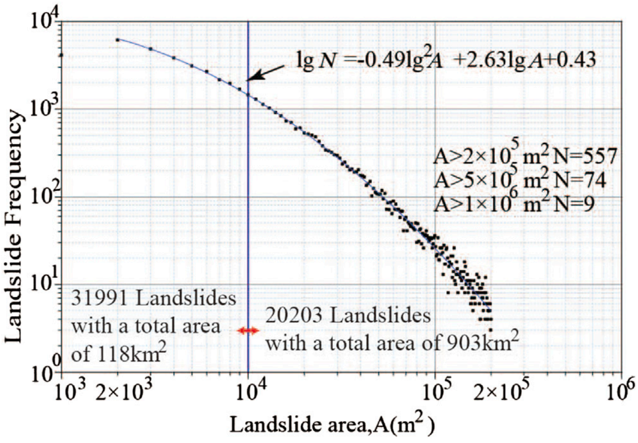

FIGURE 8 | Relationship between the cumulative number and area of landslides in the Wenchuan earthquake (Du et al., 2020a).

large-scale earthquake landslides may also be characterized by continuous activity due to rainfall after the earthquake.

Regional Control Characteristics of Strong Historical Earthquake Landslides

The landslides in the dense area are mainly distributed along the north side of the Longxian–Qishan–Mazhao Fault with an asymmetric distribution. According to the analysis, the Loess Plateau and river terraces lie toward the southwest side of the fault while the Loess Plateau and mountain hills lie toward the northeast side. Limited by topographical conditions, dense landslides do not occur on the southern and western sides of the fault; therefore, "sand liquefaction" and "seismic soil" will more likely form in soft areas, such as river terraces and valleys, due to violent earthquake vibrations (**Figure 11**). According to the characteristics, landslides triggered by strike-slip fault activities are mainly distributed on both sides of the fault (Chen et al., 2014). If the geological engineering conditions on the south side of the Longxian–Qishan–Mazhao Fault are the same as those on the north side, there may also be dense historical landslides.

780 BC Qishan Earthquake Parameters

The 780 BC Qishan earthquake is an earthquake that is historically difficult to interpret, with a long elapsed time and unknown historical records. Determining the intensity/isoseismic distribution is difficult. However, for a major earthquake that triggers a secondary disaster, the range of its extreme earthquake zone/severely damage zone can be obtained through the spatial distribution and characteristics of secondary disasters revealed by high-resolution remote sensing images. The center of the macroscopic damage zone is the macroscopic epicenter. Therefore, the epicenter of the 780 BC Qishan earthquake may be located northwest of Qishan, closer to Fengxiang.

The Longxian–Qishan–Mazhao Fault has been the most active fault in the Longxian–Baoji Fault zone since the late Quaternary. The National Earthquake Administration (1988) divided the fault into three sections: Xinjichuan–Longxian section, Longxian–Qishan section, and Qishan–Mazhao section. Historical landslides in dense areas are mainly concentrated in the range of 90 km between Longxian and Qishan, corresponding to the Longxian–Qishan section of the Longxian–Qishan–Mazhao Fault.

The extension of the severe damage zone of a major earthquake along the seismogenic fault can represent an extension of the fracture. The surface rupture zone produced by the Wenchuan earthquake spread within the IX intensity zone.

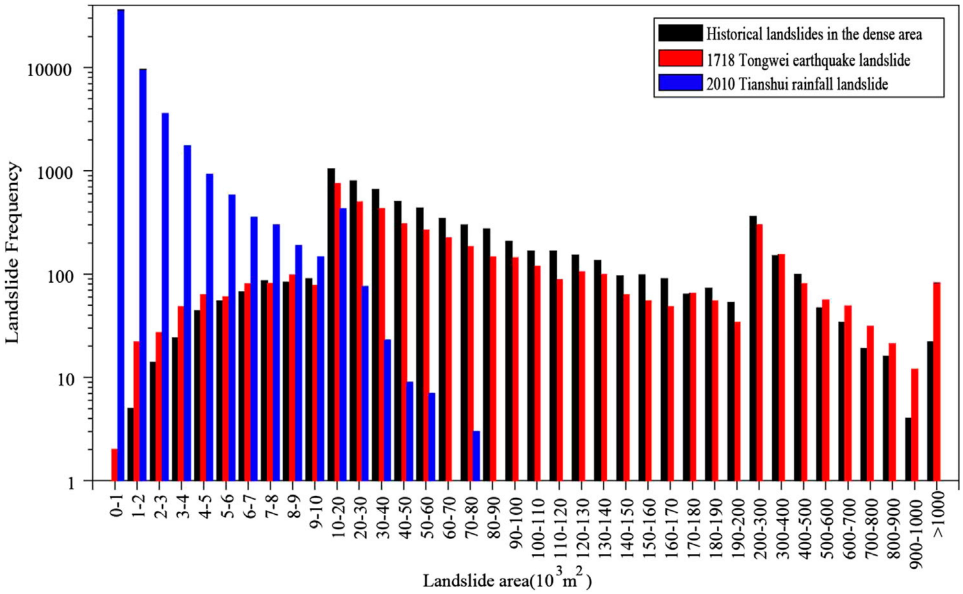

FIGURE 9 | Comparison of the dominant area of the rainfall landslide and the 1718 Tongwei earthquake landslide (Xu et al., 2020a; Xu et al., 2020b) and the historical landslide area in Long County, Qishan

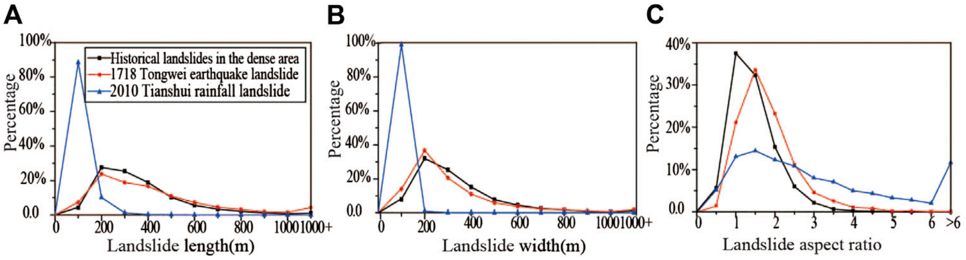

FIGURE 10 | Comparison of the lengths, widths, heights, and aspect ratio of landslides: **(A)** comparison chart of landslide lengths; **(B)** comparison chart of landslide widths; and **(C)** comparison chart of landslide aspect ratios.

The area of landslides within the IX zone accounted for 81.1% of the total area, and the number of landslides in the IX zone accounted for 76.9% of the total landslides. We suggest that the landslide-intensive area within a range of 90 km between Long and Qishan Counties can represent the rupture area of the 780 BC Qishan earthquake, as well as the severely damaged area. Therefore, the minimum possible rupture length for the rupture zone of the 780 BC Qishan earthquake was 90 km.

We assumed that the Longxian–Qishan section of the Longxian–Qishan–Mazhao Fault is completely broken. According to the global empirical formula, i.e., Mw = 5.16 + 1.12lgL (Wells and Coppersmith, 1994), for the rupture length and magnitude of strike-slip faults, the moment magnitude is Mw 7.35 According to the empirical formula, i.e., M = 5.303 + 1.181lgL (Ran, 2011), for the strike-slip fault magnitude-fracture parameter in western China, the magnitudes is 7.61. According to the empirical formula, i.e., Ms = 5.704 + 0.9871lgL (Sun et al., 2016), the surface wave magnitude is Ms 7.63.

The earthquake disasters due to six strong earthquakes of magnitude 8 on the Loess Plateau are comparable to the 780 BC Qishan earthquake. For example, for the AD 1739 Ningxia Pingluo and Yinchuan *M*8 earthquake that occurred on the plains, there were no records of landslides, but the other five earthquakes produced documented landslides. The six *M*8 earthquakes have records of spring overflowing/river overflowing similar to the "boiled rivers" (**Table 4**). This shows that the intensity of the 780 BC Qishan earthquake may have been similar to the six *M*8 earthquakes.

For the magnitude of the 780 BC Qishan earthquake, except for the "Catalog of China's Historical Strong Earthquakes" published in 1995, which set the magnitude as ≥ 7, other historical earthquake catalogs all set the magnitude at 6–7. Based on the distribution and scale of landslide disasters, we posit that the magnitude of the 780

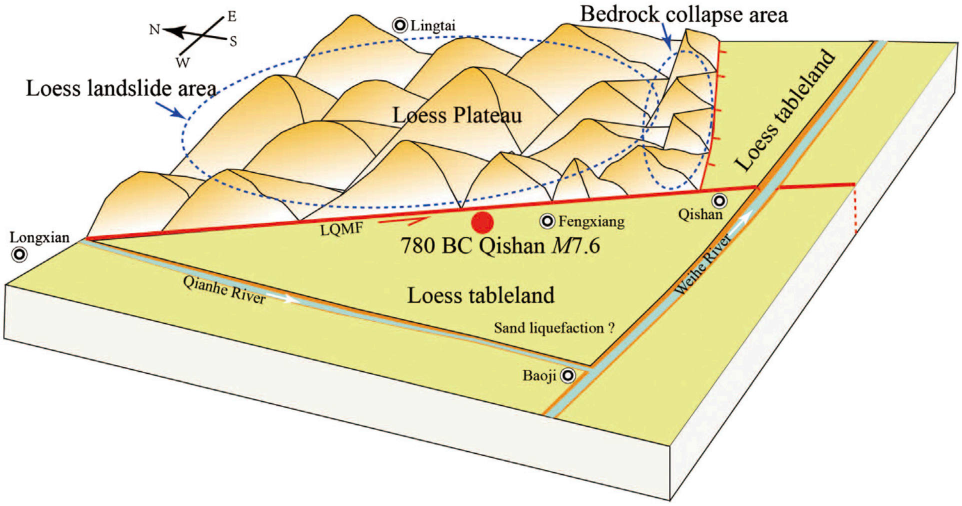

FIGURE 11 | Relationship between the distribution pattern of landslides in the dense area in this study and the 780 BC Qishan earthquake.

TABLE 4 | Historical records of earthquake damage due to 6 strong M8 earthquakes in or around China's Loess Plateau (Gu, 1983).

Historical earthquake	Phrases that appear numerous times in records of earthquake geological disasters
780 BC Qishan *M*7.6	Three rivers are exhausted, Qishan falls/Hundred rivers boil, and hills collapse. High banks become valleys, deep valleys become mausoleums
1,303 Hongtong *M*8.0	Ground fissure/ground gushing sand/water/city subsidence/landslide
1,556 Huaxian *M*8.0	Water surges and sand overflows/mountains move, ground rifts/mountains are exhausted/wells are exhausted, Luohe and Weihe rivers can be waded/landslides and rivers surge
1,654 Tianshui *M*8.0	Landslides and water stagnated, blocked as river ponds/ground fissures/gushing water
1739 Yinchuan *M*8.0	Ground fissure/city subsidence/gushing yellow sand and black water
1879 Wudu *M*8.0	Mountain fissure/water surge/landslide/landslide/river choked, then re-washed, the water was turbulent
1920 Haiyuan *M*8.5	The ground may become high tombs or sink into deep valleys, landslides and ground fissures, cliffs and landslides/blocked rivers/gushing water belts, black sand/mountains move away, peaks and valleys interchange/loess landslides/landslides

BC Qishan earthquake should be higher than the magnitude reported in the historical earthquake catalog, i.e., a magnitude of approximately 7.6 (Mw7.3). This is similar to the maximum moment magnitude Mw7.2 ± estimated by Du et al. (2018) for potential earthquakes in the Longxian–Baoji Fault zone.

CONCLUSION

Combining historical records and referring to current interpretation methods for strong earthquake landslides, we used high-resolution Google Earth images to extract historical landslides along the southwestern margin of the Ordos Block.

The results showed that there are 6,876 historical landslides in the landslide-intensive area along the southwestern margin of the Ordos Block, with a total area of 643 km^2. The landslide-intensive areas are mainly distributed unilaterally along the Longxian–Qishan–Mazhao Fault in the loess valley area on the northeast side of the fault. The southwest side of the fault is Loess Pateau and river terraces; owing to the topographical conditions, there is no dense landslide distribution in this area. Through a comprehensive analysis, combined with the dating results of existing landslides and bedrock collapses, the dense historical landslides on the southwestern margin of the Ordos Block were linked with the 780 BC Qishan earthquake. According to studies of landslides due to the Wenchuan earthquake, large-scale landslides in dense coseismic landslide areas can represent the main body of coseismic landslides. Finally, according to the spatial distribution characteristics of the landslide, we suggested that the epicenter of the Qishan earthquake may be located in northwestern Qishan, near Fengxiang, with a possible magnitude of Mw7.3 (M7.6) and possible seismogenic structure belonging to the Longxian–Qishan–Mazhao Fault along the Longxian–Qishan segment.

We note that if landslides in a target area can be confirmed to have been triggered by a single strong historical earthquake, a "relatively complete" coseismic landslide database of historical earthquakes can be obtained using current high-resolution satellite images. This could provide more objective evidence for the revision of source parameters associated with strong historical earthquakes as compared with the use of historical records.

DATA AVAILABILITY STATEMENT

The original contributions presented in the study are included in the article/Supplementary Material, further inquiries can be directed to the corresponding author.

AUTHOR CONTRIBUTIONS

XY proposed and participated in designing the study; DP designed the study, analyzed the data and wrote the manuscript; TQ participated in designing the study and improved the paper; LW participated in designing the study; All authors approved the final version of the manuscript.

FUNDING

The authors would like to extend their thanks to the National Natural Science Foundation of China (No. 42072248), the National Key Research and Development Program (No. 2019YFE0108900), the Seismic Active Fault Exploration Project based on High-Resolution Remote Sensing Interpretation Technology by the Department of Earthquake Damage Defense, CEA (No. 15230003), and the China Scholarship Council (No. 201604190021).

REFERENCES

Chen, X., Hui, H., and Zhao, Y. (2014). Study on the fault mechanics influences on the landslides distribution: a case study from the Wenchuan earthquake. *Seismol. Geol.* 36, 358–367. doi:10.3969/j.issn.0253-4967.2014.02.007 (in Chinese).

Cheng, J., Rong, Y., Magistrale, H., and Chen, G. (2017). An mw-based historical earthquake catalog for mainland China: an MW-based historical earthquake catalog for mainland China. *Bull. Seismol. Soc. Am.* 107, 2490–2500. doi:10.1785/0120170102

Dadson, S., Hovius, N., Chen, H., Dade, W., Lin, J., and Hsu, M. (2004). Earthquake-triggered increase in sediment delivery from an active mountain belt. *Geology* 32, 733–736. doi:10.1130/G20639.1

Deng, Q. (2011). *The Climatic evolution during the Holoeene in the Bao ji region.* Xi'an: Chang'an University, 1–64. (in Chinese).

Department of Earthquake Disaster Prevention National Earthquake Administration. (1995). *Catalog of historical strong earthquakes in China.* Beijing: Earthquake Press, 1–514. (in Chinese).

Du, F., Wen, X., Feng, J., Liang, M., Long, F., and Wu, J. (2018). Seismo-tectonics and seismic potential of the Liupanshan fault zone (LPSFZ), China. *Chin. J. Geophys.* 61, 545–559. doi:10.6038/cjg2018L0181 (in Chinese).

Du, P., Xu, Y., Tian, Q., Zhang, W., and Liu, S. (2020a). The spatial distribution and attribute parameter statistics of landslides triggered by the may 12th, 2008, Mw7.9 wenchuan earthquake. *Earthq. Res. China* 34, 29–49.

Du, P., Xu, Y., Li, W., Tian, Q., and Chen, L. (2020b). Volume calculation of landslides and dammed lake sediments triggered by a strong historical earthquake on the loess plateau: a case study of Qiuzigou, gansu province, northwest China. *Earthq. Res. China.*, 34, 54–59. (in press).

Gu, G. (1983). *Catalog of earthquakes in China (1831–1969 BC).* Beijing: Science Press. (in Chinese).

Lanzhou Institute of Earthquake Research, National Seismological Administration (1985). *Catalog of strong earthquakes in the four provinces (regions) of Shaanxi, Gansu, Ningxia and Qinghai.* Xi'an: Shaanxi Science and Technology Press. (in Chinese).

Larsen, I., Montgomery, D., and Korup, O. (2010). Landslide erosion controlled by hillslope material. *Nat. Geosci.* 3, 247–251. doi:10.1038/ngeo776

Li, C. (2019). The Relationship between strain accumulation characteristics and seismic moment release on the southwestern margin of Ordos block. (in Chinese)

Li, S. (1960). *Catalog of earthquakes in China.* Beijing: Seismological Press. (in Chinese).

Li, W., Huang, R., Pei, X., and Zhang, X. (2015). Historical co-seismic landslides inventory and analysis using Google Earth: a case study of 1920 M8.5 Haiyuan earthquake, China. *Eng. Geol. Soc. Territ.*, 2. Switzerland: Springer, 709–712.

Li, X. (2018). Deformation pattern based on geometry and kinematics of active tectonics in the southwestern Ordos block. *Recent Dev. World Seismol.* 5, 43–45. doi:10.3969/j.issn.0253-4975.2018.05.009 (in Chinese).

Li, X., Feng, X., Li, X., Li, C., Zheng, W., Zhang, P., et al. (2019). Geological and geomorphological evidence for active faulting of the southern Liupanshan fault zone, NE Tibetan plateau. *Geomorphology* 345, 1–11. doi:10.1016/j.geomorph.2019.106849

Li, Z., Yang, L., Wang, G., Hou, J., Xin, Z., Liu, G., et al. (2019). Current status, problems and countermeasures of soil erosion control in the Loess Plateau. *Acta Ecol. Sin.* 39, 7398–7409. doi:10.5846/stxb201909021821 (in Chinese).

Meunier, P., Hovius, N., and Haines, J. (2008). Topographic site effects and the location of earthquake induced landslides. *Earth Planet Sci. Lett.* 275, 221–232. doi:10.1016/j.epsl.2008.07.020

National Earthquake Administration. (1988). *Ordos peripheral active fault system.* Beijing: Seismological Press. (in Chinese).

Parker, R., Densmore, A., Rosser, N., De, M., Li, Y., Huang, R., et al. (2011). Mass wasting triggered by the 2008 Wenchuan earthquake is greater than orogenic growth. *Nat. Geosci.* 4, 449–452. doi:10.1038/ngeo1154

Peng, J. (1992). Structural evolution and seismicity of the Weihe fault zone. *Seismol. Geol.* 14, 113–120. (in Chinese).

Ran, H. (2011). Empirical relations between earthquake magnitude and parameters of strike-slip seismogenic active faults associated with historical earthquakes in western China. *Seismol. Geol.* 33, 577–585. doi:10.3969/j.issn.0253-4967.2011.03.008 (in Chinese).

Song, F., Yuan, D., Chen, G., Ge, W., Cheng, J., and Su, H. (2007). Pattern and combination features of the surface ruptures of the 1125 A.D. Lanzhou M7 earthquake. *Seismol. Geol.* 29, 834–844. doi:10.3969/j.issn.0253-4967.2007.04.014 (in Chinese).

Sun, P., LiJiang, R. h., Lgwe, O., and Shi, J. (2017). Earthquake-triggered landslides by the 1718 Tongwei earthquake in gansu province, northwest China. *Bull. Eng. Geol. Environ.* 76, 1281–1295. doi:10.1007/s10064-016-0949-4

Sun, Y., Xu, G., Long, H., and Xu, L. (2016). Relationship between magnitude and rupture length. *Acta Seismol. Sin. (Chin. Ed.).* 38 (5), 803–806. doi:10.11939/jass.2016.05.014

Wang, A., Yuan, D., and Lei, Z. (2018). The distribution characteristics of seismic hazard and seismogenic structure of the southern Tianshui M6.0 Earthquake in 1936. *Earthq. Res. China* 34, 788–799. doi:10.3969/j.issn.1001-4683.2018.04.019 (in Chinese).

Wang, L. M. (2003). *Loess dynamics.* Beijing: Seismological Press. (in Chinese).

Wang, S. (2018). *Late Cenozoic structural deformation characteristics of the Liupanshan–Baoji fault zone on the northeastern margin of the Qinghai–Tibet Plateau.* Kirkland: Northwest University. (in Chinese).

Wells, D., and Coppersmith, K. (1994). Empirical relationships among magnitude, rupture length, rupture area, and surface displacement. *Bull. Seismol. Soc. Am.* 84, 974–1002. doi:10.1007/BF00808290

Xu, C., Xu, X., Yao, X., and Dai, F. (2014). Three (nearly) complete inventories of landslides triggered by the May 12, 2008 Wenchuan Mw 7.9 earthquake of China and their spatial distribution statistical analysis. *Landslides* 11, 441–461. doi:10.1007/s10346-013-0404-6

Xu, C., Xu, X., Zheng, W., Min, W., Ren, Z., and Li, Z. (2013). Landslides triggered by the 2013 Minxian-Zhangxian, Gansu province Ms6.6 earthquake and its tectonic analyses. *Seismol. Geol.* 35, 616–626. doi:10.3969/j.issn.0253-4967.2013.03.015 (in Chinese).

Xu, Y., Allen, M., Zhang, W., Li, W., and He, H. (2020a). Landslide characteristics in the loess plateau, northern China. *Geomorphology* 359, 107150. doi:10.1016/j.geomorph.2020.107150

Xu, Y., Du, P., Li, W., Zhang, W., Tian, Q., Xiong, R., et al. (2020b). A case study on AD 1718 Tongwei M7.5 earthquake triggered landslides—application of landslide database triggered by historical strong earthquakes on the Loess Plateau. *Chin. J. Geophys.* 63, 1235–1248. doi:10.6038/cjg2020N0146

Xu, Y., Liu-Zeng, J., Allen, M., Zhang, W., and Du, P. (2020c). Landslides of the 1920 Haiyuan earthquake, northern China. *Landslides* doi:10.1007/s10346-020-01512-5

Xu, Y., Zhang, W., Li, W., He, H., and Tian, Q. (2018). Distribution characteristics of the ad 1556 Huaxian earthquake triggered disasters and its implications. *Seismol. Geol.* 40, 721–737. doi:10.3969/j.issn.0253-4967.2018.04.001

Yang, X., Feng, X., Huang, X., Song, F., Li, G., Chen, X., et al. (2015). The Late Quaternary activity characteristics of the Lixian-Luojiabu fault: a discussion on the seismogenic mechanism of the Lixian M8 earthquake in 1654. *Chin. J. Geophys.* 58, 504–519. doi:10.6O38/cjg2O15O214

Ye, M., Meng, G., and Su, X. (2018). Locking characteristics and slip deficits of the main faults in the northeast margin of Tibetan plateau. *Earthquake* 38, 1–12. doi:10.3969/j.issn.1000-3274.2018.03.001

Yuan, D., Ge, W., Chen, Z., Li, C., Wang, Z., Zhang, H., et al. (2013). The growth of northeastern Tibet and its relevance to large-scale continental geodynamics: a review of recent studies. *Tectonics* 32, 1358–1370. doi:10.1002/tect.20081

Yuan, D., Lei, Z., and Wang, A. (2017). Additional textual criticism of southern Tianshui M8 earthquake in gansu province in 1654. *China Earthq. Eng. J.* 39, 0509–0520. 10.1155/2012/461863

Yuan, R., Deng, Q., Cunningham, D., Xu, C., Xu, X., and Chang, C. (2013). Density distribution of landslides triggered by the 2008 Wenchuan earthquake and their relationships to peak ground acceleration. *Bull. Seismol. Soc. Am.* 103, 2344–2355. doi:10.1785/0120110233

Zhang, B., He, W., Fang, L., Pang, W., Zhao, Z., and Liu, X. (2015). Surveys on surface ruptures phenomena of gansu kangle M6 3/4 earthquake in 1936. *J. Seismol. Res.* 38, 262–271. doi:10.3788/gzxb20184703.0324003

Zheng, D., Wang, W., Wan, J., Yuan, D., Liu, C., Zheng, W., et al. (2017). Progressive northward growth of the northern qilian Shan–hexi corridor (northeastern tibet) during the cenozoic. *Lithosphere* 9, 5877–5891. doi:10.1130/L587.1

Zheng, W., Lei, Z., Yuan, D., He, W., Ge, W., and Liu, X. (2007). Structural research on the 1837 northern Minxian M6 earthquake in Gansu Province and its causative structure. *Earthquake* 27, 120–130. doi:10.3969/j.issn.1000-3274.2007.01.016

Zheng, W., Zhang, P., He, W., Yuan, D., Shao, Y., Zheng, D., et al. (2013). Transformation of displacement between strike-slip and crustal shortening in the northern margin of the Tibetan Plateau: evidence from decadal GPS measurements and late Quaternary slip rates on faults. *Tectonophysics* 584, 267–280. doi:10.1016/j.tecto.2012.01.006

Conflict of Interest: The authors declare that the research was conducted in the absence of any commercial or financial relationships that could be construed as a potential conflict of interest.

frontiers
in Earth Science

ORIGINAL RESEARCH
published: 23 February 2021
doi: 10.3389/feart.2021.633117

Monitoring and Assessment for the Susceptibility of Landslide Changes After the 2017 Ms 7.0 Jiuzhaigou Earthquake Using the Remote Sensing Technology

Xinyi Guo[1,2]*, Bihong Fu*[1]**, Jie Du*[3]*, Pilong Shi*[1]*, Jingxia Li*[1,2]*, Zhao Li*[1,2]*, Jiaxin Du*[1,2]*, Qingyu Chen*[1,2] *and Han Fu*[1,2]

[1]*Key Laboratory of Digital Earth Science, Aerospace Information Research Institute, Chinese Academy of Sciences, Beijing, China,* [2]*University of Chinese Academy of Sciences, Beijing, China,* [3]*Jiuzhaigou Administration Bureau, Sichuan, China*

Monitoring the change of post-seismic landslides could provide valuable information for geological disaster treatment. The 2017 Jiuzhaigou Ms 7.0 earthquake has triggered a large number of landslides in the Jiuzhaigou United Nations Educational, Scientific and Cultural Organization (UNESCO) Natural Heritage site, which provides a unique opportunity for monitoring the spatio-temporal characteristics and exploring the impact factors of post-seismic landslides change. In this study, the spatio-temporal characteristics of landslides and their post-seismic changes are analyzed using multi-source, multi-temporal, and multi-scale remote sensing data combining with the field study. The Support Vector Machine classification, visual interpretation, field investigation, and Geographic Information System technology are employed to extract landslides and analyze their spatial distribution patterns. Moreover, the Certainty Factor method is used to explore the susceptibility of landslides and to find key impact factors. Our results show that the net increase area of landslide is 1.2 km^2 until September 27th, 2019, which are induced by the expansion of coseismic landslide, the post-seismic landslide, and the expansion of vegetation degradation. Moreover, the area expansion of the coseismic and post-seismic landslides is mainly related to the increase of debris flow induced by the post-seismic torrential rainfalls. The highest net increase rate of post-seismic landslide change does not distribute on the regions with the highest density of coseismic landslides. The susceptibility of post-seismic landslide change is greatly influenced by slope, altitude, aspect, peak ground acceleration fault, and strata. It is higher in the coseismic landslide area with low susceptibility. This study also suggests that the potential landslides will most likely occur in the unstable slope region affected by the additional driving force. Therefore, great attention should be paid to identify and prevent the potential landslides on unstable slopes in addition to treatments of the sliding slopes. This study provides a good example for the monitoring and assessment of post-seismic landslides in mountainous regions with a steep slope and deep valley.

Keywords: jiuzhaigou earthquake, post-seismic landslide, spatio-temporal variation, certainty factor method, Susceptibility analysis

OPEN ACCESS

Edited by:
Chong Xu,
Ministry of Emergency Management (China), China

Reviewed by:
Jia-wen Zhou,
Sichuan University, China
Fenghuan Su,
Institute of Mountain Hazards and Environment (CAS), China
Muhammad Shafique,
University of Peshawar, Pakistan

***Correspondence:**
Bihong Fu
fubh@aircas.ac.cn

Specialty section:
This article was submitted to Environmental Informatics and Remote Sensing, a section of the journal Frontiers in Earth Science

Received: *24 November 2020*
Accepted: *18 January 2021*
Published: *23 February 2021*

Citation:
Guo X, Fu B, Du J, Shi P, Li J, Li Z, Du J, Chen Q and Fu H (2021) Monitoring and Assessment for the Susceptibility of Landslide Changes After the 2017 Ms 7.0 Jiuzhaigou Earthquake Using the Remote Sensing Technology. Front. Earth Sci. 9:633117. doi: 10.3389/feart.2021.633117

HIGHLIGHTS

(1) Both coseismic landslides and post-seismic landslide change are concentrated in Jiuzhaitiantang-Panda Lake;
(2) The susceptibility of post-seismic landslide change is mainly influenced by slope, altitude, aspect, PGA, fault, and strata;
(3) The risk of post-seismic landslide change reduces in the high susceptibility area of coseismic landslide, but it increases in the low susceptibility area of coseismic landslide.

INTRODUCTION

This general term of landslides comprises almost all varieties of mass movements on slopes, including some, such as debris flows, rock falls, and rock slides (Varnes, 1984; Cruden and Varnes, 1996; Fan et al., 2019). In this study, landslides refer to the exposed rocks and soil area caused by mass movements on slopes, including their provenance, scraping, and accumulation areas, which are secondary disasters related to the seismic events. According to the triggers, the landslides related to earthquakes can be divided into 1) The slopes slide due to the strong force generated by earthquakes, which are called coseismic landslides; 2) The loose and unstable slopes affected by earthquakes are triggered by additional forces, such as heavy rainfall and other forces. They are called post-seismic landslides (Wang, 2004; Fan et al., 2018). In this study, the post-seismic landslide changes include the increase of landslides and the decrease of landslides after the earthquake, such as post-seismic landslides and restored landslides.

The strong earthquake will trigger large-scale coseismic landslides, which will cause great damage to people, buildings, natural and cultural heritages, such as the Ms 7.6 Chi-Chi earthquake in 1999 (Khazai and Sitar, 2004), the Ms 7.6 Pakistan earthquake in 2005 (Khattak et al., 2010), the Ms 8.0 Wenchuan earthquake in 2008 (Yin et al., 2009), the Ms 8.1 Nepal earthquake in 2015 (Regmi et al., 2016), and the Ms 7.0 Jiuzhaigou earthquake in 2017 (Dai et al., 2017; Fan et al., 2018). However, the effect of destructive earthquakes on landslides is not only in the coseismic stage but also in several years after the earthquake. Because of the destruction of earthquakes, the rock and soil are broken and the stability of slopes is reduced, resulting in active post-seismic landslides. The disaster activity time may last more than 10 years (Cui et al., 2011). Nakamura et al. (2000) studied the landslides for the periods after the 1923 M 7.9 Kanto Earthquake in Japan and considered that the most active stage of landslides was 15 years after the earthquake. The stage made the landslide area in a constantly changing process of increasing and recovering. To summarize the change characteristics of landslides and analyze the susceptibility of the impact factors can obtain the trend and the change rules of landslides, which has great significance for the post-seismic landslide treatment and ecological restoration.

At present, the previous studies on the post-seismic landslide change using multi-temporal remote sensing images have become a common concern in seismic landslide researches. The studies on different landslides show that the characteristics of post-seismic landslide change are as follows: 1) The restoration of landslide collapse area is worse than that of accumulation area (Lin et al., 2008); 2) The restoration ratio of landslides in two years after the earthquake is low (Khattak et al., 2010); 3) There is a good correlation between landslide restoration and terrain factors such as slope and altitude (Lu et al., 2012); 4) The restoration of landslides is related to lithology (Li et al., 2016). There are also some studies on the change characteristics of post-seismic landslide susceptibility, but the number of studies is small.

The post-seismic landslide change is still regarded as a part of coseismic landslides in the previous studies. There are essential differences between post-seismic landslides and coseismic landslides. Generally, the factors affecting landslides are mainly divided into background factors and trigger factors. Background factors are the necessary conditions for landslide occurrence, and trigger factors are the sufficient conditions for landslide occurrence (Qiao, 2010). For coseismic landslides, ground motion during earthquakes is the direct trigger factor. For post-seismic landslides, earthquake shaking is the background factor, which breaks the critical stability of the slope, and the trigger factors which directly trigger sliding are often external dynamic conditions such as heavy rainfall. Therefore, the post-seismic landslides should be studied as a separate landslide event and choose impact factors. Currently, since the post-seismic landslide changes and coseismic landslides are not considered separately, the characteristics of post-seismic landslide change obtained from the previous studies are not prominent enough, and the applicability of the characteristics is not common among different research areas.

There are few susceptibility studies on the selection of factors in the susceptibility analysis and the susceptibility change law of each factor in the process of landslide change after the earthquake. In previous studies, because the influence of some factors which are chosen is not significant, these factors have little contribution to susceptibility evaluation and the laws summarized from one impact factor can only be applied to this impact factor. There are almost no laws from the previous studies that can be used in different factors. Therefore, it is necessary to further study how to choose the factors and summarize the laws of the factors of the post-seismic landslide change.

On August 8th, 2017, a Ms 7.0 earthquake struck Jiuzhaigou, Sichuan Province, China. This earthquake triggered a large number of landslides (Wu et al., 2018), causing great damage to the Jiuzhaigou UNESCO Natural Heritage site. It is of great significance to study post-seismic landslide change for implementing the landslide treatments and the heritage site restoration. At the same time, because of detailed observation, dense vegetation, and significant change, the Jiuzhaigou area can provide a natural laboratory for studying the characteristics and impact factors of post-seismic landslide change. In the process of the dynamic change of landslide after the earthquake, it is necessary to extract landslides quickly and effectively, analyze their spatial distribution, summarize the characteristics of post-seismic landslide change, discuss the impact factors of post-seismic landslide change, conduct the multi-stage susceptibility analysis, and put forward the scientific treatment suggestions,

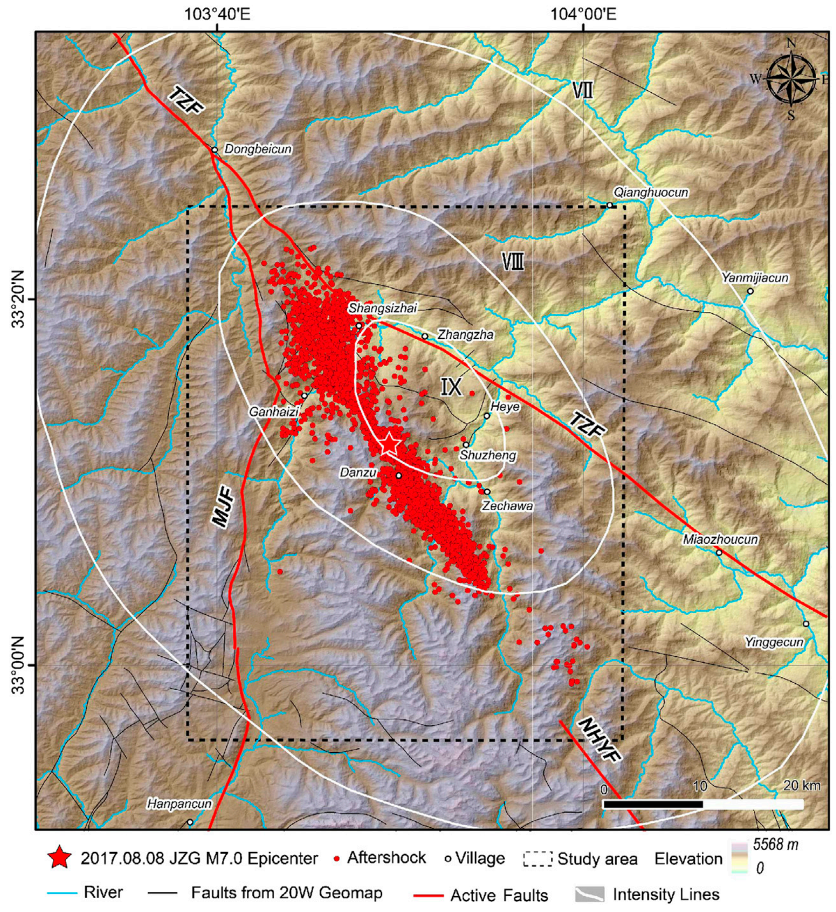

FIGURE 1 | Active tectonic map of the 2017 Jiuzhaigou Earthquake. MJF: Minjiang Fault, NHYF: North Huya Fault, TZF: Tazang Fault.

which are of great significance and value for the reconstruction of landslide areas.

In the Jiuzhaigou area with dense vegetation, bare land can be used as a symbol to identify landslides and even accurately extract the location and area of landslides. In this study, landslides are extracted by combining the SVM classification, visual interpretation, and field investigation. This study will analyze the pattern of spatial distribution and control factors of the post-seismic landslide change and the coseismic landslide. Then, the susceptibility of the landslide is explored by using the CF method, and the change rule is found out, the reasons for the change are summarized, and reasonable treatment suggestions are put forward.

STUDY AREA AND DATA

Study Area

Jiuzhaigou is located in the northeastern Tibetan Plateau. The terrain is high in the South and low in the North. It is the transition zone from the Tibetan Plateau to the Sichuan Basin and is also the turning point in front of the ridge of the highest terrain step in China (Guo et al., 2000). The area features deep-incized gullies and high mountains, the maximum peak is over 4700 m a.s.l. the minimum elevation is about 1200 m a.s.l. and the slope gradient is higher than 30° (Fan et al., 2018) (**Figure 1**).

The study area features outcrops of Devonian to Triassic sedimentation. The most representative lithology is a thick sequence of deep marine deposits, including limestone, flysch complex, and sandstone. The main lithology of Devonian strata is stratiform limestone and massive dolomite, the main lithology of Carboniferous stratum is layered and dense massive limestone, the main lithology of Permian stratum is siliceous limestone and sandy limestone, the lithology of Triassic stratum is mainly limestone and sandstone, and Quaternary loose deposits are distributed in river valleys (Dai et al., 2017).

At 21:19:46 on August 8th, 2017, a Ms 7.0 earthquake occurred in Jiuzhaigou County, Aba Autonomous Prefecture, Sichuan Province, China with an epicenter of (33.20°N, 103.82°E). The area affected by the Jiuzhaigou earthquake is more than 4,000 km^2 (VII degrees earthquake intensity and above). Due to the high magnitude, shallow source, and high intensity of the earthquake, as well as the fragile geological environment (high slope gradient, fragile lithology), the earthquake triggered thousands of landslides (Dong et al., 2020).

Data Description

To study the quantity, scale, and spatial distribution characteristics of post-seismic landslides, we used Sentinel-2 images (10 m) before and after the earthquake for preliminary identification of landslides. Erial images (1 m and 0.16 m) and a series of pre-earthquake images including Google Earth were used for more careful identification and verification. In this study, three Sentinel-2 images with low cloud and good data quality were selected and processed. Before the earthquake, the image on July 29th, 2017, was selected. After the earthquake, to ensure that the phenological differences have the least impact on the change detection results, the images on September 7th, 2017, and September 27th, 2019, in the same season after the earthquake were selected. All images cover the area of VII degree Jiuzhaigou earthquake intensity and above, where most of the disasters are distributed. The ortho-level erial remote sensing image of emergency observation after the earthquake is from the large aircraft of the Bureau of Surveying and mapping on August 10th, 2017, with a spatial resolution of 1 m. It covers the Shuzheng Gully Jianzhu Lake area about 97.17 km^2. The ortho-level unmanned erial vehicle (UAV) image after the earthquake is from the UAV (CW-15) image taken on June 10th, 2020, with a spatial resolution of 0.16 m. It covers the Shuzheng Gully Five Flower Lake area about 92.06 km^2. The images on Google Earth are from remote sensing images on August 13th, 2013, and October 21st, 2015. Terrain data, stratigraphical data, and seismic data are used to analyze the control factors of disasters and to evaluate their susceptibility. Terrain data are downloaded from ALOS DEM with a spatial resolution of 12.5 m. Stratigraphical data come from the 1:200,000 geological map. Seismic data obtained from the open data of the Jiuzhaigou earthquake on the USGS website (http://earthquake. usgshakemap.gov).

Data Preprocessing

The Sentinel-2 images in this study are L1C products, which are the top of atmosphere (TOA) reflectance products. They have been corrected by radiometric correction and orthorectification. This study uses the Sen2Cor plug-in provided by ESA for atmospheric correcting which converts TOA reflectance products into surface reflectance products (L2A products). The data resampled and format conversion are processed by SNAP. Finally, image products are under WGS 1984 coordinate system and UTM projection.

There may be geometric distortion and offset between the images in 2017 and 2019, which may cause errors in change detection. This study uses ENVI to register remote sensing images until the accuracy of registration is higher than 0.5 pixels, which can meet the requirements of landslide change detection.

METHODS

Landslide Identification

The Jiuzhaigou area has dense vegetation, with a coverage rate of 85.5% (Deng, 2011). In most landslide events, the vegetation on the slopes will be destroyed. So, it is easy to identify the bare land where vegetation is damaged by landslides. However, the vegetation of the area above 3700 m a.s.l. is sparse due to frost weathering and permanent snow. Previous studies have shown that landslides above 3700 m are rare in the Jiuzhaigou area (Wu et al., 2018). Therefore, this study extracts landslides in areas lower than 3,700 m a.s.l.

In landslide identification studies, visual interpretation is the most reliable method to identify landslides (Sun et al., 2020). However, due to the large number of landslides induced by the earthquake, the visual interpretation of landslides requires a large number of human resources and consumes a lot of time, which limits the landslide identification efficiency. We used a more efficient method to identify landslides. Firstly, based on Sentinel-2 and UAV remote sensing images, this study uses SVM classification (Vapnik, 1998) which selects samples manually and automatically classifies them by software with high accuracy and efficiency to extract the bare land within 2055 km^2 of the Jiuzhaigou area. It obtains the preliminary classification results of the bare land. Then, visual interpretation is used to verify the bare land represents the landslide results or not, and eliminate the false detection areas. For key areas or uncertain areas, field investigation is carried out to verify the results.

Change Detection

The accuracy of the image preprocessing results in *Data Preprocessing* is verified before the change detection. This study found that the error of the total area of landslide changes obtained by change detection can be controlled within 10^{-3} when the registration accuracy is within 0.5 pixels. It can meet the accuracy of change detection.

After obtaining the accurate landslides extraction results of 2017 and 2019, this study used the 2017 landslide area to erase the 2019 landslide area and used the 2019 landslide area to erase the 2017 landslide area, obtaining the new landslide area and the restored landslide area respectively, by the ArcGIS-Analysis-Erase tool, as shown in **Figure 2**.

The change of the total landslide area is the net change which is the sum of the new landslide area and the restored landslide area. The net change is the result of the difference between the new landslide area in 2019 and the restored landslide area in 2017. This study also named it the net increase. When the net increase was positive, it meant that the landslide area of 2019 increased; when the net increase was negative, it meant that the landslide area of 2019 recovered. This study assumes that the landslide area in 2019 is increased by "m" and restored by "n", compared with that in 2017. If the two images have offset which is left even after the registration, the results will have an error "i" which will be generated during the erasing operation. It means that the area of landslides in 2019 increases "$m + i$" and restores "$n + i$", as shown in **Figure 3**. However, when the net increase area is calculated by the difference between the increase and the recovery, that is "$(m + i) - (n + i)$", the net increase result is still "$m - n$", which is consistent with the result without error. In other words, when the offset after registration is small, it hardly has any effect on the result of change detection.

Influencing Factors Selection and Net Increase Rate Calculation

Previous studies suggested that landslides related to earthquakes are mainly affected by seismic factors, topographic factors, and geological factors (Keefer, 2000; Huang and Li, 2008). The

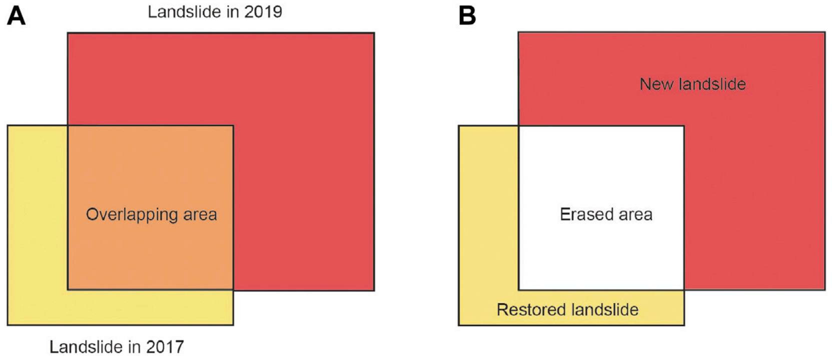

FIGURE 2 | Principle of change detection **(A)** Assumed range of landslides in 2017 and 2019 **(B)** Change detection of the new landslide and the restored landslide.

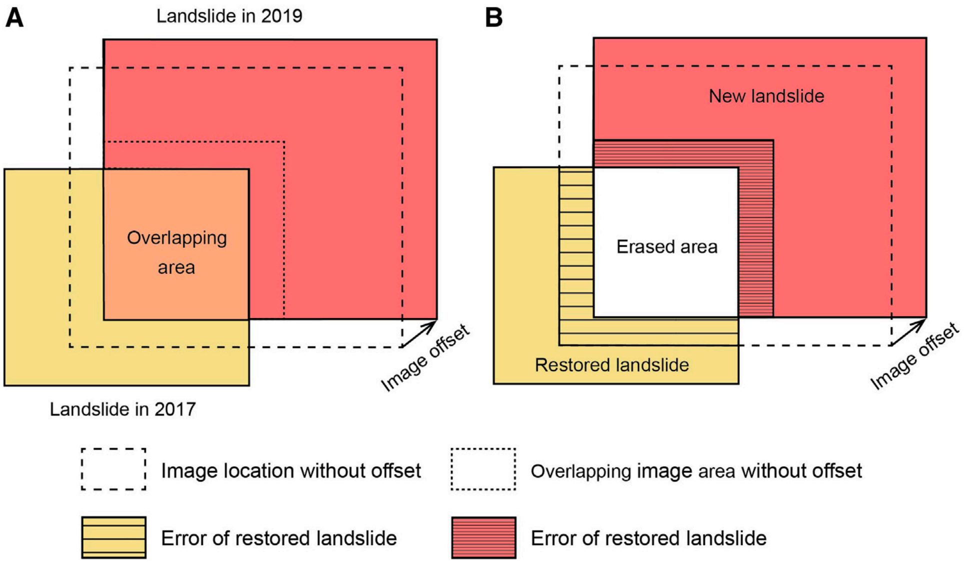

FIGURE 3 | Principle of change detection with offset **(A)** Dislocation in the two images **(B)** Change detection of landslide with image offset. The error of restored landslide: The change detection error of the new landslide is caused by an image offset. The error of restored landslide: The change detection error of the restored landslide is caused by an offset.

post-seismic landslide change is affected not only by seismic factors, topographical factors, and geological factors but also by external factors such as rainfall and the human's engineering treatments after earthquakes. However, the rainfall for the susceptibility of post-seismic landslide change is a trigger factor, not a background factor, and is difficult to predict in advance. So, this study does not select rainfall and selects the other eight factors. Seismic factors, topographic factors, and geological factors include PGA, slope, aspect, altitude, strata, and distance to the fault. Considering that landslide treatment work and human activities mainly distribute on both sides of the roads and rivers, the distance to the rivers and roads is also selected as an influencing factor.

In terms of slope, the slopes below 30° are divided by 10° intervals, and the slopes above 30° with dense landslides are divided by 5° interval; in terms of altitude, all the factors are divided by 200 m; in terms of aspect, it is divided by 45° interval, and the flat area without downhill direction is divided into Flat; in terms of strata, the strata are divided, according to stratigraphic age; in terms of PGA, when PGA is lower than 0.24 g, it is divided by an equal interval of 0.04 g, and when PGA is higher than 0.24 g, it is divided by an equal interval of 0.02 g; in terms of fault, rivers, and roads, as they are all linear elements, buffer zones with an equal interval of 1 km are generated on both sides. The spatial distribution histogram of landslides in 2017 was analyzed by GIS.

To conveniently display the landslide density under each classification, this study calculates the relative probability of landslide in the classification subsets of every factor, which is called the landslide area density (Landslide area/Classification area). Then this study normalizes it and colored it according to the normalized index (Dai et al., 2017).

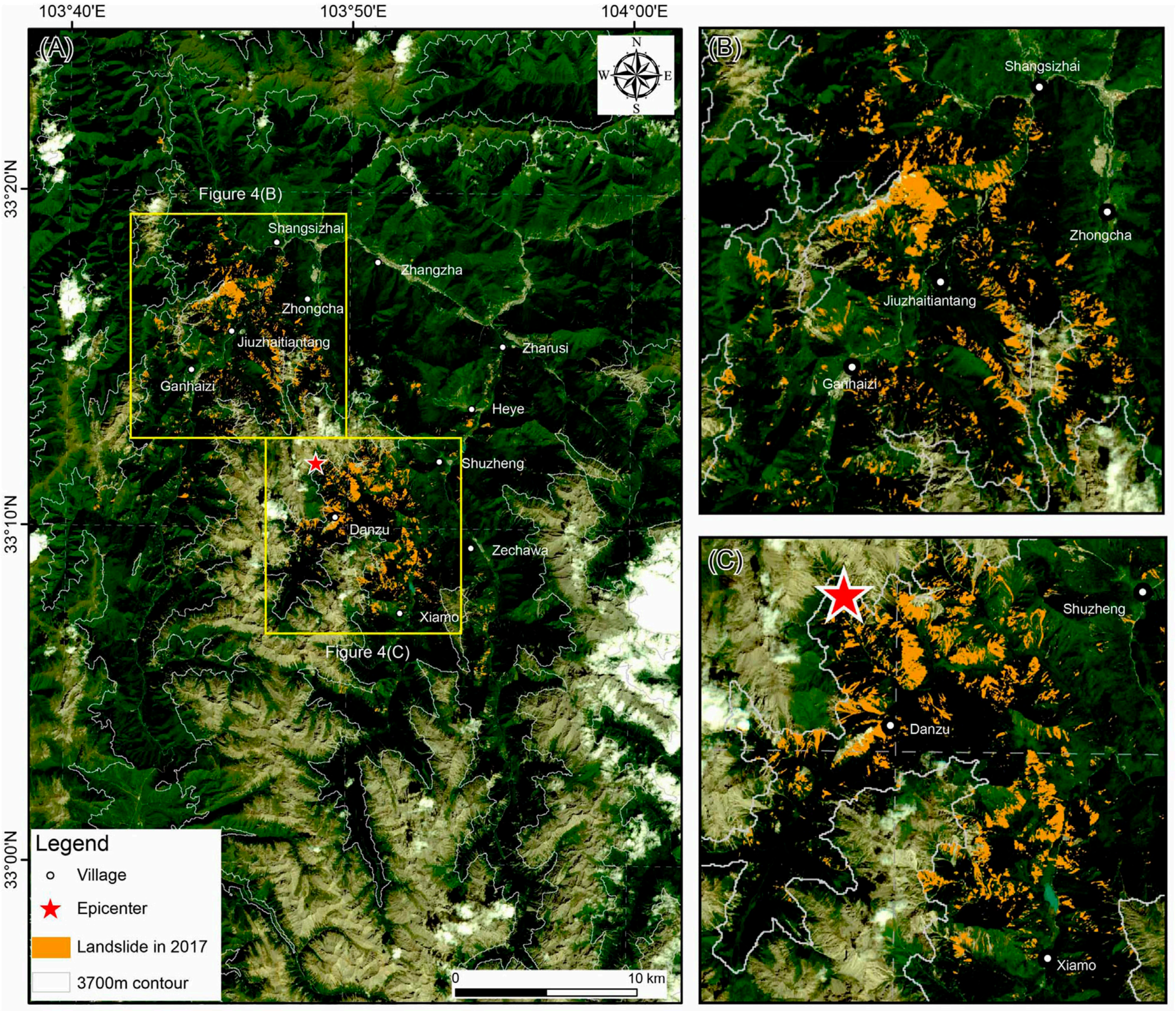

FIGURE 4 | Inventory map of the landslide in 2017 **(A)** Landslide map **(B)** Landslide map of Jiuzhaitiantang **(C)** Landslide map of Panda Lake.

In terms of post-seismic landslide change, this study defines a net increase rate to measure the change range of landslide under the classification subsets of every factor based on the net increase area. **Eq. 1** is listed as follows:

$$R_a = \frac{N_a - F_a}{F_a} \times 100\% \tag{1}$$

Where R_a is the net increase rate of the landslide in category "a", N_a is the area of current landslides in category "a", and F_a is the area of previous landslides in category "a". When $R_a > 0$, it means that the increase of landslide is greater than the restoration of the landslide, and the larger R_a is, the greater the increased range of landslide is; when $R_a < 0$, it means that the increase of landslide is less than the restoration of the landslide, and the smaller R_a is, the larger of landslide restoration is; when $R_a = 0$, it indicates that the increase and restoration of landslide reach a dynamic balance.

Susceptibility Calculation

The CF method is a probability function. It was first proposed by Shortliffe and Buchanan (Shortliffe and Buchanan, 1987) to analyze the susceptibility of various factors affecting the occurrence of an event. Lan et al. applied the CF method to the susceptibility analysis of regional landslides (Lan and Wu, 2002). **Eq. 2** is listed as follows:

$$CF = \begin{cases} \dfrac{P_a - P_s}{P_s(1 - P_a)}, P_a < P_s \\ \dfrac{P_a - P_s}{P_a(1 - P_s)}, P_a \geq P_s \end{cases} \tag{2}$$

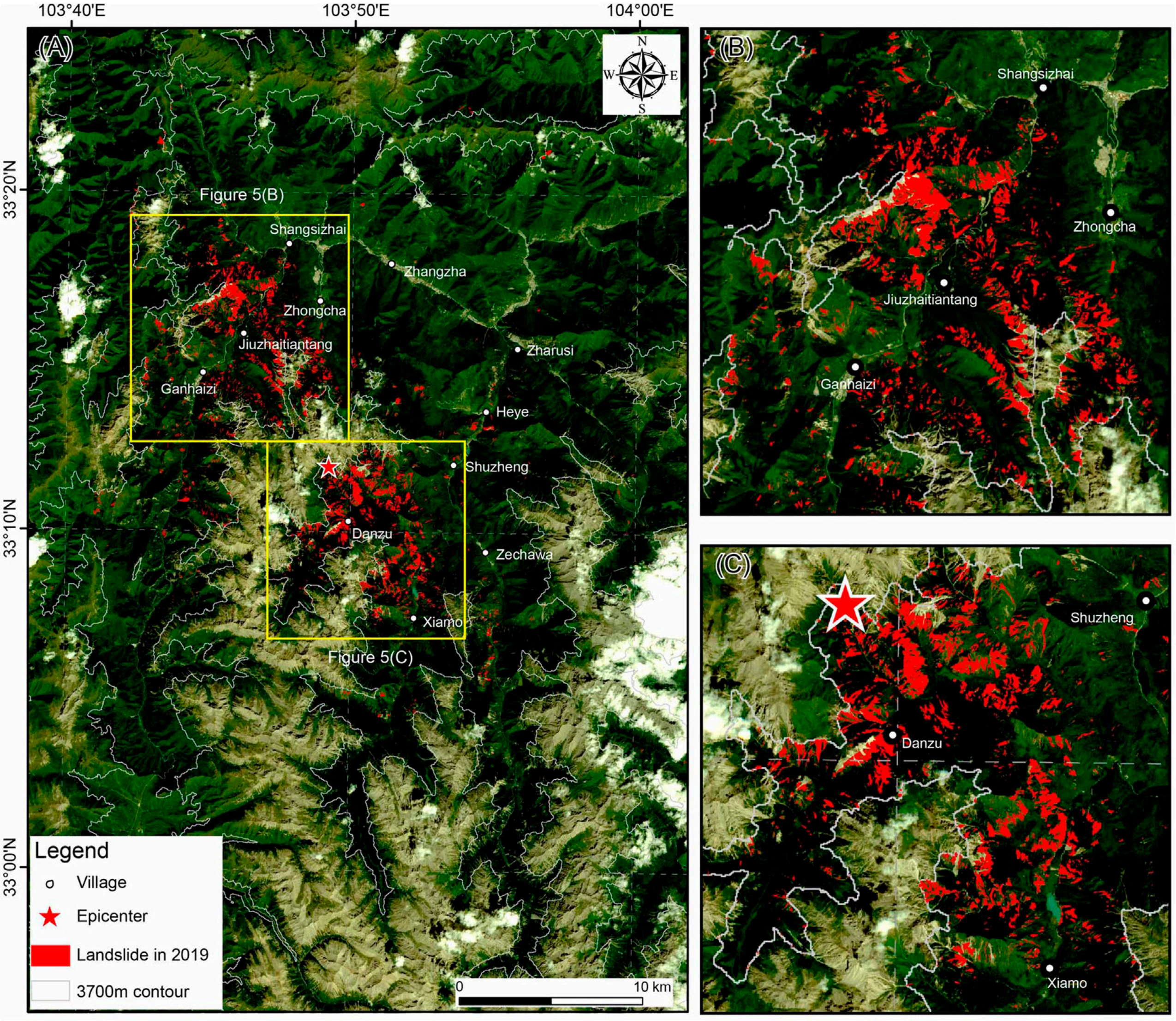

FIGURE 5 | Inventory map of the landslide in 2019 **(A)** Landslide map **(B)** Landslide map of Jiuzhaitiantang **(C)** Landslide map of Panda Lake.

Where P_a is the conditional probability of landslide occurrence in category "a", and P_s is the prior probability of landslide occurrence in the whole study area. P_a represents the ratio of the landslide area to the background area of the category "a"; P_s represent the ratio of the total landslide area to the total area of the study area. The range of CF is $[-1, 1]$. When $CF > 0$, the larger CF is, the more likely the slope will slide; when $CF < 0$, the smaller CF is, the less likely the slope will slide; when $CF = 0$, it indicates that the probability of slope sliding may not be determined.

RESULTS

Inventories of Coseismic Landslide and Post seismic Landslide Change

This study extracted the landslides in the Jiuzhaigou area within 2055 km^2. This scope almost covers the whole Jiuzhaigou landslide area. There were 4,456 landslides with an area of 13.7 km^2 in September 2017 (**Figure 4**) and 4,076 landslides with an area of 14.9 km^2 in September 2019 (**Figure 5**). In terms of post-seismic landslide change, the net increase area is 1.2 km^2, including the increased area of 3.6 km^2 (**Figure 6**) and the restored area of 2.4 km^2 (**Figure 7**).

Spatial Distribution of Coseismic and Post-seismic Landslides

The post-seismic landslide changes include the increased and restoration of landslides. They are distributed in the whole landslide area and are similar to the landslide distribution of 2017 and 2019. There are two gathering areas in space. One of the gathering areas is the area of Jiuzhaitiantang which is outside the scenic area, the other gathering area is the area of Panda Lake

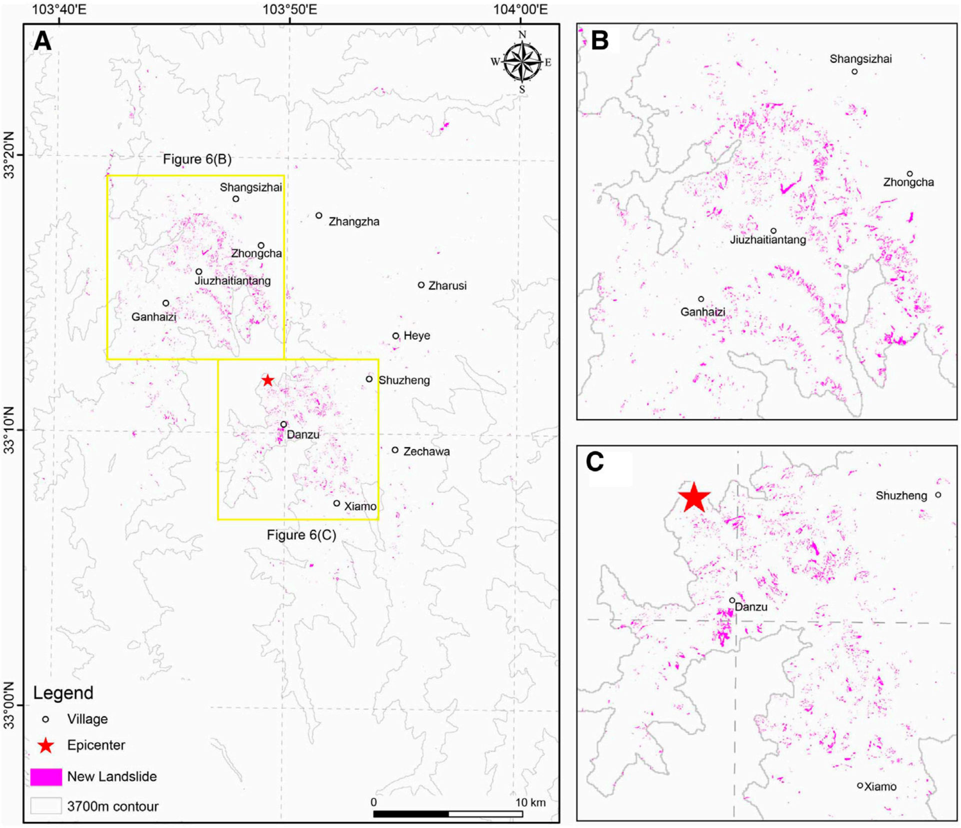

FIGURE 6 | Inventory map of new landslide area **(A)** New landslide map **(B)** New landslide map of Jiuzhaitiantang **(C)** New landslide map of Panda Lake.

which is in the scenic area. There are a small number of landslides along Shuzheng Gully and Zechawa Gully (**Figure 6**, **Figure 7**).

The post-seismic landslide changes type contains the expansion of coseismic landslide, the new post-seismic landslide, the expansion of vegetation degradation, and the landslide restoration. The expansion of coseismic landslide and the new post-seismic landslide belong to the post-seismic landslides which are mainly triggered by rainfall in the Jiuzhaigou area. The expansion of vegetation degradation is the result of vegetation damages caused by coseismic landslides. The landslide restoration is caused by natural succession or human treatments.

For the new landslide area, through remote sensing images and field investigation, it is found that the increased area comes from the expansion of coseismic landslide, the new post-seismic landslide, and the expansion of vegetation degradation. The expansion of coseismic landslide mostly occurs on the slopes with accumulated landslide materials (**Figure 8**), and the area is the largest; the new post-seismic landslides with significant changes are distributed in the whole disaster area (**Figure 9**), and the area is less than the expansion of the coseismic landslide area; the expansion of vegetation degradation which is affected by landslides on the slope is common (**Figure 10**), and the area is the smallest.

Through remote sensing images and field investigation, the landslide restoration caused by natural succession is distributed in all landslide areas and the landslide restoration caused by the engineering treatments is mainly distributed around roads, scenic spots, and residential areas, which is the most significant (**Figure 11**).

The relationship between the distribution of coseismic landslides, post-seismic landslide changes and seismic factors, topographic factors, geological factors, and human activities is shown in **Figure 12**.

Slope: Coseismic landslides are mainly distributed on the slopes of 30°–55° (**Figure 12A**) which is consistent with previous study results (Fan et al., 2018; Wang et al., 2018). However, for post-seismic landslide change, the slopes of 0°–10° and 20°–30° are the areas of landslide increasing significantly. On the slopes of 0°–10°, the net increase area is 0.0476 km^2 and the net increase rate is 216%. On the slopes of 20–30°, the net increase area is 1.6522 km^2 and the net increase rate is 209%. The net increase area and the net increase rate are both very large on the slope of 20–30°. The reason is that the post-seismic increase of landslide area in the Jiuzhaigou area is mainly caused by the expansion of coseismic landslide whose deposits will expand to the area with gentle slope under the additional force. This phenomenon also occurred in the process of post-seismic landslide change after the 2008 Ms 8.0 Wenchuan earthquake (Li, et al., 2018). With the increase of the slope and the landslide density, the net increase rate of landslide decreases. When the slopes above 50° have high landslide density, landslides hardly increase or even recover.

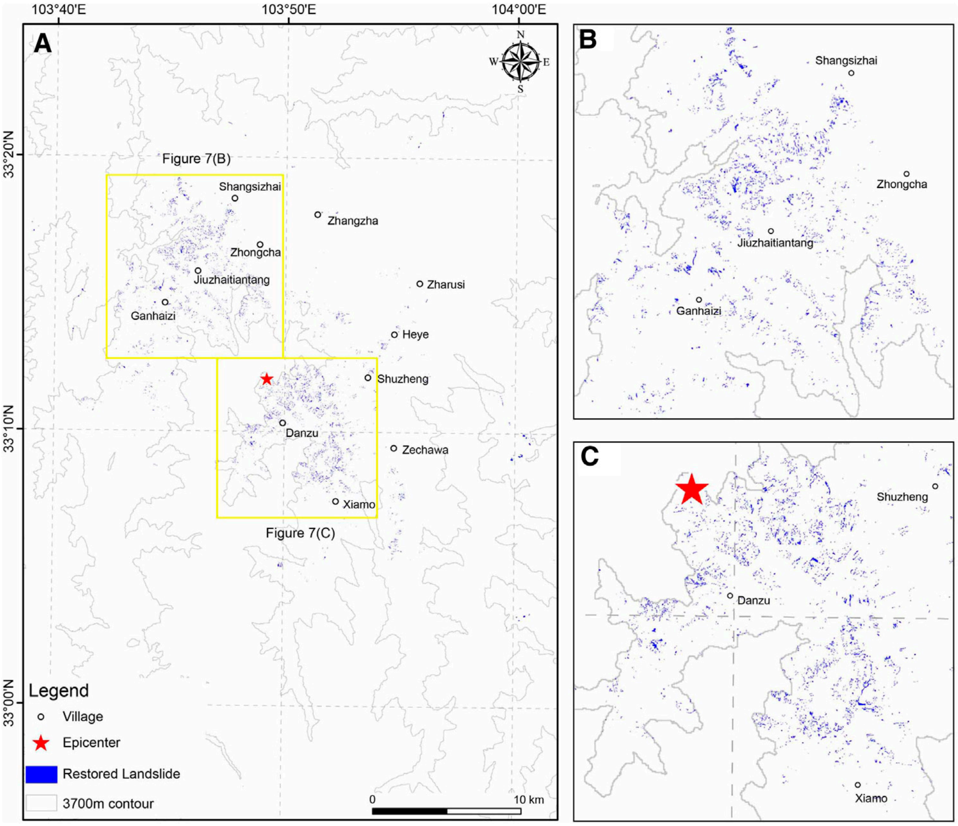

FIGURE 7 | Inventory map of the restored landslide area **(A)** Restored landslide map **(B)** Restored landslide map of Jiuzhaitiantang **(C)** Restored landslide map of Panda Lake.

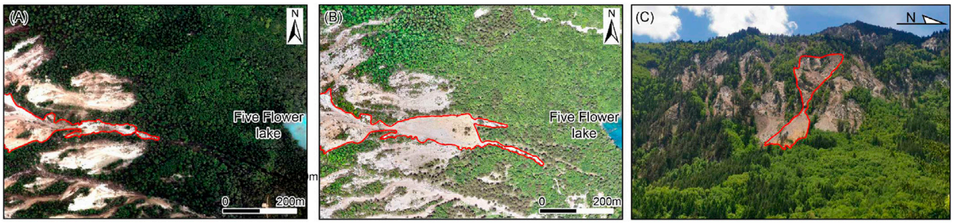

FIGURE 8 | Expansion of coseismic landslide **(A)** Coseismic landslide in 2017 **(B)** Expansion of coseismic landslide in 2020 **(C)** Field photo showing the expansion of coseismic landslide.

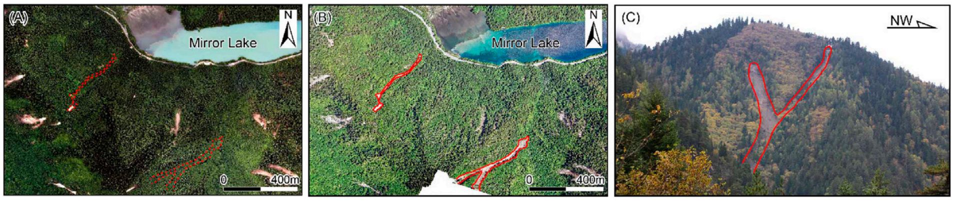

FIGURE 9 | Post-seismic landslide **(A)** Slope in 2017 **(B)** Post-seismic landslide in 2020 **(C)** Field photo showing the post-seismic landslide.

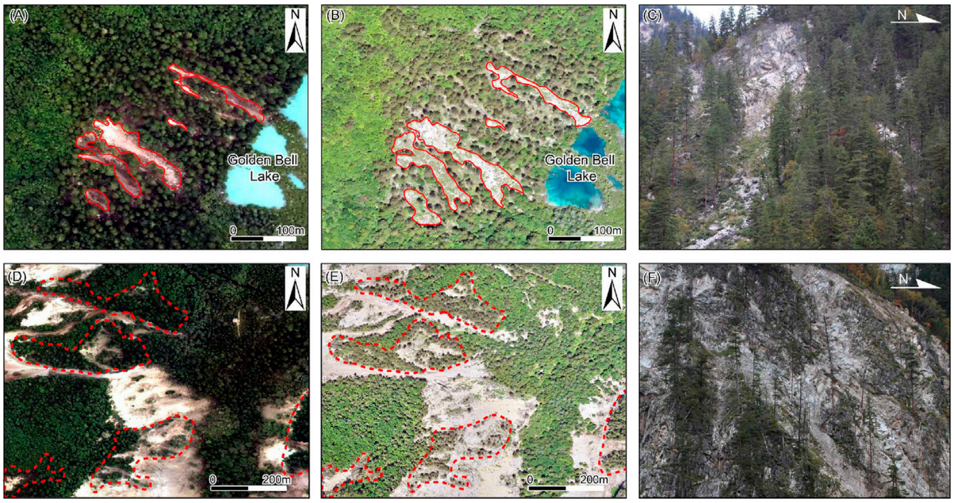

FIGURE 10 | Expansion of vegetation degradation **(A)** Coseismic landslides in 2017 **(B)** Hidden damage of landslide appears in 2020 **(C)** Field photo showing the damage caused by coseismic landslides **(D)** Vegetation damaged by the coseismic landslides in 2017 **(E)** Vegetation degradation on landslides in 2020 **(F)** Field photo showing the vegetation degradation caused by landslides.

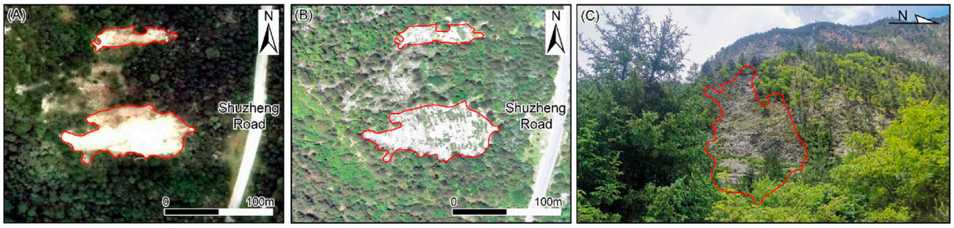

FIGURE 11 | Landslide restoration after treatment **(A)** Coseismic landslides in 2017 **(B)** The landslides with vegetation in 2020 **(C)** Field photo showing the landslide with vegetation.

Altitude: Coseismic landslides are mainly distributed on the slopes of 2,800–3,600 m a.s.l. (**Figure 12B**). However, for post-seismic landslide change, there is a great difference between the post-seismic landslide changes of 3,000–3,200 m a.s.l. and that of 3,200–3,400 m a.s.l. showing an opposite change pattern. The landslides of 3,000–3,200 m a.s.l. with the highest density show a significant recovery with a net increase rate of -20%. But, the landslides of 3,200–3,400 m a.s.l. with low landslide density show a significant increase with a net increase rate of nearly 60%.

Aspect: Coseismic landslides have a "back-slope effect" (Dai et al., 2017; Xie et al., 2018). They are mainly concentrated in the NE-S direction (**Figure 12C**). However, for post-seismic landslide change, the increase of post-seismic landslides is mainly concentrated on the slopes of SW, W, NW N, and NE which have low landslide density. The net increase rates of NW, N, and NE-facing slopes are high, with an average net increase rate of about 55%. On the slopes of E-S with high landslide density, the change of landslide shows a significant recovery. The landslides of flat land also recover.

PGA: Coseismic landslides are mainly concentrated in the area where the PGA is greater than 0.20 g (**Figure 12D**) (Yi et al., 2020). However, for post-seismic landslide change, the net increase rate of the landslide on the slopes of 0.2 g–0.26 g is not very high. The net increase rate of the landslide is 88% at 0.08 g and 170% at 0.12 g. The increase rate is 3% at 0.26 g, which is close to the constant state.

Fault: Coseismic landslides are mainly concentrated within 2 km away from the fault (**Figure 12E**) (Fan et al., 2018). With the increase of distance, the area and density of landslides decrease. However, for post-seismic landslide change, the net increase rate of landslides within 2 km is not very high. The net increase rate of landslides peaks at 67% in 9–10 km.

Strata: Coseismic landslides are mainly distributed in the area of Carboniferous and Permian strata (**Figure 12F**). The main lithology in the Carboniferous and Permian strata is limestone and dolomite. For post-seismic landslide change, the net increase rate of landslides in the strata of Carboniferous is 8% and in Permian is −2%, while that in the strata of Devonian, Triassic, and Quaternary with low landslide density are 17, 22, and 35% respectively.

Rivers: Coseismic landslides are mainly concentrated within 2 km away from the rivers (**Figure 12G**). With the increase of

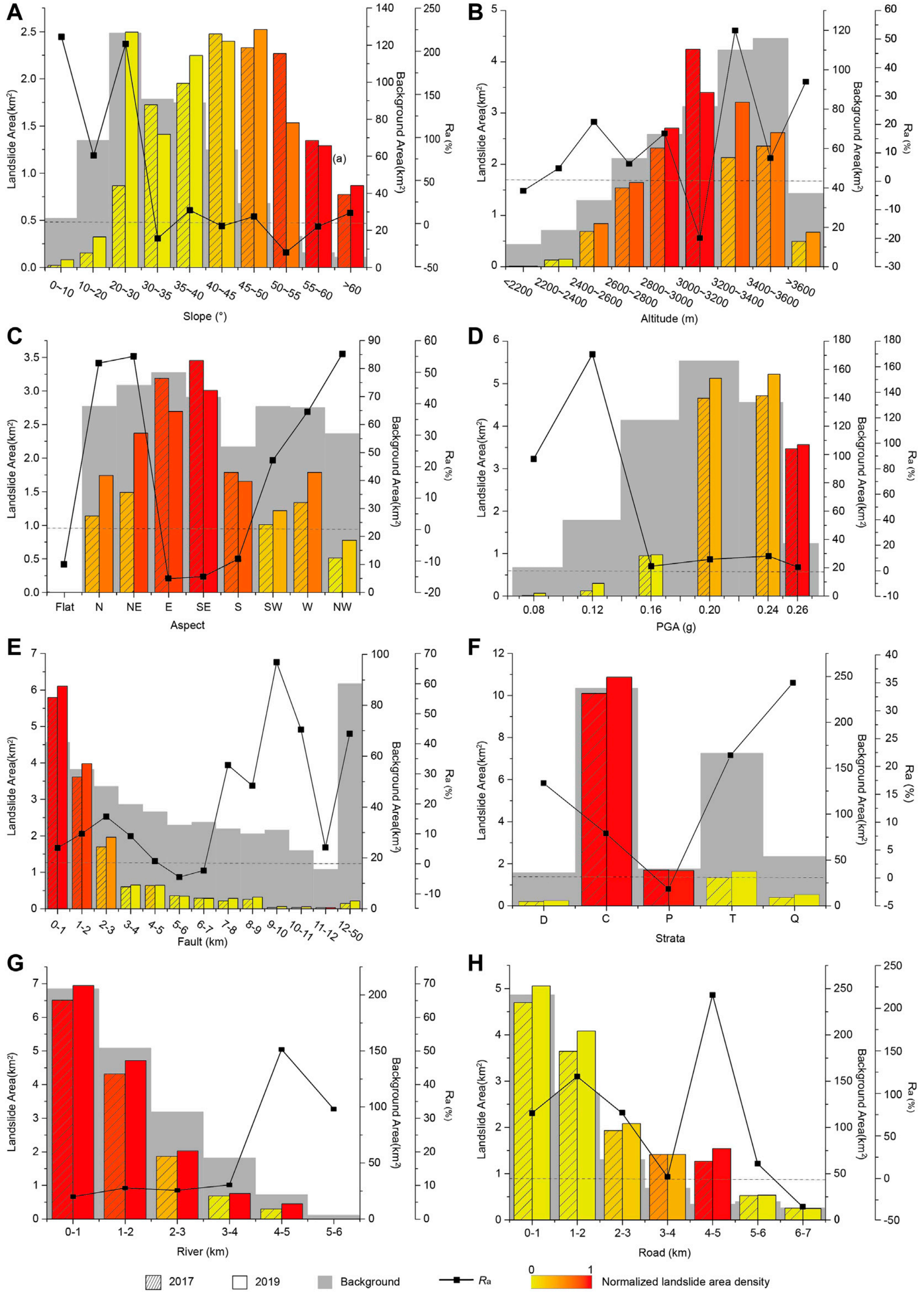

FIGURE 12 | Distribution of coseismic landslides and post-seismic landslide change **(A)** Slope **(B)** Altitude **(C)** Aspect **(D)** PGA **(E)** Distance to fault **(F)** Strata **(G)** Distance to rivers **(H)** Distance to roads.

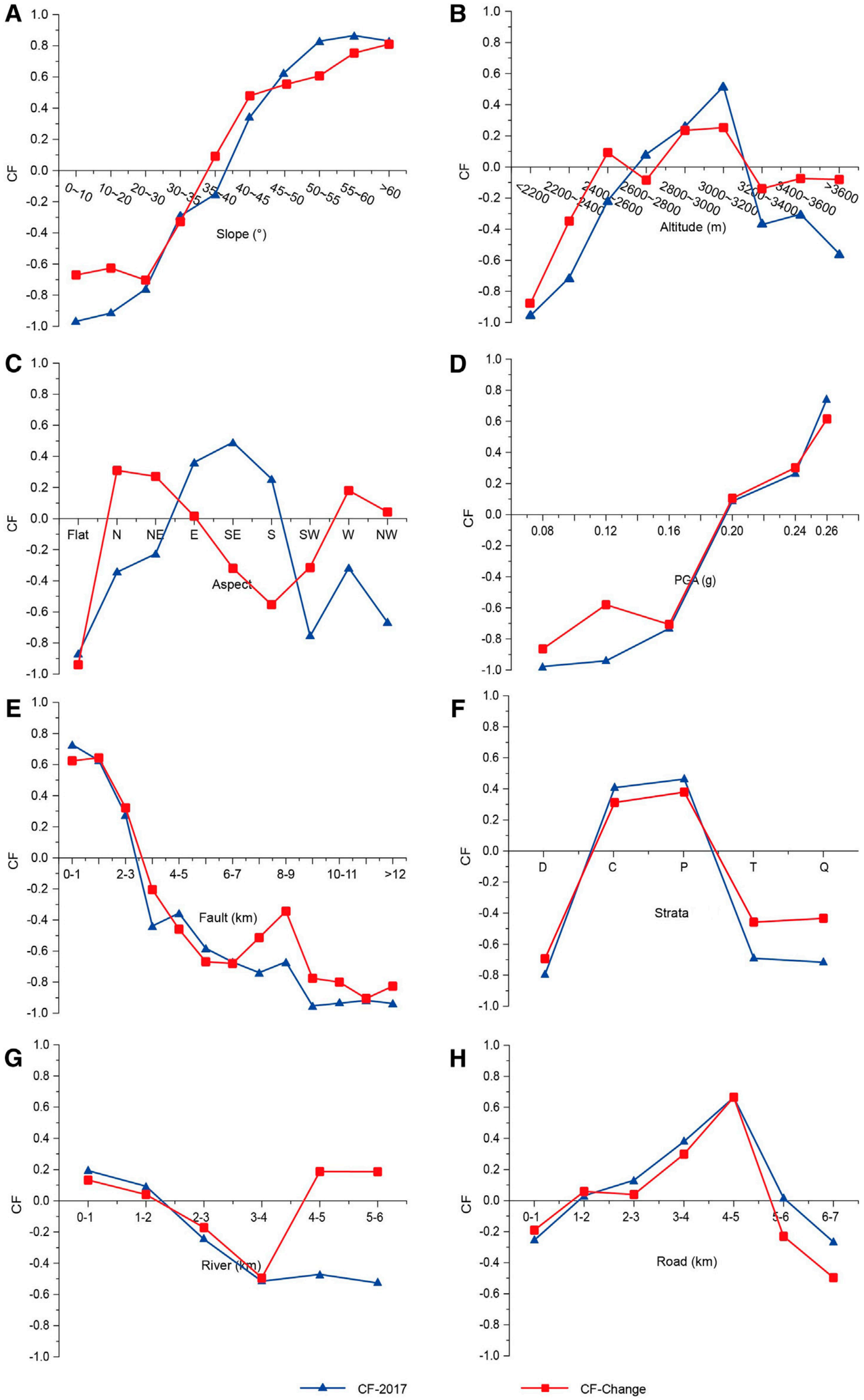

FIGURE 13 | Susceptibility of coseismic landslides and post-seismic landslide change **(A)** Slope **(B)** Altitude **(C)** Aspect **(D)** PGA **(E)** Distance to fault **(F)** Strata **(G)** Distance to rivers **(H)** Distance to roads.

distance, the area and density of landslides decreases. However, for post-seismic landslide change, the net increase rate of landslides in 0–2 km is not very high. The net increase rate peaks at 50% at 4–5 km.

Roads: Coseismic landslides are mainly concentrated within 2 km from the roads (**Figure 12H**). However, for post-seismic landslide change, the net increase rate of landslides in 0–2 km is close to the average net increase rate, which is not high. The net increase rate peaks at 22% in the area from the roads about 4–5 km.

The Susceptibility of Coseismic Landslide and Post-seismic Landslide Change

The susceptibilities of eight factors related to coseismic landslides and post-seismic landslide change are shown in **Figure 13.**

Slope: For coseismic landslides, the range of CF values is from −0.96–0.86. The CF values increase rapidly with the increase of slope and peak on the slope of 55°–60° (**Figure 13A**). The steeper the slope is, the more likely the landslide will slide. For post-seismic landslide change, the trend of CF values is consistent with that of coseismic landslides. However, the range of CF values is from −0.67 to 0.81, which is smaller than that of coseismic landslides. The CF values of post-seismic landslide change are higher than that of coseismic landslides on the slope within 45°, and the CF values of change landslides are less than that of coseismic landslides on the slope above 45°. The susceptibility of landslide varies widely and is significantly affected by the slope.

Altitude: For coseismic landslides, the range of CF values is from −0.96 to 0.52 (**Figure 13B**). The CF values increase with the increase of altitude when the altitude is lower than 3,000–3,200 m a.s.l. and decreases with the increase of altitude when the altitude is higher than 3,000–3,200 m a.s.l. The CF value peaks at 3,000–3,200 m a.s.l. indicating that the possibility of slope sliding is the highest. For post-seismic landslide change, the trend of CF values is consistent with that of coseismic landslides. However, the range of CF values is from −0.88 to 0.25, which is smaller than that of coseismic landslides. Within the altitude of 2,800 m a.s.l. coseismic landslides are not easy to slide. The CF values of post-seismic landslide change is a little higher than that of coseismic landslides in this area. Above 3,200 m a.s.l. the CF values have similar characteristics.

Aspect: For coseismic landslides, the range of CF values is from −0.87 to 0.49 (**Figure 13C**). The CF values on E, SE, and S-facing slopes are positive, which indicates that the slopes may slide. The CF value peaks on SE-facing slopes, indicating that SE-facing slopes have the highest possibility of sliding. They are negative in other aspects and flat, which shows that these slopes are not easy to slide. However, for post-seismic landslide change, the range of CF value of landslides is smaller than that of coseismic landslides, ranging from −0.94 to 0.31. In the slopes where coseismic landslides are not easy to slide, post-seismic landslides are more likely to slide. In the slopes where coseismic landslides are easy to slide, post-seismic landslides are not easy to slide. The CF values of N, NE, W, and NW-facing slopes are positive, which indicates that the landslide may slide. The CF value peaks on the N-facing slope, which indicates the sliding probability is higher. The CF values of other slopes are negative or close to 0, which indicates the sliding probability is low.

PGA: For coseismic landslides, the range of CF values is from −0.98 to 0.75 (**Figure 13D**). The CF values increase with the increase of PGA and peak at the maximum of PGA, indicating that the larger the PGA is, the more likely the landslide will slide. For post-seismic landslide change, the trend of CF values is consistent with that of coseismic landslides. However, the range of the CF values is from −0.89 to 0.61. It is smaller than the CF values of coseismic landslides. The susceptibility of the landslide is significantly affected by PGA.

Fault: For coseismic landslides, the range of CF values is from −0.95 to 0.73 (**Figure 13E**). The CF values decrease with the increase of the distance to the fault. It indicates that the closer the distance is to the fault, the more likely the landslide will slide. For post-seismic landslide change, the trend of CF values is consistent with that of coseismic landslides. However, the range of CF values is from −0.91 to 0.64. It is smaller than the CF values of coseismic landslides.

Strata: For coseismic landslides, the range of CF values is from −0.72 to 0.46 (**Figure 13F**). The CF values are high in the area of Carboniferous and Permian strata, and they are 0.41 and 0.46 respectively. The CF values are −0.80, −0.69, −0.72 respectively in areas of Devonian, Triassic, and Quaternary strata, which means the possibilities of sliding in those areas are low. For post-seismic landslide change, the trend of CF values is consistent with that of coseismic landslides while the range of CF values which is from −0.70 to 0.38 is a little smaller than that of coseismic landslides.

Rivers: For coseismic landslides, with the increase of the distance to the rivers, the CF values vary slightly, ranging from −0.53 to 0.19 (**Figure 13G**). Within 2 km away from the rivers, the CF values are positive, which is beneficial to slide, but the possibility is not too high. The CF values are negative over 2 km, which is not easy to slide. However, for post-seismic landslide change, the CF values within 2 km or more than 4 km are positive. The maximum of CF values is only 0.19, and the susceptibility is not very high. The CF values change with the change of the distance to the fault is not significant. So, there is no significant correlation between the susceptibility and the distance to the rivers.

Roads: For coseismic landslides, the range of CF values is from −0.66 to 0.27 (**Figure 13H**). The CF values increase with the increase of the distance within 4 km away from the roads and decrease with the increase of the distance over 5 km. It peaks at 0.66 when the range of distance is 4–5 km, indicating that the possibility of landslide sliding is the highest. It is positive when the distance is between 2 and 6 km, which shows that it is easy to slide. For post-seismic landslide change, the trend of CF values is consistent with that of coseismic landslides. However, the range of CF values is a little bigger than that of coseismic landslides.

DISCUSSION

Integrity and Accuracy of the Coseismic Landslide Database and Spatial Distribution

Incomplete landslide databases may mislead the studies of landslide distribution and they may mislead the studies of susceptibility assessment (Xu and Xu, 2014). A complete landslide database can provide accurate information for fault studies or other studies, such as assisting in identifying the blind fault on the unexposed surface of the Jiuzhaigou earthquake (Fan et al., 2018). In the previous studies of Jiuzhaigou, their landslide areas are not consistent. It indicates that their landslide databases may be incomplete, which leads to inconsistencies in landslide distribution studies, such as the studies of Tian et al. (2019), Dai et al. (2017), Wu et al. (2018), and Liang et al. (2019). In these studies, the results of the distribution are incompletely consistent, especially the slope distribution.

Landslides are extracted from the satellite and erial remote sensing images by the monitoring technology of integrated space-air-ground. SVM classification is used to extract landslides. Visual interpretation and field investigation are used to verify the extracted result. This method can improve the speed and accuracy of landslide interpretation. It avoids the problem that visual interpretation needs the cooperation of many people with different interpretation experience which is easy to get inaccurate interpretation results. Therefore, the landslides extracted in this study is more comprehensive and the distribution results are more accurate.

Post-seismic Landslide Change

Causes of Post-seismic Landslide Change

The landslide area of Jiuzhaigou is larger in 2019 than that in 2017. A previous study on the landslides related to the 2008 Wenchuan earthquake shows that the frequency of the landslides increased significantly within 5 years after the earthquake. Compared with the pre-seismic records, the number of post-seismic landslides is 2–5 times higher than that before the earthquake (Huang and Li, 2014). Strong earthquakes not only trigger a large number of coseismic landslides but also induce relaxation and cracks in the rocks and soils which make these rocks and soils vulnerable to instability during subsequent aftershocks or rainfall events (Fu et al., 2020). Some cracks can become the boundary of the post-seismic landslides and the main permeable path for subsequent rainwater (Huang et al., 2019). Moreover, coseismic landslides will also produce a large number of loose deposits on the slope. The deposits on the slope can remobilize and turn into debris flow during heavy rainy seasons. Three heavy rainfall events occurred in September 2017, August 2018, and August 2019 after the 2017 Jiuzhaigou earthquake, all of which induced mass geological disasters (Huang et al., 2020). When the speed of landslide occurrence is faster than that of landslide recovery, the landslide area will increase. Only 2 years after the 2017 Jiuzhaigou earthquake, the post-seismic recovery needs a longer period. Therefore, the landslide area will increase in recent and future times.

Rules and Causes of Spatial Distribution of Post-seismic Landslide Change

In this study, the net increase rate is used to measure the post-seismic landslide change. The spatial distribution pattern of post-seismic landslide change and coseismic landslides is quite different in the factors of earthquake, topography, geology, and human activities. This study suggests that the areas with high landslide density are most affected by the strong earthquake shaking and the unstable slopes have already slipped during the earthquake. Thus, there are almost no new landslides in these areas within two years after the earthquake. In other areas, the earthquakes did not trigger too many coseismic landslides. But these slopes (Delgado et al., 2011) and their ecological environment (Lu et al., 2012) have been weakened by the earthquakes. The earthquakes induced relaxation and cracks and produced deposits on them. Therefore, these slopes become the main increase areas of landslides triggered by other additional forces after the earthquake. There is a general rule across the factors: the highest net increase rate of post-seismic landslide change does not distribute on the regions with the highest density of coseismic landslides; on the contrary, the areas with the highest density of coseismic landslides show that the net increase rates of landslides are close to 0. For slope and PGA, the net increase rate is close to 0 in the area with the highest density of coseismic landslides. For altitude and aspect, the net increase rate is negative in the area with the highest density of coseismic landslides. For faults, strata, and rivers, the net increase rate in the areas with the highest density of coseismic landslides is small and not more than 10%.

The increase areas of landslides can be divided into three cases as described in *Spatial Distribution of Coseismic and Post-seismic Landslides*: 1) Some landslides with deposits on the slope do not reach the state of stress balance, which is conducive to expansion under the trigger of additional driving forces, such as rainfall after the earthquake. This case is the most common in the Jiuzhaigou area, such as the landslide areas around Five Flower Lake (**Figure 8**); 2) There is no landslide on the slope weakened by the earthquake, but if the slope is affected by additional driving forces, post-seismic landslides will happen in this area, which changes most significantly, such as the post-seismic landslide at Mirror Lake (**Figure 9**); 3) There has been small collapse or displacement on the slopes due to the earthquake. But the damage is not easy to be detected due to the shelter of the vegetation. So, the impact is not significant in the early stage after the earthquake. However, the change of slope will cause some disturbance to the adjacent or overlying vegetation. The vegetation will degenerate with time (Guo et al., 2020), and then landslides can be detected. This case is also very common, but the area is not too big (**Figure 10**).

Rules and Causes of Susceptibility of Post-seismic Landslide Change

In this study, the susceptibilities of the coseismic landslides and the post-seismic landslide change are calculated respectively. The susceptibility of post-seismic landslide change changed significantly with slope, altitude, aspect, PGA, fault, and strata (**Figure 13**). Reasons for the susceptibility anomaly of post-seismic landslide change are consistent with the spatial distribution anomaly. From the distribution of susceptibility, there are general rules across the factors: the susceptibility peak value of the post-seismic landslide change is lower than that of the coseismic landslide; the susceptibility of the post-seismic landslide change is lower than that in the coseismic landslide area with high susceptibility, which indicates that the landslide risk reduces; the susceptibility of the post-seismic landslide change is higher than that in the coseismic landslide area with low susceptibility, which indicates that the landslide risk increases.

The potential landslides in the area with high landslide density have already slipped in the earthquake, which results in that the susceptibility decrease. In the original low susceptibility areas which have been weakened by the earthquake events, new landslides will occur due to the influence of additional driving force after the earthquake, which results in that the susceptibility increase.

In the process of post-seismic landslide change, rainfall is one of the important forces that trigger the post-seismic landslide change, especially the expansion of coseismic landslide. It will remobilize the deposits on the slope which will expand to the area with a more gentle slope and lower altitude and cause damage to these areas. It results in the susceptibility of these areas with low susceptibility increases. This dynamic situation will last for a long time in the future.

Suggestions for the Investigation and Mitigation of the Post-seismic Landslides

This study suggests that landslides are investigated by the monitoring technology of integrated space-air-ground which includes multi-source, multi-temporal, and multi-scale remote sensing data and field study. The SVM classification, visual interpretation, field investigation, and GIS technology are employed in this study. They can create complete and accurate landslide inventories and analyze the spatio-temporal characteristics of landslides and their post-seismic changes.

According to the characteristics of spatial distribution and susceptibility, this study proposes some opinions for the treatments of landslides in the post-seismic change process. For the coseismic landslides, the expansion is caused by the remobilization of landslide deposits on slopes, accounting for the largest proportion of the increase of landslide area. These slopes should be reinforced and the landslide deposits should be cleared. However, because of the huge amount of landslide deposits, it is difficult to clear them in a short time. We suggest that reasonable dredging and reuse treatments of deposits should be implemented. For the small-scale coseismic collapses or potential post-seismic landslides triggered by the additional driving force, they are difficult to be found with the shelter of the vegetation. But, vegetation anomalies can be used as good indicators to identify them in the concealed unstable slopes. Great attention should be paid to extract the potential landslides by identifying the vegetation anomaly in the concealed unstable slopes. These unstable slopes also should be reinforced to prevent sliding.

CONCLUSION

(1) Coseismic landslides and post-seismic landslide change are concentrated in the Jiuzhaitiantang-Panda Lake area. The increased area of the landslide is 3.6 km^2, the restored area is 2.4 km^2, and the net increase area is 1.2 km^2, compared with the coseismic landslide, until September 27th, 2019. The expansion includes the expansion of coseismic landslide, the post-seismic landslide, and the expansion of vegetation degradation. The area expansion of the coseismic and post-seismic landslides is mainly related to the increase of debris flow induced by the post-seismic torrential rainfalls. The reduction contains the restoration caused by natural succession or the engineering treatments.

(2) The susceptibility of post-seismic landslide change is greatly influenced by slope, altitude, aspect, PGA, fault, and strata. Due to the post-seismic changes of stress and slope stability, the risk of post-seismic landslide change reduces in the high susceptibility area of coseismic landslide and it increases in the low susceptibility area of coseismic landslide.

(3) The slope with coseismic landslides should be reinforced and the landslide deposits should be cleared, dredged, or reused. The concealed unstable slope which may have potential landslides should be paid great attention to identify the potential landslides by extracting the vegetation anomaly to prevent potential landslides.

DATA AVAILABILITY STATEMENT

The original contributions presented in the study are included in the article/Supplementary Material, further inquiries can be directed to the corresponding author.

AUTHOR CONTRIBUTIONS

XG and BF designed this study, analyzed the data, and wrote the manuscript; Jie D, PS, JL, ZL, Jia D, QC, and HF worked on the processing of remote sensing data and field investigations. All authors approved the final version of the manuscript.

FUNDING

This work was funded by the Second Tibetan Plateau Scientific Expedition and Research Program (STEP, Grant No. 2019QZKK0901) and Project on Integrated Space-Air-Ground of Jiuzhaigou World Natural Heritage Site supported by the Jiuzhaigou Administration Bureau (Grant No. E0H20501).

ACKNOWLEDGMENTS

We are grateful for the helpful discussion with Yueren Xu of the Institute of Earthquake Forecasting, China Earthquake Administration. We really appreciate the constructive comments and suggestions from three reviewers, which are helpful to improve the quality of our manuscript.

REFERENCES

Cruden, D. M., and Varnes, D. J. (1996). Landslide types and processes. Special Report. Transportation Research Board, National Research Council, 247, 36–75. Available at: https://onlinepubs.trb.org/Onlinepubs/sr/sr247/sr247-003.pdf (Accessed August 17, 1996).

Cui, P., He, S. M., Yao, L. K., Wang, Z. Y., and Chen, X. Q. (2011). *Formation mechanism and risk control of mountain disaster caused by the Wenchuan earthquake*. Science Press, 2.

Dai, L. X., Xu, Q., Fan, X. M., Chang, M., Yang, Q., Yang, F., et al. (2017). A preliminary study on spatial distribution patterns of landslides triggered by Jiuzhaigou earthquake in Sichuan on August 8th, 2017, and their susceptibility assessment. *J. Eng. Geol.* [in Chinese, with English summary].

Delgado, J., Garrido, J., López-Casado, C., Martino, S., and Peláez, J. A. (2011). On far field occurrence of seismically induced landslides. *Eng. Geol.* 123 (3), 204–213. doi:10.1016/j.enggeo.2011.08.002

Deng, G. P. (2011). Study of Tourism Geosciences Landscape Formation and Protection of Jiuzhaigou World Natural Heritage Site. Dissertation/doctor's thesis. Chengdu (China): Chengdu University of Technology.

Dong, X. J., Xu, Q., She, J. X., Li, W. L., Liu, F., and Zou, X. X. (2020). Preliminary study on interpretation of geological hazards in Jiuzhaigou based on multi-source remote sensing data. Geomatics and Information Science of Wuhan University, 45 (3), 432–441 [in Chinese, with English summary]. doi:10.13203/j.whu-gis20130532

Fan, X. M., Scaringi, G., Korup, O., West, A. J., Westen, C. J. V., Tanyas, H., et al. (2019). Earthquake-induced chains of geologic hazards: patterns, mechanisms, and impacts. *Rev. Geophys.* 57, 421–503. doi:10.1029/2018RG000626

Fan, X. M., Scaringi, G., Xu, Q., Zhan, W. W., Dai, L. X., Li, Y. S., et al. (2018). Coseismic landslides triggered by the 8th August 2017 MS 7.0 Jiuzhaigou earthquake (sichuan, China): factors controlling their spatial distribution and implications for the seismogenic blind fault identification. *Landslides* 15 (5), 967–983. doi:10.1007/s10346-018-0960-x

Fu, X. D., Sheng, Q., Li, G., Zhang, Z. P., Zhou, Y. Q., and Du, Y. X. (2020). Analysis of landslide stability under seismic action and subsequent rainfall: a case study on the Ganjiazhai giant landslide along the Zhaotong-Qiaojia road during the 2014 Ludian earthquake, Yunnan, China. *Bull. Eng. Geol. Environ.* 79, 5229–5248. doi:10.1007/s10064-020-01890-z

Guo, J. Q., Peng, D., Cao, J., and Yang, J. Y. (2000). Geomorphology and quaternary geology in Jiuzhai Valley. *Acta geologica sichuan* [in Chinese, with English summary].

Guo, X. Y., Guo, Q., and Feng, Z. K. (2020). Relationship between landslide creep and vegetation anomalies in remote sensing images. *J. Remote Sens.* 24 (6), 776–786 [in Chinese, with English summary]. doi:10.11834/jrs.20208330

Huang, D., Li, Y. Q., Song, Y. X., Xu, Q., and Pei, X. J. (2019). Insights into the catastrophic Xinmo rock avalanche in Maoxian county, China: combined effects of historical earthquakes and landslide amplification. *Eng. Geol.* 258, 105158. doi:10.1016/j.enggeo.2019.105158

Huang, H., Shi, S. W., Yang, S., Tian, Y., Yang, D. X., and Liu, J. K. (2020). Study on the debris flow mitigation engineering damage in the national parks caused by the 8th August 2017 Jiuzhaigou earthquake. *Chinese J. Rock Mech. Eng.* [in Chinese, with English summary]. doi:10.13722/j.cnki.jrme.2020.0099

Huang, R. Q., and Li, W. L. (2014). Post-earthquake landsliding and long-term impacts in the Wenchuan earthquake area, China. *Eng. Geol.* 182, 111–120 [in Chinese, with English summary]. doi:10.1016/j.enggeo.2014.07.008

Huang, R. Q., and Li, W. L. (2008). Research on development and distribution rules of geohazards induced by Wenchuan earthquake on 12th May 2008. *Chin. J. Rock Mech. Eng.* 27 (12), 2585–2592 [in Chinese, with English summary].

Keefer, D. K. (2000). Statistical analysis of an earthquake-induced landslide distribution—the 1989 Loma Prieta, California event. *Eng. Geol.* 58 (3), 231–249. doi:10.1016/S0013-7952(00)00037-5

Khattak, G. A., Owen, L. A., Kamp, U., and Harp, E. L. (2010). Evolution of earthquake-triggered landslides in the Kashmir Himalaya, northern Pakistan. *Geomorphology* 115 (1–2), 102–108. doi:10.1016/j.geomorph.2009.09.035

Khazai, B., and Sitar, N. (2004). Evaluation of factors controlling earthquake-induced landslides caused by Chi-Chi earthquake and comparison with the Northridge and Loma Prieta events. *Eng. Geol.* 71, 79–95. doi:10.1016/S0013-7952(03)00127-3

Lan, H. X., and Wu, F. Q. (2002). Analysis on susceptibility of gis based landslide triggering factors in Yunnan Xiaojiang watershed. *Chin. J. Rock Mech. Eng.* 21 (10), 1500–1506 [in Chinese, with English summary].

Li, C. R., Wang, M., and Liu, K. (2018). A decadal evolution of landslides and debris flows after the wenchuan earthquake. *Geomorphology* 323, 1–12. doi:10.1016/j.geomorph.2018.09.010

Li, L. J., Yao, X., Zhang, Y., Zhang, Y. S., Iqbal, J., Chen, J., et al. (2016). Surface recovery of landslides triggered by 2008 Ms 8.0 wenchuan earthquake (China): a case study in a typical mountainous watershed. *Landslides* 13 (4), 787–794. doi:10.1007/s10346-015-0594-1

Liang, J., Pei, X. J., Wen, Y., Luo, L. G., and Qin, D. J. (2019). Research on development and distribution rules of geohazards in Jiuzhaigou earthquake in 2017. *J. Nat. Disasters* 28 (05), 181–188.

Lin, W. T., Chou, W. C., and Lin, C. Y. (2008). Earthquake-induced landslide hazard and vegetation recovery assessment using remotely sensed data and a neural network-based classifier: a case study in central taiwan. *Nat. Hazards* 47 (3), 331–347. doi:10.1007/s11069-008-9222-x

Lu, T., Zeng, H. C., Luo, Y., Wang, Q., Shi, F. S., Sun, G., et al. (2012). Monitoring vegetation recovery after China's May 2008 Wenchuan earthquake using Landsat TM time-series data: a case study in Mao County. *Ecol. Res.* (27), 955–966. doi:10.1007/s11284-012-0976-y

Nakamura, H., Tsuchiya, S., Inoue, K., and Ishikawa, Y. (2000). *Sabo against earthquakes*. Tokyo: Kokon Shoin, 190–220 [in Japanese, with English summary].

Qiao, J. P. (2010). *Theory and practice of landslide risk zoning*. Sichuan University Press, 173 [in Chinese, with English summary].

Regmi, A. D., Dhital, M. R., Zhang, J. Q., Su, L. J., and Chen, X. Q. (2016). Landslide susceptibility assessment of the region affected by the 25 April 2015 Gorkha earthquake of Nepal. *J. Mt. Sci.* 13 (011), 1941–1957. doi:10.1007/s11629-015-3688-2

Shortliffe, E. H., and Buchanan, B. G. (1987). A model of inexact reasoning in medicine. *Math. Biosci.* 23 (3–4), 351–379. doi:10.1016/0025-5564(75)90047-4

Sun, G. Q., Chen, F., Yu, B., and Wang, N. (2020). Landslide change and its influence factors in central Nepal from 2001 to 2017. *J. Univ. Chin. Acad. Sci.* 37 (3), 308–316 [in Chinese, with English summary].

Tian, Y. Y., Xu, C., Ma, S. Y., Xu, X. W., Wang, S. Y., and Zhang, H. (2019). Inventory and spatial distribution of landslides triggered by the 8th August 2017 MW 6.5 Jiuzhaigou earthquake, China. *J. Earth Sci.* 30 (1), 206–217. doi:10.1007/s1258.3-018-0869-2

Vapnik, V. N. (1998). "Statistical learning theory," in *Encyclopedia of the sciences of Learning*. 41 (4), 3185.

Varnes, D. J. (1984). *Landslide hazard zonation: a review of principles and practice*. Natural Hazards 3.

Wang, G. X. (2004). *Landslide science and landslide control technology*. China Railway Press, 100 [in Chinese, with English summary].

Wang, J., Jin, W., Cui, Y., Zhang, W., Wu, C., and Alessandro, P. (2018). Earthquake-triggered landslides affecting a UNESCO natural site: the 2017 Jiuzhaigou earthquake in the World national park, China. *J. Mt. Sci.* 15 (7), 1412–1428. doi:10.1007/s11629-018-4823-7

Wu, C. H., Cui, P., Li, Y. S., Irasema, A. A., Huang, C., and Yi, S. J. (2018). Seismogenic fault and topography control on the spatial patterns of landslides triggered by the 2017 Jiuzhaigou earthquake. *J. Mt. Sci.* 15 (4), 793–807, doi:10.1007/s11629-017-4761-9

Xie, Z. J., Zheng, Y., Yao, H. J., Fang, L. H., Zhang, Y., Liu, C. L., et al. (2018). Preliminary analysis on the source properties and seismogenic structure of the 2017 Ms 7.0 Jiuzhaigou Earthquake. *Sci. China Earth Sci.* 61, 339–352 [in Chinese, with English summary]. doi:10.1007/s11430-017-9161-y

Xu, C., and Xu, X. (2014). Statistical analysis of landslides caused by the MW 6.9 yushu, China, earthquake of April 14, 2010. *Nat. Hazards* 72 (2), 871–893. doi:10.1007/s11069-014-1038-2

Yi, Y. N., Zhang, Z. J., Zhang, W. C., Jia, H. H., and Zhang, J. Q. (2020). Landslide susceptibility mapping using multiscale sampling strategy and convolutional neural network: a case study in Jiuzhaigou region. *Catena* 195, 104851. doi:10.1016/j.catena.2020.104851

Yin, Y. P., Wang, F. W., and Sun, P. (2009). Landslide hazards triggered by the 2008 Wenchuan earthquake, Sichuan, China. *Landslides* 6 (2), 139–152. doi:10.1007/s10346-009-0148-5

Conflict of Interest: The authors declare that the research was conducted in the absence of any commercial or financial relationships that could be construed as a potential conflict of interest.

frontiers
in Earth Science

ORIGINAL RESEARCH
published: 25 February 2021
doi: 10.3389/feart.2021.633665

Investigation of the Effect of the Dataset Size and Type in the Earthquake-Triggered Landslides Mapping: A Case Study for the 2018 Hokkaido Iburu Landslides

Resul Comert*

Department of Geomatics Engineering, Faculty of Engineering and Natural Sciences, Gumushane University, Gumushane, Turkey

Rapid mapping of landslides that occur after an earthquake is important for rapid crisis management. In this study, experimental research was conducted on the size of the model area and the data types used in developing classifiers for the supervised classification approaches used in rapid landslide mapping. The Hokkaido Iburu earthquake zone that occurred on September 6, 2018, was selected as the study area. PlanetScope pre-event and post-event images and ALOS-PALSAR Digital Elevation Model (DEM) were used in the analysis processes. In this context, five model areas with different sizes and one test area were determined. Object-based image analysis (OBIA) was used as a landslide mapping approach. Random Forest classifier, which is a supervised classification algorithm, was performed in the mapping of image objects produced by the segmentation stage of OBIA. Two different data sets were created for landslide mapping: change-based dataset and post-event dataset. The change-based dataset is generated from change data such as the difference of normalized difference vegetation index (δNDVI), change detection Image (CDI), princiable component analysis (PCA), and Independent component analysis (ICA) which are used in change detection applications. The post-event dataset was created from data generated from post-event image bands. When the obtained results were examined, higher accuracy results were obtained with the post-event dataset. Increasing the size of the model area, in other words, increasing the training data slightly increases the accuracy of landslide mapping. However, a model area that represents the region to be mapped in small sizes to make rapid decisions provides a 94% F-measure accuracy for earthquake-triggered landslide detection.

Keywords: OBIA (object based image analysis), random forest, landslide mapping, hokkaido earthquake, planetScope

Edited by:
Tolga Gorum,
Istanbul Technical University, Turkey

Reviewed by:
Fushun Balik Sanli,
Yıldız Technical University, Turkey
Zeinab Shirvani,
Technische Universität Dresden, Germany

***Correspondence:**
Resul Comert
rcomert@gumushane.edu.tr

Specialty section:
This article was submitted to Geohazards and Georisks, a section of the journal Frontiers in Earth Science

Received: *25 November 2020*
Accepted: *11 January 2021*
Published: *25 February 2021*

Citation:
Comert R (2021) Investigation of the Effect of the Dataset Size and Type in the Earthquake-Triggered Landslides Mapping: A Case Study for the 2018 Hokkaido Iburu Landslides. Front. Earth Sci. 9:633665. doi: 10.3389/feart.2021.633665

INTRODUCTION

Earthquakes are natural events that cause great damage to nature, buildings, engineering structures, and cause human death (Gorum and Carranza 2015). Moderate and severe magnitude earthquakes trigger thousands of landslides, especially in rugged and high-slope mountainous regions (Gorum et al., 2013; Tanyaş et al., 2017). For example, in the 2008 Wenchuan, China Mw 7.9 earthquake, there were about 200,000 landslides (Tian et al., 2019), about 5,000 landslides in the January 12, 2010 Mw 7.0 Haiti earthquake (Gorum et al., 2013), more than 2,000 landslides in the 2015 Gorkha, Nepal Mw 7.8 earthquake, and about 6,000 landslides in the 2018 Hokkaido Iburu Mw 6.7 earthquake (Yamagishi and Yamazaki 2018). Landslides that appear as a secondary effect of earthquakes cause human deaths and economic losses. Fatal landslides occurred in 76 of the 196 earthquakes between 1811 and 2016. These fatalities correspond to 17.7% (213,913 people) of deaths caused by earthquakes (Jessee et al., 2020). Earthquake-triggered landslides accounted for 5.2% ($ 170 billion) of economic damage from earthquakes between 1900 and 2016 (Daniell et al., 2017). Therefore, rapid mapping of landslides is important for rapid response to disaster areas and crisis management.

Active and passive remote sensing systems offer great advantages in rapid landslide mapping (Aimaiti et al., 2019). With remote sensing systems, Optical images (Zhao et al., 2017; Shao et al., 2019), synthetic aperture radar (SAR) (Aimaiti et al., 2019; Adriano et al., 2020), LIDAR systems (Liu et al., 2019), Unmanned Aerial Vehicle (UAV) systems (Comert et al., 2019) or synthesis of optical and SAR images (Shirvani et al., 2019) can be used in the landslide mapping. The most common method preferred in mapping landslides is visual image interpretation (Guzzetti et al., 2012; Rosi et al., 2018). Although the image interpretation provides high accuracy, it is a slow method that is not suitable at the time of rapid intervention since the landslides are mapped by the expert with image interpretation and manual digitization (Guzzetti et al., 2012). Therefore, automatic landslide mapping is an important factor for post-disaster crisis management. Image classification approaches (Vamsee et al., 2018) and change detection methods (Lu et al., 2019) are used in automatic landslide mapping. Since change detection methods require pre-event images, they present a disadvantage in mapping the landslide events triggered by the earthquake. However, it is a useful method in case of the pre-event image available (Yang and Chen 2010; Lu et al., 2019). Classification methods are generally carried out on post-event images (Stumpf and Kerle 2011; Dou et al., 2015). The disadvantage of this method in making rapid decisions is that it takes time to generate the training dataset. However, when the classification model is developed over the appropriate training dataset, the mapping process is shortened (Danneels et al., 2007; Stumpf and Kerle 2011; Mondini et al., 2011).

Image classification is used in landslide mapping in two approaches, pixel-based image analysis (PBIA) (Danneels et al., 2007) and object-based image analysis (OBIA) (Martha et al., 2010; Stumpf and Kerle 2011; Hölbling et al., 2015; Shirvani et al., 2019). After the landslide events, different sizes of landslides can occur in the relevant area. High spatial resolution images offer great advantages to detect landslides of different sizes. OBIA has become more popular in landslide mapping in the last decade since misclassified pixels have emerged from the landslide mapping from high spatial resolution images with PBIA (Guzzetti et al., 2012; Zhong et al., 2020). OBIA is applied in two different ways in landslide mapping: rule-based (Martha et al., 2010; Hölbling et al., 2012; Comert et al., 2019) and supervised mapping (Stumpf and Kerle 2011; Shirvani et al., 2019). In the landslide mapping process, landslides should be separated from different land use classes. A large number of object features must be used for this process. Rule-based mapping is a slow method for complex areas. since the object features and threshold values that separate the classes must be determined by an expert (Stumpf and Kerle, 2011). In supervised mapping performed with a selected algorithm such as random forest, the features used to separate the classes are automatically determined, and rapid results are produced by the mapping process made on the training data to be produced in the appropriate size and number (Stumpf and Kerle 2011; Shirvani et al., 2019; Shirvani, 2020). Therefore, supervised mapping process will give rapid results in rapid intervention in crisis management.

In this study, the success of the size of the model area selected for training data, and the dataset type to be used in classification in the rapid detection of earthquake-triggered landslides were investigated. In particular, the following questions have been addressed:

- How enlarging the model area selected for training data affect earthquake-triggered landslide mapping accuracy?
- Which of the datasets used in the classification stage is more useful?
- Which image object feature from the selected data sets is important for landslide mapping?

For these purposes, the Hokkaido Iburu earthquake zone in Japan was chosen as the study area. PlanetScope images and ALOS-PALSAR Digital Elevation Model (DEM) were used as analysis data. OBIA was preferred as the mapping approach and the Random Forest (RF) algorithm was used as the classification method in the OBIA. RF algorithm, which is a fast machine learning classifier, was preferred in this study because it gives successful results in many areas such as landslide susceptibility mapping (Dou et al., 2019; Shirvani 2020), landslide mapping (Stumpf and Kerle 2011; Chen et al., 2017; Shirvani et al., 2019; Maxwell et al., 2020), burnt area mapping (Ramo and Chuvieco 2017).

STUDY AREA AND DATASET

Study Area

The study area is located in the southwest of the Hokkaido region (**Figure 1A**). The dominant land cover of the study area consists of forests and paddy fields and has a rugged, mountainous, and high slope topography (Zhang et al., 2019; Adriano et al., 2020). Hokkaido, which includes the study area, is a tectonically active region in the world. The faults and active faults in the region develop near the north-south strike (Zhang et al., 2019).

On September 6, 2018, an earthquake with a magnitude of 6.7 Mw and a depth of 37 km occurred in the Iburu subprefecture of the southern Hokkaido province of Japan. With the powerful ground motion of the event, structural damage in buildings,

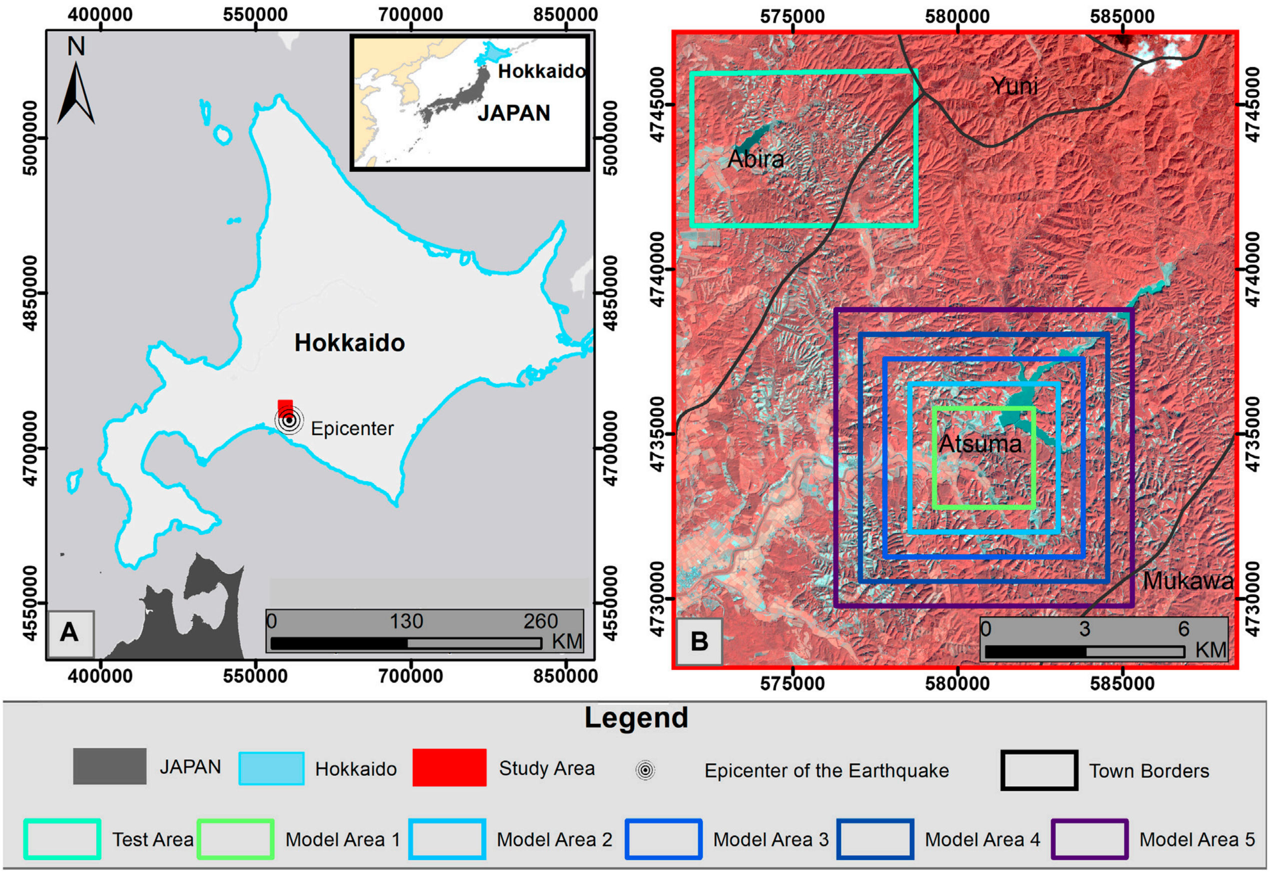

FIGURE 1 | The study area selected for analysis: **(A)** The location of the epicenter of the earthquake and the study area (red polygon) in Hokkaido, **(B)** Model development and test areas determined for landslide mapping.

liquefaction on the ground, and thousands of landslides occurred in areas close to the epicenter (42.691°N, 142.007°E) of the earthquake. Due to the earthquake, 41 people died and 691 people were injured; 390 buildings were destroyed, 1061 buildings were damaged, approximately 6000 landslides occurred (Yamagishi and Yamazaki 2018; Zhang et al., 2019). The reason for the large number of landslides triggered by the earthquake in the region is that the earthquake occurred one day after the typhoon Jebi, which accumulated approximately 100 mm of precipitation in the region (Yamagishi and Yamazaki 2018). The majority of the coseismic landslides in the region consist of typical shallow debris landslides with a width of approximately 250 m. The types of landslides are classified as planar and spoon type landslides such as rainfall-induced landslides (Yamagishi and Yamazaki 2018; Zhang et al., 2019). The areas selected within the scope of this study are located in the towns of Atsuma and Abira, where slope failures are densely distributed (**Figure 1B**).

Data Sets

PlanetScope is a satellite constellation operated by Planet Labs that contains 130+ CubeSats (size: 10 cm by 10 cm by 30 cm; weight: 4 kg) that move in the sun-synchronous orbit. Using this satellite constellation, images are collected in an area of 200 M + km^2/day. PlanetScope images consist of 4 spectral bands with 3.7 m spatial, 16-bit radiometric, and 1-day temporal resolution (**Table 1**) (Planet, 2017). In this study, PlanetScope Level 3B multispectral surface reflectance products were used to create the change-based dataset and the post-event datasets. Level 3B surface reflectance products, which are orthorectified, are geometrically corrected images using Ground Control Points (GCPs) and fine Digital Elevation Models (DEMs) (Wicaksono and Lazuardi 2018; Planet, 2017). Also, the atmospheric corrections of these products were made by Planet Labs using the 6S radiative transfer model with ancillary data from MODIS (Cheng et al., 2020). After atmospheric and geometric corrections, the orthorectified images are presented to users by Planet Labs at 3 m spatial resolution (Planet 2017). Within the scope of the study, images belonging to two different dates as pre-event (August 03, 2018) and post-event (September 21, 2018) were used (**Table 1**). These images were selected as the dates closest to each other, with no clouds on the study area. Also, ALOS-PALSAR 30 m spatial resolution DEM data dated July 14, 2006 were used as auxiliary data to obtain the slope map of the study area.

TABLE 1 | PlanetScope Leve 3 B product specification and image dates.

Band	Band range (nm)	Resolution	Image dates	
			Pre-event	Post-event
Blue	455–515	3 m spatial res	August 3, 2018	September 21, 2018
Green	500–590	16-Bit radiometric res		
Red	590–670	1-day revisit time		
NIR	780–860			

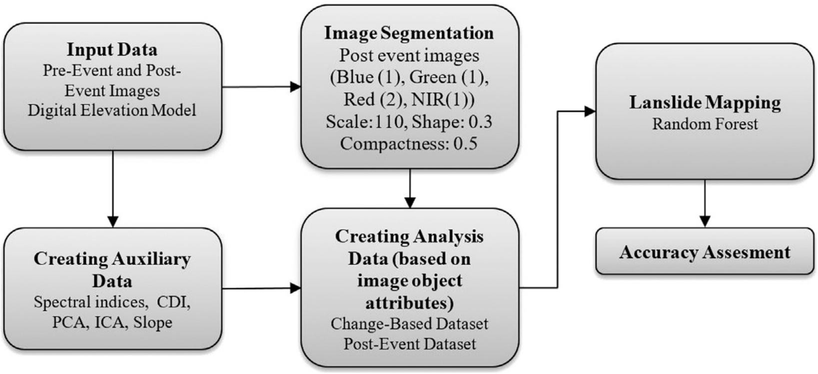

FIGURE 2 | The methodology applied for the rapid detection of earthquake-triggered landslides in the study.

Five different model areas have been created to develop classifiers to be used in the mapping of landslides over the area chosen as the study area (**Figure 1B**). The smallest of these model areas (Model Area 1) is 3 × 3 km in size. While determining this area, it has been taken into consideration that the test area has similar land use characteristics such as water, agricultural areas, roads, small settlements, landslides, and forest. Other model areas were obtained by enlarging the edges of the previous model area by 1.5 km. The largest model area (Model Area 5) created in the area is 9 × 9 km in size.

METHODS

The methodology applied within the scope of the study is shown in **Figure 2**. The landslide mapping process was carried out using the OBIA approach. OBIA and PBIA are two different approaches used in image classification. Spectral values of pixels are used when classifying images with PBIA, while spectral, geometric, textural, and spatial values of image objects are used for classification with OBIA. OBIA was preferred in this study because it reduces the problem of misclassification error in high spatial resolution images includes different image object metrics in addition to spectral features and reduces the data size (Zhong et al., 2020).

Creating Auxiliary Data

Auxiliary data such as band indices and change detection indices were generated to achieve change-based dataset and post-event datasets. Normalized difference vegetation index (NDVI), normalized difference water index (NDWI) and brightness index (BI), principal component analysis (PCA), change detection image (CDI), independent component analysis (ICA) were additional data generated.

NDVI (Tucker 1979) is an effective index used in the separation of green vegetation area from landslides. Therefore, it is used both in landslide mapping with change detection (Lu et al., 2019) and in landslide mapping from post-event images (Martha et al., 2010). $\mathrm{NDVI}_{\mathrm{post}}$ was used for the post-event dataset, δNDVI was used for the change-based dataset. NDWI (McFeeters 1996) was included in the post-event dataset to distinguish the water areas from the landslides (Shirvani et al., 2019).

$$\mathrm{NDVI} = \frac{\rho_{\mathrm{NIR}} - \rho_{\mathrm{Red}}}{\rho_{\mathrm{NIR}} + \rho_{\mathrm{Red}}}, \tag{1}$$

$$\delta\mathrm{NDVI} = \mathrm{NDVI}_{\mathrm{pre}} - \mathrm{NDVI}_{\mathrm{post}}, \tag{2}$$

$$\mathrm{NDWI} = \frac{\rho_{\mathrm{Green}} - \rho_{\mathrm{NIR}}}{\rho_{\mathrm{Green}} + \rho_{\mathrm{NIR}}}, \tag{3}$$

where ρ_{Green}, ρ_{Red}, and ρ_{NIR} are green, red, and near-infrared (NIR) bands of images, respectively.

BI has been used in post-event landslide mapping from satellite images in many studies. This index is obtained by dividing the sum of the spectral values of the bands ($c_{i(vis)}$) by the total number of bands ($\mathrm{n}_{\mathrm{vis}}$) (Stumpf and Kerle 2011). BI was calculated using the four bands of PlanetScope post-event image bands.

$$\mathrm{BI} = \frac{1}{\mathrm{n}_{\mathrm{vis}}} \sum_{i=1}^{\mathrm{n}_{\mathrm{vis}}} c_{i(vis)}. \tag{4}$$

PCA, a linear transformation method, converts a set of correlated numerical variables into non-correlated variables in a different orthogonal coordinate system. When a data set with N bands is given with PCA, the desired number of main components is calculated. The first PCA component contains the largest variance between the input bands, the second contains the second major variance not defined in the first component, and so on. In the calculation of the principal components, the n-dimensional data set is defined by the $X^T = [X_1 \ldots X_n]$ matrix and the C covariance matrix. With the first scaled eigenvectors (e_{1i}) calculated from the covariance matrix, the first principal components (Y_1) are calculated as in **Eq. 5**. The other desired principal components are calculated similarly using the relevant eigenvector (Mondini et al., 2011). In this study, two different PCA data sets were produced. The first one is four main components produced from post-event image bands to use in the post-event dataset. The second one, for the change-based dataset, four main components were generated by using the red and NIR bands of pre-event and post-event images as Lu et al. (2019) stated in their articles.

$$Y_1 = \sum_{i=1}^{n} e_{1i} X_i. \tag{5}$$

ICA is a geometric transformation that transforms variables used as inputs into statistically independent components. ICA is calculated by **Eq. 6**. Where A is the mixing matrix, s is the matrix of independent components and X represents the vector of input variables (Hyvärinen and Oja 2000).

$$\mathrm{X} = sA = \sum_{i=1}^{n} a_i s_i. \tag{6}$$

CVA is a method used for mapping landslides from pre-and post-event images (Li et al., 2016; Lu et al., 2019). In this method, a change detection image (CDI) is created by determining the changes between multi-temporal image bands. The value of a pixel in the CDI is calculated by **Eq. 7**. where, the pixel value at pre-event t_1 time is I_{t1}, the pixel value at post-event time t_2 is l_{t2}. b represents the number of satellite images band being processed.

$$\rho(I) = \left[\sum_{b=1}^{n} (I_{t1} - I_{t2})_b^2\right]^{1/2.} \tag{7}$$

Image Segmentation

Image segmentation is the first step of the OBIA process. At this stage, it is aimed to produce meaningful image objects from the layers subjected to segmentation. Multi-resolution segmentation (MRS) is the most preferred segmentation method in OBIA. In this method, the segmentation process starts at a pixel level, and the merging process takes place according to the spatial and spectral heterogeneity of the candidate selected image object with neighboring image objects (Benz and Schreier 2001; Jensen 2005). To create optimum image objects with the MRS method, the scale, shape, compactness, and layer weights must be determined by the user. The scale parameter controls the size or heterogeneity level of the image objects to be formed. If the scale parameter is defined as a large value, large image objects are produced, if a small value is defined, small image objects are produced. The shape parameter, which takes values between 0–1, is used to determine the weights of spatial and spectral functions in the calculation of the merging factor. The compactness parameter controls the compactness and smoothness of the resulting image objects in the calculation of the shape function. Layer weights are used to define the importance of segmentation layers compared to other layers (Baatz et al., 2000). MRS parameters can be determined by automatic methods such as Estimation Scale Parameter-2 (ESP-2) (Drăguţ et al., 2014), optimum scale parameter selector (OSPS) (Vamsee et al., 2018), or by the trial and error method (Martha et al., 2010; Hölbling et al., 2012; Shirvani et al., 2019) based on visual analysis. In this study, the trial-error method was used to determine the appropriate segmentation parameters.

Creating Analysis Data

After the segmentation steps, image object attributes (features) were calculated. Image object attributes are the features used in classifying image objects. Textural, spectral, spatial, geometric, and contextual metrics can be used in landslide mapping (Martha et al., 2010; Shirvani et al., 2019). Two different data sets containing image object features were created for the mapping of landslides. These were change-based dataset and post-event dataset. Layers produced from pre-event and post-event bands were used in the creation of the change-based dataset, post-event bands and layers produced from them were used in the creation of the post-event dataset. The features of both datasets used in mapping landslides were selected using eCognition Developer 9.0 software. As a result of the literature review (Martha et al., 2010; Shirvani et al., 2019) and visual analysis, 40 image object features were selected for the change-based dataset (**Table 2**) and 43 for the post-event dataset (**Table 3**). Since it does not provide any discrimination in visual analysis, geometric features are not included in the datasets.

Landslide Mapping

The random forest (RF) algorithm was used for the landslide mapping. RF is an ensemble learning algorithm that generates multiple decision trees using randomly selected variables and subsets in a dataset. To generate the decision tree with the RF classifier, the user must determine the number of variables (m) used in each node and the number of randomly generated trees (N) to determine the best split. For a dataset consisting of M variables, the number of m variables to be randomly selected is determined as a value equal to or close to the $\sqrt{M}$. With the determined parameters, trees with high variance and low bias are created by the algorithm. The final classifier is decided according to the voting for the power of decision trees to separate classes. The tree with the most votes is used for the respective class (Breiman 2001). While the classifier is developed with the RF algorithm, 2/3 of the dataset is used as training data and 1/3 as test data (Belgiu and Drăguţ 2016). This ratio can be chosen between 80 and 20% to increase the number of data in the training dataset (Ramo and Chuvieco 2017). Another method used in model training is k-fold cross-validation, which is used in cases where there is limited validation data (Karlson et al., 2015). In the study, in the selection of optimum parameters for the RF classifier for

TABLE 2 | Selected image object features used for the change-based dataset.

Type	Features	Num. of features
Spectral	Mean of (ICA1, ICA2, ICA3, ICA4, CDI, δNDVI, PCA1$_{change}$, PCA2$_{change}$, PCA3$_{change}$, PCA4$_{change}$) Std. Dev. of (ICA1, ICA2, ICA3, ICA4, δNDVI, PCA2$_{change}$, PCA3$_{change}$, PCA4$_{change}$) and Max. Diff	19
Spatial	Mean of slope	1
Textural	GLCM all direction Contrast of (PCA3$_{change}$, PCA4$_{change}$, ICA3) Dissimilarity of (PCA4$_{change}$, PCA3$_{change}$, ICA3, CDI) Entropy of (ICA1, ICA2, ICA3, ICA4, CDI, δNDVI, PCA1$_{change}$, PCA2$_{change}$, PCA3$_{change}$, PCA4$_{change}$) Homogeneity of (ICA3, PCA3$_{change}$, PCA4$_{change}$)	20

CDI, change detection image; ICA, independent component analysis; Max. Diff., maximum difference; PCA$_{change}$, change based principal component analysis; Std. Dev., standard deviation.

TABLE 3 | Selected image object features used for the post-event dataset.

Type	Features	Num. of features
Spectral	Mean. of (R, G, B, NIR, NDVI, NDWI, BI, PCA1$_{post}$, PCA2$_{post}$, PCA3$_{post}$, PCA4$_{post}$), Max. Diff., std. Dev. of (R, G, B, NIR, NDVI, BI, PCA1$_{post}$, PCA2$_{post}$, PCA3$_{post}$, PCA4$_{post}$)	22
Spatial	Mean and std. dev. of slope	2
Textural	GLCM all direction Contrast of (R, NIR, NDWI, BI) Dissimilarity of (NIR, R, BI, PCA2$_{post}$, PCA4$_{post}$) Entropy of (R, NIR, NDVI, BI) Homogeneity of (R, NIR, NDVI, BI, PCA2$_{post}$, PCA4post)	19

B, blue; BI, brightness index; G, green; NDVI, normalized difference vegetation index; NDWI, normalized difference water index; NIR, near infrared; PCA$_{post}$, post-event principal component analysis; R, red.

each model area, the data belonging to the model areas were used as 80% training data and 20% test data. Classifier success to the obtained optimum parameters has been tested on the test area.

Accuracy Assessment

The success of the created classifiers on the test area was calculated according to the accuracy measures developed on the confusion matrix used in two-class classification applications (Eqs 8–11) (Sokolova and Lapalme 2009). The correctly classified of LS and NLS image objects on the test data of the developed models were achieved by using the overall accuracy measures (Eq. 12) (Banko 1998).

	Reference	
Predicted	**T**rue **P**ositive	**F**alse **P**ositive
	False **N**egative	**T**rue **N**egative

$$Recall\ (TP\ Rate) = \frac{TP}{TP+FN} \tag{8}$$

$$FP\ Rate = \frac{FP}{FP+TN} \tag{9}$$

$$Precision = \frac{TP}{TP+FP} \tag{10}$$

$$F-Measure = 2 * \frac{precision * recall}{precision + recall} \tag{11}$$

$$Overall\ Accuracy = \frac{correctly\ clasified\ image\ objects\ (LS+NLS)}{total\ number\ of\ image\ objects} \tag{12}$$

RESULTS

In the segmentation stage, different combinations of post-event image bands and layers produced for image difference were tried to identify appropriate input bands to create image objects representing landslides. As a result of the experiments, it was seen that the landslide objects were best obtained from the post-event R, G, B, NIR bands. Therefore, these layers were used as input bands in the segmentation process for all data sets. Different scale parameters (from 10 to 150 by 10), shape, compactness, and layer weights were tested in determining the optimum parameters for MRS. As a result of trial and error, suitable parameters were determined as a scale: 110, shape: 0.3, compactness: 0.7, layer weights as B = G = NIR = 1, R = 2. These values have been applied to be the same for all data sets. These values were used to create image objects for all data sets. Landslides in the image objects obtained result of the segmentation process consists of more than one image object. When the scale parameter was set to more than 110, it has been observed that especially small landslides mix with other land use classes. Image objects created by segmentation for model and test areas were labeled as Landslide (LS) and Non-Landslide (NLS) using pre-event and post-event images. The data sets created for the RF classifier and the numbers of image objects belonging to LS and NLS included in them are shown in **Table 4**.

The RF classifier development process was carried out using WEKA (Waikato Environment for Knowledge Analysis) data mining software. The process of determining the optimum number of trees and the minimum variable was carried out separately for each model area. The number of random trees was applied as different values from 100 to 1500. The number of m variables was applied to the model data sets as 6, 7, 8, 9 values. As a result of the experiments, the m value was determined as 8

TABLE 4 | The number of Landslide (LS) and Non-Landslide (NLS) image objects labeled for the models and test datasets to be used in the analysis process.

Data sets	Number of NLS image objects	Number of LS image objects	Total number of image objects	Area (km^2)
Model Set1	1669	458	2127	9.00
Model Set2	3521	1193	4714	20.25
Model Set3	6070	2156	8226	36.00
Model Set4	9259	3425	12684	56.25
Model Set5	12804	4802	17606	81.00
Test set	4869	1855	6724	31.64

TABLE 5 | Accuracy assessment on the test area with RF classifiers developed for model areas.

Model name	Post-event dataset				
	Recall (TP rate)	FP rate	Precision	F-measure	Overall accuracy
Model area 1	0.92	0.016	0.95	0.938	96.68
Model area 2	0.932	0.017	0.955	0.943	96.94
Model area 3	0.934	0.018	0.952	0.943	96.86
Model area 4	0.934	0.020	0.947	0.941	97.22
Model area 5	0.950	0.023	0.940	0.945	96.90
Model name	**Change-based dataset**				
	Recall (TP rate)	**FP rate**	**Precision**	**F-measure**	**Overall accuracy**
Model area 1	0.896	0.021	0.942	0.919	95.44
Model area 2	0.881	0.020	0.943	0.911	95.27
Model area 3	0.871	0.011	0.967	0.917	95.62
Model area 4	0.892	0.013	0.962	0.926	96.04
Model area 5	0.890	0.009	0.973	0.930	96.28

for all data sets. The number of trees was defined as 600 for model areas 2 and model area 3 in the change-based dataset. The number of trees in model area 4 was determined as 400 for both the change-based dataset and the post-event dataset. The number of trees was set as 500 for the remaining classifiers. The success of the RF classifiers created for model areas according to the determined parameters on the test area is shown in **Table 5**. The overall accuracy success of RF classifiers on the test site for separating LS and NLS areas has been achieved by over 95% with all classifiers in both datasets (**Table 5**).

When the accuracy results were examined (**Table 5**), it was seen that TP Rate increases in the post-event dataset when the model area expands. With the classifier developed for Model Area 1, 92% of the image objects belonging to the LS in the test area were successfully mapped. This ratio was obtained with 3% more accuracy in the largest dataset. When the number of training data is increased by expanding the model area, the FP rate, which defines the mapping rate of NLS image objects as LS, slightly increased. This change had reduced the precision rate of classifiers. When the success of the developed classifiers for landslide mapping was evaluated, it is observed that very close F-measure values were obtained, but a little more success was achieved in the largest dataset.

When the accuracies for the change-based datasets are investigated, the TP ratio of LS image objects was obtained approximately 90% for the smallest dataset. This ratio decreased by 1 and 2% in model area 2 and model area 3, respectively. In the largest dataset, very close results were obtained with model area 1. When the size of the model dataset was increased, it was seen that the sensitivity of the FP ratio increased and the extraction of NLS objects as LS decreased. This condition has increased the precision ratio and the F-measure value of the developed classifiers.

Comparing the results obtained for the change-based dataset and post-event dataset, landslides were obtained with a higher TP Rate in all model areas where RF classifiers were developed. When the FP Rate values were compared, it was seen that when the data size was increased, the classification of NLS image objects as LS with the change-based data set decreased, and the developed classifiers map the NLS areas with higher accuracy. When the overall success of the classifiers for two datasets was evaluated according to F-measure, it was indicated that landslide mapping with post-event dataset gave higher accuracy values.

In this study, 40 different features were used for the change-based dataset and 43 different features for the post-event dataset. When the feature importance of the variables was investigated, it was observed that the same variables were effective in all model areas. δNDVI in change-based RF classifiers and slope and NDVI in post-event RF classifiers were the most effective features. In **Figure 3**, the top ten features in the classifier created for the model area 5 based on change-based datasets were shown according to the mean decrease of accuracy and mean decrease of Gini index. When **Figure 3** is examined, it is seen that the most important parameters in classification according to mean decrease accuracy were mean values of δNDVI, slope, PCA3, and ICA2. The most important variables that affect the purity of the classifier when extracted from the dataset were mean values of δNDVI, ICA3, PCA3, and PCA4. In **Figure 4**, the top ten features obtained for Model Area 5 with the post-event dataset were given. The most important features for the developed classifier were obtained as mean values of the slope, NDVI, PCA4, PCA3, and Maximum Difference. The most important parameters that increase the purity of the model were NDVI, PCA2, NDWI, Max Difference, and Red

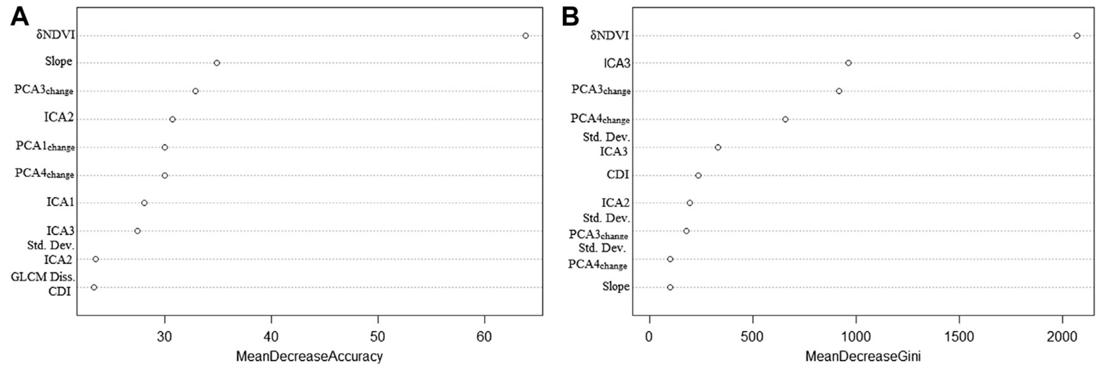

FIGURE 3 | The ten most important features for the classifier developed with change-based dataset in model area 5: **(A)** shows how selected features affect model accuracy when removed from the dataset, **(B)** indicates how selected features affect model purity when removed from the dataset.

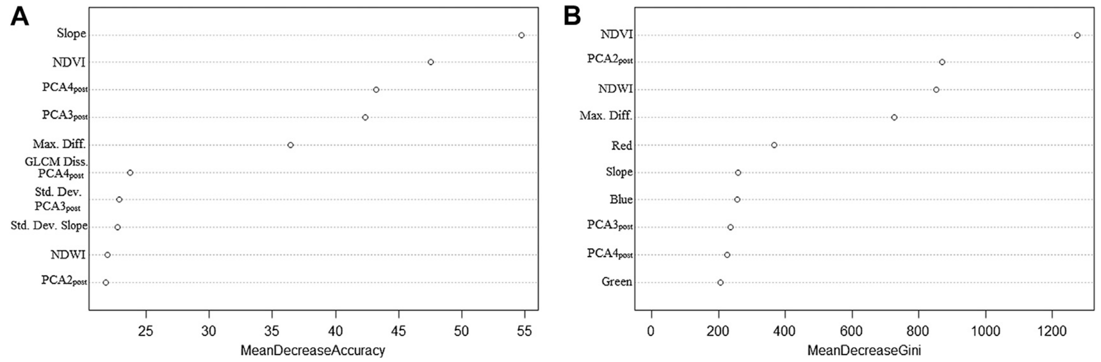

FIGURE 4 | The ten most important features for the classifier developed with post-event dataset in model area 5: **(A)** shows how selected features affect model accuracy when removed from the dataset, **(B)** indicates how selected features affect model purity when removed from the dataset.

(**Figure 4**). When the importance of properties for different datasets is evaluated, it is seen that spectral properties and spatial properties are more effective in mapping landslides according to textural properties.

DISCUSSION

In this study, the influence of model development area size and dataset types in landslide mapping during the post-earthquake crisis management phase was investigated. In this context, ten landslide mapping models have been developed with OBIA-RF classifier using two different datasets, namely change-based and post-event dataset, at five model development areas with different sizes. The success of the developed classifier models has been investigated on a determined test area. When the obtained results were examined, although landslide mapping results were obtained with high accuracy from all developed models, higher accuracy values were obtained in classifier models using post-event datasets (**Table 5**). These results show that while pre-event and post-event images are useful to create or update the landslide inventory maps (Yang and Chen, 2010; Đurić et al., 2017), post-event images without the need for any archive images in crisis management are sufficient in detecting the locations where the dense landslide events occurred. In the comparison of dataset size in this study, it was observed that increasing the dataset size slightly increased the mapping accuracy (**Table 5**). Therefore, large model areas are not required in the post-disaster decision-making phase. The model development process, which is carried out on a small area that best represents the area to be mapped, is useful for rapid decision-making.

The RF algorithm for landslide mapping was applied to datasets produced by using PlanetScope images and ALOS-PALSAR DEM data in the study. The RF algorithm, which gives successful results in extracting the desired feature in datasets with large sizes and many variables in different application areas (Stumpf and Kerle, 2011; Ramo and Chuvieco, 2017; Shirvani et al., 2019; Maxwell et al., 2020; Shirvani, 2020), has also produced high accuracy results from the datasets used (**Table 5**). With this research, it has been demonstrated that PlanetScope satellites, which offer daily high spatial resolution images, provide successful results in the detection of earthquake-triggered landslide areas with high accuracy. To produce the slope map of the study area, 30 m

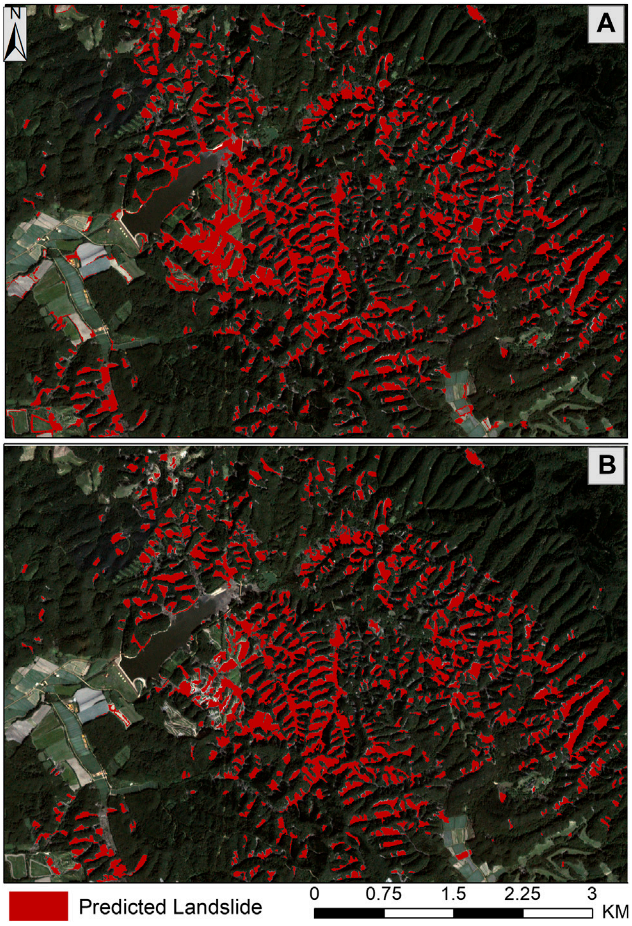

FIGURE 5 | Estimated landslides on the test area for model area 5 with RF classifier: **(A)** post-event dataset result, **(B)** change-based dataset result.

resolution ALOS-PALSAR DEM data were used as elevation data. Although this DEM is sufficient for this application in terms of presenting the general slope characteristics of topographic surfaces where landslides occur in the study area, it is insufficient in terms of producing induvial landslide inventory mapping. During the segmentation phase, landslides were obtained as multiple image objects. By merging these image objects, holistic landslides can be obtained (**Figure 5**). However, these landslides were not individual. The main reason for this is the high reflection of fresh landslides in satellite bands. In the segmentation stage, adjacent landslides with the same spectral value fall into the same image object. For these landslides to be used in susceptibility and hazard maps, the necessary ones should be converted into individual landslides. For this process, post-event high-resolution DEM data of the area is required (Marc and Hovius 2015).

While determining the object features in the datasets, firstly, the visual evaluation of the image object features to be included in the datasets on the image objects created as a result of the segmentation stage was made. Since the landslide areas consist of more than one image object, geometric features such as length/width, size, shape were not added in the datasets because there was no distinctive finding was observed on these features. Variable importance analysis was performed for the image object features used in datasets. The ten most important features for the datasets were shown in **Figures 3**, **4**. NDVI, which is an effective feature in separating green vegetation areas from landslides, is a frequently preferred feature in landslide mapping with change detection (Mondini et al., 2011; Hölbling et al., 2015; Lu et al., 2019) and classification method (Martha et al., 2010; Shirvani et al., 2019). Since the application areas were chosen in this study were covered with dense forest areas and agricultural land, it has been revealed that NDVI and δNDVI were important features in both the change-based dataset and the post-event dataset (**Figures 3**, **4**). The slope value is especially in the separation of low-slope areas such as roads and bare soil spectrally similar to landslides from landslides (Comert et al., 2019). The slope feature was seen to be an important feature that increases the accuracy of landslide mapping for both the change-based dataset and post-event dataset in this study (**Figures 3**, **4**).

PCA and ICA, which are non-parametric feature extraction methods, are the preferred approaches in landslide mapping with change detection (Mondini et al., 2011; Lu et al., 2019). PCA4, ICA2, ICA3, and ICA4 components produced from pre-event and post-event NIR and Red bands gave successful results (Lu et al., 2019). In this study, $PCA1_{change}$, $PCA3_{change}$, and $PCA4_{change}$, which were among the PCA components produced for the change-based dataset, were found to be important features that increase the accuracy of the classifiers and ensure the purity of the decision trees used in landslide mapping (**Figure 3**). ICA3, one of the ICA components produced for the change-based dataset, has been seen to be the second most important component that provides the homogeneity of decision trees used in the separation of LS and NLS areas (**Figure 3**). Also, ICA2 was the fourth feature that positively affects classifier accuracy (**Figure 3**). In the study, four PCA components were generated from post-event image bands and included in the post-event dataset. Among these features, $PCA2_{post}$, $PCA3_{post}$, and $PCA4_{post}$ were found to be important features that increase classification accuracy and provide decision tree purity (**Figure 4**). According to the variable important results, it shows that the non-parametric components obtained by PCA analysis can be used in landslide mapping studies based on the post-event images.

When examining other features obtained by variable important analysis, it was seen that the Max. Diff. the feature was important in both classifier accuracy and model homogeneity for the post-event dataset. Also, Red, Green Blue bands were obtained as important properties in providing model purity for the post-event dataset. CDI is used in landslide mapping with change detection from multi-temporal images (Li et al., 2016; Lu et al., 2019). In this study, it was seen that for the change-based data set, it was an important parameter in terms of classifiers model homogeneity, although not as much as, δNDVI, PCA, and ICA components.

CONCLUSION

In this study, the success of different datasets and different data sizes produced from remote sensing images in rapid earthquake-triggered landslide mapping were investigated. In this context, change-based and post-event datasets were created for five model areas and one test area. When RF classifiers developed on model areas were applied to the test area, high accuracies are obtained for all model areas and datasets. However, slightly higher accuracy results have been achieved with post-event datasets compared to change-based dates. Similarly, slightly higher accuracy was obtained when the model area size was increased. When these results are evaluated, in rapid detection of the location where earthquake-triggered landslides occur: 1) models to be used in mapping landslides can be developed over a small area that best represents the area to be mapped, 2) in the landslide mapping process, landslides can be successfully detected from the post-event images without the archive image of the relevant area. In the study, the importance of image object features used in datasets in the mapping process was investigated. When the importance levels of the object features are examined, it has been observed that the highly important features are similar to the features used in the literature. Also, PCA components generated from post-event images are included in the post-event data. Since these components positively affect the classification accuracies, they can be included in the post-event datasets in future studies. The approach presented in this study is an appropriate method for detecting large landslide areas that occur after a natural disaster and to respond rapidly. The presented method needs improvement to create landslide inventory maps. In future studies, both crisis management and inventory mapping research will be conducted from platforms that offer higher spatial resolution images and DEMs such as Unmanned Aerial Vehicle.

DATA AVAILABILITY STATEMENT

The original contributions presented in the study are included in the article/Supplementary Material, further inquiries can be directed to the corresponding author.

AUTHOR CONTRIBUTIONS

This study was prepared individually by RC.

ACKNOWLEDGMENTS

The author thanks PlanetScope for providing satellite images. I also thank ALOS for providing Digital Elevation Data.

REFERENCES

Adriano, B., Yokoya, N., Miura, H., Matsuoka, M., and Koshimura, S. (2020). A semiautomatic pixel-object method for detecting landslides using multitemporal ALOS-2 intensity images. *Rem. Sens.* 12 (3), 561. doi:10.3390/rs12030561

Aimaiti, Y., Liu, W., Yamazaki, F., and Maruyama, Y. (2019). Earthquake-induced landslide mapping for the 2018 Hokkaido eastern iburi earthquake using PALSAR-2 data. *Rem. Sens.* 11 (20), 2351. doi:10.3390/rs11202351

Baatz, M., Schäpe, A., Strobl, J., Blaschke, T., and Griesebner, G. (2000). Multiresolution Segmentation-an optimization approach for high quality multi-scale image segmentation. *Angewandte Geographische Informationsverarbeitung* 12 12–23.

Banko, G. (1998). Report No.: IR-98-081. "A review of assessing the accuracy of classifications of remotely sensed data and of methods including remote sensing data in forest inventory Laxenburg, Austria: International Institute for Applied Systems Analysis (IIASA) Interim Report.

Belgiu, M., and Drăguţ, L. (2016). Random forest in remote sensing: a review of applications and future directions. *ISPRS J. Photogrammetry Remote Sens.* 114, 24–31. doi:10.1016/j.isprsjprs.2016.01.011

Benz, U., and Schreier, G. (2001). Definiens Imaging GmbH: object oriented classification and feature detection. *IEEE Geoscience and Remote Sensing Society Newsletter* 9, 16–20.

Breiman, L. (2001). Random forests. *Mach. Learn.* 45 (1), 5–32. doi:10.1023/a:1010933404324

Chen, T., Trinder, J., and Niu, R. (2017). Object-oriented landslide mapping using ZY-3 satellite imagery, random forest and mathematical morphology, for the Three-Gorges Reservoir, China. *Rem. Sens.* 9 (4), 333. doi:10.3390/rs9040333

Cheng, Y., Vrieling, A., Fava, F., Meroni, M., Marshall, M., and Gachoki, S. (2020). Phenology of short vegetation cycles in a Kenyan rangeland from PlanetScope and Sentinel-2. *Remote Sens. Environ.* 248, 112004. doi:10.1016/j.rse.2020.112004

Comert, R., Avdan, U., Gorum, T., and Nefeslioglu, H. A. (2019). Mapping of shallow landslides with object-based image analysis from unmanned aerial vehicle data. *Eng. Geol.* 260, 105264. doi:10.26833/ijeg.455595

Daniell, J. E., Schaefer, A. M., and Wenzel, F. (2017). Losses associated with secondary effects in earthquakes. *Front. Built. Environ.* 3 (30), 1–4. doi:10.3389/fbuil.2017.00030

Danneels, G., Pirard, E., and Havenith, H.-B. (2007). "Automatic landslide detection from remote sensing images using supervised classification methods," in IEEE International Geoscience and Remote Sensing Symposium, Barcelona, Spain, July, 2007.

Dou, J., Yunus, A. P., Tien Bui, D., Merghadi, A., Sahana, M., Zhu, Z., et al. (2019). Assessment of advanced random forest and decision tree algorithms for modeling rainfall-induced landslide susceptibility in the Izu-Oshima Volcanic Island, Japan. *Sci. Total Environ.* 662, 332–346. doi:10.1016/j.scitotenv.2019.01.221

Dou, J., Chang, K.-T., Chen, S., Yunus, A., Liu, J.-K., Xia, H., et al. (2015). Automatic case-based reasoning approach for landslide detection: integration of object-oriented image analysis and a genetic algorithm. *Rem. Sens.* 7 (4), 4318–4342. doi:10.3390/rs70404318

Drăguţ, L., Csillik, O., Eisank, C., and Tiede, D. (2014). Automated parameterisation for multi-scale image segmentation on multiple layers. *ISPRS J. Photogramm. Remote Sens.* 88, 119–127. doi:10.1016/j.isprsjprs.2013.11.018

Đurić, D., Mladenović, A., Pešić-Georgiadis, M., Marjanović, M., and Abolmasov, B. (2017). Using multiresolution and multitemporal satellite data for post-disaster landslide inventory in the Republic of Serbia. *Landslides* 14 (4), 1467–1482. doi:10.1007/s10346-017-0847-2

Gorum, T., and Carranza, E. J. M. (2015). Control of style-of-faulting on spatial pattern of earthquake-triggered landslides. *Int. J. Environ. Sci. Technol.* 12 (10), 3189–3212. doi:10.1007/s13762-015-0752-y

Gorum, T., van Westen, C. J., Korup, O., van der Meijde, M., Fan, X., and van der Meer, F. D. (2013). Complex rupture mechanism and topography control symmetry of mass-wasting pattern, 2010 Haiti earthquake. *Geomorphology.* 184, 127–138. doi:10.1016/j.geomorph.2012.11.027

Guzzetti, F., Mondini, A. C., Cardinali, M., Federica, F., Santangelo, M, and Chang, K.-T. (2012). Landslide inventory maps: new tools for an old problem. *Earth Sci. Rev.* 112 (1-2), 42–66. doi:10.1016/j.earscirev.2012.02.001

Hölbling, D., Friedl, B., and Eisank, C. (2015). An object-based approach for semi-automated landslide change detection and attribution of changes to landslide classes in northern Taiwan. *Earth Sci. India* 8 (2), 327–335. doi:10.1007/s12145-015-0217-3

Hölbling, D., Füreder, P., Antolini, F., Cigna, F., Casagli, N., and Lang, S. (2012). A semi-automated object-based approach for landslide detection validated by persistent scatterer interferometry measures and landslide inventories. *Rem. Sens.* 4 (5), 1310–1336. doi:10.3390/rs4051310

Hyvärinen, A., and Oja, E. (2000). Independent component analysis: algorithms and applications. *Neural Network* 13 (4-5), 411–430. doi:10.1016/s0893-6080(00)00026-5

Jensen, J. R. (2005). "Thematic information extraction: pattern recognition," in *Introductory Digital Image Processing: A Remote Sensing Perspective*. Upper Saddle River, NJ: Prentice Hall, 337–406.

Jessee, M. A. N., Hamburger, M. W., Ferrara, M. R., McLean, A., and FitzGerald, C. (2020). A global dataset and model of earthquake-induced landslide fatalities. *Landslides* 187, 1363–1376. doi:10.1007/s10346-020-01356-z

Karlson, M., Ostwald, M., Reese, H., Sanou, J., Tankoano, B., and Mattsson, E. (2015). Mapping tree canopy cover and aboveground biomass in Sudano-Sahelian woodlands using Landsat 8 and random forest. *Rem. Sens.* 7 (8), 10017–10041. doi:10.3390/rs70810017

Li, Z., Shi, W., Lu, P., Yan, L., Wang, Q., and Miao, Z. (2016). Landslide mapping from aerial photographs using change detection-based Markov random field. *Remote Sens. Environ.* 187, 76–90. doi:10.1016/j.rse.2016.10.008

Liu, W., Yamazaki, F., and Maruyama, Y. (2019). Detection of earthquake-induced landslides during the 2018 kumamoto earthquake using multitemporal airborne lidar data. *Rem. Sens.* 11 (19), 2292. doi:10.3390/rs11192292

Lu, P., Qin, Y., Li, Z., Mondini, A. C., and Casagli, N. (2019). Landslide mapping from multi-sensor data through improved change detection-based Markov random field. *Remote Sens. Environ.* 231, 111235. doi:10.1016/j.rse.2019.111235

Marc, O., and Hovius, N. (2015). Amalgamation in landslide maps: effects and automatic detection. *Nat. Hazards Earth Syst. Sci.* 15, 723–733. doi:10.5194/nhess-15-723-2015

Martha, T. R., Norman, K., Jetten, V., Cees, J. v. W., and Kumar, K. V. (2010). Characterising spectral, spatial and morphometric properties of landslides for semi-automatic detection using object-oriented methods. *Geomorphology* 116 (1-2), 24–36. doi:10.1016/j.geomorph.2009.10.004

Maxwell, A. E., Sharma, M., Kite, J. S., Donaldson, K. A., Thompson, J. A., Bell, M. L., et al. (2020). Slope failure prediction using random forest machine learning and LiDAR in an eroded folded mountain belt. *Rem. Sens.* 12 (3), 486. doi:10.3390/rs12030486

McFeeters, S. K. (1996). The use of the normalized difference water index (NDWI) in the delineation of open water features. *Int. J. Rem. Sens.* 17 (7), 1425–1432. doi:10.1080/01431169608948714

Mondini, A. C., Chang, K.-T., and Yin, H.-Y. (2011). Combining multiple change detection indices for mapping landslides triggered by typhoons. *Geomorphology* 134 (3-4), 440–451. doi:10.1016/j.geomorph.2011.07.021

Planet (2017). *Planet imagery product specification*. San Francisco, CA: Planet Labs.

Ramo, R., and Chuvieco, E. (2017). Developing a random forest algorithm for MODIS global burned area classification. *Rem. Sens.* 9 (11), 1193. doi:10.3390/rs9111193

Rosi, A., Tofani, V., Tanteri, L., Tacconi Stefanelli, C., Agostini, A., Catani, F., Casagli, N., et al. (2018). The new landslide inventory of Tuscany (Italy) updated with PS-InSAR: geomorphological features and landslide distribution. *Landslides* 15 (1), 5–19. doi:10.1007/s10346-017-0861-4

Shao, X., Ma, S., Xu, C., Zhang, P., Wen, B., Tian, Y., et al. (2019). Planet image-based inventorying and machine learning-based susceptibility mapping for the landslides triggered by the 2018 Mw6.6 tomakomai, Japan earthquake. *Rem. Sens.* 11 (8), 978. doi:10.3390/rs11080978

Shirvani, Z. (2020). A holistic analysis for landslide susceptibility mapping applying geographic object-based random forest: a comparison between protected and non-protected forests. *Rem. Sens.* 12 (3), 434. doi:10.3390/rs12030434

Shirvani, Z., Abdi, O., and Buchroithner, M. (2019). A synergetic analysis of sentinel-1 and -2 for mapping historical landslides using object-oriented random forest in the hyrcanian forests. *Rem. Sens.* 11 (19), 2300. doi:10.3390/rs11192300

Sokolova, M., and Lapalme, G. (2009). A systematic analysis of performance measures for classification tasks. *Inf. Process. Manag.* 45 (4), 427–437. doi:10.1016/j.ipm.2009.03.002

Stumpf, A., and Kerle, N. (2011). Object-oriented mapping of landslides using random forests. *Remote Sens. Environ.* 115 (10), 2564–2577. doi:10.1016/j.rse.2011.05.013

Tanyaş, H., CeesVan Westen, J., E Allstadt, K., Anna Nowicki Jessee, M., Görüm, T., Jibson, R. W., et al. (2017). Presentation and analysis of a worldwide database of earthquake-induced landslide inventories. *J. Geophys. Res.: Earth Surface* 122 (10), 1991–2015. doi:10.1002/2017JF004236

Tian, Y., Xu, C., Hong, H., Zhou, Q., and Wang, D. (2019). Mapping earthquake-triggered landslide susceptibility by use of artificial neural network (ANN) models: an example of the 2013 minxian (China) Mw 5.9 event. *Geomatics, Nat. Hazards Risk* 10 (1), 1–25. doi:10.1080/19475705.2018.1487471

Tucker, C. J. (1979). Red and photographic infrared linear combinations for monitoring vegetation. *Remote Sens. Environ.* 8 (2), 127–150. doi:10.1016/0034-4257(79)90013-0

Vamsee, A. M., Kamala, P., Martha, T. R., Kumar, K. V., Sankar, G. J., and Amminedu, E. (2018). A tool assessing optimal multi-scale image segmentation. *J. Indian Soc. Remote. Sens.* 46 (1), 31–41. doi:10.1007/s12524-017-0685-7

Wicaksono, P., and Lazuardi, W. (2018). Assessment of PlanetScope images for benthic habitat and seagrass species mapping in a complex optically shallow water environment. *Int. J. Rem. Sens.* 39 (17), 5739–5765. doi:10.1080/01431161.2018.1506951

Yamagishi, H., and Yamazaki, F. (2018). Landslides by the 2018 Hokkaido iburi-tobu earthquake on september 6. *Landslides* 15 (12), 2521–2524. doi:10.1007/s10346-018-1092-z

Yang, X., and Chen, L. (2010). Using multi-temporal remote sensor imagery to detect earthquake-triggered landslides. *Int. J. Appl. Earth Obs. Geoinf.* 12 (6), 487–495. doi:10.1016/j.jag.2010.05.006

Zhang, S., Li, R., Wang, F., and Iio, A. (2019). Characteristics of landslides triggered by the 2018 Hokkaido eastern iburi earthquake, northern Japan. *Landslides* 16 (9), 1691–1708. doi:10.1007/s10346-019-01207-6

Zhao, W., Li, A., Nan, X., Zhang, Z., and Lei, G. (2017). Postearthquake landslides mapping from Landsat-8 data for the 2015 Nepal earthquake using a pixel-based change detection method. *IEEE J. Sel. Top. Appl. Earth Observations Remote Sensing* 10 (5), 1758–1768. doi:10.1109/jstars.2017.2661802

Zhong, C., Liu, Y., Gao, P., Chen, W., Li, H., Hou, Y., et al. (2020). Landslide mapping with remote sensing: challenges and opportunities. *Int. J. Rem. Sens.* 41 (4), 1555–1581. doi:10.1080/01431161.2019.1672904

Conflict of Interest: The author declares that the research was conducted in the absence of any commercial or financial relationships that could be construed as a potential conflict of interest.

frontiers
in Earth Science

ORIGINAL RESEARCH
published: 16 March 2021
doi: 10.3389/feart.2021.649543

A Historical Earthquake-Induced Landslide Damming Event at the Qiaojia Reach of the Jinsha River, SE Tibetan Plateau: Implication for the Seismic Hazard of the Xiaojiang Fault

Mengmeng Hu[1,2], Zhonghai Wu[1], Klaus Reicherter[3], Sajid Ali[3,4], Xiaolong Huang[1] and Jiameng Zuo[1,5]*

[1]Key Laboratory of Neotectonic Movement and Geohazard, The Institute of Geomechanics, Chinese Academy of Geological Sciences, Beijing, China, [2]School of Earth and Space Sciences, Peking University, Beijing, China, [3]Neotectonics and Natural Hazards, RWTH Aachen University, Aachen, Germany, [4]Department of Earth Sciences, COMSATS University Islamabad, Abbottabad Campus, Abbottabad, Pakistan, [5]China University of Geosciences, Beijing, China

OPEN ACCESS

Edited by:
*Chong Xu,
Ministry of Emergency
Management, China*

Reviewed by:
*Ming Zhang,
China University of Geosciences
Wuhan, China
Xiangli He,
China Earthquake
Administration, China
Yulong Cui,
Anhui University of Science and
Technology, China*

***Correspondence:**
*Zhonghai Wu
wuzhonghai8848@foxmail.com*

Specialty section:
*This article was submitted to
Geohazards and Georisks,
a section of the journal
Frontiers in Earth Science*

Received: *05 January 2021*
Accepted: *08 February 2021*
Published: *16 March 2021*

Citation:
*Hu M, Wu Z, Reicherter K, Ali S, Huang X and Zuo J (2021) A Historical Earthquake-Induced Landslide Damming Event at the Qiaojia Reach of the Jinsha River, SE Tibetan Plateau: Implication for the Seismic Hazard of the Xiaojiang Fault.
Front. Earth Sci. 9:649543.
doi: 10.3389/feart.2021.649543*

In bedrock mountainous areas where active faults and deep river valleys interact, earthquake-induced landslides can be used to explore local seismic hazards. The intersection of the highly active Xiaojiang Fault and the Jinsha River and its main tributaries in southwest China is a site of abundant earthquake-induced landslides. We found some boulders inappropriately scattered on the east bank of the Qiaojia reach of the Jinsha River, where the Qiaojia Segment of the Xiaojiang Fault passes through. We investigated the lithology and topography nearby and confirmed its source area, as well as the existence of a landslide damming event in the field. A high-resolution Digital Surface Model (DSM) generated from Unmanned Aerial Vehicle (UAV) images was used to analyze its characteristics and calculate its parameters. Optically Stimulated Luminescence (OSL) and ^{14}C dating methods on the related dammed lake sand shows the age of the landslide, which is not later than 878 AD. The characteristics of large size with limited depositional extent, spatial relevance between the landslide and Xiaojiang Fault, and temporal-coincidence of the landslide with 624 AD earthquake support the seismic origin of this landslide. Moreover, the 624 AD earthquake was reanalyzed for its magnitude and macro-epicenter based on the coseismic displacement of the Heishui River floodplain. It was calculated to be Mw7.7 or Ms7.9 and relocated to the Qiaojia area. No M ≥ 7 earthquakes have occurred on the Qiaojia Segment for nearly 1,400 years since 624 AD. The elapsed time is close to the average recurrence interval of large earthquakes on the Qiaojia Segment. Therefore, the seismic hazard of the Qiaojia area should be considered in the future.

Keywords: Qiaojia, Jinsha River, earthquake-induced landslide, seismic hazard assessment, Xiaojiang Fault

INTRODUCTION

Landslides are a widely distributed geological process, commonly found in mountainous areas (Evans and Clague, 1994). Moreover, large landslides usually develop along rivers, giving rise to dammed lakes, which may eventually cause a subsequent catastrophic breach-flood. Based on morphology, displaced material type, mechanism of initiation, and other factors, landslides have been classified into many types (Bolt et al., 1977; Varnes, 1978; Highland and Bobrowsky, 2008), among which earthquakes can trigger every type. Landslides here are called earthquake-induced landslides. These landslides account for a large number of deaths and high economic losses, damaging engineering structures including settlements, dams, bridges, and communication systems (Keefer, 1984).

Earthquake-induced landslides can be used as indirect evidence to reconstruct the seismic history of a region without surface ruptures or environmental effects of earthquakes and should be implemented in hazard and risk studies (Jibson, 1996), which primarily focus on the likelihood, potential magnitude, and recurrence interval of large earthquakes in a region. Adams (1981) proposed that the magnitudes of prehistoric earthquakes could be estimated by comparing the extents of landslide dams of recent earthquakes with those of landslide dams in historical ones. Similarly, he has assessed the magnitude of the historical or prehistorical earthquake by comparing coseismal landslide distributions of prehistorical events with well-documented recent earthquakes in New Zealand and Central Asia (Adams, 1981). Practically, Zeng et al. (2020) used the empirical equations of the total volume of all paleolandslides triggered in an earthquake and the moment magnitude (Keefer, 1984) to evaluate the earthquake magnitude that triggered the Nixu rock avalanche event (~Mw7.0–7.2). Taking Soviet Central Asia as an example, Nikonov (1988) had an understanding: large seismo-gravitational dislocations, such as landslides, occur due to earthquakes of magnitude 6–6.5 or more and are always located within the highest isoseismal (about 10–25 km), tending to be along its major axis. Moreover, the number, size, and areal extent of the landslides are proportional to the size of an earthquake (Solonenko, 1977). Tibaldi et al. (1995) reconstructed the geometry of seismogenic faults by correlating the elongation of the landslide distribution with the location and dimensions of the faults. According to a statistical analysis of 40 historical worldwide earthquakes, the relationship between landslide distribution and seismic parameters was analyzed (Keefer, 1984). Later, the upper bound of the maximum distance to landslides from the epicenter and fault rupture zone for earthquakes of different magnitudes was determined (Jibson, 1996; Jibson, 2009; McCalpin, 2009). Meunier et al. (2007) derived an expression for the spatial variation of landslide density analogous with regional seismic attenuation laws, based on the observation on landsliding associated with large earthquakes on three thrust faults: the Northridge earthquake in California, Chi-Chi earthquake in Taiwan, and two earthquakes on the Ramu-Markham fault. Massey et al. (2018) investigated the landslides accompanying with the 2014 November 2016 Mw7.8 Kaikōura earthquake, and found: 1) seven of the largest eight landslides (from 5 to 20 Mm^3) occurred on faults that ruptured to the surface during the earthquake; 2) the average landslide density within 200 m of a mapped surface fault rupture is three times than that at a distance of 2,500 m or more from a mapped surface fault rupture.

The SE Tibetan Plateau, located between the Eastern Himalayan Syntaxis and the Sichuan Basin, contains numerous active faults, large relief, and a well-developed river network. Three major rivers, the Jinsha, the Lancang, and the Nu, flow from NW to SSE in parallel (Liu et al., 2009). A series of landslide blocking events were found along the rivers previously. Using the Interferometric synthetic aperture radar (InSAR) method, 22 active landslides were identified and mapped over more than 2,500 km^2 in the reservoir of the Wudongde hydropower station, Jinsha River (Zhao et al., 2018). The ancient Zhaizicun landslide blocked the Jinsha River, and the lacustrine sediments developed upstream of the landslide dam (Xu et al., 2011; Zhang et al., 2012). The Chongjianghe landslide, a giant landslide discovered by Zhang et al. (2013) in the Chongjianghe Screw Bay Power Station, a branch of the Jinsha River in northwestern Yunnan, is located in the step over of a regional active fault.

We found some boulders inappropriately scattered on the east bank of the Qiaojia reach of the Jinsha River in the field, where the Qiaojia Segment of the Xiaojiang Fault passes through. Lithology and surrounding topography indicate its source location, implying a landslide damming event occurred before. A high-resolution DSM generated from UAV images was used to analyze the characteristics and calculate the parameters of this landslide. Simultaneously, OSL and ^{14}C dating methods were used to determine its age. Moreover, we attempted to demonstrate its seismic origin mechanism. Combined with the analysis of a coseismic displacement on the Qiaojia Segment near this landslide, we discussed the seismic hazard of the Qiaojia Segment.

REGIONAL SETTINGS

Geography

At the Qiaojia reach of the Jinsha River, the curve traces of three major active faults (the northern segment of the Xiaojiang Fault (Qiaojia Segment), Zemuhe Fault, and Daliangshan Fault) intersect, forming the Qiaojia Pull-Apart Basin (**Figure 1**). The Yaoshan Mountains and the Jinsha River, to the east and the west respectively, bound the Qiaojia Basin, while Hulukou and Xiaotianba restrict it in the north and south (**Figure 2**). The overall shape of the basin is a 15 km long and 4 km wide narrow wedge, having an N-S orientation and an average slope of about 7°. Significantly, the north-flowing Jinsha River conferred a ladder terrain, including three terraces and a flood platform. These terraces lie between 640 and 750 m elevation and the flood platform exists between 750 and 1,000 m elevation from the back-end of the terrace to the foot of the Yaoshan Mountains (**Figure 3**). In addition, some incised valleys and terraces developed across the platform. The west side of the Jinsha River is divided by the Zhilu Gully, having the Wushenggong

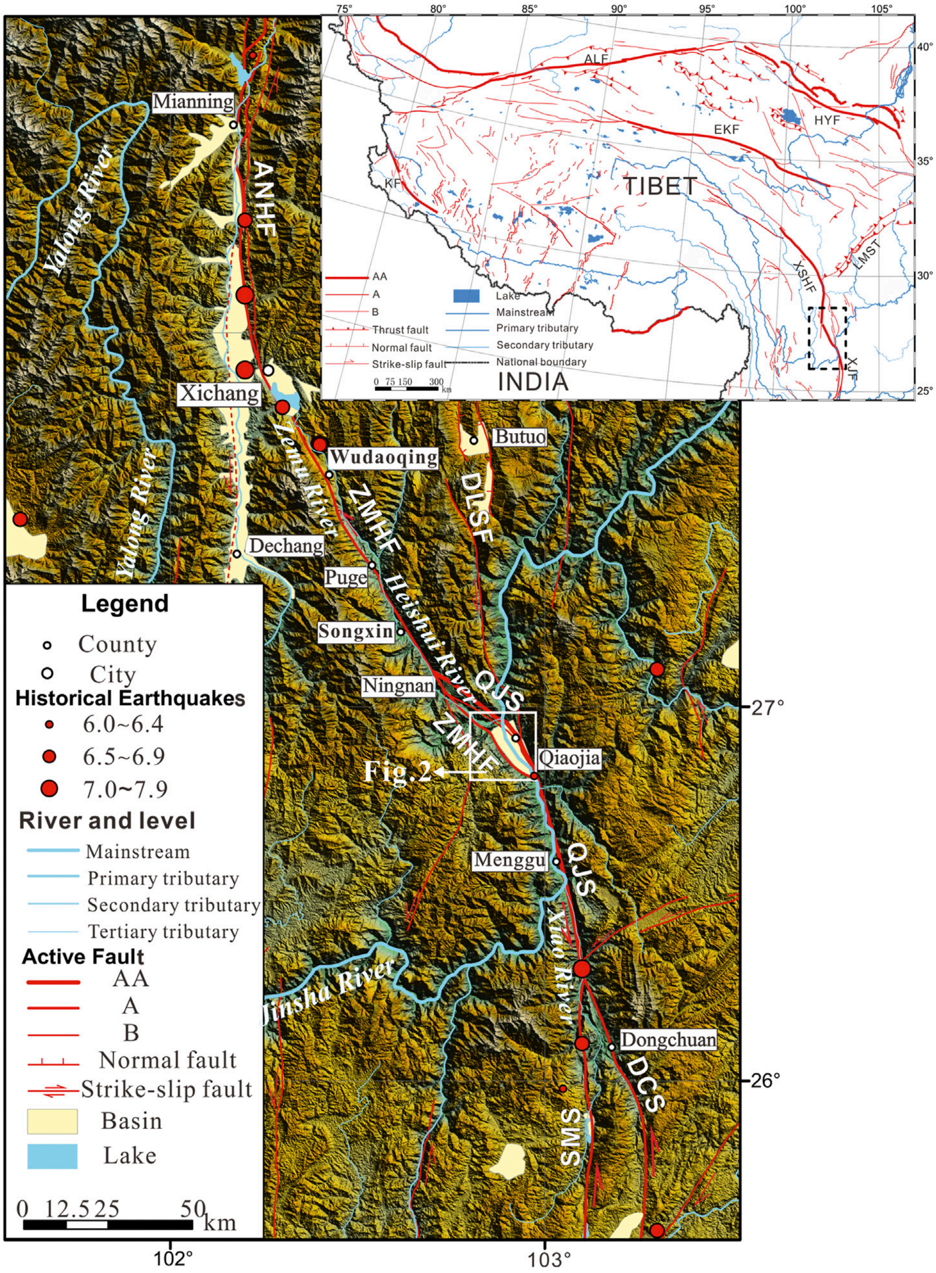

FIGURE 1 | Principal active faults, historical earthquakes with magnitude ≥ 6.0, basins, rivers, and main towns in the study area mapped on a Digital Elevation Model (ASTER GDEM res-30 m). KF = Karakoram Fault; ALF = Altyn Tagh Fault; EKF = East Kunlun Fault; XSHF = Xianshuihe Fault; ANHF = Anninghe Fault; ZMHF = Zemuhe Fault; DLSF = Daliangshan Fault; XJF = Xiaojiang Fault; LMST = Longmenshan Thrust; QJS = Qiaojia Segmeny; DCS = Dongchuan Segment; SMS = Songming Segment. For the active faults, AA, A, and B indicate their activity of extremely strong, strong, and medium. Dashed rectangle in the inset marks the location of the study area. All vector data from Wu and Zhou (2018).

Ridge (up to an elevation of 1,060 m) to its north and the Low Mountain, hilly landform with medium fluctuation to its south. Close to the boulders, the topography of both sides of the Jinsha River is significantly different (**Figure 4**). On the east side, a Q_3 proluvial-alluvial fan originates from a mountain pass, with a low slope angle (4.6°), spreading at least 2 km from the east bank to the mountain foot. On the west side, the valley shoulder (elevation 870 m, and 240 m above the river surface) of the Wushenggong Ridge separates the gently sloping terrain above it from the alternate terrain of the abrupt wall and the narrow gentle slope below it. The comprehensive terrain slope under the valley shoulder is about 42°. Separated from the Wushenggong Ridge by a gully, the accumulational hill is 760 m high at most, occupying an area of 0.13 km^2. Moreover, the limestone bedrock hill between Hulukou Town and the Heishui River locates at the site where the width of the Jinsha River abruptly narrows from

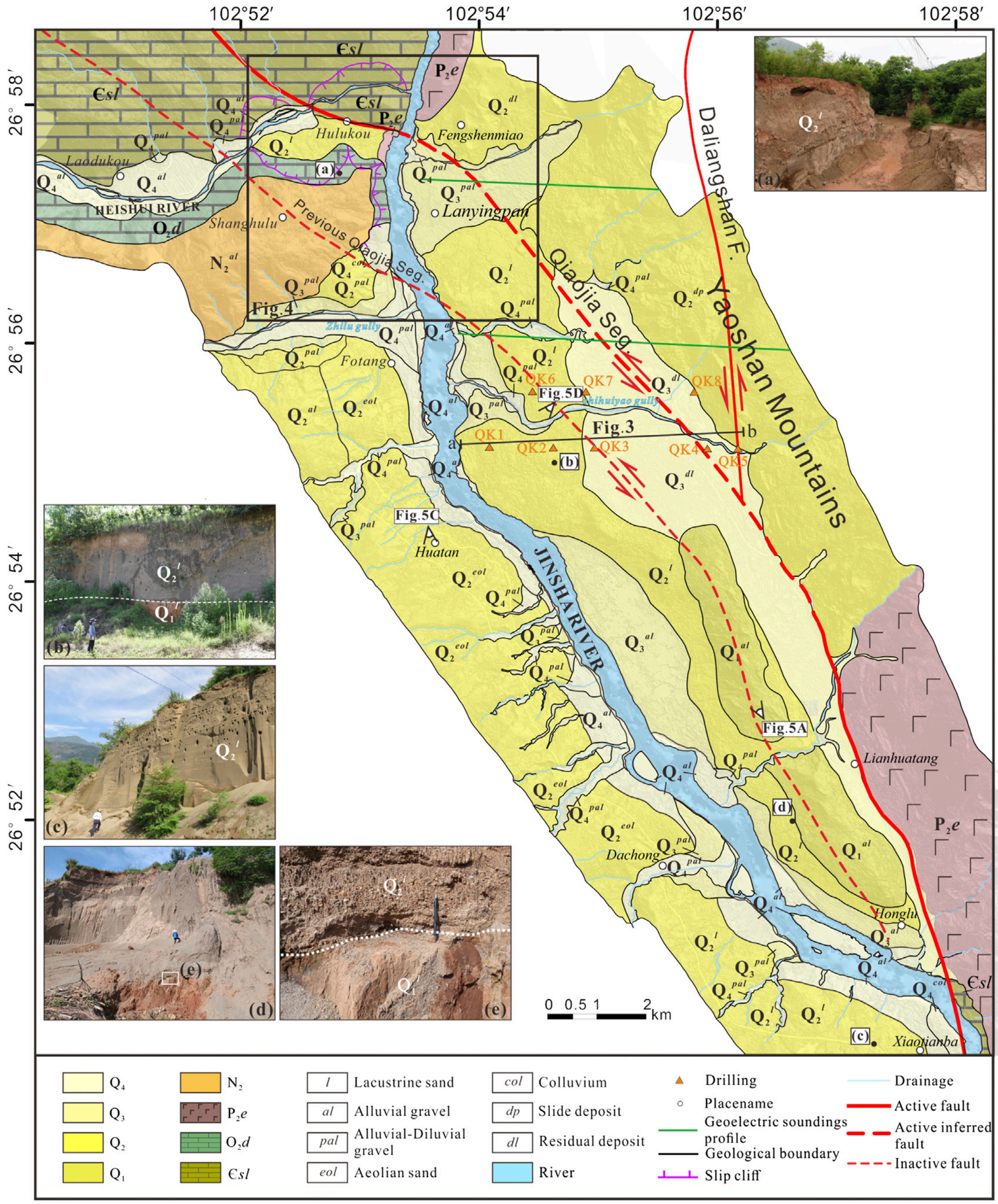

FIGURE 2 | Stratigraphic units of the Qiaojia Basin; the insert photos show two sets of lacustrine sediments with ages of Q_2 and Q_1.

200 to 120 m. Its top elevation is 866 m. The Qiaojia Segment traces on its south side, forming a fault scarp.

The climate in the dry-hot valley of the Jinsha River is arid, and the water and heat are extremely unbalanced. Located in the river valley, Qiaojia Basin has an annual average temperature of more than 20°C. The average temperature of the hottest month, July, is 27.4°C, and the average temperature of the coldest month, January, is 12.2°C. According to the data of major climate stations in the Qiaojia area, the annual precipitation varies from 600 to 1,600 mm from Jinsha River Valley to the mountains above 3,000 m.

Geology

The Qiaojia Basin is mainly controlled by the Qiaojia Segment (**Figure 2**). About 80 km long, the Qiaojia Segment extends nearly N-S with an almost upright dip angle from Daduo in the south and north of Qiaojia in the north. The trace and location of this segment in the Qiaojia Basin can only be identified from the offset

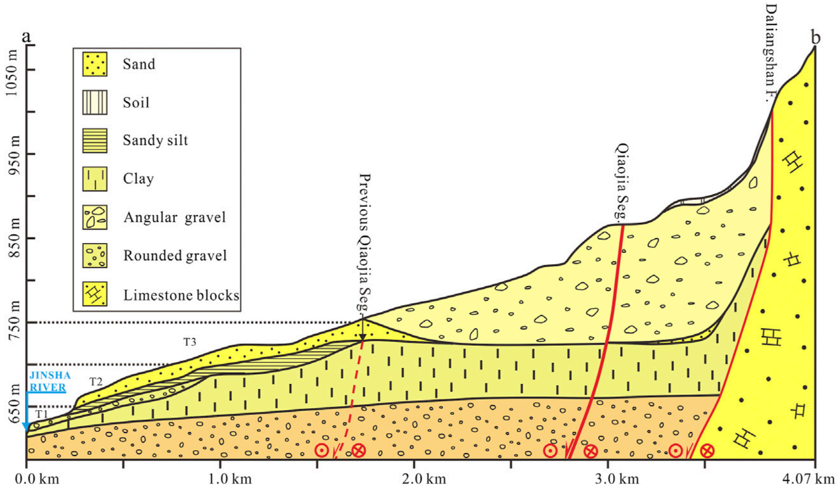

FIGURE 3 | Cross-section of Qiaojia Basin, showing the three terraces of the Jinsha River and a flood platform behind them; from the drill data of Li et al. (2016); see the location of the drills in **Figure 1**.

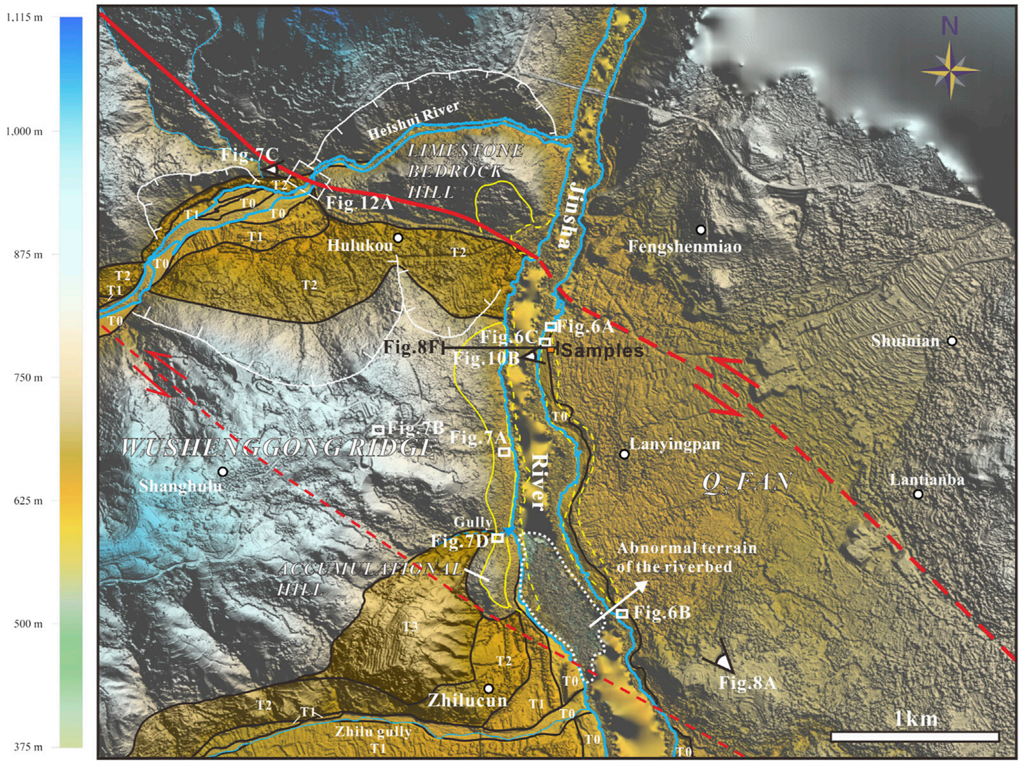

FIGURE 4 | DSM (res-0.6 m) of the topography around the landslide; red solid line and thick red dashed line indicate the current Qiaojia Segment trace, thin red dashed line indicates the previous Qiaojia Segment trace; jagged white lines show the crown of the early landslides; yellow solid lines circle the source of the failed slope collapse to be discussed in this paper, yellow dashed lines to the west of the Jinsha River indicate the near-source deposit, and the yellow dashed line to the east of the Jinsha River circles the spatial distribution of boulders from this failed slope collapse. All terraces are outlined with black lines. Solid orange rectangle shows the sample locations, as well as the locations in **Figure 9**.

of several stream channels and the geoelectric soundings at overlying thick Quaternary sediment sites. It changes trend from nearly N-S to a NW direction, crossing the basin and connecting to the Zemuhe Fault near Ningnan. The strike-slip rate of the Qiaojia Segment was estimated at 7.0–10 mm/yr on a multiple-temporal scale from Late Quaternary to the modern

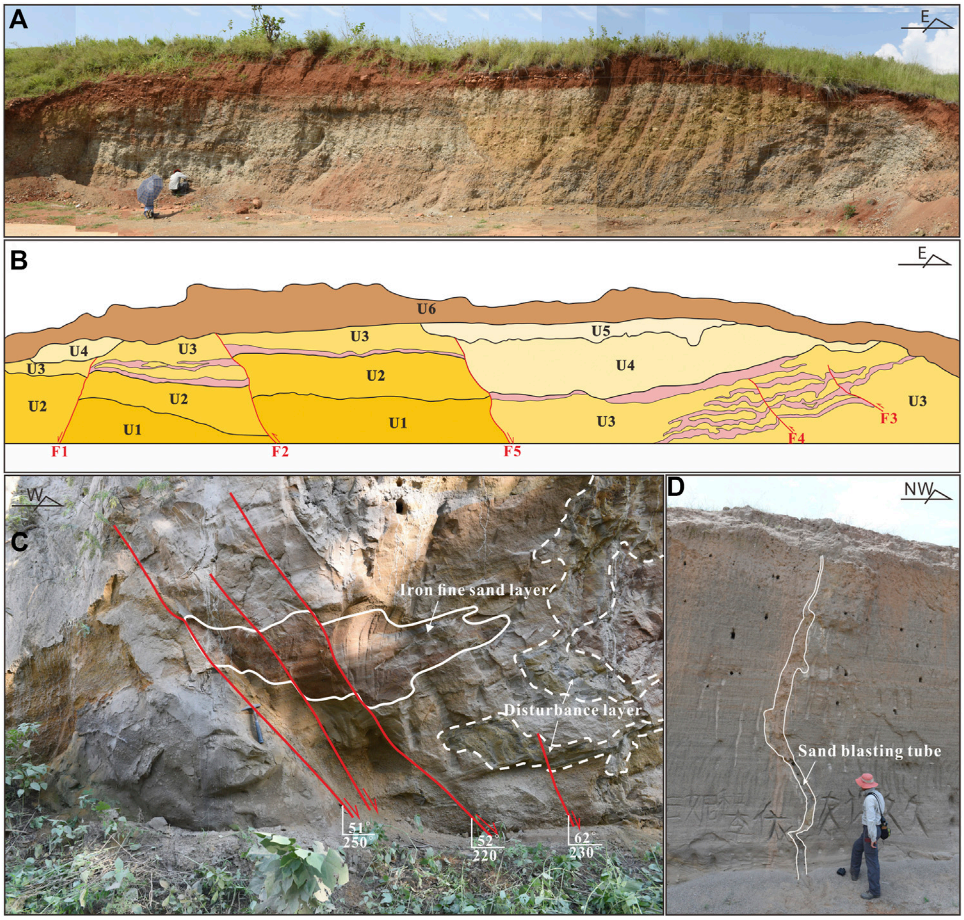

FIGURE 5 | Earthquake-induced effects in different sedimentary units (see the locations in **Figure 1**). **(A)** Small faults in Q_1^{al}; **(B)** the interpretation of **(A)**, U1: gray gravel layer; U2: light grayish-green gravel layer; U3: inter-bedding of gray gravel layer and brown gray fine silty sand bearing gravel; U4: yellow-brown sand layer bearing gravel; U5: off-white calcareous consolidated gravel layer; U6: eolian brownish-red gravel layer **(lower)** and sand layer bearing gravel **(upper)**; **(C)** Small faults and disturbance layer in Q_2^{al} brownish-yellow fluvial sand layer, the marker layer of a fault dislocation is an iron fine sand layer; the lime-green sand layer was disturbed; **(D)** sandblasting tube in Q_2^{l} medium-coarse lacustrine sand, the walls of the tube are calcareous cemented.

time (Wen et al., 2011; Wei et al., 2012; Zhao et al., 2015). Its previous trace was located to the west of the modern trace, proven to have ceased its activity by the latest dislocation strata dated to Q_2.

Under the dual role of the north-flowing Jinsha River and the gullies from the eastern mountain, the Qiaojia Basin is characterized by a large amount of Quaternary fluvial sediments accumulated in the interior, including fluvial terraces, proluvial-alluvial fans, and lacustrine sediments. Among them, a large proportion of the lacustrine sediments are remarkable, with a wide exhibition range (**Figure 2**). Generally, we recognized two sets of lacustrine sediments linking to two large landslide damming events, referring to Q_1^{l} and Q_2^{l} according to the criterion of stratigraphic sedimentary sequence, which is constrained by strata of known age. These unconsolidated deposits are mainly sand and gravel and are more than 300 m thick. The Qiaojia Segment at Qiaojia Basin significantly fractured the bedrock on the west of the Jinsha River, which would facilitate the occurrence of landslides. Accordingly, it has been observed that some landslides take place in some places downstream, damming the Jinsha River or its main tributaries (**Figure 4**).

Earthquakes

Seven historical earthquakes with magnitude ≥ 6.0 from Xichang to Dongchuan, mainly concentrated at the two end sites, with the maximum one occurred at Dongchuan in 1733 (M $7^3/_4$) (Department of Earthquake Damage Prevention, State Seismological Bureau, 1995) (**Figure 1**). The earthquakes recorded in the Qiaojia area were not as numerous as expected due to its special tectonic location. The historical earthquake catalog of the area indicates a seismic gap relative to the whole Xiaojiang Fault (Wen et al., 2011; Xu et al., 2017). Since 1500 AD, this area has been characterized by only one strong earthquake event (Qiaojia M6 earthquake). Coseismic surface ruptures correspond to this earthquake distribution,

TABLE 1 | Results of OSL dating on the lacustrine sand.

Sample number	Material	Burial depth/m	Moisture content/%	Ambient dose rate/(Gy/ka)	Equivalent dose/Gy	Age/ka
SQ3	Medium-fine sand	0.1	6 ± 3	2.82 ± 0.08	5.02 ± 0.16	1.78 ± 0.07
SQ4	Medium-fine sand	0.35	8 ± 4	3.20 ± 0.10	5.65 ± 0.26	1.77 ± 0.10

TABLE 2 | Results of ^{14}C dating.

Laboratory number	Sample code number	Material	Conventional radiocarbon age	2 sigma calendar calibrated results
Beta-509563	SQ1	Calcium film	43,310 ± 620 years BP	46,122–43,422 cal BC
Beta-509564	SQ2	Snail shell	1,110 ± 30 years BP	878–1,013 cal AD

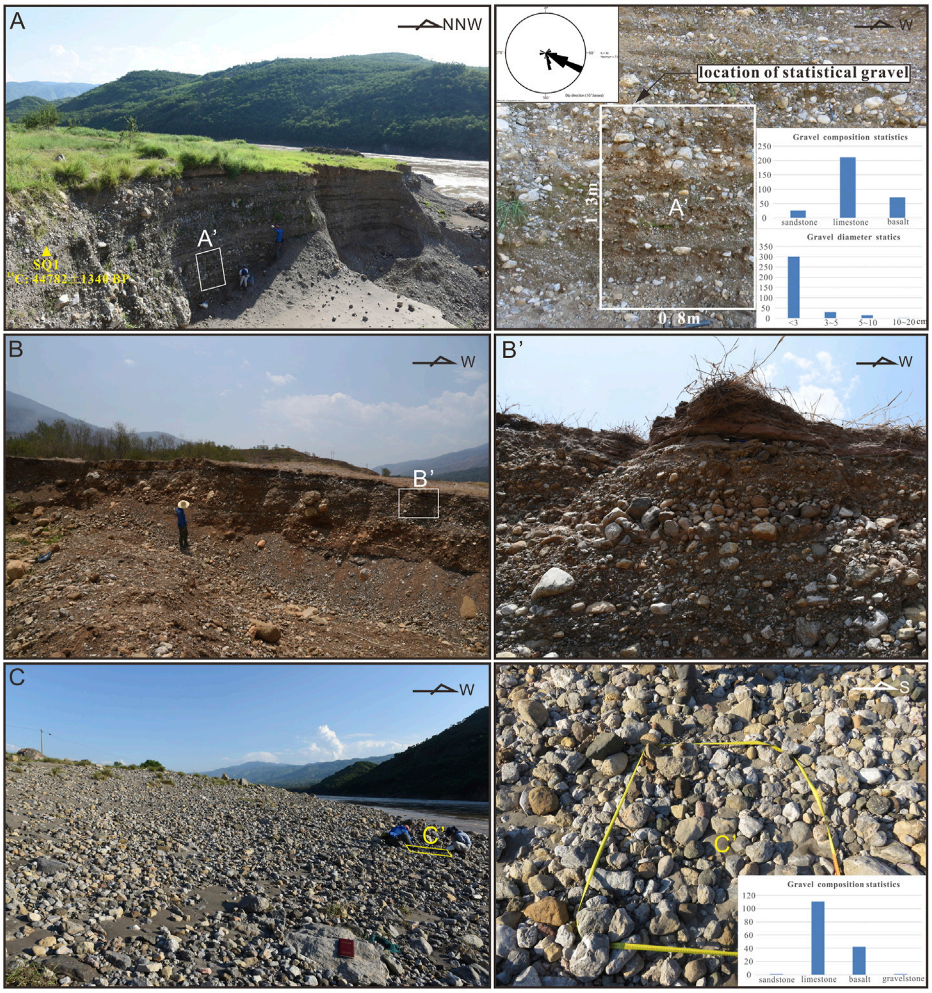

FIGURE 6 | Gravel statistical locations (see the location in **Figure 3**). **(A)** and **(B)** Photos note the sidewalls and gravels of the Q_3 fan north and south of Lanyingpan, respectively; the white rectangle in **(A)** indicates the gravel statistical location, the rose diagram shows the paleo-flow direction, and the two histograms show the composition and size of gravels; **(C)** Photo of the gravel of the Jinsha River floodplain, with the gravel statistical location in the yellow rectangle.

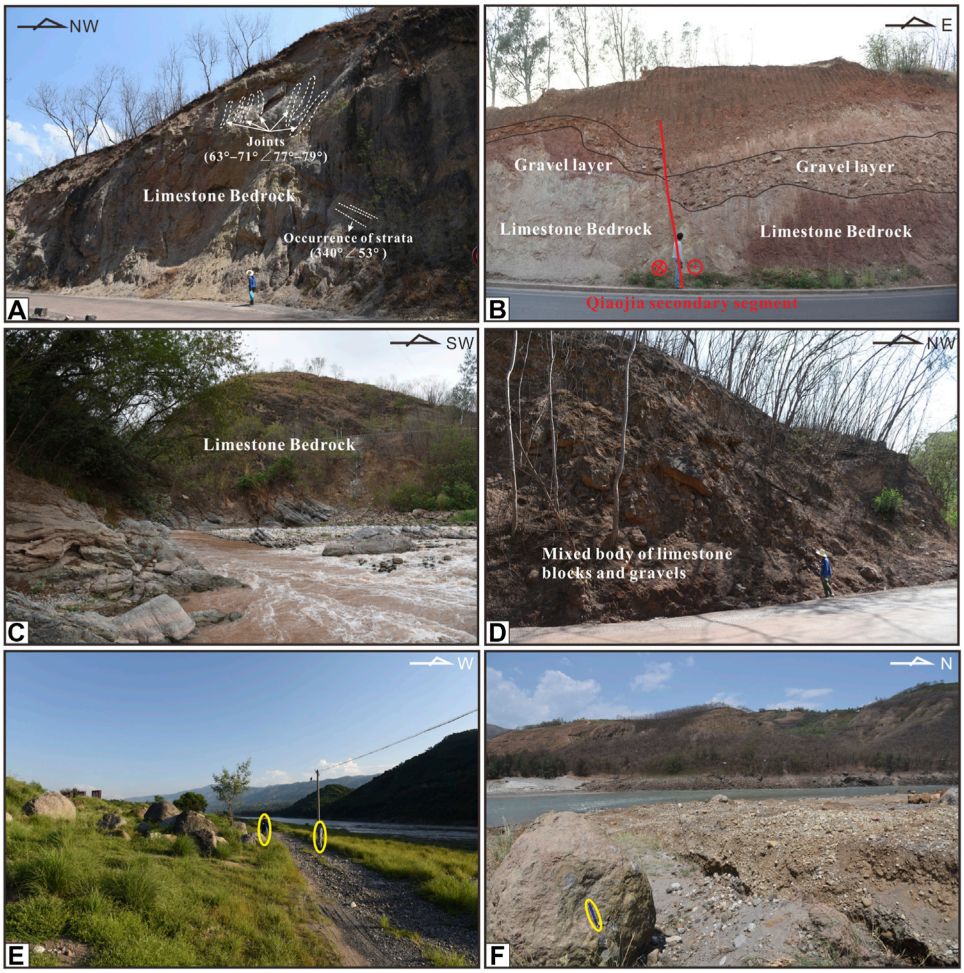

FIGURE 7 | Materials of the Wushenggong Ridge and its adjacent hills. **(A)** limestone bedrock of the Wushenggong Ridge; **(B)** terrace gravel layer overlying the limestone bedrock, in the Wushenggong Ridge. The Qiaojia secondary segment can also be seen in this profile; **(C)** limestone bedrock of the hill north of Wushenggong Ridge; **(D)** Mixed body of limestone boulders and gravels of the hill south of Wushenggong Ridge. All locations are illustrated in **Figure 3**. **(E)**, **(F)** Field views of boulders at north and south of Lanyingpan, respectively, and person/pencil-outlined for scale. Locations in **Figure 7**.

which preserves a non-rupture section around the Qiaojia area (Wen et al., 2011). Paradoxically, a series of effects of earthquake-induced landslides are well preserved in the strata pre-Holocene, including small faults, disturbance layers, and sandblasting tubes (**Figure 5**), indicating the long-term earthquake silence in this area is abnormal.

DATA AND METHODS

Mapping the Landslide

In order to determine the characteristics and origin of this landslide, a combination of field investigation, satellite images from Google Earth, and a high-resolution DSM (res-0.6 m) generated with Structure from Motion (SfM) processing of UP30 Autopilot System photography were used. The SfM is an emerging and widely used photogrammetric method for reconstructing a 3-D structure using large sets of high-resolution images with a high degree of overlap derived from a moving sensor (Snavely et al., 2008; Westoby et al., 2012; Lucieer et al., 2014). A detailed explanation of the SfM process is described in Snavely et al. (2008). Our collected images were processed using Agisoft Photoscan Pro software1 with processing workflow procedures similar to that of Johnson et al. (2014). Hillshade was created in Global Mapper[2] from the high-resolution DSM and further processed in Coreldraw X7 for geomorphic mapping. To view and calculate the distribution and parameters of the landslide, we used the "Acute3D viewer" software[3] to visualize the 3D demos generated from ContextCapture[4].

---

[1] www.agisoft.com

[2] https://www.bluemarblegeo.com/

[3] https://acute3d-viewer.software.informer.com/

[4] https://www.bentley.com/en/products/brands/contextcapture

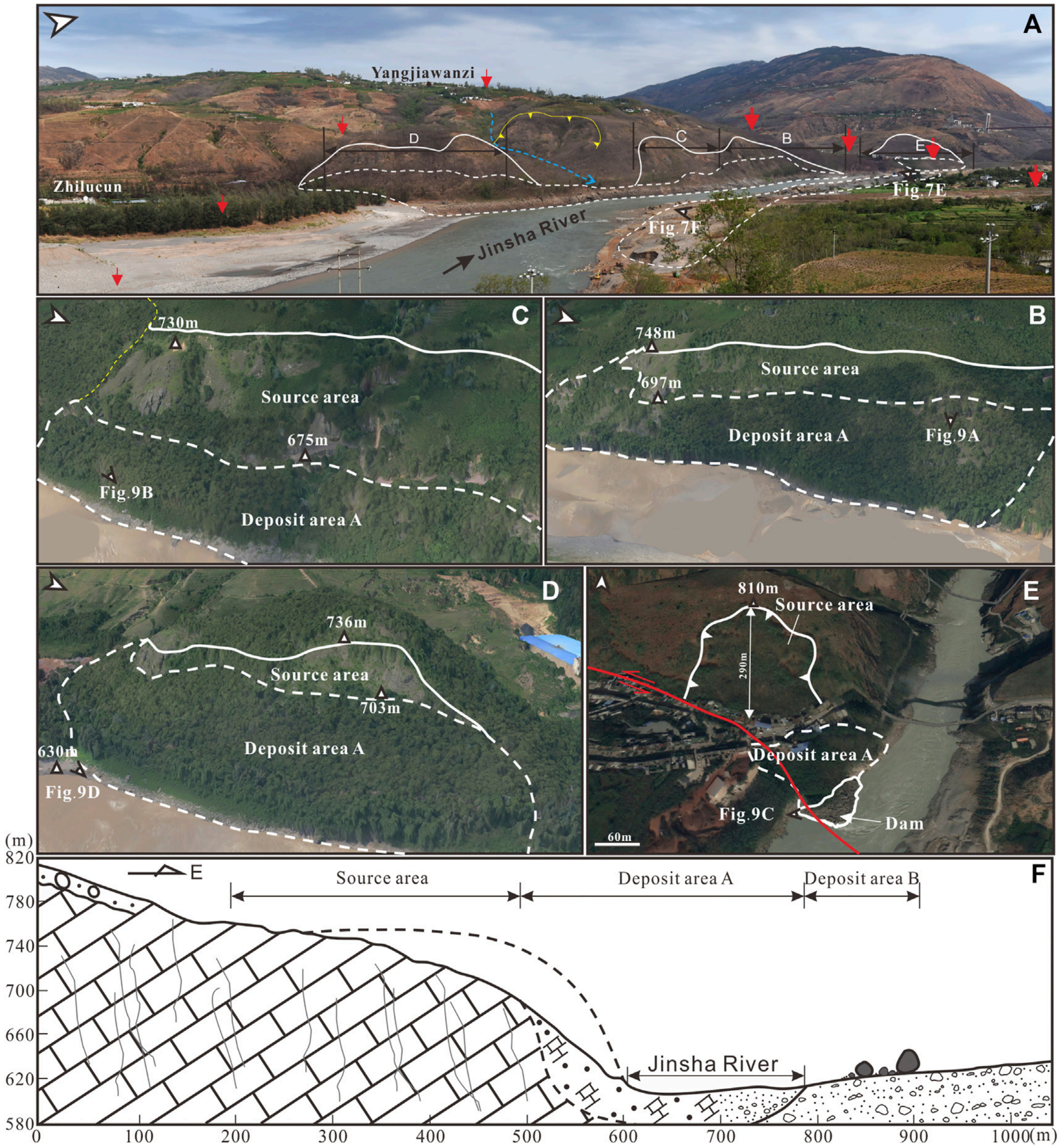

FIGURE 8 | Landslide morphology **(A)** Field panoramic photo of the failed slope collapse (location in **Figure 3**). Source area, deposit area, and boulders are indicated with white solid lines, and white dashed line, respectively. Yellow jagged line shows the crown of the early landslides, as well as the gully and villages with a blue dashed line and white/black solid circles. The Qiaojia Segment and the previous Qiaojia Segment are indicated with larger red arrows and smaller red arrows. **(B)–(D)** Air photos show the details of the failed slope collapse at different sections. The elevations of the crown and the foot of the source area are marked. **(E)** Google Earth Image of the rock fall located at the north side of Qiaojia Segment; the crown elevation of the source area and the maximum travel path of the deposit are indicated; the dam, which is inside the range of the Jinsha River, is also circled with a white solid line. **(F)** Longitudinal profile of the failed slope collapse, and the location is in **Figure 3**.

TABLE 3 | Characteristics of the failed slope collapse at different sections.

Section	Materials	Crown Elevation (m)	Drop (m)	Cut Volume (m^3)	Fill Volume (m^3)
B	Limestone bedrock	748	118	2,557,072.98	941,062.93
C	Limestone bedrock	730	100	1,326,247.92	118,034.27
D	Mixed body of limestone bedrock and gravels	736	106	717,513.26	627,118.52
E	Limestone bedrock	810	180	2,837,946.70	854,919.42

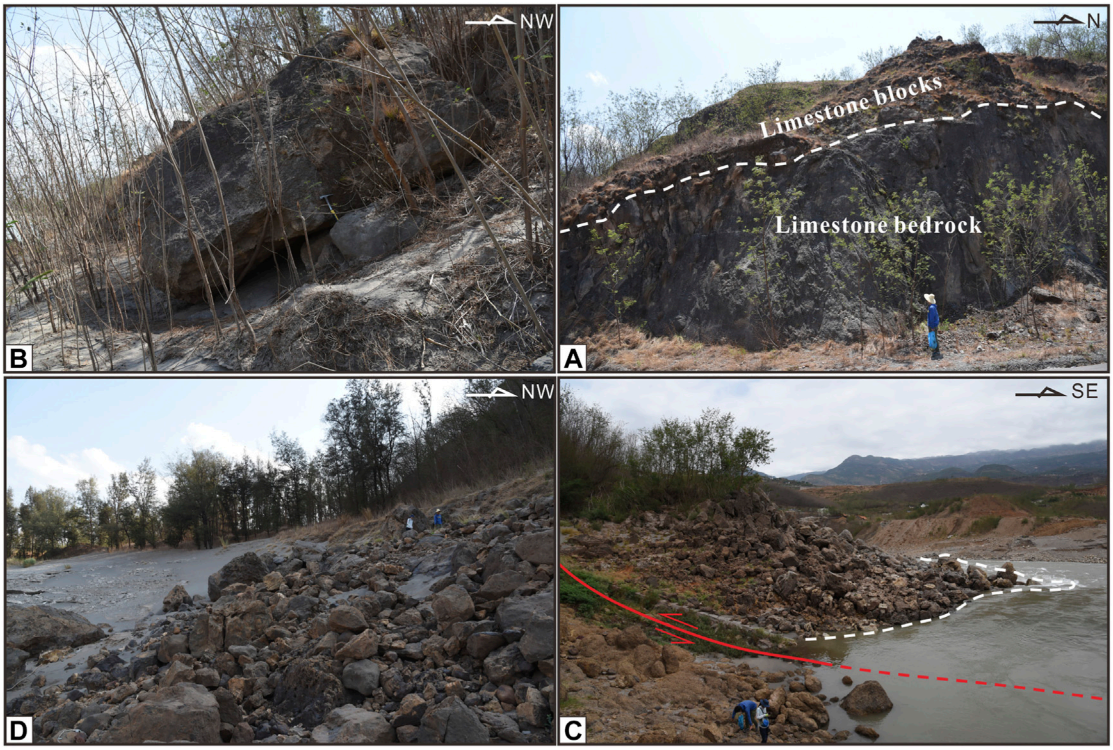

FIGURE 9 | **(A)** and **(B)** limestone boulders from the rock falls at sections **(B)** and **(C)**; **(C)** Field view of the dam at the north side of Qiaojia Segment; **(D)** limestone boulders scatter on the west bank of the Jinsha River from the rock fall at section **(D)**. All locations in **Figure 7**.

Dating

In this study, two OSL samples and two ^{14}C samples were dated. They are summarized in **Tables 1** and **2**, respectively.

The OSL samples were collected using stainless steel tubes (20 cm long and 5 cm diameter). The tubes were hammered into the sediment, and after completely filling, both ends were immediately sealed with aluminum foil and taped to prevent light leakage and loss of water during transport and storage. The sand can be easily sorted, and sizes of quartz particles in the range of 90–125 μm were chosen to date the sand. The whole dating process was carried out at the OSL/TL Geochronology Laboratory, Institute of Geology, China Seismological Bureau. Detailed processing and analytical procedures are reported in a previous study (Chen et al., 2013). The ^{14}C dating method used on the fossil snail shells buried in the sand precisely constrained the age of the sand. The sample was carried out at Beta Analytic Testing Laboratory, and the age was calibrated based on the INTCAL13 database on BetaCal3.21 software with 2σ (95% confidence limits). All the ages referred to hereafter in this paper are calendar years obtained from conventional radiocarbon ages.

RESULTS OF THE INVESTIGATION

Existence of a Landslide

At the north of Lanyingpan, the fan underlying the boulders was dated to 44,782 ± 1,340 years BP using AMS-^{14}C (Sample: SQ1, **Table 2**). It is characterized by the inter-bedding of the coarse and fine gravel layers, with the gravel-bearing coarse sand lens occurring locally (**Figure 6A**). The gravel is mainly limestone, accounting for 85%–90%, with the remaining 10–15% being sandstone and basalt. The general flat-surface of the gravels inclines to the SEE, indicating it origined from the east mountain pass. The diameter of the gravels is predominantly several centimeters with few over 1 m. At the south of Lanyingpan, the gravels of the fan change in diameter to a smaller level, and the composition is also different from the above site, in which basalt is predominant, followed by limestone and sandstone (**Figure 6B**).

The gravels in the floodplain of the Jinsha River are mainly sub-angular and sub-circular in shape (**Figure 6C**). Their diameter is mainly 2–20 cm, followed by 20–30 cm, and a few 20–50 cm. In composition, limestone accounts for 70%, followed by basalt with 20–25%, and sandstone with 5–10%.

The Wushenggong Ridge mainly consists of limestone bedrock, with sandstone and basalt developed locally, and a thick gravel layer overlain (**Figure 2**). The presence of the Qiaojia Segment has resulted in the limestone (340°∠53°) being intensely fragmented, having a set of steep joints (63°–71°∠77°–79°), which is consistent with the Qiaojia Segment on the strike (**Figure 7A**). The existing structures cause a reduction in the strength of the bedrock. Specifically, they may initiate small amounts of movement in a sliding mass and provide a path for potential water flow, which can cause

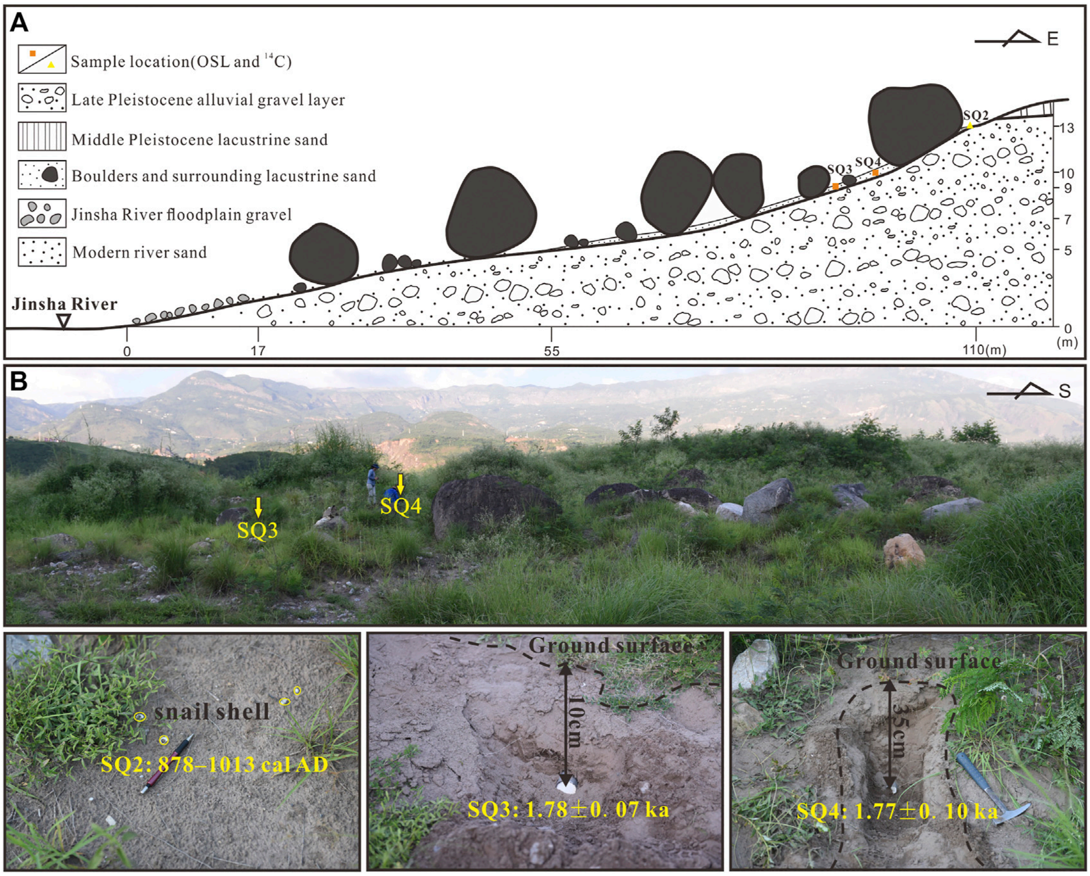

FIGURE 10 | Samples site. **(A)** Schematic profile of the sampling locations; **(B)** close-up photos of the sampling locations where one can see boulder sizes, sand, and vegetation cover.

substantial engineering or construction difficulties, especially in the valley or canyon area (Bolt et al., 1977). The gravel layer is about 18–20 m thick and is characterized by alternating layers of coarse and fine gravel layers, where the gravel is dominantly extremely circular, with a maximum diameter above 50 cm and a primary composition of sandstone, spreading from an elevation of 770–1,060 m. It is cemented with calcareous material and forms a set of terrace gravel from the Heishui River (**Figure 7B**). The gravels are mainly sandstone with a diameter of 10–40 cm, which is consistent with the one on the Wushenggong Ridge. Moreover, the hill between Hulukou Town and the Heishui River is a limestone bedrock hill with the limestone extremely deformed (**Figure 7C**). The accumulational hill south of the Wushenggong Ridge is characterized by a mixed body of limestone boulders and sub-round but poorly sorted gravels, without underlying limestone bedrock (**Figure 7D**).

The boulders on the east bank of the river extend about 1.5 km long from north to south, centrally scattering at two sites. At the north of Lanyingpan, the boulders are even larger than a person (≤3.5 m) (**Figure 7E**). Limestone is their main composition, with a roundness of sub-angular to sub-circular. The farthest boulder is 13 m above the river surface and is 100 and 287 m away from the east and west edges, respectively. At the south of Lanyingpan, the diameter of the boulders ranges from 0.8 to 1.4 m, with the same roundness and different compositions, mainly including limestone, followed by basalt breccia (**Figure 7F**).

Considering the coincidence of the composition and size between the boulders and materials of the Wushenggong Ridge and its adjacent hills, the source status of the ridge and its adjacent hills appear to be linked with the boulders. In addition, the steep topography on the west of Jinsha River, the spatial-correspondence between the boulders distribution and the range of the west slope, as well as the similar deposit on the foot of the west slope, all support the uniqueness of this origin. The Yaoshan Mountains east of Qiaojia Basin are exactly to land sliding, with several reports and research attesting to this (Wang, 1996; Feng et al., 2019). However, the ancient huge landslide occurred one hundred thousand years ago, and its stability has been proved. Over 10 m thick younger sediments overlay the frontal margin material of the landslide, as we introduced the stratum of Qiaojia Basin according to the field investigation and drill data. Thus, it is confirmed that a landslide originated from the Wushenggong Ridge and its adjacent hills.

TABLE 4 | Historical earthquakes before 878 AD in Xichang-Dongchuan area.

Date	Epicenter		Magnitude (Ms)	MMI	Description
	Latitude, longitude	References location			
624/08/15	27.9°, 102.2°	Xichang area	>6	VIII	Mountains shook, rivers were blocked with the dam
814/04/02	27.9°, 102.2°	Xichang area	7	IX	The aftershock lasted for 80 days, more than 100 people were crushed to death, and compression occurred within 15 km

Landslide Characteristics

The over 2 km long eastern flank of the Wushenggong Ridge, the accumulational hill south of it, and the bedrock hill north of it were observed as an entire failed slope (**Figure 8A**). It consists of several individual simultaneous landslides of different scales, crown elevations, materials, and slope angle (**Table 3**), complying with the criteria of a rock fall cluster (Keefer, 1984). The volumes of the total source area and the total deposit on the west bank are about 7 × 10^6 and 2.5 × 10^6 m^3 respectively (extracted from the "Acute 3D Viewer" software). According to the classification of landslides on the basis of their magnitude (Parkash, 2012), this failed slope collapse was placed in an enormous category.

For the Wushenggong Ridge, two individual rock falls were focused (**Figures 8B,C**). At section C, fragment limestone blocks originated from an elevation of about 748 m, which is 118 m higher than the river surface (**Figure 8B**). The cut volume is far more than the fill volume, indicating a large amount of the materials transported into the river. The deposit on the west bank of the river is mainly composed of limestone boulders, with diameters ranging from 0.5 to 5 m (**Figures 9A,B**). The rock fall at section D shows similar features as the above one, with the crown elevation somewhat lower (730 m) (**Figure 8C**).

The materials of the accumulational hill failed with a wide range of collapse that occurred at a maximum elevation of 736 m (**Figure 8D**). The scattered limestone boulders (1–8 m diameter) on the west bank of the Jinsha River (**Figure 9D**) are products of the rock fall at this site.

At the south side of the limestone bedrock hill, Qiaojia Segment passes through, forming a fault scarp, which is prone to collapse. The limestone bedrock hill started to collapse at an elevation of 810 m. From crown to foot, the longest travel path of the rock masses is 290 m (**Figure 8E**). The accumulation of the limestone boulders (0.5–8 m diameter) stacked on the west bank of the Jinsha River is fresh without fillings, indicating the young age of the rock fall here. It even occupied half of the modern Jinsha River (**Figure 9C**) and was considered as a dam resulting in the dammed lake. With the boulders transported to the east bank of the Jinsha River, a dammed lake formed, and gray medium-fine sand spread around those boulders. This provides us an appropriate window to learn about the age limit of the landslide, which is almost equal to the age of the dammed lake sand.

Landslide Age

The 10–35 cm thick gray gravel-bearing medium-fine dammed lake sand layer begins to appear around the boulders 55 m away from the east edge of the river, spreading eastward to the end of the boulders. We sampled with the profile perpendicular to the Jinsha River direction, where the boulders were exposed (**Figure 10**). The two dates from OSL samples (Samples: SQ3, SQ4) aged from 1770 to 1780 years BP (~240 AD) are older than the age of the ^{14}C sample (Sample: SQ2, 878–1013 AD). According to the Timing principle of the OSL dating method, it determines the age of the last sunlight exposure event of the sample, thus more reliable result needs high degree of sunlight exposure and low residual OSL signals for the sample. However, as researched before (Zhang et al., 2015), when this method is applied with fluvial-lacustrine facies sand, the result could be used as a reference rather than accurate result, in the presence of other more reliable dating methods. In addition, the sand layer we sampled has experienced a rapid and transient sedimentary process, meaning an incomplete sunlight exposure. Thus, it is believed that the dammed lake formed before 878 AD.

DISCUSSION

Seismic Origin of the Landslide

A landslide occurs when the downslope component of the forces acting on the earth or rock mass exceeds the strength or shearing resistance of the material. The transition from a stable hillside to an active slide implies that either the acting force or the soil or rock resistance has changed for some reasons (Bolt et al., 1977). Several contributory causes were proposed, mostly including rainfall, earthquake, human activity, and so on (Cornforth, 2005). The annual precipitation of Qiaojia Basin is placed in the regionally low level and is the less rainy area. Considering the cluster characteristics of the landslide in a range of 2 km long, which cannot be realized with rainfall as a triggering factor, it is suggested that rainfall should be ruled out as a possible trigger of such a wide range of slope collapse. As a remote mountainous area, Qiaojia County is not a densely populated area historically, so human activity should also be excluded.

Uniqueness of the cause of landslide will be correlated with earthquake when some characteristics of the landslide possess. Spatial-relevance between landslides and active fault indicates that the landslides are seismically triggered (Burrows, 1975). Crozier (1992) proposes six criteria to support a seismic origin generally: 1) ongoing seismicity in the region, which has triggered landslides, 2) coincidence of landslide distribution with an active fault or seismic zone, 3) geotechnical slope-stability analyses showing that earthquake shaking would have been required to induce slope failure, 4) large size of landslides, 5) presence of liquefaction features associated with

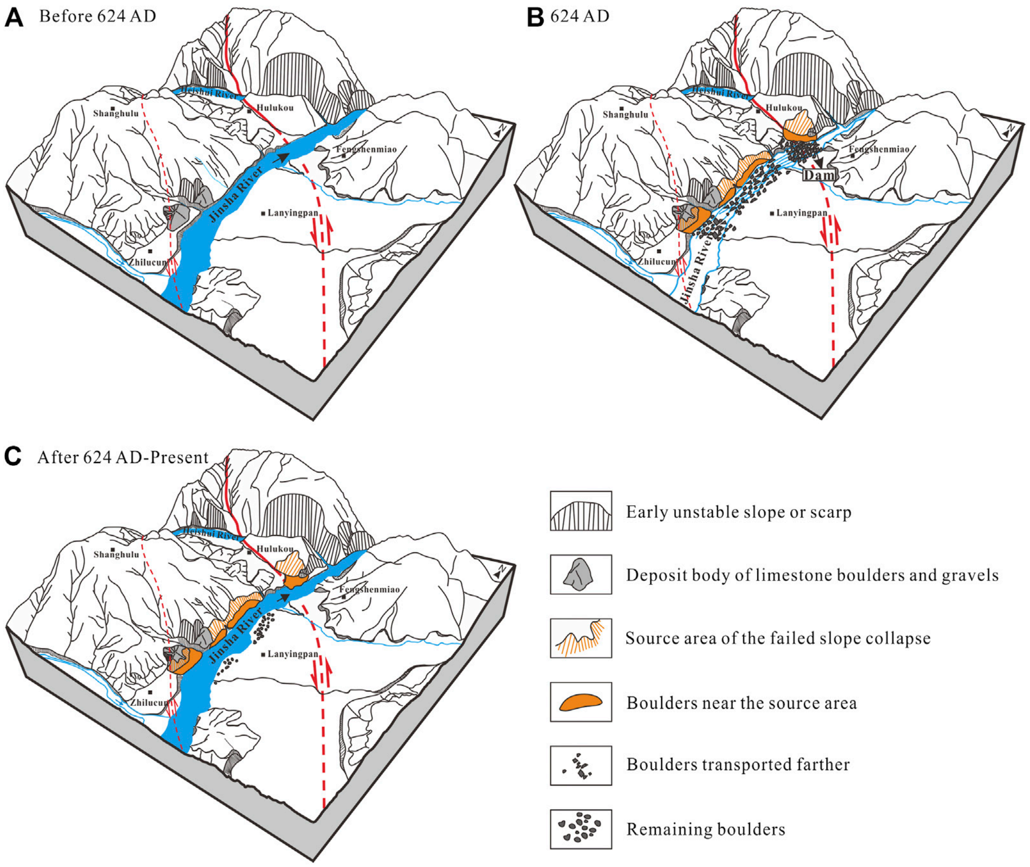

FIGURE 11 | The sketch process of the 624 AD failed slope collapse.

landslides, and 6) landslide distribution that cannot be explained solely on the basis of geological or geomorphic conditions. Obviously, the more of these criteria that are satisfied, the stronger the case for seismic origin (Jibson, 1996). Keefer (1994) also mentions that in active seismic regions landslides with huge energy releases, large volumes and long runout distances have much higher probability of seismic origin than non-seismic origin. In addition, spatio-temporally correlating landslides with known or assumed earthquakes can increase the certainty of landslide seismic origin (Pánek, 2015). The landslide here meets several criteria of them.

Large Size With Limited Depositional Extent

A characteristic of the earthquake-induced landslide is its rapid occurrence, within a few minutes after the termination of the earthquake. The corresponding result of the rapid process of the landslide is its more limited depositional extent, which is different from that of the landslides that occur in intense rainfall conditions, characterized by more fluidity and a tendency to spread out farther across a depositional area (Perrin and Hancox, 1992). As mentioned above, this failed slope collapse is enormous in magnitude, with a characteristic of cluster. The boulders on the east bank distributed 1.5 km long in an N-S direction. We concluded that the general extent of the deposit did not exceed the range of the source area (2 km long) transversely. The long horizontal distance against the small drop supports the effect of an earthquake. Further considering the blocky appearance of the deposits, we roughly confirm the seismic origin of this landslide.

Spatial Relevance Between the Landslide and Xiaojiang Active Fault

Zhang et al. (2018) recognized 94 landslides in the Qiaojia to Dongchuan area along the middle and northern segments of the Xiaojiang Fault based on GIS. The banded distribution of these landslides shows an obvious control by the fault, which corresponds with the surface rupture zone of strong earthquakes. Thus, it is believed that the Xiaojiang Fault controls the occurrence of landslides. Song et al. (2012) researched the deformation of the left bank of the Jinsha River around Baihetan Hydropower, about 40 km downstream of the Qiaojia Basin. He pointed out that the gently dipping faulted bedding belt and the NW trending fault are the main controlling factors of the deformation. For the left bank in the Qiaojia Basin, i.e., Wushenggong Ridge, a set of steep joints (63°–71°∠77°–79°) is consistent with the previous Qiaojia Segment on the strike. The small faults in the strata before the Holocene (**Figure 5A**) indicate

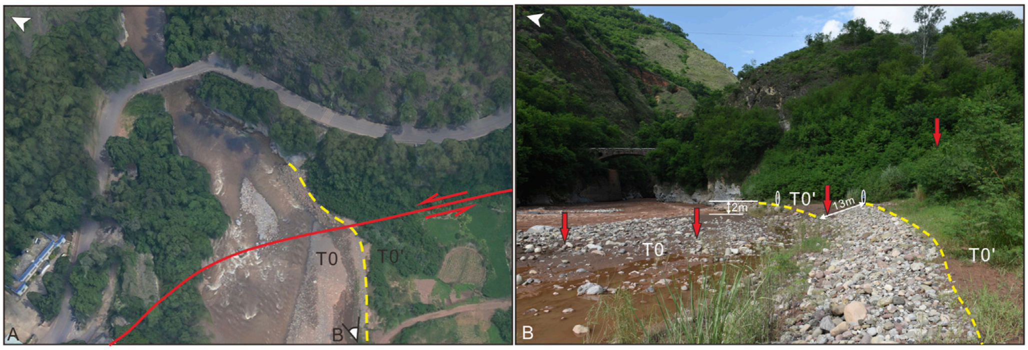

FIGURE 12 | (A) Air photo of the displacement of the Heishui River floodplain (see the location in **Figure 3**); **(B)** field view of the displacement of the Heishui River floodplain.

the existence of the non-active previous Qiaojia Segment, which is suggested to be the early location of the current Qiaojia Segment. The joints in the limestone of the Wushenggong Ridge are located within the fault of the previous segment and present the rock fragmentation effect of its activity. Under such unstable slope conditions, the Wushenggong Ridge is prone to collapse. After migrating to the Basin-Mountain margin east of Qiaojia County, the Qiaojia Segment has been acting in the extreme, having the potential to initiate earthquakes. As Jibson (2015) mentioned: landslides triggered in the immediate vicinity of active faults commonly are seismically triggered. The landslide in this paper straddles the Qiaojia Segment, indicating the possibility of being triggered by an earthquake event relevant to the activity of the fault.

Temporal-Coincidence of the Landslide With 624 AD Earthquake

Two earthquakes that occurred earlier than 878 AD in the study area are the 624 AD earthquake and the 814 AD earthquake (Lou, 1996). The former triggered landslides, resulting in river damming, whereas the latter was mainly characterized by ground compression (**Table 4**). Seismically induced permanent ground deformation is defined as any earthquake-generated process that leads to deformations within a soil medium, which, in turn, results in permanent horizontal or vertical displacements of the ground surface (Stewart and Wren, 2005). It includes the following modes: Surface fault rupture, liquefaction, seismically induced land sliding, and seismic compression. The requisite conditions for land sliding are the presence of sloping ground and the presence of combined static and dynamic shear stresses that exceed material strengths, whereas seismic compression needs relatively strong shaking and unsaturated soil of a flat site. These two modes correspond to the effects of the 624 AD earthquake and the 814 AD earthquake respectively, according to their descriptions. This means that the 814 AD earthquake probably occurred in a flat area such as Xichang Basin, while the 624 AD earthquake was more likely to have occurred in valley areas between Xichang and Qiaojia. And as mentioned before (Nikonov, 1988), large landslides, which are triggered by earthquakes of magnitude 6–6.5 or more, are always located within the highest isoseismal (about 10–25 km), tending to be along its major axis. Thereby, we confirmed the macro-epicenter of the 624 AD earthquake at somewhere of the Heishui valley, not far 25 km away from this landslide. Considering the remoteness of the ancient Xichang–Qiaojia area and the larger population in Xichang than in Qiaojia, it is understandable to arrange the Xichang as the macro-epicenter of the 624 AD earthquake in the historical catalog. The description of the 624 AD earthquake and its spatial proximity to the studied landslide support its greater plausibility as the trigger of this landslide than the 814 AD earthquake.

Accordingly, the seismic origin of this landslide is basically determined, termed as a coseismic event of the 624 AD earthquake.

Process of the Landslide

Long-term activities of the Qiaojia Segment have led to the fragmentation of rock masses on both sides of the fault. Weakened erosion resistance and reduced stability of the rock mass laid a foundation for the large-scale instability of the marginal slope. Under this condition, the eastern flank of the Wushenggong Ridge is prone to have slope failures, and it is ascertained by a deposit body of limestone boulders and gravels overlying the limestone bedrock (**Figure 11A**).

In 624 AD, a strong earthquake caused the entire eastern slope of the Wushenggong Ridge to collapse, including the above deposit body and a hill north of the ridge. This earthquake caused an over 2 km long slope collapse with a total volume exceeding 7 × 106 m^3 failing. The boulders spread from the frontal edge of the source area to the east bank of the Jinsha River, with a maximum horizontal distance of 550 m. Most of the boulders fell into the Jinsha River, and a small amount of them lie on both banks of the river in a limited range. At the point where the Jinsha River narrowed, a large number of boulders blocked the river, forming a dam and a temporary lake. In a relatively still water environment, a set of lacustrine sand was preserved in a limited area (**Figure 11B**).

The dammed lake had not existed long from the evidence of the thin lacustrine sand layer (10–35 cm thick). As researched previously, landslide dammed lakes may last from several

TABLE 5 | Parameters of earthquakes with intensity ≥ IX from Xichang to Dongchuan.

No	Date	Magnitude	Macroscopic epicenter	Epicentral intensity	Epicentral region		Seismogenic fault	Data sources
					(Major axis, minor axis) km	Trend		
1	624/8/18	7.9	Qiaojia	X	(158,33)**	N31°W	Qiaojia Fault	a
2	814/4/6	7	Xichang	IX	—	—	Anninghe Fault	b
3	1489/1/15	$6^{3}/_{4}$	Xichang and Yuexi	IX	(39,18)*	N6°W	Zemuhe Fault	c
4	1732/1/29	$6^{3}/_{4}$	Xichang	IX	(50,21)*	N23°W	Zemuhe Fault	b
5	1733/8/2	$7^{3}/_{4}$	Dongchuan	X	(152,42)*	N11°W	Qiaojia fault and dongchuan Fault	b
6	1850/9/12	$7^{1}/_{2}$	Xichang-puge	X	(116,29)*	N25°W	Zemuhe Fault	b
7	1966/2/5	$6^{1}/_{2}$	Dongchuan	IX	(97,53)*	N44°W	Songming Fault	b

*Annotation: * from documented data; ** calculated according to the formula (3) in the text; - no data; a. This paper; b. Department of Earthquake Damage Prevention (1995); c. Wen, 2000.*

minutes to several thousand years, depending on factors such as volume, size, geometry, sorting of blockage materials, rates of seepage through the blockage, and rates of sediments and water that flow into the newly formed lake (Costa and Schuster, 1988; Peng and Zhang, 2011). Combined with cases in southwest China (Peng and Zhang, 2011), where the longevity of landslide dams is a few hours or more than 10 h, here we suppose several that several hours later, the dam broke and the river reopened its flow (**Figure 11C**). The boulders in the water were either swept away by the current or settled on the bottom of the riverbed. The remaining boulders even affected the terrain of the riverbed (**Figure 4**). The boulders on the east bank have experienced a free movement without friction among boulders, which resulted in the boulders having better roundness. With the later influence of artificial reconstruction, the boulders became fewer in number.

Seismic Hazard Assessment of Qiaojia Segment

About 1.3 km NW of the landslide, the floodplain of Heishui River shows a left-lateral displacement of 13 m, which was measured in the field with the laser rangefinder and was considered surface coseismic displacement of one or several earthquakes (**Figure 12**). Chen and Zhao (1988) found that the Jinsha River and its main tributaries all have more than six terraces. The depositional age of the terraces of the Jinsha River and its first tributaries, such as Nu, Nanpan, Niulan, and Xiao Rivers were obtained (Ji et al., 2000). It is indicated that the T1 terrace of the first tributaries was deposited in 4,500–11,000 years BP, which is later than that of the Jinsha River (9,000–17,000 years BP). The stream trenching rate of the Jinsha River near Qiaojia was also taken into account to constrain the forming age of the Heishui River floodplain. Huang et al. (2010) calculated the stream trenching rate on the Baihetan reach of the Jinsha River for the construction needs of the Baihetan Hydropower station. The results show the average trenching rate is about 1.2 mm/yr since 25 ka, showing an increasing trend since 100 ka. Ding et al. (2017) later took the climate factor into account and gave a 1.17 mm/yr trenching rate since 23.5 ka at Qiaojia. In combination with our field measurement of the 2 m height of the floodplain, we believe that the lower limit of the age of the floodplain is no earlier than 1700 years BP. As recorded, the earliest earthquake recorded in the Xichang area is the Xichang 111 BC earthquake (Xichang City Chronicle Compilation Committee of Sichuan Province, 1996). In the absence of omissions, there is only one earthquake with a magnitude of M ≥ 6 since then, that is, the 624 AD earthquake. Apparently, the 624 AD earthquake alone bore the 13 m displacement of the Heishui River floodplain. In addition, it is further confirmed that the macro-epicenter of this earthquake is at this coseismic displacement location. Furthermore, according to the functional relationship between the maximum coseismic displacement and the moment magnitude of Wells and Coppersmith (1994),

$$Mw = 6.81 + 0.78 * \log(MD) \quad (1)$$

Where the MD refers to maximum displacement (m); the moment magnitude of the 624 AD earthquake is calculated to be about 7.7.

Similarly, the functional relationship between the maximum coseismic displacement and the surface wave magnitude of Bonilla et al. (1984),

$$Ms = 7 + 0.78 * \log(MD) \quad (2)$$

Where the MD also refers to maximum displacement (m), giving a result of Ms7.9. As we discussed above, the 624 AD earthquake should have occurred in valley areas south of Xichang, and near Qiaojia. This transforms the Qiaojia area from a historical seismic gap to a potential seismic area.

For the eastern margin of the Tibetan Plateau, M6.5 may represent the magnitude threshold of the surface rupture along the active faults in the region (Xu et al., 2017). Earthquakes with a magnitude less than this threshold generally do not have surface ruptures, and occasionally have secondary surface fractures (Wells and Coppersmith, 1994). Earthquakes with a magnitude greater than or equal to this threshold can form several kilometers to one hundred kilometers of coseismic surface rupture and several meters of coseismic displacement, which directly controls the spatial distribution

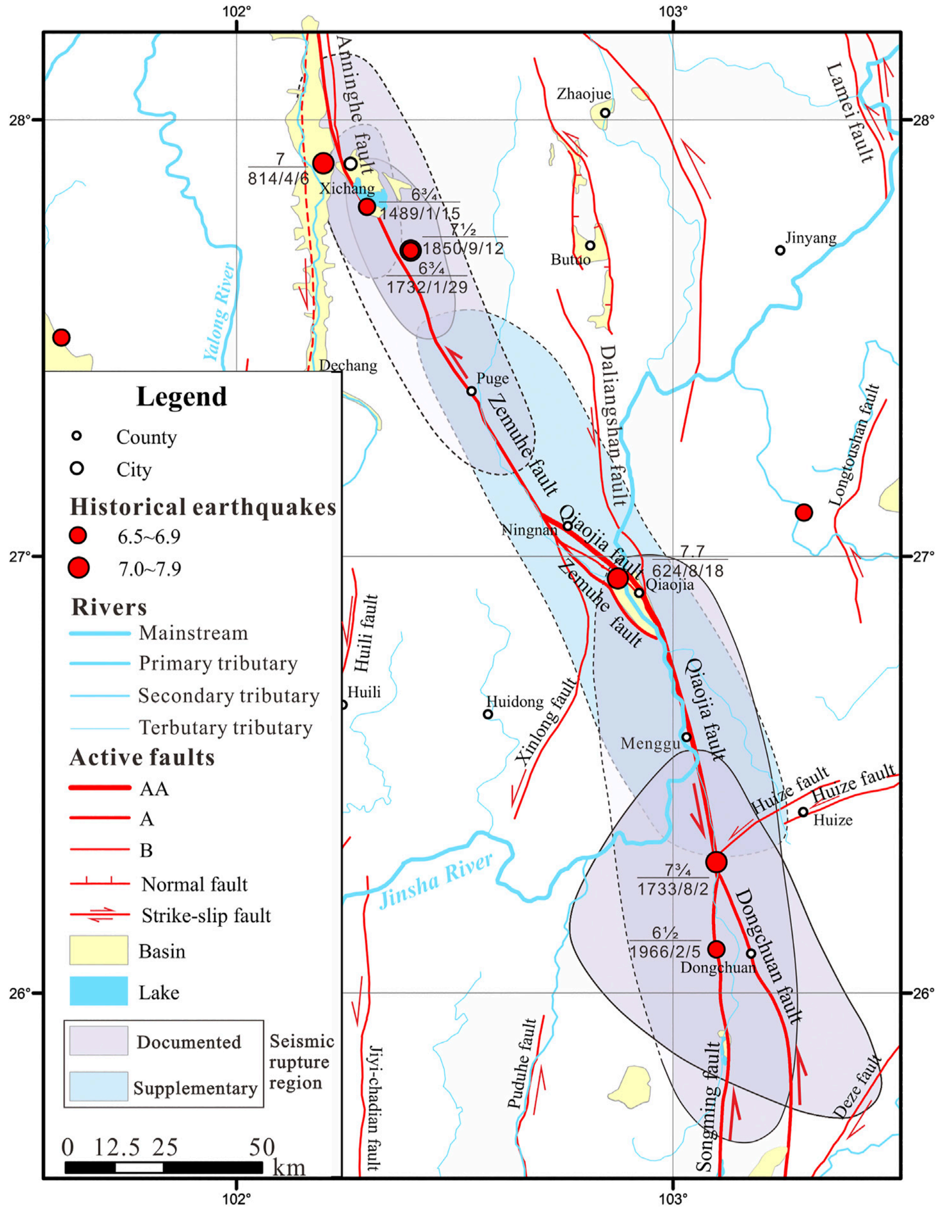

FIGURE 13 | Rupture areas with intensity ≥ IX for the historical earthquakes from Xichang to Dongchuan. The dashed circle indicates the area not verified in the field. For the active faults, AA, A, and B indicate their activity of extremely strong, strong, and medium.

of the serious earthquake disaster zone in the Meizoseismal area. Therefore, the distribution of seismic gaps on a fault can be seen directly by statistical analysis of the historical earthquakes with magnitudes ≥ 6.5 and delineation of their rupture areas with intensity ≥ IX. Based on this, the authors reorganized the historical earthquakes with intensity ≥ IX from Xichang to Dongchuan that involves the Anninghe Fault, the Zemuhe Fault, and the Xiaojiang Fault, from north to south (**Table 5**). Apart from the 624 AD and 814 AD earthquakes, the rupture areas of other historical earthquakes are all referred to in historical data or previous studies. It should be noted that the rupture area of the 1489 AD earthquake is the same as the focal area of the $6^3/_4$-magnitude earthquake (Wen, 2000), and the VIII area was adopted as the rupture area of the 1952 earthquake. Furthermore, according to the regression of surface rupture length and displacement (Wells and Coppersmith, 1994),

$$\text{Log}(\text{SRL}) = 1.49 + 0.64 * \log(\text{MD}) \quad (3)$$

The long axis of the rupture area of the 624 AD earthquake was calculated to be158 km based on the 13 m displacement of the Heishui River floodplain (**Figure 13**).

No M ≥ 7 earthquakes have occurred on Qiaojia Segment for the nearly 1,400 years since 624 AD. Such a long elapsed time is close to the average recurrence interval of large earthquakes on the segment around Dongchuan (1,447 ± 822 years) as estimated by Shen et al. (1998). In addition, the late Quaternary strike-slip rate of the Qiaojia Segment is 8.5 ± 1.5 mm/yr, therefore, the strain accumulated since about 1,400 yrs could occur an earthquake with a comparable magnitude. Apparently, the seismic hazard of the Qiaojia area should be considered in the future.

CONCLUSION

Based on the field investigation, the use of high-resolution topographic data, and the OSL and ^{14}C methods, we can conclude:

In 624 AD, a nearly 2 km long failed slope collapse occurred on the west bank of the Qiaojia reach of the Jinsha River, resulting in a temporary dammed lake. This failed slope collapse is suspected to be seismic origin, with several evidences support, including: The landslide is located in the seismic region, its large size with cluster form, the instability of the source area, the limited distribution of landslide mass, and the temporal-coincidence with 624 AD earthquake.

The macro epicenter of the 624 AD earthquake was relocated to Qiaojia, and its magnitude was recalculated to be Mw7.7 or Ms7.9 according to the coseismic displacement of the Heishui River floodplain. Further combining with the rupture regions of other historical earthquakes in the Xichang-Dongchuan area, it is considered that the 624 AD earthquake filled the seismic gap in the Qiaojia area. However, the nearly 1,400 a long-time elapsed time is close to the average recurrence interval of large earthquakes on the Qiaojia Segment. Therefore, the seismic hazard of the Qiaojia area should be considered in the future.

DATA AVAILABILITY STATEMENT

The original contributions presented in the study are included in the article/Supplementary Material, further inquiries can be directed to the corresponding author.

AUTHOR CONTRIBUTIONS

MH designed the study, analyzed the data, and wrote the manuscript; ZW proposed and participated in designing the study, and reviewed the paper; KR participated in designing the study, and reviewed the paper; SA improved and polished the paper; XH and JZ participated in the field investigation. All authors approved the final version of the manuscript.

FUNDING

This research has been funded by the China Geology Survey Projects (Grant Nos. 12120114002101, DD20160268) and the financial grants from the National Natural Scientific Foundation of China (Grant No. U2002211).

ACKNOWLEDGMENTS

The authors are grateful to the editor and three reviewers for their thorough and constructive reviews, which greatly improved the quality of this manuscript. The authors also would like to thank Guanghao Ha for his kind help during the fieldwork. In addition, the first author thanks the China Scholarship Council (CSC) for the scholarship and financial support.

REFERENCES

Adams, J. (1981). Earthquake-dammed lakes in New Zealand. *Geology* 9, 215–219. doi:10.1130/0091-7613(1981)9<215:elinz>2.0.co;2

Bolt, A. B., Horn, L. W., Macdonald, A. G., and Scott, F. R. (1977). *Geological hazards*. New York, NY: Springer-Verlag.

Bonilla, M. G., Mark, R. K., and Lienkaemper, J. J. (1984). Statistical relations among earthquake magnitude, surface rupture length, and surface fault displacement. *Bull. Seismol. Soc. America* 74 (6), 2379–2411.

Burrows, C. J. (1975). A 500-year-old landslide in the Acheron River valley, Canterbury. *N. Z. J. Geology. Geophys.* 18, 357–360. doi:10.1080/00288306.1975.10418206

Chen, F. B., and Zhao, Y. T. (1988). *The neotectonics in the panzhihua-xichang region of China*. Chengdu, China: Sichuan Science and Technology Press.

Chen, Y., Li, S.-H., Sun, J., and Fu, B. (2013). OSL dating of offset streams across the Altyn Tagh Fault: channel deflection, loess deposition and implication for the slip rate. *Tectonophysics* 594, 182–194. doi:10.1016/j.tecto.2013.04.002

Cornforth, D. H. (2005). *Landslides in practice: investigation, analysis, and remedial preventative options in soils*. Chichester, United Kingdom: John Wiley & Sons.

Costa, J. E., and Schuster, R. L. (1988). The formation and failure of natural dams. *Geol. Soc. Am. Bull.* 100, 1054–1068. doi:10.1130/0016-7606(1988)100<1054:tfafon>2.3.co;2

Crozier, M. J. (1992). "Determination of paleoseismicity from landslide," in *Landslides (Glissemnets de terrain)*. Editor D. H. Bell (New Zealand: Balkema), 1173–1180.

Department of Earthquake Damage Prevention, State Seismological Bureau (1995). *Catalog of strong earthquakes in China (23rd century B.C.-1911 A.D)*. Beijing, China: Seismological Press.

Ding, Y. Y., Zhang, X. J., He, Z. X., Hu, D. G., and Wang, C. Q. (2017). River incision behavior response to climate change during the last glacial period. *Geoscience* 31 (2), 394–405. (in Chinese with English abstract).

Evans, S. G., and Clague, J. J. (1994). Recent climatic change and catastrophic geomorphic processes in mountain environments. *Geomorphology* 10, 107–128. doi:10.1016/0169-555x(94)90011-6

Feng, Z., Wu, Z. H., Cao, J. W., Hu, M. M., Ha, G. H., and Kang, H. X. (2019). Engineering geological characteristics of gigantic pre-historic landslide along Qiaojia section of the Xiaojiang fault. *Acta Geosci. Sin.* 40 (4), 629–636. doi:10.3975/cagsb.2019.012401 (in Chinese with English abstract).

Highland, L. M., and Bobrowsky, P. (2008). *The landslide handbook–a guide to understanding landslides*, Reston, Virginia: U.S. Geological Survey Circular. 129.

Huang, D., Yang, D. Y., Lu, F., Li, L. P., Ge, Z. S., Shi, A. C., et al. (2010). Incision rates of the baihetan section of the Jinsha River. *Quat. Sci.* 30 (5), 872–876. (in Chinese with English abstract).

Ji, F. J., Zheng, R. Z., Li, J. P., and Yin, J. H. (2000). Chronological research of geomorphic surface of lower terraces along several major rivers in the east and west of Yunnan province. *Seismol. Geology.* 22 (3), 265–276. (in Chinese with English abstract).

Jibson, R. W. (1996). Use of landslides for paleoseismic analysis. *Eng. Geol.* 43, 291–323. doi:10.1016/s0013-7952(96)00039-7

Jibson, W. R. (2015). "Paleoseismology and landslides," in *Encyclopedia of earthquake engineering*. Editors M. Beer, I. A. Kougioumtzoglou, E. Patelli, and S. K. Au (Heidelberg: Springer).

Jibson, W. R. (2009). "Using landslides for paleoseismic analysis," in *Paleoseismology*. Editor P. J. McCalpin (Cambridge, MA: Academic Press), 565–601.

Johnson, K., Nissen, E., Saripalli, S., Arrowsmith, J. R., McGarey, P., Scharer, K., et al. (2014). Rapid mapping of ultrafine fault zone topography with structure from motion. *Geosphere* 10 (5), 969–986. doi:10.1130/ges01017.1

Keefer, D. K. (1984). Landslides caused by earthquakes. *Geol. Soc. America Bull.* 95, 406–421. doi:10.1130/0016-7606(1984)95<406:lcbe>2.0.co;2

Keefer, D. K. (1994). The importance of earthquake-induced landslides to long-term slope erosion and slope-failure hazards in seismically active regions. *Geomorphology* 10, 265–284. doi:10.1016/0169-555x(94)90021-3

Li, T.-T., Pei, X.-J., Huang, R.-Q., and Jin, L.-D. (2016). The formation and evolution of the Qiaojia pull-Apart Basin, north Xiaojiang fault zone, southwest China. *J. Mt. Sci.* 13, 1096–1106. doi:10.1007/s11629-015-3778-1 (in Chinese with English abstract).

Liu, J., Zeng, L. S., Ding, L., Tapponnier, P., Gaudemer, Y., Wen, L., et al. (2009). Tectonic geomorphology, active tectonics and lower crustal channel flow hypothesis of the southeastern Tibetan Plateau. *Chin. J. Geology.* 44 (4), 1227–1255. (in Chinese with English abstract).

Lou, B. T. (1996). *A comprehensive complication of historic and recent earthquakes disaster status in China*. Beijing, China: Seismological Press.

Lucieer, A., Jong, S. M. D., and Turner, D. (2014). Mapping landslide displacements using structure from motion (SfM) and image correlation of multi-temporal UAV photography. *Prog. Phys. Geogr. Earth Environ.* 38 (1), 97–116. doi:10.1177/0309133313515293

Massey, C., Townsend, D., Rathje, E., Allstadt, K. E., Lukovic, B., Kaneko, Y., et al. (2018). Landslides triggered by the 14 november 2016 Mw 7.8 Kaikōura earthquake, New Zealand. *Bull. Seismol. Soc. America* 108 (3B), 1630–1648. doi:10.1785/0120170305

McCalpin, P. J. (2009). “Application of paleoseismic data to seismic hazard assessment and neotectonic research,” in *Paleoseismology*. Editor P. J. McCalpin (Cambridge, MA: Academic Press), 1–106.

Meunier, P., Hovius, N., and Haines, A. J. (2007). Regional patterns of earthquake-triggered landslides and their relation to ground motion. *Geophys. Res. Lett.* 34, L20408. doi:10.1029/2007GL031337

Nikonov, A. A. (1988). Reconstruction of the main parameters of old large earthquakes in Soviet Central Asia using the paleoseismogeological method. *Tectonophysics* 147, 297–312. doi:10.1016/0040-1951(88)90191-6

Pánek, T. (2015). Recent progress in landslide dating. *Prog. Phys. Geogr. Earth Environ.* 39 (2), 168–198. doi:10.1177/0309133314550671

Parkash, S. (2012). *Training module on comprehensive landslides risk management*. New Delhi, India: National Institute of Disaster Management, 282

Peng, M., and Zhang, L. M. (2011). Breaching parameters of landslide dams. *Landslides* 9 (1), 13–31. doi:10.1007/s10346-011-0271-y

Perrin, N. D., and Hancox, G. T. (1992). “Landslide-dammed lakes in New Zealand - preliminary studies on their distribution, causes and effects,” in *Landslides (Glissements de terrain)*. Editor D. H. Bell (New Zealand: Balkema), 1457–1466.

Shen, J., Wang, Y. P., Song, F. M., and Li, Y. Z. (1998). Relative creep rate and characteristic earthquake recurrence interval–an example from the Xiaojiang Fault Zone in Yunnan, China. *Seismol. Geology.* 20 (4), 328–331. (in Chinese with English abstract).

Snavely, N., Seitz, S. M., and Szeliski, R. (2008). Modeling the world from internet photo collections. *Int. J. Comput. Vis.* 80 (2), 189–210. doi:10.1007/s11263-007-0107-3

Solonenko, V. P. (1977). Landslides and collapses in seismic zones and their prediction. *Bull. Int. Assoc. Eng. Geol.* 15, 4–8. doi:10.1007/bf02592633

Song, X. B., Shi, A. C., Zheng, W. F., and Jin, R. X. (2012). Analysis of slope deformation characteristics and mechanism in left bank of Baihetan Hydropower Station Jinsha River. *Chin. J. Rock Mech. Eng.* 31 (S2), 3533–3538. (in Chinese with English abstract).

Stewart, J., and Wren, J. (2005). “Geotechnical aspects,” in *Consortium of Universities for Research in Earthquake Engineering (CUREE), Engineering guidelines for the assessment and repair of earthquake damage in residential wood frame buildings* (USA: CUREE Publication). No. EDA-06 Version 2005-4.

Tibaldi, A., Ferrari, L., and Pasquarè, G. (1995). Landslides triggered by earthquakes and their relations with faults and mountain slope geometry: an example from Ecuador. *Geomorphology* 11, 215–226. doi:10.1016/0169-555x(94)00060-5

Varnes, D. J. (1978). “Slope movement types and processes,” in *Landslides, analysis and control, transportation research board, special report no. 176*. Editors R. L. Schuster and R. J. Krizek (Washington DC: National Academy of Sciences), 11–33.

Wang, Z. H. (1996). Remote sensing investigation for a huge landslide—Qiaojia county landslide. *Remote sensing Environ. China* 11 (4), 280–284. (in Chinese with English abstract).

Wei, W. X., Jiang, Z. S., Wu, Y. Q., Liu, X. X., Zhao, J., Li, Q., et al. (2012). Study on motion characteristics and strain accumulation of the Xiaojiang Fault Zone. *J. Geodesy Geodynamics* 32 (2), 11–15. (in Chinese with English abstract).

Wells, D. L., and Coppersmith, K. J. (1994). New empirical relationships among magnitude, rupture length, rupture width, rupture area, and surface displacement. *Bull. Seismol. Soc. America* 84 (4), 974–1002.

Wen, X., Du, F., Long, F., Fan, J., and Zhu, H. (2011). Tectonic dynamics and correlation of major earthquake sequences of the Xiaojiang and Qujiang-Shiping fault systems, Yunnan, China. *Sci. China Earth Sci.* 54 (10), 1563–1575. doi:10.1007/s11430-011-4231-0

Wen, X. Z. (2000). The character of rupture segmentation of the Xianshuihe-Anninghe-Zemuhe Fault Zone, western Sichuan. *Seismol. Geology.* 22 (3), 239–249. (in Chinese with English abstract).

Westoby, M. J., Brasington, J., Glasser, N. F., Hambrey, M. J., and Reynolds, J. M. (2012). ’Structure-from-Motion’ photogrammetry: a low-cost, effective tool for geoscience applications. *Geomorphology* 179, 300–314. doi:10.1016/j.geomorph.2012.08.021

Wu, Z. H., and Zhou, C. J. (2018). *Distribution map of active faults in China and its adjacent seas (1:5,000,000) and its specification*. Beijing, China: Geological Publishing House.

Xichang City Chronicle Compilation Committee of Sichuan Province (1996). *Xichang chronicles*. Chengdu, China: Sichuan Renmin Press.

Xu, X. W., Wu, X. Y., Yu, G. H., Tan, X. B., and Li, K. (2017). Seismo-Geological signatures for identifying M≥7.0 earthquake risk area and their premilimary application in mainland China. *Seismol. Geology.* 39 (2), 219–275. (in Chinese with English abstract).

Xu, Z. M., Zhao, W. L., and Huang, R. Q. (2011). Engineering geological characteristics of Zhaizicun giant ancient landslide along Jinsha River and its occurrence mechanisms. *Chin. J. Rock Mech. Eng.* (S2), 3539–3550. (in Chinese with English abstract).

Zeng, Q. L., Yuan, G. X., McSaveney, M., Ma, F. S., Wei, R. Q., Liao, L. Y., et al. (2020). Timing and seismic origin of Nixu rock avalanche in southern Tibet and its implications on Nimu active fault. *Eng. Geology.* 268, 1–14. doi:10.1016/j.enggeo.2020.105522

Zhang, J. M., Xu, Z. M., Li, Q. K., Zhang, W. F., and Fu, B. (2012). New findings of ancient landslide and geological tectonics constraints along the Jinsha River near Zhaizicun, Yongsheng, Yunnan, China. *J. Jinlin Univ. (Earth Sci. Edition)* 42 (S3), 206–213. (in Chinese with English abstract).

Zhang, K. Q., Wu, Z. H., Lv, T. Y., and Feng, H. (2015). Review and progress of OSL dating. *Geol. Bull. China* 34 (1), 183–203. (in Chinese with English abstract).

Zhang, X., Wang, Y. S., and Liang, R. F. (2018). Assessment of landslide hazard in the middle and northern Xiaojiang Fault Zone based on GIS. *Geology. Exploration* 54 (3), 623–633. (in Chinese with English abstract).

Zhang, Y. S., Guo, C. B., and Zhou, N. J. (2013). Characteristics of Chongjianghe landslide at a branch of Jinsha River and its local reactivation mechanism. *Chin. J. Geotechnical Eng.* 35 (3), 445–453. (in Chinese with English abstract).

Zhao, C., Kang, Y., Zhang, Q., Lu, Z., and Li, B. (2018). Landslide identification and monitoring along the Jinsha River catchment (Wudongde reservoir area), China, using the InSAR method. *Rem. Sens.* 10, 1–20. doi:10.3390/rs10070993

Zhao, J., Jiang, Z. S., Niu, A. F., Liu, J., Wu, Y. Q., Wei, W. X., et al. (2015). Study on dynamic characteristics of fault locking and fault slip deficit in the eastern boundary of the Sichuan-Yunnan rhombic block. *Chin. J. Geophys.* 58 (3), 872–885. (in Chinese with English abstract).

Conflict of Interest: The authors declare that the research was conducted in the absence of any commercial or financial relationships that could be construed as a potential conflict of interest.

frontiers in Earth Science

ORIGINAL RESEARCH
published: 12 April 2021
doi: 10.3389/feart.2021.609896

A One-Class-Classifier-Based Negative Data Generation Method for Rapid Earthquake-Induced Landslide Susceptibility Mapping

Shuai Chen[1], Zelang Miao[1]*, Lixin Wu[1], Anshu Zhang[2], Qirong Li[1] and Yueguang He[3]

[1]School of Geoscience and Info-Physics, Central South University, Changsha, China, [2]Department of Land Surveying and Geo-Informatics, The Hong Kong Polytechnic University, Kowloon, Hong Kong, [3]School of Traffic and Transportation Engineering, Changsha University of Science and Technology, Changsha, China

OPEN ACCESS

Edited by:
Tolga Gorum,
Istanbul Technical University,
Turkey

Reviewed by:
Jie Dou,
Nagaoka University of Technology,
Japan
Aykut Akgün,
Karadeniz Technical University,
Turkey

***Correspondence:**
Zelang Miao
zelang.miao@csu.edu.cn

Specialty section:
This article was submitted to Environmental Informatics and Remote Sensing,
a section of the journal
Frontiers in Earth Science

Received: *25 September 2020*
Accepted: *10 February 2021*
Published: *12 April 2021*

Citation:
Chen S, Miao Z, Wu L, Zhang A, Li Q and He Y (2021) A One-Class-Classifier-Based Negative Data Generation Method for Rapid Earthquake-Induced Landslide Susceptibility Mapping.
Front. Earth Sci. 9:609896.
doi: 10.3389/feart.2021.609896

Machine learning with extensively labeled training samples (e.g., positive and negative data) has received much attention in terms of addressing earthquake-induced landslide susceptibility mapping (LSM). However, the extensive amount of labeled training data required by machine learning, particularly the precise negative data (i.e., non-landslide area), cannot be easily and efficiently collected. To address this issue, this study presents a one-class-classifier-based negative data generation method for rapid earthquake-induced LSM. First, an incomplete landslide inventory (i.e., positive data) was produced with the aid of change detection using before-and-after satellite images and the Geographic Information System (GIS). Second, a one-class classifier was utilized to compute the probability of landslide occurrence based on the incomplete landslide inventory followed by the negative data generation from the low landslide susceptibility areas. Third, the positive data as well as the generated negative data (i.e., non-landslide) were compounded to train a traditional binary classifier to produce the final LSM. Experimental results suggest that the proposed method is capable of achieving a result that is comparable to methods using the complete landslide inventory, and it displays good correspondence with recent landslide events, making it a suitable method for rapid earthquake-induced LSM. The findings in this study would be useful in regional disaster planning and risk reduction.

Keywords: earthquake-induced landslide, landslide susceptibility mapping, one class classifier, incomplete landslide inventory, negative data

1 INTRODUCTION

Many mountainous areas in the world, such as southwest China, are prone to seismic events and, consequently, landslides (Fan et al., 2018; Cao et al., 2019). Seismic landslides are widely distributed and of large scales, and the damage they cause is often great. In addition, large earthquakes may change the local geological structure and create unstable slopes that may slide in the future (Huang and Li, 2014; Yunus et al., 2020). For instance, after the Wenchuan Mw 7.9 earthquake and Jiuzhaigou Mw 6.5 earthquake, many landslides occurred and brought about extensive damages to southwest China (Gorum et al., 2011; Fan et al., 2018). Therefore, timely monitoring of landslide susceptibility after the earthquake is very critical for post-earthquake rehabilitation and reconstruction as well as early disaster monitoring and prevention (Guzzetti et al., 2006).

Multiple methods have been designed for landslide susceptibility mapping (LSM). Field surveys are utilized with great frequency due to their high accuracy and robustness. This method, however, depends heavily on expert experience and is time-consuming and labor-intensive, so it is not suitable for regional/global LSM (Keefer, 2002). Furthermore, it is challenging for field surveys to map landslide susceptibility at full spatial coverage, particularly for some inaccessible areas. In recent years, automated and/or semi-automated LSM has been developed based on remote sensing technology and the Geographic Information System (GIS), and the methods include the heuristic method (Ruff and Czurda, 2008), deterministic method (Jibson, 1993; Jibson et al., 2000; Tsai et al., 2019), and machine learning method (Reichenbach et al., 2018). By use of the heuristic method, investigators rank and weigh the causative factors based on their importance in causing landslides. The result depends on the investigator's understanding of the real causative factors, which may lead to subjective LSM results (Mandal and Mandal, 2018). The deterministic method employs the simplified and physically-based landslide modeling schemes to analyze the stability using simple limit equilibrium models (e.g., the Newmark model) or more sophisticated approaches. The accuracy of this method depends on the reliability of the geotechnical and hydrological input data (Dreyfus et al., 2013). The machine learning method comprehensively considers the correlation between landslide distribution and regional geological environment and thus obtains reliable landslide susceptibility map (Reichenbach et al., 2018). It also has the widest application in LSM among the three methods (Pourghasemi et al., 2018).

A complete and accurate coseismic landslide inventory map (LIM) is an important prerequisite for landslide susceptibility analysis. An ideal coseismic LIM would cover the entire earthquake-affected area, accurately locate all the landslides triggered by the earthquake, and depict the true shapes of landslides in the form of a vector polygon (Harp et al., 2011). The landslide distribution information from such inventories can then be used for the seismic landslide susceptibility analysis and other quantitative analyses (Tanyaş et al., 2017). However, it is difficult or even impossible to obtain a detailed and complete landslide inventory after an earthquake. On the one hand, due to the cloudy and rainy weather, the available optical images are limited and do not have sufficient spatial coverage for the whole earthquake area. On the other hand, a large earthquake often induces many landslides, which are widely distributed and often deeply seated. Existing technology thus faces challenges to mapping all these landslides quickly in the short time following the earthquake.

Besides the detailed LIM, massive labeled training data are also important for the machine learning methods. Most statistical learning methods for predicting landslide-prone distribution depend on data sets with both positive (landslide presence) and negative (landslide absence) data (Conoscenti et al., 2016). The positive data are relatively fixed and are mainly selected from the landslide body cells in the inventory. The negative data are usually uncertain and are randomly selected as individual pixels outside of the landslide body. Then, the LSM can be established using the machine learning models trained on both positive and negative data. To improve the LSM reliability, efforts have been made to optimize the selection strategy of negative data. First, we randomly select negative data from the non-landslide area or the area with a certain distance from the landslide body (Su et al., 2017). This is the most commonly used method for generating negative data, but it requires a complete LIM that covers all landslides. Besides, the earthquake changes the local geological structure, resulting in a lot of shatter mountains or unstable slopes, which still belong to the non-landslide area in LIM but are unsuitable to serve as the negative data. Secondly, we convert positive data into negative data by changing the feature space attribute information. The most representative method of this type is the target space exteriorization sampling (TSES) (Xiao et al., 2010). Since the negative data constructed by this method are from the feature space and the corresponding location cannot be found in the real world, it is difficult to conduct field verification. In addition, this method also requires a complete LIM. Lastly, generate the negative data by clustering analysis. This method clusters the data sets into multiple categories based on feature similarities and automatically generates negative data in the category that contains the fewest landslides. The commonly used clustering methods include the self-organizing map (SOM) (Huang et al., 2017) and similarity-based sampling (SBS) Zhu et al. (2019). Since this method is based on feature similarity, a complete LIM is still required to reflect the true feature space of seismic landslides.

All these negative data generation methods require a complete LIM, which is very difficult to obtain in a short time. It is easy to establish an incomplete LIM using remote sensing and GIS technologies. Thus, if the incomplete LIM can be used for generating reliable negative data, rapid LSM after the earthquake is possible. However, there are only a few studies on the LSM based on incomplete LIM, and this is due to the uncertainty in the generation of negative data (Chen et al., 2020). Therefore, efforts should be made on the generation of negative data based on incomplete LIM.

Based on the aforementioned analysis, this study presents a one-class-classifier-based negative data generation method for earthquake-induced LSM. Using the proposed method, we calculate the landslide susceptibility based on the incomplete LIM, and then automatically generate pseudo labeling of negative data from areas with low landslide susceptibility. After that, the generated negative data and the positive data (i.e., the incomplete LIM) are applied to train the traditional binary classifier to produce the final landslide susceptibility map. **Figure 1** shows the flowchart of the presented method. The left of this study is organized as follows. **Section 2** presents the study area and materials used in this study. **Section 3** introduces the proposed one-class-classifier-based negative data generation method for earthquake-induced LSM. **Section 4** presents the experimental results and discussions, and **Section 5** draws some conclusions.

2 STUDY AREA AND MATERIALS

Wenchuan, situated in Sichuan province, southwest China, has complex terrains and is the site of much intense neotectonic

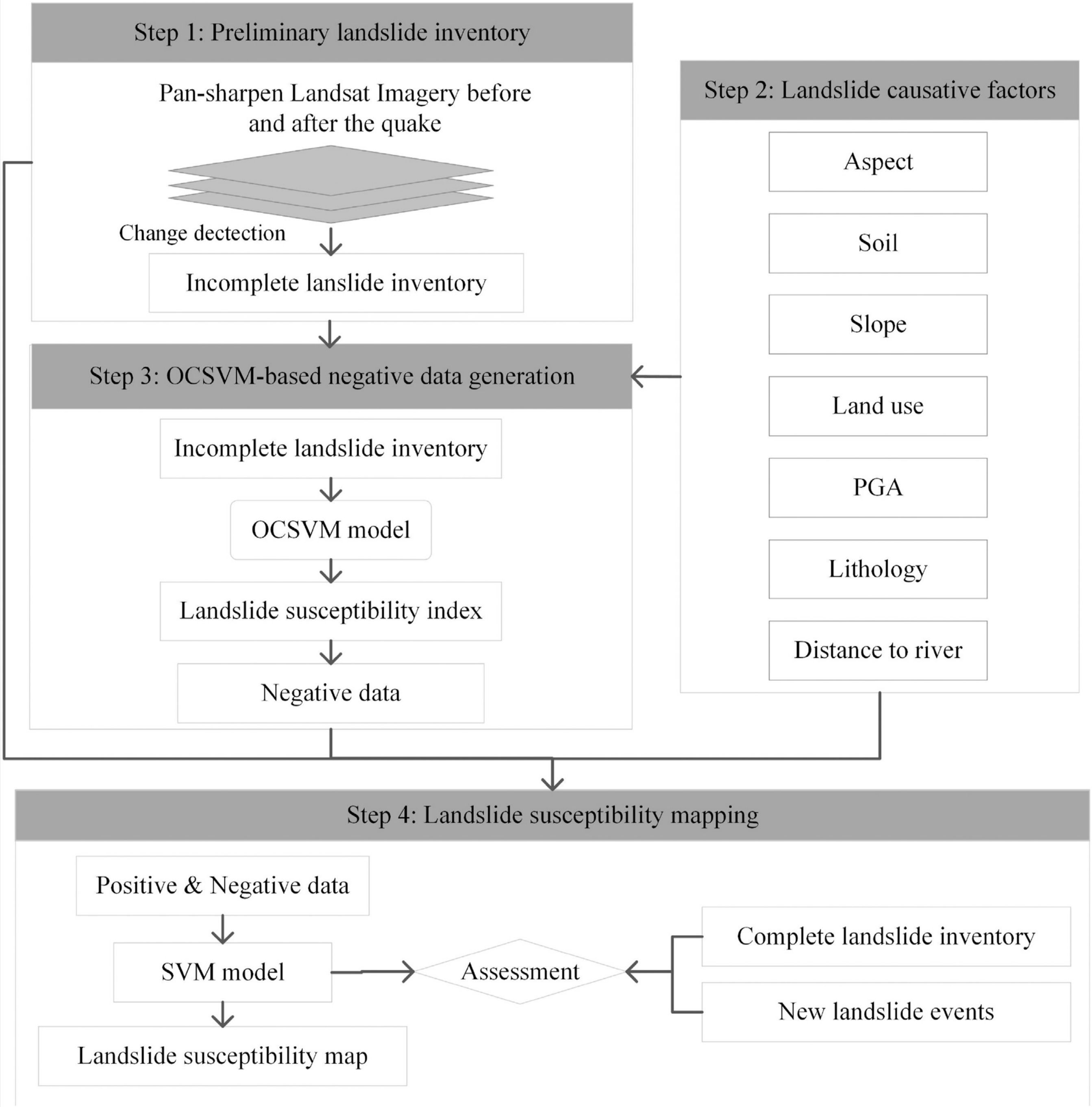

FIGURE 1 | Flowchart of the presented method.

activity. The region features high ridges, lofty mountains, and crisscrossing gorges and valleys. The elevation fluctuates greatly from 782 m to 5,896 m. The neotectonic activities in this area are intense, and the Longmenshan thrust belt, which is composed of three main faults, namely, the Yingxiu-Beichuan fault, Guanxian-Anxian fault, and Mao-wen fault, runs across the whole of Wenchuan. Among them, the Yingxiu-Beichuan fault is inferred as the main structure of the 2008 earthquake (Li et al., 2008). The complex terrain and intense structure make this region a area prone to seismic and geological disasters (Wu et al., 2020). For instance, the 2008 Wenchuan Mw7.9 earthquake occurred in this region and induced a large number of coseismic landslides, see **Figure 2**.

The data sources used in this study include pre- and post-earthquake Landsat 7 satellite images (acquisition dates: April 22, 2008, and May 25, 2008), a digital elevation model (DEM), river,

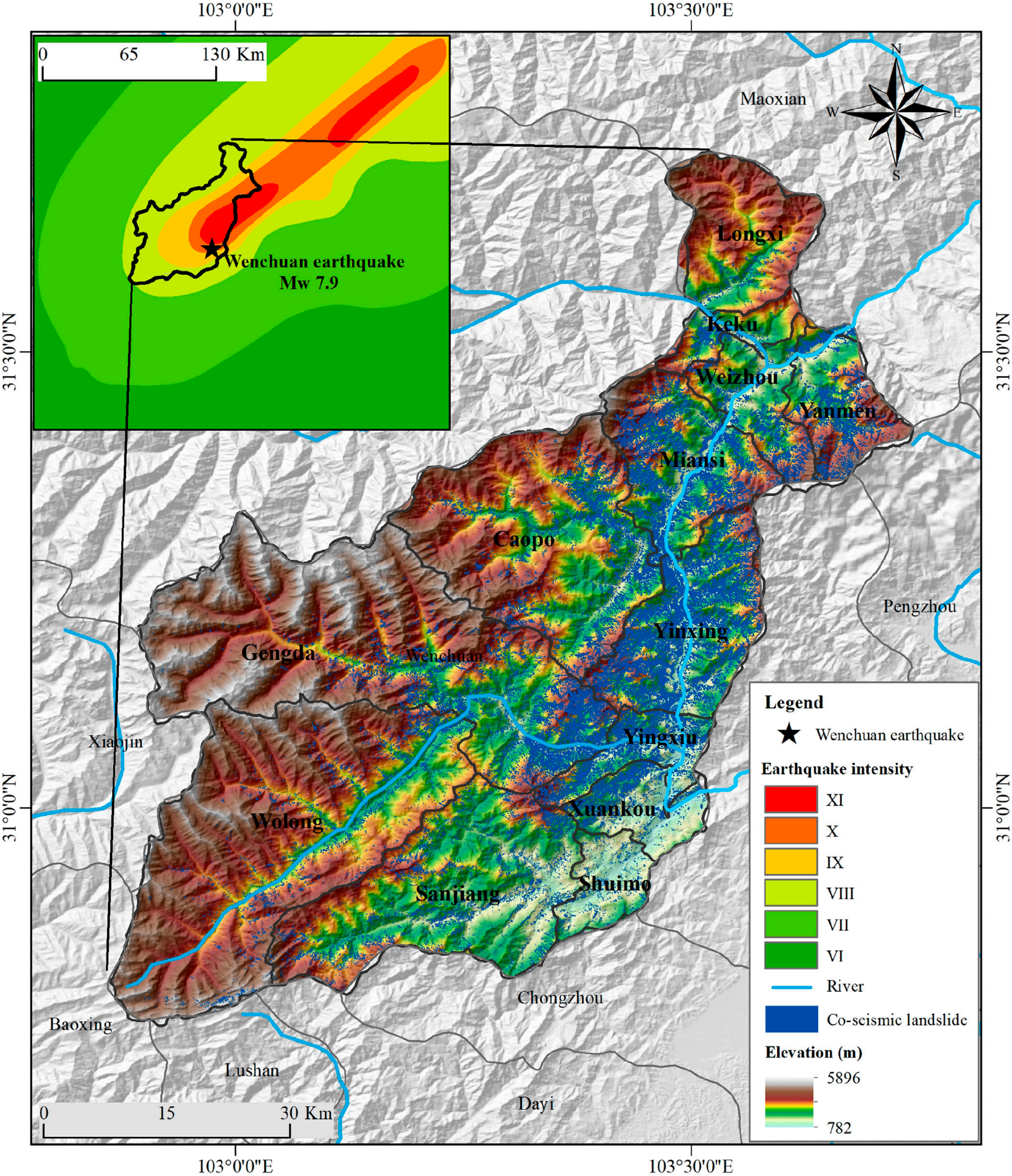

FIGURE 2 | Distribution of coseismic landslides induced by the 2008 Wenchuan earthquake.

TABLE 1 | Data sources used in this study.

Data	Resolution	Application	Data source
Landsat 7	Panchromatic: 15 m; Multispectral: 30 m	Co-seismic landslide	https://earthexplorer.usgs.gov/
DEM	30 m	Causative factor	https://gdex.cr.usgs.gov/gdex/
River	Vector	Causative factor	https://www.webmap.cn/
Lithology	1:200,000	Causative factor	http://geocloud.cgs.gov.cn/
Land use	30 m	Causative factor	http://www.resdc.cn/data.aspx/
Soil	30 m	Causative factor	http://www.resdc.cn/data.aspx/
PGA	Vector	Inducing factor	https://earthexplorer.usgs.gov/
Complete LIM	Vector	Evaluation	https://earthquake.usgs.gov/earthquakes/

lithology, land use, soil, peak ground acceleration (PGA), and the complete LIM (see **Table 1**). The slope and aspect were derived from the DEM. The complete LIM was produced by the integration of field survey and rigorous analysis of very-high-resolution satellite images acquired by multiple platforms/sensors (e.g., aerial photo, IKONOS, and QuickBird) (Xu et al., 2014). The post-earthquake images used for the complete landslide inventory ranged from May 23, 2008, to June 13, 2008. The acquisition date of images used for two landslide inventories have a substantial overlap, which compresses the influence of the area and spatial distribution differences of landslides caused by time.

3 METHODOLOGY

3.1 Data Preparation

3.1.1 Acquisition of the Incomplete LIM Through Change Detection

This study compares satellite images before and after the earthquake to extract the landslides by change detection. To reduce the influence of terrain, atmosphere, and sensors, these images are preprocessed through radiation correction, atmospheric correction, orthographic correction, image registration, and a cloud mask. As the landslides will cause surface damage, especially vegetation damage, the normalized difference vegetation index (NDVI) (Ramos-Bernal et al., 2018), sensitive to vegetation change, is adopted as the main feature for change detection. Finally, the change area is separated from the background by the image difference method (Fung, 1990) in which the threshold is determined by **Eq. 3** (Lv et al., 2018).

$$NDVI = \frac{(NIR - R)}{(NIR + R)} \tag{1}$$

$$I_{diff} = \left| NDVI_{post} - NDVI_{pre} \right| \tag{2}$$

$$X_{I_{diff}} = \begin{cases} \text{landslide} & \text{if} \quad I_{diff} > m + k*\sigma \\ \text{background} & n = x + 2y \end{cases} \tag{3}$$

where m and σ are the mean value and standard deviation corresponding to I_{diff}, respectively. k is an adjustable parameter, and we determine the value of k in this study by trial-and-error method and get $k = 1.5$. After we remove the interference of pseudo-change information by morphology operation and manual interaction, the co-seismic LIM is finally obtained.

Figure 3 shows the coseismic LIM obtained from multi-temporal Landsat images. This inventory contains most medium-large landslides but fails to detect landslides in cloudy areas. Besides, limited by the image resolution, this inventory does not include small landslides with an area less than 5,000 m^2. A complete LIM (Xu et al., 2014) was taken as the ground truth to validate the extracted LIM. The completeness of the landslide extraction results is determined by the ratio of the area of the correctly extracted landslides to that of the real coseismic landslides. Specifically, the correctly extracted landslide in this study is 159.46 km^2, and the real coseismic landslide is 359.6 km^2, so the completeness of the result is 49%, which is far less than the real coseismic landslide. Therefore, the established landslide inventory is an incomplete LIM.

3.1.2 Slope Unit Generation

Mapping units, fundamental to LSM (Van Den Eeckhaut et al., 2009; Erener and Düzgün, 2012), include the pixel unit, slope unit (SU), watershed, unique condition unit, and terrain unit (Reichenbach et al., 2018). The pixel unit and slope unit are more widely used than the other three types. The pixel unit is a regular raster unit and capable of processing the resolution differences of data sources using very simple operations. Despite its popularity, the pixel unit is difficult to work with in complex terrain and struggles to distinguish landslide sources from accumulation areas, impacting the performance of LSM. SU represents a slope or a part of a slope. Landslides are geological hazards that develop on slopes; the number of landslides that occur on a slope reflects the slope stability (Sun et al., 2020). Also, SU suppresses the bias introduced by the incomplete LIM (Reichenbach et al., 2018). Based on its advantages, we chose SU as the mapping unit.

This study applies the hydrological analysis of DEM to extract SUs, including the acquisition of positive and negative DEM, extraction of flow direction and accumulated flow, generation of the river network and watershed, and SU generation (Wang et al., 2017). In this process, the accumulative flow threshold corresponding to the river network is the key to obtaining satisfactory SUs. This study sets the optimal accumulative flow threshold through trial and error. To further improve the accuracy of SUs, we use GIS editing tools to manually adjust the boundaries of SUs and eliminate unqualified SUs. Finally, we get 1,351 SUs, see **Figure 4**.

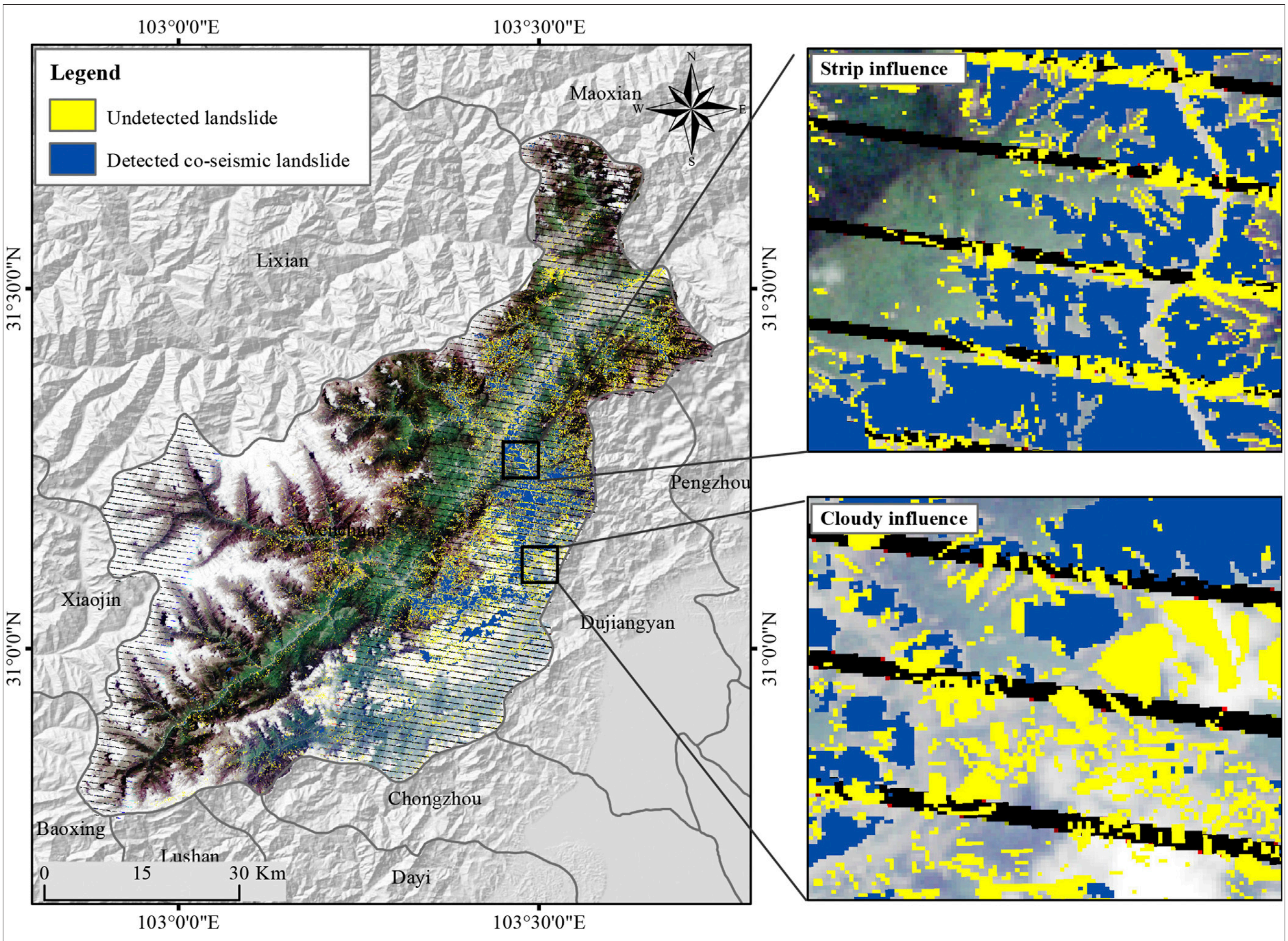

FIGURE 3 | The incomplete LIM extracted from multi-temporal Landsat images.

3.1.3 Selection of Causative Factors

A landslide is controlled by a series of causative factors (Pradhan and Lee, 2010), and thus accurately identifying the causative factors is critical for reliable LSM. Through analysis of the publication from 2005 to 2016 (Pourghasemi et al., 2018), this study selected the seven most widely used causative factors for earthquake-induced LSM in Wenchuan: slope angle, slope aspect, distance to river, lithology, soil, land use, and peak ground acceleration (PGA).

3.1.3.1 Slope Angle

Slope angle is a key factor that determines the failure of a landslide. Generally, slope angles between 30° and 40°are considered to be prone to landslides (Xu et al., 2014), as slope angles in this interval can enhance the shear force and surface water penetration, which provide favorable conditions for landslide occurrence. The slope information of the study area is obtained based on the digital elevation model (DEM), and the spatial analysis tool of ArcGIS is used to calculate the ratio of the maximum elevation difference between adjacent grids to the horizontal distance, which is the slope information of this grid. In this paper, the extracted slope information in the study area was divided into nine categories at an interval of 10°: 1) <10°; 2) 10–20°; 3) 20–30°; 4) 30–40°; 5) 40–50°; 6) 50–60°; 7) 60–70°; 8) 70–80°; and 9) >80°, see **Figure 5A**.

3.1.3.2 Slope Aspect

The slope aspect also affects the distribution of coseismic landslides, as slopes with different aspects carry different seismic effects (Zhou et al., 2016). In addition, there are differences in sunshine and rock weathering in different slope aspects, which leads to obvious differences in coseismic landslides in different slope aspects. For example, the spatial distribution of coseismic landslides in Wenchuan shows that the east, southeast, and south are the dominant slope aspects of seismic landslides [1]. Based on the DEM, this paper uses the spatial analysis tool of GIS to identify the downhill direction with the largest change rate from the current grid to the upper value of its adjacent grid direction, namely, the slope aspect, and divides the slope aspect into nine groups: 1) Flat (-1); 2) N (North, 0–22.5°and 337.5–360°); 3) NE (Northeast, 22.5–67.5°); 4) E (East, 67.5–112.5°); 5) SE (Southeast, 112.5–157.5°); 6) S (South,

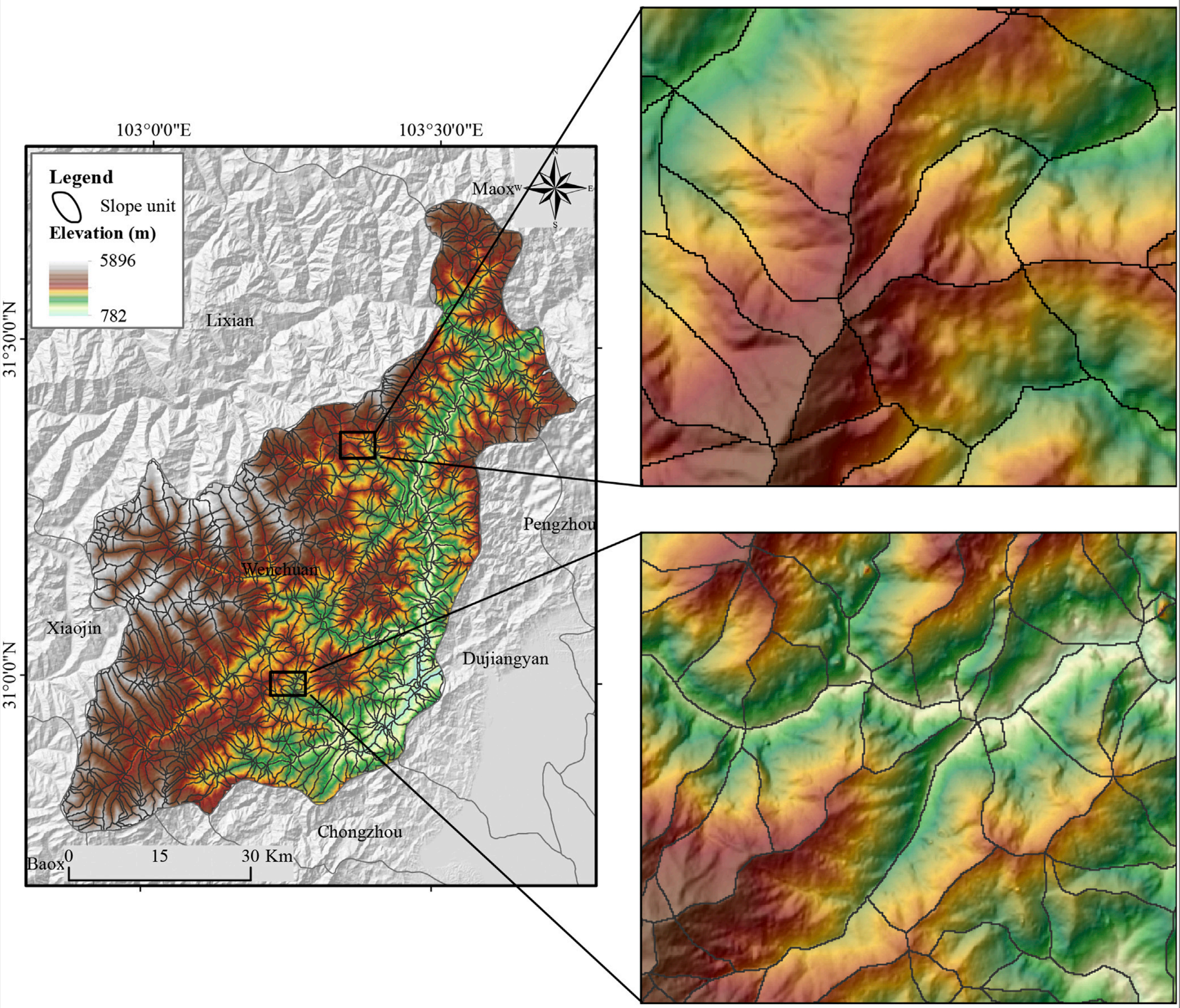

FIGURE 4 | Slope units of the study area.

157.5–202.5°); 7) SW (Southwest, 202.5–247.5°); 8) W (West, 247.5–292.5°); and 9) NW (Northwest, 292.5–337.5°); see **Figure 5B**.

3.1.3.3 Distance to Rivers

The river controls the seismic landslide distribution through the action of groundwater and the erosion of water flow (Kamp et al., 2008). This study considers the distance between slopes and rivers and creates buffers around rivers to analyze the correlation between seismic landslides and their distance to rivers. According to the basic geographic information provided by the National Geographic Information System (NGIS), the initial river network in the study area was extracted. To guarantee the river network quality, we overlayed the initial river network on a cloud-free Landsat-5 mosaic in 2007 of the study area. We deleted parts of the initial river network that did not exhibit rivers on our Landsat mosaic images. Rivers exhibited on Landsat mosaic image but not on the initial river network were added to the initial river network. Finally, we divide the distance to rivers into 10 groups with a step of 2.5 km: 1) 0–2.5 km; 2) 2.5–5 km; 3) 5–7.5 km; 4) 7.5–10 km; 5) 10–12.5 km; 6) 12.5–15 km; 7) 15–17.5 km; (8)17.5–20 km; 9) 20–22.5 km, and (10) >22.5 km see **Figure 5C**.

3.1.3.4 Lithology

The lithology is considered to be another important factor in dealing with landslide susceptibility assessment and hazards (Reichenbach et al., 2018). Lithology influences the topographic character of the landscape and how seismic energy is transmitted, particularly through elastic and

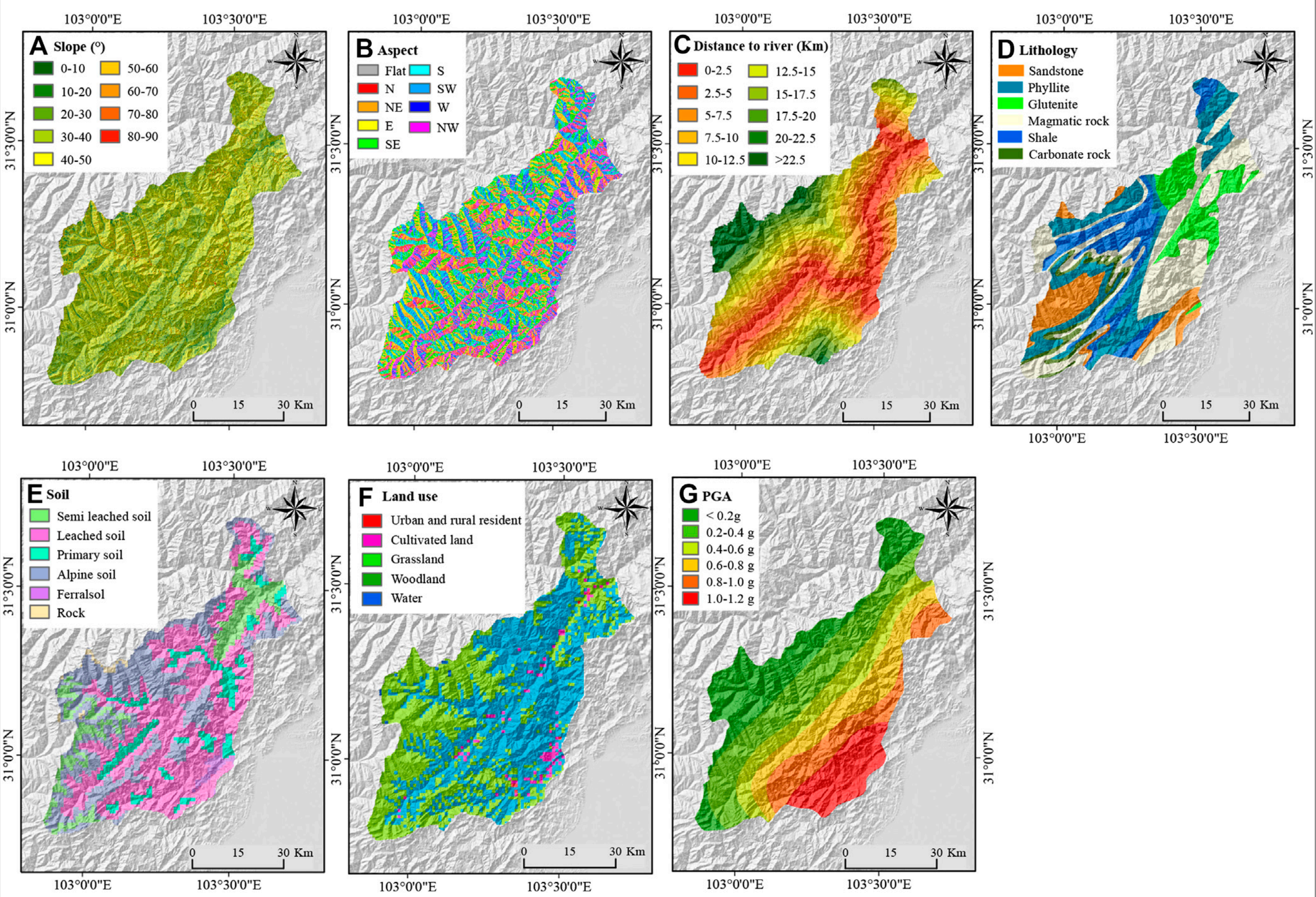

FIGURE 5 | The landslide causative factors used in this study. **(A)** Slope, **(B)** Aspect, **(C)** Distance to river, **(D)** Lithology, **(E)** Soil, **(F)** Land use, **(G)** PGA.

brittle/elastic properties of the rock, chemical weathering and its control of erosion and slope, fracture development and fault displacement, and seismic wave interactions with topography and lithological structures (Kargel et al., 2016). Using rock mass rating containing lithologic factors to conduct landslide hazard assessment is reasonable but, due to lack of enough field and laboratory data, cannot be applied to a large area (Tang et al., 2011). To determine the relative influence of bedrock lithology on the occurrence of landslides in a large area, the sensitivity index of the landslide occurrence of each rock type is calculated by comparing the landslide density in the area occupied by each rock type. In this paper, the relative influence of rock mass is determined by referring to the existing studies on Wenchuan earthquake landslides. The lithology data in the study area was generated by digitizing the hard copies of the 1:200,000 geological maps released by the China Geological Bureau. After that, the digitized lithology data were re-projected to WGS-84 coordinates and rasterized at 30 m resolution. Based on lithological similarities, the rock types were grouped into six classes, including 1) shale; 2) phyllite; 3) sandstone; 4) glutenite; 5) magmatic rock; and 6) carbonate rock, as shown in **Figure 5D**. The existing studies showed that the seismic landslides in hard rock layers, including magmatic rock, carbonate rock, and glutenite, were the most developed and that the development density of shale, phyllite, and sandstone were the second (Huang and Li, 2009; Li et al., 2013).

3.1.3.5 Soil

The composition of the soil determines the permeability of the soil, the better the permeability of the soil, the more conducive it is to flood discharge; generally, sand particles are coarser, as they do not as easily produce runoff or small flow. The permeability of clay is poor; it is easy to erode, and geological disasters are occur with relative ease. For instance, granular, nonplastic, and low plasticity soils are more susceptible than fine soils (Maharaj, 1993). The soil data were generated from 1:1,000,000 soil distribution data in China provided by the data processing center of the Chinese Academy of Sciences. Similar to the vectorization process of the lithology data, the digitized data of soil was re-projected to WGS-84 and re-sampled to 30 m. The study area mainly contains six soil types, including 1) semi-leached soil, 2) leached soil, 3) primary soil, 4) alpine soil, 5) ferralsol, and 6) rock, see **Figure 5E**.

3.1.3.6 Land Use

Human activities have changed the land surface and caused great damage to the natural environment, making it easier for landslides to form alongside earthquake disturbances. Studies have shown that there is a strong correlation between the distribution of landslides and land use. However, obtaining land use data at a specific time is exceedingly difficult. Based on the land use map of 2005 collected from the data processing center of the Chinese Academy of Sciences, the initial land use map of 2007 before the Wenchuan earthquake was obtained by combining supervised classification and visual interpretation with a cloud-free Landsat-5 mosaic image acquired in 2007. Supervised classification consists of three steps: 1) to select training samples for five land-use types by visual interpretation, 2) to train the support vector machine using the training samples and classify the whole Landsat-5 mosaic image, and 3) to repeat the classification steps five times and select the land-use map with the highest accuracy. We compare the classified land use map and the initial land use map to produce the most reliable land use map. The study area mainly includes five land-use types: 1) residential area; 2) cultivated land; 3) grassland; 4) the forest land; and 5) water, see **Figure 5F**.

3.1.3.7 PGA

The strong ground motion that causes short-lived disturbances in the balance of forces within hill slopes is the main reason for slope failure (Li et al., 2013). Strong ground motion directly induces coseismic landslides. PGA is simply the maximum peak acceleration on the acceleration time history curve recorded at a site in the earthquake. It is often used as a parameter to describe strong ground motion (Ma and Xu, 2019). Previous studies have shown that there is a positive correlation between PGA and seismic landslide, and the greater the PGA value, the easier it is to trigger a landslide (Xu et al., 2014). After the Wenchuan earthquake, according to the ground motion peak recorded by the seismic sensor, the United States Geological Survey (USGS) established the PGA map of Wenchuan by interpolation method, field amplification correction, and ground motion attenuation model. In this paper, the latest PGA was download from USGS website, and the study area was divided into six groups, including: 1) <0.2 g, 2) 0.2–0.4 g, 3) 0.4–0.6 g, 4) 0.6–0.8 g, 5) 0.8–1 g, and 6) >1 g, see **Figure 5G**.

3.1.4 Multi-Collinearity Analysis of Landslide Causative Factors

Landslide causative factors have intra-correlations, which increases the data dimension and affects the model reliability. To separate the influence of causative factors, we employ the tolerance and variance inflation factor (VIF) (Chen et al., 2019) to conduct a multicollinearity test. Tolerance and VIF are expressed as follows:

$$Tolerance = 1 - R_j^2 \tag{4}$$

$$VIF = \left[\frac{1}{Tolerance}\right] \tag{5}$$

TABLE 2 | Multicollinearity analysis for the landslide causative factors.

Causative factors	Collinearity statistics	
	Tolerance	VIF
Soil	0.907	1.102
Slope	0.913	1.096
Lithology	0.974	1.027
Land-use	0.787	1.27
Aspect	0.979	1.021
Distance to river	0.821	1.218
PGA	0.722	1.385

where R_j^2 is the regression determination coefficient of landslide causative factors. If the VIF is high, the multi-collinearity influence is serious. This study sets VIF < 10 and tolerance > 0.1 (Chen et al., 2019) as the multi-collinearity threshold. **Table 2** presents the tolerance and VIF values of the seven landslide causative factors. The largest VIF and smallest tolerance are 1.385 and 0.722, respectively. The results suggest that there is no multi-collinearity relationship among the seven landslide causative factors, and thus all these factors are used for LSM.

3.2 Negative Data Generation

Traditionally, negative data are randomly selected from the areas outside the LIM. However, non-landslide areas often contain a large number of unstable slopes, which are not identified in the LIM. Besides, there are also many unrecognized landslides in non-landslide areas. The unstable slopes and unrecognized landslides cannot be used to select negative data. To overcome these shortcomings, this study presents a one-class support vector machine (OCSVM) (Schölkopf et al., 2000) based negative data generation method. The OCSVM maps the samples from low dimension to high dimension space through the kernel function and finds the optimal hyperplane between the origin and the high dimension space. Specifically, the distance between the sample and the hyperplane indicates the correlation between the sample and a specific class. The decision function is defined as the following:

$$f(x) = \operatorname{sign}\big((\omega.\Phi(x)) - \rho\big) \tag{6}$$

where $\Phi(x)$ represents the mapping function, weight ω, and threshold ρ of the support vector are obtained by solving the quadratic programming problem.

$$\min \frac{1}{2}\|\omega\|^2 + \frac{1}{\nu N}\sum_{i=1}^{N}\xi_i - \rho \tag{7}$$

$$\text{s.t.}\ (\omega.\Phi(x_i)) \geqslant \rho - \xi_i\ \xi_i \gg 0$$

where ξ_i is the relaxation variable, and $\nu \in (0,1)$ controls the proportion of support vectors in the training samples. By introducing the kernel function $k(x)$, the above optimization problem is transformed into a dual form:

$$\min_a \frac{1}{2}\sum_{i=1}^{N}\sum_{j=1}^{N} a_i a_j k\left(x_i, x_j\right) \tag{8}$$

$$\text{s.t.} 0 \leqslant a_i \leqslant \frac{1}{vN} \sum_{i=1}^{N} a_i = 1$$

where $\rho = \sum_{i=1}^{N} a_i K(x_i, x_j)$ denotes the threshold value, and weight ω determines the optimal hyperplane. The Gaussian kernel is selected as the kernel function to construct OCSVM that is run with the LIBSVM software package (Chang and Lin, 2011). The optimal hyper-parameters are obtained through five-fold cross-validation.

Selecting negative data from non-landslide areas is a commonly used method for LSM, but its feasibility relies on a complete LIM. By contrast, this study uses an incomplete LIM obtained by change detection to generate negative data. Suppose S represent the data sets of the study area. L_i and L_c represent landslides in the incomplete LIM and in the complete LIM, respectively. $N_i = \overline{L_i} \cap S$ and $N_c = \overline{L_c} \cap S$ represent non-landslides in the incomplete LIM and in the complete LIM, respectively. $N_p = \overline{L_i} \cap \overline{L_c}$ represents the pseudo non-landslide, and N_{OCSVM} denotes the extremely low susceptibility areas in the LSM produced by OCSVM.

To analyze the influence of different negative data generation strategies on LSM, we designed four negative data generation strategies:

1. Negative data T_c are randomly selected from N_c (i.e., $T_c \in N_c$)
2. Negative data T_p are randomly selected from N_p i.e., $T_p \in N_p$)
3. Negative data T_i are randomly selected from N_i (i.e., $T_i \in N_i$)
4. Negative data T_{OCSVM} are randomly selected from N_{OCSVM} (i.e., $T_{OCSVM} \in N_{OCSVM}$)

3.3 LSM

The aforementioned steps produce training samples to train a statistical learning algorithm. The support vector machine (SVM) is a common machine learning algorithm that is capable to build a stable and reliable statistical model with a small number of samples (Suykens and Vandewalle, 1999). Therefore, this study selects SVM to compute the landslide susceptibility values for SUs. The decision function is expressed as follows:

$$y = \sum_{i=1}^{n} \omega_i x_i + b \tag{9}$$

where ω is the support vector weight and b the intercept. To suppress the noise influence, the relaxation variables ξ is introduced, and the corresponding convex quadratic programming of SVM is expressed as follows:

$$\begin{gathered} \min_{\omega,b} \frac{1}{2}\omega^2 + C\sum_{i=1}^{n}\xi_i \\ \text{s.t.} y_i(\omega \cdot x_i + b) \geqslant 1 - \xi_i \\ i = 1, 2, 3, \ldots n \end{gathered} \tag{10}$$

where C represents the penalty coefficient. The optimal hyperplane can be obtained by converting the appeal planning problem into a dual problem that is expressed as follows:

$$\begin{gathered} \min_{a} \frac{1}{2}\sum_{i=1}^{n}\sum_{j=1}^{n} a_i a_j y_i y_j \left(x_i \cdot x_j\right) - \sum_{i=1}^{n} a_i \\ \text{s.t.} \sum_{i=1}^{n} a_i y_i = 0 \\ 0 \leqslant a_i \leqslant C, i = 1, 2, 3, \ldots n \end{gathered} \tag{11}$$

where $(x_i \cdot x_j)$ represents the kernel function that projects samples to high dimensional space to handle complex nonlinear problems. This study chooses the Gaussian kernel as the kernel function, and the optimal hyper-parameters are obtained by the five-cross validation (Hong et al., 2017). This study implements SVM by the LIBSVM package (Chang and Lin, 2011).

3.4 Model Evaluation

The reliability of LSM is mainly determined by the accuracy of the model. But there is no uniform standard to assess the model accuracy. The common method is to use a set of independent data sets for accuracy assessment. Test sets reserved in the early data preparation phase are widely used for model evaluation (Irigaray et al., 2007; Dou et al., 2019). Considering that the data set used in this study is the incomplete LIM, and the actual complete LIM does not participate in the model construction, the complete LIM is taken as the test set for model evaluation.

Receiver operating characteristics (ROC) is an important tool for model evaluation (Swets, 1988). It calculates the true positive rate and false positive rate of the model according to different discriminant standards and draws a curve with the true positive rate and the false positive rate as the x-axis and the y-axis, respectively. The area under the curve (AUC), generally between 0.5-1, is often used to reflect the model performance. The greater the AUC value, the better the model performance will be.

$$\text{TruePositiveRate} = \text{Sensitivity} = \frac{TP}{TP + FN} \tag{12}$$

$$\text{TrueNegativeRate} = \text{Specificity} = \frac{TN}{TN + FP} \tag{13}$$

$$\text{FalsePositiveRate} = 1 - \text{Specificity} = \frac{FP}{TN + FP} \tag{14}$$

where TN, TP, FP, and FN represent true negative, true positive, false positive, and false negative, respectively.

As LSM reflects the landslide occurrence possibility in the earthquake-affected region (Guzzetti et al., 2006), this study counts the number of new landslides that occurred in the hazardous areas to further verify the model performance. To this end, this study collected 11 landslide events that occurred in the study area after 2008 from the website of the China Geological Survey (referred to as new landslides hereafter). The higher number of new landslides in hazardous areas of LSM, the better the model performance will be. In this study, the hazardous areas include areas with extremely high susceptibility, high susceptibility, and moderate susceptibility levels.

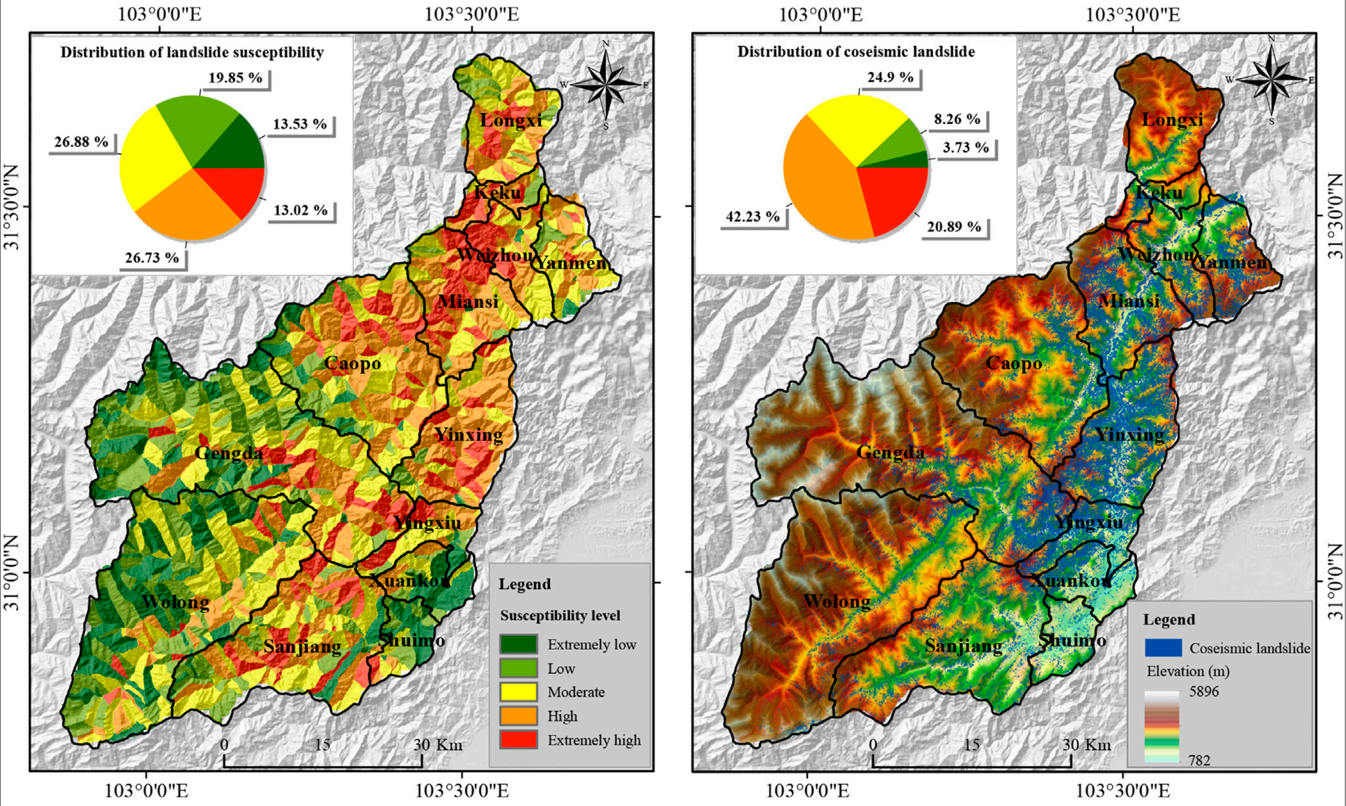

FIGURE 6 | Landslide susceptibility map generated by OCSVM.

4 EXPERIMENTAL RESULTS

4.1 Evaluation of the Reliability of the Negative Data Generation Method Based on OCSVM

Figure 6 shows the LSM derived from OCSVM. It can be seen that 88.02% of the landslides fall into the hazard area (e.g., extremely high susceptibility, high susceptibility, and moderate susceptibility areas). This suggests that OCSVM can obtain a reliable landslide susceptibility map using positive data only. Meanwhile, extremely low susceptibility areas cover 13.53% of the study area and share 3.73% landslides. In other words, landslides rarely occur in extremely low susceptibility areas derived from OCSVM, which in turn guarantees the quality of the generated labeled negative data sets.

4.2 Accuracy Assessment of LSMs Derived From Different Strategies

Figure 7 shows the landslide susceptibility maps produced by SVM based on different training sample sets. The hazard area percentages of four methods ranges from 46.70% to 60.39%. The generated LSM maps show apparent differences in the spatial distribution of susceptibility area. As both the machine learning algorithm and the positive data are fixed, this difference comes from negative data generation strategies. This indicates that negative data generation strategy and the LSM performance have a close relationship. To quantitatively evaluate the model performance, **Figure 8** presents ROC curves for four methods. The AUC values derived from ROC curves are 0.8164, 0.7673, 0.7928, and 0.8100, respectively. Among four methods, SVM based on T_c achieves the highest AUC value (i.e., 0.8164), while SVM based on T_p achieved the lowest AUC value (i.e., 0.7673). The AUC value of the presented method is 0.81, which is close to the best performance achieved by T_c. The AUC difference between the presented method and T_c is marginal, suggesting that the presented method based on the incomplete LIM is capable of achieving a comparable performance to that of the traditional method based on the complete LIM. Therefore, the presented method is suitable for rapid earthquake-triggered landslide susceptibility mapping when only the incomplete landslide inventory is efficient and timely in terms of obtaining data after the occurrence of an earthquake.

This study applies the natural break classification to divide the landslide susceptibility into five levels: extremely high, high, moderate, low, and extremely low susceptibility. By overlaying the actual coseismic landslide distribution (i.e., the complete LIM), the areas of different landslide susceptibility levels and corresponding coseismic landslide areas were computed. **Table 3** shows that the evaluation results corresponding to different negative data sets are quite different, and thus the negative

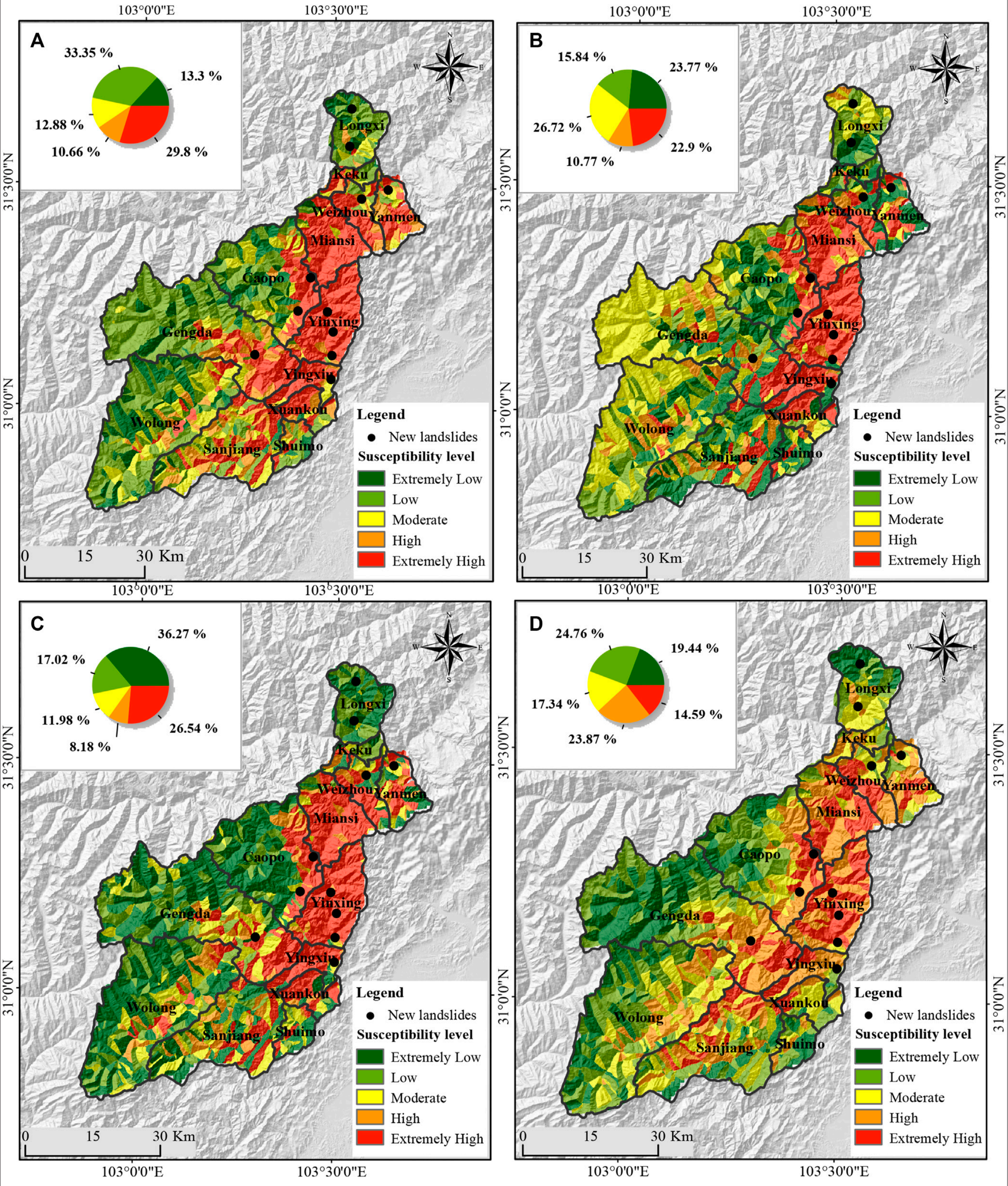

FIGURE 7 | Landslide susceptibility map obtained based on the SVM using different negative data: **(A)** T_c, **(B)** T_p, **(C)** T_i, and **(D)**.T_{OCSVM}

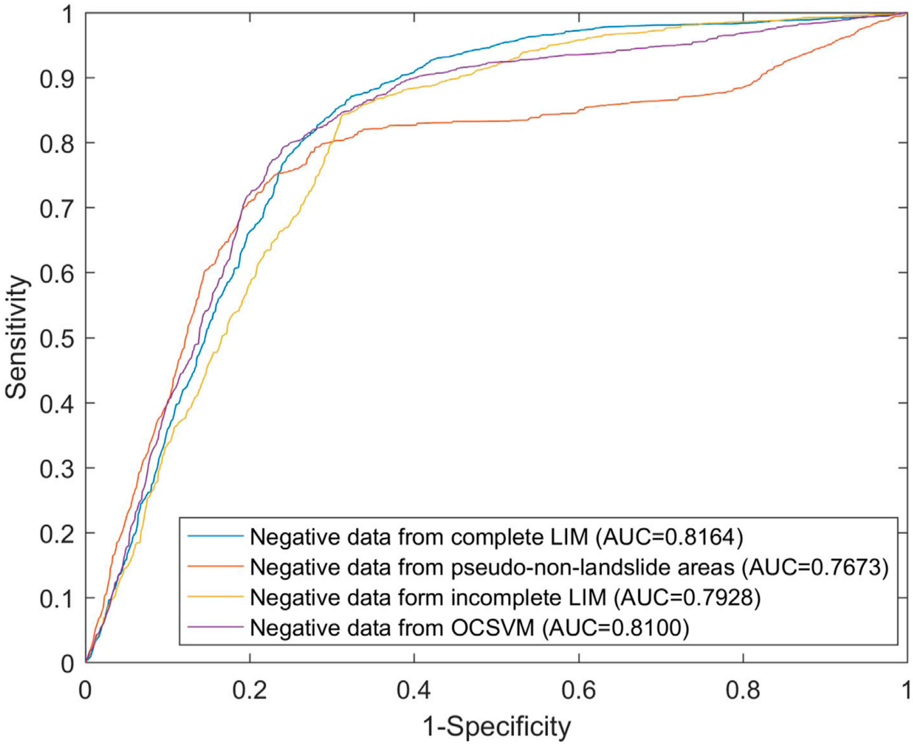

FIGURE 8 | ROC curves of four negative data generation strategies.

TABLE 3 | Landslide susceptibility levels and density of landslides in the study area.

Susceptibility level	Area (km^2)	Percent of area	Area of landslide (km^2)	Percent of landslide	Density
T_c					
Extremely low	536.28	0.13	6.88	0.02	0.01
Low	1,344.24	0.33	18.19	0.05	0.01
Moderate	519.34	0.13	27.66	0.08	0.05
High	429.85	0.11	36.23	0.1	0.08
Extremely high	1,201.32	0.3	267.48	0.75	0.22
T_p					
Extremely low	958.07	0.24	58.03	0.16	0.06
Low	638.49	0.16	14.14	0.04	0.02
Moderate	1,077.06	0.27	18.86	0.05	0.02
High	434.34	0.11	35.81	0.1	0.08
Extremely high	923.08	0.23	229.61	0.64	0.25
T_i					
Extremely low	1,461.92	0.36	31.85	0.09	0.02
Low	686.22	0.17	14.01	0.04	0.02
Moderate	483.12	0.12	27.33	0.08	0.06
High	329.85	0.08	28.27	0.08	0.09
Extremely high	1,069.93	0.27	254.98	0.72	0.24
T_{OCSVM}					
Extremely low	783.83	0.19	8.33	0.02	0.01
Low	998.04	0.25	22.29	0.06	0.02
Moderate	698.86	0.17	34.14	0.1	0.05
High	962.21	0.24	158.87	0.45	0.17
Extremely high	588.1	0.15	132.82	0.37	0.23

TABLE 4 | The percentage of coseismic landslides in the hazardous areas of towns and villages detected by the LSM using different negative data.

Subarea unit	Percent of coseismic landslide (%)	Coseismic landslides distribution			
		T_c	T_p	T_i	T_{OCSVM}
Yinxing	24.85	1.00	0.99	0.98	1.00
Gengda	14.90	0.90	0.73	0.81	0.87
Miansi	14.13	0.96	0.92	0.96	0.97
Caopo	9.12	0.84	0.75	0.8	0.93
Yingxiu	8.24	0.95	0.89	0.94	0.93
Sanjiang	6.56	0.58	0.48	0.39	0.70
Yanmen	6.50	0.96	0.67	0.71	0.87
Weizhou	4.35	0.88	0.66	0.75	0.95
Wolong	4.24	0.45	0.41	0.55	0.44
Xuankou	3.66	0.85	0.75	0.93	0.83
Keku	1.47	0.59	0.25	0.58	0.98
Shuimo	1.18	0.57	0.45	0.50	0.36
Longxi	0.80	0.38	0.03	0.35	0.98

data generation strategy has an essential influence on the performance of LSM. Specifically, for negative data T_c, 93% of the coseismic landslide exists in 54% of the hazardous areas of LSM, which is consistent with the coseismic landslide distribution. However, for negative data T_p, only 80% of the coseismic landslides occurred in 61% of the hazardous area of LSM. This indicates that the model does not evaluate the landslide susceptibility well. The main reason is that the negative data are from the pseudo-stability area, that is, the negative data belong to the unstable area of the study area. Negative data T_i has considerable uncertainty, due to the incomplete LIM and high concealment of potentially unstable slopes, resulting in significant fluctuations in the results. In this study, 87% of the coseismic landslides are distributed in 47% of the hazardous area of LSM. OCSVM can effectively obtain the stable area of the study area, so the influence of the potentially unstable slopes and the incomplete LIM can be well eliminated. Finally, 92% of coseismic landslides occurred in 56% of the hazardous area of LSM, which is higher than that of other negative data sources generated based on incomplete LIM.

To analyze the site scale accuracy of the LSMs generated from different negative data, we took towns and villages as the subarea unit. We calculated the ratio of coseismic landslide to the hazardous areas in each subarea. **Table 4** shows the percentage of the coseismic landslide distributed in the hazardous areas in each subarea. The landslide susceptibility maps show remarkable differences in towns and villages, especially the unrecognized landslide area in the incomplete LIM. Specifically, for the results of T_c, the percentage of the coseismic landslides in the hazardous area of several towns is less than 60%. Especially in Longxi Town, the coseismic landslide distributed in the detected hazardous area is as low as 38%. The results indicate that although the negative data are from the ideal non-landslide area, there are some unstable slopes affecting the accuracy of LSM. For negative data T_p, the distribution of the landslide susceptibility area is inconsistent with that of a coseismic landslide, especially in Longxi Town, where the percentage of a coseismic landslide is only 3%. For T_i, the percentage of coseismic landslides in the detected hazardous areas is less than 60%. In Longxi Town, only 35% of the coseismic landslide are distributed in the detected hazardous areas, and the landslide susceptibility of this area was also not well evaluated. Finally, for the negative data T_{OCSVM}, the model estimated results are consistent with the coseismic landslide distribution for most towns. Only the percentages of two towns are less than 60%. Longxi Town is not covered by the incomplete LIM, but 98% of the coseismic landslides that occurred here are in the detected hazardous area. **Table 4** also shows that T_c, T_i, and T_{OCSVM} achieved the best performance in five, two, and seven administrative districts, respectively. T_p delivered the poorest performance among all subareas, suggesting that T_p is not suitable to train statistical learning algorithms for LSM. The third interesting finding is that T_{OCSVM} achieved a comparable or even better performance to that of T_c in most cases. However, in two subareas (i.e., Keku and Longxi), T_{OCSVM} achieved a substantial improvement compared to T_c. Thus, T_{OCSVM} shows a great advantage in areas with a low percent of coseismic landslides.

We also applied 11 new landslides that occurred after 2008 to further verify the performance of LSM. **Figure 7** shows the superposition of new landslides over the landslide susceptibility maps. We counted the number of new landslides that occurred in the hazardous areas to assess the LSM reliability. **Table 5** shows that 9, 7, 9, and 10 new landslides occurred in the hazardous areas produced by T_c, T_p, T_i, and T_{OCSVM}, respectively. Among four negative data generation strategies, T_{OCSVM} achieves the highest match rate with new landslides while T_p the lowest match rate with new landslides. Therefore, the presented negative data generation strategy can effectively assess the landslide susceptibility in earthquake-affected areas.

4.3 The Influence of One-Class Classifier Selection

To test the influence of one-class classifier (OCC) selection on the performance of LSM, another two benchmark OCCs, including SOM and TSES, are selected to compare with OCSVM. SOM is a kind of autonomic learning neural network without tutors. Its hierarchy consists of an input layer and competition layer (Huang et al., 2017). The input layer accepts external input variables, and the competition layer realizes clustering by analyzing and comparing the input variables. The data of one class have similar features, so the negative data can be generated by cluster analysis. In this study, five classes were selected as the final clustering results. TSES directly generates pseudo negative data based on positive data in feature space (Xiao et al., 2010). It exteriorizes positive data to become negative by replacing the value of one of its features with a new one outside the value range of this feature of all positive data.

We produced LSMs using the SVM based on different negative data sets generated by OCSVM, SOM, and TSES, respectively. The results are referred to as LSM-OCSVM, LSM-SOM, and LSM-TSES, see **Figure 9**. LSM-OCSVM is consistent with the distribution of coseismic landslides, suggesting the proposed OCSVM method gets high accuracy landslide susceptibility in

TABLE 5 | LSM and new landslide events.

New landslides	Lon	Lat	T_c	T_p	T_i	T_{OCSVM}
2009.7.25 (Chediguan bridge)	103.48	31.21	Extremely high	Extremely high	Extremely high	Extremely high
2010.5.30 (Suoqiao village)	103.64	31.49	Moderate	Extremely low	Moderate	Moderate
2010.6.12 (Jinbo village)	103.41	31.22	Extremely high	Extremely high	Extremely high	High
2011.7.3 (Dongjienao village)	103.50	31.12	Extremely high	High	High	High
2011.7.3(Fengxiangshu village)	103.50	31.06	High	Extremely high	Extremely high	Moderate
2011.7.3 (Maojiawang)	103.50	31.17	Extremely high	Extremely high	Extremely high	Extremely high
2013.7.22 (Zuwang village)	103.44	31.29	Extremely high	High	Extremely high	Extremely high
2018.4.8 (Aer village)	103.54	31.67	Low	Low	Extremely low	Extremely low
2018.7.26 (Minjiang bridge)	103.57	31.45	High	High	High	Moderate
2019.8.20 (Longtan village)	103.3	31.12	Moderate	Low	Extremely high	High
2020.6.20 (Kuapo village)	103.54	31.59	Extremely low	Extremely low	Extremely low	Moderate

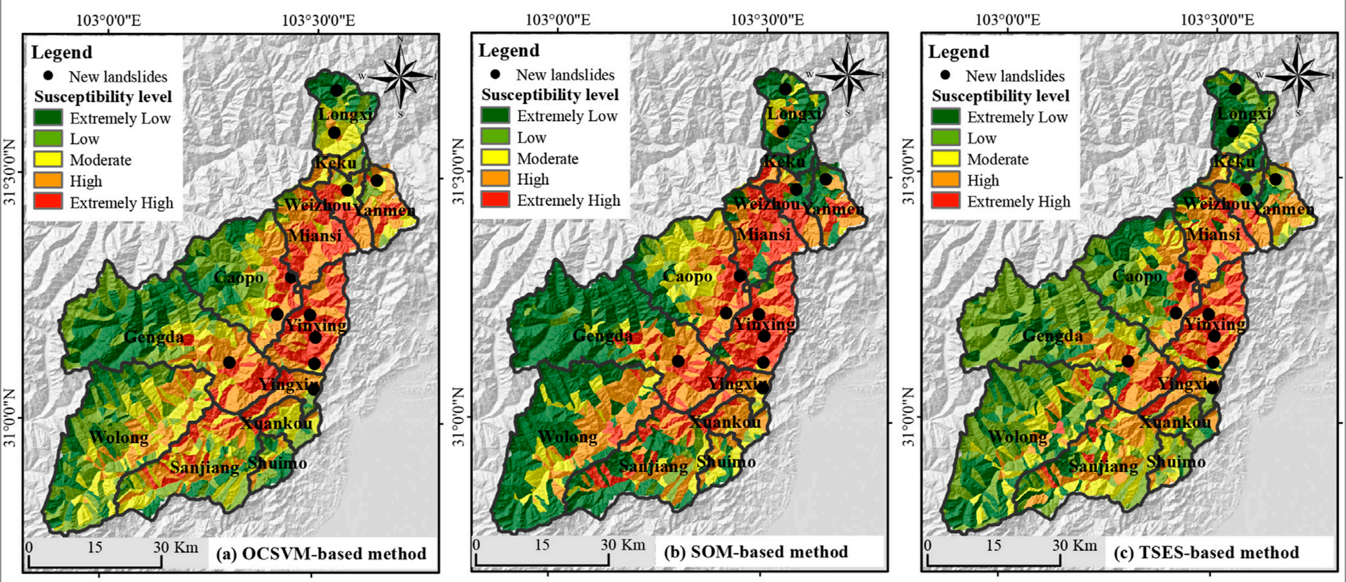

FIGURE 9 | Landslide susceptibility maps produced by: **(A)** OCSVM-based method, **(B)** SOM-based method, and **(C)** TSES-based method.

the post-earthquake area. Most of the LSM-SOM is consistent with the coseismic landslide distribution. However, the results are quite different from the actual situation at the junction of Miansi Town and Yingxiu Town. The TSES-based method underestimates the degree of earthquake disturbance, so many coseismic landslides are in the low susceptibility area.

To quantitatively evaluate the accuracy of the LSM obtained from different negative data generation strategies, we used the complete LIM to draw the ROC curves and calculate the corresponding AUC values. **Figure 10** shows that AUC values of OCSVM, SOM, and TSES are 0.8100, 0.7909, and 0.7641, respectively. Among three OCCs, OCSVM achieves the highest AUC value and TSES the lowest value. This result suggests that the selection of OCC has an influence on the performance of LSM, and thus the OCC should be carefully selected. **Table 6** shows the area percentage of coseismic landslides that occurred in the hazardous areas. The proposed OCSVM method has the highest value with a percentage of 92%, and this was followed by the TSES method at 86% and the SOM method at 84%. Specifically, 10 of 11 new landslides occurred in the hazardous area of the landslide susceptibility map obtained by the OCSVM negative data generation method. In contrast, the results based on SOM and TSES correspond to eight and six new landslide events, respectively. The main reasons for this result are as follows. Firstly, the result of the negative data generation method based on cluster analysis depends on two aspects. The clustering analysis in this study was carried out based on the frequency ratio of each causative factor, which depends on the LIM in the study area. Therefore, the clustering analysis is also affected by the incomplete LIM. Besides, as the clustering analysis needs to determine the category in advance. To compare this with the method presented in this study, the data sets in the study area were also divided into five categories, and the categories with fewer coseismic landslides were selected as the negative data source. Similarly, there are still a small number of coseismic landslides in the selected category, which affects the evaluation results of the model. Secondly, TSES transforms positive data

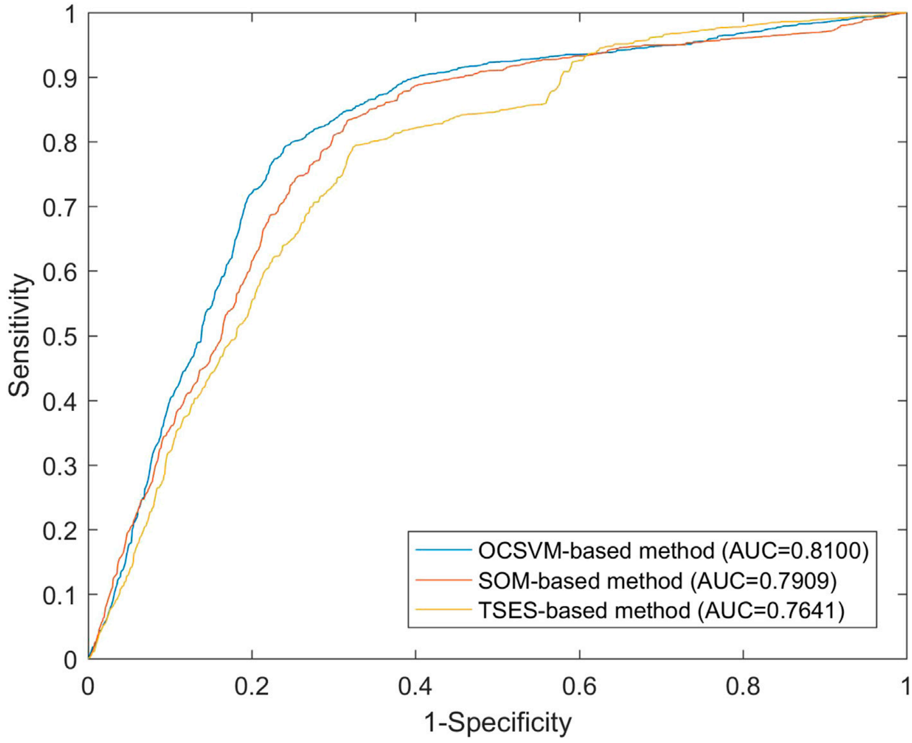

FIGURE 10 | ROC curves of the presented method based on three OCCs.

TABLE 6 | The co-seismic landslide and new landslide events in the hazardous area of LSM with different negative data generation methods.

Methods	Hazardous area of LSM	
	Co-seismic landslide (%)	New landslides
SVM-OCSVM	0.92	10
SVM-SOM	0.84	8
SVM-TSES	0.86	6

into negative data by replacing the value of a randomly selected causative factor with a value outside the range. This method is also affected by two factors. The LIM represents the landslide-affected area. On the other hand, the SUs used in this study are small-scale units that cannot accurately reflect the spatial differences of the feature corresponding to coseismic landslides. Therefore, there is still considerable uncertainty in the negative data generation based on inaccurate feature space information. In addition, TSES assumes that the weight of each causative factor is equal, while the existing research shows that the impact of the seismic landslide causative factor is different. Therefore, simply replacing the attribute value of a causative factor cannot generate a reliable negative data set. In summary, the method proposed in this study can effectively obtain the negative data, which has little dependence on the complete LIM and can quickly obtain the landslide susceptibility map after the earthquake.

4.4 DISCUSSION

A reliable and complete LIM is an important data source for rapid assessment of earthquake-induced landslides (Van Westen et al., 2008; Harp et al., 2011). As stated in the introduction, most statistical learning methods for predicting the distribution of landslide-prone areas depend on data sets with both positive (landslide presence) and negative (landslide absence) data (Hong et al., 2019). However, the complete LIM is difficult or impossible to obtain, which hampers the rapid LSM and hazard analysis after an earthquake (Reichenbach et al., 2018). By contrast, incomplete LIM is easy to obtain and is a potential data source for rapid LSM after an earthquake (Xu et al., 2013; Monsieurs et al., 2018; Chen et al., 2020; Du et al., 2020). The results of this paper show that satisfactory results of earthquake-induced LSM can also be obtained based on incomplete LIM provided that the negative data provided by the incomplete LIM is properly processed. Compared with earthquake-induced LSM based on the complete LIM, the approach by using incomplete LIM, proposed in this paper, has the advantages of high efficiency and low economic cost.

This study also finds that the one-class classifier can generate reliable negative data based on incomplete LIM. In this study, a comparative experiment is carried out for the uncertainty of negative data come from incomplete LIM. Compared with using complete LIM, the landslide susceptibility model has higher uncertainty when the negative data come from incomplete LIM, which is basically consistent with the existing research (Huang and Zhao, 2018; Dou et al., 2020b). However, the negative data generation method based on the one-class classifier can effectively reduce the uncertainty of the negative data and obtain a more stable and reliable model. Incomplete LIM provides negative data that may stem from unrecognized landslides, and false-negative data will reduce the reliability of the landslide susceptibility model. Even within the negative data obtained from complete LIM, there are inevitably unstable areas (Huang et al., 2017; Hong et al., 2019; Zhu et al., 2019), that is, the potential landslide areas in the deformation process. The data for such areas are between the negative data and the positive data, and simply taking them as negative data also increases the uncertainty of the samples. To overcome these challenges, the one-class classifier can construct a screening negative data model based on single class samples, which can eliminate the influence of unrecognized landslide area and potential landslide area and obtain more reliable negative data. Compared with other one-class classifiers, OCSVM can deal with complex nonlinear problems based on small sample data (Schölkopf et al., 2000), which can precisely represent the complex nonlinear relationship between seismic landslides and causative factors.

The performance of machine learning algorithms (e.g., SVM and OCSVM, which are used in this study) varies in accordance with topographic variables, suggesting that the patterns in causative factors are highly complex and variable for the different facets of causative factor attributes (e.g., spatial scale) (Chang et al., 2019). Thus, finding a general approach suitable for all regions and/or topographic variables is unlikely. And instead, evaluation of multiple machine learning algorithms (Merghadi et al., 2020; Wang et al., 2020) and/or ensemble of different machine learning algorithms (Dou et al., 2020a; Pham et al., 2020) should be standard procedure in developing satisfactory LSMs with highly complex landslide causative factors.

Focusing on overcoming the uncertainty of negative data that comes from an incomplete LIM, the method presented in this paper can quickly carry out seismic LSM under data-scarce environments conditions. Inevitably, some open problems require further study. First, we must find out how we can best define an incomplete LIM and explore the relationship between the completeness level of LIM and LSM performance, as these are not discussed in detail in this paper. In addition, the method presented in this paper is mainly based on incomplete LIM and is still a data-driven method. The quality of the results still depends on source data quality (Broeckx et al., 2018). With the rapid development of Synthetic Aperture Radar, 3D deformation information of earthquake-affected area can be obtained quickly after an earthquake, which can be effectively used to identify the hidden landslide area (Xie et al., 2020). More reliable negative data may be obtained by integrating the stable area in 3D deformation and the non-landslide area in LIM. More accurate LSM may be achieved by extending the proposed method based on OCSVM to incorporate such negative data with higher quality.

5 CONCLUSION

This study proposed a negative data generation method based on one class classifier, which can effectively make use of incomplete LIM. Based on the binary classifier established by the generated negative data, we performed LSM for the landslides of the 2008 Wenchuan earthquake. The reliability of the result was analyzed and verified using the coseismic landslides and new landslide events in the study area. The results show the following: 1) the two-class support vector machine is susceptible to the negative data, especially in the absence of complete LIM, and the landslide susceptibility model/mapping obtained from different negative data are quite different; 2) an incomplete LIM is easy to obtain, which is important data for rapid evaluation of landslide susceptibility; 3) the method presented in this study can effectively reduce the uncertainty of negative data and can significantly improve the performance of the landslide susceptibility model even without complete LIM. To sum up, the method in this study can be used to evaluate the landslide susceptibility quickly after the earthquake and provide an important reference for emergency rescue and land planning in post-earthquake regions.

DATA AVAILABILITY STATEMENT

The original contributions presented in the study are included in the article/Supplementary Material, further inquiries can be directed to the corresponding author.

AUTHOR CONTRIBUTIONS

ZM, LW, and SC proposed and participated in designing the study; SC, ZM, AZ and QL designed the study, analyzed the data and wrote the manuscript; AZ and YH participated in designing the study and improved the paper; AZ polished the paper. All authors approved the final version of the manuscript.

FUNDING

This work was supported in part by the National Key R& D Program of China under Grant 2018YFC15035, in part by National Natural Science Foundation of China under Grant 41701500 and Grant 41930108, in part by the Natural Science Foundation of Hunan Province under Grant 2018JJ3641 and Grant 2019JJ60001, in part by Talents Gathering Program of Hunan Province under Grant 2018RS3013, in part by Innovation-Driven Project of Central South University under Grant 2020CX036, in part by Early-Stage Research Start-up Grants funded by Central South University under Grant 502045001 and Grant 506030101, and in part by Natural Science Foundation of Jiangsu Province (BK20190785).

ACKNOWLEDGMENTS

The authors would like to thank two reviewers for their constructive comments that greatly improve this article.

REFERENCES

Broeckx, J., Vanmaercke, M., Duchateau, R., and Poesen, J. (2018). A data-based landslide susceptibility map of africa. *Earth-Science Rev.* 185, 102–121. doi:10.1016/j.earscirev.2018.05.002

Cao, J., Zhang, Z., Wang, C., Liu, J., and Zhang, L. (2019). Susceptibility assessment of landslides triggered by earthquakes in the western sichuan plateau. *Catena* 175, 63–76. doi:10.1016/j.catena.2018.12.013

Chang, C.-C., and Lin, C.-J. (2011). Libsvm. *ACM Trans. Intell. Syst. Technol.* 2, 1–27. doi:10.1145/1961189.1961199

Chang, K.-T., Merghadi, A., Yunus, A. P., Pham, B. T., and Dou, J. (2019). Evaluating scale effects of topographic variables in landslide susceptibility models using gis-based machine learning techniques. *Scientific Rep.* 9, 1–21. doi:10.1038/s41598-019-48773-2

Chen, S., Miao, Z., Wu, L., and He, Y. (2020). Application of an incomplete landslide inventory and one class classifier to earthquake-induced landslide susceptibility mapping. *IEEE J. Sel. Top. Appl. Earth Observations Remote Sensing* 13, 1649–1660. doi:10.1109/jstars.2020.2985088

Chen, W., Yan, X., Zhao, Z., Hong, H., Bui, D. T., and Pradhan, B. (2019). Spatial prediction of landslide susceptibility using data mining-based kernel logistic regression, naive bayes and rbfnetwork models for the long county area (China). *Bull. Eng. Geol. Environ.* 78, 247–266. doi:10.1007/s10064-018-1256-z

Conoscenti, C., Rotigliano, E., Cama, M., Caraballo-Arias, N. A., Lombardo, L., and Agnesi, V. (2016). Exploring the effect of absence selection on landslide susceptibility models: a case study in sicily, Italy. *Geomorphology* 261, 222–235. doi:10.1016/j.geomorph.2016.03.006

Dou, J., Yunus, A. P., Bui, D. T., Merghadi, A., Sahana, M., Zhu, Z., et al. (2020a). Improved landslide assessment using support vector machine with bagging, boosting, and stacking ensemble machine learning framework in a mountainous watershed, Japan. *Landslides* 17, 641–658. doi:10.1007/s10346-019-01286-5

Dou, J., Yunus, A. P., Merghadi, A., Shirzadi, A., Nguyen, H., Hussain, Y., et al. (2020b). Different sampling strategies for predicting landslide susceptibilities are deemed less consequential with deep learning. *Sci. total Environ.* 720, 137320. doi:10.1016/j.scitotenv.2020.137320

Dou, J., Yunus, A. P., Tien Bui, D., Sahana, M., Chen, C.-W., Zhu, Z., et al. (2019). Evaluating gis-based multiple statistical models and data mining for earthquake and rainfall-induced landslide susceptibility using the lidar dem. *Remote Sensing* 11, 638. doi:10.3390/rs11060638

Dreyfus, D., Rathje, E. M., and Jibson, R. W. (2013). The influence of different simplified sliding-block models and input parameters on regional predictions of seismic landslides triggered by the northridge earthquake. *Eng. Geology.* 163, 41–54. doi:10.1016/j.enggeo.2013.05.015

Du, J., Glade, T., Woldai, T., Chai, B., and Zeng, B. (2020). Landslide susceptibility assessment based on an incomplete landslide inventory in the jilong valley, tibet, Chinese himalayas. *Eng. Geology.* 270, 105572. doi:10.1016/j.enggeo.2020.105572

Erener, A., and Düzgün, H. S. B. (2012). Landslide susceptibility assessment: what are the effects of mapping unit and mapping method?. *Environ. Earth Sci.* 66, 859–877. doi:10.1007/s12665-011-1297-0

Fan, X., Scaringi, G., Xu, Q., Zhan, W., Dai, L., Li, Y., et al. (2018). Coseismic landslides triggered by the 8th August 2017 Ms 7.0 Jiuzhaigou earthquake (Sichuan, China): factors controlling their spatial distribution and implications for the seismogenic blind fault identification. *Landslides* 15, 967–983. doi:10.1007/s10346-018-0960-x

Fung, T. (1990). An assessment of tm imagery for land-cover change detection. *IEEE Trans. Geosci. remote sensing* 28, 681–684. doi:10.1109/igarss.1989.577758

Gorum, T., Fan, X., van Westen, C. J., Huang, R. Q., Xu, Q., Tang, C., et al. (2011). Distribution pattern of earthquake-induced landslides triggered by the 12 may 2008 wenchuan earthquake. *Geomorphology* 133, 152–167. doi:10.1016/j.geomorph.2010.12.030

Guzzetti, F., Reichenbach, P., Ardizzone, F., Cardinali, M., and Galli, M. (2006). Estimating the quality of landslide susceptibility models. *Geomorphology* 81, 166–184. doi:10.1016/j.geomorph.2006.04.007

Harp, E. L., Keefer, D. K., Sato, H. P., and Yagi, H. (2011). Landslide inventories: the essential part of seismic landslide hazard analyses. *Eng. Geology.* 122, 9–21. doi:10.1016/j.enggeo.2010.06.013

Hong, H., Miao, Y., Liu, J., and Zhu, A.-X. (2019). Exploring the effects of the design and quantity of absence data on the performance of random forest-based landslide susceptibility mapping. *Catena* 176, 45–64. doi:10.1016/j.catena.2018.12.035

Hong, H., Pradhan, B., Bui, D. T., Xu, C., Youssef, A. M., and Chen, W. (2017). Comparison of four kernel functions used in support vector machines for landslide susceptibility mapping: a case study at suichuan area (China). *Geomatics, Nat. Hazards Risk* 8, 544–569. doi:10.1080/19475705.2016.1250112

Huang, F., Yin, K., Huang, J., Gui, L., and Wang, P. (2017). Landslide susceptibility mapping based on self-organizing-map network and extreme learning machine. *Eng. Geology.* 223, 11–22. doi:10.1016/j.enggeo.2017.04.013

Huang, R., and Li, W. (2014). Post-earthquake landsliding and long-term impacts in the wenchuan earthquake area, China. *Eng. Geology.* 182, 111–120. doi:10.1016/j.enggeo.2014.07.008

Huang, R. Q., and Li, W. L. (2009). Analysis of the geo-hazards triggered by the 12 may 2008 wenchuan earthquake, China. *Bull. Eng. Geol. Environ.* 68, 363–371. doi:10.1007/s10064-009-0207-0

Huang, Y., and Zhao, L. (2018). Review on landslide susceptibility mapping using support vector machines. *Catena* 165, 520–529. doi:10.1016/j.catena.2018.03.003

Irigaray, C., Fernández, T., El Hamdouni, R., and Chacón, J. (2007). Evaluation and validation of landslide-susceptibility maps obtained by a gis matrix method: examples from the betic cordillera (southern Spain). *Nat. Hazards* 41, 61–79. doi:10.1007/s11069-006-9027-8

Jibson, R. W., Harp, E. L., and Michael, J. A. (2000). A method for producing digital probabilistic seismic landslide hazard maps. *Eng. Geology.* 58, 271–289. doi:10.1016/s0013-7952(00)00039-9

Jibson, R. W. (1993). Predicting earthquake-induced landslide displacements using newmark's sliding block analysis. *Transportation Res. Rec.* 1411, 9–17.

Kamp, U., Growley, B. J., Khattak, G. A., and Owen, L. A. (2008). Gis-based landslide susceptibility mapping for the 2005 kashmir earthquake region. *Geomorphology* 101, 631–642. doi:10.1016/j.geomorph.2008.03.003

Kargel, J. S., Leonard, G. J., Shugar, D. H., Haritashya, U. K., Bevington, A., Fielding, E. J., et al. (2016). Geomorphic and geologic controls of geohazards induced by nepals 2015 gorkha earthquake. *Science* 351, 8353. doi:10.1126/science.aac8353

Keefer, D. K. (2002). Investigating landslides caused by earthquakes–a historical review. *Surv. Geophys.* 23, 473–510. doi:10.1023/a:1021274710840

Li, W.-l., Huang, R.-q., Tang, C., Xu, Q., and van Westen, C. (2013). Co-seismic landslide inventory and susceptibility mapping in the 2008 wenchuan earthquake disaster area, China. *J. Mt. Sci.* 10, 339–354. doi:10.1007/s11629-013-2471-5

Li, X., Zhou, Z., Yu, H., Wen, R., Lu, D., Huang, M., et al. (2008). Strong motion observations and recordings from the great wenchuan earthquake. *Earthquake Eng. Eng. Vibration* 7, 235–246. doi:10.1007/s11803-008-0892-x

Lv, Z. Y., Shi, W., Zhang, X., and Benediktsson, J. A. (2018). Landslide inventory mapping from bitemporal high-resolution remote sensing images using change detection and multiscale segmentation. *IEEE J. Sel. Top. Appl. Earth Observations Remote Sensing* 11, 1520–1532. doi:10.1109/jstars.2018.2803784

Ma, S., and Xu, C. (2019). Assessment of co-seismic landslide hazard using the Newmark model and statistical analyses: a case study of the 2013 Lushan, China, Mw6.6 earthquake. *Nat. Hazards* 96, 389–412. doi:10.1007/s11069-018-3548-9

Maharaj, R. J. (1993). Landslide processes and landslide susceptibility analysis from an upland watershed: a case study from st. andrew, Jamaica, west indies. *Eng. Geology.* 34, 53–79. doi:10.1016/0013-7952(93)90043-c

Mandal, B., and Mandal, S. (2018). Analytical hierarchy process (ahp) based landslide susceptibility mapping of lish river basin of eastern darjeeling himalaya, India. *Adv. Space Res.* 62, 3114–3132. doi:10.1016/j.asr.2018.08.008

Merghadi, A., Yunus, A. P., Dou, J., Whiteley, J., ThaiPham, B., Bui, D. T., et al. (2020). Machine learning methods for landslide susceptibility studies: a comparative overview of algorithm performance. *Earth-Science Rev.* 207, 103225. doi:10.1016/j.earscirev.2020.103225

Monsieurs, E., Jacobs, L., Michellier, C., Basimike Tchangaboba, J., Ganza, G. B., Kervyn, F., et al. (2018). Landslide inventory for hazard assessment in a data-poor context: a regional-scale approach in a tropical african environment. *Landslides* 15, 2195–2209. doi:10.1007/s10346-018-1008-y

Pham, B. T., Nguyen-Thoi, T., Qi, C., Phong, T. V., Dou, J., Ho, L. S., et al. (2020). Coupling rbf neural network with ensemble learning techniques for landslide susceptibility mapping. *Catena* 195, 104805. doi:10.1016/j.catena.2020.104805

Pourghasemi, H. R., Yansari, Z. T., Panagos, P., and Pradhan, B. (2018). Analysis and evaluation of landslide susceptibility: a review on articles published during 2005–2016 (periods of 2005–2012 and 2013–2016). *Arabian J. Geosciences* 11, 193. doi:10.1007/s12517-018-3531-5

Pradhan, B., and Lee, S. (2010). Landslide susceptibility assessment and factor effect analysis: backpropagation artificial neural networks and their comparison with frequency ratio and bivariate logistic regression modelling. *Environ. Model. Softw.* 25, 747–759. doi:10.1016/j.envsoft.2009.10.016

Ramos-Bernal, R., Vázquez-Jiménez, R., Romero-Calcerrada, R., Arrogante-Funes, P., and Novillo, C. (2018). Evaluation of unsupervised change detection methods applied to landslide inventory mapping using aster imagery. *Remote Sensing* 10, 1987. doi:10.3390/rs10121987

Reichenbach, P., Rossi, M., Malamud, B. D., Mihir, M., and Guzzetti, F. (2018). A review of statistically-based landslide susceptibility models. *Earth-Science Rev.* 180, 60–91. doi:10.1016/j.earscirev.2018.03.001

Ruff, M., and Czurda, K. (2008). Landslide susceptibility analysis with a heuristic approach in the eastern alps (vorarlberg, Austria). *Geomorphology* 94, 314–324. doi:10.1016/j.geomorph.2006.10.032

Schölkopf, B., Williamson, R. C., Smola, A. J., Shawe-Taylor, J., and Platt, J. C. (2000). "Support vector method for novelty detection," in *Advances in neural information processing systems*, 582–588.

Su, Q., Zhang, J., Zhao, S., Wang, L., Liu, J., and Guo, J. (2017). Comparative assessment of three nonlinear approaches for landslide susceptibility mapping in a coal mine area. *Ijgi* 6, 228. doi:10.3390/ijgi6070228

Sun, X., Chen, J., Han, X., Bao, Y., Zhan, J., and Peng, W. (2020). Application of a gis-based slope unit method for landslide susceptibility mapping along the rapidly uplifting section of the upper jinsha river, south-western China. *Bull. Eng. Geol. Environ.* 79, 533–549. doi:10.1007/s10064-019-01572-5

Suykens, J. A. K., and Vandewalle, J. (1999). Least squares support vector machine classifiers. *Neural Process. Lett.* 9, 293–300. doi:10.1023/a:1018628609742

Swets, J. (1988). Measuring the accuracy of diagnostic systems. *Science* 240, 1285–1293. doi:10.1126/science.3287615

Tang, C., Zhu, J., and Qi, X. (2011). Landslide hazard assessment of the 2008 wenchuan earthquake: a case study in beichuan area. *Can. Geotech. J.* 48, 128–145. doi:10.1139/T10-059

Tanyaş, H., Van Westen, C. J., Allstadt, K. E., Anna Nowicki Jessee, M., Görüm, T., Jibson, R. W., et al. (2017). Presentation and analysis of a worldwide database of earthquake-induced landslide inventories. *J. Geophys. Res. Earth Surf.* 122, 1991–2015. doi:10.1002/2017JF004236

Tsai, H.-Y., Tsai, C.-C., and Chang, W.-C. (2019). Slope unit-based approach for assessing regional seismic landslide displacement for deep and shallow failure. *Eng. Geology.* 248, 124–139. doi:10.1016/j.enggeo.2018.11.015

Van Den Eeckhaut, M., Reichenbach, P., Guzzetti, F., Rossi, M., and Poesen, J. (2009). Combined landslide inventory and susceptibility assessment based on different mapping units: an example from the flemish ardennes, Belgium. *Nat. Hazards Earth Syst. Sci.* 9, 507–521. doi:10.5194/nhess-9-507-2009

Van Westen, C. J., Castellanos, E., and Kuriakose, S. L. (2008). Spatial data for landslide susceptibility, hazard, and vulnerability assessment: an overview. *Eng. Geology.* 102, 112–131. doi:10.1016/j.enggeo.2008.03.010

Wang, F., Xu, P., Wang, C., Wang, N., and Jiang, N. (2017). Application of a gis-based slope unit method for landslide susceptibility mapping along the longzi river, southeastern Tibetan plateau, China. *Ijgi* 6, 172. doi:10.3390/ijgi6060172

Wang, W.-D., He, Z., Han, Z., and Li, Y. (2020). "Landslide susceptibility mapping based on the deep belief network: a case study in sichuan province, China," in *Workshop on world landslide forum* (Springer), 201–213.

Wu, R., Zhang, Y., Guo, C., Yang, Z., Tang, J., and Su, F. (2020). Landslide susceptibility assessment in mountainous area: a case study of sichuan–tibet railway, China. *Environ. Earth Sci.* 79, 1–16. doi:10.1007/s12665-020-8878-8

Xiao, C., Tian, Y., Shi, W., Guo, Q., and Wu, L. (2010). A new method of pseudo absence data generation in landslide susceptibility mapping with a case study of shenzhen. *Sci. China Technol. Sci.* 53, 75–84. doi:10.1007/s11431-010-3219-x

Xie, M., Zhao, W., Ju, N., He, C., Huang, H., and Cui, Q. (2020). Landslide evolution assessment based on insar and real-time monitoring of a large reactivated landslide, wenchuan, China. *Eng. Geology.* 277, 105781. doi:10.1016/j.enggeo.2020.105781

Xu, C., Xu, X., Dai, F., Wu, Z., He, H., Shi, F., et al. (2013). Application of an incomplete landslide inventory, logistic regression model and its validation for landslide susceptibility mapping related to the may 12, 2008 wenchuan earthquake of China. *Nat. Hazards* 68, 883–900. doi:10.1007/s11069-013-0661-7

Xu, C., Xu, X., Yao, X., and Dai, F. (2014). Three (nearly) complete inventories of landslides triggered by the may 12, 2008 wenchuan mw 7.9 earthquake of China and their spatial distribution statistical analysis. *Landslides* 11, 441–461. doi:10.1007/s10346-013-0404-6

Yunus, A. P., Fan, X., Tang, X., Jie, D., Xu, Q., and Huang, R. (2020). Decadal vegetation succession from modis reveals the spatio-temporal evolution of post-seismic landsliding after the 2008 wenchuan earthquake. *Remote Sensing Environ.* 236, 111476. doi:10.1016/j.rse.2019.111476

Zhou, S., Chen, G., and Fang, L. (2016). Distribution pattern of landslides triggered by the 2014 ludian earthquake of China: implications for regional threshold topography and the seismogenic fault identification. *Ijgi* 5, 46. doi:10.3390/ijgi5040046

Zhu, A.-X., Miao, Y., Liu, J., Bai, S., Zeng, C., Ma, T., et al. (2019). A similarity-based approach to sampling absence data for landslide susceptibility mapping using data-driven methods. *Catena* 183, 104188. doi:10.1016/j.catena.2019.104188

Conflict of Interest: The authors declare that the research was conducted in the absence of any commercial or financial relationships that could be construed as a potential conflict of interest.

frontiers
in Earth Science

ORIGINAL RESEARCH
published: 01 June 2021
doi: 10.3389/feart.2021.676470

Quantitative Analysis of the Effects of an Earthquake on Rainfall Thresholds for Triggering Debris-Flow Events

Shuang Liu[1], Kaiheng Hu[1]*, Qun Zhang[2], Shaojie Zhang[1], Xudong Hu[3] and Desheng Tang[2]

[1]Key Laboratory of Mountain Hazards and Earth Surface Processes, Institute of Mountain Hazards and Environment, Chinese Academy of Sciences, Chengdu, China, [2]Sichuan Institute of Land and Space Ecological Restoration and Geological Hazard Prevention, Chengdu, China, [3]College of Civil Engineering and Architecture, China Three Gorges University, Yichang, China

The impacts of destructive earthquakes on rainfall thresholds for triggering the debris flows have not yet been well investigated, due to lacks of data. In this study, we have collected the debris-flow records from the Wenchuan, Lushan, and Jiuzhaigou earthquake-affected areas in Sichuan Province, China. By using a meteorological dataset with 3 h and 0.1° resolutions, the dimensionless effective rainfall and rainfall intensity-duration relationships were calculated as the possible thresholds for triggering the debris flows. The pre- and post-seismic thresholds were compared to evaluate the impacts of the various intensities of earthquakes. Our results indicate that the post-quake thresholds are much smaller than the pre-seismic ones. The dimensionless effective rainfall shows the impacts of the Wenchuan, Lushan, and Jiuzhaigou earthquakes to be ca. 26, 27, and 16%, respectively. The Wenchuan earthquake has the most significant effect on lowering the rainfall intensity-duration curve. Rainfall threshold changes related to the moment magnitude and focal depth are discussed as well. Generally, this work may lead to an improved post-quake debris-flow warning strategy especially in sparsely instrumented regions.

Keywords: debris flows, seismic effects, regional rainfall threshold, early warning, disaster prevention

Edited by:
Tolga Gorum,
Istanbul Technical University, Turkey

Reviewed by:
Hans-Balder Havenith,
University of Liège, Belgium
Joern Lauterjung,
German Research Centre for Geosciences, Germany

****Correspondence:***
Kaiheng Hu
khhu@imde.ac.cn

Specialty section:
This article was submitted to Geohazards and Georisks, a section of the journal Frontiers in Earth Science

Received: *05 March 2021*
Accepted: *10 May 2021*
Published: *01 June 2021*

Citation:
Liu S, Hu K, Zhang Q, Zhang S, Hu X and Tang D (2021) Quantitative Analysis of the Effects of an Earthquake on Rainfall Thresholds for Triggering Debris-Flow Events. Front. Earth Sci. 9:676470. doi: 10.3389/feart.2021.676470

INTRODUCTION

Massive earthquake-induced loose deposits on slopes or channels can be mobilized by heavy rainfalls and evolve into debris flows. The increased unconsolidated sediment reduces the rainfall threshold for the debris-flow occurrence and significantly augments the magnitude of post-quake debris flows (Chen and Petley, 2005; Ma et al., 2013). The post-quake hazards can remain highly frequent for 5–10 years, even longer as 20 years (Cui et al., 2011). Quantifying the impact of strong earthquakes on the rainfall threshold is essential for post-quake debris-flow early warning (Zhang and Zhang, 2017).

Numerous studies have reported the rainfall threshold variation after strong earthquakes. As an example, the mean value of the accumulated rainfall decreased from 867 mm for 67 debris flows in 1996 to 146 mm for 197 debris flows in 2001 in the intensive-ground-motion areas of the 1999 Chi-Chi earthquake in Taiwan (Liu et al., 2008). Similarly, the maximum effective cumulative precipitation decreased from 950 to 200 mm in the Mt. Ninety-Nine area of Taiwan during the first year after the earthquake (Shieh et al., 2009). After the 2008 Wenchuan earthquake, the accumulated rainfall threshold decreased by 15–22% while the critical value for the hourly rainfall intensity decreased by 25–32% (Tang et al., 2009). Likewise, a sudden drop in the rainfall threshold

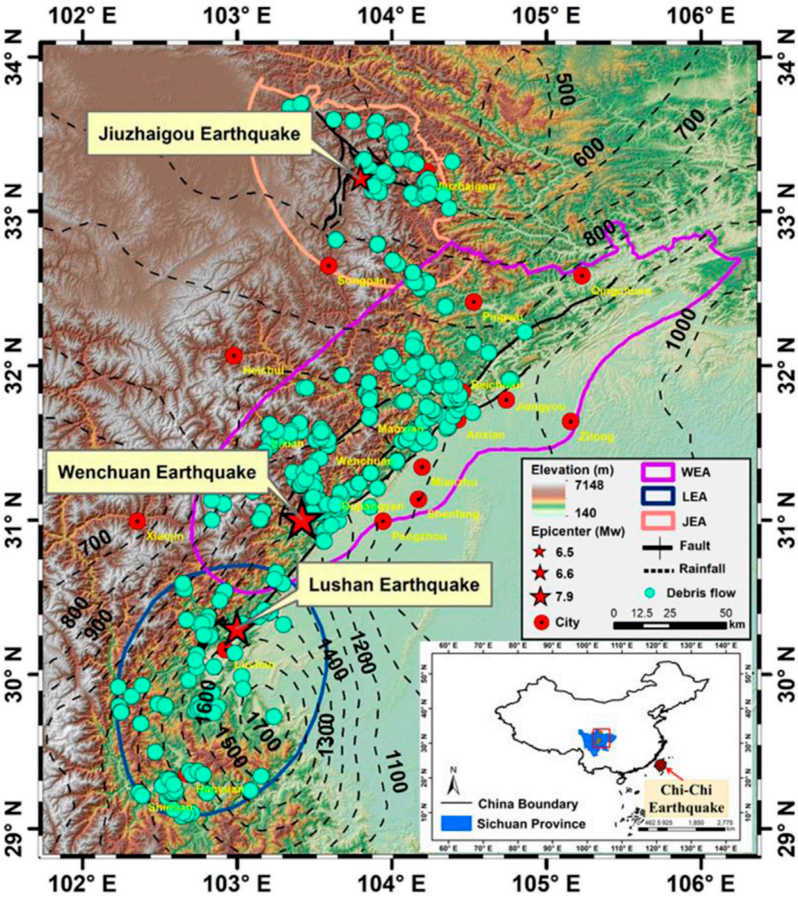

FIGURE 1 | Location of study areas in Sichuan Province, China. The ranges, elevations, main faults, debris-flow records (filled dot), epicenters (pentagram), moment magnitude (Mw), and mean annual rainfall (contour with 100 mm interval) are shown for the WEA (Chinese seismic intensity ≥ VIII), LEA (Chinese seismic intensity ≥ VI), and JEA (Chinese seismic intensity ≥ VI), respectively. The location of the Chi-Chi earthquake in Taiwan Province is also marked in the subplot.

was found in the Gaochuan River basin near the Wenchuan earthquake's epicenter (Li et al., 2016). The rainfall intensity-duration (I-D) thresholds normalized by the mean annual maximum hourly rainfall, indicate a reduction of at least 30% compared to the pre-quake level (Ma et al., 2017). Yu et al. (2014) found that the ratio of the thresholds before and after the earthquake decreased with increasing peak ground acceleration. However, due to data limitation, the impacts of destructive earthquakes on rainfall thresholds have not been well investigated quantitatively.

The recent three severe earthquakes occurred in Sichuan Province, Southwest China, namely the Wenchuan earthquake in 2008, the Lushan earthquake in 2013 and the Jiuzhaigou earthquake in 2017 have different magnitudes (**Figure 1**), which provides valuable cases to quantitatively examine the influence of the earthquake magnitude on the rainfall thresholds. We have collected debris-flow records in the Wenchuan earthquake-affected area (WEA), Lushan earthquake-affected area (LEA), and Jiuzhaigou earthquake-affected area (JEA) to examine how much an earthquake can affect the rainfall threshold for triggering debris flows. Two kinds of rainfall thresholds, including the dimensionless effective rainfall and the rainfall I-D curve, were calculated based on the China Meteorological Forcing Dataset from National Tibetan Plateau Data Center to show the seismic effects.

MATERIALS AND METHODS

Study Area

The study area is located at the eastern edge of the Tibetan Plateau, which has been affected by the three earthquakes (**Figure 1**). The Mw 7.9 Wenchuan earthquake (the "5.12" earthquake) ruptured along the Longmenshan thrust belt on May 12, 2008 (Xu et al., 2009). The shock-induced collapses and landslides produced approximately 2.6×10^9 m^3 of loose material (Parker et al., 2011), indicating that debris flows may occur frequently following the earthquake (Cui et al., 2011). Huang and Li (2009) found that there were 8,627 geo-hazards, including 3,627 landslides, 2,383 slope collapses, and 837 debris flows in the 42 earthquake-hit regions of Sichuan Province. The Mw 6.6 Lushan earthquake

TABLE 1 | Debris-flow numbers and the time range in each area.

	WEA		LEA		JEA	
	Period	Count	Period	Count	Period	Count
Pre-seismic	2000–2007	21	2000–2012	88	2010–2016	58
Post-seismic	2008–2010	246	2013–2017	21	2017–2018	12

occurred in the Longmen Shan fold-and-thrust belt, Sichuan Province, China, on April 20, 2013, causing 196 deaths and 13,484 injuries (Li et al., 2014). The earthquake has reduced hillslope stability and moderately increased the possibility of debris flows occurrence (Cui et al., 2014). On August 8, 2017, the Mw 6.5 earthquake with a focal depth of 20 km hit the Jiuzhaigou World Natural and Cultural Heritage site and its surroundings (Hong et al., 2018). The epicenter was at 33.2° N, 103.82° E, approximately 5 km west of the Jiuzhaigou core scenic area (Hu et al., 2019). 1883 earthquake-induced geological hazards were identified by remote sensing within the 840 km^2 area affected by the earthquake (Fan et al., 2018).

Considering the sufficient earthquake intensity and available debris-flow records for comparisons, we choose the WEA with the Chinese seismic intensity ≥ VIII, the LEA with the intensity ≥ VI, and the JEA with the intensity ≥ VI as regions of interest. The moist monsoon dominates the regional climate, providing water conditions for debris flows (Cui et al., 2014). In addition, the Mw 7.6 Chi-Chi Earthquake in Taiwan is also used for discussion.

Data Sources

Collection of Debris-Flow Data

The debris flows mentioned in this study limit to the torrential flow of a mixture of water, mud, and debris in the gully or channel of a small catchment, even on a hill slope. The time span of the collected debris-flow events to the earthquakes does not exceed 15 years. Data of some debris-flow events when near-zero rainfall was recorded from a gridded rainfall dataset are excluded (more details in 2.2.2). Then, 267 debris-flow records for 2000–2010 in the WEA, 109 for 2000–2017 in the LEA, and 70 for 2010–2018 in JEA were collected through field survey and data gathering from Sichuan Provincial Natural Resources Department (**Figure 1**; **Table 1**). In the WEA, the debris flows that happened on the same day with the earthquake are classified as post-earthquake events, which can be used to show extremely post-seismic impacts on the rainfall conditions. Unlike debris flows in the WEA, we collected no co-seismic debris-flow records in the LEA and JEA.

Gridded Rainfall Data

The gridded near-surface meteorological dataset was developed for evaluating land surface processes in China (He et al., 2020). The dataset was made through the fusion of remote sensing products (e.g., Tropical Rainfall Measuring Mission 3B42 v7), a reanalysis dataset (e.g., Global Land Data Assimilation System and Modern-Era Retrospective Analysis), and *in-situ* observations at weather stations (e.g., daily data from approximately 700 stations of China Meteorological Administration and sub-daily data from the National Oceanic and Atmospheric Administration's National Centers for Environmental Information). The time of the data ranges from January 1979 up to December 2018 with a temporal resolution of 3 h and a spatial resolution of 0.1°. For each 0.1° grid cell, a rainfall record with Greenwich Mean Time (GMT) stands for a mean value of rainfall intensities (mm/h) taken every three hours. So, each grid cell represents 8 records on each day. The data have been adjusted to match the Beijing time, i.e., 8 h ahead of the GMT.

Based on the data, the mean annual rainfall of 1979–2018 is ca. 950, 1,360, and 660 mm for the WEA, the LEA, and the JEA, respectively. According to the time ranges in **Table 1**, the mean annual rainfall of 937 mm after 2008 in the WEA is 7% higher than before 2008. However, the number of debris flows per year has increased ca. 30 times compared with the period before the Wenchuan earthquake. The decrease in the number of debris flows in both the LEA and the JEA cannot be directly linked with the change in the mean annual rainfall, suggesting that more short-term rainfall conditions should be discussed.

Regional Rainfall Threshold

Dimensionless Effective Rainfall

Effective rainfall is considered as a function of the regressive rainfall index (Li et al., 2011; Zhuang et al., 2015). We use the ratio of effective rainfall to annual rainfall as the dimensionless effective rainfall (DER) to eliminate the impacts of different annual climate. The equation for calculating DER can be written as:

$$DER = \frac{\sum_{i=1}^{n} K^i P_i + P_0}{P_{annual}} \tag{1}$$

where P_0 is the total rainfall on the day of debris-flow occurrence; P_i is the accumulative daily rainfall (mm) on the ith day before the occurrence; K^i indicating K to the power of i is the decay factor of precipitation on the ith day before the occurrence; and P_{annual} is the total rainfall for each year. The study areas belong to the Hengduan Mountains in the southwest region of China, therefore, the K is empirically set to 0.84 (Liu et al., 2020). n is set to 3, 7, 11, and 15, respectively, for comparison. The median of DER in each earthquake-affected area is regarded as a proxy of regional rainfall threshold.

Rainfall Intensity-Duration Relationship

The so-called rainfall intensity-duration (I-D) relationship was proposed firstly by Caine (1980). It is a fairly common type of debris-flow threshold (Guzzetti et al., 2007). The original expression of the relationship is of discrepant dimension as the following:

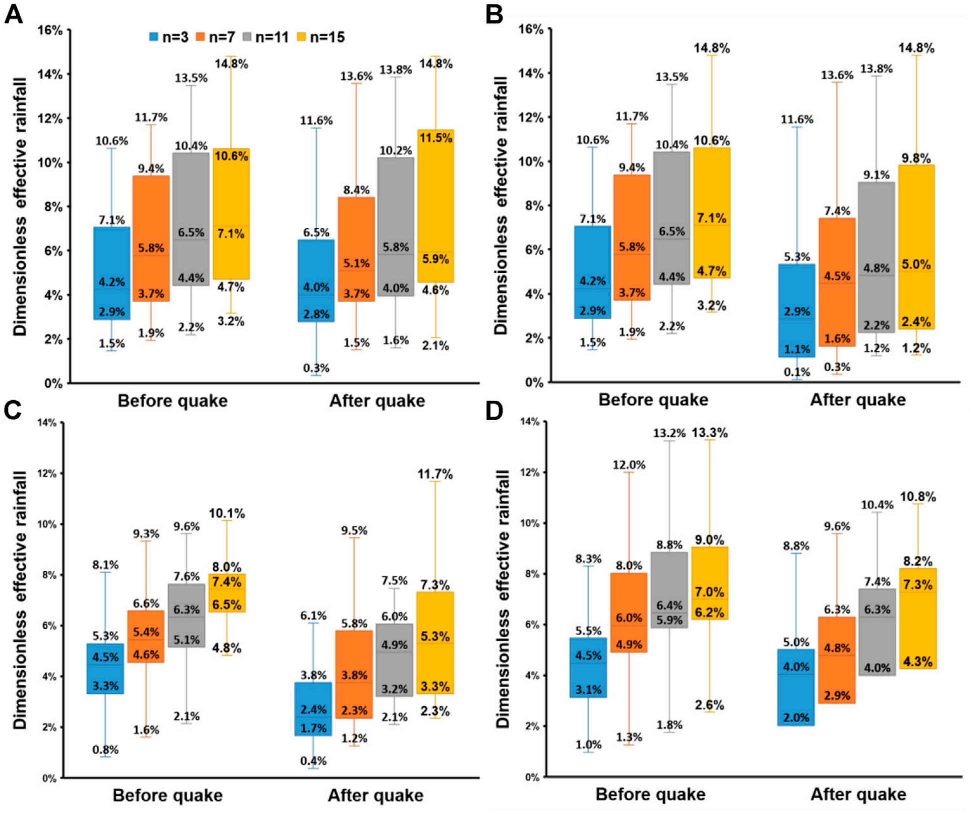

FIGURE 2 | Boxplots of DER for Wenchuan **(A, B)**, Lushan **(C)**, and Jiuzhaigou **(D)** earthquakes. Subplot **(A)** excludes the debris flows occurring on May 12, 2008, while subplot **(B)** includes those events. *n* denotes effective antecedent rainy days. The first quartile marks the bottom of the box, and the third quartile marks the other end of the box. The backline in the box denotes the median.

$$I = \alpha D^{-\beta} \tag{2}$$

where the term I denotes the mean hourly rainfall intensity (mm/h) of a continuous rainfall process that triggers a debris-flow event; D is the rainfall duration (h) for triggering a debris-flow event; and α and β are coefficients. Then, when the curve is drawn in a double logarithmic coordinate system, the α can reflect the intercept, while β can reflect the slope of the straight line. The rainfall conditions above the curve are more likely to trigger debris flows. Although some studies emphasize the physical interpretation of parameters in I-D curve, it is now restricted to some specific kind of debris flows such as runoff-generated debris flows with enough *in-situ* observations (Berti et al., 2020).

To eliminate the impacts of different annual climates before and after an earthquake, the ratio (I_{new}, h^{-1}) of mean hourly rainfall intensity (mm/h) to annual rainfall (mm) is used to replace the term I in the **Eq. 2** as follows:

$$I_{new} = \alpha_{new} D^{-\beta_{new}} \tag{2a}$$

where α_{new} and β_{new} are new coefficients. It is noteworthy that only the "day" information of debris-flow occurrence is available. It is assumed that a continue rainfall process begins if when averaged hourly rainfall intensity of grid cells covering the debris-flow gully is greater than 0.05 mm/h. Thus, the I_{new} and D of such rainfall event were used to describe the rainfall process for triggering debris flows.

Impacts of the Earthquake on the Thresholds

The impact of each earthquake on the thresholds is determined by the following equation:

$$Impact = \frac{\left(Thre_{pre} - Thre_{post}\right)}{Thre_{pre}} \times 100\% \tag{3}$$

where $Thre_{pre}$ denotes the median DER or the parameters of I-D curve before the earthquake; and $Thre_{post}$ indicates those after the earthquake. For the DER, the positive value of *Impact* indicates the decrease of the regional rainfall threshold. For the parameters of I-D curve, the positive impact on α indicates a decrease of the scaling constant after an earthquake, α_{new} of I_{new} at $D = 1$ in the power-law relationship indicates that post-earthquake rainfall intensity is smaller or greater than the pre-earthquake intensity. The positive impact on β_{new} indicates a decrease of the shape slope, which should be combined with α_{new} change for threshold analysis.

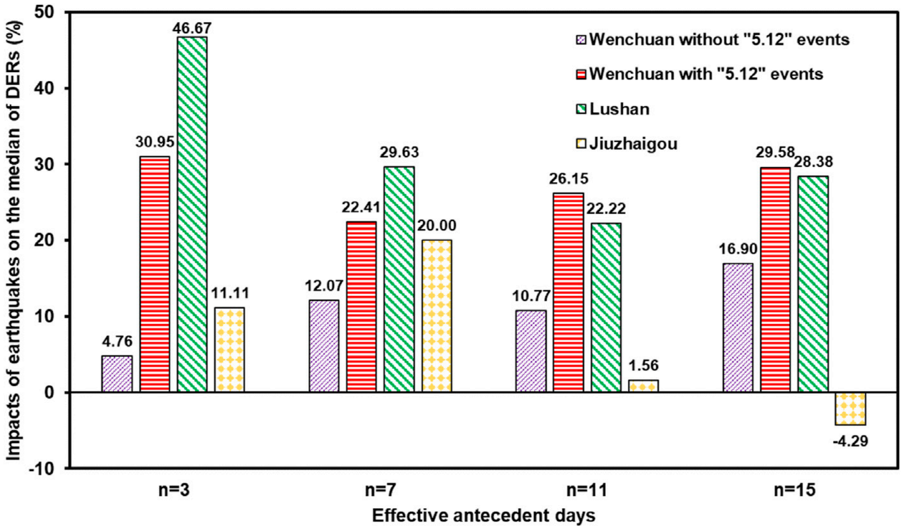

FIGURE 3 | Impacts of each earthquake on rainfall thresholds with different n settings. n is effective antecedent rainy days. The positive value indicates the decrease of the regional rainfall threshold.

RESULTS AND DISCUSSION

Seismic Impacts on Dimensionless Effective Rainfall Thresholds

In the WEA, the regional rainfall thresholds are ca. 4.2, 5.8, 6.5, and 7.1% of the annual rainfall for effective antecedent rainy-day settings of 3, 7, 11, and 15, respectively, (**Figure 2A**). After the Wenchuan earthquake, the threshold decreased. When excluding the debris-flow samples on the day when the earthquake occurred, the thresholds are ca. 4.0, 5.1, 5.8, and 5.9% of the annual rainfall. When considering the debris-flow records on that day, the thresholds dropped more significantly (**Figure 2B**). The mean reduction of ca. 18% represent the most serious impact of Wenchuan earthquake on the rainfall condition. It suggests that once such earthquake happens, the short-term rainfall threshold could be much lower than that obtained from data in the following several years.

Before the Lushan earthquake, the thresholds are ca. 4.5, 5.4, 6.3, and 7.4% of the annual rainfall. Then, they reduce to 2.4, 3.8, 4.9, and 5.3% after the quake (**Figure 2C**). Similarly, the thresholds in the JEA are ca. 4.5, 6.0, 6.4, and 7.0% before the earthquake (**Figure 2D**). After the shock, they decrease to ca. 4.0, 4.8, and 6.3% for antecedent rainy-day settings of 3, 7, and 11, respectively. However, the threshold unexpectedly increases slightly when the number of antecedent rainy days is set to 15.

In most cases, the earthquake lowered the DER thresholds (**Figure 3**). The regional impacts show a significant variation when n is set to 3. However, when n is set to other values rather than 3, the impacts only show lower variations. Based on the results with $n = 7$, 11, and 15, the mean impacts (mean level of seismic effects with different n settings) of the Wenchuan (including co-seismic events) and Lushan earthquakes are ca. 26 and 27%, respectively. When excluding the co-seismic samples ("5.12" events), the mean impact of Wenchuan is ca. 13%. When n is set to 11 and 15, the impacts are not significant in the JEA. Maybe the drier climate of Jiuzhaigou in the northern Sichuan province leads to fewer days of DER. When n is equal to 3 or 7, the mean impact of the Jiuzhaigou earthquakes is ca. 16%.

Seismic Impacts on Rainfall Intensity–Duration Relationships

All post-seismic I-D curves are lower than the pre-seismic ones, indicating that triggering post-quake debris flows needs smaller rainfall intensity or shorter duration (**Figure 4**). When drawing the "5.12" events for the Wenchuan earthquake in the picture (the purple crosses in **Figure 4A**), the triggering rainfall level becomes much lower than the post-seismic mean status, indicating extremely low rainfall threshold for co-seismic debris flows. For the WEA, there are more scattered debris-flow records for a shorter duration than a longer duration. Data shows more discrete records after Wenchuan earthquake than before the quake (**Figure 4A**). It may indicate more randomness on the rainfall intensity to trigger debris flows, which is consistent with the random effect of an earthquake on reducing the stability of the surface material (Zhao et al., 2020). Similar results occur at 3 and 9 h durations in both LEA and JLA (**Figure 4B,C**).

According to the **Eq. 3**, impacts of earthquakes on the parameter α_{new} are ca. 45, 24, and 3% in the WEA, the LEA, and the JEA, respectively (**Figure 5**). Impact of the Wenchuan earthquake on the parameter β_{new} is ca. 12%, while those of the Lushan and Jiuzhaigou earthquakes are ca. −34 and ca. −46%. It indicates that, though the impacts of the Lushan and Jiuzhaigou earthquakes on α_{new} are smaller, the increased slopes also made the threshold lower (**Figure 4B,C** and **Figure 5**). However, it should be noted that a little change of β_{new} may not be important

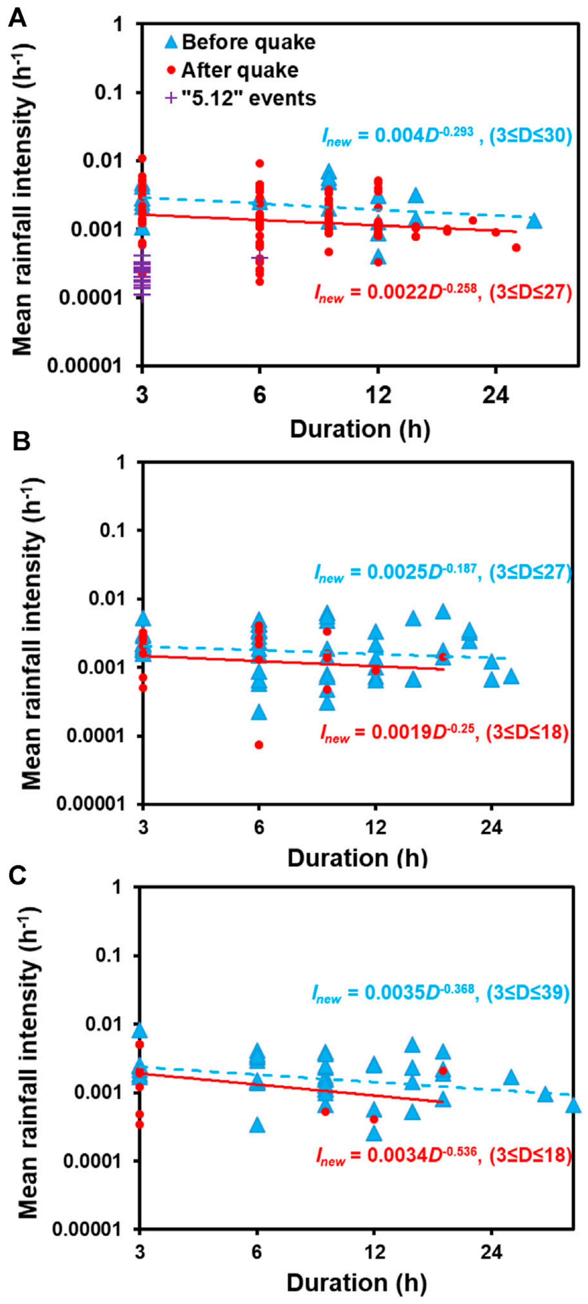

FIGURE 4 | I-D curves for debris flows. The blue and red lines indicate I-D curves for debris flows before and after the Wenchuan **(A)**, Lushan **(B)**, and Jiuzhaigou **(C)** earthquakes. In the WEA, the pre-quake I-D curve is fitted with 21 debris-flow events from 2000 to 2007, while post-quake one is fitted with 183 events from 2008 to 2010 when excluding the samples on the day of "5.12" earthquake. The red circle denotes debris flows occurring after May 12, 2008, while the purple cross represents the debris flows occurring on that day. All sample points and fitted curves are drawn in the double logarithmic coordinate system.

due to the limited rainfall duration indicated by the observations. Under these circumstances, the changes of the α_{new} could be considered as the more important aspect affected by the earthquakes.

Discussion

Rainfall Threshold Change

The impact of the Wenchuan earthquake is reported to be ca. 20–30% (Tang et al., 2009; Ma et al., 2017). Compared with these studies, debris-flow records from more timely and detailed investigations after earthquakes have been collected, especially for the Wenchuan earthquake, meaning more debris flows with smaller rainfall have been included for statistical analysis. In addition, we supplemented the data analysis on the Lushan earthquake in 2013 and the recent Jiuzhaigou earthquake in 2017, and further explored the impacts of the earthquake on regional rainfall threshold. The impacts of the Lushan and Jiuzhaigou earthquakes on I-D rainfall thresholds are smaller, which may be due to the fact that moderate magnitude earthquakes (Mw 6–7) produce less landslide-associated loose materials (Stoffel et al., 2014).

Lin et al. (2004) concludes that the triggering thresholds such as cumulative antecedent rainfall and hourly rainfall intensity significantly decreased by 33% after the Chi-Chi Earthquake compared to the values before the earthquake. Shieh et al. (2009) surveyed the Wushihkeng watershed and the Mt. Ninety-Nine watershed in the Chi-Chi earthquake area. The maximum effective cumulative rainfall threshold was about 50% of that before the earthquake. Similar outcomes can be found in the Chen-Yu-Lan watershed (Chen, 2011). The 30–50% change caused by the Chi-Chi earthquake is indeed similar to that by the Wenchuan earthquake.

Implication for Post-quake Debris-Flow Warning

As shown in **Table 2**, the moment magnitude of the Wenchuan earthquake reached 7.9, much higher than the others. Although the change in the median DER is close to that influenced by the Lushan earthquake, the α_{new} of the I-D curve in the WEA has been changed by 45%, which is nearly double in the LEA. With a similar moment magnitude, different focal depths affect the results. The change in the median DER in the LEA with a 13 km focal depth is 11% larger than the JEA with 20 km focal depth.

A warning strategy, including the DER and I-D curves can be considered by using similar settings of methods and data as in this study. The DER threshold should be the initial focus. The antecedent rainfall can be obtained from up-to-date meteorological data, such as near-real-time precipitation produced by the land data assimilation system (CLDAS) from the China Meteorological Data Service Center (http://data.cma.cn/), satellite data, and *in-situ* observation. The daily rainfall data is obtained from the weather forecast. When the earthquake magnitude is ca. 6.5 and the focal depth is ca. 20 km, the change in the rainfall threshold condition can be estimated by referring to ca. 15% in the JEA. When the magnitude is greater than 6.5, but focal depth is less than 15 km, we can refer to a threshold change of 26% in the LEA and WEA. When the DER exceeds the median DER, we may think the rainfall can reach a warning level at the first stage. However, earthquake-affected areas responded differently to the statistical approaches (**Table 2**), which may be attributed to the heterogeneity of rainfall for triggering debris flows under different surface conditions. Thus, the hourly I-D

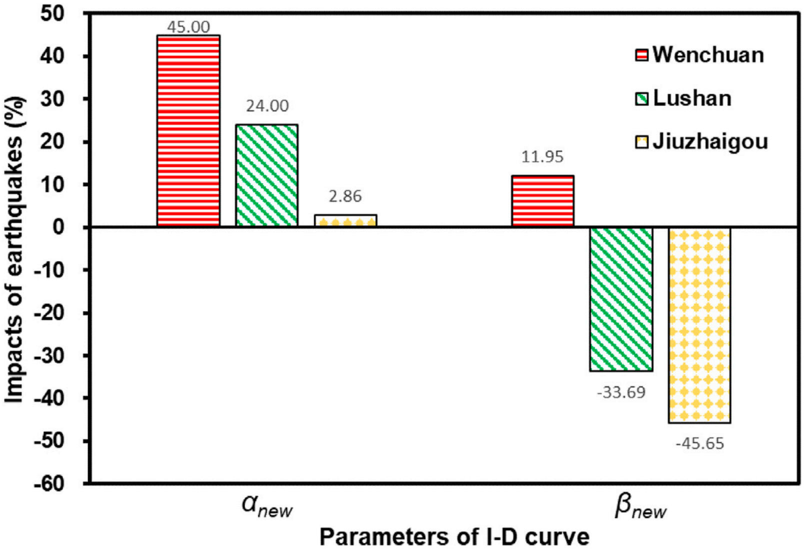

FIGURE 5 | Impacts of each earthquake on the I-D curve parameters for debris flows. The positive impact on α_{new} indicates the decrease of the scaling constant. The positive impact on β_{new} means the decrease of the shape slope.

TABLE 2 | Earthquake attributes and their impacts on regional rainfall thresholds.

Earthquake	Mw	Focal depth (km)	Impacts	
			Median of DER (%)	α_{new} (%)
Wenchuan	7.9	14	26.05	45.00
Lushan	6.6	13	26.74	24.00
Jiuzhaigou	6.5	20	15.56	2.86

curve can be used. The degree of I-D curve lowering after a strong shock are referred in **Table 2**. When the mean hourly rainfall intensity is above the curve, a regional warning should be issued.

Due to the lack of meteorological *in-situ* observations, advanced satellite-based rainfall data can be used as an effective alternative for near real-time analysis, which is widely adopted for disaster research (Jia et al., 2020). The Global Precipitation Measurement (GPM) mission, led by the National Aeronautics and Space Administration and the Japanese Aerospace Exploration Agency has been the latest generation of rainfall products since March 2014 (Hou et al., 2013). With the resolution of 0.1° and 0.5 h, the up-to-date GPM products may be suitable for near real-time analysis based on long-term historical records, which have been expanded back to start-ups (in 2000) by calibration (Huffman et al., 2019). We use the gridded rainfall dataset to check the reliability of the new GPM data for future application in debris-flow monitoring and warning. Correlation coefficients of 0.67, 0.53, and 0.56 are obtained for Jiuzhaigou, Wenchuan, and Lushan areas, respectively, (**Figure 6**), which indicates that the reliability needs to be further improved, as also confirmed by Liu et al. (2019). Though any satellite-based method will cause inevitable uncertainties (Carr et al., 2015), a combination with the methods used in this study could be an important supplement for debris-flow warning in ungauged areas with earthquakes.

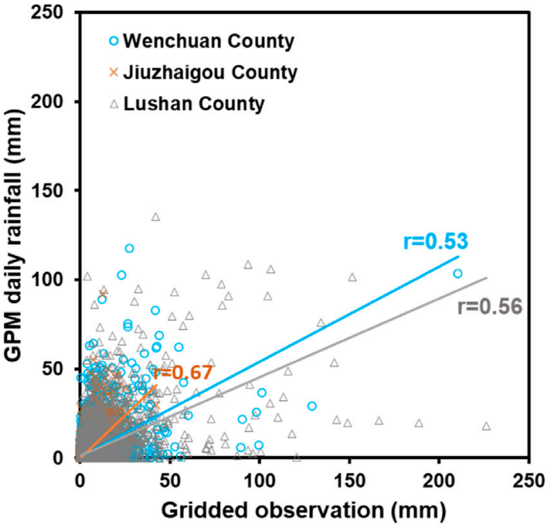

FIGURE 6 | Comparison between GPM daily rainfall data and gridded observations.

Uncertainty and Limitation

The 40 years gridded rainfall data can provide enough information for this study, but the 3 h resolution and GMT format could cause uncertainty for determining the accurate time of debris-flow occurrence. Furthermore, even if eliminating the effects of fluctuant annual rainfall, the rainfall thresholds cannot avoid abnormal distribution of rainfall within certain year. The statistics in small regions (specified high earthquake-intensity areas) depend on the local information and temporal variability (Nikolopoulos et al., 2017; Gariano et al., 2020). However, most debris-flow disasters always occur in places where there is insufficient or ineffective instrumental observation.

Figure 4 shows that effects of the Lushan and Jiuzhaigou earthquake in the curves are not very obvious as that of Wenchuan earthquake. I-D scatters obtained by other study also support the point (Guo et al., 2021). Guo et al. (2021) pointed that debris flows after Lushan earthquake are triggered by shorter-duration rainfall than in most other regions, including the Wenchuan earthquake area, which may magnify the uncertainty from the rainfall data. In addition, some regional I-D threshold is difficult to be obtained, due to the limited data which cannot meet demand for a rigorous fitting. That is why we emphasize more on the change in the I-D relationships rather than the accurate threshold.

Van Asch et al. (2014) made a link between the rainfall thresholds and sediment material delivered by seismic landslides retained in gullies. Thousands of landslides triggered by the Lushan earthquake have become the material source of debris flows (Tang et al., 2015). But the erosion of channel deposits by overland runoff after Lushan earthquake was the dominant mechanism of debris-flow formation in the LEA (Guo et al., 2021). Compared with the WEA, the debris-flow volume in the LEA is smaller, which may be due to the smaller earthquake magnitude and the wetter climate for vegetation recovery. In addition, free placement of wastes produced in post-quake reconstruction can be initiated more easily to form debris flows. The complex spatial heterogeneity of natural and anthropogenic factors makes great differences of critical rainfall conditions for debris flows in different regions. Even so, it is still difficult to isolate any other factors for discussing the earthquake effects on rainfall for triggering the debris flows.

CONCLUSION

We collected the debris-flow records in the Wenchuan, Lushan, and Jiuzhaigou earthquake-affected areas in Sichuan Province, China. Based on the gridded meteorological dataset with 3 h and 0.1° resolutions, the DER and I-D thresholds were calculated. Then, comparison of the pre and post-seismic rainfall thresholds shows the impacts of the earthquakes with different magnitudes on the rainfall thresholds. Our results demonstrate that the post-quake thresholds are much smaller than the pre-seismic thresholds. The mean impacts of the Wenchuan, Lushan, and Jiuzhaigou earthquakes are ca. 26, 27, and 16%, respectively, with respect to the DER. For the Wenchuan earthquake we found a significantly lowered I-D curve. The impacts of the Wenchuan and Chi-Chi earthquakes are comparable. In general, this work is useful for calibrating and improving the rainfall thresholds of post-quake debris-flow warning.

DATA AVAILABILITY STATEMENT

Because of tough field survey and requirements of the cooperative institutions, the debris-flow records should be requested upon approval of the corresponding author.

AUTHOR CONTRIBUTIONS

SL and KH analyzed the results, and wrote the manuscript. SL, QZ, and DT documented all the data. KH, SZ, and XH reviewed and enhanced the paper.

FUNDING

This work was supported by the National Key R&D Program of China (2018YFC1505205, 2020YFD1100701), the Science and Technology Research and Development Plan of China State Railway Group Co., Ltd. (K2019G006), and Research and Demonstration Program of Precise Warning and the Emergence Disposal Technologies against geo-hazards in the Jiuzhaigou scenic area (KJ-2018–23).

ACKNOWLEDGMENTS

We sincerely appreciate all the constructive and detailed comments from the editor Tolga Gorum and the reviewers including Joern Lauterjung and Hans-Balder Havenith. We also thank the CAS "Light of West China" Program. The 90 m elevation data can be collected from the website (http://srtm.csi.cgiar.org/srtmdata/). The gridded meteorological dataset can be accessed from National Tibetan Plateau Data Center (https://data.tpdca.aca.cn) or the website of the journal Scientific Data (https://www.nature.com/articles/s41597-020-0369-y). GPM precipitation products can be accessed from the website (https://disca.gsfca.nasa.gov/).

REFERENCES

Berti, M., Bernard, M., Gregoretti, C., and Simoni, A. (2020). Physical Interpretation of Rainfall Thresholds for Runoff-Generated Debris Flows. *J. Geophys. Res. Earth Surf.* 125, e2019JF005513. doi:10.1029/2019jf005513

Caine, N. (1980). The Rainfall Intensity - Duration Control of Shallow Landslides and Debris Flows. *Geografiska annaler: Ser. A, Phys. Geogr.* 62, 23–27. doi:10.1080/04353676.1980.11879996

Carr, N., Kirstetter, P.-E., Hong, Y., Gourley, J. J., Schwaller, M., Petersen, W., et al. (2015). The Influence of Surface and Precipitation Characteristics on TRMM Microwave Imager Rainfall Retrieval Uncertainty. *J. Hydrometeorology* 16, 1596–1614. doi:10.1175/jhm-d-14-0194.1

Chen, H., and Petley, D. N. (2005). The Impact of Landslides and Debris Flows Triggered by Typhoon Mindulle in Taiwan. *Q. J. Eng. Geology. Hydrogeology* 38, 301–304. doi:10.1144/1470-9236/04-077

Chen, J.-C. (2011). Variability of Impact of Earthquake on Debris-Flow Triggering Conditions: Case Study of Chen-Yu-Lan Watershed, Taiwan. *Environ. Earth Sci.* 64, 1787–1794. doi:10.1007/s12665-011-0981-4

Cui, P., Chen, X.-Q., Zhu, Y.-Y., Su, F.-H., Wei, F.-Q., Han, Y.-S., et al. (2011). The Wenchuan Earthquake (May 12, 2008), Sichuan Province, China, and Resulting Geohazards. *Nat. Hazards* 56, 19–36. doi:10.1007/s11069-009-9392-1

Cui, P., Zhang, J., Yang, Z., Chen, X., You, Y., and Li, Y. (2014). Activity and Distribution of Geohazards Induced by the Lushan Earthquake, April 20, 2013. *Nat. Hazards* 73, 711–726. doi:10.1007/s11069-014-1100-0

Fan, X., Scaringi, G., Xu, Q., Zhan, W., Dai, L., Li, Y., et al. (2018). Coseismic Landslides Triggered by the 8th August 2017 Ms 7.0 Jiuzhaigou Earthquake

(Sichuan, China): Factors Controlling Their Spatial Distribution and Implications for the Seismogenic Blind Fault Identification. *Landslides* 15, 967–983. doi:10.1007/s10346-018-0960-x

Gariano, S. L., Melillo, M., Peruccacci, S., and Brunetti, M. T. (2020). How Much Does the Rainfall Temporal Resolution Affect Rainfall Thresholds for Landslide Triggering? *Nat. Hazards* 100, 655–670. doi:10.1007/s11069-019-03830-x

Guo, X., Chen, X., Song, G., Zhuang, J., and Fan, J. (2021). Debris Flows in the Lushan Earthquake Area: Formation Characteristics, Rainfall Conditions, and Evolutionary Tendency. *Nat. Hazards* 106, 2663–2687. doi:10.1007/s11069-021-04559-2

Guzzetti, F., Peruccacci, S., Rossi, M., and Stark, C. P. (2007). Rainfall Thresholds for the Initiation of Landslides in central and Southern Europe. *Meteorol. Atmos. Phys.* 98, 239–267. doi:10.1007/s00703-007-0262-7

He, J., Yang, K., Tang, W., Lu, H., Qin, J., Chen, Y., et al. (2020). The First High-Resolution Meteorological Forcing Dataset for Land Process Studies over China. *Scientific Data* 7, 25. doi:10.1038/s41597-020-0369-y

Hong, S., Zhou, X., Zhang, K., Meng, G., Dong, Y., Su, X., et al. (2018). Source Model and Stress Disturbance of the 2017 Jiuzhaigou Mw 6.5 Earthquake Constrained by InSAR and GPS Measurements. *Remote Sensing* 10, 1400. doi:10.3390/rs10091400

Hou, A. Y., Kakar, R. K., Neeck, S., Azarbarzin, A. A., Kummerow, C. D., Kojima, M., et al. (2013). The Global Precipitation Measurement Mission. *Bull. Am. Meteorol. Soc.* 95, 701–722.

Hu, X., Hu, K., Tang, J., You, Y., and Wu, C. (2019). Assessment of Debris-Flow Potential Dangers in the Jiuzhaigou Valley Following the August 8, 2017, Jiuzhaigou Earthquake, Western China. *Eng. Geology.* 256, 57–66. doi:10.1016/j.enggeo.2019.05.004

Huang, R. Q., and Li, W. L. (2009). Analysis of the Geo-Hazards Triggered by the 12 May 2008 Wenchuan Earthquake, China. *Bull. Eng. Geol. Environ.* 68, 363–371. doi:10.1007/s10064-009-0207-0

Huffman, G. J., Stocker, E. F., Bolvin, D. T., Nelkin, E. J., and Tan, Jackson. (2019). "GPM IMERG Final Precipitation L3 1 Day 0.1 Degree X 0.1 Degree V06," in *Goddard Earth Sciences Data and Information Services Center (GES DISC)*. Editor A. Savtchenko, (Greenbelt, MD: National Aeronautics and Space Administration).

Jia, G., Tang, Q., and Xu, X. (2020). Evaluating the Performances of Satellite-Based Rainfall Data for Global Rainfall-Induced Landslide Warnings. *Landslides* 17, 283–299. doi:10.1007/s10346-019-01277-6

Li, C., Ma, T., Zhu, X., and Li, W. (2011). The Power-Law Relationship between Landslide Occurrence and Rainfall Level. *Geomorphology* 130, 221–229. doi:10.1016/j.geomorph.2011.03.018

Li, T.-T., Huang, R.-Q., and Pei, X.-J. (2016). Variability in Rainfall Threshold for Debris Flow after Wenchuan Earthquake in Gaochuan River Watershed, Southwest China. *Nat. Hazards* 82, 1967–1980. doi:10.1007/s11069-016-2280-6

Li, Y., Jia, D., Wang, M., Shaw, J. H., He, J., Lin, A., et al. (2014). Structural Geometry of the Source Region for the 2013 Mw 6.6 Lushan Earthquake: Implication for Earthquake hazard Assessment along the Longmen Shan. *Earth Planet. Sci. Lett.* 390, 275–286. doi:10.1016/j.epsl.2014.01.018

Lin, C.-W., Shieh, C.-L., Yuan, B.-D., Shieh, Y.-C., Liu, S.-H., and Lee, S.-Y. (2004). Impact of Chi-Chi Earthquake on the Occurrence of Landslides and Debris Flows: Example from the Chenyulan River Watershed, Nantou, Taiwan. *Eng. Geology.* 71, 49–61. doi:10.1016/s0013-7952(03)00125-x

Liu, C.-N., Huang, H.-F., and Dong, J.-J. (2008). Impacts of September 21, 1999 Chi-Chi Earthquake on the Characteristics of Gully-type Debris Flows in central Taiwan. *Nat. Hazards* 47, 349–368. doi:10.1007/s11069-008-9223-9

Liu, S., Hu, K., Zhang, S., and Zeng, Y. (2019). Comprehensive Evaluation of Satellite-Based Precipitation at Sub-Daily Time Scales over a High-Profile Watershed with Complex Terrain. *Earth Space Sci.* 6, 2347–2361. doi:10.1029/2019ea000855

Liu, S., Wei, L., and Hu, K. (2020). Topographical and Geological Variation of Effective Rainfall for Debris-Flow Occurrence from a Large-Scale Perspective. *Geomorphology* 358, 107134. doi:10.1016/j.geomorph.2020.107134

Ma, C., Hu, K., and Tian, M. (2013). Comparison of Debris-Flow Volume and Activity under Different Formation Conditions. *Nat. Hazards* 67, 261–273. doi:10.1007/s11069-013-0557-6

Ma, C., Wang, Y., Hu, K., Du, C., and Yang, W. (2017). Rainfall Intensity-Duration Threshold and Erosion Competence of Debris Flows in Four Areas Affected by the 2008 Wenchuan Earthquake. *Geomorphology* 282, 85–95. doi:10.1016/j.geomorph.2017.01.012

Nikolopoulos, E. I., Destro, E., Maggioni, V., Marra, F., and Borga, M. (2017). Satellite Rainfall Estimates for Debris Flow Prediction: An Evaluation Based on Rainfall Accumulation-Duration Thresholds. *J. Hydrometeorology* 18, 2207–2214. doi:10.1175/jhm-d-17-0052.1

Parker, R. N., Densmore, A. L., Rosser, N. J., De Michele, M., Li, Y., Huang, R., et al. (2011). Mass Wasting Triggered by the 2008 Wenchuan Earthquake Is Greater Than Orogenic Growth. *Nat. Geosci* 4, 449–452. doi:10.1038/ngeo1154

Shieh, C. L., Chen, Y. S., Tsai, Y. J., and Wu, J. H. (2009). Variability in Rainfall Threshold for Debris Flow after the Chi-Chi Earthquake in central Taiwan, China. *Int. J. Sediment Res.* 24, 177–188. doi:10.1016/s1001-6279(09)60025-1

Stoffel, M., Mendlik, T., Schneuwly-Bollschweiler, M., and Gobiet, A. (2014). Possible Impacts of Climate Change on Debris-Flow Activity in the Swiss Alps. *Climatic Change* 122, 141–155. doi:10.1007/s10584-013-0993-z

Tang, C., Ma, G., Chang, M., Li, W., Zhang, D., Jia, T., et al. (2015). Landslides Triggered by the 20 April 2013 Lushan Earthquake, Sichuan Province, China. *Eng. Geology.* 187, 45–55. doi:10.1016/j.enggeo.2014.12.004

Tang, C., Zhu, J., Li, W. L., and Liang, J. T. (2009). Rainfall-triggered Debris Flows Following the Wenchuan Earthquake. *Bull. Eng. Geol. Environ.* 68, 187–194. doi:10.1007/s10064-009-0201-6

Van Asch, T. W. J., Tang, C., Alkema, D., Zhu, J., and Zhou, W. (2014). An Integrated Model to Assess Critical Rainfall Thresholds for Run-Out Distances of Debris Flows. *Nat. Hazards* 70, 299–311. doi:10.1007/s11069-013-0810-z

Xu, X., Wen, X., Yu, G., Chen, G., Klinger, Y., Hubbard, J., et al. (2009). Coseismic Reverse- and Oblique-Slip Surface Faulting Generated by the 2008 Mw 7.9 Wenchuan Earthquake, China. *Geology* 37, 515–518. doi:10.1130/g25462a.1

Yu, B., Wu, Y., and Chu, S. (2014). Preliminary Study of the Effect of Earthquakes on the Rainfall Threshold of Debris Flows. *Eng. Geology.* 182, 130–135. doi:10.1016/j.enggeo.2014.04.007

Zhang, S., and Zhang, L. M. (2017). Impact of the 2008 Wenchuan Earthquake in China on Subsequent Long-Term Debris Flow Activities in the Epicentral Area. *Geomorphology* 276, 86–103. doi:10.1016/j.geomorph.2016.10.009

Zhao, L., Huang, Y., Chen, Z., Ye, B., and Liu, F. (2020). Dynamic Failure Processes and Failure Mechanism of Soil Slope under Random Earthquake Ground Motions. *Soil Dyn. Earthquake Eng.* 133, 106147. doi:10.1016/j.soildyn.2020.106147

Zhuang, J., Cui, P., Wang, G., Chen, X., Iqbal, J., and Guo, X. (2015). Rainfall Thresholds for the Occurrence of Debris Flows in the Jiangjia Gully, Yunnan Province, China. *Eng. Geology.* 195, 335–346. doi:10.1016/j.enggeo.2015.06.006

Conflict of Interest: The authors declare that the research was conducted in the absence of any commercial or financial relationships that could be construed as a potential conflict of interest.

frontiers in Earth Science

ORIGINAL RESEARCH
published: 08 June 2021
doi: 10.3389/feart.2021.659152

Spatial Patterns and Scaling Distributions of Earthquake-Induced Landslides—A Case Study of Landslides in Watersheds Along Dujiangyan–Wenchuan Highway

Xuemei Liu[1,2,3]†, Pengcheng Su[1,2], Yong Li[1,2]*, Rui Xu[3], Jun Zhang[1,2], Taiqiang Yang[1,2], Xiaojun Guo[1,2] and Ning Jiang[1,2]*

[1] Key Laboratory of Mountain Hazards and Surface Processes, Institute of Mountain Hazards and Environment, Chinese Academy of Sciences, Chengdu, China, [2] University of Chinese Academy of Sciences, Beijing, China, [3] Sichuan Earthquake Administration, Chengdu, China

OPEN ACCESS

Edited by:
Chong Xu,
National Institute of Natural Hazards,
Ministry of Emergency Management
(China), China

Reviewed by:
R. M. Yuan,
China Earthquake Administration,
China
Hans-Balder Havenith,
University of Liège, Belgium
Yingying Tian,
Institute of Geology, China Earthquake
Administration, China

***Correspondence:**
Pengcheng Su
supengcheng@imde.ac.cn
Yong Li
ylie@imde.ac.cn

†ORCID:
Xuemei Liu
orcid.org/0000-0001-5179-5913

Specialty section:
This article was submitted to
Geohazards and Georisks,
a section of the journal
Frontiers in Earth Science

Received: 27 January 2021
Accepted: 03 March 2021
Published: 08 June 2021

Citation:
Liu X, Su P, Li Y, Xu R, Zhang J, Yang T, Guo X and Jiang N (2021) Spatial Patterns and Scaling Distributions of Earthquake-Induced Landslides—A Case Study of Landslides in Watersheds Along Dujiangyan–Wenchuan Highway. Front. Earth Sci. 9:659152. doi: 10.3389/feart.2021.659152

Earthquake-induced landslide has various spatial characteristics that can be effectively described with the frequency–area curve. Nevertheless, the widely used power-law curve does not reflect well the spatial features of the distribution, and the power exponent does not show the association with the background factors. There is a lack of standards for building the relationship, and its implication on the spatial distribution of landslides has never been analyzed. In this study, we propose a new form of frequency distribution and explore the parameters in the typical watersheds along the highway from Dujiangyan to Wenchuan in the Wenchuan earthquake region. The obtained parameters are related to the landslide density and proportions of the large-scale landslides. Furthermore, a hot spot analysis of landslides in the watersheds is conducted to assess the relationship between the parameters and the spatial cluster patterns of landslides. The hot spots highlight the size and distance of landslide areas that cluster together, whereas the distribution parameters reflect the density and proportions of landslides. This research introduces a new method to analyze the distribution of landslides and their association with the spatial features, which can be applied to the landslide distribution in relation to other influential factors.

Keywords: earthquake landslide, hot spot analysis, frequency curve, scaling distribution, spatial pattern

INTRODUCTION

Earthquake-induced landslides have different spatial distribution characteristics, which depend on the tectonic features of the earthquake and the geomorphological conditions of landslides. For example, the 2002 Alaska earthquake is a surface rupture earthquake with the induced landslides that were obviously distributed along the long axis in the NW–SE direction of the seismic Denali fault (Gorum et al., 2011). The 2013 Lushan earthquake occurred in a hidden fault and resulted in the relatively scattered landslides with distribution over the affected area (Xu et al., 2015).

Studies have observed that landslides follow the power-law frequency–area relationship (Malamud et al., 2004; Chong et al., 2013; Xu et al., 2014; Tanyaş et al., 2017), yet there is no standard criterion for determining the power-law exponent. Cumulative and noncumulative frequency–area curves are used for the research and creation of the landslide inventories that have rainfall or earthquake origin (Fujii, 1969; Hovius et al., 1997, 2000). Landslide inventories in different regions seem to have different exponents, yet without comparability in relation to the landslide backgrounds. The landslide frequency–area curve is generally used to show the completeness of the landslide inventory. According to some researchers, the phenomenon that the tail of the frequency–area curve obeys the power law cannot be attributed to the incompleteness of data. The overall variables of landforms, especially the different forms of the slope, control the two parts of the frequency–area curve. The frequency–area distribution is the combined result of the distance to slope and the actual terrain constraints of landslide (Pelletier et al., 1997; Hovius et al., 2000; Guthrie and Evans, 2004). Some scholars have quantified the spatial distribution characteristics of the earthquake-induced landslides (Harp and Jibson, 1996; Cardinali et al., 2000; Bucknam et al., 2001; Stark and Hovius, 2001; Guzzetti et al., 2002; Brardinoni and Church, 2004; Guthrie and Evans, 2004; Malamud et al., 2004; Korup, 2005; Van Den Eeckhaut et al., 2007; Corominas and Moya, 2008; Guan, 2018). In some cases, the special probability distributions (e.g., the three-parameter inverse-gamma distribution) fit the landslide area distribution well (Malamud et al., 2004), yet no physical implications are found in the parameters. Moreover, the landslide distribution varies with time (Fan et al., 2018), but there are still no specific associations with the utilized distribution parameters.

In summary, previous studies have used the power-law distribution for the entire landslide inventory in an earthquake area, often confusing landslides with different seismic and landform conditions or even including landslides from different historical events. Therefore, the power-law exponents have no relationship with any of the specific influential factors. Furthermore, it is frequently noticed that the landslides in the subregions of the earthquake-affected area do not follow the power-law distribution at large scales. This requires a more effective method to describe the size distribution and spatial patterns of landslides in an earthquake area.

This study investigates landslides in several watersheds in the Wenchuan earthquake area based on the latest complete inventory of seismic landslides (Xu et al., 2014). A new distribution form of landslide area is proposed, and then the distribution parameters in relation to the spatial characteristics of the landslides are discussed. This method is expected to be applicable for the landslide distribution characteristics under other influencing factors.

DISTRIBUTION OF LANDSLIDES INDUCED BY THE WENCHUAN EARTHQUAKE

Data Source and the Frequency–Area Curve

The landslide inventory used in the study was published in 2014 (Xu et al., 2014). It is based on 86 high-resolution images with pre- and post-earthquake interpretations, including aerial photographs with 1-, 2-, 2. 4-, and 5-m resolutions, SPOT 5 with a 2.5-m resolution, CBERS02B with a 19.5-m resolution, IKONOS with a 1-m resolution, ASTER with a 15-m resolution, IRS-P5 with a 2.5-m resolution, QuickBird with 0.6- and 2.4-m resolutions, and ALOS with a 2.5-m resolution. The inventory contains 197,481 landslides with a total area of 1,160 km^2, and individual landslide areas range from 0.00003 to 6.972824 km^2, covering an area of 110,000 km^2 (**Figure 1**). This inventory provides more detailed landslide data and is referenced according to Harp's earthquake landslide distribution cataloging and mapping rule. Accordingly, more small-scale landslides were identified, and the result is more complete and closer to the actual situation of the Wenchuan earthquake landslide (Harp and Jibson, 1996; Xu et al., 2014).

In the process of obtaining the frequency–area curve, binning is used to divide landslide areas, and both equivalent and inequivalent bin widths are used. The inequivalent bin width increased with the increase of landslide area, so the bin widths are approximately equal in logarithmic coordinates (Malamud et al., 2004). Each bin includes the proportion of the area occurrence, and both cumulative and noncumulative proportions are used. It is generally observed that the frequency–area curve has a straight line for medium and large landslides, which implies that the distribution satisfies the power law:

$$P(> A) = cA^{-\alpha} \tag{1}$$

where A is the landslide area, $P(>A)$ is the cumulative proportion of landslides with areas greater than A, and c and α are parameters. Similarly, the noncumulative curve also applies to the distribution in many cases:

$$p(A) = c'A^{-\beta} \tag{2}$$

where $p(A)$ is the noncumulative proportion of landslides, and c' and β are parameters.

For the present case, we put forward the cumulative frequency–area curve of the entire landslides (**Figure 2**), which shows the power-law range from 0.1 to 1 km^2, with $c = 1.234 \times 10^{-5}$, $\alpha = 2.46741$, and $R^2 = 0.9976$.

This differs remarkably in the power exponent compared with the result of Xu et al. (2014), who used the same data and obtained $c = 13$, $\alpha = 2.0745$, and $R^2 = 0.9931$, ranging from 0.01 to 1 km^2. It illustrates that the power-law curve strongly depends on the processing method and that the same data may result in different exponents. Moreover, even if the power-law curve holds, it covers only a very small portion of the landslide (about less than 10 or 1%). There is no detailed study on the power-law parameters, partly because in the process of obtaining the landslide frequency–area relationship, some researchers used an equivalent bin width, whereas others used inequivalent, some used cumulative frequency–area, whereas others used noncumulative (Fujii, 1969; Hovius et al., 1997, 2000). There is no uniform standard for the bin width and proportion of area, and the valid range of fitting line is greatly influenced by subjective factors, which has greatly influenced the distribution of parameters. Therefore, it is difficult to analyze

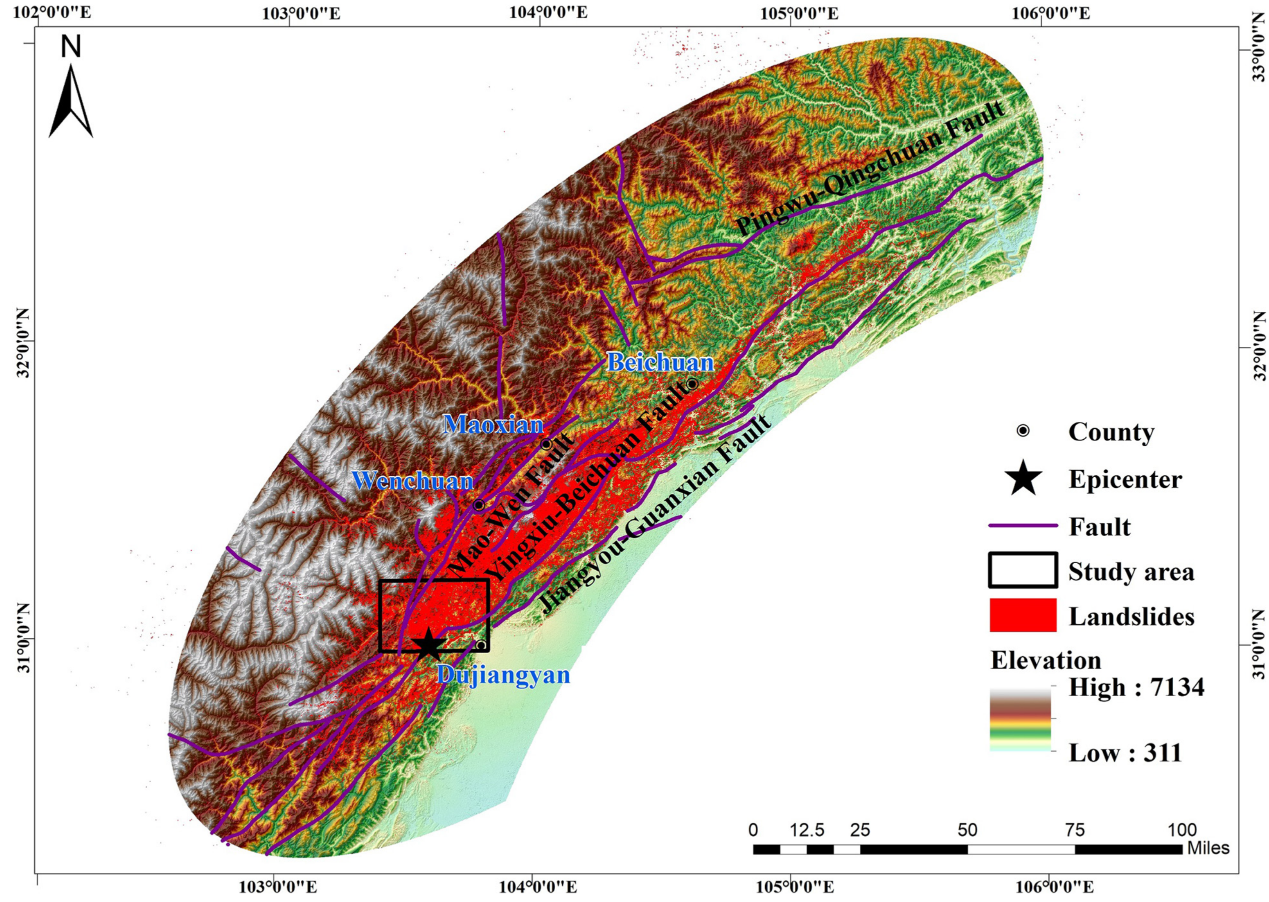

FIGURE 1 | Spatial distribution of landslides in the Wenchuan earthquake region.

these parameters and to use them for the analysis of the spatial characteristics of landslides.

Study Area

The power-law curve is usually applied to the entire inventory of earthquake-induced landslides. This inevitably confuses landslides with different geological and geomorphological conditions and makes the power exponent meaningless in relation to the influencing factors. Therefore, it is necessary to consider landslides in certain control conditions. For example, we can consider landslides in watersheds under similar seismic and geological conditions, and it should reflect the landslide distribution under geomorphological conditions. Watershed is taken as a unit area because it is a natural site where landslides occur, and all influential factors can be conveniently determined in an individual watershed.

The suitable area for this study should have the following characteristics: (i) different landslide density distributions, (ii) different topographies, and (iii) greatly affected by earthquakes, namely with a similar background but local differences. Thus, for the study area, we selected the region along the highway from Dujiangyan to Wenchuan (DW) in the Wenchuan county in the Sichuan province. The study area is approximately 1,200 km^2. The Wenchuan earthquake created 1×10^9 m^3 of landslides along the highway, damaged 80% of the road, more than 10 km was completely covered by the collapsed material, more than 50 bridges were damaged, and traffic was disrupted, causing great difficulties for disaster relief (Zhuang et al., 2010). The epicenter is near the region and lies in its middle and lower part, with the Longmenshan (LMS) fault passing through the region from southwest to northeast. The fault broke from the epicenter to the northeast, so landslides were more severe in the northeast from the epicenter than in the southwest (**Figure 1**).

The distance to the fault in the study area is from 3 to 18 km, and the peak ground acceleration is from 0.56 to 1.32 g in the Wenchuan earthquake. Mountains and steep gorges characterize this region, the high terrain is in the northwest, and the low terrain is in the southeast, the elevation is from 1,014 to 4,450 m, and the average slope angle is from 30 to 35°. Lithologies are mainly granitoid and intermediate with coal seam, pyroxene, and other sedimentary rocks. Belonging to the mountainous subtropical humid monsoon climate zone, it is one of the rainfall centers in the western Sichuan province, where heavy rain often occurs.

In this study, a digital elevation model with a resolution of 30 m was adopted, and a SWAT modular of ArcGIS was used

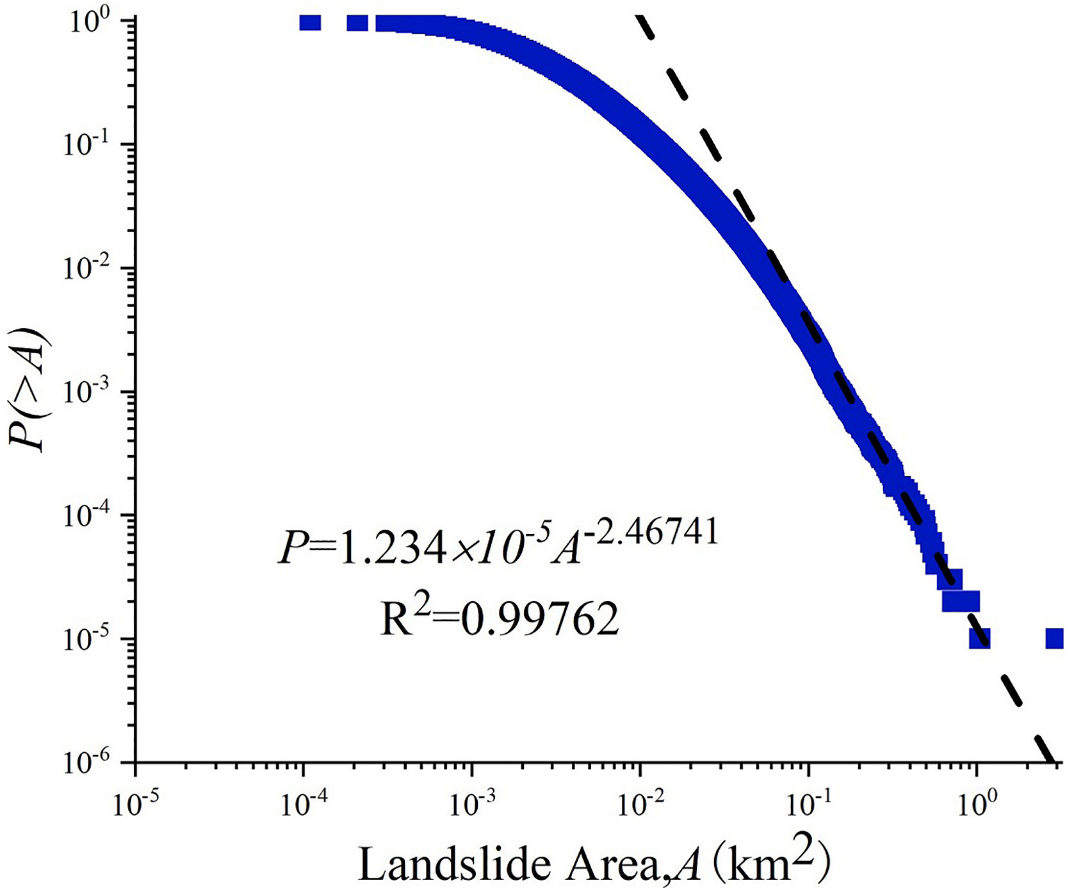

FIGURE 2 | Double logarithm chart of the cumulative frequency–area of the landslides.

to divide the study area into watersheds. This study included 11 watersheds along the DW highway and a total of 11,631 landslides with an area of 66.82 km^2. The watersheds are the Longtan (LT) watershed, the Xingfu (XF) watershed, the Taiping (TP) watershed, the Yeniu (YN) watershed, the Chediguan (CDG) watershed, the Luoquanwan (LQW) watershed, the Dayin (DY) watershed, the Huanglian (HL) watershed, the Xiaogou (XG) watershed, the Zhuanjinglou (ZJL) watershed, and the Qicenglou (QL) watershed. Among them, the XG watershed has the largest total number of landslides (TNl) (2,441), whereas the smallest number of landslides (166) is in the ZJL watershed. The largest total landslide area (TAl) (11.11021 km^2) is in the XG watershed, whereas the smallest is in the ZJL watershed (0.421146 km^2), as shown in **Figure 3** and **Table 1**.

LANDSLIDE DISTRIBUTION IN WATERSHEDS

Scaling Distribution

Considering the characteristics of landslide distribution in the study area, we used the equivalent bin width. The bin interval was set at 0.0001 km^2, and by using the cumulative curves, we found that the curves do not follow the power-law form even on the tails (**Figure 4**). Rather, we found that the landslides of all scales are subject to a scaling distribution (Eq. 3) that combines the power-law with the exponential distribution (Yong et al., 2013, 2017):

$$P(>A) = CA^{-\rho}\exp(-A/A_c) \tag{3}$$

where, C, ρ, and A_c are the parameters listed in **Table 2**.

We found that C and ρ are related by a logarithmic relation (**Figure 5**), which means C is not independent, and the distribution is determined by the parameters ρ and A_c. It is expected to be derived from some underlying probability distributions. Accordingly, the distribution is reduced to the pair ρ and A_c.

We found that ρ can well reflect the density of the landslide area (Dl), and A_c coincides with Pl, the proportion of large landslides, with a lower limit of 0.01 km^2 as determined by A_c (**Figure 6**).

As for ρ and A_c, we found that they are linearly related in six watersheds and show a discrepancy in the other five watersheds. Two points (CDG watershed, LQW watershed) have deviated from the fitting line and are located on the left and above the line, whereas three of them (TP watershed, XG watershed, LT watershed) are on the right and below the line, meaning that

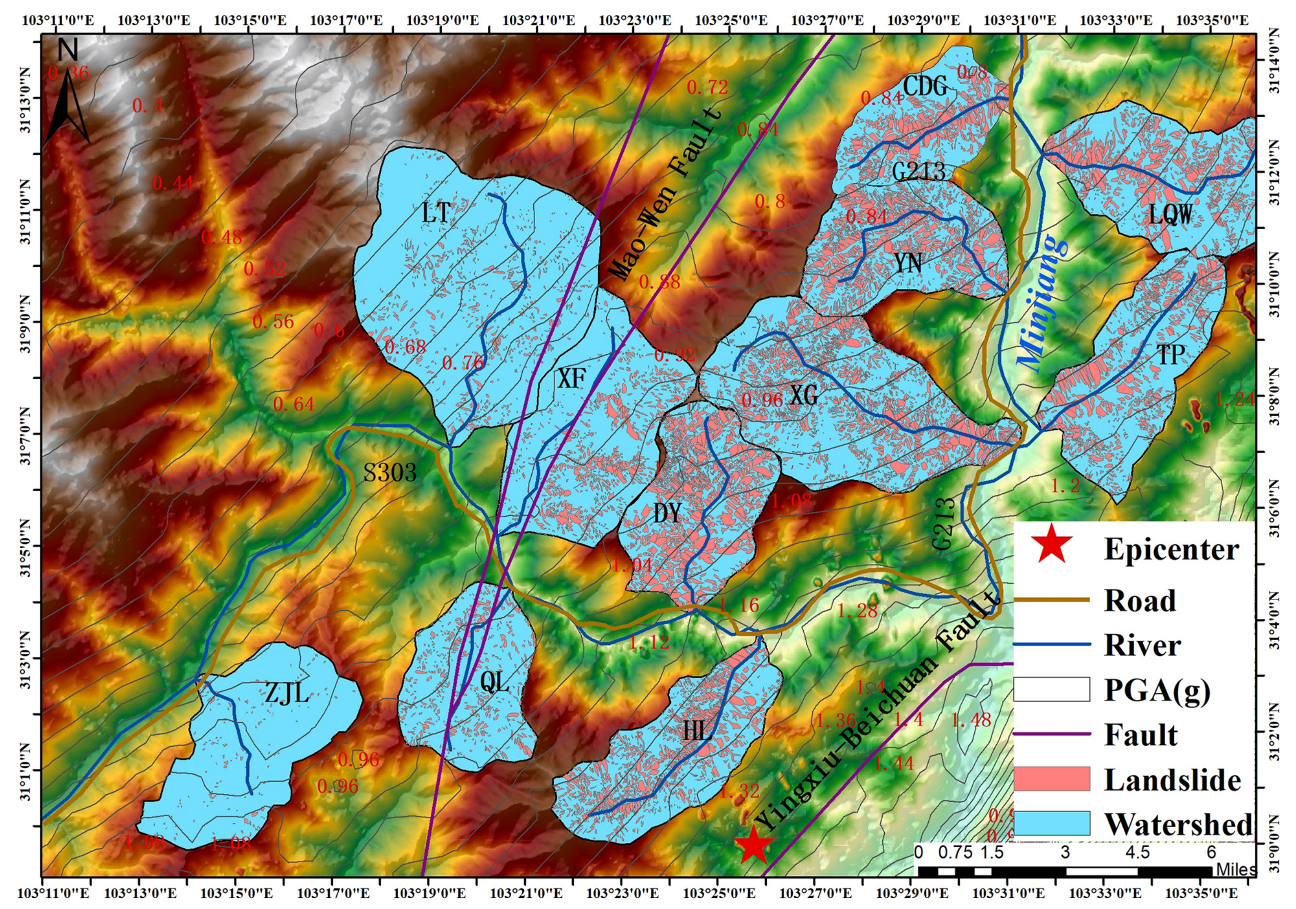

FIGURE 3 | Landslides within 11 watersheds along the highway from Dujiangyan to Wenchuan (DW).

TABLE 1 | Attributes of Watersheds.

Watershed	Elevation (m)	Df (km)	PGA (g)	TAw (km^2)	TNI	Tal (km^2)	NI	DI	PI	MI
LT	1,617–4,450	18	0.56–0.88	55.0178	892	2.7234	45	0.0495	0.0504	0.0454
XF	1,666–3,291	11	0.92–1	32.4855	830	4.2417	84	0.1306	0.1012	0.1169
TP	1,014–3,478	4	1.08–1.24	25.3097	1116	6.5060	139	0.2571	0.1246	0.1882
YN	1,117–3,689	10	0.84–0.96	23.2927	1409	8.8280	221	0.3790	0.1568	0.1521
CDG	1,072–2,984	15	0.8–0.84	16.8441	627	5.2091	135	0.3093	0.2153	0.1181
LQW	1,317–3,433	8	0.88–1.12	28.2474	967	8.2407	215	0.2917	0.2223	0.2340
DY	1,625–3,975	8	0.96–1.12	23.4656	1390	10.1355	237	0.4319	0.1705	0.2694
HL	1,236–3,775	3	1.16–1.28	24.6464	1233	7.0097	183	0.2844	0.1484	0.1159
XG	1,030–3,460	5	0.88–1.16	40.1529	2441	11.1102	255	0.2767	0.1045	0.2135
ZJL	2,053–2,956	14	0.84–1.04	27.8276	166	0.4211	5	0.0151	0.0301	0.0179
QL	1,549–3,734	10	0.96–1.08	21.0836	560	2.3943	45	0.1136	0.0804	0.0550

Distance to fault (Df); Total area of watershed (TAw); Total number of landslides (TNl); Total area of landslides (TAl); Number of large-scale landslides (Nl); Density of landslide area (Dl); Proportion of large-scale landslides (Pl); Maximum landslide area (Ml); Peak ground acceleration (PGA). A large-scale landslide has a landslide area greater than 0.01 km^2.

A_c of the CDG watershed and the LQW watershed are higher than ρ, whereas A_c of the TP watershed, the XG watershed, and the LT watershed are lower than ρ (**Figure 7**). Accordingly, we considered that the number of large-scale landslides is more than small-scale landslides in the CDG and LQW watersheds, but the small-scale landslides have a major part within the TP watershed and the XG watershed.

The tail landslide distribution within watersheds did not satisfy the power law. Landslides of all scales are subject to the scaling distribution and not just the tail of the distribution. ρ and

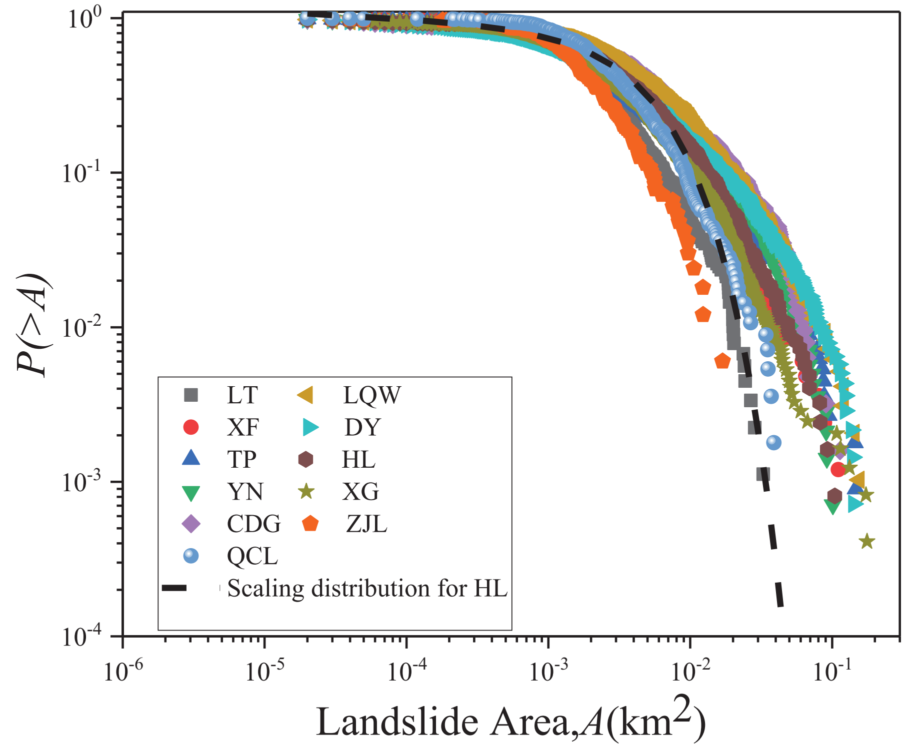

FIGURE 4 | Scaling distribution of landslides within 11 watersheds.

Ac can reflect the density of the landslide area and the proportion of the large landslides, respectively.

Spatial Analysis

After the analysis discussed earlier, we examine the spatial distribution characteristics of landslides within the watersheds. We have noticed that landslides inside the watersheds can be clarified in three categories, as shown in **Figure 8**. The first type includes the watersheds ZJL, QL, LT, and XF. Their ρ values are negative, their landslide densities and areas are small, and distributions are dispersed (**Figure 8A**). The second type includes the watersheds HL, CDG, LQW, and XG. Their ρ values are from 0.0455 to 0.0642, and their landslide densities and the degree of concentration are higher than in the four watersheds mentioned before (**Figure 8B**). The third type includes the watersheds TP, YN, and DY. Their ρ values (from 0.0817 to 0.1191) and densities are the highest among the three types of watersheds (**Figure 8C**). From the analysis discussed earlier, it can be seen

TABLE 2 | Landslide distribution parameters in watersheds.

Watershed	C	ρ	A_c	R^2
LT	1.2889	−0.0161	0.0022	0.9915
XF	1.0721	−0.0036	0.0037	0.9926
TP	0.4832	0.0817	0.0044	0.9785
YN	0.4117	0.0971	0.0065	0.9874
CDG	0.6144	0.0468	0.0081	0.9933
LQW	0.6046	0.0538	0.0075	0.9891
DY	0.3207	0.1191	0.0079	0.9851
HL	0.6578	0.0455	0.0051	0.9895
XG	0.5545	0.0642	0.0043	0.9898
ZJL	2.0410	−0.0699	0.0017	0.9948
QL	1.3378	−0.0249	0.0032	0.9938

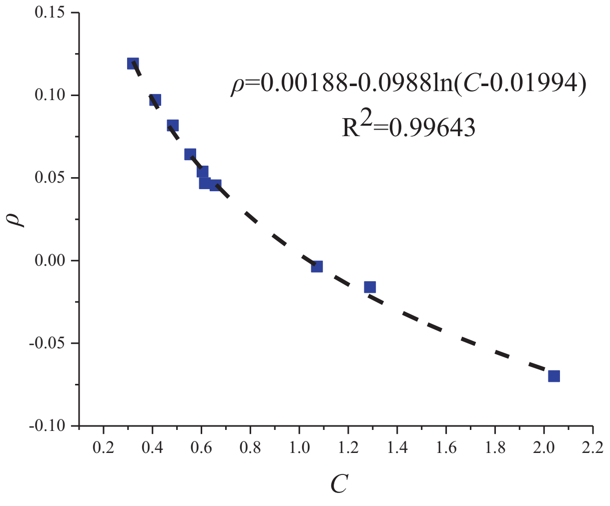

FIGURE 5 | *C*–ρ relationship of the distribution.

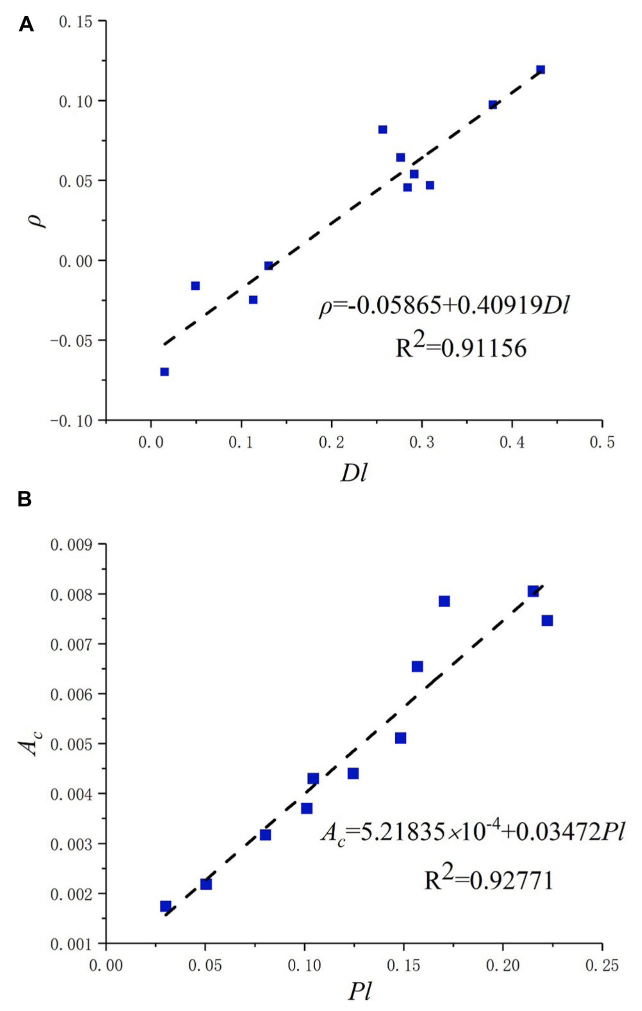

FIGURE 6 | (A) ρ–Dl and **(B)** A_c–Pl relationship for landslides in the study watersheds.

that ρ value could reflect the landslide density. We then analyzed the relationship between A_c and the spatial distribution of landslides. The proportions of the large-scale landslides are small within the watersheds ZJL, LT, QL, and XF, and their A_c values are the smallest and range from 0.0017 to 0.0037 (**Figure 9A**). Higher proportions of the large-scale landslides are noticed within the watersheds XG, TP, HL, and YN, and their A_c values range from 0.0043 to 0.0065 (**Figure 9B**). The number and the degree of concentration of the large-scale landslides within the watersheds LQW, DY, and CDG are higher, and their A_c values are the highest and range from 0.0075 to 0.0081 (**Figure 9C**).

In addition, we found that the watersheds with the lowest A_c values are also those with the lowest ρ values, such as the watersheds ZJL, LT, QL, and XF (**Figures 8A**, **9A**). However, the medium and large values of the two parameters are not consistent. For example, the CDG watershed and the LQW watershed have medium ρ values and large A_c values. We then assessed their spatial distribution characteristics and found that the CDG watershed and the LQW watershed have more large-scale landslides than other watersheds. These landslides are concentrated together, and despite their medium densities, their A_c values are large, and ρ values are medium (**Figures 8**, **9**). In contrast, more medium- and small-scale landslides are dispersed within the TP watershed despite large densities in the watershed; their A_c values are medium, and ρ values are large (**Figures 8**, **9**). This characteristic may well prove our conclusion that the proportion of the large-scale landslides is higher than the small-scale landslides within the CDG and LQW watersheds, but within the TP watershed is the opposite. We found that the CDG watershed has the highest A_c value, and the landslide concentrate degree of this watershed is one of the greatest. Thus, we conjectured that A_c could reflect the concentration degree of large landslides, which is expected to be confirmed by sufficient data.

HOT SPOT ANALYSIS

Z-Scores for the Watersheds

To analyze the concentrated degree of landslides within the watersheds, we performed a hot spot analysis using the Getis-Ord Gi* tool of ArcGIS, which provides a value related to the clustering of landslides. Taking the landslide area as weight, this tool works by looking at each landslide in the context of a neighboring landslide to calculate which features with either high or low values are spatially clustered. In our research, high and low values correspond to large and small landslide areas, respectively. A landslide with a large area surrounded by landslides with a large area will be defined as a statistically significant hot spot. The local sum for one landslide and its neighbors is proportionally compared with the sum of all landslides in the region. When the local sum is very different from the expected local sum and when that difference is too large to result from a random chance, a statistically significant Z-score will be generated (Eq. 4). The larger the value of the statistically significant positive Z-scores, the more intensive is the clustering of high values (hot spot). For statistically significant negative Z-scores, the smaller the Z-score, the more intensive the clustering of low values (cold spot). There is no obvious spatial clustering if the Z-score is close to zero (not significant) [Copyright(C) 1995–2013 Esri]:

$$Z = \frac{\sum_{j=1}^{n} \omega_{i,j} x_j - \bar{X} \sum_{j=1}^{n} \omega_{i,j}}{S\sqrt{\frac{[n\sum_{j=1}^{n} \omega_{i,j}^2 - (\sum_{j=1}^{n} \omega_{i,j})^2}{n-1}}} \tag{4}$$

where x_j is the area of jth landslide, $\omega_{i,j}$ is the weight of the distance between ith landslide and landslide jth, and n is the total number of landslides:

$$\bar{X} = \frac{\sum_{j=1}^{n} x_j}{n} \tag{5}$$

$$S = \sqrt{\frac{\sum_{j=1}^{n} x_j^2}{n} - (\bar{X})^2} \tag{6}$$

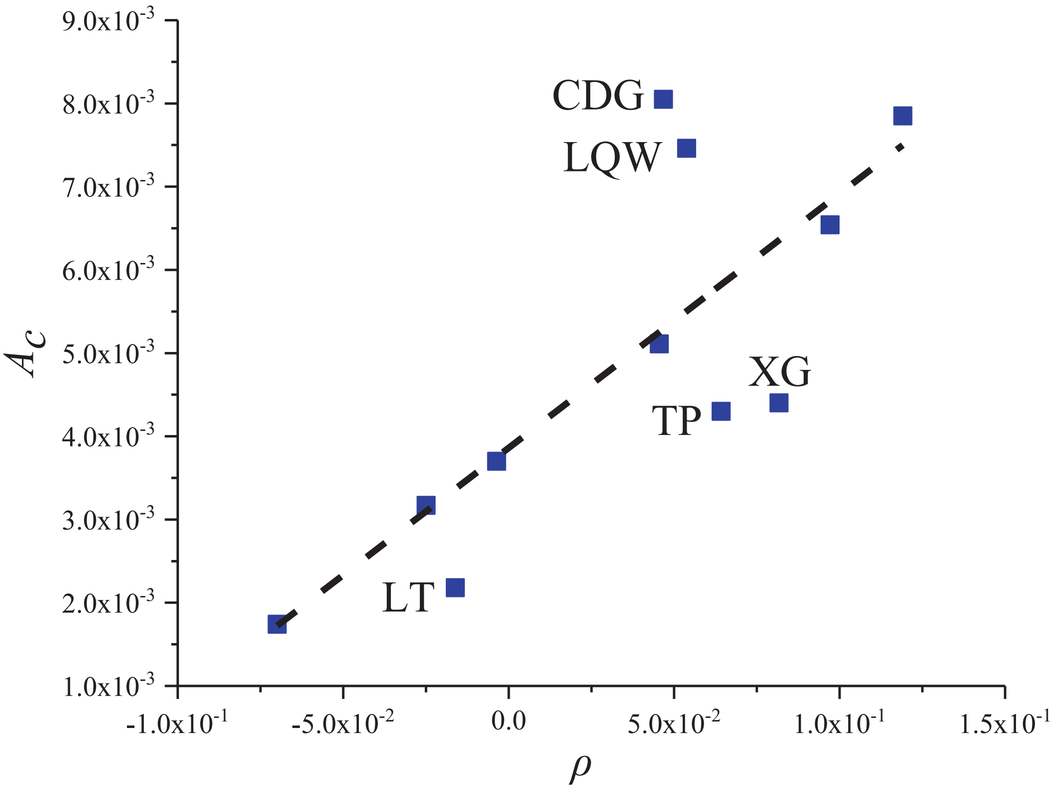

FIGURE 7 | ρ–A_C relationship for landslides in 11 watersheds.

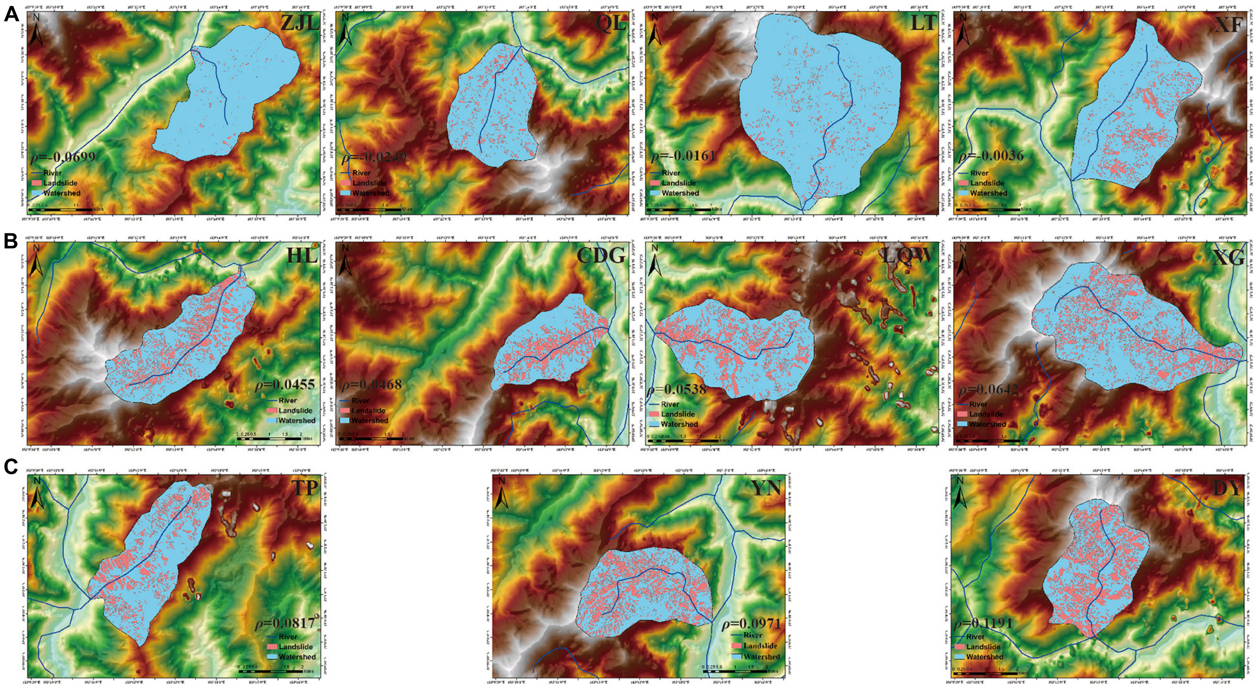

FIGURE 8 | Classified ρ and corresponding spatial distribution of landslides within watersheds.

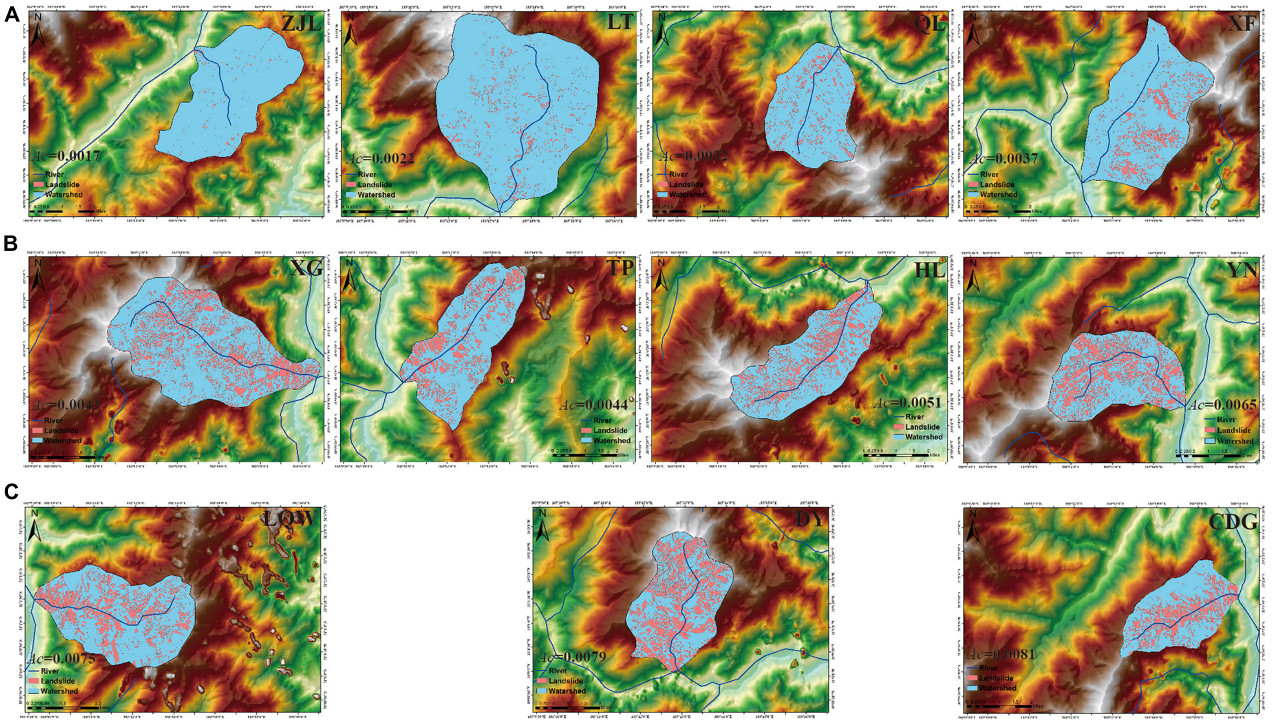

FIGURE 9 | Classified A_c and corresponding spatial distribution of landslides within watersheds.

To analyze the clustering degrees within the watersheds, we calculated the Z-score sum for hot spots (Zsh), the number of hotspots (Nh), the average Z-score for hot spots (Zah), the number of cold spots (Nc), the Z-score sum for cold spots (Zsc), and the average Z-score for cold spots (Zac), as shown in **Table 3**.

Distribution Parameters and Z-Scores

The sum of the Z-scores for hot spots (Zsh) and the sum of the Z-scores for cold spots (Zsc) have corresponding relations with ρ, as shown in **Figures 10A,B**. However, the Z-scores have no linear relationship with A_c, as shown in **Figures 10C,D**. (Notes: The ZJL watershed does not have a cold spot, and there are only 10 watersheds for Zsc-ρ and Zsc-A_c.)

Although the CDG watershed has the highest A_c, the sum of the Zsh is not the highest in this watershed, but it is the highest in the XG watershed, as shown in **Tables 2**, **3**. We then observed the hot spots distribution of landslides with the two watersheds (**Figure 11**) and found that the CDG watershed has many concentrated landslides, but their areas are not as large as the landslides inside the XG watershed. As the Z-score is affected by the landslide area, the larger area leads to a higher Z-score. That is why the Z-score for hot spots of the CDG watershed is lower than the XG watershed. In addition, despite the total number of landslides within the CDG watershed is smaller than in the XG watershed, the proportion of the large-scale landslides with the CDG watershed is greater than within the XG watershed, so A_c of the CDG watershed is greater. We then analyzed the watersheds with small-scale landslides to determine whether they conform to this rule. The XF watershed and the QL watershed have low landslide density, low A_c and ρ values, low sums of Zsh, but the sum of the Zsc are high because of small-scale landslides within the two watersheds are in the majority (**Table 3** and **Figure 11**). We consider that A_c of the total landslide within the watershed could not reflect the local spatial clustering degree of landslides. Because the hot spots analysis is more focused on the size and distance of landslides that are clustered together, A_c is more focused on the proportion of the large-area landslides within the watershed.

TABLE 3 | Z-scores of watersheds.

Watershed	Zsh	Nh	Zah	Nc	Zsc	Zac
LT	414.5329	143	2.8988	172	−339.0281	−1.9711
XF	282.9456	92	3.0755	19	−33.8098	−1.7795
TP	448.2614	100	4.4826	283	−604.0893	−2.1346
YN	586.8547	195	3.0095	350	−820.0218	−2.3429
CDG	311.6820	128	2.4350	75	−163.3526	−2.1780
LQW	383.3916	131	2.9720	161	−320.6247	−1.9915
DY	550.4717	191	2.8821	549	−1716.4727	−3.1265
HL	399.0793	129	3.1178	173	−358.7550	−2.0737
XG	854.9474	281	3.0425	433	−962.4430	−2.2227
ZJL	80.3711	29	2.7714	0	–	–
QL	169.6324	64	2.6505	45	−86.8006	−1.9289

ZJL watershed does not have a cold spot because the distance between landslides with a small area in this watershed is too far to meet the clustering conditions.

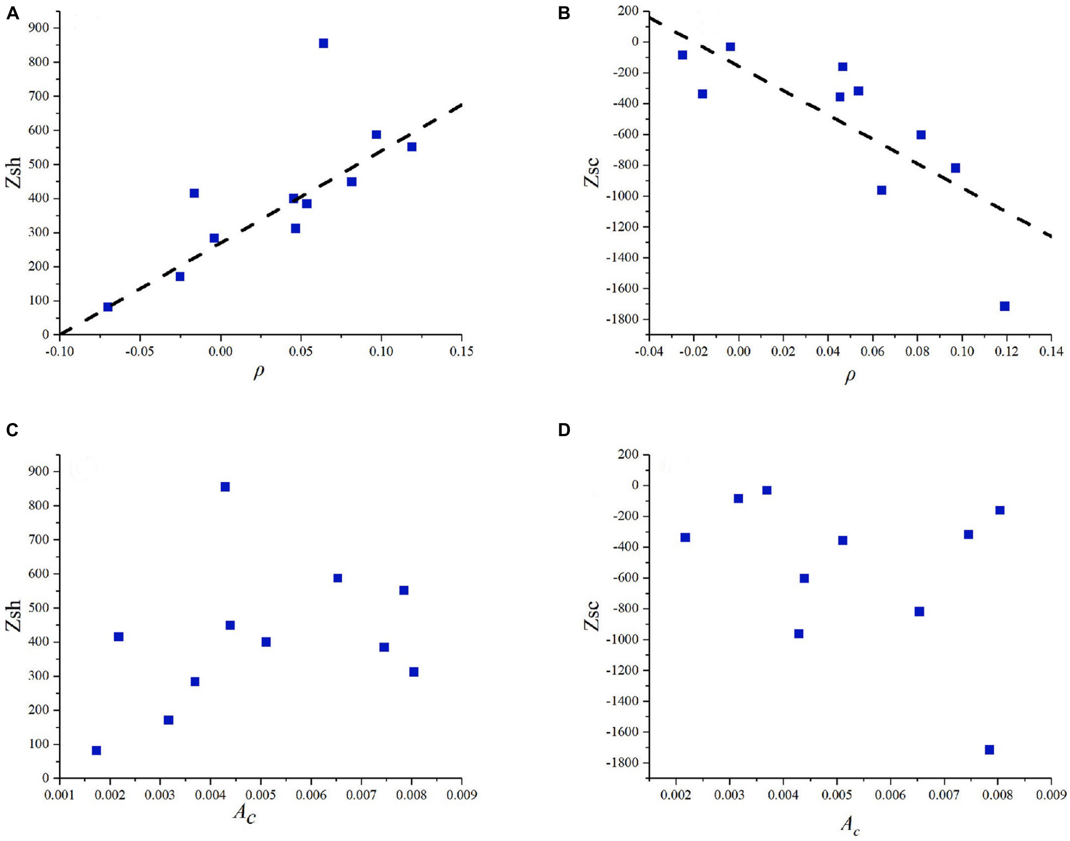

FIGURE 10 | Distribution parameters in relation to hot spot **(A)** Zsh–ρ a, **(B)** Zsc–ρ, **(C)** Zsh–A_c, **(D)** Zsc–A_c relationship.

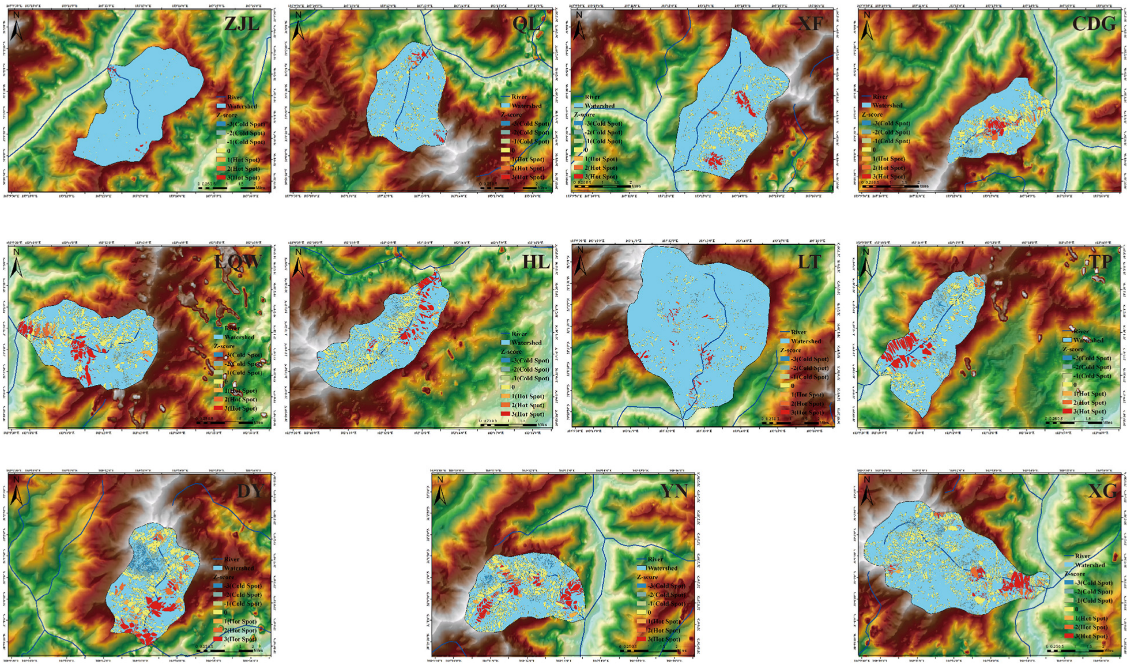

FIGURE 11 | Distribution of hot spots and cold spots within watersheds.

In addition, by analyzing the hot spots, we found that the large-scale landslides are located in the lower part of the watersheds and concentrated near the outlets of the watersheds or the sub-watersheds; the small-scale landslides are located in the middle or upper part of the watersheds and were always far from the outlets, as shown in **Figure 11**.

DISCUSSION AND CONCLUSION

Research generally considers that the tail of the landslide frequency–area relationship fits the power law, but the relationship between parameters and the spatial distributions has never been analyzed. There is no standard for building the frequency–area, and the range of fitting with power-law is greatly influenced by subjective factors. Therefore, it is difficult to relate the power exponent to the spatial distribution of landslides. We considered landslides in typical watersheds and found that the cumulative frequency satisfies the scaling distribution. The watershed with low density, small area of landslides, and low proportion of the large-scale landslides and clustering degree has small ρ, *Ac,* and Z-score values. If A_c is greater than ρ, then the large-scale landslides are more frequent than the small-scale landslides, whereas when ρ is greater than A_c, the landslide distribution characteristics are the opposite. Watershed can have a high Z-score and high density of landslides, yet not necessarily high A_c because the Z-score is affected by the landslide area. On the contrary, a watershed with a large proportion of large-scale landslides and high A_c yet the small landslides area will reduce the Z-score.

In our research, the cumulative frequency–area of landslides within several watersheds satisfies a scaling distribution that derives two parameters: the exponent ρ and the characteristic area A_c. It was found that the two parameters reflect the landslide density and the proportion of the large-scale landslides, respectively, and that the relationships are determined by the data. We then performed a hot spot analysis to investigate the relationship between the parameters and the spatial clustering degree of landslides. From the analysis, we consider that the hot spot analysis emphasizes the size and distance of landslide area, which clusters together. A_c emphasizes the proportion of the large-area landslide within the watershed, whereas ρ emphasizes the density of the landslides.

In addition, considering the watershed as a spatial cell rather than a grid is more in line with the natural characteristics of the landslide and can provide more details on the spatial distribution of landslides within a watershed. In this research, the watershed is considered as a factor of landslide division; it is expected that the same method can be easily used for landslide distribution under other influential factors.

DATA AVAILABILITY STATEMENT

The original contributions presented in the study are included in the article/supplementary material, further inquiries can be directed to the corresponding author/s.

AUTHOR CONTRIBUTIONS

All authors listed have made a substantial, direct and intellectual contribution to the work and approved it for publication.

FUNDING

This study was supported by the Strategic Priority Research Program of the Chinese Academy of Sciences (Grant No. XDA23090202), the Key International S&T Cooperation Project (Grant No. 2016YFE0122400), the Key consulting projects of Chinese Academy of Engineering (2019-XZ-18), the NSF of China (No. 42074023), the NSF of China (No. 41704014), the Earthquake Science and Technology Spark Project (XH20051), the Key R&D Projects of Sichuan Province (2020YFS0451), the Special Seismic Science and Technology Project of Sichuan Earthquake Administration (LY1814), and the Technology Innovation Fund of Sichuan Earthquake Agency (No. 201803).

REFERENCES

Brardinoni, F., and Church, M. (2004). Representing the landslide magnitude–frequency relation: Capilano River basin, British Columbia. *Earth Surf. Proces. Landform. J. Br. Geomorphol. Res. Group* 29, 115–124. doi: 10.1002/esp.1029

Bucknam, R. C., Coe, J. A., Chavarría, M. M., Godt, J. W., Tarr, A. C., Bradley, L. A., et al. (2001). *Landslides Triggered by Hurricane Mitch in Guatemala–Inventory and discussion. US Geological Survey Open File Report*. Reston, VA: U.S. Geological Survey, 1.

Cardinali, M., Ardizzone, F., Galli, M., Guzzetti, F., and Reichenbach, P. (2000). "Landslides triggered by rapid snow melting: the December 1996–January 1997 event in Central Italy," in *Proceedings of the 1st Plinius Conference on Mediterranean Storms*, (Cosenza: Bios), 439–448.

Chong, X. U., Xiwei, X., Xiyan, W. U., Fuchu, D. A. I., Xin, Y., and Qi, Y. (2013). Detailed catalog of landslides triggered by the 2008 Wenchuan earthquake and statistical analyses of their spatial distribution. *J. Eng. Geol.* 21, 25–44.

Corominas, J., and Moya, J. (2008). A review of assessing landslide frequency for hazard zoning purposes. *Eng. Geol.* 102, 193–213. doi: 10.1016/j.enggeo.2008.03.018

Fan, X., Domènech, G., Scaringi, G., Huang, R., Xu, Q., Hales, T. C., et al. (2018). Spatio-temporal evolution of mass wasting after the 2008 M w 7.9 Wenchuan earthquake revealed by a detailed multi-temporal inventory. *Landslides* 15, 2325–2341. doi: 10.1007/s10346-018-1054-5

Fujii, Y. (1969). Frequency distribution of landslides caused by heavy rainfall. *J. Seismol. Soc. Jpn.* 22, 244–247.

Gorum, T., Fan, X., van Westen, C. J., Huang, R. Q., Xu, Q., Tang, C., et al. (2011). Distribution pattern of earthquake-induced landslides triggered by the 12 May 2008 Wenchuan earthquake. *Geomorphology* 133, 152–167. doi: 10.1016/j.geomorph.2010.12.030

Guan, X. (2018). *Study on Risk Assessment of Landslide in Yunnan Province*. Ph.D. dissertation. Beijing: China University of Mining and Technology.

Guthrie, R. H., and Evans, S. G. (2004). Magnitude and frequency of landslides triggered by a storm event, Loughborough Inlet, British Columbia.

Nat. Hazard. Earth Syst. Sci. 4, 475–483. doi: 10.5194/nhess-4-475-2004

Guzzetti, F., Malamud, B. D., Turcotte, D. L., and Reichenbach, P. (2002). Power-law correlations of landslide areas in central Italy. *Earth Planet. Sci. Lett.* 195, 169–183. doi: 10.1016/s0012-821x(01)00589-1

Harp, E. L., and Jibson, R. W. (1996). Landslides triggered by the 1994 Northridge, California, earthquake. *Bull. Seismol. Soc. Am.* 86, S319–S332.

Hovius, N., Stark, C. P., and Allen, P. A. (1997). Sediment flux from a mountain belt derived by landslide mapping. *Geology* 25, 231–234. doi: 10.1130/0091-7613(1997)025<0231:sffamb>2.3.co;2

Hovius, N., Stark, C. P., Hao-Tsu, C., and Jiun-Chuan, L. (2000). Supply and removal of sediment in a landslide-dominated mountain belt: central Range, Taiwan. *J. Geol.* 108, 73–89. doi: 10.1086/314387

Korup, O. (2005). Geomorphic imprint of landslides on alpine river systems, southwest New Zealand. *Earth Surf. Proces. Landform.* 30, 783–800. doi: 10.1002/esp.1171

Malamud, B. D., Turcotte, D. L., Guzzetti, F., and Reichenbach, P. (2004). Landslide inventories and their statistical properties. *Earth Surf. Proces. Landform.* 29, 687–711. doi: 10.1002/esp.1064

Pelletier, J. D., Malamud, B. D., Blodgett, T., and Turcotte, D. L. (1997). Scale-invariance of soil moisture variability and its implications for the frequency-size distribution of landslides. *Eng. Geol.* 48, 255–268. doi: 10.1016/s0013-7952(97)00041-0

Stark, C. P., and Hovius, N. (2001). The characterization of landslide size distributions. *Geophys. Res. Lett.* 28, 1091–1094. doi: 10.1029/2000gl008527

Tanyaş, H., Van Westen, C. J., Allstadt, K. E., Anna Nowicki Jessee, M., Görüm, T., Jibson, R. W., et al. (2017). Presentation and analysis of a worldwide database of earthquake−induced landslide inventories. *J. Geophys. Res. Earth Surface* 122, 1991–2015. doi: 10.1002/2017jf004236

Van Den Eeckhaut, M., Poesen, J., Govers, G., Verstraeten, G., and Demoulin, A. (2007). Characteristics of the size distribution of recent and historical landslides in a populated hilly region. *Earth Planet. Sci. Lett.* 256, 588–603. doi: 10.1016/j.epsl.2007.01.040

Xu, C., Xu, X., and Shyu, J. B. H. (2015). Database and spatial distribution of landslides triggered by the Lushan, China Mw 6.6 earthquake of 20 April 2013. *Geomorphology* 248, 77–92. doi: 10.1016/j.geomorph.2015.07.002

Xu, C., Xu, X., Yao, X., and Dai, F. (2014). Three (nearly) complete inventories of landslides triggered by the May 12, 2008 Wenchuan Mw 7.9 earthquake of China and their spatial distribution statistical analysis. *Landslides* 11, 441–461. doi: 10.1007/s10346-013-0404-6

Yong, L., Chengmin, H., Baoliang, W., Xiafei, T., and Jingjing, L. (2017). A unified expression for grain size distribution of soils. *Geoderma* 288, 105–119. doi: 10.1016/j.geoderma.2016.11.011

Yong, L., Xiaojun, Z., Pengcheng, S., Yingde, K., and Jingjing, L. (2013). A scaling distribution for grain composition of debris flow. *Geomorphology* 192, 30–42. doi: 10.1016/j.geomorph.2013.03.015

Zhuang, J. Q., Cui, P., Ge, Y. G., Zhu, Y. Y., Liu, Y. H., and Pei, L. Z. (2010). Risk assessment of collapses and landslides caused by 5.12 wenchuan earthquake—a case study of dujiangyan–wenchuan highway. *Chin. J. Rock. Mech. Eng.* 29, 3736–3742.

Conflict of Interest: The authors declare that the research was conducted in the absence of any commercial or financial relationships that could be construed as a potential conflict of interest.

frontiers in Earth Science

ORIGINAL RESEARCH
published: 10 June 2021
doi: 10.3389/feart.2021.673137

Evaluation of Remote Mapping Techniques for Earthquake-Triggered Landslide Inventories in an Urban Subarctic Environment: A Case Study of the 2018 Anchorage, Alaska Earthquake

S. N. Martinez*, L. N. Schaefer†, K. E. Allstadt and E. M. Thompson

U.S. Geological Survey, Geologic Hazards Science Center, Golden, CO, United States

Earthquake-induced landslide inventories can be generated using field observations but doing so can be challenging if the affected landscape is large or inaccessible after an earthquake. Remote sensing data can be used to help overcome these limitations. The effectiveness of remotely sensed data to produce landslide inventories, however, is dependent on a variety of factors, such as the extent of coverage, timing, and data quality, as well as environmental factors such as atmospheric interference (e.g., clouds, water vapor) or snow and vegetation cover. With these challenges in mind, we use a combination of field observations and remote sensing data from multispectral, light detection and ranging (lidar), and synthetic aperture radar (SAR) sensors to produce a ground failure inventory for the urban areas affected by the 2018 magnitude (M_w) 7.1 Anchorage, Alaska earthquake. The earthquake occurred during late November at high latitude (~61°N), and the lack of sunlight, persistent cloud cover, and snow cover that occurred after the earthquake made remote mapping challenging for this event. Despite these challenges, 43 landslides were manually mapped and classified using a combination of the datasets mentioned previously. Using this manually compiled inventory, we investigate the individual performance and reliability of three remote sensing techniques in this environment not typically hospitable to remotely sensed mapping. We found that differencing pre- and post-event normalized difference vegetation index maps and lidar worked best for identifying soil slumps and rapid soil flows, but not as well for small soil slides, soil block slides and rock falls. The SAR-based methods did not work well for identifying any landslide types because of high noise levels likely related to snow. Some landslides, especially those that resulted in minor surface displacement, were identifiable only from the field observations. This work highlights the importance of the rapid collection of field observations and provides guidance for future mappers on which techniques, or combination of techniques, will be most effective at remotely mapping landslides in a subarctic and urban environment.

Edited by:
Hakan Tanyas,
International Institute for Geo-Information Science and Earth Observation, Netherlands

Reviewed by:
Pukar Amatya,
Universities Space Research Association (USRA), United States
Federica Fiorucci,
National Research Council (CNR), Institute for Geo-Hydrological Protection (IRPI), Italy
Michele Santangelo,
National Research Council (CNR), Institute for Geo-Hydrological Protection (IRPI), Italy

***Correspondence:**
S. N. Martinez
snmartinez@usgs.gov

†ORCID:
L. N. Schaefer
orcid.org/0000-0003-3216-7983

Specialty section:
This article was submitted to Environmental Informatics and Remote Sensing, a section of the journal Frontiers in Earth Science

Received: *26 February 2021*
Accepted: *25 May 2021*
Published: *10 June 2021*

Citation:
Martinez SN, Schaefer LN, Allstadt KE and Thompson EM (2021) Evaluation of Remote Mapping Techniques for Earthquake-Triggered Landslide Inventories in an Urban Subarctic Environment: A Case Study of the 2018 Anchorage, Alaska Earthquake. Front. Earth Sci. 9:673137. doi: 10.3389/feart.2021.673137

Keywords: NDVI, amplitude change detection, DEM differencing, image thresholding, Google Earth Engine (GEE), urban

INTRODUCTION

The November 30, 2018 magnitude (M_w) 7.1 Anchorage, Alaska earthquake, triggered substantial ground failure throughout Anchorage and surrounding areas (Grant et al., 2020b; Jibson et al., 2020). The earthquake was an intraslab event with a focal depth of about 47 km and an epicenter about 16 km north of the city of Anchorage. Most of the landslides triggered by the earthquake were small ($<15{,}000\ m^2$), and shallow, attributed to the relatively short duration of ground motion (1 min) and deep source, which resulted in widespread shaking but without high peak ground accelerations (Grant et al., 2020b; Jibson et al., 2020). Peak ground accelerations reached ~30% g. Despite the relatively subdued ground failure, geotechnical damage to buildings and structures was widespread (Franke et al., 2019). The last major earthquake to significantly damage Anchorage was the 1964 M 9.2 Great Alaska earthquake, a subduction zone earthquake that shook the city at similar levels to the 2018 earthquake but for 4–7 min and caused extensive landslide damage, including large translational landslides in developed areas of the city (Hansen, 1965).

The 2018 earthquake is an important ground failure event to document thoroughly not only because of the region's history of earthquake-triggered ground failure, but also as a key dataset needed to improve hazard characterization in other geologically and climatically similar regions in the world. Documenting events with subdued ground failure is important because these events are underrepresented in existing inventories. Field-based observations, photos, and ground failure features recorded by U.S. Geological Survey (USGS) scientists during the 10 days immediately following the earthquake are summarized in Grant et al. (2020a) and Jibson et al. (2020). However, around the time of the earthquake, Anchorage was experiencing approximately 6 h of daylight between 09:45 and 15:50, which limited field observations. A cumulative total of 0.109 m of snowfall occurred in Anchorage the 10 days following the earthquake (NOAA/NWS Interactive Snow Information https://www.nohrsc.noaa.gov/interactive), which also obscured overflight observations, particularly at higher elevations (Grant et al., 2020b; Jibson et al., 2020). Partial or complete snow coverage persisted until late March (NOAA/NWS Interactive Snow Information). Grant et al. (2020b) and Jibson et al. (2020) note that their observations are generally incomplete due to these adverse conditions experienced while collecting data.

Our long-term goal is to produce a complete and high-quality landslide inventory associated with this event. The data collected in the field, however, were not sufficient to build such an inventory. The adverse conditions experienced indicate that an inventory built solely on these data would be incomplete because some landslide features may have been obscured by snowfall or simply not documented (i.e., those landslides in areas not easily accessible). Thus, we built an inventory by using both the field observation data and remotely sensed data as they supplement one another. To assemble our inventory, we first identified the location of landslide features by comparing the field observation data (photos) to high-resolution satellite imagery (WorldView-2, WorldView-3, GeoEye-1). Once the location of the landslide was determined, we used a variety of remote sensing methods to locate the head scarp of the landslide feature and to also delineate the landslide where possible. In creating our inventory, we found that the effectiveness of remote sensing data to identify and delineate landslides in this environment varied. In our study area, some field-verified landslides could be identified and delineated using multiple methods while others could not be identified at all. Our inventory allowed us to determine the capabilities and limitations of remotely sensed data to map landslides in an environment such as Anchorage. This knowledge can be used to guide remote mapping beyond the field area and help us achieve our goal of eventually creating a complete landslide inventory.

We use the landslide inventory to retroactively evaluate the effectiveness of the three remote sensing methods used: 1) light detection and ranging (lidar) elevation differencing, 2) normalized difference vegetation index (NDVI) differencing, and 3) synthetic aperture radar (SAR) amplitude change detection (ACD). We compare these methods against the inventory data in a subarea of Anchorage for which data for all three methods are available. For clarity, we refer to this subarea as the study area. We describe the effectiveness of each method to identify certain landslide types and why some methods may have outperformed others. Additionally, we identify environmental and data-type specific challenges. While such an analysis will help in our efforts to build a complete inventory beyond the study area, this work can aid others in remote mapping as well.

BACKGROUND

The location, size, and spatial distribution of landslides can help define regional landslide trends, reveal geologic and structural patterns of a given environment, and inform landslide hazard and susceptibility models (e.g., Keefer, 1984; Mirus et al., 2020). Landslide inventories have long provided the foundation for a wide variety of landslide research, such as updating and improving landslide susceptibility models (Stanley and Kirschbaum, 2017; Nowicki Jessee et al., 2018), optimizing empirical and deterministic criteria for landslide early warning systems (Baum et al., 2010; Mirus et al., 2018), or understanding the role of hillslope erosion in landscape evolution (Larsen and Montgomery, 2012). Thus, compiling landslide inventories after triggering events (e.g., earthquake, rainfall) is highly beneficial for landslide hazard assessment and risk reduction efforts.

Recent studies have emphasized the importance of landslide inventory quality across a variety of triggering scenarios, landscapes, and climates for landslide studies and model development (Tanyaş et al., 2017; Mirus et al., 2020; Tanyaş

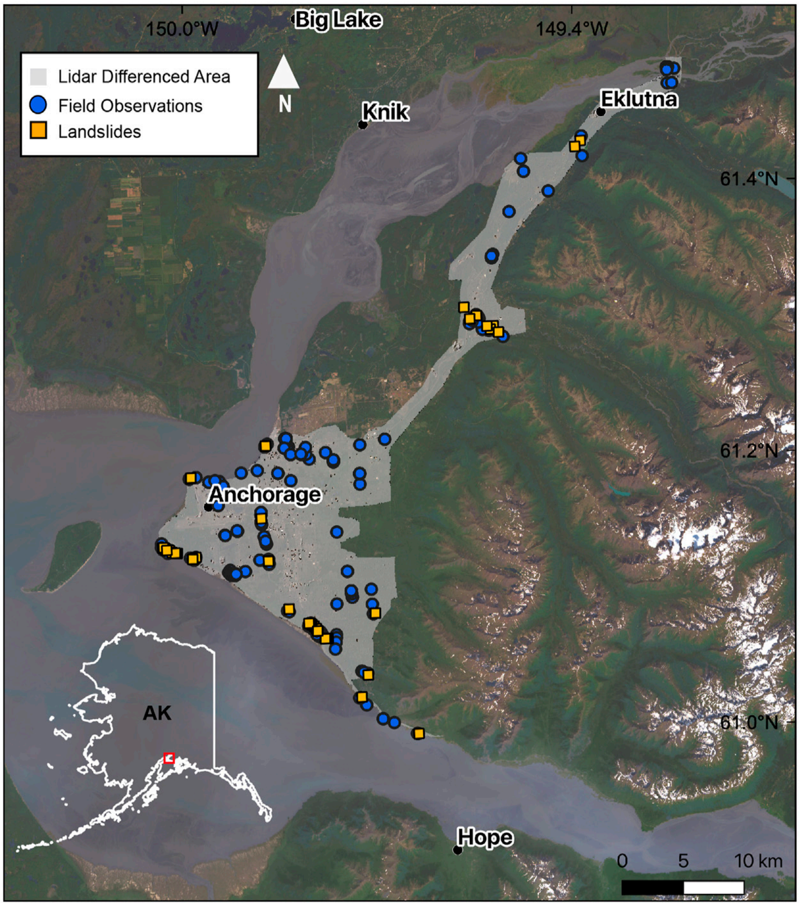

FIGURE 1 | Location of the study area within Anchorage, AK. The extent of the lidar differenced area is shown in gray. Landslides are shown as orange squares whereas he approximate location of field observations are shown as blue circles. The field observations consist of multiple photos of all types of ground failure (including ground failure as a result of liquefaction) taken from various vantage points (ground, helicopter). Orange squares are locations that are included in the landslide inventory for this study, which also have corresponding field observations in most cases.

and Lombardo, 2020). The accuracy and completeness of landslide inventories vary due to data quality, accessibility, and availability, as well as event-specific field conditions and accessibility. Limitations in data resolution or field observations also result in infrequent documentation of the smallest landslides triggered by a seismic or rainfall event (Guzzetti et al., 2012). Additionally, the end goals and purpose for creating landslide inventories differ between authors and across organizations, resulting in varying levels of detail and data inclusion (e.g., Mirus et al., 2020).

Many advancements in landslide mapping and inventory quality can be linked to the increasing availability and attainability of remotely sensed imagery that aid in large scale mapping (Guzzetti et al., 2012), complementing traditional field observations. Manual image interpretation or automatic detection methods can be used with a variety of aerial and satellite data products, such as optical (visual) images, multispectral images, laser scanning, and radar sensors to develop inventories (Booth et al., 2009; Martha et al., 2011; Harp et al., 2016; Mondini et al., 2019). The quality of inventories developed using each approach varies, however, and is dependent on a few variables. For example, manual interpretation of imagery can be limited by the resolution of data and experience of the mapper and can be time intensive depending on the level of detail desired (Galli et al., 2008). Automatic methods tend to increase the speed at which inventories can be generated but have been shown to overestimate the landslide-affected area resulting in a high false positive rate (Li et al., 2014). Additionally, each data product has inherent advantages and disadvantages. For example, optical images can be hampered by poor weather conditions, poor lighting, clouds, or snow. Active radar methods typically avoid some barriers associated with optical imaging; radar satellites emit their own energy and thus can collect images at night, and the longer wavelengths used allow imaging through clouds and other adverse weather conditions. However, radar methods are still limited by geometric distortions (e.g., layover, foreshortening, or shadowing), ground moisture, dense vegetation or heavy snowfall, and atmospheric noise (Colesanti and Wasowski, 2006; Rott and Nagler, 2006). Imagery-based landslide mapping can be enhanced with the continued improvement of image filtering, clustering,

TABLE 1 | The spatial resolution, wavelength, revisit time, and coverage offered by the sensors whose data were used in this study.

Data source	Spatial resolution	Wavelength	Revisit time	Global coverage
Sentinel-1 imagery	~14 m	C-band (5.6 cm)	12 days	Yes
Sentinel-2 imagery	10 m	NA	5 days	Yes
DGGS (2015) lidar	1 m	NA	NA	No
DGGS (2018) lidar	1 m	NA	NA	No
ALOS-2	~10 m	L-band (22.9 cm)	14 days	Yes

classification, change detection, multi-data integration, or other techniques (Guzzetti et al., 2012 and references therein). Thus, carefully examining the performance of these methods under various circumstances can help improve the overall efficacy of landslide mapping for others.

DATA AND METHODS

In this study, we constrain our study area to the extent covered by the post-earthquake lidar (lidar differenced area, **Figure 1**) because it is relatively well characterized by field observations (Grant et al., 2020a). In addition to this, all other data we examine (optical and SAR imagery) have coverage in this area (details of all data used can be found in **Table 1**). We first used a combination of field observations (Grant et al., 2020a), manual inspection of optical imagery, and three different remote sensing methods (lidar differencing, NDVI differencing, and SAR amplitude change detection), to produce a landslide inventory in the study area. We describe each method and the accompanying datasets in detail in the following subsections. For each landslide, we identify the approximate center of the head scarp as a point and delineate the shape of the landslide if possible. Delineation of each landslide involved creating a polygon of the landslide affected area. The landslide-affected area includes both the landslide scar and deposit. We classify each landslide according to Keefer (1984) and note whether the landslide is new or reactivated.

Using this manually compiled inventory, we then retrospectively evaluate the effectiveness of the three remote sensing methods to identify and delineate the different types of mapped landslides individually without the benefit of manual analysis and combined data sources. We do this by comparing the probability distribution of landslide pixels and the non-landslide pixels for each method. The intention of this exercise is to explore how well these methods might work for automated mapping. Our evaluation methods are detailed in Evaluation of Method Effectiveness.

Field Observations and Optical Imagery

For this study, we used the 1,301 geotagged photos from the ground and helicopter reconnaissance collected by Grant et al. (2020a) within the study area to help map and delineate 43 landslides (**Figure 1**). Because of the differences in vantage points and cameras used, the accuracy of coordinates associated with each photo varies, thus this field observation database is used primarily with comparisons against high-resolution optical satellite imagery (WorldView-2, WorldView-3, GeoEye-1). We use the high-resolution optical imagery to determine a more accurate location for the manifestations of ground failure in the field photos by matching geographic features seen in the photos to those in the optical imagery (i.e., houses, structures, roads).

Elevation Differencing

Elevation differencing determines the change in elevation between two time periods using digital elevation models (DEMs). The difference in elevation is determined at the pixel scale by subtracting the change in elevation between two aligned pixels (James et al., 2012). This method has proven effective for mapping landslides in a variety of environments and climates (e.g., Bull et al., 2010; Ventura et al., 2011; Prokešová et al., 2014; Mora et al., 2018). The extent of the effectiveness of this method for landslide mapping, however, is dependent on the spatial and temporal resolution of the DEMs, quality of the data, and the extent of coverage.

This study uses 1-m pre- and post-earthquake DEMs derived from lidar data acquired by the state of Alaska and made available via the Alaska Division of Geological and Geophysical Surveys (DGGS) elevation portal (DGGS Staff, 2013). The pre-event data were collected in May 2015 while the post-event data were acquired in December 2018, the week following the earthquake. The reported vertical accuracy for the 2015 DEM is 9.25 cm. Vertical accuracy of the 2018 DEM has not yet been reported by the acquisition team. More information and metadata for these datasets can be downloaded via the DGGS elevation portal (DGGS Staff, 2013). The 2015 DEM was provided in feet, so this raster was converted to meters to remove a vertical offset between the DEMs. The DEMs were aligned by first clipping each to the area of which they both overlap. Then, using the "raster align" tool in QGIS (3.10; https://www.qgis.org/), the clipped DEMs were aligned to one another. Aligning the DEMs involves rescaling and reprojecting the DEMs as needed to ensure that the individual pixels in each image are aligned to one another. After alignment, the DEMs are differenced using the raster calculator in QGIS. The elevation differenced map is computed as

$$\text{Elevation Difference} = \text{DEM}_{\text{Post}} - \text{DEM}_{\text{Pre}} \tag{1}$$

in which DEM_{Post} refers to the 2018 DEM while DEM_{Pre} refers to the 2015 DEM.

After creating the elevation differenced map, landslides were identified by examining areas within the differenced map that suggested there had been a significant increase or decrease in elevation (relative to surrounding landscape) since the $\mathrm{DEM}_{\mathrm{Pre}}$ was acquired (2015). The landslides are visually easy to identify, as most of the study area experienced very little change in elevation. Despite this, a majority of the areas that experienced dramatic changes in elevation since 2015 were related to development and mining activity. Thus, it is necessary to differentiate elevation change that is solely due to landsliding from these other events. To do so, we used high-resolution optical imagery (WorldView-2, WorldView-3, GeoEye-1) to rule out the changes that were the result of development or mining activity.

Normalized Difference Vegetation Index Differencing

NDVI is used to map the relative distribution of vegetation in landscapes. This can be useful for landslide mapping because slope failure often results in damage to vegetation. NDVI maps are generated using the near-infrared (NIR) and red (R) image bands contained within a multispectral image (Deering and Haas, 1980):

$$\mathrm{NDVI} = \frac{\mathrm{NIR} - \mathrm{R}}{\mathrm{NIR} + \mathrm{R}} \tag{2}$$

Because vegetation absorbs visible light and reflects near-infrared light, this index gives an indication of the health of existing vegetation at the pixel scale. It also maps the relative distribution of vegetation in a landscape because non-vegetated areas are classified with a lower NDVI value. Thus, NDVI differencing maps can reveal areas where vegetation has been damaged or stripped away from the landscape (i.e., due to landslides). Differencing maps can be generated by subtracting the pre-event NDVI pixels from the post-event NDVI pixels. Then, within the change detection image, those pixels that correspond to large changes in NDVI can be further assessed visually to determine whether the change corresponds to a landslide. As previously mentioned, we use optical imagery (WorldView-2, WorldView-3, GeoEye-1) to determine if the NDVI change corresponds to other phenomena such as urban development and/or mining activity.

The lack of sunlight and presence of snow prohibited the creation of accurate NDVI maps in the days immediately preceding and following the event, so we instead used summer NDVI composites from 2018 to 2019 to generate a NDVI differencing map spanning the time of the earthquake. The summer composites were produced using Google Earth Engine (Gorelick et al., 2017) using satellite imagery from the European Space Agency's Sentinel-2 multispectral satellite. The 10 m resolution composites are generated by taking the median value of each pixel within an image collection after filtering out pixels containing clouds. The composites are then used to produce NDVI maps for the summers preceding and following the earthquake and then differenced to isolate areas where landslides triggered by the earthquake may have caused damage to the normal vegetative cover. The NDVI differenced map is computed as

$$\mathrm{NDVI\,Difference} = \mathrm{NDVIComp}_{\mathrm{Pre}} - \mathrm{NDVIComp}_{\mathrm{Post}} \tag{3}$$

in which $\mathrm{NDVIComp}_{\mathrm{post}}$ refers to the summer 2019 NDVI composite and $\mathrm{NDVIComp}_{\mathrm{Pre}}$ refers to the summer 2018 NDVI composite.

Synthetic Aperture Radar Amplitude Change Detection

Synthetic aperture radar (SAR) amplitude images measure the proportion of microwave backscattered from that area on the ground, which depends on a variety of factors such as the type, size, shape, orientation, roughness, moisture content, and dielectric constant of reflectors within a given pixel. SAR amplitude change detection (ACD) compares the amplitude intensities between two dates to detect changes in amplitude intensity that may indicate surface changes (e.g., floods, mass movements, or liquefaction events).

Three sets of images are used for change detection before and after the earthquake from the Sentinel-1 and ALOS-2 satellites (**Supplementary Table S1**). Scene pairs include ascending Sentinel-1 on November 17, 2018 and January 26, 2019, descending Sentinel-1 data on November 22, 2018 and December 4, 2018, and ascending ALOS-2 data on November 17, 2018 and January 26, 2018. Images were processed using SNAP 7.0 software (SNAP - ESA Sentinel Application Platform v7.10, http://step.esa.int). Both Sentinel and ALOS-2 products were radiometrically calibrated to radar reflectivity per unit area, filtered for speckle using a Lee filter operating as a 3 × 3 pixel moving window, corrected for geometric/terrain distortions using a range doppler orthorectification, and composited to determine amplitude changes between the pre-event and post-event image. Pixel intensity was converted to the backscattering coefficient measured in decibel (dB) units that ranges from c. +10 dB for very bright objects to −40 dB for very dark surfaces. Differencing these data that are converted to decibel units is equivalent to the log-ratio method used in other studies (Mondini et al., 2019; Jung and Yun, 2020; Lin et al., 2021) to determine the change in amplitude between SAR scenes. These studies compute the log-ratio value as

$$\mathrm{A}_{\mathrm{ratio}} = \log_{10}\left(\frac{\mathrm{A}_{\mathrm{pre}}}{\mathrm{A}_{\mathrm{post}}}\right) \tag{4}$$

in which the $\mathrm{A}_{\mathrm{pre}}$ and $\mathrm{A}_{\mathrm{post}}$ values correspond to the radar brightness coefficient values (Mondini et al., 2019; Jung and Yun, 2020; Lin et al., 2021). Once we converted our data to dB units, the images were then simply differenced as

$$\mathrm{Amplitude\,Difference} = \mathrm{Amp}_{\mathrm{Pre}} - \mathrm{Amp}_{\mathrm{Post}} \tag{5}$$

Additionally, an amplitude change detection time series of Sentinel-1 images between 2015/11/29 and 2020/11/01 was generated using Google Earth Engine (see *Data Availability Statement*). This approach produces pre- and post-event time series maps utilizing Sentinel-1 ground range detected (GRD) products. GRD products are processed to remove thermal noise and are radiometrically and terrain calibrated. The processed data are also provided in dB units, so the composited time-series maps are differenced as

$$\text{Amplitude Difference} = \text{AmpComp}_{\text{Pre}} - \text{AmpComp}_{\text{Post}} \quad (6)$$

In the workflow, image composites are generated for time periods preceding and following the event of interest utilizing VH (vertical transmit, horizontal receive) polarization images. The method utilizes both ascending and descending data to generate the composites. Different polarizations and seasonal composites (i.e., summer months only) did not impact the results. List of the SAR scenes used can be found in the **Supplementary Data Sheet S1**.

Evaluation of Method Effectiveness

Manual mappers visually look for discontinuities in remote sensing products that correspond to landslides. They typically use knowledge of where landslides are more likely to occur (e.g., steep coastal bluffs, riverbanks) to guide their efforts. Automatic mapping relies on a similar approach and can be implemented using either pixel-based or object-based image analysis methods. Pixel-based methods are those that classify imagery at the pixel scale and do not take into consideration neighboring pixels (Scaioni et al., 2014). Object-based image analysis typically involves the use of thresholding and segmentation techniques (Martha et al., 2011). Thresholding typically entails removing or masking the areas within target images where landslides are least likely to occur, similar to the way in which a manual mapper uses their knowledge of landslide susceptibility to guide their efforts. Segmentation groups the portions of the image into objects comprising similar pixels (Hölbling et al., 2015) working the same way as a human would to identify continuous sets of pixels that may correspond to a landslide. A set of rules, which can be prescribed by the mapper or determined using machine learning algorithms, can be applied to the target image to determine which of the objects or pixel clusters correspond to landslides. Automatic methods tend to struggle with differentiating similar objects from one another, resulting in a large number of false positives (Li et al., 2014). Because of this, automatic methods tend to be more successful when those landslide pixels and subsequently the objects to which they correspond are markedly different from the surrounding pixels (Rosin and Hervas, 2005).

With these concepts in mind, the performance of each of the three remote sensing methods is compared using the probability distributions of landslide pixels versus landscape pixels for each method. This is done in order to determine which methods would be more useful at delineating landslides of different types in this environment using both manual and automatic mapping methods without prior knowledge of the exact location of the landslides. Those landslide pixels that are markedly different from the remaining pixels in the target image would have a probability distribution that differs from the general landscape distribution and thus, likely be more easily identifiable using both manual and automatic approaches.

To generate the probability distributions for each method, we sampled the landslide pixels and landscape pixels of each corresponding raster. We sampled the values at all landslide pixels and then randomly sampled an equal number of pixels from the landscape (non-landslide areas). We then plotted the probability distributions of the sampled landslide and landscape pixels for each method to facilitate comparison. To determine the effect of noise removal on the distributions and to smooth all layers to roughly the same resolution for more direct comparison, the elevation and NDVI differenced raster images were smoothed using a Gaussian filter with a standard deviation of ~15 m. The results of this smoothing on the distributions can be seen in **Supplementary Figure S2**. Noise removal did not significantly impact the results, so we do not filter the final data. We show the percentage of observed landslide pixels as a point over each bin in the probability distributions for each method. This displays, for each method, the range of values where landslides are likely to be found.

LANDSLIDE DETECTION AND METHOD EFFECTIVENESS

Landslide Inventory

Within the study area, we were able to successfully document the location of 43 landslides using the combined methodologies, including three soil block slides, nine soil slumps, 20 soil slides, nine rapid soil flows, and two rock falls (those landslides that were not classified by those who gathered field observations were classified using the field photos and remote sensing data). Of these landslides, we were able to delineate 39 (90%) as they were easy to identify visually using the remotely sensed data; the remaining 4 (9%) were mapped with a point at the approximate location that was determined using field observations. Field photos of these undelineated landslides (two soil slides and two incipient soil slumps) can be seen in **Figure 2**. Of the 43 landslide events, 38 (88%) were identifiable using the elevation differenced map and 21 landslides (48%) were identifiable using the NDVI differenced map. No landslides could be delineated using the ACD methods. Remote mapping methods failed to aid in the identification and delineation of four landslides identified in the field, and five landslides not observed in the field were mapped using remote mapping methods. A visual representation of each method is presented in **Figure 3**. Because the data we used have varying degrees of spatial and temporal resolution, the accuracy of each mapped landslide varies. Accuracy refers to the location of the landslide, the existence of the landslide (i.e., whether it can be confidently attributed to the earthquake) and the delineation. Mapping uncertainty associated with each feature can be found in **Supplementary Table S3**.

Method Performance Summary

As previously mentioned, elevation and NDVI differencing were able to aid in the identification and delineation of most landslides whereas ACD methods were largely ineffective. This statement is supported by **Figures 4A,B**, where the probability distributions of the landslide pixels in the elevation and NDVI change maps differ greatly from those of the remaining landscape in comparison to results from the amplitude-based methods (**Figures 4C–F**) which are essentially indistinguishable. The distributions of the landscape and landslide pixels for the ACD methods are similar, which suggest that the data are generally too noisy to identify and delineate landslides.

FIGURE 2 | The map on the left **(A)** shows the location of landslides by type as well as the location of those landslides that could not be delineated using remote sensing mapping methods (labeled **B–E** on the map). Corresponding photos of those landslides can be seen to the right of the map. The top center photo shows a **(B)** soil slide with a person for scale. The top right **(C)** and bottom center **(D)** show incipient soil slumps and the bottom right **(E)** shows a soil slide. (Photo Credits: USGS).

For the elevation differenced map, the probability distribution for the landslide pixels is negatively skewed. Because a negative change in elevation corresponds to erosion, this suggests that the landslides mapped are mostly erosional (i.e., soil slides, rapid soil flows). The NDVI change distribution is positively skewed, suggesting that the mapped landslides are those that are severe because they remove vegetation and leave a significant scar on the landscape. The minimum landslide area mapped using elevation differencing was 26 m^2 while the minimum area mapped by the NDVI differencing method was 355 m^2. SAR ACD methods were ineffective primarily due to noise (possibly caused by atmospheric interference, snowfall, moisture, and dense vegetation) hindering the delineation and identification of landslides. Additionally, the amplitude values of the resulting landslide scar or deposit were similar to the original landscape (i.e., soil slide occurring in areas of unvegetated, exposed soil), preventing the utility of this method. Geometric distortion also prevented any delineation of landslides along coastal bluffs using the SAR ACD methods. Because of these issues with SAR ACD methods, we will only discuss the effectiveness of elevation and NDVI differencing to delineate landslide types in subsequent sections.

Elevation Differencing

The probability distributions for the soil slumps, soil slides, and rapid soil flows suggest that elevation differencing was more effective at delineating these landslide types than the others (soil block slides and rock falls) in our study area (**Figures 5C, E, G**). This is based on the fact that the distribution of landslide pixels for these landslide types differs from the general landscape distribution and also because, over a certain range of elevation change values, a relatively high percentage of landslide pixels is observed. Landslide pixels associated with soil block slides and rock falls (**Figures 5A,I**) are too similar to the remaining landscape distribution to state that elevation differencing can be effective at delineating those landslide types automatically. Despite this, the field observations allowed us to identify and delineate the soil block slides using the elevation differenced map. So, in regard to manual mapping, the differencing was helpful to delineate these types of landslides but only with prior knowledge of likely landslide locations. This suggests that automatic methods may not be able to systematically map soil block slides using elevation differencing. Rock falls, in our study area, were not able to be delineated using the lidar differenced map. Even with knowledge that they occurred and the general vicinity in which they occurred, delineation was challenging. This could be attributed to their deposits being thin and the time difference between the lidar datasets producing noise that corresponds to non-earthquake related changes. Only two rock falls were mapped in the study area, which limits our observations of these features.

Normalized Difference Vegetation Index Differencing

The probability distributions for the soil slumps and rapid soil flows suggest that NDVI differencing was more effective at delineating these landslide types than the others (**Figures 5D,H**). This is based on the fact that the distribution of landslide pixels for these landslide types differs from the general landscape distribution and also because, over a certain range of NDVI change values a relatively high percentage of landslide pixels is observed. Soil block slides, soil slides, and rock falls (**Figures 5B, F, J**) are too similar to the remaining landscape

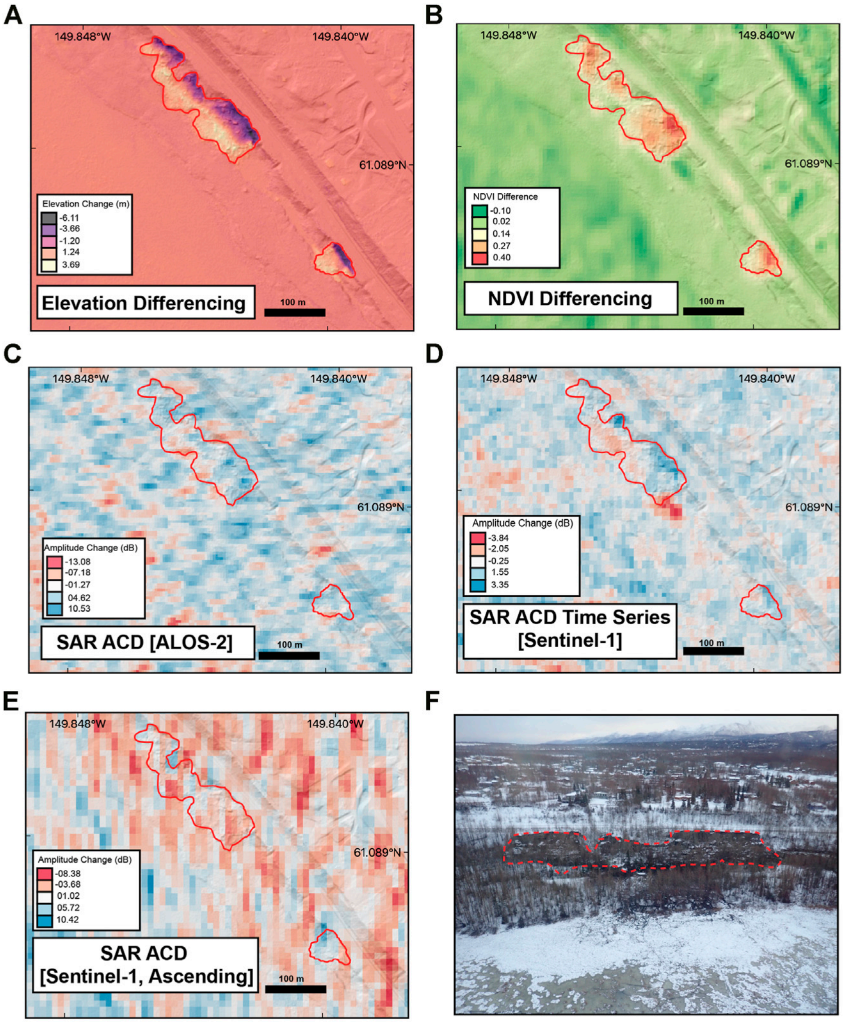

FIGURE 3 | An example of the performance of each method at detecting rapid soil flows (outlined in red). Panel **(A)** shows the performance of elevation differencing and **(B)** shows the performance of NDVI differencing. Panels **C–E** display the performance of the remaining SAR ACD methods. An aerial photo of these rapid soil flows can be seen in panel **(F)** (Photo Credit: USGS).

distribution to state that NDVI differencing is effective at delineating these landslide types.

DISCUSSION

In this study, lidar elevation differencing and NDVI differencing are proven to be more effective at identifying and delineating landslides in an urban subarctic environment than SAR ACD methods. Elevation differencing proved useful to identify and delineate soil slumps, soil slides and rapid soil flows, while NDVI differencing is more effective at capturing soil slumps and rapid soil flows. The success of the elevation differencing method at delineating soil slumps, soil slides and rapid soil flows can be attributed to the fact that they have distinct erosional or depositional signatures which increases the extent of the landslide affected area. Because soil slumps tend to result in a large, semi-coherent landslide deposit left in the landscape, the probability distribution for this landslide type is positively skewed and thus, these landslides are easy to delineate using elevation differenced data. Soil slides and rapid soil flows have an elongated erosional signature with small and thin deposits, which result in a negatively skewed probability distribution.

The success of the NDVI differencing method at delineating soil slumps and rapid soil flows can be attributed to their severity and size, with the major limiting factor being that landslides need to occur in vegetated areas in order for NDVI methods to be useful. Because soil slumps and rapid soil flows are disruptive to the overlying vegetation, they have the potential to have a lasting impact on the landslide affected area. Even though the images used in our study are a year apart, these landslides are still able to be delineated due to their severity and ability to leave a lasting scar on the landscape. Thus, in scenarios where these landslide types are known to have been triggered, the methods presented here could prove useful at identifying those landslides and delineating them.

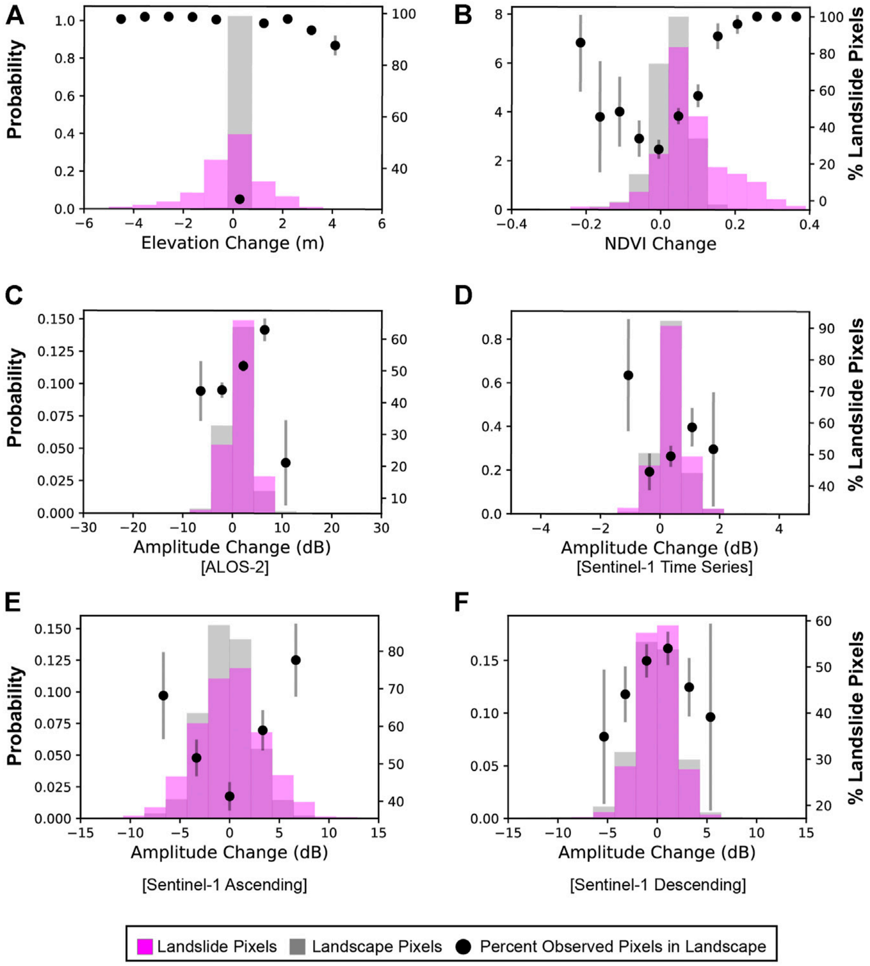

FIGURE 4 | Probability distributions comparing landslide pixels to landscape pixels for each method. Panel **(A)** and **(B)** display the distributions for the elevation and NDVI differencing, respectively. Panels **(C–F)** display the distributions of the remaining SAR ACD methods. Confidence interval for each point shown as gray line (significance level 0.05).

Although the earthquake occurred in late fall with winter conditions, seasonal NDVI composites preceding and following the earthquake were shown to be effective at identifying and delineating landslides. Because the NDVI composites were generated using widely available Sentinel-2 data, the method can be easily implemented in future studies. The resolution of this data (10 m resolution), however, may fail to map smaller landslides. In this study, for instance, the minimum landslide area that could be mapped using the NDVI differenced data was 355 m^2. While not widely available, higher resolution imagery containing NIR bands, such as from the WorldView sensors, may be able to generate higher resolution NDVI differencing maps.

Challenges to Overcome

While we were able to effectively identify and delineate landslides observed in the field using the remote sensing methods, and delineate an additional five that were not identified in the field, we also faced many challenges that prevented us from mapping all landslides in our study area. Snow accumulation and lack of sunlight were the primary challenges associated with landslide mapping using field and multispectral data, but the expression of the landslides due to the nature of the ground motion also played a crucial role. Despite the November 30 earthquake being the largest earthquake since the M 9.2 Great Alaska earthquake to affect the Anchorage area, the landslides triggered were generally small, shallow, and limited in number (Jibson et al., 2020). Many slope failures consisted of minor slope cracking and deformation (e.g., **Figure 2**) that may result in costly damage to structures but are too subtle to identify via the remote sensing methods. In addition, many of these geotechnical failures were repaired prior to the date of the post-event imagery used in this study (we had to wait until the Spring or Summer for post-event images to be of sufficient quality for mapping). To summarize, producing a complete and high-quality landslide inventory is challenging for this particular earthquake due to the environmental conditions as well as the subdued surface expression of the landslides.

Within our study area, we failed to delineate soil slides and soil slumps that were identified in the field with remotely sensed data. This is primarily attributed to the resolution of the NDVI (~10 m) and elevation data (1 m) because these failures were small. This may also result in a failure to effectively map rock falls as well.

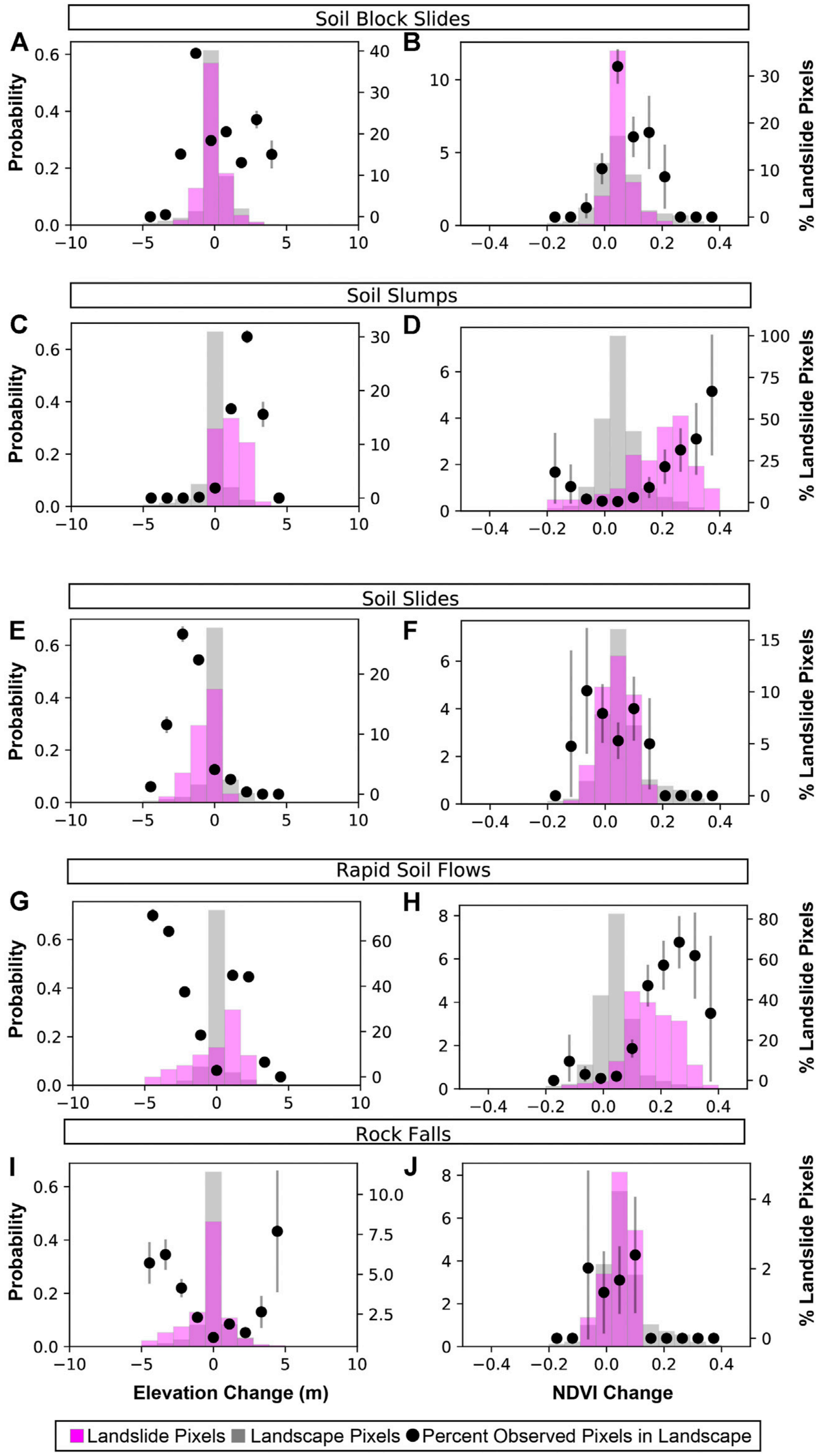

FIGURE 5 | Probability distributions comparing landslide pixels to landscape pixels by landslide type for the elevation and NDVI differencing methods. Panels **(A)** and **(B)** display the distributions that correspond to soil block slides for the elevation and NDVI differencing methods, respectively. Similarly, panels **(C)** and **(D)** correspond to soil slumps, panels **(E)** and **(F)** correspond to soil slides, **(G)**and **(H)** correspond to rapid soil flows and **(I)** and **(J)** correspond to rock falls. Confidence interval for each point shown as gray line (significance level 0.05).

However, there were only two rock falls in our study area so with this small sample size it is difficult to definitively say if rock falls are generally challenging to map using the methods presented here. Additionally, NDVI may have failed to capture some landslides due to the composites being produced from images taken several months before and after the earthquake event, if vegetation disruption was minor, the vegetative cover could have fully recovered in that time. While we were able to successfully use NDVI differencing to map other landslides in our study area, this method is unfortunately not applicable above tree line in arid or semi-arid environments due to a lack of vegetation and thus lack of changes in vegetation due to landslide scouring. Though outside the study area, there were some rock falls above tree line in the mountainous areas east of Anchorage (Grant et al., 2020b; Jibson et al., 2020). Elevation differencing can solve these issues, however there are limitations related to data availability as well as the spatial and temporal resolution of the data. Here, our mapping was limited by the extent of the 1-m DEM data and the 3-year time difference between the pre- and post-DEMs. One way to overcome this may be to use the DEMs available as part of the ArcticDEM project (Porter et al., 2018). The ArcticDEM data are derived from stereo satellite imagery and made available for a large portion of the northern latitudes at 2 m resolution. The data are periodically released, however, and at the time of publication the latest release did not include any post-earthquake DEMs. Depending on data access and computer processing power, one could also generate these DEMs using stereo satellite imagery and the NASA AMES stereo pipeline (Beyer et al., 2018). One limitation, however, is that unlike lidar methods, the ArcticDEM project produces a digital surface model (DSM) that does not remove vegetation. This emphasizes the importance of collecting regular "pre-event" baseline data to facilitate rapid and reliable mapping.

Despite the many advantages of using SAR sensors for mapping surface changes, SAR ACD methods were not effective at mapping landslides in this study due to several geomorphologic, radiometric, and image processing factors (see Mondini et al., 2021 for a recent review). During image pre-processing, both horizontal-horizontal (HH) and horizontal-vertical (HV) polarization scenes were considered. HV scenes typically had lower (darker) backscatter and did not improve landslide detection, therefore only HH scene results are shown herein. Additionally, we found that a Lee filter operating as a 3 × 3 pixel moving window sufficiently reduced speckle, as determined visually and by comparing the variance in the intensity image before and after filtering.

Multiple platforms with different SAR bands and look directions were used to optimize landslide detection. A direct comparison of C-band (Sentinel-1) versus L-band (ALOS-2) performance is challenging due to the different temporal and spatial resolutions of the scenes. While the L-band scene contained less speckle than the C-band scenes, it did not result in an improvement in landslide detection. Landslide events must cause surface changes of a significant magnitude to be recognizable in the SAR imagery, thus changes in the amplitude were not sufficiently higher than the noise or speckle effect to identify surface changes. One of the most significant limiting factors for landslide detection in this study was illumination issues caused by the side-looking geometry of the SAR system, which results in geometric distortions in steep terrain, such as layover (top of a backscattering object is recorded closer to the radar than the lower parts of the objects) and radar shadows (lack of radar illumination). While both ascending and descending scenes were considered, steep, south-facing slopes where many of the landslides occurred still experienced significant geometric distortions, preventing landslide detection.

SAR can penetrate clouds and image during the day or a night, providing a potential workaround for mapping in the dark in subarctic and arctic regions. However, the snow coverage may have resulted in the large amount of noise present in our SAR scenes. Thus, the main question arising from this work is what other methods can we further develop to help with landslide mapping in dark, snow covered environments? A second questions is: what methods will help to map small and subdued landslides? The motivation for the first question is due to the need for mapping in subarctic regions, the second question arises from the fact that in many instances' landslide inventories are produced for events that are extreme and leave an easily discernible mark on the landscape (Tanyaş et al., 2018). Thus, the landslide inventories that are generally used for modeling efforts tend to rely on information from these dramatic events and not events that result in smaller landslides. This situation results in subsequent models relying on these inventories to be biased. The answer to both questions can be obtained by further testing and developing methods in such an environment (where visibility is limited due to snow and lack of sunlight) and under similar conditions (limited surface expression of landslide damage).

Our work indicates the value of closely analyzing and further developing remote mapping methods in environments such as Anchorage, AK, and for events that result in minor surface deformation. A similar earthquake event occurred on March 31, 2020, in Stanley, Idaho. After the M_w 6.5 earthquake, USGS field reconnaissance efforts were restricted due to the ongoing COVID-19 pandemic. In addition, local response was stymied due to avalanche risk and late season snow limiting ground visibility via aircraft (Idaho Geological Survey, 2020). The Idaho event is just one example that highlights the utility of remote mapping in an environment such as Anchorage, AK. Anthropogenic climate change has also been shown to alter the characterization and frequency of landslides occurring in subarctic conditions (Coe et al., 2018; Coe, 2020) suggesting that developing such methods will be of high importance into the future. Here, we suggest that exploring remote mapping methods systematically can lead to a better understanding of landslide mapping in such an environment. Such development in the field could then greatly improve earthquake-triggered landslide susceptibility and hazard models.

The challenges left to overcome relate mainly to the resolution and quality of the data available. ArcticDEM data could potentially be used to map landslides in subarctic environments. Additionally, higher resolution satellite imagery could be used to generate NDVI maps. Digital image correlation (DIC) of high-resolution satellite imagery may be more effective at capturing coherent landslides such as soil block slides (Bickel et al., 2018). Despite the ineffectiveness of the SAR ACD methods, InSAR (Interferometric Synthetic Aperture Radar) could be used to map coherent deformation, such as lateral spreading, as well (Saroli et al., 2005). The NASA-ISRO SAR mission

(NISAR) with a projected launch date of 2022, will have a long (L-band) wavelength, 3–10 m resolution, temporal resolution of 12 days, and will be freely available and open to the public. Since L-band radar can penetrate the tree canopy at greater depths than C-band, these new data may be useful in detecting landslides in forested areas (Rosen et al., 2017).

CONCLUSION

In our study, we provide evidence that remote mapping can augment field-based inventories by aiding in the discovery of previously unobserved landslides and also help to better delineate the landslide-affected area. Simultaneously, we also highlight the importance of rapid post-earthquake field observations in environments such as Anchorage, AK, as these allowed us to build an adequate inventory and also develop methods to map the remaining area affected by the earthquake.

Broadly, we demonstrate a gap in our knowledge of earthquake-triggered ground failure in arctic and subarctic environments in winter conditions because of difficulties in remote mapping under such circumstances. With many earthquake-prone areas subject to such circumstances (northern Japan, Alaska, Canada, Iceland) and many other regions prone to similar geologic conditions and winter weather, there is merit in determining an effective way to map landslides in such an environment. To date, few earthquake-induced landslide inventories are located in these subarctic environments despite the relatively high amount of seismic activity (Tanyaș et al., 2018). Many of the identified challenges are not unique to Alaska; thus, the observations and mapping methods described in this study can provide the foundation for others to develop workflows for mapping landslides in subarctic and urban regions and improve response and landslide inventory efforts in these challenging environments.

DATA AVAILABILITY STATEMENT

Snowfall data were accessed using the Interactive Snow Information website maintained by the National Operational Hydrologic Remote Sensing Center (https://www.nohrsc.noaa.gov/interactive). High-resolution satellite imagery was downloaded using the MAXAR Global Enhanced GEOINT Delivery (G-EGD) system. The Google Earth Engine code used to create the synthetic aperture radar (SAR) amplitude change detection (ACD) time series maps can be accessed via GitHub at the following link: https://github.com/MongHanHuang/GEE_SAR_landslide_detection(https://doi.org/10.5281/zenodo.4060268). The landslide inventory used in our analysis is provided by Martinez et al. (2021). Field observation data can be found in Grant et al. (2020a).

AUTHOR CONTRIBUTIONS

The study was conceived by KEA, EMT, LNS, and SNM. Field inventory and landslide inventory were created by SNM. Elevation, NDVI differencing, and SAR ACD time series maps were derived by SNM. ALOS-2 and Sentinel-1 SAR ACD maps were derived by LNS. Probability distribution analysis was carried out by SNM. KEA and EMT guided the structure of the work. All authors contributed to discussion of findings and implications for future work.

ACKNOWLEDGMENTS

We would like to acknowledge Rob Witter, Alex Grant, and Randall W. Jibson (U.S. Geological Survey) for their constructive feedback throughout the duration of this project as well as for their contributions to the field observations database. We would also like to thank Barrett Salisbury from the Alaska Department of Natural Resources (Alaska DNR) for his support in regard to data accessibility and information regarding the earthquake event. Thank you to Stephen Slaughter and Jeffrey Coe (U.S. Geological Survey) for their helpful suggestions and comments. And lastly, thank you to the reviewers for their careful review and constructive feedback.

SUPPLEMENTARY MATERIAL

The Supplementary Material for this article can be found online at: https://www.frontiersin.org/articles/10.3389/feart.2021.673137/full#supplementary-material

REFERENCES

Baum, R. L., Godt, J. W., and Savage, W. Z. (2010). Estimating the Timing and Location of Shallow Rainfall-Induced Landslides Using a Model for Transient, Unsaturated Infiltration. *J. Geophys. Res. Earth Surf.* 115, 1–26. doi:10.1029/2009jf001321

Beyer, R. A., Alexandrov, O., and McMichael, S. (2018). The Ames Stereo Pipeline: NASA's Open Source Software for Deriving and Processing Terrain Data. *Earth Space Sci.* 5, 537–548. doi:10.1029/2018ea000409

Bickel, V., Manconi, A., and Amann, F. (2018). Quantitative Assessment of Digital Image Correlation Methods to Detect and Monitor Surface Displacements of Large Slope Instabilities. *Remote Sens.* 10 (6), 865. doi:10.3390/rs10060865

Booth, A. M., Roering, J. J., and Perron, J. T. (2009). Automated Landslide Mapping Using Spectral Analysis and High-Resolution Topographic Data: Puget Sound Lowlands, Washington, and Portland Hills, Oregon. *Geomorphology* 109 (3–4), 132–147. doi:10.1016/j.geomorph.2009.02.027

Bull, J. M., Miller, H., Gravley, D. M., Costello, D., Hikuroa, D. C. H., and Dix, J. K. (2010). Assessing Debris Flows Using LIDAR Differencing: 18 May 2005 Matata Event, New Zealand. *Geomorphology* 124, 75–84. doi:10.1016/j.geomorph.2010.08.011

Coe, J. A. (2020). Bellwether Sites for Evaluating Changes in Landslide Frequency and Magnitude in Cryospheric Mountainous Terrain: A Call for Systematic, Long-Term Observations to Decipher the Impact of Climate Change. *Landslides* 17, 2483–2501. doi:10.1007/s10346-020-01462-y

Coe, J. A., Bessette-Kirton, E. K., and Geertsema, M. (2018). Increasing Rock-Avalanche Size and Mobility in Glacier Bay National Park and Preserve, Alaska Detected From 1984 to 2016 Landsat Imagery. *Landslides* 15, 393–407. doi:10.1007/s10346-017-0879-7

Colesanti, C., and Wasowski, J. (2006). Investigating Landslides With Space-Borne Synthetic Aperture Radar (SAR) Interferometry. *Eng. Geol.* 88, 173–199. doi:10.1016/j.enggeo.2006.09.013

Deering, D. W., and Haas, R. H. (1980). Using Landsat Digital Data for Estimating Green Biomass. *NASA Tech. Memo.* 80727, 1.

DGGS Staff (2013). Elevation Datasets of Alaska: Alaska Division of Geological & Geophysical Surveys Digital Data Series 4. Available at: https://maps.dggs.alaska.gov/elevationdata/ (Accessed June 1, 2020).

Franke, K. W., Koehler, R. D., Beyzaei, C. Z., Cabas, A., Pierce, I., Stuedlein, A., et al. (2019). Geotechnical Engineering Reconnaissance of the 30 November 2018 Mw 7.0 Anchorage, Alaska Earthquake. GEER Report GEER-059, 1–46. (Accessed June 1, 2020).

Galli, M., Ardizzone, F., Cardinali, M., Guzzetti, F., and Reichenbach, P. (2008). Comparing Landslide Inventory Maps. *Geomorphology* 94, 268–289. doi:10.1016/j.geomorph.2006.09.023

Gorelick, N., Hancher, M., Dixon, M., Ilyushchenko, S., Thau, D., and Moore, R. (2017). Google Earth Engine: Planetary-Scale Geospatial Analysis for Everyone. *Remote Sens. Environ.* 202, 18–27. doi:10.1016/j.rse.2017.06.031

Grant, A. R., Jibson, R. W., Witter, R. C., Allstadt, K., Thompson, E., Bender, A. M., et al. (2020a). Field Reconnaissance of Ground Failure Triggered by Shaking During the 2018 M7.1 Anchorage, Alaska, Earthquake: U.S. Geological Survey Data Release. Open-File Report 2020-1043. (Accessed June 1, 2020).

Grant, A. R. R., Jibson, R. W., Witter, R. C., Allstadt, K. E., Thompson, E. M., and Bender, A. M. (2020b). Ground Failure Triggered by Shaking during the November 30, 2018, Magnitude 7.1 Anchorage, Alaska, Earthquake: U.S. Geological Survey. Open-File Report 2020-1043. (Accessed June 1, 2020).

Guzzetti, F., Mondini, A. C., Cardinali, M., Fiorucci, F., Santangelo, M., and Chang, K.-T. (2012). Landslide Inventory Maps: New Tools for an Old Problem. *Earth-Sci. Rev.* 112, 42–66. doi:10.1016/j.earscirev.2012.02.001

Hansen, W. R. (1965). Effects of the Earthquake of March 27, 1964, at Anchorage, Alaska. Washington, DC. US Government Printing Office.

Harp, E. L., Jibson, R. W., and Schmitt, R. G. (2016). Map of Landslides Triggered by the January 12, 2010, Haiti Earthquake: Scientific Investigations Map Reston, VA. U.S. Geological Survey, 15.

Hölbling, D., Friedl, B., and Eisank, C. (2015). An Object-Based Approach for Semi-Automated Landslide Change Detection and Attribution of Changes to Landslide Classes in Northern Taiwan. *Earth Sci. Inform.* 8, 327–335. doi:10.1007/s12145-015-0217-3

Idaho Geological Survey (2020). M6.5 Stanley, ID Earthquake Aerial Reconnaissance Report. Available at: https://www.idahogeology.org/pub/Other/IGS_Stanley_EQ_Recon_Summary_20200406.pdf. (Accessed June 1, 2020).

James, L. A., Hodgson, M. E., Ghoshal, S., and Latiolais, M. M. (2012). Geomorphic Change Detection Using Historic Maps and DEM Differencing: The Temporal Dimension of Geospatial Analysis. *Geomorphology* 137, 181–198. doi:10.1016/j.geomorph.2010.10.039

Jibson, R. W., R. Grant, A. R., Witter, R. C., Allstadt, K. E., Thompson, E. M., and Bender, A. M. (2020). Ground Failure From the Anchorage, Alaska, Earthquake of 30 November 2018. *Seismol. Res. Lett.* 91 (1), 19–32. doi:10.1785/0220190187

Jung, J., and Yun, S.-H. (2020). Evaluation of Coherent and Incoherent Landslide Detection Methods Based on Synthetic Aperture Radar for Rapid Response: A Case Study for the 2018 Hokkaido Landslides. *Remote Sens.* 12 (2), 265. doi:10.3390/rs12020265

Keefer, D. K. (1984). Landslides Caused by Earthquakes. *Geol. Soc. Am. Bull.* 95, 406–421. doi:10.1130/0016-7606(1984)95<406:lcbe>2.0.co;2

Larsen, I. J., and Montgomery, D. R. (2012). Landslide Erosion Coupled to Tectonics and River Incision. *Nat. Geosci.* 5, 468–473. doi:10.1038/ngeo1479

Li, G., West, A. J., Densmore, A. L., Jin, Z., Parker, R. N., and Hilton, R. G. (2014). Seismic Mountain Building: Landslides Associated with the 2008 Wenchuan Earthquake in the Context of a Generalized Model for Earthquake Volume Balance. *Geochem. Geophys. Geosyst.* 15, 833–844. doi:10.1002/2013gc005067

Lin, S.-Y., Lin, C.-W., and Van Gasselt, S. (2021). Processing Framework for Landslide Detection Based on Synthetic Aperture Radar (SAR) Intensity-Image Analysis. *Remote Sens.* 13 (4), 644. doi:10.3390/rs13040644

Martha, T. R., Kerle, N., van Westen, C. J., Jetten, V., and Kumar, K. V. (2011). Segment Optimization and Data-Driven Thresholding for Knowledge-Based Landslide Detection by Object-Based Image Analysis. *IEEE Trans. Geosci. Remote Sens.* 49, 4928–4943. doi:10.1109/tgrs.2011.2151866

Martinez, S. N., Schaefer, L. N., Allstadt, K. E., and Thompson, E. M. (2021). Initial Observations of Landslides Triggered by the 2018 Anchorage, Alaska Earthquake. USGS Data Release (Accessed June 1, 2020).

Mirus, B. B., Becker, R. E., Baum, R. L., and Smith, J. B. (2018). Integrating Real-Time Subsurface Hydrologic Monitoring with Empirical Rainfall Thresholds to Improve Landslide Early Warning. *Landslides* 15, 1909–1919. doi:10.1007/s10346-018-0995-z

Mirus, B. B., Jones, E. S., Baum, R. L., Godt, J. W., Slaughter, S., Crawford, M. M., et al. (2020). Landslides Across the USA: Occurrence, Susceptibility, and Data Limitations. *Landslides* 17, 2271–2285. doi:10.1007/s10346-020-01424-4

Mondini, A. C., Guzzetti, F., Chang, K. T., Monserrat, O., Martha, T. R., and Manconi, A. (2021). Landslide Failures Detection and Mapping Using Synthetic Aperture Radar: Past, Present and Future. *Earth-Sci. Rev.* 216, 103574. doi:10.1016/j.earscirev.2021.103574

Mondini, A., Santangelo, M., Rocchetti, M., Rossetto, E., Manconi, A., and Monserrat, O. (2019). Sentinel-1 SAR Amplitude Imagery for Rapid Landslide Detection. *Remote Sens.* 11 (7), 760. doi:10.3390/rs11070760

Mora, O., Lenzano, M., Toth, C., Grejner-Brzezinska, D., and Fayne, J. (2018). Landslide Change Detection Based on Multi-Temporal Airborne LiDAR-Derived DEMs. *Geosciences* 8, 23. doi:10.3390/geosciences8010023

Nowicki Jessee, M. A., Hamburger, M. W., Allstadt, K., Wald, D. J., Robeson, S. M., Tanyas, H., et al. (2018). A Global Empirical Model for Near-Real-Time Assessment of Seismically Induced Landslides. *J. Geophys. Res. Earth Surf.* 123, 1835–1859. doi:10.1029/2017jf004494

Porter, C., Morin, P., Howat, I., Noh, M.-J., Bates, B., Peterman, K., et al. (2018). ArcticDEM. Harvard Dataverse, V1. https://www.pgc.umn.edu/data/arcticdem/ (Accessed June 1, 2021).

Prokešová, R., Kardoš, M., Tábořík, P., Medveďová, A., Stacke, V., and Chudý, F. (2014). Kinematic Behaviour of a Large Earthflow Defined by Surface Displacement Monitoring, DEM Differencing, and ERT Imaging. *Geomorphology* 224, 86–101.

Rosen, P., Hensley, S., Shaffer, S., Edelstein, W., Kim, Y., Kumar, R., et al. (2017). "The NASA-ISRO SAR (NISAR) Mission Dual-Band Radar Instrument Preliminary Design," in 2017 IEEE International Geoscience and Remote Sensing Symposium (IGARSS) Fort Worth, TX, July 23–28, 2017, 3832–3835.

Rosin, P. L., and Hervás, J. (2005). Remote Sensing Image Thresholding Methods for Determining Landslide Activity. *Int. J. Remote Sens.* 26, 1075–1092. doi:10.1080/01431160512331330481

Rott, H., and Nagler, T. (2006). The Contribution of Radar Interferometry to the Assessment of Landslide Hazards. *Adv. Space Res.* 37, 710–719. doi:10.1016/j.asr.2005.06.059

Saroli, M., Stramondo, S., Moro, M., and Doumaz, F. (2005). Movements Detection of Deep Seated Gravitational Slope Deformations by Means of InSAR Data and Photogeological Interpretation: Northern Sicily Case Study. *Terra Nova* 17 (1), 35–43. doi:10.1111/j.1365-3121.2004.00581.x

Scaioni, M., Longoni, L., Melillo, V., and Papini, M. (2014). Remote Sensing for Landslide Investigations: An Overview of Recent Achievements and Perspectives. *Remote Sens.* 6 (10), 9600–9652. doi:10.3390/rs6109600

Stanley, T., and Kirschbaum, D. B. (2017). A Heuristic Approach to Global Landslide Susceptibility Mapping. *Nat. Hazards* 87, 145–164. doi:10.1007/s11069-017-2757-y

Tanyaş, H., Allstadt, K. E., and van Westen, C. J. (2018). An Updated Method for Estimating Landslide-Event Magnitude. *Earth Surf. Process. Landf.* 43, 1836–1847. doi:10.1002/esp.4359

Tanyaş, H., and Lombardo, L. (2020). Completeness Index for Earthquake-Induced Landslide Inventories. *Eng. Geol.* 264, 105331. doi:10.1016/j.enggeo.2019.105331

Tanyaş, H., Van Westen, C. J., Allstadt, K. E., Anna Nowicki Jessee, M., Görüm, T., Jibson, R. W., et al. (2017). Presentation and Analysis of a Worldwide Database of Earthquake-Induced Landslide Inventories. *J. Geophys. Res. Earth Surf.* 122, 1991–2015. doi:10.1002/2017JF004236

Ventura, G., Vilardo, G., Terranova, C., and Sessa, E. B. (2011). Tracking and Evolution of Complex Active Landslides by Multi-Temporal Airborne LiDAR Data: The Montaguto Landslide (Southern Italy). *Remote Sens. Environ.* 115, 3237–3248. doi:10.1016/j.rse.2011.07.007

Disclaimer: Any use of trade, firm, or product names is for descriptive purposes only and does not imply endorsement by the U.S. Government.

Conflict of Interest: The authors declare that the research was conducted in the absence of any commercial or financial relationships that could be construed as a potential conflict of interest.

frontiers
in Earth Science

ORIGINAL RESEARCH
published: 06 July 2021
doi: 10.3389/feart.2021.700546

New Insight into Post-seismic Landslide Evolution Processes in the Tropics

Hakan Tanyaş[1,2,3]*†, Dalia Kirschbaum[2]†, Tolga Görüm[4]†, Cees J. van Westen[1]† and Luigi Lombardo[1]†

[1]Faculty of Geo-Information Science and Earth Observation (ITC), University of Twente, Enschede, Netherlands, [2]Hydrological Sciences Laboratory, NASA Goddard Space Flight Center, Greenbelt, MD, United States, [3]Universities Space Research Association (USRA), Columbia, MD, United States, [4]Eurasia Institute of Earth Sciences, Istanbul Technical University, Istanbul, Turkey

Edited by:
Carmine Galasso,
University College London,
United Kingdom

Reviewed by:
Joern Lauterjung,
German Research Center for
Geosciences, Germany
Mariano Di Napoli,
University of Genoa, Italy

***Correspondence:**
Hakan Tanyaş
h.tanyas@utwente.nl

†ORCID:
Hakan Tanyaş
orcid.org/0000-0002-0609-2140
Dalia Kirschbaum
orcid.org/0000-0001-5547-2839
Tolga Görüm
orcid.org/0000-0001-9407-7946
Cees J. van Westen
orcid.org/0000-0002-2992-902X
Luigi Lombardo
orcid.org/0000-0003-4348-7288

Specialty section:
This article was submitted to
Geohazards and Georisks,
a section of the journal
Frontiers in Earth Science

Received: 26 April 2021
Accepted: 22 June 2021
Published: 06 July 2021

Citation:
Tanyaş H, Kirschbaum D, Görüm T,
van Westen CJ and Lombardo L
(2021) New Insight into Post-seismic
Landslide Evolution Processes in
the Tropics.
Front. Earth Sci. 9:700546.
doi: 10.3389/feart.2021.700546

Earthquakes do not only trigger landslides in co-seismic phases but also elevate post-seismic landslide susceptibility either by causing a strength reduction in hillslope materials or by producing co-seismic landslide deposits, which are prone to further remobilization under the external forces generated by subsequent rainfall events. However, we still have limited observations regarding the post-seismic landslide processes. And, the examined cases are rarely representative of tropical conditions where the precipitation regime is strong and persistent. Therefore, in this study, we introduce three new sets of multi-temporal landslide inventories associated with subsets of the areas affected by 1) 2016 Reuleuet (Indonesia, M_w = 6.5), 2) 2018 Porgera (Papua New Guinea, M_w = 7.5) and 3) 2012 Sulawesi (Indonesia, M_w = 6.3), 2017 Kasiguncu (Indonesia, M_w = 6.6) and 2018 Palu (Indonesia, M_w = 7.5) earthquakes. Overall, our findings show that the landslide susceptibility level associated with the occurrences of new landslides return to pre-seismic conditions in less than a year in the study areas under consideration. We stress that these observations might not be representative of the entire area affected by these earthquakes but the areal boundaries of our study areas.

Keywords: landslide, earthquake, precipitation, landslide recovery, post-seismic landslides

INTRODUCTION

Based on the number of casualties, earthquakes and precipitation are the most common landslide triggers (Petley, 2012) and near-real-time global landslide susceptibility assessment methods are separately available for both earthquake- (e.g., Nowicki Jessee et al., 2018; Tanyaş et al., 2019) and rainfall-triggered (Kirschbaum and Stanley, 2018) landslides. However, none of these statistically based methods are capable of accounting for the coupled effect of earthquakes and precipitation. Nevertheless, characterizing these interactions is critical to advance effective landslide susceptibility assessment because various studies show that the combined effect of earthquakes and rainfall could increase landslide susceptibility (e.g., Sassa et al., 2007; Sæmundsson et al., 2018; Wistuba et al., 2018; Bontemps et al., 2020; Chen et al., 2020a). Specifically, earthquakes are recognized as an important predisposing factor increasing post-seismic landslide susceptibility either by disturbing the strength and/or geometry of hill slope materials or by producing co-seismic landslide deposits, which are prone to instabilities mostly due to subsequent rainfall events (e.g., Lin et al., 2004; Parker et al., 2015; Tanyaş et al., 2021).

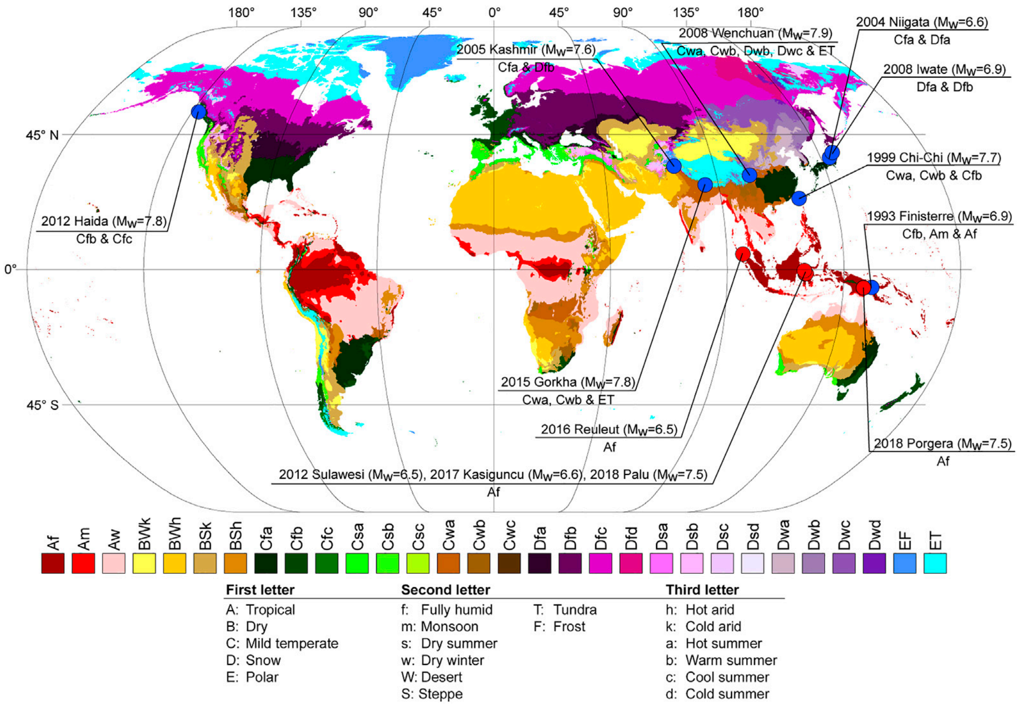

FIGURE 1 | World map of the Köppen-Geiger climate classification (Kriticos et al., 2012) overlaid by the spatial distribution of cases (blue points) in which post-seismic landslide evolution processes were examined *via* multi-temporal landslide inventories. Red points indicate the sites where we mapped multi-temporal inventories for this study.

Either way, the seismic effect can cause a reduction in rainfall thresholds in post-seismic periods (e.g., Liu et al., 2008, Liu et al., 2021; Tanyaş et al., 2021).

To capture the preconditioning effect of seismic shaking for a rainfall-triggered landslide susceptibility assessment, we first need to understand the evolution of landslides in post-seismic periods.

In the geoscientific literature, the post-seismic landslide evolution is examined on the basis of the temporal variation of several parameters such as landslide rate (km^2/year, in Barth et al., 2020), landslide density (m^2/km^2, in Marc et al., 2019), climate normalized landslide rate (Marc et al., 2015), number of landslides (Saba et al., 2010), total landslide area (Shafique, 2020) and cumulative landslide area/volume (Fan et al., 2018). The timespan of the post-seismic period required to restore a given area to pre-seismic landslide susceptibility levels is called landslide recovery time (e.g., Marc et al., 2015; Kincey et al., 2021). And, it is mostly identified using one of the parameters listed above.

Various factors can be interchangeably and/or simultaneously used to explain the mechanisms behind landslide recovery time. Positive correlations between landslide recovery time and various factors such as the amount of co-seismic landslide deposits (e.g., Chen et al., 2020b; Tian et al., 2020; Yunus et al., 2020), the intensity of seismicity in terms of both mainshocks and aftershocks (Fan et al., 2018; Tian et al., 2020) or revegetation rate (e.g., Chen et al., 2020; Xiong et al., 2020; Yunus et al., 2020) are emphasized in the literature. However, there is no agreement in the geoscientific community on the actual meaning of the term landslide recovery. On one hand, some geoscientists define the recovery as a mechanical healing process where the strength of hill slope material is restored (e.g., Marc et al., 2015). On the other hand, others argue that healing on strength of hill slope materials is not possible through natural processes under low pressure and temperature conditions (e.g., Parker et al., 2015).

Regardless of the landslide recovery definition, our knowledge regarding the post-seismic mass wasting processes mostly, if not entirely, depends on landslide inventories. In particular, multi-temporal landslide inventories are vital to understand the spatial and temporal evolution of landslides in post-seismic periods. However, cloud-free aerial images required to create multi-temporal landslide inventories especially for large areas are rarely available and therefore, multi-temporal inventories are not common (Guzzetti et al., 2012). To date, only nine earthquakes in the literature have been associated with post-seismic landslides recorded in a multi-temporal scheme (see **Figure 1**). These earthquakes correspond to: 1) 1993 Finisterre (Papua New Guinea, $M_w = 6.9$) (Marc et al., 2015), 2) 1999 Chi-Chi (Taiwan, $M_w = 7.7$) (e.g., Shou et al., 2011; Marc et al., 2015), 3) 2004 Niigata (Japan, $M_w = 6.6$) (Marc et al., 2015), 4) 2005 Kashmir (India-Pakistan, $M_w = 7.6$) (Saba et al., 2010; Shafique, 2020), 5) 2008 Iwate (Japan, $M_w = 6.9$) (Marc et al., 2015), 6) 2008 Wenchuan (China, $M_w = 7.9$) (e.g., Tang et al., 2016; Zhang et al., 2016; Yang et al., 2017; Fan et al., 2018; Chen et al., 2020b), 7) 2012 Haida Gwaii (Canada, $M_w = 7.8$) (Barth et al., 2020) and 9) 2015 Gorkha (Nepal, $M_w = 7.8$) (Marc et al., 2019; Kincey et al., 2021). Based on the analyses executed on these events, there is a general agreement that earthquakes elevate the landslide susceptibility in post-seismic periods and the landscape returns to pre-seismic susceptibility level over time.

Nevertheless, the agreement reported above within the geoscientific community leaves room for an equal amount of disagreements on the duration of the recovery. In fact, even for the same earthquake, there are different observations regarding the time through which the elevated landslide susceptibility persists in post-seismic periods. For instance, Shafique (2020) examines a subset of the area affected by the 2005 Kashmir earthquake from 2004 to 2018 using multi-temporal landslide inventories and indicates that 13 years after the earthquake the level of landslide susceptibility is still larger than the level estimated in pre-seismic conditions. Conversely, Khan et al. (2013) monitored a sample of the hill slopes that failed during the Kashmir earthquake and suggested that the landscape returned to pre-seismic susceptibility level within five years after the earthquake.

In the same way as above, different timespans of elevated landslide susceptibility have also been suggested for other large earthquakes such as Chi-Chi (e.g., Shou et al., 2011; Marc et al., 2015), Wenchuan (e.g., Fan et al., 2018; Chen et al., 2020b) and Gorkha (e.g., Marc et al., 2019; Kincey et al., 2021) earthquakes. Notably, the inconsistency between different observations could be related to the boundaries of examined areas (e.g., Shafique, 2020; Yunus et al., 2020) because the ground shaking level spatially varies, hence its effect varies as well. In other words, the damage produced by ground motion is not homogeneous throughout the area affected by an earthquake. Kincey et al. (2021) elaborate on this issue and refer to both methodological and conceptual issues. They note that the method used to map landslides and, in particular, the data used for the mapping may play a role. They also indicate that post-seismic landslide evolution could be assessed by monitoring new landslides or both new landslides and reactivated co-seismic landslides. In turn, based on the target post-seismic landsliding processes, different conclusions regarding the post-seismic evolution of landslides could arise.

Taking aside these uncertainties, the actual landslide recovery time could also be different in each earthquake-affected area because of the diversity in environmental conditions (e.g., Kincey et al., 2021). For instance, landslide recovery time could be longer in areas affected by stronger earthquakes (e.g., Fan et al., 2018) and/or stronger and more numerous earthquake aftershocks (Tian et al., 2020). Also, the amount of co-seismic landslide deposits and precipitation patterns could influence the landslide recovery time (e.g., Tian et al., 2020). This shows that different seismic and climatic conditions could shape the general characteristics of post-seismic landslide evolution processes. In this context, new cases reflecting different environmental conditions are essential to better understand the post-seismic processes.

Specifically, new cases from the high-relief mountainous environments where the precipitation rate is high and persistent could provide valuable information regarding landslide recovery time because such conditions could trigger more landslides and allow us to create high-resolution, multi-temporal landslide inventories. However, the literature summarized above shows that post-seismic landslide evolution is rarely examined for fully humid, tropical conditions (**Figure 1**). The only case belonging to this climate zone is the 1993 Finisterre earthquake (Marc et al., 2015). Therefore, in this paper, we aim to contribute to the current literature by introducing three new sets of multi-temporal landslide inventories (two sites from Indonesia and one from Papua New Guinea) where the post-seismic periods are governed by strong and persistent precipitation regimes.

MATERIALS AND METHODS

We examined the post-seismic landslide evolution associated with five earthquakes (**Figure 1**): 1) August 18, 2012 Sulawesi (Indonesia, $M_w = 6.3$), 2) May 29, 2017 Kasiguncu (Indonesia, $M_w = 6.6$), 3) September 28, 2018 Palu (Indonesia, $M_w = 7.5$), 4) December 6, 2016 Reuleuet (Indonesia, $M_w = 6.5$) and 5) February 25, 2018 Porgera (Papua New Guinea, $M_w = 7.5$). In each case, we investigated subsets of areas affected by co-seismic landslides and created multi-temporal inventories by only mapping new landslides (**Table 1**).

The area affected by the Reuleuet earthquake is the first site we examined (**Figure 2**). The second area is affected by the Porgera earthquake (**Figure 3**). The third site is affected by three earthquakes: the Sulawesi, Kasiguncu and Palu earthquakes (**Figure 4**). We should note that the aggregated version of the inventories mapped for the first and the third sites were also examined by Tanyaş et al. (2021) to investigate the legacy of earthquakes as a predisposing factor in susceptibility assessments run for rainfall-induced landslides in post-seismic periods. Specifically, the authors run statistically based multivariate analyses to monitor the contribution of Peak Ground Acceleration (PGA) through time from co-seismic to post-seismic periods. However, landslide recovery time was not elaborated by Tanyaş et al. (2021) as we focus on in this contribution.

To map multitemporal inventories we used PlanetScope (3–5 m), Rapid Eye (5 m) images acquired from Planet Labs (Planet Team, 2018) and high-resolution Google Earth scenes. The details of the satellite images we used are presented in **Supplementary Tables S1, S2 and S3** (see **Supplementary Material**). We systematically examined the satellite images through visual observation, which is the ideal mapping technique reported in the literature (e.g., Xu 2015; Tanyaş et al., 2021). We did not differentiate source and depositional areas of landslides and delineated them as a part of the same polygon.

For each earthquake-affected area, we initially examined all available remotely sensed scenes and choose the largest available cloud-free regions. In turn, all the multitemporal images we used for mapping convey the real landslide distribution over time during pre- and post-seismic periods. Notably, we could not follow a fixed temporal resolution to create the inventories. We mapped as many inventories as the imagery availability allowed (**Table 1**). In each inventory, we eliminated landslides that have previously occurred and only include new failures.

The 2012 Reuleuet earthquake occurred along a strike-slip fault and it triggered only 60 co-seismic landslides over a scanned area of 1356 km^2 (**Figure 2**). We created one landslide inventory associated with pre-seismic conditions, a co-seismic landslide inventory and three post-seismic ones (**Table 1**). Intermediate, basic volcanic and mixed sedimentary rocks are the dominant lithologic units (Sayre et al., 2014) in which landslides are triggered. Based on our interpretation, the co-seismic failures are primarily characterized by shallow translational slides (60 landslides, 0.4 km^2 landslide area). The percentage of post-seismic landslides that interact with previously occurred failures is negligible (<1% of the post-seismic

TABLE 1 | Details of the multi-temporal landslide inventories.

Reuleut earthquake

	Acquisition date of		# Of landslides	Total landslide area (m^2)
	Pre-images	Post-images		
Pre-seismic	12-Jul-15	27-Jul-16	65	514,396
Co-seismic (6-12-2016)	27-Jul-16	14-Dec-16	60	373,600
Post-seismic1	14-Dec-16	25-Mar-17	742	839,696
Post-seismic2	25-Mar-17	12-Feb-18	105	509,187
Post-seismic3	12-Feb-18	5-Jan-19	162	689,646

Porgera earthquake

	Acquisition date of		# Of landslides	Total landslide area (m^2)
	Pre-images	Post-images		
Pre-seismic1	11-Jul-16	30-Sep-17	67	126,458
Pre-seismic2	30-Sep-17	4-Feb-18	66	227,392
Co-seismic (25-2-2018)	4-Feb-18	25-Mar-18	1177	10,402,050
Post-seismic1	25-Mar-18	7-May-18	5	14,715
Post-seismic2	7-May-18	16-Feb-19	35	142,476
Post-seismic3	16-Feb-19	19-Oct-19	14	53,256

Sulawesi, Kasiguncu and Palu earthquakes

	Acquisition date of		# Of landslides	Total landslide area (m^2)	
	Pre-images	Post-images			
Co-seismic-A (18-8-2012)	17-Aug-12	20-Aug-13	520	1,248,485	Sulawesi
Post-seismic-A1	20-Aug-13	6-Feb-14	15	26,647	
Post-seismic-A2	6-Feb-14	5-Jul-15	40	111,938	
Post-seismic-A3	5-Jul-15	19-Oct-15	62	146,584	
Post-seismic-A4	19-Oct-15	16-Feb-16	21	28,999	
Post-seismic-A5	16-Feb-16	25-Apr-17	20	28,375	
Co-seismic-B (29 5-2017)	25-Apr-17	7-Jun-17	386	494,619	Kasiguncu
Post-seismic-B1	7-Jun-17	7-Aug-17	76	67,193	
Post-seismic-B2	7-Aug-17	27-Sep-17	55	50,840	
Post-seismic-B3	27-Sep-17	8-Mar-18	38	45,389	
Post-seismic-B4	8-Mar-18	10-Jun-18	29	35,118	
Post-seismic-B5	10-Jun-18	14-Jul-18	2	2,054	
Post-seismic-B6	14-Jul-18	1-Aug-18	3	2,252	
Post-seismic-B7	1-Aug-18	26-Sep-18	1	682	
Co-seismic-C (2-11-2018)	26-Sep-18	2-Oct-18	725	2,494,215	Palu
Post-seismic-C1	2-Oct-18	22-Oct-18	29	41,595	
Post-seismic-C2	22-Oct-18	17-Mar-19	83	147,493	
Post-seismic-C3	17-Mar-19	9-Sep-19	197	312,380	

landslide population) and no remobilization was observed in the post-seismic period. In other words, most post-seismic failures are characterized by new landslides.

As for the 2018 Porgera earthquake, which occurred on a thrust fault, we examined a 491 km^2 window and mapped a co-seismic landslide inventory including 1,168 landslides with a total surface of 9.8 km^2 (**Figure 3**). Landslides were triggered in basic volcanic and carbonate sedimentary rocks (Sayre et al., 2014). Rock/debris avalanches and translational landslides are observed as part of the co-seismic landslide inventory. We also mapped two pre-seismic and three post-seismic landslide inventories (**Table 1**). Despite the relatively large deposits of co-seismic landslides, we did not observe any connection between post-seismic landslides and those within previously occurred deposits or sliding surfaces. In other words, we mapped only new landslides.

The areas affected by the 2012 Sulawesi (strike-slip), 2017 Kasiguncu (normal fault) and 2018 Palu (strike-slip) earthquakes overlap (**Figure 4**). We mapped the landslides associated with the three earthquakes over an area of 1078 km^2. The co-seismic landslide inventories we created for the overlapping area contained 520 (1.2 km^2), 386 (0.5 km^2) and 725 landslides (2.3 km^2), respectively. We also mapped five, seven and three post-seismic landslide inventories for Sulawesi, Kasiguncu and Palu earthquakes, respectively (**Table 1**). In each case, we interpret the majority of landslides as shallow slides which were triggered in metamorphic and acid plutonic rocks (Sayre et al., 2014). Also, in each case, post-seismic landslides appeared as new failures regardless of the locations of co-seismic landslides and their deposits. The percentage of the post-seismic landslides that appeared to have interacted with previous failures is less than 5%.

Once the multi-temporal inventories were compiled, we examined the temporal evolution of land sliding based on the changes in both the number of landslides and landslide rates. We

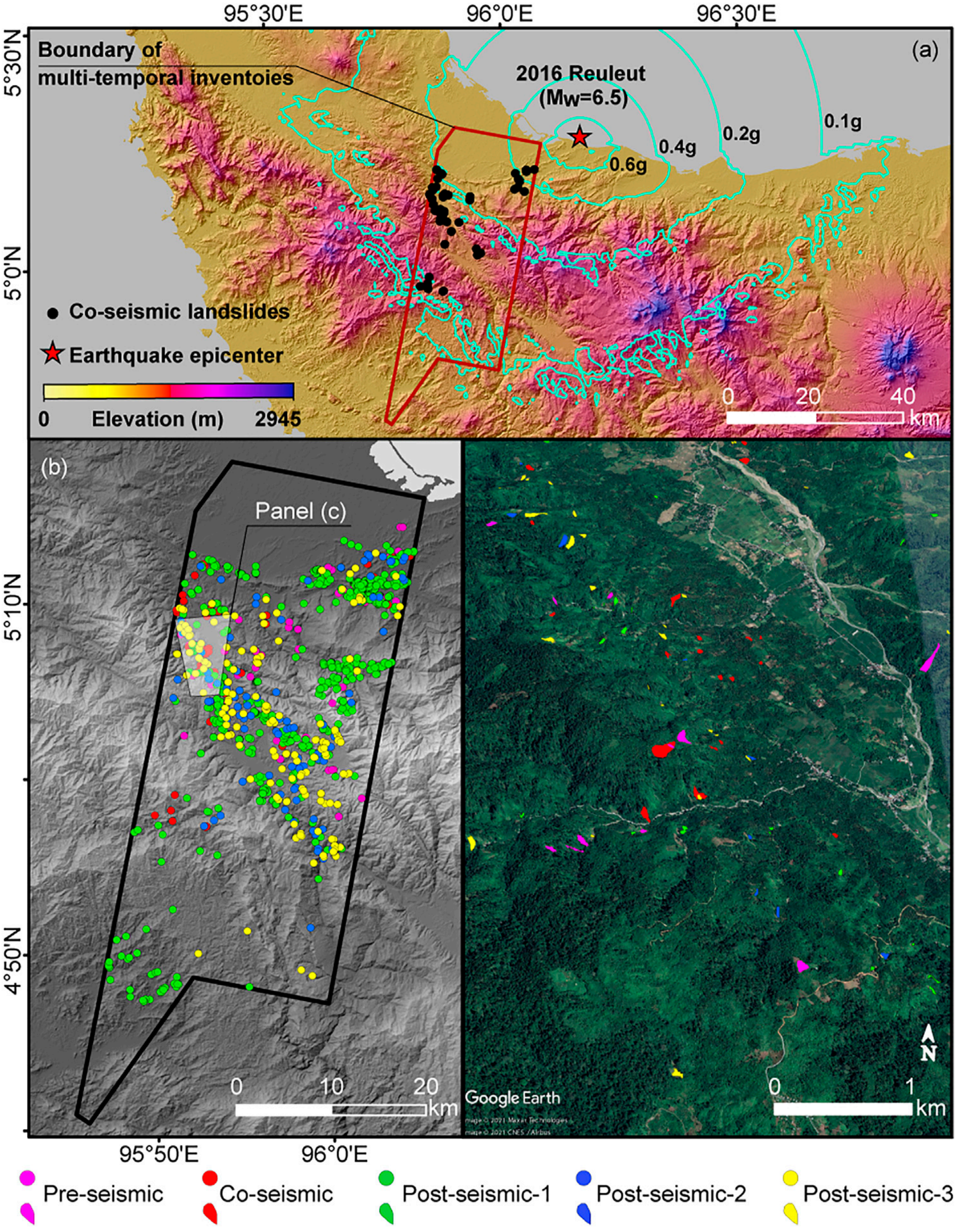

FIGURE 2 | Maps showing **(A)** areal extent of multi-temporal inventories we mapped for the 2017 Reuleut earthquake, **(B)** spatial distribution of mapped landslides and **(C)** Google Earth scene as a sample view of multi-temporal landslide inventories for a subset of the area. In **Panel A** cyan contour lines show PGA values are acquired from the USGS ShakeMap system (Worden and Wald, 2016).

calculated the landslide rates as the total landslide area divided by the length of the scanned time window (m^2/year).

We also analyzed the variation in the precipitation regime to evaluate the role of rainfall. We used the Integrated Multi-Satellite Retrievals (IMERG) Final Run product (Huffman et al., 2015), which is available through Giovanni (v.4.32) (Acker and Leptoukh, 2007) online data system. Using this product, we first calculated the mean and standard deviation of daily accumulated precipitation from a 20-years (from January 1, 2000 to March 31, 2020) time series and compared it with variation in landslide occurrences. Second, we created boxplots of daily accumulated precipitation for each time window that we mapped a landslide inventory and again compared it with variation in landslide occurrences.

RESULTS

For the area affected by the Reuleuet (December 6, 2016) earthquake, we compiled one landslide inventory associated with pre-earthquake conditions, a co-seismic landslide inventory and three post-seismic ones (**Table 1**). We observed

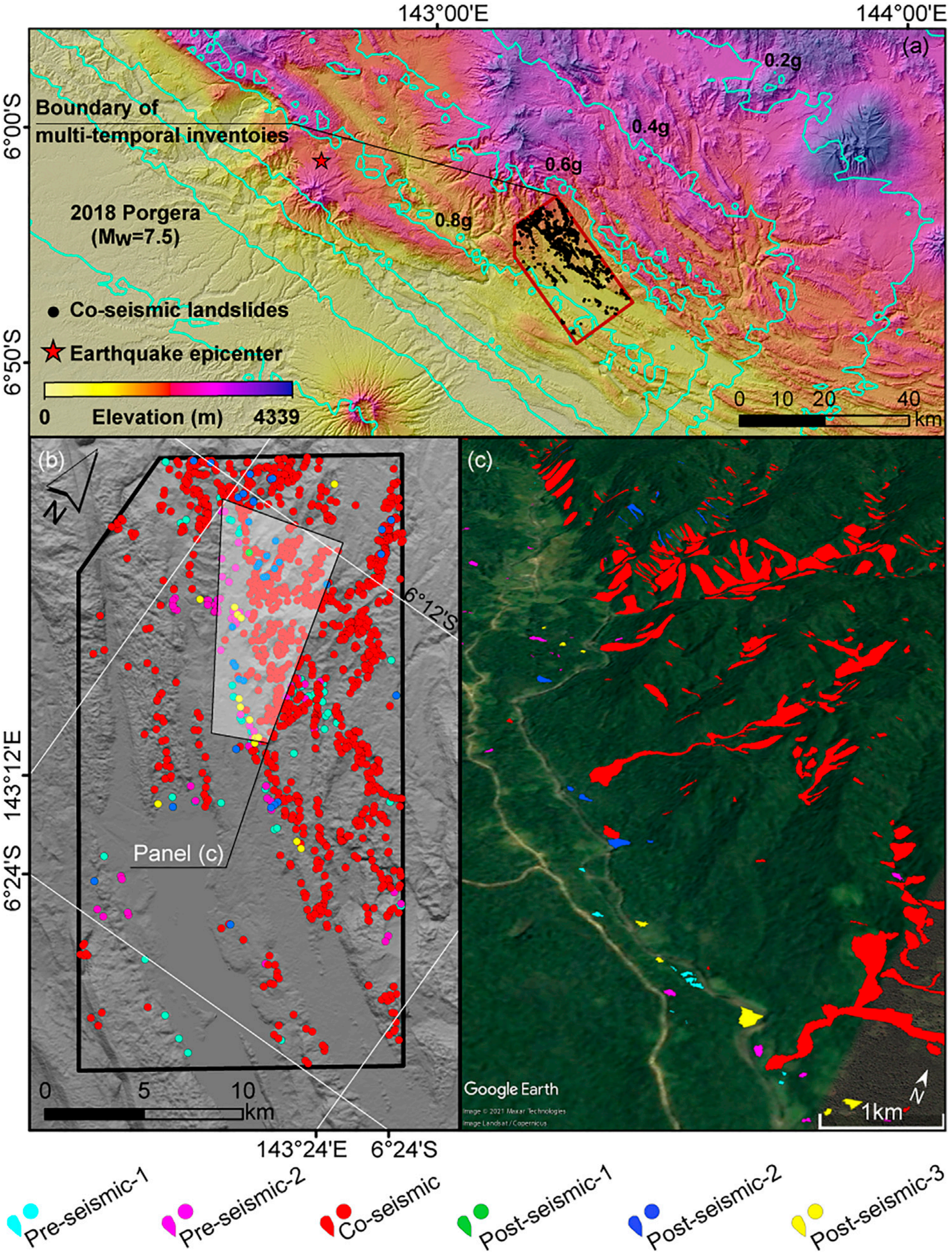

FIGURE 3 | Maps showing **(A)** areal extent of multi-temporal inventories we mapped for the 2018 Porgera earthquake, **(B)** spatial distribution of mapped landslides and **(C)** Google Earth scene as a sample view of multi-temporal landslide inventories for a subset of the area. In **Panel A** cyan contour lines show PGA values are acquired from the USGS ShakeMap system (Worden and Wald, 2016).

the peak landslide rate in our first post-seismic inventory that we created comparing the imageries acquired on December 14, 2016 and March 25, 2017. After the first post-seismic inventory, a strong decline in landslide rates arises toward pre-seismic conditions (**Table 1** and **Figure 5**).

We created the second post-seismic landslide inventory comparing the imageries acquired on March 25, 2017 and February 12, 2018. Precipitation amounts show that during the period that we mapped the second post-seismic inventory, the study area was exposed to more intense rainfall events compared to the pre-seismic period we examined (**Figure 5**). Also, the time window we scanned to create both pre-seismic and second post-seismic landslide inventories have approximately the same length, which is one year. However, the landslide rates and the number of landslides triggered by rainfall are still at the same level in both phases. This shows that landslide rates that we calculated for the occurrences of new landslides return to pre-seismic levels by February 12, 2018 (**Figure 5**). This case shows that the elevated

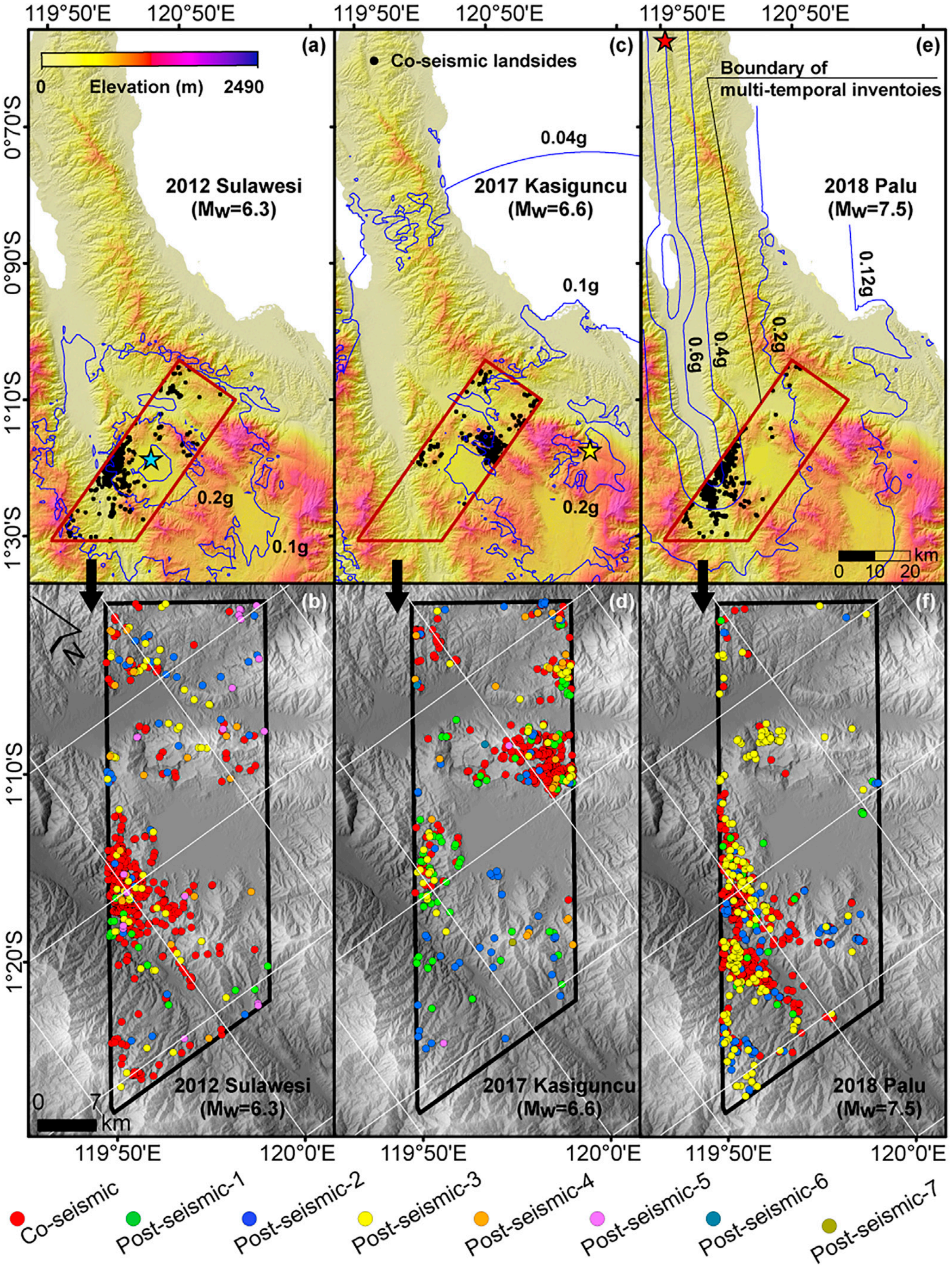

FIGURE 4 | Maps showing areal extent of the examined area and spatial distribution of landslides we mapped for **(A–B)** 2012 Sulawesi **(C–D)** 2017 Kasiguncu and **(E–F)** 2018 Palu earthquakes. In **Panels A**, **C** and **E** blue contour lines show PGA values are acquired from the USGS ShakeMap system (Worden and Wald, 2016).

landslide susceptibility is only valid until March 25, 2017. Also, we note that the highest daily accumulated precipitation for this four-month time window (i.e., between the Reuleut earthquake and March 25, 2017) is observed soon after the earthquake on January 4, 2017. However, due to the lack of availability of more frequent imagery, we could not create a landslide event inventory for that specific rainfall event.

It is worth noting that the landslide rate of landslides triggered by the Reuleut earthquake provided a rare observation where the co-seismic landslide rate is smaller than their post-seismic counterpart (Tanyaş et al., 2021). The peak landslide rate is mostly introduced by co-seismic landslide events in the literature (e.g., Saba et al., 2010; Fan et al., 2018). However, in this case, the earthquake does not trigger widespread co-seismic

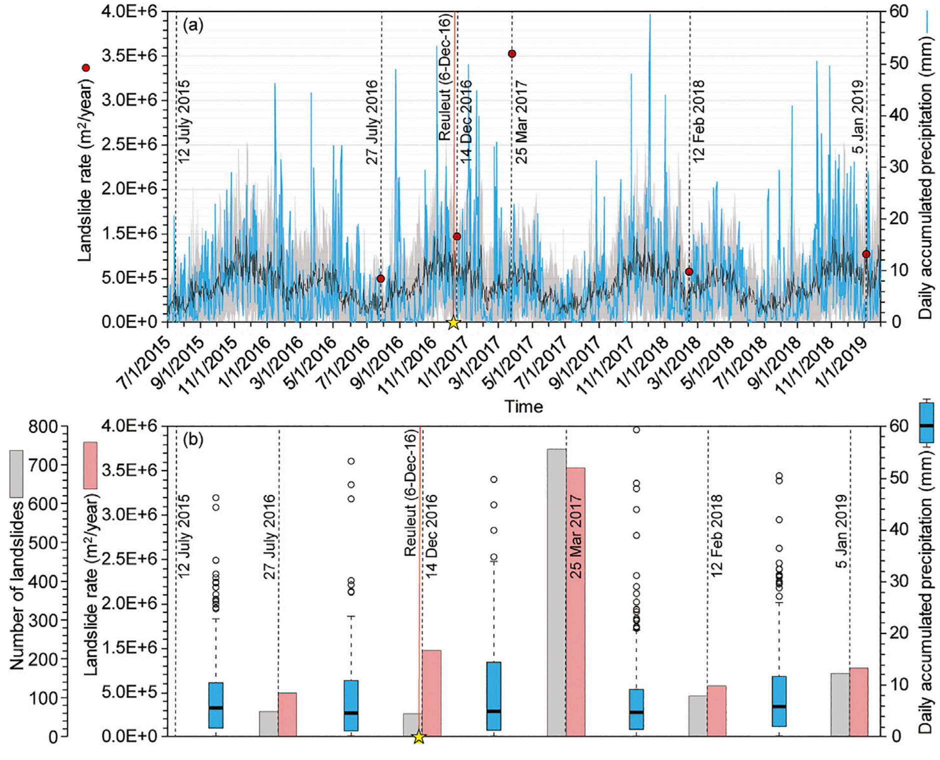

FIGURE 5 | Landslide rates, number of landslides and daily precipitation regarding the examined time windows for the 2016 Reuleuet earthquakes. Yellow stars show the date of the earthquake. Vertical dashed black lines indicate the dates of the satellite imagery used for mapping. In **Panel A**, the mean and standard deviation of daily accumulated precipitation of the respective time windows are calculated from a 20-years time series are shown by black and gray lines, respectively. In **Panel B**, boxplots show minimum, median and maximum precipitation amounts as well as first, third quartiles and outliers.

landslides although it most likely disturbs hill slope materials and makes them more susceptible. As a result, the subsequent rainfall event causes a higher landslide rate compared to the co-seismic phase (Tanyaş et al., 2021).

Regarding the Porgera (February 25, 2018) earthquake, we created two landslide inventories for pre-earthquake conditions, a co-seismic one and three additional post-seismic inventories (**Table 1**). We compared two sets of images from February 4, 2018 and March 25, 2018 to map the co-seismic landslides. We observed the peak landslide rate in the co-seismic phase and then all post-seismic inventories gave rates in the same range with pre-seismic observations (**Table 1** and **Figure 6**). This shows that landslide rates that we calculated for the occurrences of new landslides return to pre-seismic levels by March 25, 2018 (**Figure 6**). Within the 50-days gap between the two sets of images we used to create our co-seismic landslide inventory, we noticed two peaks in daily accumulated precipitation on March 12th and 21st. Therefore, those rainfall events may have already triggered some of the post-seismic landslides and our co-seismic inventory may also include post-seismic landslides. However, we do not have landslide inventories capturing those specific rainfall events.

In the third site, affected by three earthquakes (2012 Sulawesi, 2017 Kasiguncu and 2018 Palu earthquakes), we separately compiled co-seismic landslide inventories for each case. Furthermore, we mapped five inventories between the 2012 Sulawesi and 2017 Kasiguncu earthquakes. Similarly, we digitized seven inventories to monitor landslide rates between the 2017 Kasiguncu and 2018 Palu earthquakes. Ultimately, we compiled three additional inventories describing post-seismic conditions with reference to the last (Palu) earthquake (**Table 1**). Below, we present each earthquake and associated pre-, co- and post-seismic landslide inventories separately.

The inventory featuring the co-seismic landslides triggered by the Sulawesi earthquake (August 18, 2012) lacked the support of pre-earthquake imageries. Moreover, we could not find cloud-free images showing the situation through the entire area until the August 20, 2013. However, we acquired some scenes, (e.g., 17th and August 21, 2012, September 4, 2012 and February 4, 2013) which allowed us to partly but consistently observe pre- and co-seismic conditions in a fraction of the study area. Therefore, the peak landslide rate we observed in the first post-seismic inventory (August 20, 2013) likely reflects the presence of some pre- and post-seismic landslides in addition to the co-seismic ones (**Figure 7**). Nevertheless, the six intra-seismic inventories mapped between the August 20, 2013 and the April 25, 2017 showed significantly lower landslide rates compared to the first post-seismic one. As a result, we can still assume that the August 20, 2013 inventory mostly encompasses co-seismic landslides.

For the Kasiguncu (May 29, 2017) earthquake, we observed another co-seismic landslide peak (**Figure 7**). We compiled this inventory using images acquired on seventh, 10th and June 26,

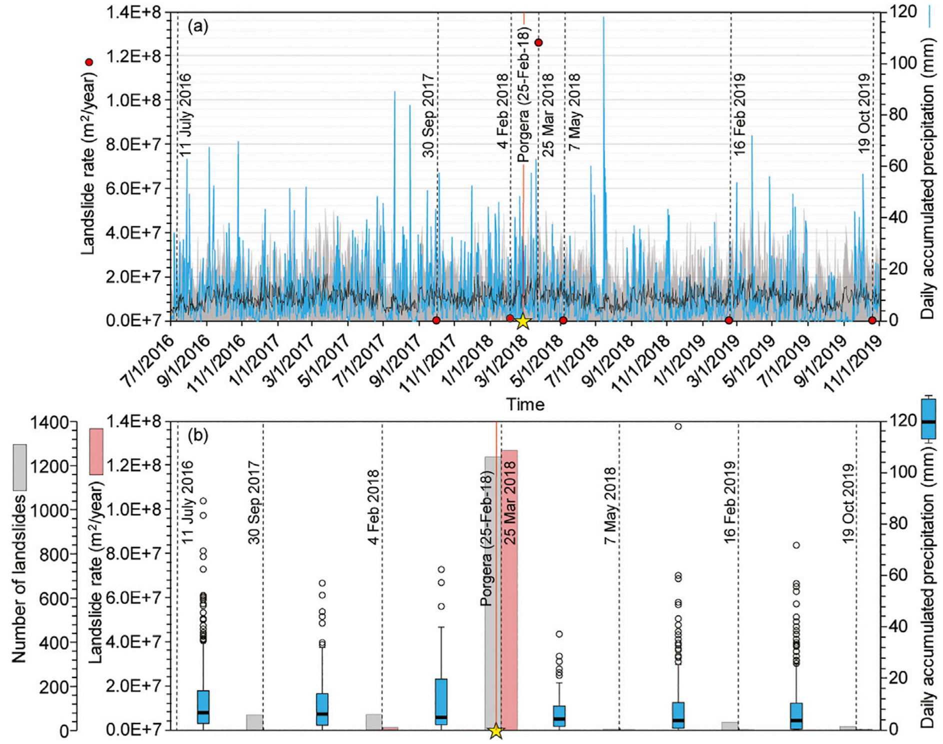

FIGURE 6 | Landslide rates, number of landslides and daily precipitation regarding the examined time windows for the 2018 Porgera earthquakes. Yellow stars show the date of the earthquake. Vertical dashed black lines indicate the dates of the satellite imagery used for mapping. In **Panel A**, the mean and standard deviation of daily accumulated precipitation of the respective time windows are calculated from a 20-years time series are shown by black and gray lines, respectively. In **Panel B**, boxplots show minimum, median and maximum precipitation amounts as well as first, third quartiles and outliers.

2017. Therefore, we can confidently argue that co-seismic landslides cause this peak. We also mapped seven intra-seismic landslide inventories before the occurrence of the Palu earthquake. The first two intra-seismic inventories showed relatively higher landslide rates than the rest (**Figure 7**). These relatively high rates can be linked to extreme precipitation discharged after the Kasiguncu earthquake (please note six rainfall peaks in **Figure 7C**), although these rates are still in range or lower than the ones before the Kasiguncu earthquake (**Figure 7**). Notably, the third post-Kasiguncu inventory (March 8, 2018) highlights a regular or pre-seismic landslide regime which implies that landslide rates that we calculated for the occurrences of new landslides return to pre-seismic levels by March 8, 2018 (**Figure 7**).

For the Palu (September 28, 2018) earthquake ($M_w = 7.5$), we also compiled a co-seismic landslide inventory using scenes acquired on second and October 5, 2018. In this case, the associated landslide rate is significantly higher due to the strong shaking with respect to the previous two earthquakes (2012 Sulawesi, Mw = 6.3 and 2017 Kasiguncu, Mw = 6.6), which took place in the same area (**Figure 4**). The three post-seismic inventories highlight a rapid decline in landslide rates, although it should be noted that these rates did not align along with the low to very low-rate trends shown in pre-Palu conditions (**Figures 7A,B**). Nevertheless, we do not have an adequate series of observations as we have for the Kasiguncu case and because of this, it is not clear whether these low landslide rates imply a return to pre-seismic levels.

DISCUSSION

As noted earlier in the text, in this study we focused on sites where post-seismic landslide processes are mostly governed by occurrences of new landslides in tropics where precipitation is high and persistent. We examined five earthquakes in total and mapped multi-temporal landslide inventories for each of them from pre-to post-seismic phases. Between five earthquakes, the landslide time series we created for Sulawesi and Palu earthquakes, on one hand, did not provide adequate information to cover the entire process of landslide evolution. In the Sulawesi case, we could not map a pre-seismic landslide inventory, whereas in the Palu earthquake our inventories did not cover a period long enough to monitor the entire post-seismic landslide evolution. On the other hand, for three of the examined cases (2012 Reuleut, 2017 Kasiguncu and 2018 Porgera), our multi-temporal inventories showed that after the earthquake the elevated landslide susceptibility levels return to pre-seismic conditions in less than a year.

We stress that these observations may not be representative of the entire area affected by these earthquakes but the areal boundaries of our study areas. This means that for the whole

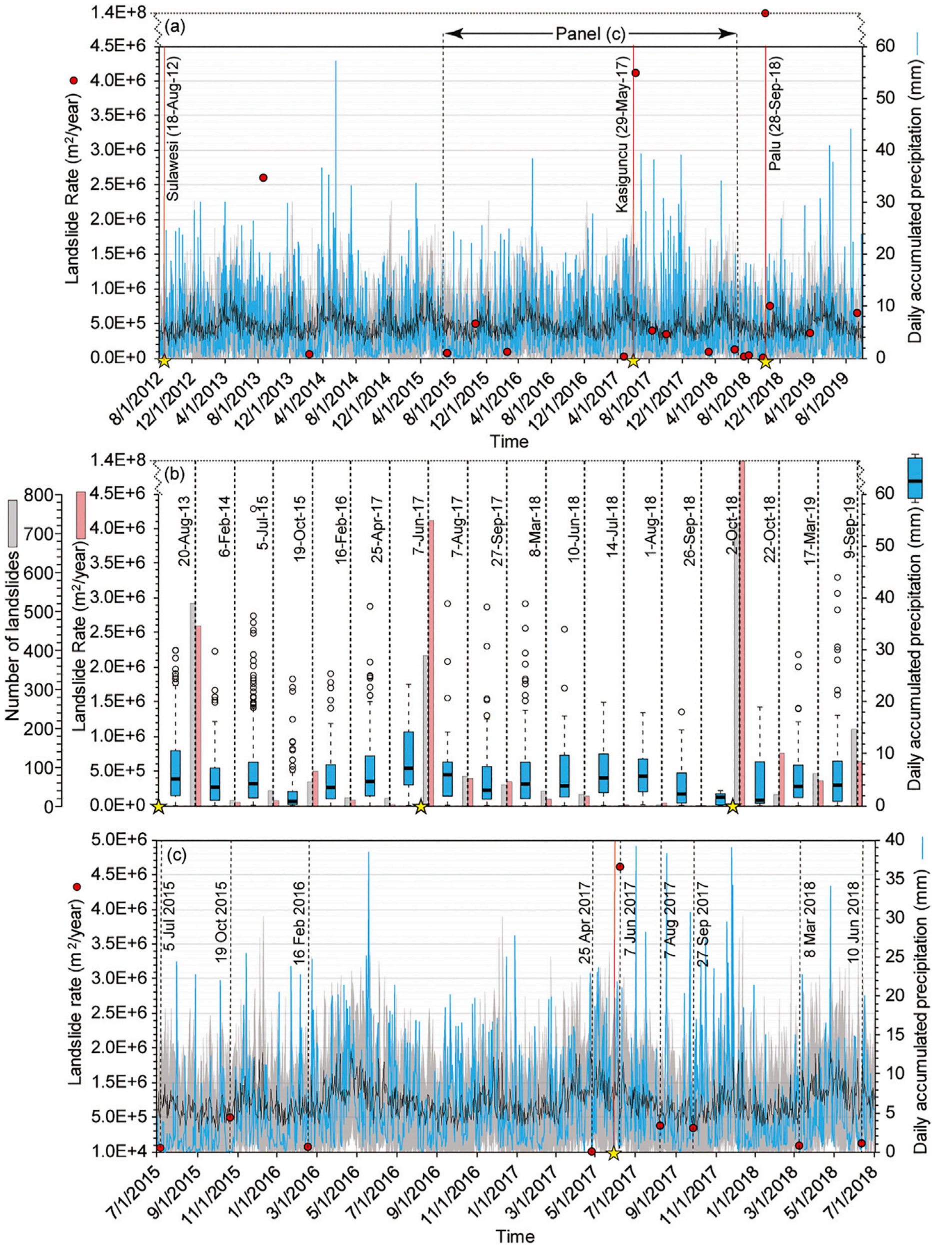

FIGURE 7 | Landslide rates, number of landslides and daily precipitation regarding **(A–B)** the largest time-window where we examined the landslides associated with three earthquakes (2012 Sulawesi, 2017 Kasiguncu and 2018 Palu earthquakes) and **(C)** a zoomed-in view plotted for pre-, co- and post-seismic landslides associated with the 2017 Kasiguncu earthquake. Yellow stars show the date of the earthquakes. Vertical dashed black lines indicate the dates of the satellite imagery used for mapping. In **Panels A** and **C**, the mean and standard deviation of daily accumulated precipitation is calculated from a 20-years time series are shown by black and gray lines, respectively. In **Panel B**, boxplots show minimum, median and maximum precipitation amounts as well as first, third quartiles and outliers.

areas affected by these earthquakes these observations may not valid. However, compared to the similar works in the literature suggesting at least a few years for returning to the pre-seismic susceptibility levels (e.g., Marc et al., 2015; Fan et al., 2018; Kincey et al., 2021), our findings still point out a relatively short period.

Among the examined cases, the 2016 Reuleut earthquake is a clear example to discuss the possible factors controlling this relatively short period to return to pre-seismic landslide rates. The Reuleut earthquake triggered only 60 shallow landslides in the examined area although, within 110 days from the earthquake, we observed 742 new landslides in the same site (**Table 1** and **Figure 5**). This later series of landslides is larger than the common landslide rate in the area. However, from this time onward, the landslide rate recovers to its pre-earthquake pattern (**Figure 5**). The limited number of shallow co-seismic landslides implies that there is not much material deposited on hill slopes and the remobilization processes through, for instance, debris flows are negligible. This shows that the post-seismic process is governed by occurrences of new landslides and therefore, returning to pre-seismic landslide rates could be relatively quick (e.g., Tian et al., 2020).

By discarding the contribution of deposit availability, the most likely explanation for the high landslide susceptibility following the earthquake can be associated with strength reduction in hillslope regolith and/or bedrock caused by ground shaking (e.g., Parker et al., 2015; Fan et al., 2019). In such cases, the post-seismic landsliding processes may be controlled by two mechanisms already postulated in the literature (e.g., Saba et al., 2010; Marc et al., 2015): 1) healing of soil and/or rock mass strength parameters and/or 2) the environmental stress due to the subsequent rainfall discharge.

The healing of soil strength parameters is a proven process under certain circumstances (Lawrence et al., 2009; Fan et al., 2015; Bontemps et al., 2020). Specifically, in tropical landscapes, we can expect relatively fast recovery rates in the vegetation cover, which may play a large role in lateral root reinforcement for shallow landslide mitigation (e.g., Schwarz et al., 2010). However, vegetation recovery is a gradually occurring process and it may take three years even for the fast-growing tree species in the tropics (Dislich and Huth, 2012). For instance, Yunus et al. (2020) examined the relationship between vegetation recovery and landslide rates *via* Normalized Difference Vegetation Index (NDVI) values and concluded that just based on the established NDVI trend, pre-seismic landslide rates can be obtained within 18 years. Moreover, considering the persistent external stress caused by the precipitation regime in Reuleut, Indonesia (i.e., in the absence of dry season), in such a short post-seismic period (i.e., 110 days), healing in soil strength parameters is not likely to take place.

The second alternative refers to the intensity and duration of the post-earthquake rainfall regime. Precipitation may negatively affect disturbed hillslopes that the earthquake has brought to a Factor of Safety (FoS) close to one. However, the rainfall may not be enough to bring the FoS to the brink of actual instability and failure. As a result, regardless of the abovementioned healing processes, post-seismic landslide rates might decrease gradually through time or might decline rapidly based on the climatic conditions, particularly based on intensity and persistence of precipitation.

We can further discuss the intensity of landslide triggers, for instance, considering post-seismic landslides following the 2005 Kashmir earthquake. After the first monsoon season following the Kashmir earthquake, Saba et al. (2010) observed only a few landslides despite the heavy precipitation. Our interpretation is in line with theirs, stating that the rainfall intensity might not be enough to trigger further landslides. On the other hand, they also note that another possible reason for the lack of landslides is that all unstable slopes might have already failed by that moment. However, the unstable slope is a relative term and a failure can occur on any slope if there is an access amount of external forces disturbing the stability conditions.

In this context, our newly developed landslide dataset allows us to elaborate on the relativity of the term "unstable slope" and to make a simplified comparison between the intensity of rainfall and earthquake events as triggering agents that exacerbate slope stability conditions. The area affected by three earthquakes (2012 Sulawesi, 2017 Kasiguncu and 2018 Palu) shows that even relatively low-intensity ground shaking might be more effective than intense precipitation at triggering landslides. After the Sulawesi earthquake, the post-seismic landslide rates remain low until the 2017 Kasiguncu earthquake, although several intense rainfall events occurred between 2014 and 2017 (**Figure 7**). However, the high landslide rate associated with the 2017 Kasiguncu earthquake occurs despite the relatively weak ground shaking estimates reported by the U.S. Geological Survey, ShakeMap system for the examined area (PGA≈0.08–0.10 g) (Worden and Wald, 2016) (**Figure 8A**). This implies that having a limited number of landslides related to rainfall events may not be due to the removal of all unstable slopes or healing on hill slope materials but because of a lack of triggers with sufficient intensity to cause failures on hill slopes, even when some of them have been previously damaged.

This research also provides some findings regarding the argument that the legacy of the previous earthquakes can be valid years after an earthquake occurs (Parker et al., 2015). The Indonesia case where we mapped three co-seismic landslide inventories for the same site shows that there is an increasing trend in the co-seismic landslide rates over time (**Figure 8B**). With co-seismic landslides, the intensity of ground shaking is naturally the main factor controlling the landslide rates. In fact, the 2018 Palu earthquake (M_w = 7.5) caused one of the biggest landslide events observed in this region, though the site was hit by several large earthquakes previously (Watkinson and Hall, 2019). The Palu earthquake created strong ground motions within our study area with PGA values ranging from 0.20 to 0.68 g (**Figure 8A**). Therefore, the peak landslide rate related to the Palu earthquake is a natural consequence of such a large earthquake. On the other hand, within the same study area, the severity of ground shaking related to the 2017 Kasiguncu earthquake (PGA≈0.08–0.10 g) was relatively lower than the 2012 Sulawesi earthquake (PGA≈0.08–0.26 g). The level of ground shaking caused by the Kasiguncu earthquake is out of the zone in which the large majority of landslides (90% of the total landslide population) are located in most of the earthquake-induced landslide inventories in the literature. Specifically, Tanyaş and Lombardo (2019) identify the 0.12 g contour as the areal boundary of the zone containing at least 90% of the landslides. They also identify 0.05 g as the minimum PGA value triggering landslides. This means that our study area is located in a zone where we do not expect so many failures caused by the Kasiguncu earthquake. However, the Kasiguncu earthquake triggered 382 landslides and the post-seismic landslide rates of Kasiguncu earthquake is relatively higher than the Sulawesi earthquake (**Figure 8B**), although there is no significant change in the precipitation regime (**Figure 7**). The relatively high landslide rates, in this case, might be explained by various factors such as frequency and/or duration of ground shaking (Jibson et al., 2004, 2019; Jibson and Tanyaş, 2020) and detailed analyses are required to better understand these controlling factors. Yet, among various possible explanations, we can also count the legacy of the Sulawesi earthquake as a factor

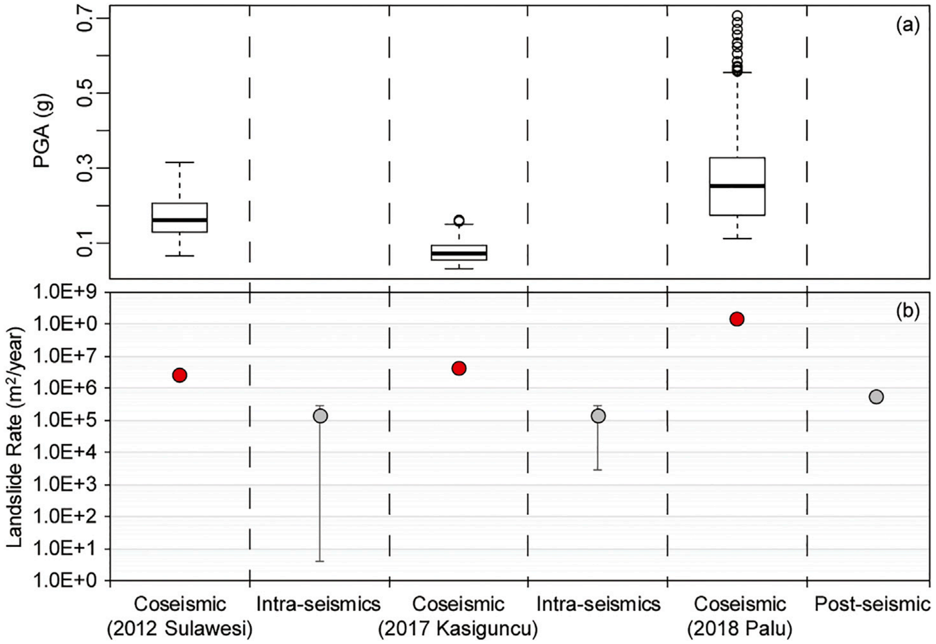

FIGURE 8 | Plot showing **(A)** central tendencies and ranges of PGA for Sulawesi, Kasiguncu and Palu earthquakes and **(B)** the evolution of landslide rates in time for both co-seismic and post-seismic (intra-seismic) landslides. The error bars are given for the first standard deviation of landslide rates for each examined and post-seismic (intra-seismic) set of landslides.

dictating the higher landslide rate concerning the Kasiguncu earthquake.

The variation in the mean (and standard deviation) of landslide rates for these three sets of post-seismic landslide inventories (see gray dots in **Figure 8B**) also suggests a similar conclusion that the legacy of the previous earthquakes might play a role in the trend of increasing post-seismic landslide rates through time. The accumulated disturbance on hill slope materials might cause a small increase in the average landslide rate of a site. As a result, the background level for the landslide susceptibility might be higher after each earthquake compared to previous earthquakes.

CONCLUSION

In this work, we examined the temporal evolution of landslides during post-seismic periods in which the combined effect of earthquakes and rainfall causes a particularly elevated landside susceptibility. Specifically, we examined some cases where rainfall acts as the main landslide trigger and seismicity plays the role of a predisposing factor. We focused on earthquakes that occurred in fully humid, tropical conditions because of two reasons. First, post-seismic landslide processes have been rarely investigated in these settings. Therefore, providing a new dataset belonging to rarely examined conditions could provide valuable information to better understand the post-seismic processes, which are mainly governed by site-specific environmental factors (e.g., seismicity, climate, etc.) (e.g., Tian et al., 2020). The second reason is due to the high and persistent precipitation regimes typical of tropical environments. In fact, these settings provide the perfect conditions for continuous genesis of slope failures, making it possible to obtain high spatial and temporal resolution time series of landslide inventories. The average temporal resolutions of our inventories are approximately eight, seven and five months for the areas affected by Reuleut, Porgera and Palu earthquakes, respectively (**Table 1**).

We observed that landslide susceptibility levels associated with the occurrences of new landslides return to pre-seismic conditions in less than a year, for the environmental settings under consideration. This implies that the elevated landslide susceptibility could disappear rapidly if the area is exposed to strong and persistent rainfall discharges. However, this does not mean that prolonged and strong precipitation regimes always bring a rapid decline in elevated landslide susceptibility. Site-specific characteristics of a study area such as seismotectonic, morphologic, geologic and climatic conditions, as well as sediment budget associated with co-seismic landslide events, govern the evolution of post-seismic periods. In this context, the possible roles of these factors need to be examined by further analyses.

DATA AVAILABILITY STATEMENT

The original contributions presented in the study are included in the article/**Supplementary Material**, the inventories we mapped for this study are shared through NASA Landslide Viewer (https://landslides.nasa.gov). Further inquiries can be directed to the corresponding author.

AUTHOR CONTRIBUTIONS

HT, DK, TG, LL and CW contributed to conception and design of the study. All authors contributed to manuscript revision, read, and approved the submitted version.

SUPPLEMENTARY MATERIAL

The Supplementary Material for this article can be found online at: https://www.frontiersin.org/articles/10.3389/feart.2021.700546/full#supplementary-material

REFERENCES

Barth, S., Geertsema, M., Bevington, A. R., Bird, A. L., Clague, J. J., Millard, T., et al. (2020). Landslide Response to the 27 October 2012 Earthquake (MW 7.8), Southern Haida Gwaii, British Columbia, Canada. *Landslides* 17, 517–526. doi:10.1007/s10346-019-01292-7

Bontemps, N., Lacroix, P., Larose, E., Jara, J., and Taipe, E. (2020). Rain and Small Earthquakes Maintain a Slow-Moving Landslide in a Persistent Critical State. *Nat. Commun.* 11, 1–10. doi:10.1038/s41467-020-14445-3

Chen, L., Mei, L., Zeng, B., Yin, K., Shrestha, D. P., and Du, J. (2020a). Failure Probability Assessment of Landslides Triggered by Earthquakes and Rainfall: a Case Study in Yadong County, Tibet, China. *Sci. Rep.* 10, 16531. doi:10.1038/s41598-020-73727-4

Chen, M., Tang, C., Xiong, J., Shi, Q. Y., Li, N., Gong, L. F., et al. (2020b). The Long-Term Evolution of Landslide Activity Near the Epicentral Area of the 2008 Wenchuan Earthquake in China. *Geomorphology* 367, 107317. doi:10.1016/j.geomorph.2020.107317

Dislich, C., and Huth, A. (2012). Modelling the Impact of Shallow Landslides on forest Structure in Tropical Montane Forests. *Ecol. Model.* 239, 40–53. doi:10.1016/j.ecolmodel.2012.04.016

Fan, L., Lehmann, P., and Or, D. (2015). Effects of Hydromechanical Loading History and Antecedent Soil Mechanical Damage on Shallow Landslide Triggering. *J. Geophys. Res. Earth Surf.* 120, 1990–2015. doi:10.1002/2015JF003615

Fan, X., Domènech, G., Scaringi, G., Huang, R., Xu, Q., Hales, T. C., et al. (2018). Spatio-temporal Evolution of Mass Wasting after the 2008 Mw 7.9 Wenchuan Earthquake Revealed by a Detailed Multi-Temporal Inventory. *Landslides* 15, 2325–2341. doi:10.1007/s10346-018-1054-5

Fan, X., Scaringi, G., Domènech, G., Yang, F., Guo, X., Dai, L., et al. (2019). Two Multi-Temporal Datasets that Track the Enhanced Landsliding after the 2008 Wenchuan Earthquake. *Earth Syst. Sci. Data* 11, 35–55. doi:10.5194/essd-11-35-2019

Guzzetti, F., Mondini, A. C., Cardinali, M., Fiorucci, F., Santangelo, M., and Chang, K.-T. (2012). Landslide Inventory Maps: New Tools for an Old Problem. *Earth-Science Rev.* 112, 42–66. doi:10.1016/j.earscirev.2012.02.001

Huffman, G. J., Bolvin, D. T., Braithwaite, D., Hsu, K., Joyce, R., Kidd, C., et al. (2015). *NASA Global Precipitation Measurement (GPM) Integrated Multi-satellitE Retrievals for GPM (IMERG) Prepared for: Global Precipitation Measurement (GPM) National Aeronautics and Space Administration (NASA); Algorithm Theoretical Basis Document Version 4.5*. Washington, DC: National Aeronautics and Space Administration, 26

Jibson, R. W., Harp, E. L., Schulz, W., and Keefer, D. K. (2004). Landslides Triggered by the 2002 Denali Fault, Alaska, Earthquake and the Inferred Nature of the strong Shaking. *Earthquake Spectra* 20, 669–691. doi:10.1193/1.1778173

Jibson, R. W., R. Grant, A. R., Witter, R. C., Allstadt, K. E., Thompson, E. M., and Bender, A. M. (2019). Ground Failure from the Anchorage, Alaska, Earthquake of 30 November 2018. *Seismol. Res. Lett.* 91, 19–32. doi:10.1785/0220190187

Jibson, R. W., and Tanyaş, H. (2020). The Influence of Frequency and Duration of Seismic Ground Motion on the Size of Triggered Landslides-A Regional View. *Eng. Geology.* 273, 105671. doi:10.1016/j.enggeo.2020.105671

Khan, S. F., Kamp, U., and Owen, L. A. (2013). Documenting Five Years of Landsliding after the 2005 Kashmir Earthquake, Using Repeat Photography. *Geomorphology* 197, 45–55. doi:10.1016/j.geomorph.2013.04.033

Kincey, M. E., Rosser, N. J., Robinson, T. R., Densmore, A. L., Shrestha, R., Pujara, D. S., et al. (2021). Evolution of Coseismic and Post-seismic Landsliding After the 2015 M W 7.8 Gorkha Earthquake, Nepal. *J. Geophys. Res. Earth Surf.* 126, e2020JF005803. doi:10.1029/2020JF005803

Kirschbaum, D., and Stanley, T. (2018). Satellite-Based Assessment of Rainfall-Triggered Landslide Hazard for Situational Awareness. *Earth's Future* 6, 505–523. doi:10.1002/2017EF000715

Kriticos, D. J., Webber, B. L., Leriche, A., Ota, N., Macadam, I., Bathols, J., et al. (2012). CliMond: Global High-Resolution Historical and Future Scenario Climate Surfaces for Bioclimatic Modelling. *Methods Ecol. Evol.* 3, 53–64. doi:10.1111/j.2041-210X.2011.00134.x

Lawrence, Z., Bodin, P., and Langston, C. A. (2009). *In Situ* measurements of Nonlinear and Nonequilibrium Dynamics in Shallow, Unconsolidated Sediments. *Bull. Seismological Soc. America* 99, 1650–1670. doi:10.1785/0120080177

Lin, C.-W., Shieh, C.-L., Yuan, B.-D., Shieh, Y.-C., Liu, S.-H., and Lee, S.-Y. (2004). Impact of Chi-Chi Earthquake on the Occurrence of Landslides and Debris Flows: Example from the Chenyulan River Watershed, Nantou, Taiwan. *Eng. Geology.* 71, 49–61. doi:10.1016/S0013-7952(03)00125-X

Liu, C.-N., Huang, H.-F., and Dong, J.-J. (2008). Impacts of September 21, 1999 Chi-Chi Earthquake on the Characteristics of Gully-type Debris Flows in central Taiwan. *Nat. Hazards* 47, 349–368. doi:10.1007/s11069-008-9223-9

Liu, S., Hu, K., Zhang, Q., Zhang, S., Hu, X., and Tang, D. (2021). Quantitative Analysis of the Effects of an Earthquake on Rainfall Thresholds for Triggering Debris-Flow Events. *Front. Earth Sci.* 9, 417, 2021. Available at: https://www.frontiersin.org/article/10.3389/feart.2021.676470. doi:10.3389/feart.2021.676470

Marc, O., Behling, R., Andermann, C., Turowski, J. M., Illien, L., Roessner, S., et al. (2019). Long-term Erosion of the Nepal Himalayas by Bedrock Landsliding: The Role of Monsoons, Earthquakes and Giant Landslides. *Earth Surf. Dynam.* 7, 107–128. doi:10.5194/esurf-7-107-2019

Marc, O., Hovius, N., Meunier, P., Uchida, T., and Hayashi, S. (2015). Transient Changes of Landslide Rates after Earthquakes. *Geology* 43, 883–886. doi:10.1130/G36961.1

Nowicki Jessee, M. A., Hamburger, M. W., Allstadt, K., Wald, D. J., Robeson, S. M., Tanyas, H., et al. (2018). A Global Empirical Model for Near-Real-Time Assessment of Seismically Induced Landslides. *J. Geophys. Res. Earth Surf.* 123, 1835–1859. doi:10.1029/2017JF004494

Parker, R. N., Hancox, G. T., Petley, D. N., Massey, C. I., Densmore, A. L., and Rosser, N. J. (2015). Spatial Distributions of Earthquake-Induced Landslides and Hillslope Preconditioning in the Northwest South Island, New Zealand. *Earth Surf. Dynam.* 3, 501–525. doi:10.5194/esurf-3-501-2015

Petley, D. (2012). Global Patterns of Loss of Life from Landslides. *Geology* 40, 927–930. doi:10.1130/G33217.1

Planet Team (2018). *Planet Application Program Interface: In Space for Life on Earth*. San Francisco, CA. Available at: https://api.planet.com (Accessed March 20, 2020).

Saba, S. B., van der Meijde, M., and van der Werff, H. (2010). Spatiotemporal Landslide Detection for the 2005 Kashmir Earthquake Region. *Geomorphology* 124, 17–25. doi:10.1016/j.geomorph.2010.07.026

Sæmundsson, Þ., Morino, C., Helgason, J. K., Conway, S. J., and Pétursson, H. G. (2018). The Triggering Factors of the Móafellshyrna Debris Slide in Northern Iceland: Intense Precipitation, Earthquake Activity and Thawing of Mountain Permafrost. *Sci. Total Environ.* 621, 1163–1175. doi:10.1016/j.scitotenv.2017.10.111

Sassa, K., Fukuoka, H., Wang, F., and Wang, G. (2007). "Landslides Induced by a Combined Effect of Earthquake and Rainfall," in *"Landslides Induced by a Combined Effect of Earthquake and Rainfall," in* Progress in Landslide Science. Editors K. Sassa, H. Fukuoka, F. Wang, and G. Wang (Berlin, Heidelberg: Springer Berlin Heidelberg)), 193–207. doi:10.1007/978-3-540-70965-7_14

Sayre, R., Dangermond, J., Frye, C., Vaughan, R., Aniello, P., Breyer, S., et al. (2014). *A New Map of Global Ecological Land Units-An Ecophysiographic Stratification Approach*. Washington, DC: Assoc. Am. Geogr.

Schwarz, M., Lehmann, P., and Or, D. (2010). Quantifying Lateral Root Reinforcement in Steep Slopes - from a Bundle of Roots to Tree Stands. *Earth Surf. Process. Landforms* 35, 354–367. doi:10.1002/esp.1927

Shafique, M. (2020). Spatial and Temporal Evolution of Co-seismic Landslides after the 2005 Kashmir Earthquake. *Geomorphology* 362, 107228. doi:10.1016/j.geomorph.2020.107228

Shou, K. J., Hong, C. Y., Wu, C. C., Hsu, H. Y., Fei, L. Y., Lee, J. F., et al. (2011). Spatial and Temporal Analysis of Landslides in Central Taiwan after 1999 Chi-Chi Earthquake. *Eng. Geology.* 123, 122–128. doi:10.1016/j.enggeo.2011.03.014

Tang, C., Van Westen, C. J., Tanyas, H., and Jetten, V. G. (2016). Analysing post-earthquake Landslide Activity Using Multi-Temporal Landslide Inventories Near the Epicentral Area of the 2008 Wenchuan Earthquake. *Nat. Hazards Earth Syst. Sci.* 16, 2641–2655. doi:10.5194/nhess-16-2641-2016

Tanyaş, H., Kirschbaum, D., and Lombardo, L. (2021). Capturing the Footprints of Ground Motion in the Spatial Distribution of Rainfall-Induced Landslides. *Bull. Eng. Geol. Environ.* 80, 4323. doi:10.1007/s10064-021-02238-x

Tanyaş, H., and Lombardo, L. (2019). Variation in Landslide-Affected Area under the Control of Ground Motion and Topography. *Eng. Geol.* 260, 105229. doi:10.1016/j.enggeo.2019.105229

Tanyas, H., Rossi, M., Alvioli, M., van Westen, C. J., and Marchesini, I. (2019). A Global Slope Unit-Based Method for the Near Real-Time Prediction of Earthquake-Induced Landslides. *Geomorphology* 327, 126–146. doi:10.1016/j.geomorph.2018.10.022

Tian, Y., Owen, L. A., Xu, C., Ma, S., Li, K., Xu, X., et al. (2020). Landslide Development within 3 Years after the 2015 Mw 7.8 Gorkha Earthquake, Nepal. *Landslides* 17, 1251–1267. doi:10.1007/s10346-020-01366-x

Watkinson, I. M., and Hall, R. (2019). Impact of Communal Irrigation on the 2018 Palu Earthquake-Triggered Landslides. *Nat. Geosci.* 12, 940–945. doi:10.1038/s41561-019-0448-x

Wistuba, M., Malik, I., Krzemień, K., Gorczyca, E., Sobucki, M., Wrońska-Wałach, D., et al. (2018). Can Low-Magnitude Earthquakes Act as a Triggering Factor for Landslide Activity? Examples from the Western Carpathian Mts, Poland. *CATENA* 171, 359–375. doi:10.1016/j.catena.2018.07.028

Worden, C. B., and Wald, D. J. (2016). *ShakeMap Manual Online: Technical Manual, User's Guide, and Software Guide*. Golden, Colorado: U. S. Geological Survey. doi:10.5066/F7D21VPQ

Xiong, J., Tang, C., Chen, M., Zhang, X., Shi, Q., and Gong, L. (2020). Activity Characteristics and Enlightenment of the Debris Flow Triggered by the Rainstorm on 20 August 2019 in Wenchuan County, China. *Bull. Eng. Geol. Environ.* 80, 873–888. doi:10.1007/s10064-020-01981-x

Xu, C. (2015). Preparation of Earthquake-Triggered Landslide Inventory Maps Using Remote Sensing and GIS Technologies: Principles and Case Studies. *Geosci. Front.* 6, 825–836. doi:10.1016/j.gsf.2014.03.004

Yang, W., Qi, W., Wang, M., Zhang, J., and Zhang, Y. (2017). Spatial and Temporal Analyses of post-seismic Landslide Changes Near the Epicentre of the Wenchuan Earthquake. *Geomorphology* 276, 8–15. doi:10.1016/j.geomorph.2016.10.010

Yunus, A. P., Fan, X., Tang, X., Jie, D., Xu, Q., and Huang, R. (2020). Decadal Vegetation Succession from MODIS Reveals the Spatio-Temporal Evolution of post-seismic Landsliding after the 2008 Wenchuan Earthquake. *Remote Sensing Environ.* 236, 111476. doi:10.1016/j.rse.2019.111476

Zhang, S., Zhang, L., Lacasse, S., and Nadim, F. (2016). Evolution of Mass Movements Near Epicentre of Wenchuan Earthquake, the First Eight Years. *Sci. Rep.* 6, 1–9. doi:10.1038/srep36154

Conflict of Interest: The authors declare that the research was conducted in the absence of any commercial or financial relationships that could be construed as a potential conflict of interest.

frontiers
in Earth Science

ORIGINAL RESEARCH
published: 26 July 2021
doi: 10.3389/feart.2021.689303

Rapid Terrain Assessment for Earthquake-Triggered Landslide Susceptibility With High-Resolution DEM and Critical Acceleration

Season Maharjan[1], Kaushal Raj Gnyawali[1,2], Dwayne D. Tannant[2], Chong Xu[3] and Pascal Lacroix[4]*

[1]Natural Hazards Section, Himalayan Risk Research Institute (HRI), Kathmandu, Nepal, [2]School of Engineering, The University of British Columbia, Kelowna, BC, Canada, [3]National Institute of Natural Hazards, Ministry of Emergency Management of China, Beijing, China, [4]ISTerre, Université Grenoble Alpes, IRD, CNRS, Grenoble, France

Earthquake ground motion often triggers landslides in mountainous areas. A simple, robust method to quickly evaluate the terrain's susceptibility of specific locations to earthquake-triggered landslides is important for planning field reconnaissance and rescues after earthquakes. Different approaches have been used to estimate coseismic landslide susceptibility using Newmark's sliding block model. This model requires an estimate of the landslide depth or thickness, which is a difficult parameter to estimate. We illustrate the use of Newmark sliding block's critical acceleration for a glaciated valley affected by the 2015 Gorkha earthquake in Nepal. The landslide data came from comparing high-resolution pre- and post-earthquake digital elevation models (DEMs) derived from Spot 6/7 images. The areas where changes were detected provided an inventory of all the landslides triggered by the earthquake. The landslide susceptibility was modeled in a GIS environment using as inputs the pre-earthquake terrain and slope angles, the peak ground acceleration from the 2015 Gorkha earthquake, and a geological map. We exploit the depth information for the landslides (obtained by DEM difference) to apply the critical acceleration model. The spatial distribution of the predicted earthquake-triggered landslides matched the actual landslides when the assumed landslide thickness in the model is close to the median value of the actual landslide thickness (2.6 m in this case). The landslide predictions generated a map of landslide locations close to those observed and demonstrated the applicability of critical acceleration for rapidly creating a map of earthquake-triggered landslides.

Keywords: rapid terrain assessment, earthquake-triggered landslides, critical acceleration, 2015 Gorkha earthquake, high resolution DEM, Newmark's sliding block, Langtang valley, landslide thickness

Edited by:
Mark Bebbington,
Massey University, New Zealand

Reviewed by:
Hans-Balder Havenith,
University of Liège, Belgium
Francesca Bozzoni,
Fondazione Eucentre, Italy

****Correspondence:***
Kaushal Raj Gnyawali
gnyawalikr@hri.org.np

Specialty section:
This article was submitted to Geohazards and Georisks, a section of the journal Frontiers in Earth Science

Received: *31 March 2021*
Accepted: *01 July 2021*
Published: *26 July 2021*

Citation:
Maharjan S, Gnyawali KR, Tannant DD, Xu C and Lacroix P (2021) Rapid Terrain Assessment for Earthquake-Triggered Landslide Susceptibility With High-Resolution DEM and Critical Acceleration. Front. Earth Sci. 9:689303. doi: 10.3389/feart.2021.689303

INTRODUCTION

Earthquake ground motion is one of the main triggering agents for catastrophic landslides worldwide. According to Keefer (1984), earthquake magnitudes greater than 6.0 Moment Magnitude (Mw) can trigger landslides over areas extending up to 500,000 square kilometers. The 1994 Northridge earthquake (Mw = 6.7) in California triggered more than 11,000 landslides over an area of ~10,000 km^2 (Harp and Jibson, 1996). The 2002 Denali Fault earthquake (Mw = 7.8) in

Alaska triggered more than 1,580 landslides in a glaciated area of 7,150 km^2 (Gorum et al., 2014). The 2008 Wenchuan earthquake (Mw = 7.9) in China caused 197,481 landslides in ~110,000 km^2 (Xu et al., 2014). In Nepal, the 2015 Gorkha earthquake (Mw = 7.8) triggered more than 25,000 landslides covering 61.5 km^2 in an area of 20,500 km^2 (Gnyawali and Adhikari, 2017; Roback et al., 2018; Tian et al., 2020).

Rapid assessment of earthquake-triggered landslide hazards is vital for planning response and recovery operations, in the immediate aftermath of an earthquake. Such landslides are widespread, so usually, the reconnaissance is carried out by flying helicopters in pre-defined priority tracks to identify the landslide hotspots, valley blocking slides, and damaged infrastructure locations. E.g., In the 2016 central Italy earthquake sequence by Stewart et al. (2018) and Lanzo et al. (2018); in the 2015 Gorkha earthquake sequence by Collins and Jibson (2015); and in the 2016 Kaikoura earthquake by Jibson et al. (2018). To efficiently plan the reconnaissance operation, as well as pre-planning of the earthquake-triggered landslide (ETL) hazards, a model to predict widespread landslide locations is pivotal for disaster management.

Newmark (1965) proposed a method for analyzing the deformation of embankments and dams caused by earthquake shaking, assuming the dam moves as a single rigid block. Although Newmark (1965) first developed this method for embankments and dams, Wilson and Keefer (1983) applied it for assessing the stability of natural slopes under earthquake shaking. Permanent displacement of the landslide occurs when the seismic acceleration exceeds a critical value (Newmark, 1965). When the seismic acceleration exceeds the critical acceleration, the block moves relative to the slope and stops when the earthquake acceleration drops below the critical acceleration. Newmark's method considers only rigid block movements with no internal deformations. Shear deformation is assumed at the base of the block (Newmark, 1965). The method has been found suitable for shallow landslides during earthquakes (Keefer, 1994; Keefer, 2002). The Newmark sliding block method has been used to assess earthquake-triggered landslides (ETL) in Los Angeles, California (Jibson et al., 2000), Greece (Chousianitis et al., 2014), Wenchuan, China (Chen et al., 2014), Longmenshan, China (Yuan et al., 2016) and Lushan, China (Jin et al., 2019).

The Newmark method has been tested for evaluating slope stability for several earthquakes. Two different approaches for using the Newmark method are popular: a) evaluate the yield displacement (Newmark's displacement) of a sliding block or b) evaluate the critical acceleration required to move a sliding block. The displacement method uses a threshold displacement as a sliding block criterion. The landslide displacement is calculated by double integrating the recorded acceleration-time record of the earthquake (Newmark, 1965) or using empirical formulae (Jibson et al., 2000; Jibson, 2007). For the acceleration method or simplified Newmark block method, the critical acceleration needed to cause a block to slide is compared with the measured peak ground acceleration (PGA). When PGA exceeds the critical acceleration, the landslide is triggered. Both approaches have been implemented to study ETL susceptibility.

Newmark's displacement method was used to study areas affected by the Chi-Chi earthquake in Taiwan and showed a good prediction of shallow landslides compared with the observed landslides (Wang and Lin, 2010). Similarly, Jin et al. (2019) used a modified Newmark's method and found that the predicted landslide map agreed well with the actual distribution of the landslides triggered by the Lushan earthquake, China. Newmark's displacement method was used to model ETL from the 2015 Gorkha earthquake (Gallen et al., 2016). Although the model results had similarities with the general landslide pattern, the detailed distribution of landslides was not captured by the Newmark model (Gallen et al., 2016). The model shortcomings were attributed to large cell sizes in the digital elevation model (90 m), aspects of the ground motion spectra that PGA does not capture, and lack of spatial variability in surface material strength. Other studies have used critical acceleration, instead of Newmark's displacement, to analyze the terrain's susceptibility to ETL (Chen et al., 2014; Xiaoli and Chunguo, 2019; Chen et al., 2020). Chen et al. (2014) compared the landslide distribution triggered by the 2008 Wenchuan earthquake with a critical acceleration map and found good correspondence with the actual landslide locations. An ETL susceptibility map can be easily prepared from a probable PGA map using the critical acceleration concept (Xiaoli and Chunguo, 2019). But to prepare a map using Newmark's displacement method, earthquake acceleration-time records are needed, which are often not available at the location of landslide-affected areas, and even less so before an earthquake disaster. These studies indicate that the critical acceleration method can help predict ETL locations *via* comparison with an independent estimate of the peak ground acceleration. Furthermore, when earthquake data are limited, critical acceleration is a better approach than Newmark's displacement for rapid assessment of the terrain's susceptibility to ETL locations.

The evaluation of the method presented here to predict ETL locations method requires a detailed inventory of actual ETL locations and an estimate of the landslide depths, which can be converted into thicknesses. Erial photographs or satellite images are commonly used to delineate landslide areas (as polygons) after an earthquake. These polygons can be used to validate the prediction results from the critical acceleration model (Wang and Lin, 2010; Chen et al., 2014; Shinoda and Miyata, 2017). These landslide inventories capture the areal information but typically lack the landslide depth data. Researchers have adopted different approaches to estimate the landslide depth. Wang and Lin (2010) estimated the depth using an empirical slope-depth relationship. Shinoda and Miyata (2017) assumed a 2 m landslide depth for the Niigata earthquake, based on a field study conducted by Kieffer et al. (2006). Ma and Xu (2019) set the landslide depth as 3 m based on field observation and previous research (Jibson et al., 2000; Dreyfus et al., 2013). Landslide depths derived from these approaches may not provide a reasonable estimate of the actual depths because they are based on regional studies or estimates from a few local field observations. Here, we determine the landslide areas and depth information by subtracting a high-resolution post-earthquake digital elevation model (DEM) from a pre-earthquake DEM. The availability of landslide depth

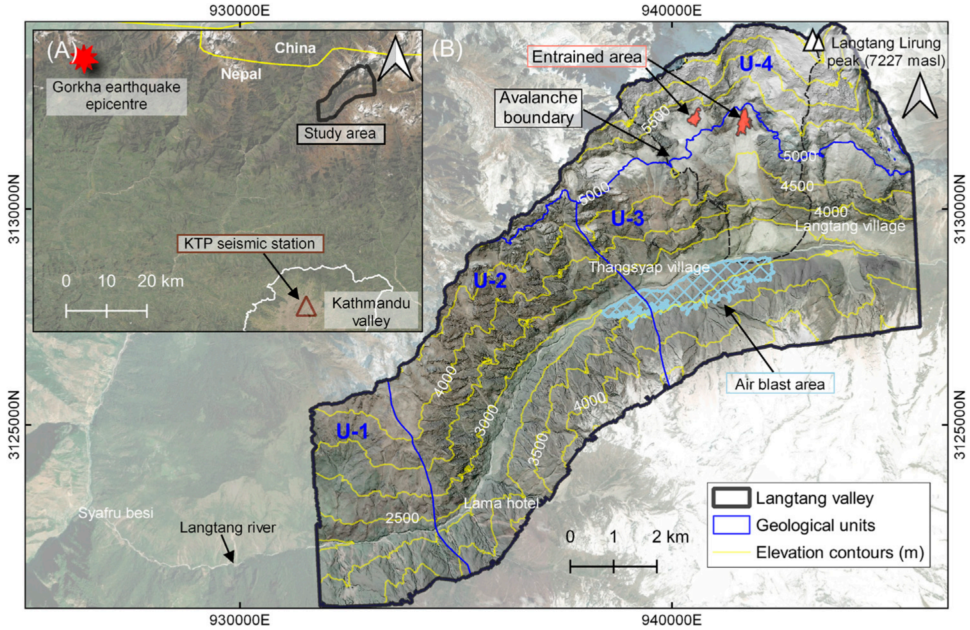

FIGURE 1 | Map of Langtang valley. **(A)** Study area lies approximately 60 km north of Kathmandu. The red star shows the epicenter of the 2015 Gorkha earthquake. **(B)** Langtang valley topography indicated by yellow elevation contours. The blue lines are boundaries of geological units (Jones et al., 2020), U-1 (Syaprubesi formation), U-2 (Bamboo formation), and U-3 (Langtang formation). U-4 is above the permanent snowline at 5,000 masl and consists of glacier ice and snow. The black dashed line shows the catastrophic Langtang avalanche boundary that originated above 5,000 masl and descended onto Langtang village at ~3,400 masl. The red polygons are the avalanche's entrainment areas (Gnyawali et al., 2020). The blue hatched polygon is the air-blast impact area on the opposite slope of the valley.

information from the DEMs enables the calibration of the critical acceleration model and allows exploration of the relationship between observed landslide thicknesses and the thickness used in the model.

STUDY AREA

Here, we focus on the Langtang area in Nepal, affected by the 2015 Gorkha earthquake (Mw7.8), to evaluate the critical acceleration method for ETL susceptibility assessment. This area is a glaciated valley and a popular tourist destination. It also had the largest and most destructive landslide triggered by the 2015 Gorkha earthquake, a rock avalanche that killed more than 350 people and buried the Langtang village (Kargel et al., 2015). An air blast created by the rock avalanche uprooted trees and flattened the forest on the opposite valley wall (Kargel et al., 2015; Lacroix, 2016). Aside from this rock avalanche, three different studies mapped between 160 and 205 landslides in the study area (Lacroix 2016; Gnyawali and Adhikari, 2017; Roback et al., 2018). The landslides varied in size from rockfalls to very large landslides, and many landslides had long-runout zones because of the steep terrain.

The valley lies approximately 60 km north of Kathmandu (**Figure 1A**). Nearly half of the Langtang valley (46% or 166 km^2) is covered by glaciers (Immerzeel et al., 2012). Langtang Khola is the main river draining the valley westwards to the Bhote Koshi River at Syabru Besi. The Langtang valley has a U-shape (Immerzeel et al., 2012) and is surrounded by high mountains with the highest peak, Langtang Lirung, 7,227 m above sea level (masl) (Lacroix, 2016). The study area is a part of the Langtang valley (91.4 km^2) and has a length and width of approximately 15 and 6 km (**Figure 1B**). The valley has steep slopes prone to landslides (Lacroix, 2016).

The Gorkha earthquake epicenter was located approximately 70 km west of the study area. The 2015 Gorkha earthquake was followed by numerous aftershocks, including five greater than 6.0 Mw between April 25 and June 10, 2015 (Kargel et al., 2015). The peak ground acceleration measured at the closest seismic station (KTP) was 2.41 m/s^2 in the east-west direction. This station was near Kathmandu, approximately 60 km south of the study area (Takai et al., 2016). The 2015 Gorkha earthquake triggered more than 25,000 landslides in Central Nepal (Gnyawali and Adhikari, 2017; Roback et al., 2018; Tian et al., 2020).

Most landslides in the study area had shallow depths (<5 m), and many occurred in surficial glacial and post-glacial soils over the bedrock (**Figure 2**). The bedrock geology is dominated by gneiss in the valley, which likely resulted in glacial soils dominated by sand and gravel particle sizes. **Figure 1** shows the bedrock units as U-1 to U-3, adapted from Jones et al. (2020). The Syaprubesi formation (U-1) consists of gneiss dominated by muscovite, biotite, and quartz, with subordinate plagioclase and garnet. Likewise, the Bamboo formation (U-2) is gneiss dominated by muscovite, biotite, and quartz, with subordinate tourmaline. The Langtang formation (U-3) consists of leucogranite, dominated by muscovite, tourmaline, epidote, and occasionally garnet. These previously glaciated areas are covered by various thicknesses of glacial materials such as

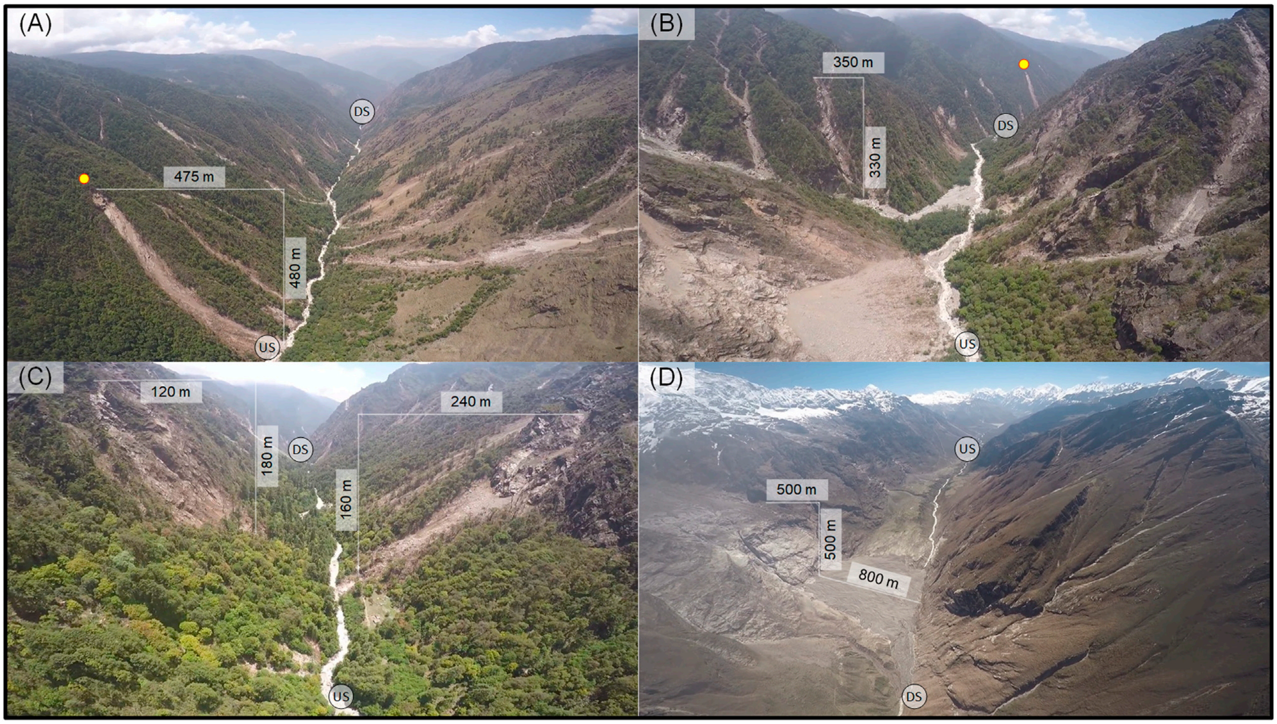

FIGURE 2 | Photos of earthquake-triggered landslides in the Langtang valley extracted from video recordings (Collins, 2015). The camera locations for each photograph **(A–D)** are shown in **Figure 3**. The yellow dot in panels **(A)** and **(B)** corresponds to the same landslide. US = upstream and DS = downstream.

TABLE 1 | Different types of data used in this study.

Data	Date	Description	Application	Source
Geological map	2019	Based on fieldwork	Lithological classification	Jones et al. (2020)
Pre-earthquake DEM	21-04-2014	4 m cell size	Determine local slope angle and aspect	Lacroix (2016)
Post-earthquake DEM	10-05-2015	4 m cell size	Create the landslide inventory	Lacroix (2016)
Gorkha earthquake ground motion	14-01-2016	On-line ground motion map	Determine peak ground accelerations	USGS ShakeMap

glacial tills and glaciofluvial sediments, as well as more recent colluvium and debris flow deposits. Terraces of glacial soils exist near the valley bottom. Permanent snow occurs above the altitude of 5,000 masl in the valley (Fujita et al., 2017), and the U-4 area is covered by glacier ice and snow. During the 2015 Gorkha earthquake, the catastrophic Langtang avalanche originated from multiple high-altitude source areas in U-4 and involved snow, ice, and rock fragments (Lacroix, 2016; Gnyawali et al., 2020). As separate rock avalanches descended, they entrained debris before merging into one large rock avalanche that traveled to the valley bottom and burying the village of Langtang (**Figure 1B**).

DATA AND METHODS

The critical acceleration method is used to map ETL susceptibility. This method compares the critical acceleration of a slope section with the expected PGA at this location to assess slope stability. The critical acceleration is calculated using topography and geology parameters. The slope angle is obtained from a high-resolution pre-earthquake DEM (Lacroix, 2016). The geotechnical parameters (cohesion, friction angle, and unit weight landslide materials) are estimated from a geology map of the Langtang valley (Jones et al., 2020). **Table 1** summarizes the different types of data used in this study. In addition, an estimate of the landslide thickness is needed to calculate the factor of safety. The landslide thickness is unknown before an earthquake, but the model can be run using various landslide thicknesses. For the Langtang Valley case history, different thicknesses were used to create predicted landslide distribution maps. The map found to best match the actual landslide distribution map was used to determine the most suitable landslide thickness. This thickness was compared to actual landslide thicknesses found from analysis of the pre-and post-earthquake DEMs.

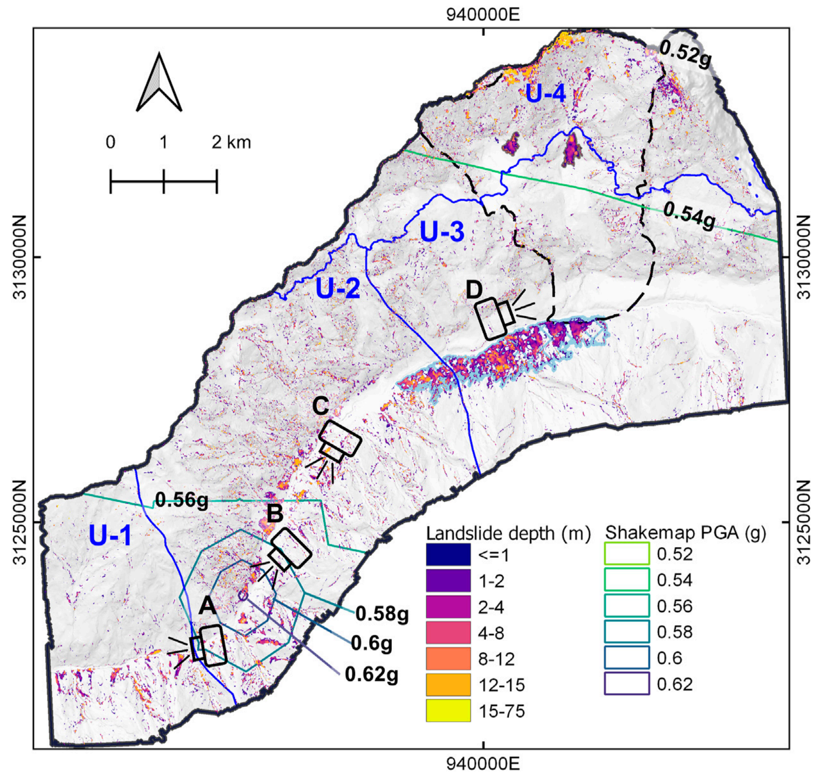

FIGURE 3 | Landslide source area cells computed from pre- and post-earthquake DEM differences and adjusted for DEM elevation accuracies, modified after Lacroix (2016). **(A–D)** are camera locations corresponding to **Figure 2**. The difference between the 2 DEMs encompasses both the landslide depth and the removal of trees over the landslide. USGS Shakemap contours of the peak ground acceleration (PGA) ranging from 0.52 g (at U-4) to 0.62 g (at U-2) are shown in shades of green to blue.

The slope angle, geotechnical parameters, and landslide thickness were used to calculate the factor of safety and critical acceleration using **Eqs 3**, **4**, respectively. The PGA values for the 2015 Gorkha earthquake came from the USGS ShakeMap for the Langtang valley (**Figure 3**). The calculated critical acceleration for each slope section (cell) was compared with the PGA from the Gorkha earthquake. If the PGA exceeds the critical acceleration, the cell is classified as unstable. The analysis yields an ETL susceptibility map using the critical acceleration of many slope cells. The entire model takes ~10 min (7 min to produce six landslide susceptibility maps and 3 min to assess accuracy) on home desktop (Intel® Core™ i5-9300H; quad-core; 8 GB RAM) to calibrate landslide thickness. The detailed methodology is described in the following sections and summarized in **Figure 4**.

Digital Elevation Model Generation

A pre-earthquake (April 2014) and a post-earthquake (March 2015) DEM at a 4 m cell size were obtained from tri-stereo SPOT 6/7 images of the Langtang valley over 100 km^2 area. The DEMs were taken from Lacroix (2016). Some voids existed in the pre-earthquake (2014) DEM created from the Spot 6/7 stereo images. These voids were filled by interpolation from neighboring cells in QGIS. The DEMs were computed using the NASA open-source software Ames Stereo Pipeline (Broxton and Edwards, 2008). The reliability of the ground elevations in the DEM varies as a function of slope gradient. The ground elevation variability, calculated through the standard deviation of the difference of the 2014 and 2015 DEMs in stable areas, ranged from 0.5 m on flat terrain up to 12 m on slopes of 80° (Lacroix, 2016).

Preparation of the Landslide Map

An initial map of landslide locations was prepared by subtracting the post-earthquake (2015) DEM from the pre-earthquake (2014) DEM. However, the inherent uncertainty in the DEMs, created from errors in the stereo pair image processing, makes this step complicated. To increase confidence in the landslide map, a DEM error map was subtracted from the DEM difference map. Only cells with positive values in a range between 1 and 75 m were used as the map of landslide locations. The negative values indicated possible deposition areas and were eliminated from further analysis.

When the catastrophic Langtang avalanche descended into the Langtang village, it created an air blast that flattened the forest canopy on the opposite face of the valley wall. This phenomenon caused a positive elevation difference in DEM subtraction, thereby falsely classifying cells as a landslide. This air-blast zone (~2 km^2) was removed from the landslide map. Furthermore, some slope area materials were entrained during the avalanche descent, causing considerable depth variation (Gnyawali et al., 2020). These sites, which covered an area of

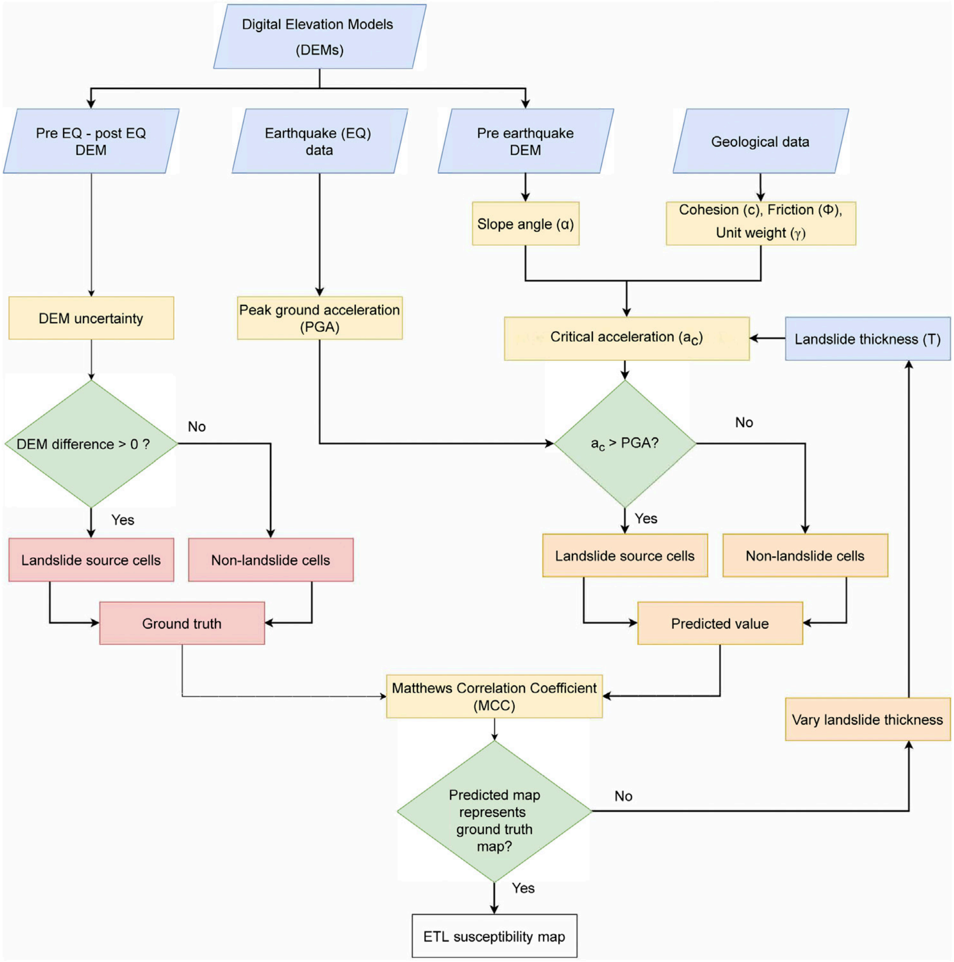

FIGURE 4 | Flowchart for creating ETL maps using DEM, critical acceleration, and earthquake PGA.

approximately 0.25 km^2, were eliminated from the map. **Figure 3** shows the resulting final map for the source areas of earthquake-triggered landslides. Landslide locations involved approximately 5.2 km^2 of the study area.

2015 Gorkha Earthquake Ground Motions

The measured ground motions caused by the Gorkha earthquake were important input for estimating ETL locations. The peak ground acceleration (PGA) closely correlates with landslide occurrence as a triggering factor (Keefer 1984; Kieffer et al., 2006; Qi et al., 2010; Dai et al., 2011; Tiwari and Ajmera, 2017). A benefit of using PGA is that probabilistic PGA maps are readily available for Nepal (Ram and Wang, 2013; Rahman and Bai, 2018). Jibson (2007) developed an empirical relationship to determine Newmark's displacement using critical acceleration and Arias intensity (Arias, 1970). Arias intensity depends upon the recorded earthquake acceleration-time history. However, earthquake acceleration-time data are not available for the study area, which makes the use of PGA attractive given the availability of USGS ShakeMap estimates of PGA around the epicentre of the Gorkha earthquake. ShakeMap provides near-real-time maps of PGA and other ground motion parameters (peak ground velocity, pseudo-spectral acceleration, intensity) following significant earthquakes, and this source for PGA was used in the critical acceleration model. ShakeMap simulates PGA by combining information from individual stations, site amplification characteristics, and ground motion prediction equations (GMPEs) for the distance to the hypocentre (Worden et al., 2010; Worden et al., 2020). We adopted PGA values from ShakeMap for this model. The PGA ranges from 0.52 g (northern part, U-4) to 0.62 g (southern part, U-2) in the study area. The PGA contours from the USGS Shakemap for the Gorkha earthquake are shown in **Figure 3**.

Critical Acceleration Method

The ETL locations are assessed in the critical acceleration method by comparing each slope section's critical acceleration and the PGA from an earthquake. If the earthquake ground acceleration surpasses a critical acceleration, the slope may fail during shaking (Chen et al., 2020). In the context of Newmark's method, the dynamic stability of a slope is related to its static stability. Before an earthquake, a block's stability is affected by its weight and the

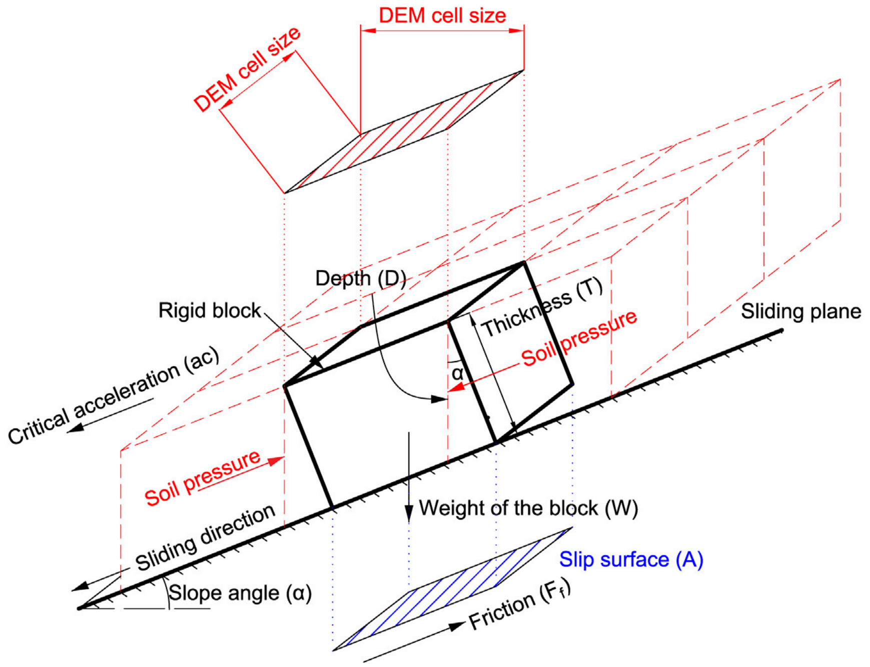

FIGURE 5 | Schematic diagram illustrating the forces acting on a block resting on an inclined plane for static (pre-earthquake) conditions on a GIS environment.

friction angle and cohesion acting along a potential sliding surface, as illustrated in **Figure 5**. The forces acting parallel to the slip surface from adjacent blocks above and below the block shown are assumed to cancel each other. The factor of safety F_S of the sliding block, as shown in **Figure 5**, can be expressed as:

$$Fs = \frac{cA + W\cos\alpha \cdot \tan\phi}{W\sin\alpha} \tag{1}$$

Where W is the weight of the block, ϕ and c are the friction angle and cohesion along the sliding surface, α is the slope angle of the slip surface, which is assumed equal to the ground surface, and A is the area of the sliding surface. The groundwater table was likely below the landslide slip surface at most locations because the 2015 Gorkha earthquake occurred during the dry season and the typical landslide depths were less than 3 m (Gallen et al., 2016). Therefore, the groundwater pressures are not included in **Eq. 1**. The critical acceleration method was applied to each cell in the pre-earthquake DEM. **Figure 5** shows a unit thick section of a block on the slope. The DEM cell size is based on a horizontal grid. Using the DEM cell size as the smallest block size in the critical acceleration analysis, **Eq. 1** can be re-written as:

$$F_S = \frac{cA}{W\sin\alpha} + \frac{W\cos\alpha \cdot \tan\phi}{W\sin\alpha}$$

$$F_S = \frac{cA}{\gamma.\,A.T.\sin\alpha} + \frac{\tan\phi}{tan\,\alpha}$$

The above equation can be simplified as **Eq. 2**, which shows that the factor of safety is influenced by topographical, geological parameters, and landslide thickness and is independent of DEM cell size.

$$F_S = \frac{c}{\gamma T \cdot \sin\alpha} + \frac{\tan\phi}{\tan\alpha} \tag{2}$$

Where γ is the unit weight of the landslide material, and T is the thickness of the sliding block. The thickness of the sliding block is $D \cdot \cos\alpha$, where the landslide depth, D, is observed from differences in DEM elevations.

In GIS implementation, cohesion raster, friction angle raster, and unit weight raster are obtained from the geology map. Similarly, slope raster is calculated from pre-earthquake DEM and block thickness is the assumed landslide thickness whose value varies in the model. **Eq. 3**. Demonstrates the use of **Eq. 2** in a GIS environment.

$$F_S = \frac{(cohesion\ raster)}{(Unit\ weight\ raster) \times block\ thickness \times \sin(slope\ raster)} + \frac{\tan(friction\ angle\ raster)}{\tan\ (slope\ raster)} \tag{3}$$

Newmark (1965) showed that the critical acceleration a_c for a potential landslide block is a simple function of the static factor of safety F_s and the slope angle.

$$a_c = (F_s - 1) \cdot \sin\alpha \cdot g \tag{4}$$

In **Eq. 4**, g is the gravitational acceleration.

Chen et al. (2014) investigated landslide areas associated with critical accelerations to determine PGA for the 2008 Wenchuan earthquake in China and showed that critical acceleration is a reliable criterion for assessing slope stability. Xiaoli and Chunguo (2019) analyzed the slope stability for the 2014 Ludian earthquake in China and showed that Newmark's critical acceleration and

TABLE 2 | Parameters used in the critical acceleration model and their uncertainty.

Geological unit	Parameter	Unit	Value	Uncertainty
U-1, Syaprubesi formation U-2, Bamboo formation U-3, Langtang formation	Cohesion, c	kPa	47	High
	Friction angle, ϕ	degree	35	Low
	Unit weight, γ	kN/m^3	1800	Low
U-4, snow and ice	Cohesion, c	kPa	27	High
	Friction angle, ϕ	degree	11.5^a	Low
	Unit weight, γ	kN/m^3	850^a	Low

[a] *Gnyawali et al. (2020).*

cohesion (c) and friction angle (ϕ) are for the sliding base of a block of fractured bedrock or colluvium; the bulk density (ρ_b) is for the equivalent of a block of fractured bedrock covered with a layer of colluvium.

PGA could be used to estimate accurate ETL locations. Similarly, Chen et al. (2020) concluded that it is possible to quickly evaluate ETL by comparing critical acceleration and PGA.

Predicting Landslide Source Areas Using Critical Acceleration Method

Input parameters for the landslide predictions include estimates of the shear strength and unit weight of the landslide materials or ice/snow, slope angles extracted from the pre-earthquake DEM (Lacroix, 2016), and PGA data obtained from USGS shakemap, **Table 2**. The values of cohesion, friction angle, and bulk density used in the analysis were adopted from published literature. Field observations of the ETLs indicated that these often occurred on steep slopes covered with a layer of colluvium. The sliding surface may have been within colluvium or slightly deeper within weathered and fractured bedrock. The assumed shear strength parameters for the sliding surface are listed in **Table 2**. The estimated friction angle and cohesion were based on published values for colluvium and increased to account for field evidence that most shallow landslides involved fractured bedrock, which likely has higher shear strength than colluvium. The bulk density for the sliding block was based on a combination of typical colluvium and fractured gneiss densities. For U-1 to U-3, the selected values were guided by values presented by Irfan and Tang (1992). The geotechnical properties for the glacier snow-ice (U-4) were obtained from Gnyawali et al. (2020).

Critical acceleration values were calculated for each cell. The DEM was resampled to generate different cell sizes, and a range of landslide thicknesses was assumed to calculate the critical accelerations for each cell using **Eq. 5**. The calculated critical acceleration at each site was compared with the PGA at each site to determine if the cell was stable or could slide during the earthquake. All cells determined to be unstable (PGA > a_c) were used to produce a predicted distribution or map of earthquake-triggered landslides. Different maps were created for different assumed landslide thicknesses and cell sizes. Finally, the predicted landslide maps were compared to those observed from DEM differencing.

An estimate of the landslide thickness was required to calculate the static factor of safety. The landslide thickness was varied until the resulting prediction of landslide locations appeared to match the landslide map obtained from DEM subtraction.

Accuracy Assessment

A quantitative assessment of the match between predicted and observed landslide locations were obtained using a confusion matrix, which is a method for assessing the accuracy of a binary classification, in this case, for cells classified as either stable or unstable. The landslide map extracted from DEM subtraction was considered as the reference map, and the critical acceleration method provided prediction maps. A correctly predicted cell consists of two classes: i) an unstable cell occurs in both maps (true positive), TP, and ii) a stable cell occurs in both maps (true negative), TN. Similarly, incorrectly predicted cells include two classes: i) an unstable cell in the reference map but a stable cell in the predicted map (false negative), FN; and ii) a stable cell in the reference map but an unstable cell in the predicted map (false positive), FP.

The Matthews correlation coefficient (MCC) is used as a measure of the quality of the classification. MCC accounts for true and false positives and negatives and is generally regarded as a balanced measure that can be used even if the classes are of very different sizes (Chicco and Jurman, 2020; Chicco et al., 2021). The MCC is a correlation coefficient between the observed and predicted binary classifications; it returns a value between −1 and +1. The MCC is calculated as:

$$MCC = \frac{TP \times TN - FP \times FN}{\sqrt{(TP + FP)(TP + FN)(TN + FP)(TN + FN)}} \tag{5}$$

The value of MCC ranges from −1 to +1, where +1 represents a perfect prediction, 0 represents a random prediction, and −1 represents a total disagreement between prediction and observation. MCC was used to evaluate the cells in the ETL prediction maps relative to the reference landslide map.

Several studies (Rong et al., 2020; Wang et al., 2020; Meena et al., 2021) have adopted MCC to evaluate landslide susceptibility maps. Rong et al. (2020) obtained MCC = 0.44 for a hazard map of rainfall-induced landslides in Shuicheng, China. Wang and Lin, 2010 compared four different landslide susceptibility mapping methods and found that MCC varied from 0.4 to 0.5. In this study, the highest MCC value was 0.13, which indicates a modest positive relationship with the reference landslide map obtained from DEM differencing.

Cell Size

Previous DEM-based investigations of ETL were performed with relatively large DEM cell sizes (greater than 10–90 m) compared to that available for the Langtang Valley. For example, Chen et al. (2014), Gallen et al. (2016), and Allstadt et al. (2018) used 90 m cell sizes. Wang and Lin (2010) used 40 m cells, and Dreyfus et al. (2013), Shinoda and Miyata (2017), and Ma and Xu (2019) used 10 m cells. An assessment of cell size on the predicted spatial distribution of unstable and stable cells was performed to assess the influence of size. The DEM cells were resampled in QGIS from 4 to 40 m cell size, using bilinear interpolation. For each resampled DEM, a series of analyses were done with varying landslide thicknesses. The landslide thickness was varied from 2 to 4.2 m with a 0.2 m increment. The critical accelerations for the various assumed landslide thicknesses were obtained. The critical accelerations were then used to create maps of predicted ETL for each assumed landslide thickness. These maps were compared with the DEM-derived landslide map.

RESULTS AND DISCUSSION

Spatial Distribution of Landslides - DEM-Derived *Versus* Satellite Imagery

Landslide inventories for the Langtang area were obtained from previously mapped landslide scars visually identified in satellite imagery (Gnyawali and Adhikari, 2017; Roback et al., 2018). As an alternative method for determining the landslide locations, the elevation differences between pre- and post-earthquake DEMs of the Langtang valley (Lacroix, 2016) were used. These maps provide a reference for comparison with predicted landslide locations obtained by applying the critical acceleration and PGA estimates.

The spatial distribution of landslide source areas obtained by DEM differencing in the Langtang valley is shown in **Figure 3**. The spatial distribution shows a cluster of landslides near the valley bottom and in the snow-covered region. As expected, the landslide map shows a high concentration of landslide source areas where the large Langtang avalanche occurred and in areas with steep slopes.

A visual comparison of the landslide sources detected using DEM differencing and existing landslide inventories (Lacroix, 2016; Gnyawali and Adhikari, 2017; Roback et al., 2018) shows some consistency. However, exceptions occurred in snow-covered regions and along the Langtang river banks, where landslides were captured in the DEM-derived map but were not found by visual interpretation of satellite imagery. Previously published maps of landslides in the Langtang Valley consisted of a relatively small number of locations compared to what was found by DEM differencing. In the snow-covered area (U-4), none of the visually prepared inventories had landslide source areas. However, the main Langtang avalanche originated from this area (Lacroix, 2016). Visual interpretation of satellite imagery for landslide mapping is a challenge if no contrast is seen between pre- and post-earthquake imagery (as in snow-covered areas) or terrain deformations do not result in long runout scars. The detection of landslide areas based on satellite image interpretation is sensitive to the image quality and the interpretation of those images. This results in landslide inventories that may miss landslides (Roback et al., 2018). However, it is important to note that DEM differencing derived landslide inventories are also subject to errors. For example, shadows, occlusions, and poor correlation can result in data gaps and residual artifacts in each of the cross-track stereo DEMs. Thus, interpretation requires caution and expert judgment. Ideally, visually prepared landslide inventories from satellite images and DEM differencing derived landslide cells should be used as complementary to each other.

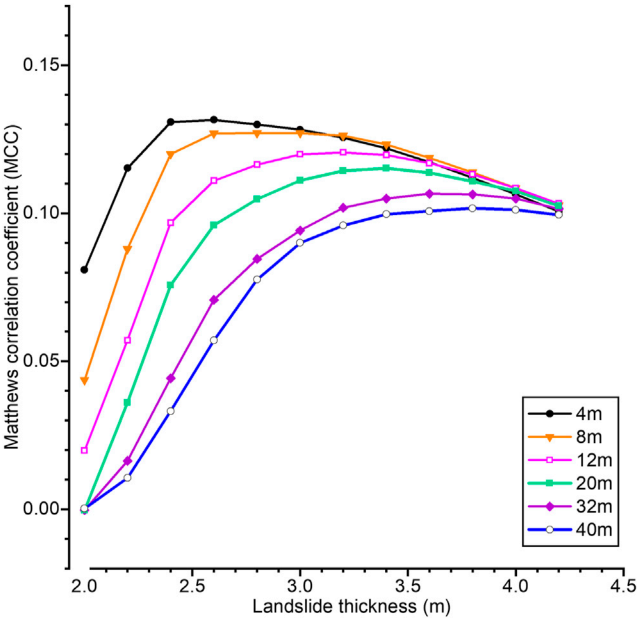

FIGURE 6 | Matthews correlation coefficient for various DEM cell sizes (4–40 m) and assumed landslide thicknesses.

The DEM differencing technique has been applied in numerous studies (Tsutsui et al., 2007; Martha et al., 2010; James et al., 2012) to study geomorphological changes, including detection of shallow landslides. Tsutsui et al. (2007) used this technique to detect landslides triggered by earthquakes in Japan and cyclones in Taiwan. They concluded that this technique delineated the large-scale landslides with an accuracy >70% for slopes under 40° and accuracy <40% for slopes over 40°. Kim et al. (2020) showed that DEM differencing could detect landslides in hilly and densely vegetated areas if the DEM uncertainty is constrained.

In this study, the DEM differencing technique was the desired approach for checking the result of the critical acceleration method because the ultimate goal is to use existing pre-earthquake DEMs and post-earthquake ShakeMap PGA to quickly generate maps of likely ETL locations to help plan field reconnaissance and rescues immediately after an earthquake. In an emergency situation, there may not be sufficient time to acquire and map many landslides using satellite imagery. Furthermore, to obtain a reliable estimate of the landslide depths for many landslides over a wide area, DEM differencing provided the best approach.

Landslide Thickness

The 2015 Gorkha earthquake triggered mostly shallow landslides. The landslide depth is measured vertically, while the landslide thickness is measured normal to the slope (**Figure 5**). The median landslide depth for all areas observed from DEM differencing was 4.8 m for cells that were 4 m in size. The median landslide depths were 3.8 m for U-1, 4.5 m for U-2, 3.6 m for U-3, and 6.7 m for U-4. U-4 was the source area of the largest rock-ice avalanche in

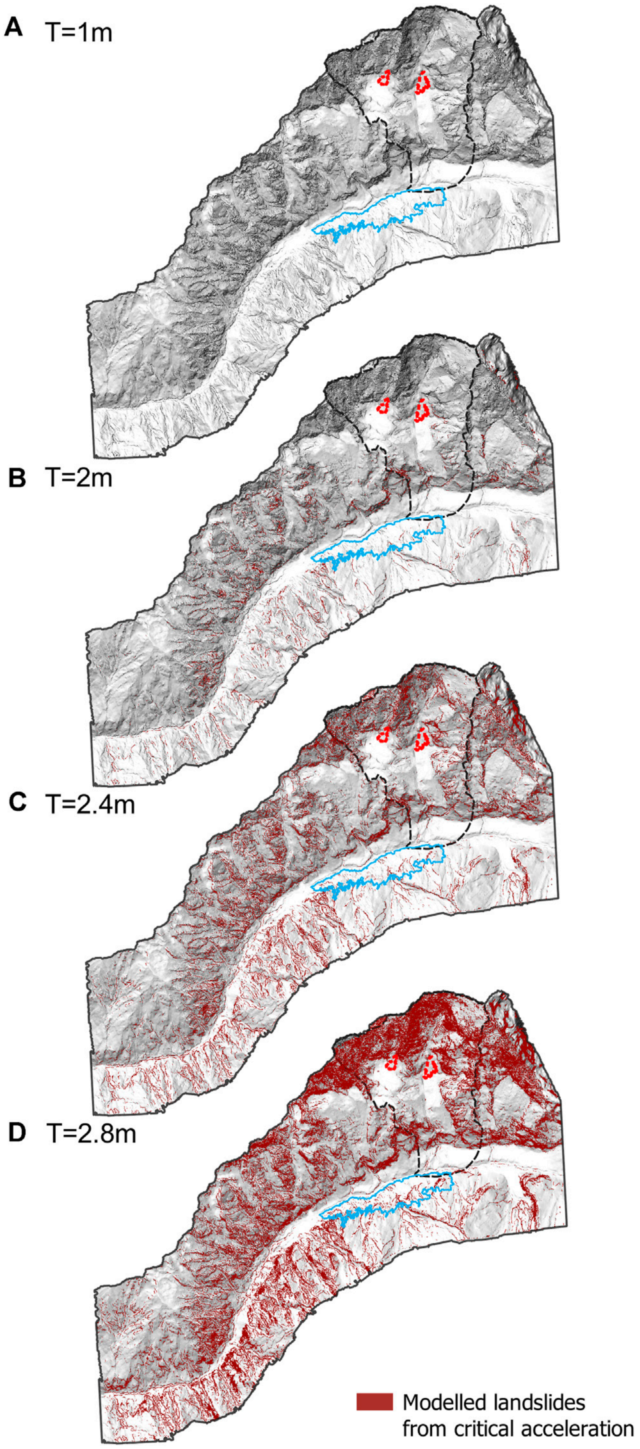

FIGURE 7 | Predicted earthquake-triggered landslide maps for different assumed landslide thicknesses **(A–D)** with a DEM cell size of 4 m.

the valley, which deposited 7 × 106 m^3 on the valley floor (Lacroix, 2016). The calculated depths from DEMs in vegetated areas can be exaggerated by vegetation loss when a shallow landslide occurs (Lacroix, 2016). The thickness (measured perpendicular to the slope) of the material that failed was calculated using the slope at each cell. The median landslide thicknesses in each area were 2.4, 2.5, 1.9, and 3.3 m for U-1 to U-4, respectively.

The sliding block's thickness is an important parameter when using the critical acceleration method with a sliding surface that has cohesion. Ma and Xu (2019) used an average landslide thickness of 3 m based on a field investigation for the 2013 Lushan earthquake in China. Shinoda and Miyata (2017) studied regional landslides using Newmark's method and found that a 2 m landslide thickness worked well for the Mid Niigata earthquake. The thickness ranged from 0.8 to 4.6 m for landslides triggered by the 2016 Kumamoto earthquake (Mw 7.1) (Saito et al., 2018). Shinoda et al. (2019) used a 3 m landslide thickness based on a JSEG (2017) report of regional landslide susceptibility for the 2016 Kumamoto earthquake. The median landslide thicknesses in the Langtang region caused by the 2015 Gorkha earthquake are similar to these other studies, and most landslides are shallow, except for a few much larger landslides.

Cell Size and MCC

Figure 6 illustrates the influence of the DEM cell size on predicting stable and unstable cells. As the DEM cell size increases, the predictive accuracy as measured by MCC decreases. This suggests that a small (4 m) cell size is best when using the analysis approach presented here. Although doubling the cell size to 8 m gives a similar prediction accuracy while reducing the amount of data to be processed and stored in the GIS. The landslide thickness used in the critical acceleration model that best matches the spatial distribution of DEM-derived stable and unstable cell locations is approximately 2.6 m, as seen by the peak in the MCC curve for the 4 m cell size in **Figure 6**. When larger DEM cells are used, a thicker landslide gives the best match with the observed ETLs. Note that when the landslide thickness was less than 1 m, almost all cells were predicted to be stable (not shown in the figure).

Wang et al. (2020) studied the influence of DEM cell size on ETL hazard assessment using Newmark's sliding block method and found that a 30 m size gave a similar prediction to a 10 m cell size. In contrast, this study shows that a smaller cell size gives better results.

The influence of the landslide thickness on the predictions of landslide locations was explored. The results using a DEM cell size of 4 m with an assumption of a constant landslide thickness of 1, 2, 2.4, and 2.8 m are shown in **Figure 7**. Pixels with a brown color represent unstable cells predicted using the critical acceleration method. This figure clearly shows how sensitive the number and locations of predicted ETLs are to the assumed landslide thickness. When the thickness is less than 2.4 m, the critical acceleration model incorrectly classifies too many cells as stable, whereas when the thickness is 2.8 m, too many cells are predicted as unstable.

Critical Acceleration Model Predictions *Versus* DEM-Derived Map

An assumed landslide thickness of 2.6 m was used to determine the predicted ETL locations using the critical acceleration

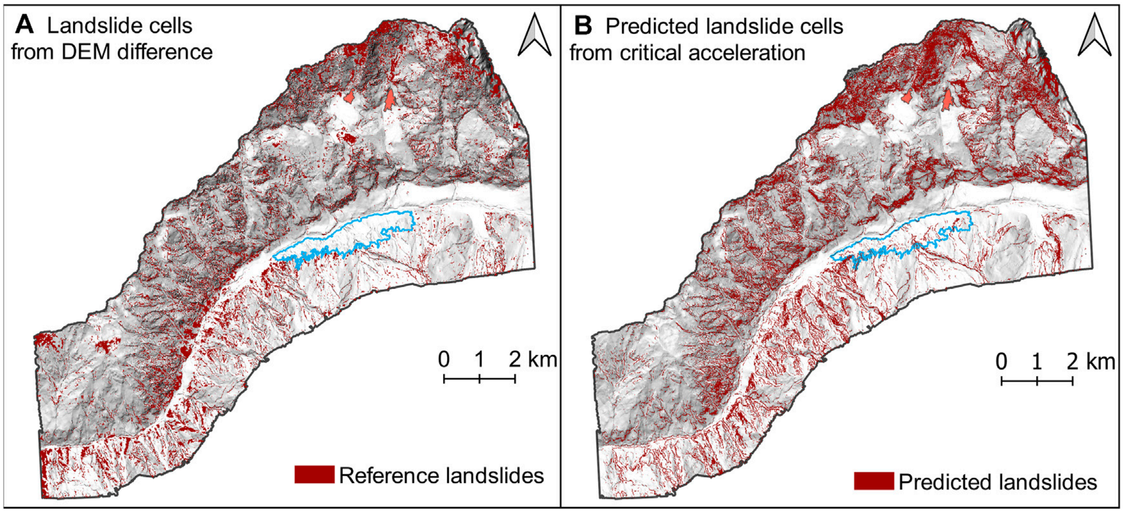

FIGURE 8 | Comparison of ETL locations from **(A)** DEM subtraction and the **(B)** critical acceleration model with an assumed landslide thickness of 2.6 m and a 4 m cell size.

method. **Figure 8** shows a comparison between the DEM-derived ETL locations and those predicted using the critical acceleration method. Cells predicted to be stable often correspond to locations where no elevation changes occurred in the DEM, which is a good match. However, cells predicted to be unstable in region U-4 are more scattered than those observed from DEM differencing.

Immediately after an earthquake occurs, the resulting thickness for ETLs is typically unknown. Gallen et al. (2016) used an aggregate strength parameter to account for the unknown landslide thickness. The aggregate strength parameter is the ratio of soil cohesion and landslide thickness. They used a range of aggregate strength parameters varying from 5 to 15 kPa m^{-1} and concluded that the lower and upper bound of the aggregate strength parameter is 10 kPa m^{-1} and 15 kPa m^{-1}. This study took advantage of the post-earthquake DEM to measure the thickness for many landslides, which gave a median value of 2.6 m. Using this value gives an aggregate strength parameter equal to 10.4 and 18 kPa m^{-1} in U-4 (glacier snow-ice) and U-1 to U-3, respectively. These values are similar to the values found by Gallen et al. (2016).

While the predicted landslide map has many similarities to the DEM-derived landslide distribution, there are differences. The prediction map is missing patches of landslides near the river in geological units U-1 and U-2. River erosion through colluvium and debris flow deposits near the valley bottom created over-steepened slopes prone to failure during the earthquake. Thus, many ETLs are observed along river banks (Tian et al., 2019). But the effect of slope undercutting or toe erosion by the river is often not captured in the DEM despite its small cell size. Thus, when running the critical acceleration model, it misses small steep slopes. Furthermore, these landslides often occur at the edges of terraces with top slopes <25°, which have a high factor of safety (**Eq. 3**). So, these cells were often classified as stable in the map showing predicted ETL. The critical acceleration method is a reliable technique for assessing earthquake-triggered landslides. However, cohesion plays an important role; thus, calibration of cohesion is critical to assessing slope stability.

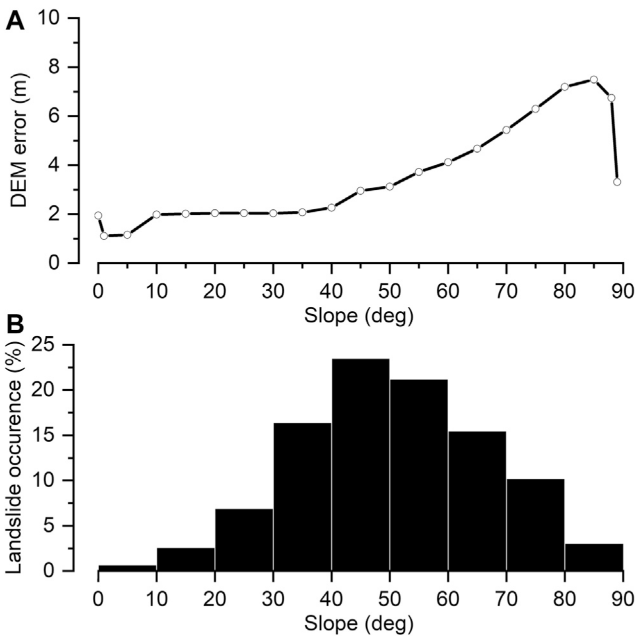

FIGURE 9 | DEM uncertainty plot. **(A)** Mean DEM error as a function of slope angle, **(B)** Distribution of landslides in different slope ranges.

Slopes

The predicted landslide distribution was examined in terms of slope angle, slope aspect, and bedrock geology. Most unstable cells (46.5%) in the study area faced southerly (SE to SW). 50 per cent of the cells in U-1 with a slope angle >78° were classified as

TABLE 3 | Metadata of USGS ShakeMap for the 2015 Gorkha earthquake.

Description	Remarks
Map version	1
Date	2020-06-03 05:35:56 (UTC[a])
Mean of map uncertainty	1.003
Empirical ShakeMap grade	C
Flagged seismic station	4
Flagged DYFI[b] stations	26
Site correction applied	GMPE native

[a] *Universal Time Coordinated.*

[b] *Did You Feel It.*

unstable during the earthquake. Similarly, 42% of cells with a slope angle >79° and 36% of cells with a slope angle >80° were unstable in U-2 and U-3, respectively. While slopes with angles between 70 and 80° had a high proportion of unstable cells, more than 45% of the unstable cells occurred for slope angles between 40 and 60°. The median slope for unstable cells in U-1, U-2, U-3, and U-4 are 41, 50, 49, and 51°, respectively.

Uncertainty in Input Parameters

Primary input parameters for the critical acceleration method are topography data, geology data, and ground motion data. The topography is obtained from a pre-earthquake DEM (Lacroix, 2016). The reliability of the ground elevations in the DEM varies as a function of slope gradient (**Figure 9**). The ground elevation variability, calculated through the standard deviation of the difference of the 2014 and 2015 DEMs in stable areas, ranged from 0.5 m on flat terrain up to 12 m on slopes of 80° (Lacroix, 2016).

The landslide distribution is more continuous in the predicted map than in the landslide inventory derived from the DEM difference. This is perhaps due to the DEM error, uncertainty in geotechnical parameters, and PGA estimates from ShakeMap. The local variation in soil strength can affect the landslide distribution. The shear strength parameters were fixed over a large area due to no knowledge of their potential variations. This simplification affects the results from the critical acceleration model. **Table 2** list the relative uncertainty in geotechnical parameters for the study area. Moreover, the absence of unstable cells near the river might be caused by ignoring potential groundwater pressures in the analysis.

USGS ShakeMap (map version 1, 2020-06-03) was used to generate an ETL susceptibility map in the Langtang valley. Two uncertainties linked with ShakeMap are (1) spatial variability of PGA near stations and (2) uncertainty in the ground-motion estimation relationships used to fill gaps between stations (Wald et al., 2008). The ShakeMap of the 2015 Gorkha earthquake has an uncertainty grade "C" (USGS, 2021a), which corresponds to a moderate quality ShakeMap (Wald et al., 2008). A middle range ("C") grade corresponds to a moderate magnitude earthquake suitably represented with a point source location (Wald et al., 2008). A description of the USGS ShakeMap for the Gorkha earthquake is given in **Table 3**.

CONCLUSION

The purpose of this paper was to demonstrate the use of a DEM and the critical acceleration method to quickly predict landslide locations after an earthquake as an aid to rapid landslide assessment and recovery after a devastating earthquake. The methodology was assessed by comparing predictions of unstable and stable cell locations with previously published ETL inventories, as well as a map of landslide locations obtained from the elevation difference between pre- and post-earthquake cells in the DEMs.

A DEM for most places on the earth is now available (e.g., Shuttle Radar Topography Mission), and DEMs are expected to improve quality over time with new satellite technologies. Thus, a critical input needed to predict the ETL locations is readily available.

Estimates of cohesion, friction angle, and unit weight of the landslide materials needed for the analysis can be inferred from geology maps (Hartmann and Moosdorf, 2012; USGS, 2021b) of the area of interest. For the case study presented here, the geological information was very limited, and the analysis only used two sets of values. However, in regions where better geological mapping is available, the shear strength parameters and bulk unit weight can vary according to the geological maps, which would help fine-tune the prediction of ETL locations.

For large earthquakes, PGA estimates are created by USGS ShakeMap soon after their occurrence. The landslide prediction method relies on comparing the critical acceleration within a GIS environment with estimates PGA for the raster cells over the area of interest. The PGA estimates from ShakeMap will likely improve as this tool becomes better calibrated, and this will contribute to better estimates of ETL locations.

The critical acceleration model is sensitive to the assumed landslide thickness when cohesion is present along the slip surface. Furthermore, it appears that the landslide thicknesses yielding the best match to observed stable and unstable cell locations can be influenced by the DEM cell size. Further research is needed to optimize the choice of a landslide thickness for conducting a regional analysis to predict ETL locations. This value will likely depend on the terrain and the soil and bedrock geology in the area of interest. However, as a starting point, evidence from past ETLs indicates that the typical landslide thickness is often in the range of 2–4 m.

ETL susceptibility mapping can be achieved in earthquake-prone mountainous regions because the basic input parameters needed for a Newmark model analysis (e.g., terrain, geology, and a probable PGA) are typically available. Therefore, applying a critical acceleration model in a GIS environment can assist with timely planning for disaster response after an earthquake. As expected, the results will be subject to error due to the simplifying assumptions used in the method. However, the results should still provide a fast way to prioritize the investigation of potential landslide areas after an earthquake. Furthermore, this approach has potential use in early planning for ETL by mapping the terrain susceptibility using readily available probabilistic PGA maps.

DATA AVAILABILITY STATEMENT

The original contributions presented in the study are included in the article/**Supplementary Material**, further inquiries can be directed to the corresponding author.

AUTHOR CONTRIBUTIONS

KG and SM conceived and designed the study. SM prepared and analyzed the data. DT guided the research through technical discussions. PL produced the DEMs. DT and PL provided crucial suggestions to improve the work. KG and SM wrote the first draft of the manuscript. DT, PL, and CX edited and reviewed the manuscript.

ACKNOWLEDGMENTS

We acknowledge the support of Frontiers Fee Support program for covering the Article Processing Charge (APC) of this paper.

SUPPLEMENTARY MATERIAL

The Supplementary Material for this article can be found online at: https://www.frontiersin.org/articles/10.3389/feart.2021.689303/full#supplementary-material

REFERENCES

Allstadt, K. E., Jibson, R. W., Thompson, E. M., Massey, C. I., Massey, C. I., Wald, D. J., Godt, J. W., et al. (2018). Improving Near–Real–Time Coseismic Landslide Models: Lessons Learned From the 2016 Kaikōura, New Zealand, Earthquake. *Bull. Seismol. Soc. Am.* 108 (3B), 1649–1664.

Arias, A. (1970). *Measure of Earthquake Intensity*. Cambridge Santiago de Chile: Massachusetts Inst. of Tech. Univ. of Chile.

Broxton, M. J., and Edwards, L. J. (2008). "The Ames Stereo Pipeline: Automated 3D Surface Reconstruction from Orbital Imagery," in Lunar and Planetary Science Conference. League City, TX, US: Meeting and Publication Services. 2419.

Chen, X.-L., Liu, C.-G., Yu, L., and Lin, C.-X. (2014). Critical Acceleration as a Criterion in Seismic Landslide Susceptibility Assessment. *Geomorphology* 217, 15–22. doi:10.1016/j.geomorph.2014.04.011

Chen, X.-L., Shan, X.-J., Wang, M.-M., Liu, C.-G., and Han, N.-N. (2020). Distribution Pattern of Coseismic Landslides Triggered by the 2017 Jiuzhaigou Ms 7.0 Earthquake of China: Control of Seismic Landslide Susceptibility. *Ijgi* 9 (4), 198. doi:10.3390/ijgi9040198

Chicco, D., and Jurman, G. (2020). The Advantages of the Matthews Correlation Coefficient (MCC) over F1 Score and Accuracy in Binary Classification Evaluation. *BMC Genomics* 21 (1), 1–13. doi:10.1186/s12864-019-6413-7

Chicco, D., Tötsch, N., and Jurman, G. (2021). The Matthews Correlation Coefficient (MCC) Is More Reliable Than Balanced Accuracy, Bookmaker Informedness, and Markedness in Two-Class Confusion Matrix Evaluation. *BioData Mining* 14 (1), 1–22. doi:10.1186/s13040-021-00244-z

Chousianitis, K., Del Gaudio, V., Kalogeras, I., and Ganas, A. (2014). Predictive Model of Arias Intensity and Newmark Displacement for Regional Scale Evaluation of Earthquake-Induced Landslide hazard in Greece. *Soil Dyn. Earthquake Eng.* 65, 11–29. doi:10.1016/j.soildyn.2014.05.009

Collins, B. D., and Jibson, R. W. (2015). Assessment of Existing and Potential Landslide Hazards Resulting from the April 25, 2015 Gorkha, Nepal Earthquake Sequence. *Geol. Surv. Open-File Rep.* 50. 1142 doi:10.3133/ofr20151142

Collins, B. D. (2015).*Video Data Files to Accompany USGS OFR 2015-1142–Assessment of Existing and Potential Landslide Hazards Resulting from the April 25, 2015 Gorkha, Nepal Earthquake Sequence*. U.S. Geological Survey data release. doi:10.5066/F7X928BN10.3133/ofr20151142

Dai, F. C., Xu, C., Yao, X., Xu, L., Tu, X. B., and Gong, Q. M. (2011). Spatial Distribution of Landslides Triggered by the 2008 Ms 8.0 Wenchuan Earthquake, China. *J. Asian Earth Sci.* 40 (4), 883–895. doi:10.1016/j.jseaes.2010.04.010

Dreyfus, D., Rathje, E. M., and Jibson, R. W. (2013). The Influence of Different Simplified Sliding-Block Models and Input Parameters on Regional Predictions of Seismic Landslides Triggered by the Northridge Earthquake. *Eng. Geology* 163, 41–54. doi:10.1016/j.enggeo.2013.05.015

Fujita, K., Inoue, H., Izumi, T., Yamaguchi, S., Sadakane, A., Sunako, S., et al. (2017). Anomalous winter-snow-amplified Earthquake-Induced Disaster of the 2015 Langtang Avalanche in Nepal. *Nat. Hazards Earth Syst. Sci.* 17, 749–764. doi:10.5194/nhess-17-749-2017

Gallen, S. F., Clark, M. K., Godt, J. W., Roback, K., and Niemi, N. A. (2016). Application and Evaluation of a Rapid Response Earthquake-Triggered Landslide Model to the April 25 2015 Mw 7.8 Gorkha Earthquake, Nepal. *Tectonophysics* 714, 173–187.

Gnyawali, K. R., and Adhikari, B. R. (2017). "Spatial Relations of Earthquake Induced Landslides Triggered by 2015 Gorkha Earthquake Mw = 7.8Spatial Relations of Earthquake Induced Landslides Triggered by 2015 Gorkha Earthquake Mw= 7.8," in Workshop on World Landslide Forum. Ljubljana, Slovenia: Springer, 85–93. doi:10.1007/978-3-319-53485-5_10

Gnyawali, K. R., Xing, A., and Zhuang, Y. (2020). Dynamic Analysis of the Multi-Staged Ice-Rock Debris Avalanche in the Langtang valley Triggered by the 2015 Gorkha Earthquake, Nepal. *Eng. Geology* 265, 105440. doi:10.1016/j.enggeo.2019.105440

Gorum, T., Korup, O., van Westen, C. J., van der Meijde, M., Xu, C., and van der Meer, F. D. (2014). Why So Few? Landslides Triggered by the 2002 Denali Earthquake, Alaska. *Quat. Sci. Rev.* 95, 80–94. doi:10.1016/j.quascirev.2014.04.032

Harp, E. L., and Jibson, R. W. (1996). Landslides Triggered by the 1994 Northridge, California, Earthquake. *Bull. Seismological Soc. America* 86 (1B), S319–S332.

Hartmann, J., and Moosdorf, N. (2012). The New Global Lithological Map Database GLiM: A Representation of Rock Properties at the Earth Surface. *Geochem. Geophys. Geosyst.* 13(12). doi:10.1029/2012gc004370

Immerzeel, W. W., Van Beek, L. P. H., Konz, M., Shrestha, A. B., and Bierkens, M. F. P. (2012). Hydrological Response to Climate Change in a Glacierized Catchment in the Himalayas. *Climatic Change* 110 (3–4), 721–736. doi:10.1007/s10584-011-0143-4

Irfan, T. Y., and Tang, K. Y. (1992). *Effect of the Coarse Fraction on the Shear Strength of Colluvium*. GEO Rep 23 GEO Special Project Report No. SPR 15/92.

James, L. A., Hodgson, M. E., Ghoshal, S., and Latiolais, M. M. (2012). Geomorphic Change Detection Using Historic Maps and DEM Differencing: The Temporal Dimension of Geospatial Analysis. *Geomorphology* 137 (1), 181–198. doi:10.1016/j.geomorph.2010.10.039

JSEG (2017). *Report of the 2016 Kumamoto, Oita Earthquake Disaster Research mission*. Japan Society of Engineering Geology (Jseg) (in Japanese).

Jibson, R. W., Allstadt, K. E., Rengers, F. K., and Godt, J. W. (2018). Overview of the Geologic Effects of the November 14, 2016, Mw 7.8 Kaikoura, New Zealand, Earthquake. *Geol. Surv. Scientific Invest. Rep. 2017–*, 39.5146 doi:10.3133/sir20175146

Jibson, R. W., Harp, E. L., and Michael, J. A. (2000). A Method for Producing Digital Probabilistic Seismic Landslide hazard Maps. *Eng. Geology* 58 (3–4), 271–289. doi:10.1016/s0013-7952(00)00039-9

Jibson, R. W. (2007). Regression Models for Estimating Coseismic Landslide Displacement. *Eng. Geology* 91 (2-4), 209–218. doi:10.1016/j.enggeo.2007.01.013

Jin, K. P., Yao, L. K., Cheng, Q. G., and Xing, A. G. (2019). Seismic Landslides hazard Zoning Based on the Modified Newmark Model: a Case Study from the Lushan Earthquake, China. *Nat. Hazards* 99 (1), 493–509. doi:10.1007/s11069-019-03754-6

Jones, J. N., Stokes, M., Boulton, S. J., Bennett, G. L., and Whitworth, M. R. Z. (2020). Coseismic and Monsoon-Triggered Landslide Impacts on Remote Trekking Infrastructure, Langtang Valley, Nepal. *Q. J. Eng. Geology Hydrogeology* 53 (2), 159–166. doi:10.1144/qjegh2019-048

Kargel, J. S., Leonard, G. J., Shugar, D. H., Haritashya, U. K., Bevington, A., Fielding, E. J., et al. (2015). Geomorphic and Geologic Controls of Geohazards Induced by Nepals 2015 Gorkha Earthquake. *Science* 351, aac8353. doi:10.1126/science.aac8353

Keefer, D. K. (2002). Investigating Landslides Caused by Earthquakes–A Historical Review. *Surv. Geophys.* 23 (6), 473–510. doi:10.1023/a:1021274710840

Keefer, D. K. (1984). Landslides Caused by Earthquakes. *Geol. Soc. America Bull.* 95 (4), 406–421. doi:10.1130/0016-7606(1984)95<406:lcbe>2.0.co;2

Keefer, D. K. (1994). "The Importance of Earthquake-Induced Landslides to Long-Term Slope Erosion and Slope-Failure Hazards in Seismically Active Regions," in *Geomorphology and Natural Hazards*. Elsevier, 265–284. doi:10.1016/b978-0-444-82012-9.50022-0

Kieffer, D. S., Jibson, R., Rathje, E. M., and Kelson, K. (2006). Landslides Triggered by the 2004 Niigata Ken Chuetsu, Japan, Earthquake. *Earthquake Spectra* 22 (1_Suppl. l), 47–73. doi:10.1193/1.2173021

Kim, M.-K., Sohn, H.-G., and Kim, S. (2020). Incorporating the Effect of ALS-Derived DEM Uncertainty for Quantifying Changes Due to the Landslide in 2011, Mt. Umyeon, Seoul. *GIScience & Remote Sensing* 57 (3), 287–301. doi:10.1080/15481603.2019.1687133

Lacroix, P. (2016). Landslides Triggered by the Gorkha Earthquake in the Langtang valley, Volumes and Initiation Processes. *Earth, Planets and Space* 68 (1), 46. doi:10.1186/s40623-016-0423-3

Lanzo, G., Tommasi, P., Ausilio, E., Aversa, S., Bozzoni, F., Cairo, R., et al. (2018). Reconnaissance of Geotechnical Aspects of the 2016 Central Italy Earthquakes. *Bull. Earthquake Eng.* 17, 5495–5532. doi:10.1007/s10518-018-0350-8

Ma, S., and Xu, C. (2019). Assessment of Co-seismic Landslide hazard Using the Newmark Model and Statistical Analyses: a Case Study of the 2013 Lushan, China, Mw6.6 Earthquake. *Nat. Hazards* 96 (1), 389–412. doi:10.1007/s11069-018-3548-9

Martha, T. R., Kerle, N., Jetten, V., van Westen, C. J., and Vinod Kumar, K. (2010). Landslide Volumetric Analysis Using Cartosat-1-Derived DEMs. *IEEE Geosci. Remote Sensing Lett.* 7 (3), 582–586. doi:10.1109/lgrs.2010.2041895

Meena, S. R., Ghorbanzadeh, O., van Westen, C. J., Nachappa, T. G., Blaschke, T., Singh, R. P., et al. (2021). Rapid Mapping of Landslides in the Western Ghats (India) Triggered by 2018 Extreme Monsoon Rainfall Using a Deep Learning Approach. *Landslides*, 18(5):1937-1950 doi:10.1007/s10346-020-01602-4

Newmark, N. M. (1965). Effects of Earthquakes on Dams and Embankments. *Géotechnique* 15 (2), 139–160. doi:10.1680/geot.1965.15.2.139

Qi, S., Xu, Q., Lan, H., Zhang, B., and Liu, J. (2010). Spatial Distribution Analysis of Landslides Triggered by 2008.5. 12 Wenchuan Earthquake, China. *Eng. Geology* 116 (1–2), 95–108. doi:10.1016/j.enggeo.2010.07.011

Rahman, M. M., and Bai, L. (2018). Probabilistic Seismic hazard Assessment of Nepal Using Multiple Seismic Source Models. *Earth Planet. Phys.* 2 (4), 327–341.

Ram, T. D., and Wang, G. (2013). Probabilistic Seismic hazard Analysis in Nepal. *Earthq. Eng. Eng. Vib.* 12 (4), 577–586. doi:10.1007/s11803-013-0191-z

Roback, K., Clark, M. K., West, A. J., Zekkos, D., Li, G., Gallen, S. F., et al. (2018). The Size, Distribution, and Mobility of Landslides Caused by the 2015 Mw7.8 Gorkha Earthquake, Nepal. *Geomorphology* 301, 121–138. doi:10.1016/j.geomorph.2017.01.030

Rong, G., Li, K., Han, L., Alu, S., Zhang, J., and Zhang, Y. (2020). Hazard Mapping of the Rainfall-Landslides Disaster Chain Based on GeoDetector and Bayesian Network Models in Shuicheng County, China. *Water* 12 (9), 2572. doi:10.3390/w12092572

Saito, H., Uchiyama, S., Hayakawa, Y. S., and Obanawa, H. (2018). Landslides Triggered by an Earthquake and Heavy Rainfalls at Aso Volcano, Japan, Detected by UAS and SfM-MVS Photogrammetry. *Prog. Earth Planet. Sci.* 5 (1), 15. doi:10.1186/s40645-018-0169-6

Shinoda, M., Miyata, Y., Kurokawa, U., and Kondo, K. (2019). Regional Landslide Susceptibility Following the 2016 Kumamoto Earthquake Using Back-Calculated Geomaterial Strength Parameters. *Landslides* 16 (8), 1497–1516. doi:10.1007/s10346-019-01171-1

Shinoda, M., and Miyata, Y. (2017). Regional Landslide Susceptibility Following the Mid NIIGATA Prefecture Earthquake in 2004 with NEWMARK'S Sliding Block Analysis. *Landslides* 14 (6), 1887–1899. doi:10.1007/s10346-017-0833-8

Stewart, J. P., Zimmaro, P., Lanzo, G., Mazzoni, S., Ausilio, E., Aversa, S., et al. (2018). Reconnaissance of 2016 Central Italy Earthquake Sequence. *Earthquake Spectra* 34, 1547–1555. doi:10.1193/080317eqs151m

Takai, N., Shigefuji, M., Rajaure, S., Bijukchhen, S., Ichiyanagi, M., Dhital, M. R., et al. (2016). Strong Ground Motion in the Kathmandu Valley during the 2015 Gorkha, Nepal, Earthquake. *Earth, Planets and Space* 68 (1), 1–8. doi:10.1186/s40623-016-0383-7

Tian, Y., Owen, L. A., Xu, C., Shen, L., Zhou, Q., and Figueiredo, P. M. (2020). Geomorphometry and Statistical Analyses of Landslides Triggered by the 2015 Mw 7.8 Gorkha Earthquake and the Mw 7.3 Aftershock, Nepal. *Front. Earth Sci.* 8, 407. doi:10.3389/feart.2020.572449

Tian, Y., Xu, C., Hong, H., Zhou, Q., and Wang, D. (2019). Mapping Earthquake-Triggered Landslide Susceptibility by Use of Artificial Neural Network (ANN) Models: an Example of the 2013 minxian (China) Mw 5.9 Event. *Geomatics, Nat. Hazards Risk* 10 (1), 1–25. doi:10.1080/19475705.2018.1487471

Tiwari, B., and Ajmera, B. (2017). "Landslides Triggered by Earthquakes from 1920 to 2015," in Workshop on World Landslide Forum. Ljubljana, Slovenia: Springer, 5–15. doi:10.1007/978-3-319-53498-5_2

Tsutsui, K., Rokugawa, S., Nakagawa, H., Miyazaki, S., Cheng, C.-T., Shiraishi, T., et al. (2007). Detection and Volume Estimation of Large-Scale Landslides Based on Elevation-Change Analysis Using DEMs Extracted from High-Resolution Satellite Stereo Imagery. *IEEE Trans. Geosci. Remote Sensing* 45 (6), 1681–1696. doi:10.1109/tgrs.2007.895209

USGS (2021a). M 7.8 - 36km E of Khudi, Nepal. Available at: https://earthquake.usgs.gov/earthquakes/eventpage/us20002926/shakemap/metadata. (Accessed May 14, 2021).

USGS (2021b). World Geologic Maps. (Accessed May 7, 2021).

Wald, D. J., Lin, K. W., and Quitoriano, V. (2008). *Quantifying and Qualifying USGS ShakeMap Uncertainty*. US Geological Survey, Reston, Virginia, U.S. 26 .

Wang, K.-L., and Lin, M.-L. (2010). Development of Shallow Seismic Landslide Potential Map Based on Newmark's Displacement: the Case Study of Chi-Chi Earthquake, Taiwan. *Environ. Earth Sci.* 60 (4), 775–785. doi:10.1007/s12665-009-0215-1

Wang, Y., Fang, Z., Wang, M., Peng, L., and Hong, H. (2020). Comparative Study of Landslide Susceptibility Mapping with Different Recurrent Neural Networks. *Comput. Geosciences* 138, 104445. doi:10.1016/j.cageo.2020.104445

Wilson, R. C., and Keefer, D. K. (1983). Dynamic Analysis of a Slope Failure from the August 6 1979 Coyote Lake, California, Earthquake. *Bull. Seismological Soc. America* 73 (3), 863–877.

Worden, C. B., Thompson, E. M., Hearne, M., and Wald, D. J. (2020). *ShakeMap Manual Online: Technical Manual, User's Guide, and Software Guide*, U. S. Geological Survey. Reston, Virginia, U.S. doi:10.5066/F7D21VPQ

Worden, C. B., Wald, D. J., Allen, T. I., Lin, K., Garcia, D., and Cua, G. (2010). A Revised Ground-Motion and Intensity Interpolation Scheme for ShakeMap. *Bull. Seismological Soc. America* 100 (6), 3083–3096. doi:10.1785/0120100101

Xiaoli, C., and Chunguo, L. (2019). "Assessment of Landslides Triggered by Earthquakes Based on the Combination of Peak Ground Motion and Critical Acceleration Analysis," in IAEG/AEG Annual Meeting Proceedings, San Francisco, California Cham: Springer, 123–129. doi:10.1007/978-3-319-93136-4_15

Xu, C., Xu, X., Yao, X., and Dai, F. (2014). Three (Nearly) Complete Inventories of Landslides Triggered by the May 12, 2008 Wenchuan Mw 7.9 Earthquake of China and Their Spatial Distribution Statistical Analysis. *Landslides* 11 (3), 441–461. doi:10.1007/s10346-013-0404-6

Yuan, R., Deng, Q., Cunningham, D., Han, Z., Zhang, D., and Zhang, B. (2016). Newmark Displacement Model for Landslides Induced by the 2013 Ms 7.0 Lushan Earthquake, China. *Front. Earth Sci.* 10 (4), 740–750. doi:10.1007/s11707-015-0547-y

Conflict of Interest: The authors declare that the research was conducted in the absence of any commercial or financial relationships that could be construed as a potential conflict of interest.

frontiers
in Earth Science

ORIGINAL RESEARCH
published: 13 August 2021
doi: 10.3389/feart.2021.706998

Detecting the Vegetation Change Related to the Creep of 2018 Baige Landslide in Jinsha River, SE Tibet Using SPOT Data

Xinyi Guo[1,2], *Qing Guo*[1]* *and Zhongkui Feng*[1]

[1]Aerospace Information Research Institute, Chinese Academy of Sciences, Beijing, China, [2]University of Chinese Academy of Sciences, Beijing, China

Edited by:
Tolga Gorum,
Istanbul Technical University, Turkey

Reviewed by:
Milad Janalipour,
K. N. Toosi University of Technology, Iran
Gaetano Pecoraro,
University of Salerno, Italy
Tapas Martha,
National Remote Sensing Centre, India

***Correspondence:**
Qing Guo
guoqing@aircas.ac.cn

Specialty section:
This article was submitted to Quaternary Science, Geomorphology and Paleoenvironment, a section of the journal Frontiers in Earth Science

Received: *19 May 2021*
Accepted: *03 August 2021*
Published: *13 August 2021*

Citation:
Guo X, Guo Q and Feng Z (2021) Detecting the Vegetation Change Related to the Creep of 2018 Baige Landslide in Jinsha River, SE Tibet Using SPOT Data.
Front. Earth Sci. 9:706998.
doi: 10.3389/feart.2021.706998

It is vital to monitor the post-seismic landslides economically and effectively in high-mountain regions for the long term. The landslide creep could cause a subtle change of the overlying vegetation after the earthquake, which will lead to the change of vegetation spectral characteristics in optical remote sensing data. The optical remote sensing technique can be used to monitor the landslide creep areas with dense vegetation in a large range at a low cost because it is easy to obtain multi-temporal, multiple-scale, and multi-spectral information. We identified and extracted the vegetation change area before the 2018 Baige landslide by the high-resolution optical remote sensing data. Firstly, the image fusion method was used to improve the accuracy of change detection. Then, vegetation coverage before the landslide was calculated. The vegetation change was identified, and qualitative and quantitative methods were used to analyze the spatio-temporal changes of vegetation coverage. Our results indicate that the creep distance of the landslide is about 50 m and the vegetation in the back scarp area and the main sliding area display a significant downward trend with time closing to the landslide comparing with that in the reference area. The vegetation change in the remote sensing image has an excellent spatio-temporal correlation with the landslide creep. This study provides a possible way and perspective for monitoring post-seismic landslide disasters.

Keywords: post-seismic landslides, vegetation change, landslide creep, high-mountain regions, optical remote sensing technique

HIGHLIGHTS

1. The changes in environmental conditions caused by the landslide creep have an impact on vegetation growth;
2. The vegetation change has an evident spatio-temporal correlation with the landslide creep;
3. The high-resolution optical remote sensing technology can be used to identify the vegetation change. For potential landslides in large-scale high-mountain areas, this method can be used for preliminary investigations economically and effectively.

INTRODUCTION

The effect of earthquakes on landslides is not only in the seismic stage but also in several years after the earthquake. The slope formed some cracks during the earthquake and did not slide immediately but formed potential landslides. Previous studies have found that these potential landslides will be in an unstable state for a long time (years to hundreds of years) after the earthquake (Khattak et al., 2010). Moreover, due to the seismic topographical amplification effect (the seismic whiplash effect) (Xu et al., 2017), cracks mainly formed in the upper part of the slope, which is hard to be reached by the field investigation. When these areas are affected by rainfall, the shear strength of the mass will reduce, and the stability of the slope will decrease. Finally, the slope becomes unstable and forms a large and destructive landslide (such as the Xinmo village landslide in 2017). Southwest China is an earthquake-prone area characterized by high and steep topography and dense vegetation. So, it is challenging to monitor the potential landslides in high-risk areas after the earthquake, especially in remote or poor accessible regions. It is vital to monitor high-risk areas economically and effectively in the long-term change process after the earthquake.

Field displacement measurement is the main method for monitoring landslides. Moreover, the common non-contact displacement monitoring methods include the global positioning system (GPS) monitoring method Wang (2011) and the synthetic aperture radar (SAR) monitoring method (Bianchini et al., 2018). But the range of GPS monitoring is limited; the monitoring network of GPS needs to be established in advance; the instruments of GPS must avoid being sheltered by vegetation during the monitoring period. The complex environment in the mountain areas will increase the difficulty of network layout and increase the cost of operation (Fan et al., 2006). The GPS monitoring method, which uses the point as the monitoring unit, is difficult to reflect the continuous change information of the land. For the interferometric synthetic aperture radar (InSAR) monitoring method, the phase unwrapping is difficult. Complex terrain and dense vegetation will cause phase decorrelation of radar data. Therefore, some slopes are difficult to be photographed (Wang et al., 2010). InSAR monitoring is not suitable for monitoring landslides in the mountain and canyon areas. The intensity tracking method of offset tracking technology which is insensitive to the coherence of SAR images is suitable for the low coherence area with significant characteristics (Yang et al., 2017). This method has been used in monitoring landslides. It matches images based on the feature information, also known as feature matching. This method generally needs bright targets (e.g., buildings and bare rocks), providing accurate and reliable estimations (Jia et al., 2020). However, it will be difficult to find buildings and bare rocks when the slopes are covered by dense vegetation.

The optical remote sensing technique, with the characteristics of non-contact, large-scale, periodic observation, multiple archived data, and rich spectral information, is an essential mean of landslide monitoring. The landslide deformation monitored by optical remote sensing mainly focuses on identifying the deformation of the slope or the cracks and bare land caused by the deformation. Sub-pixel phase correlation of optical remote sensing images can be used to obtain deformation. The deformation can be obtained by calculating the offset between two optical remote sensing images, reflecting the position deviation of points in the two images. It has been used in some earthquake cases (Michel and Avouac, 2002; Dominguez et al., 2003; Binet and Bollinger, 2005). However, when the deformation, cracks, and bare land are hidden by vegetation, the method will be helpless.

Vegetation is the first layer of Earth observation. The weak information of vegetation change can reflect the geological activities, which has been applied in the investigation of mine and the identification of the fault (Zhao, 2013). Many slopes have a slow creep stage before the landslide. Sometimes cracks and small landslides will form on the creep slopes. The deformation in this stage will change the rock, soil, water, and other things in the surrounding areas, influencing the overlying vegetation (Ding et al., 2013; Du et al., 2013). Finally, it will lead to the change of vegetation spectral characteristics in optical remote sensing data. These vegetation change phenomena are common in geological investigations.

When the landslide deformation is hidden by vegetation, the vegetation can be considered the monitoring object. The spectral characteristics of vegetation can be used to indicate landslide creep. The image fusion can enhance the weak information of vegetation variations and explore the relationship between the vegetation change and the landslide in the remote sensing data before the landslide (Guo et al., 2020). The vegetation spectral change in optical remote sensing data can be used to identify the deformation of the land effectively. It can delineate the potential geological hazards and study the dynamic evolution process and characteristics of disaster deformation by the multi-temporal remote sensing data, which is helpful to determine the risk degree of hidden danger. This monitoring method can make up for the deficiency of the existing monitoring technique in the dense vegetation and high-mountain areas and assist in monitoring the landslide in the long-term change process after the earthquake. This method can be used to preliminary investigations of potential landslides economically and effectively in large-scale areas. Then it can combine with visual interpretation, SAR, and other techniques for further confirmation in the key areas. This study focuses on the Baige landslide in the Jinsha River, SE Tibet, to monitor the landslide after the earthquake through the vegetation change.

STUDY AREA AND DATA

Study Area

The Baige landslide with a source volume of 23 million m^3 on October 11, 2018, occurred on the western bank of Jinsha River, a junction of Baiyu County (Ganzi Prefecture, Sichuan Province) and Jiangda County (Changdu City, Tibet Autonomous Region) (**Figure 1**). A second slide occurred at the same location on November 3, 2018. The second landslide volume was about 3.5 million m^3, and the entrainment volume was about 8.5 million m^3 (Fan et al., 2020). The landslide blocked the trunk stream of the Jinsha River and formed a barrier lake, which endangered Baiyu County, Batang County, and Delong County.

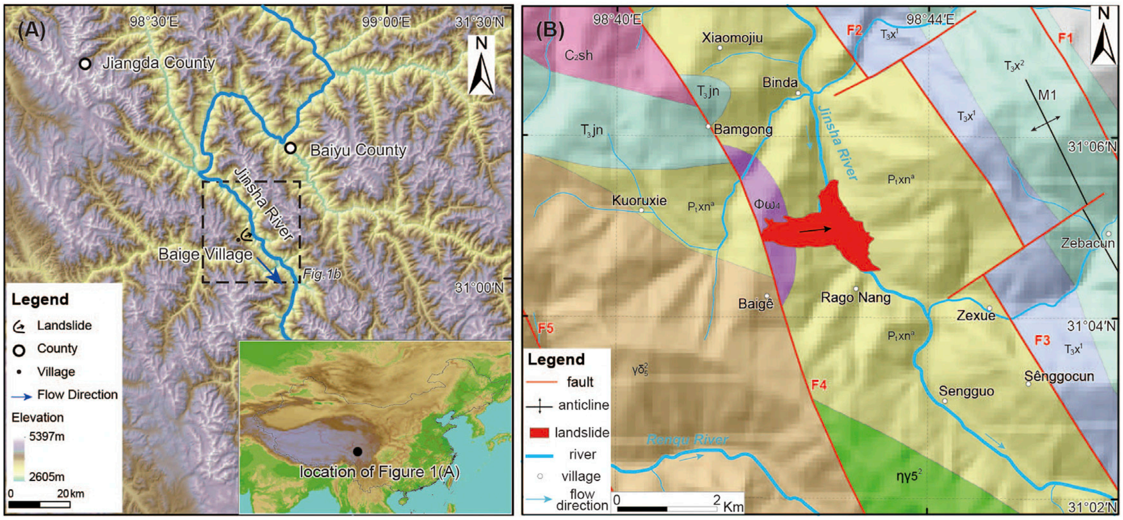

FIGURE 1 | Topographic and geologic maps of Baige landslide **(A)** Topographic map (The insert shows the location of the study area in China). **(B)** Geological map (modified from Fan et al., 2019). F1: Xuenqing-Longgang Fault; F2: Zhuying-Gonda Fault; F3: Zeba-Xietang Fault; F4: Boluo-Muxie Fault; F5: Gangda-Dizhong Fault; M1: Shandong-Baba Anticline; T_3jn: Upper Triassic Jingu Formation; T_3x^2: Upper Segment of Upper Triassic Xianisongduo Formation; T_3x^1: Lower Segment of Upper Triassic Xianisongduo Formation; C_2sh: Upper Carboniferous Shengpa Formation; P_txn^a: Upper Proterozoic Xiongsong Group Gneiss Formation; $\varphi\omega_4$: Late Paleozoic Variscan Jinshajiang ultramafic belt and serpentinite; $\eta\gamma5^2$: Yanshanian Gepo superunit fine grained monzonitic granite; $\gamma\delta_5{}^2$: Yanshanian Zeba superunit Muzha fine-grained granodiorite and quartz diorite.

The Baige landslide is located in the Southeastern Tibetan Plateau, which has steep topography, fierce landform incision, and broken rocks. Several structures are striking in the NW direction; significant among them are the Bolou-Muxie, Zhuying-Gonda, Xuenqing-Longgang faults, and the Shandong-Baba Anticline. The landslide is located on the edge of the BolouMuxie fault. The strata outcropping in the landslide area mainly consist of gneiss (P_txn^a), granite ($\gamma\delta_5{}^2$), limestone (T_3jn), and serpentinite ($\varphi\omega_4$) (An et al., 2021). The landslide headscarp developed within the serpentinite from Variscan orogeny. The landslide body is mainly composed of gneiss and serpentinite. The borehole data show that the rock masses are extremely broken in the study area. The water in Bogong Gully has infiltrated the landslide body for a long time (Zhong et al., 2021). Zhang et al. (2020) think that serpentine in the Baige landslide was altered into clay minerals, such as montmorillonite or illite. Clayey altered rock is a weak interlayer, which significantly reduces the shear strength of the potential slip zone. It is rich in clay minerals and has good water absorption. The engineering properties of the altered soft rock, which shrink/swell with drying and wetting, are weak under the influence of water (Zhang et al., 2011). It will further deteriorate the slope rock structure. Finally, the serpentine strata gradually transformed into a creep zone (Fan et al., 2019).

In history, several strong earthquakes occurred around the Baige area, such as the 1842 Mw7.3 Zongguo earthquake, the 1870 Mw7.2 Batang earthquake, and the 1989 Mw6.5 earthquake (SSB, 1995; Ambraseys and Douglas, 2004). In recent years, earthquakes occurred around this area, including the 2013 Ms6.1 Changdu earthquake. The Changdu earthquake induced 37 new potential hazards in Jiangda county and 57 new potential hazards in Baiyu County (Wang et al., 2019). These earthquakes intensified the deformation of some potential landslides and promoted the occurrence of the Baige landslide. Finally, under the rainfall and the long-term gravity, the Baige landslide loses stability.

TABLE 1 | Remote sensing data covering the Baige landslide.

Image source	Time of acquisition	Spatial resolution/m
SPOT-6	2014/05/18	PAN-1.5, MS (B, G, R, NIR)-6
SPOT-7	2015/05/30	PAN-1.5, MS (B, G, R, NIR)-6
SPOT-7	2017/05/08	PAN-1.5, MS (B, G, R, NIR)-6

Data Description

In this study, the images used for vegetation change detection need to be of good quality, from the same period each year, and without clouds. SPOT images have Ortho-Level images, which have been done ortho-rectification with few geometric distortion and good quality. According to the geographic conditions of the Baige landslide and the limited free image data available, a minimum number of SPOT-6 and SPOT-7 Ortho-Level images were selected. Panchromatic (PAN) band and multispectral (MS) bands (B, G, R, NIR) of SPOT-6 and SPOT-7 images were both used in this study. These images without clouds can provide reliable data sources for acquiring vegetation growth information before the landslide. These images come from the same period of 3 years (2014–2017), which reduces the interferences of the season (including rainfall, temperature, and other factors) to vegetation change. The information on remote sensing data is shown in **Table 1**.

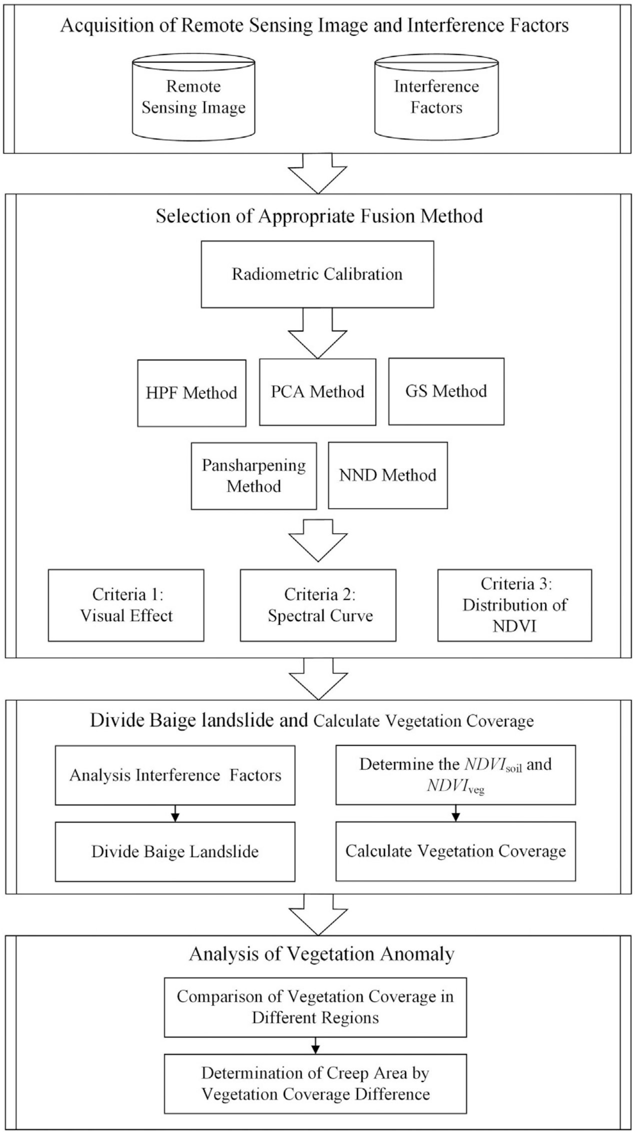

FIGURE 2 | Procedural flow chart of this study.

METHODS

The steps to detect vegetation change are listed as follows (**Figure 2**): 1) Acquire remote sensing images and interference factors; 2) select appropriate fusion method; 3) divide Baige landslide and calculate vegetation coverage; and 4) analyze vegetation anomaly.

Selection of Image Fusion Method

The recognition ability of vegetation change in remote sensing images should be enhanced before the landslides. It is necessary to improve the spatial and spectral resolutions and then integrate them as much as possible. The remote sensing image fusion method can integrate the spatial and spectral information of multiple images, which can provide more abundant and complete information than that of any single image. It is an important step in remote sensing image processing, such as information extraction, change detection, and target recognition. However, different image fusion methods have different results. Some results may interfere with vegetation change detection. We try to guarantee the detected vegetation anomaly caused by the landslide creep rather than the fusion method. So, we chose five fusion algorithms for comparative experiments to select the fusion method with the least interference, including high pass filtering (HPF) (Ranchin and Wald, 2000), principal components analysis (PCA) (María et al., 2004), Gram-Schmidt (GS) (Clayton, 1971), Pansharpening (Zhang and Mishra, 2012) and nearest-neighbor diffusion-based pan-sharpening algorithm (NND) (Sun et al., 2014).

The Pansharpening method has been used in the SPOT fusion-level products. So, the SPOT fusion-level product can be used as the fused result of the Pansharpening method. But the SPOT fusion-level products are not processed by the atmospheric correction. Referring to the processing flow of the SPOT fusion-level products, we do not implement the atmospheric correction for the experimental images to ensure the consistency of the image processing flow. The panchromatic (PAN) and multispectral (MS) images of SPOT were directly calibrated to the reflectance image. Then, the five fusion methods were used to fuse the image.

Finally, we evaluated the results of image fusion and chose the appropriate fusion method. In this study, vegetation and bare land were the key objects that can reflect vegetation growth on the surface. Owing to the spectral fidelity of remote sensing data relating to the monitoring results of vegetation, the quality of the fused image is evaluated from the visual effect evaluation, spectral curves of vegetation and bare land, and distributions of normalized difference vegetation index (*NDVI*). We select the best image fusion method which is suitable for monitoring vegetation.

Division of the Baige Landslide

This paper aims to study the vegetation change caused by landslide creep. Besides, human activities and other factors will also interfere with vegetation. So, it is necessary to control the environment variables and obtain a single environment variable zone. The zoning excludes unrelated factors such as human activities to ensure the consistency of vegetation growth conditions within the same physical geographical units. Therefore, we combined the interpretation of high-resolution remote sensing data to divide the slope into different units before the Baige landslide.

Firstly, the main sliding area at the back part of the Baige landslide, with dense vegetation, was identified. In previous studies, the visual interpretation of historical satellite images shows that the site has experienced creep deformation in the last 50 years. Cracks and slight surface disruption had shown in 1966. The slope might have been already deforming and prone to failure. In this study, the interpretation results of Google Earth's high-resolution remote sensing data (**Figure 3A**) show that the vegetation area had slipped and formed the back scarp of the landslide before 2011 (Fan et al., 2019). Since 2011, the displacement of vegetation area at the back part of the landslide increased rapidly, and the shear fractures on both sides formed. The road in the vegetation area was significantly

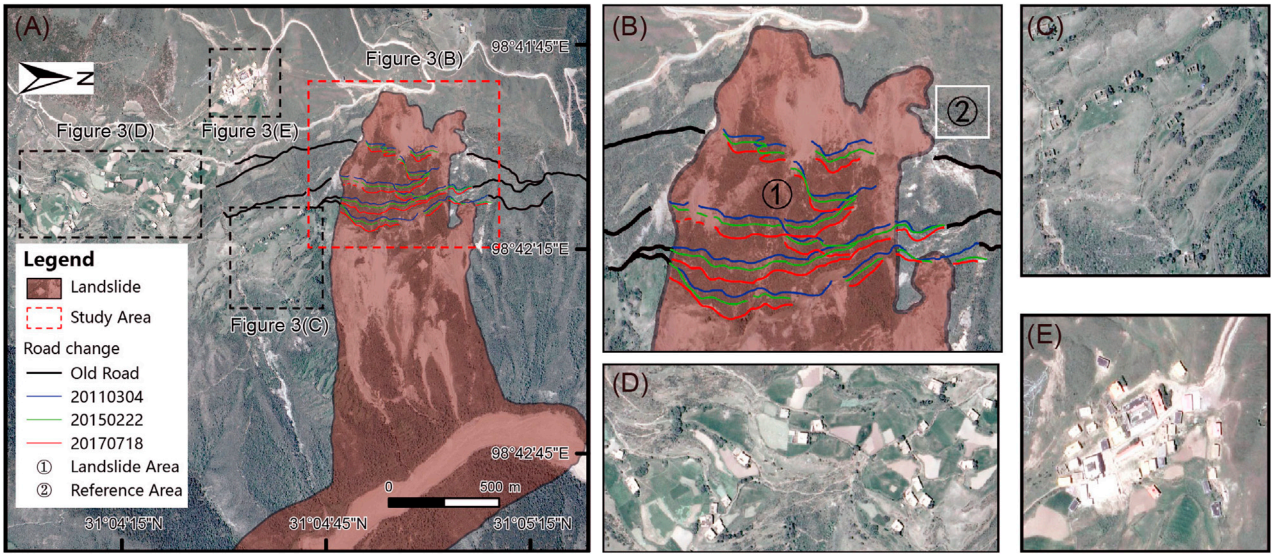

FIGURE 3 | The Baige landslide **(A)** Interpretation map of Baige landslide (modified from State Key Laboratory of Geohazard Prevention and Geoenvironment Protection, 2018 (http://www.sklgp.cdut.edu.cn/info/1018/2247.htm)) **(B)** Deformation map of the road **(C)** Community-1 **(D)** Community-2 **(E)** Community-3.

dislocated at the shear crack. As time went by, the road was abandoned, and the sliding distance of the road increased (**Figure 3B**). Therefore, the vegetation area at the back part of the landslide was determined as the main sliding area, and the area shown in the red box (**Figure 3A**) was determined as the focus area.

Then, according to the interpretation result of human activities, this study made a detailed division. In the selected red box area, the landslide edge was taken as the boundary to divide this area into two parts: the landslide area (area ①) and the external area of the landslide. In the external area of the landslide, there were many communities on the left side, as shown in **Figures 3C–E**. They may interfere with the vegetation. However, there were no communities near the right side. Since the road was abandoned, the right side of the landslide had few human activities, especially the area drawn by the white box hardly was disturbed by human activities, as shown in **Figure 3B**. This area was on the same slope as the landslide, which had the same natural conditions as the landslide. It was helpful to verify the effect of the landslide creeps on vegetation. So, the area in the white box was regarded as the reference area (area ②).

Vegetation Coverage Information Acquisition

Vegetation coverage can directly show the surface vegetation situation and is often used as an evaluation factor in geological hazard assessment, prevention, and mitigation. We used the dimidiate pixel model to calculate the vegetation coverage maps.

The dimidiate pixel method assumes that the land in a pixel is composed of vegetation area and non-vegetation area (soil or bare land). The spectral information of this land observed by remote sensing sensor is also composed of these two elements by linear weighting. The weight of each element is the proportion of their respective area in the pixel. The vegetation coverage can be regarded as the weight of vegetation (Leprieur et al., 1994; Chen et al., 2001; Zribi et al., 2003).

NDVI is also a kind of quantitative value that reflects the growth of vegetation on the land. It is calculated from the spectral information of land objects received by remote sensing sensors, as shown in **Eq. 1**. Since the atmospheric correction was not conducted in this study, *NDVI* can partly eliminate the atmospheric influence to reduce the atmospheric disturbance as much as possible. According to the dimidiate pixel model, the *NDVI* value of a pixel can be expressed as the information of $NDVI_{\mathrm{veg}}$ contributed by vegetation and the information of $NDVI_{\mathrm{soil}}$ contributed by non-vegetation (soil or bare land). Moreover, it is shown that different indicators used to calculate vegetation coverage have different characteristics, among which NDVI is the most widely used in previous studies (Li, 2003). Therefore, the vegetation coverage can be expressed by the following formulas:

$$NDVI = \frac{\rho_{\mathrm{NIR}} - \rho_R}{\rho_{\mathrm{NIR}} + \rho_R} \tag{1}$$

where ρ_{NIR} is the reflectance of the near-infrared band; ρ_R. is the reflectance of the red band.

$$F_c = \begin{cases} 0, NDVI \le NDVI_{\mathrm{soil}} \\ (NDVI - NDVI_{\mathrm{soil}})/\left(NDVI_{\mathrm{veg}} - NDVI_{\mathrm{soil}}\right), NDVI_{\mathrm{soil}} \le NDVI \le NDVI_{\mathrm{veg}} \\ 1, NDVI \ge NDVI_{\mathrm{veg}} \end{cases} \tag{2}$$

where F_c is the vegetation coverage value; $NDVI_{\mathrm{soil}}$ is the *NDVI* of the area entirely covered by soil; $NDVI_{\mathrm{veg}}$ is the *NDVI* of the area entirely covered by vegetation.

In theory, $NDVI_{\mathrm{soil}}$ and $NDVI_{\mathrm{veg}}$ should be determined by the field investigation. However, due to the Baige landslide has already happened, we can not verify $NDVI_{\mathrm{soil}}$ and $NDVI_{\mathrm{veg}}$ by the field investigation. Previous studies usually use the statistics of

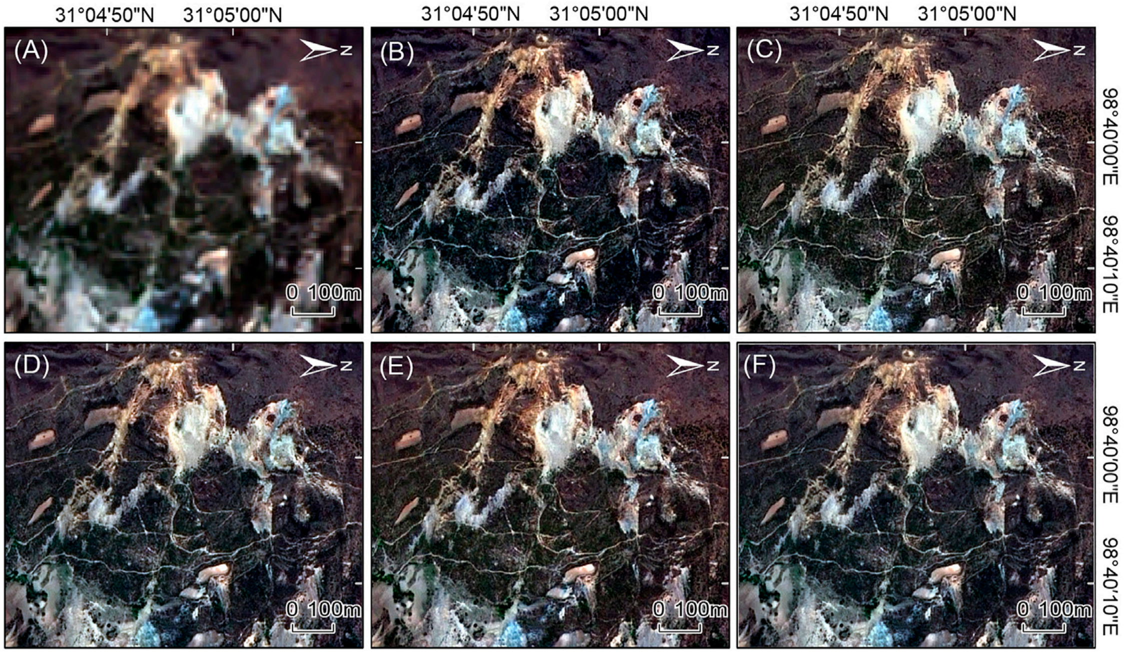

FIGURE 4 | Visual effects of different fusion methods **(A)** MS image **(B)** Pansharpening fused image **(C)** HPF fused image **(D)** GS fused image **(E)** PCA fused image **(F)** NND fused image.

$NDVI$ to get the cumulative percentage of each $NDVI$ and then set the confidence interval of the cumulative percentage to determine the $NDVI_{soil}$ and $NDVI_{veg}$ (Li et al., 2014). Therefore, we count the cumulative percentage of each $NDVI$ value in the remote sensing image at first. Secondly, we use the visual interpretation of remote sensing images to determine the vegetation area and the bare land area. Then, we use different confidence intervals to obtain the vegetation area and the bare land area. Finally, we compare the area obtained by different confidence intervals with the area obtained by visual interpretation to determine the suitable confidence interval. However, this method relies too much on visual interpretation. Sometimes there may be a slight deviation in the confidence interval of the best matching state obtained by visual interpretation of images in different phases. To obtain the consistent and best consistent vegetation coverage, we unify the confidence intervals of the three phases, getting 2%–98% as the confidence interval.

According to the confidence interval, this study determined the $NDVI_{soil}$ and $NDVI_{veg}$. The $NDVI$, whose accumulated percentage was 2% in the Baige landslide, was defined as $NDVI_{soil}$ (i.e., The pixel's $NDVI$, which was less than $NDVI_{soil}$, was entirely covered by soil). The $NDVI$, whose accumulated percentage was 98% in the Baige landslide, was defined as $NDVI_{veg}$ (i.e., The pixel's $NDVI$, which was more than $NDVI_{veg}$, was entirely covered by vegetation). Finally, the vegetation coverage of the Baige landslide was calculated according to **Eq. 2**. Besides, the vegetation coverage from high to low was transformed into the corresponding color from red to purple by the pseudo-color density segmentation. The calculation of vegetation coverage and pseudo-color enhancement can highlight the subtle vegetation changes related to landslide creep.

RESULTS

Effect of Image Fusion

In the comparative experiment, the original MS reflectance image was taken as the reference image. The fused images obtained by different fusion methods were compared. The results of the fused images are shown in **Figure 4**. Owing to the PAN and MS images in the fusion experiment gotten from the same sensor in the same phase, the color differences of most fused images were inconspicuous. They can effectively improve image clarity and visual effect.

The spectral fidelity of vegetation and bare land was analyzed from the shape and scope of the reflectance spectrum curve in different fused images, as shown in **Figure 5** and **Figure 6**. In **Figure 5**, the spectral reflectance curve of the vegetation in the NND fused image is the most consistent with that in the MS image, and the fidelity of the NND fused image is the best. Although the shapes of these spectral reflectance curves of Pansharpening, HPF, GS, and PCA fused images are not significantly different from that of the MS image, these reflectance values of fused images are high and spectral fidelity is poor. In **Figure 6**, the spectral reflectance curves of the bare land in the NND and PCA fused image have the same trend and good fidelity as that of the MS image. The curve trend of the HPF fused image is inconsistent with the MS image. Although the shapes of these spectral reflectance curves of Pansharpening and GS fused images are not significantly different from that of the

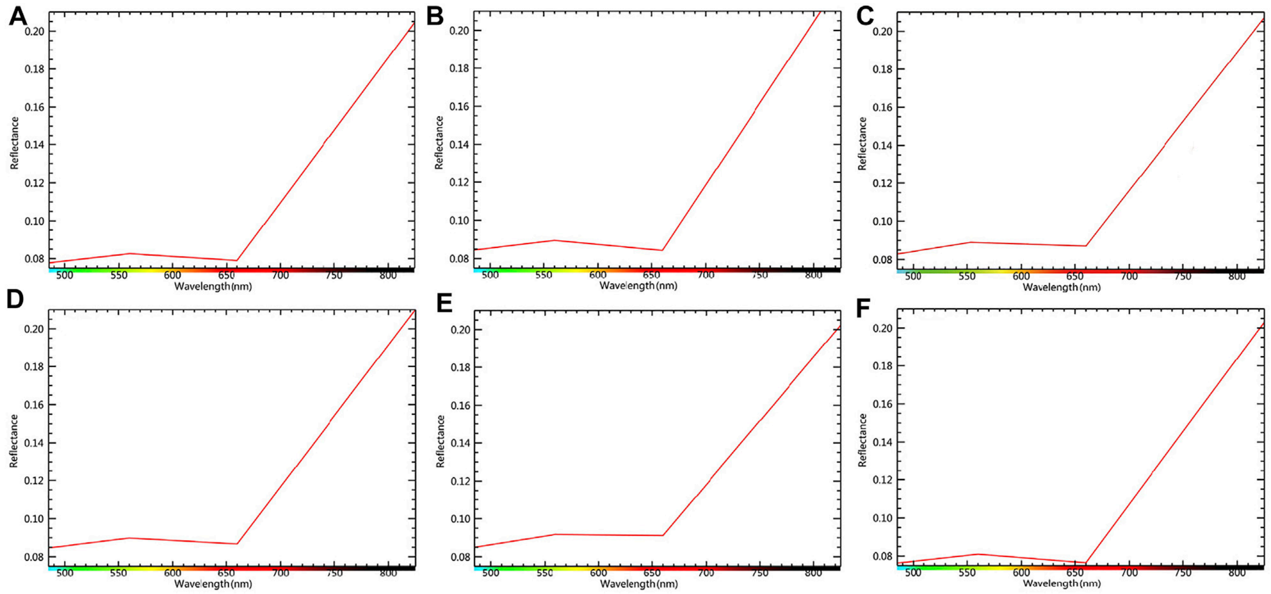

FIGURE 5 | The spectral reflectance curves of vegetation with different image fusion methods **(A)** MS image **(B)** Pansharpening fused image **(C)** HPF fused image **(D)** GS fused image **(E)** PCA fused image **(F)** NND fused image.

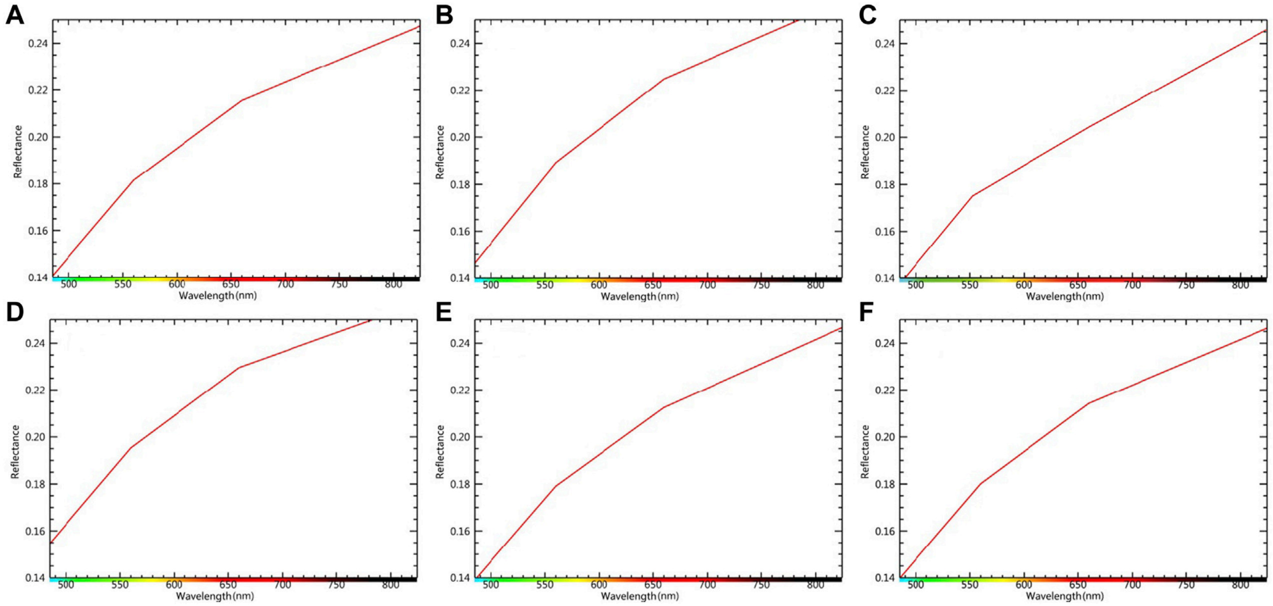

FIGURE 6 | The spectral reflectance curves of bare land with different image fusion methods **(A)** MS image **(B)** Pansharpening fused image **(C)** HPF fused image **(D)** GS fused image **(E)** PCA fused image **(F)** NND fused image.

spectral reflectance curve of MS image, these reflectance values of fused images are high, and their spectral fidelity is poor.

This study calculated the *NDV*I values of the MS image and fused images. The main objects in the selected study area are mainly bare land and vegetation, without clouds, water, and snow. So, the *NDVI* distribution values range from 0 to 1. The distributions of *NDVI* from these images are shown in **Figure 7**. The *NDVI* of the MS image was regarded as the actual value to compare with other *NDVI* values of the fused images (**Table 2**): 1) The maximum and minimum values of each *NDVI* result were counted. *NDVI* values are mainly distributed between 0.25 and 0.45 in the MS image. The distribution of *NDVI* values obtained by PCA fusion is mainly distributed between 0.25 and 0.5. In the MS image, *NDVI* appears most frequently around 0.4. In GS fused

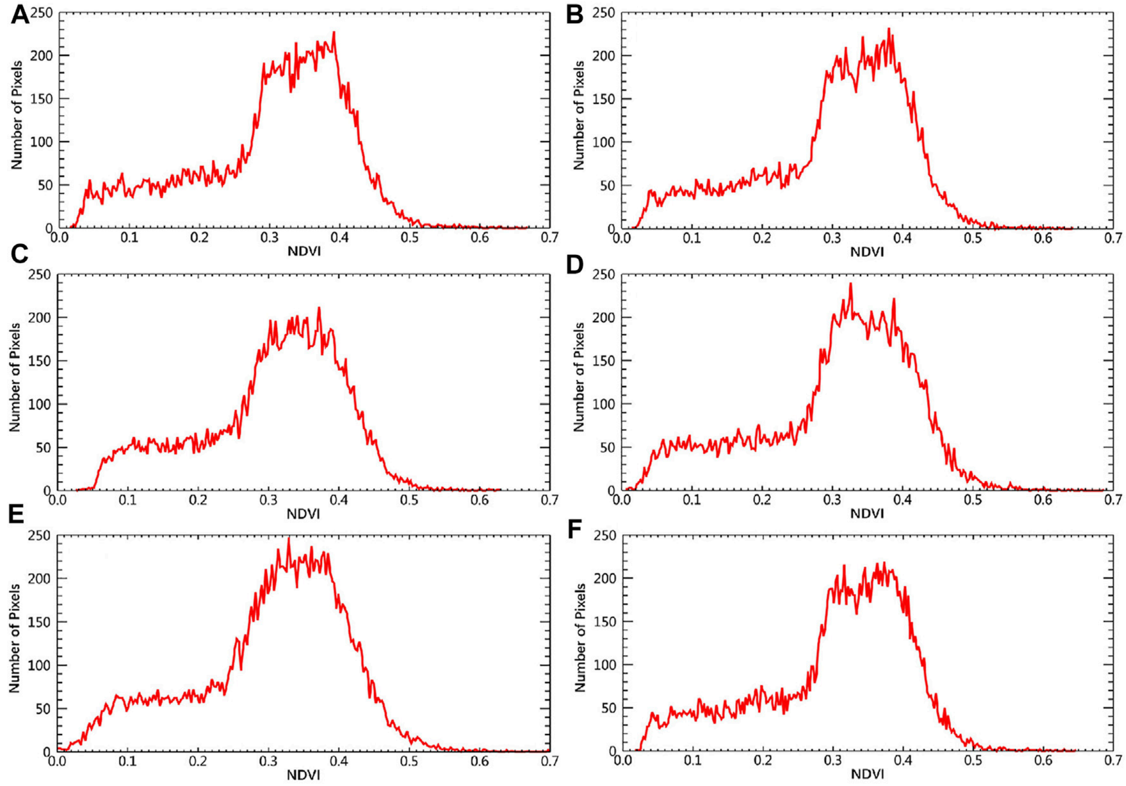

FIGURE 7 | NDVI distribution of different fused images **(A)** MS image **(B)** Pansharpening fused image **(C)** HPF fused image **(D)** GS fused image **(E)** PCA fused image **(F)** NND fused image.

TABLE 2 | NDVI of the fused image.

NDVI	MS image	Pansharpening	HPF	GS	PCA	NND
Mean	0.305	0.305	0.306	0.305	0.305	0.305
Max	0.668	0.645	0.630	0.687	0.724	0.647
Min	0.015	0.014	0.026	0.006	−0.028	0.017
RMSE	—	30.474	58.569	65.924	82.298	32.810

image, *NDVI* appears most frequently around 0.3. 2) In the mean *NDVI*, the approximation ratio of the mean *NDVI* was calculated. The approximation ratios of the mean *NDVI* obtained by these fused images and the *MS image* can almost reach 100%, except HPF fused image. 3) In the distribution of *NDVI*, we calculated the root mean squared error (RMSE) of the *NDVI* to measure the deviation between the *NDVI* values of the fused images and the actual *NDVI* value. This study compared the *NDVI* distribution of the fused images with that of the MS image. We found that the *NDVI* distribution of the fused images is similar to that of the MS image when RMSE is within 50. So, this study used RMSE as the criteria. The *NDVI* distribution of the NND and Pansharpening fused images are the most similar to the actual distribution.

According to the visual effect, the spectral curve of vegetation and bare land, and the distribution of *NDVI*, we found that the NND fusion method is superior to the other four fusion methods for this study. It can keep the actual spectrum of bare land and vegetation and keep the actual distribution of *NDVI*. So, it is the best method for bare land and vegetation and selected as the fusion algorithm of this study. Moreover, the experiment also proves that calculating *NDVI* by suitable fused remote sensing images to monitor the vegetation is reasonable.

Vegetation Change Related to the Creep

The study obtained the fused remote sensing image (**Figures 8A–C**), the maps of vegetation coverage (**Figures 8D–F**), and the maps of vegetation change (**Figures 8G–I**) of the Baige landslide. We can judge whether the landslide is sliding or not through the visual interpretation of fusion image, qualitative and quantitative study of vegetation coverage. For landslides with a long creep distance, we can outline the boundary of the landslide according to the change of vegetation coverage and judge the creep distance of the landslide.

The range of bare land and the landslide boundary can be identified from the remote sensing image. The solid black line in **Figure 3** is the landslide boundary, which is consistent with the first landslide boundary of the Baige landslide designated by the State Key Laboratory of Geohazard Prevention and Geoenvironment Protection (2018) (http://www.sklgp.cdut.edu.cn/info/1018/2247.htm). Moreover, the creep history can be

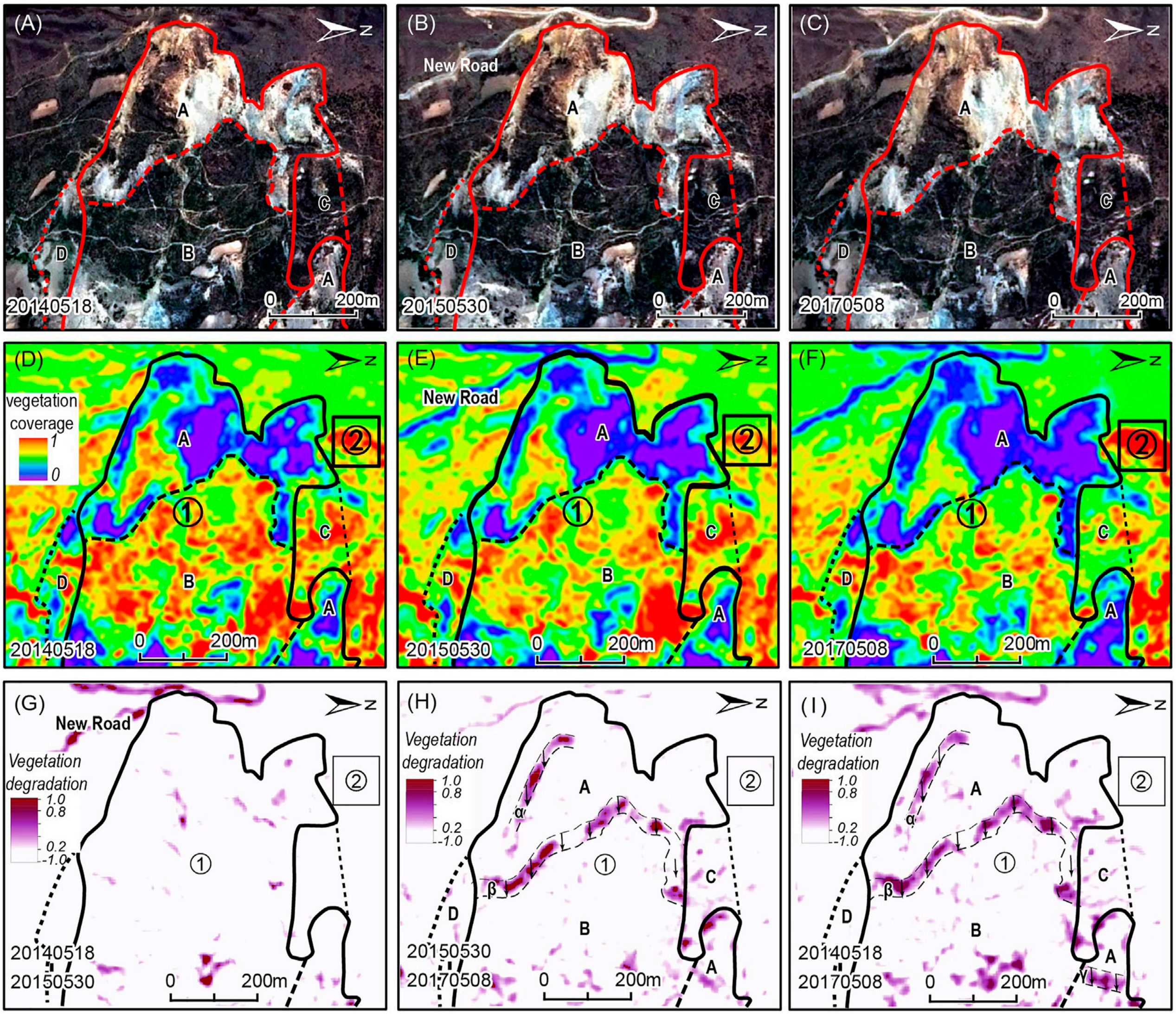

FIGURE 8 | Remote sensing data and vegetation coverage map of Baige landslide **(A)** SPOT-6 image of May 18, 2014 **(B)** SPOT-7 image of May 30, 2015 **(C)** SPOT-7 image of May 8, 2017 **(D)** Vegetation coverage map of May 18, 2014 **(E)** Vegetation coverage map of May 30, 2015 **(F)** Vegetation coverage map of May 8, 2017 **(G)** Vegetation coverage change map of 2014–2015 **(H)** Vegetation coverage change map of 2015–2017 **(I)** Vegetation coverage change map of 2014–2017.

determined according to the road displacement within the landslide (as shown in **Figure 3**).

The vegetation coverage change in the study area with time has significant spatial heterogeneity. It indicates that the vegetation in the study area is disturbed by the uneven distribution of influencing factors. We think that the main influencing factor may be landslide creep, according to the displacement of the road in **Figures 8A–C**. Therefore, the vegetation anomaly area at the middle part of the study area is the landslide-prone area that needs to be paid attention to. The change of vegetation coverage on both sides of the study area is complex. Therefore, we further divided the study area according to **Figures 8A–C**. The study area was divided into four zones: A-D. Area A is the back scarp of the landslide, where the bedrock is exposed because of the previous sliding. Area B is the main sliding area of the landslide, where the vegetation is still preserved. There is a significant boundary between area A and area B. It can be used as a marker for monitoring the creep distance of the landslide. Area C and area D are located out of the first landslide area and may be disturbed by the main landslide area. Area C had been creeping since 2014, and it slid in the second landslide. There are significant cracks on the left side of area D caused by the earlier sliding. After that, area D tends to be stable. There is still no sliding in the second landslide, which can be used as a reference area for the study of area C.

The change of vegetation coverage can be used to monitor the landslide creep. As the reference, the vegetation coverage in the reference area (area ②), which is unlikely to slide, decreased from 2014 to 2015 and then increased from 2015 to 2017. It is regarded as the background value of the vegetation coverage change. Before the first landslide, the vegetation coverage of area B decreased

TABLE 3 | Statistics of vegetation coverage difference.

Vegetation coverage difference	Percentage of vegetation coverage difference area/(%)		
	2014–2015	2015–2017	2014–2017
−1–0.2	93.88	88.00	83.87
0.2–0.4	4.10	9.35	10.92
0.4–0.6	1.82	2.23	4.21
0.6–0.8	0.19	0.42	0.92
0.8–1.0	0.01	0.00	0.08

Note: The positive number means "vegetation coverage decrease"; the negative number means "vegetation coverage increase."

significantly, and the creep of the landslide can be identified. The scope of area A gradually expanded with time. It means that area A and area B, which compose area ① (landslide area), are dangerous. The vegetation coverage of area C has decreased before the first landslide. According to the displacement of roads in area C, this area has crept from 2014. It means that area C is also dangerous. Then this area slid in the second landslide. Vegetation coverage change of area D is not significant before the first landslide, which means the danger of area D is not high. Area D did not slide in the first and second landslides (Ouyang et al., 2019).

It is not intuitive to show the creep of landslides only through the change of vegetation coverage. So, we calculated the vegetation coverage difference in 2014–2017. The negative value indicates the increase of vegetation coverage, and the positive value indicates the decrease of vegetation coverage. According to the vegetation coverage change in the area ② (reference area), we think that the vegetation coverage change at 0–0.2 is normal and reasonable in 2014–2017. Because the area ② is in the natural state and unlikely to be disturbed by landslides, human activities, and other interference factors, we use a 0.2 reduction of vegetation as the threshold of the vegetation coverage change in 2014–2017. When the difference of vegetation coverage is between −1 and 0.2, it means that the vegetation is in the natural state or vegetation coverage is increasing. The difference map of vegetation coverage was counted, and the results are shown in **Table 3**. As time goes on, the proportion of vegetation coverage differences between −1 and 0.2 decreases by more than 10%; the proportion of vegetation coverage difference between 0.2 and 0.8 increased rapidly. In this study, the difference map was colored with pseudo color at an interval of 0.2. The areas in the natural state or with increasing vegetation coverage or are set as colorless. We obtained maps of vegetation coverage difference in 2014–2015 (**Figure 8G**), 2015–2017 (**Figure 8H**), and 2014–2017 (**Figure 8I**). The vegetation coverage of areas not affected by landslides increases or remains unchanged (e.g. area ②), while the vegetation coverage of the landslide area decreases significantly (e.g. areas A, B, C).

The road construction caused the abnormal decrease of vegetation coverage in the upper part of the study area (**Figure 8I**). Moreover, according to the scope of vegetation coverage reduction area, the shape of the creeping landslide can be roughly outlined (**Figure 8I**). Although area D has bare land and its vegetation coverage is low (**Figures 8D–F**), the vegetation coverage change is similar to that of the background value, which contrasts with that of area C (**Figure 8I**). Area C and D did not slide in the first landslide, but area C slid in the second landslide. The decrease of vegetation coverage in 2014–2015 is far smaller than that in 2015–2017. Therefore, the creep distance of the landslide in 2014–2015 is far less than that in 2015–2017. At the same time, there are three significant strips α, β, and γ in the region, respectively corresponding to the exposed area of the back scarp of the landslide mass. According to the width of strips α, β, and γ in the east direction, we estimate that the creep distance of the three strips is roughly the same, about 50 m.

DISCUSSION

Validation of Vegetation Coverage Change Related to the Creep

In this study, the displacement of the landslide caused the vegetation coverage change. With the increase of the displacement, the vegetation coverage change became more and more significant. Vegetation coverage change in the remote sensing data had a spatio-temporal correlation with the landslide creep before the landslide occurred (**Figure 8**).

This study is compared with other studies employing multiple methods for validation. In the Baige landslide, Ding et al. (2021) identified the active landslide region with a mass advancing motion from west to east (i.e., from up to down). It is consistent with the local topography. The spatial heterogeneity in the displacement velocity field is significant. So, the main landslide body can divide into several blocks. Area B, where the vegetation coverage change is significant, is the dominant deformation area. The State Key Laboratory of Geohazard Prevention and Geoenvironment Protection (2018) (**Figure 6**) also found that the landslide slid intermittently in blocks and grades since 2011 (http://www.sklgp.cdut.edu.cn/info/1018/2247.htm). Liu et al. (2020) found that the cumulative deformations of area B in the satellite line of sight direction and the azimuth direction reached −60.2 and 12.6 m, respectively. Xiong et al. (2020) found that area B has the maximum average displacement velocity, and its largest horizontal deformation rate exceeds 5.8 m/yr. The sliding speed became faster after January 15, 2017. It shows that the result of this study is consistent with other studies. The change of vegetation coverage can be used to identify potential landslides in the area with dense vegetation.

Common Vegetation Change in the Landslide Area

The phenomenons of vegetation change before landslides are common in the mountainous area of southwest China, such as the Xinmo village landslide. The Xinmo village landslide is a ridge-top landslide on June 24, 2017 in Maoxian county, Sichuan Province (Yin et al., 2017). This area has dense vegetation coverage and may be affected by the Diexi earthquake in 1933, the Pingwu-Songpan earthquake in 1976, and the Wenchuan earthquake in 2008. A previous study found that the vegetation change also exited before the Xinmo village landslide (Guo et al., 2020).

In the previous study, the inherent relationship between the vegetation change and the creep of the Xinmo village landslide was detected by high-resolution optical remote sensing images. In the upper landslide area, the vegetation coverage affected by the creep of landslide declined from 2014 to 2016. With the distance from the bare land edge of Xinmo village landslide increasing, the smaller the effect of landslide creep is, the better the status of vegetation gradually becomes. As time goes on, the more significant the impact of landslide creep is, the worse the vegetation becomes. In the middle potential impact area, the vegetation coverage around the springs and gullies declines with the more significant effect of landslide creep as the landslide time approaches. The vegetation change of the upper landslide area and the middle potential impact area has an evident spatio-temporal correlation with the landslide creep.

It proves that the phenomenon of vegetation change in the landslide creep stage is universal and can be detected by high-resolution optical remote sensing images. For potential landslides in large-scale earthquake-affected areas, this monitoring method is robust and can be used for preliminary investigations. Then it can combine with visual interpretation, SAR, and other techniques for further confirmation in the key areas.

Application Conditions and Potential

The method is mainly used in large-scale surveys after earthquakes, especially in poor accessible high-mountain areas. The field investigation and GPS data may not be effectively used in poorly accessible areas, and even SAR data cannot be obtained in these areas with dense vegetation. It monitors landslide-prone areas economically and effectively in the long-term natural evolution, which applies to the case without significant environmental change, such as no earthquake event or no rare heavy rain event. This method will be used in a large range and at a low cost as a valuable supplement to the GPS and SAR. If there are earthquakes and rare heavy rain in natural evolution or this is a key area, we will consider combining it with GPS, SAR, and other methods. The fusion technology of optical remote sensing images and SAR images can be used to improve the method.

In the future, Sentinel-2A/B remote sensing images widely used in the study of landslides (Guo et al., 2021) can also be used as a new data source. It has the advantages of free access, short revisit cycle, high spatial resolution, and red edge band, which usually be used to monitor vegetation. Sentinel-2A/B remote sensing images have great potential for the application of this method. Moreover, this method can detect changes over time-series images in a larger range and a longer time, combined with the machine learning method.

CONCLUSION

This study can validate the indicative effect of vegetation change in the landslide creep stage. The changes in environmental conditions caused by the creep of landslides impact the vegetation growth, which can be identified by the optical image fusion of multi-temporal remote sensing data. The change of vegetation coverage can reflect the landslide creep.

The vegetation coverage in the back scarp area and the main sliding area of the Baige landslide significantly decreased compared to that in the normal area. The extent of vegetation coverage reduction can reflect the degree of creep, and the reduced area can show the outline of the potential landslide area. The vegetation change has an evident spatio-temporal correlation with the landslide creep in the Baige landslide.

This study can provide a new light to monitor potential landslides in high-mountain regions after the earthquake. For potential landslides in large-scale high-mountain areas, this method can be used to preliminary investigations economically and effectively. Then for the key areas, it can combine with visual interpretation, SAR, and other techniques for further confirmation.

DATA AVAILABILITY STATEMENT

The original contributions presented in the study are included in the article/Supplementary Material, further inquiries can be directed to the corresponding author.

AUTHOR CONTRIBUTIONS

XG and QG designed this study; XG analyzed the data, and wrote the manuscript; QG and ZF polished the paper. All authors approved the final version of the manuscript.

FUNDING

This research was funded by the National Natural Science Foundation of China (grant number 61771470) and the Strategic Priority Research Program of the Chinese Academy of Sciences (grant number XDA19010401).

ACKNOWLEDGMENTS

The authors are grateful for the helpful discussion with Weiheng Zhang of the Institute of Geology, China Earthquake Administration. We would like to thank the editor and reviewers for their valuable input, time, and suggestions to improve the quality of the manuscript.

REFERENCES

Ambraseys, N. N., and Douglas, J. (2004). Magnitude calibration of north Indian earthquakes. *Geophys. J. Int.* 159, 165–206. doi:10.1111/j.1365-246X.2004.02323.x

An, H., Ouyang, C., and Zhou, S. (2021). Dynamic process analysis of the Baige landslide by the combination of DEM and long-period seismic waves. *Landslides* 18 (3), 1625–1639. doi:10.1007/s10346-020-01595-0

Bianchini, S., Raspini, F., Solari, L., Del Soldato, M., Ciampalini, A., Rosi, A., et al. (2018). From Picture to Movie: Twenty Years of Ground Deformation Recording over Tuscany Region (Italy) with Satellite InSAR. *Front. Earth Sci.* 6, 177. doi:10.3389/feart.2018.00177

Binet, R., and Bollinger, L. (2005). Horizontal coseismic deformation of the 2003 Bam (Iran) earthquake measured from SPOT-5 THR satellite imagery. *Geophys. Res. Lett.* 32 (L02307), 1–4. doi:10.1029/2004gl021897

Chen, J., Chen, Y. H., He, C. Y., and Shi, P. J. (2001). Sub-pixel model from vegetation fraction estimation based on land cover classification. *J. Remote Sensing* 5 (6), 416–422.

Clayton, D. G. (1971). Gram-Schmidt orthogonalization. *Appl. Stat.* 20 (3), 355–338. doi:10.2307/2346771

Ding, C., Feng, G., Liao, M., Tao, P., Zhang, L., and Xu, Q. (2021). Displacement history and potential triggering factors of Baige landslides, china revealed by optical imagery time series. *Remote Sensing Environ.* 254, 112253. doi:10.1016/j.rse.2020.112253

Ding, Y. L., Lei, S. G., Bian, Z. F., and Qie, C. L. (2013). Distortion-resistant ability of Tetraena mongolica root at the mining subsidence area. *J. China Univ. Mining Tech.* 42, 970–974+981. doi:10.13247/j.cnki.jcumt.2013.06.014

Dominguez, S., Avouac, J. P., and Michel, R. (2003). Horizontal coseismic deformation of the 1999 Chi-Chi earthquake measured from SPOT satellite images: Implications for the seismic cycle along the western foothills of central Taiwan. *J. Geophys. Res.* 108 (B2), 1–19. doi:10.1029/2001JB000951

Du, T., Bi, Y. L., Zou, H., Zheng, J. L., and Liu, S. (2013). Effects of surface cracks caused by coal mining on microorganisms and enzyme activities in rhizosphere of Salix psammophila. *J. China Coal Soc.* 38 (12), 2221–2226. doi:10.13225/j.cnki.jccs.2013.12.0016

Fan, Q. S., Tang, C. L., Chen, Y., and Zhang, X. D. (2006). Applications of GPS and InSAR in monitoring of landslide studies. *Surv. Mapp. Sci.* 031 (5), 60–62. doi:10.3771/j.issn.1009-2307.2006.05.019

Fan, X., Xu, Q., Alonso-Rodriguez, A., Subramanian, S. S., Li, W., Zheng, G., et al. (2019). Successive landsliding and damming of the Jinsha River in eastern Tibet, China: prime investigation, early warning, and emergency response. *Landslides* 16, 1003–1020. doi:10.1007/s10346-019-01159-x

Fan, X., Yang, F., Siva Subramanian, S., Xu, Q., Feng, Z., Mavrouli, O., et al. (2020). Prediction of a multi-hazard chain by an integrated numerical simulation approach: the Baige landslide, Jinsha River, China. *Landslides* 17 (1), 147–164. doi:10.1007/s10346-019-01313-5

Guo, X., Fu, B., Du, J., Shi, P., Li, J., Li, Z., et al. (2021). Monitoring and Assessment for the Susceptibility of Landslide Changes after the 2017 Ms 7.0 Jiuzhaigou Earthquake Using the Remote Sensing Technology. *Front. Earth Sci.* 9, 633117. doi:10.3389/feart.2021.633117

Guo, X. Y., Guo, Q., and Feng, Z. K. (2020). Relationship between landslide creep and vegetation anomalies in remote sensing images. *J. Remote Sensing* 24 (6), 776–786. doi:10.11834/jrs.20208330

Jia, H., Wang, Y., Ge, D., Deng, Y., and Wang, R. (2020). Improved offset tracking for predisaster deformation monitoring of the 2018 Jinsha River landslide (Tibet, China). *Remote Sensing Environ.* 247, 111899. doi:10.1016/j.rse.2020.111899

Khattak, G. A., Owen, L. A., Kamp, U., and Harp, E. L. (2010). Evolution of earthquake-triggered landslides in the Kashmir Himalaya, northern Pakistan. *Geomorphology* 115 (1-2), 102–108. doi:10.1016/j.geomorph.2009.09.035

Leprieur, C., Verstraete, M. M., and Pinty, B. (1994). Evaluation of the performance of various vegetation indices to retrieve vegetation cover from AVHRR data. *Remote Sensing Rev.* 10 (10), 265–284. doi:10.1080/02757259409532250

Li, K., Sun, Y. D., Jiang, B. H., Guo, J. J., Wang, Y. Q., and Yue, D. X. (2014). Analysis on spatial-temporal patterns of the vegetation coverage and landslides in Bailongjiang River Basin based on the Dimidiate Pixel Model. *J. Lanzhou Univ. (Natural Sciences)* 50 (3), 376–382. doi:10.13885/j.issn.0455-2059.2014.03.013

Li, M. M. (2003). *The Method of Vegetation Fraction Estimation by Remote Sensing.* [Beijing: Institute of Remote Sensing Applications, Chinese Academy of Sciences. [M.D. thesis].

Liu, X., Zhao, C., Zhang, Q., Lu, Z., and Li, Z. (2020). Deformation of the Baige Landslide, Tibet, China, Revealed through the Integration of Cross-Platform ALOS/PALSAR-1 and ALOS/PALSAR-2 SAR Observations. *Geophys. Res. Lett.* 47 (3), 1–8. doi:10.1029/2019GL086142

María, G. A., José, L. S., Catalan, R. G., and García, R. (2004). Fusion of multispectral and panchromatic images using improved IHS and PCA mergers based on wavelet decomposition. *IEEE Trans. Geosci. Remote Sensing.* 42 (6), 1291–1299. doi:10.1109/TGRS.2004.825593

Michel, R., and Avouac, J. P. (2002). Deformation due to the 17 August 1999 Izmit, Turkey, earthquake measured from SPOT images. *J. Geophys. Res.* 107 (B4), ETG 2-1–ETG 2-6. doi:10.1029/2000JB000102

Ouyang, C., An, H., Zhou, S., Wang, Z., Su, P., Wang, D., et al. (2019). Insights from the failure and dynamic characteristics of two sequential landslides at Baige village along the Jinsha River, China. *Landslides* 16, 1397–1414. doi:10.1007/s10346-019-01177-9

Ranchin, T., and Wald, L. (2000). Fusion of high spatial and spectral resolution images: The ARSIS concept and its implementation. *Photogrammetric Eng. Remote Sensing* 66, 49–61. doi:10.1002/2014WR016042

SSB (1995). *Chinese historical catalog from 2300 B.C to 1911 A*. Beijing, China: D. Seismological Press.

State Key Laboratory of Geohazard Prevention and Geoenvironment Protection (2018). "Continuous release: Since 2011, the maximum downslope displacement of the Baige landslide area in Jinsha River is close to 50 meters," in *State Key Laboratory of Geohazard Prevention and Geoenvironment Protection Physics Web*. http://www.sklgp.cdut.edu.cn/info/1018/2247.htm (Accessed on October 17, 2018).

Sun, W., Chen, B., and Messinger, D. W. (2014). Nearest-neighbor diffusion-based pan-sharpening algorithm for spectral images. *Opt. Eng.* 53 (1), 013107. doi:10.1117/1.oe.53.1.013107

Wang, G. (2011). GPS Landslide Monitoring: Single Base vs. Network Solutions - A case study based on the Puerto Rico and Virgin Islands Permanent GPS Network. *J. Geodetic Sci.* 1 (3), 191–203. doi:10.2478/v10156-010-0022-3

Wang, G. J., Xie, M. W., Qiu, C., and Jiangqi, Z. L. (2010). Application of D-InSAR technology in large-scale landslide monitoring. *Geotechnical Mech.* 4, 333–340. doi:10.16285/j.rsm.2010.04.010

Wang, L. C., Wen, M. S., Feng, Z., Sun, W. F., Wei, Y. J., Li, J. F., et al. (2019). Researches on the Baige landslide at Jinshajiang River, Tibet, China. *Chin. J. Geol. Hazard Control.* 30 (01), 1–9. doi:10.16031/j.cnki.issn.1003-8035.2019.01.01

Xiong, Z. Q., Feng, G. C., Feng, Z. X., Miao, L., Wang, Y. D., Yang, D. J., et al. (2020). Pre- and post-failure spatial-temporal deformation pattern of the Baige landslide retrieved from multiple radar and optical satellite images. *Eng. Geo.* 279, 105580. doi:10.1016/j.enggeo.2020.105880

Xu, Q., Li, W. L., Dong, X. J., Xiao, X. X., Fan, X. M., and Pei, X. J. (2017). The Xinmocun landslide on 24 June , 2017 in Maoxian, Sichuan: characteristics and failure mechanism. *Chin. J. Rock Mech. Eng.* 36 (11), 2612–2628. doi:10.13722/j.cnki.jrme.2017.0855

Yang, Z., Li, Z., Zhu, J., Preusse, A., Yi, H., Hu, J., et al. (2017). Retrieving 3-d large displacements of mining areas from a single amplitude pair of SAR using offset tracking. *Remote Sensing* 9 (4), 338. doi:10.3390/rs9040338

Yin, Y. P., Wang, W. P., Zhang, N., Yan, J. K., Wei, Y. J., and Yang, L. W. (2017). Long runout geological disaster initiated by the ridge-top rockslide in a strong earthquake area: A case study of the Xinmo landslide in Maoxian County, Sichuan Province. *Geology China* 44 (5), 827–841.

Zhang, Y., Guo, C., Qu, Y., and Song, Y. (2011). Engineering geological properties of altered rocks and implications for railway construction in the Sanjiang orogenic belt, Southwest China. *Bull. Eng. Geol. Environ.* 70 (1), 143–152. doi:10.1007/s10064-010-0294-y

Zhang, Y., and Mishra, R. K. (2012). A review and comparison of commercially available pan-sharpening techniques for high resolution satellite image fusion. *Geosci. Remote Sensing Symp. (Igarss) 2012 IEEE Int.*, 182–185. doi:10.1109/IGARSS.2012.63516072012

Zhang, Y. S., Ba, R. J., Ren, S. S., and Li, Z. L. (2020). An analysis of geo-mechanism of the Baige landslide in Jinsha River, Tibet. *Geology China* 47 (6), 1637–1645. doi:10.12029/gc20200603

Zhao, Y. S. (2013). "Geology remote sensing," in *Principles and methods of Remote sensing application*. 2nd. (Beijing: Science Press), Vol. 16, 487–488.

Zhong, Z., Chen, N. S., Ni, H. Y., Liu, E. L., and Han, Z. (2021). Engineering Geology and Hydrogeological Characteristics of Jinsha River in Baige Landslide. *Sci. Tech. Eng.* 21 (13), 5262–5269.

Zribi, M., Le Hégarat-Mascle, S., Taconet, O., Ciarletti, V., Vidal-Madjar, D., and Boussema, M. R. (2003). Derivation of wild vegetation cover density in semi-arid regions: ERS2/SAR evaluation. *Int. J. Remote Sensing* 24 (6), 1335–1352. doi:10.1080/01431160210146668

Conflict of Interest: The authors declare that the research was conducted in the absence of any commercial or financial relationships that could be construed as a potential conflict of interest.

Advantages of publishing in Frontiers

OPEN ACCESS
Articles are free to read
for greatest visibility
and readership

FAST PUBLICATION
Around 90 days
from submission
to decision

HIGH QUALITY PEER-REVIEW
Rigorous, collaborative,
and constructive
peer-review

TRANSPARENT PEER-REVIEW
Editors and reviewers
acknowledged by name
on published articles

Frontiers
Avenue du Tribunal-Fédéral 34
1005 Lausanne | Switzerland

Visit us: www.frontiersin.org
Contact us: frontiersin.org/about/contact

REPRODUCIBILITY OF RESEARCH
Support open data
and methods to enhance
research reproducibility

DIGITAL PUBLISHING
Articles designed
for optimal readership
across devices

FOLLOW US
@frontiersin

IMPACT METRICS
Advanced article metrics
track visibility across
digital media

EXTENSIVE PROMOTION
Marketing
and promotion
of impactful research

LOOP RESEARCH NETWORK
Our network
increases your
article's readership